UNIVERSITÀ DEGLI STUDI FIRENZE

DOTTORATO DI RICERCA
INTERNATIONAL DOCTORATE IN STRUCTURAL BIOLOGY

CICLO XXXVI

COORDINATOR Prof. Lucia Banci

NMR relaxation of paramagnetic systems and biomolecules

Settore Scientifico Disciplinare CHIM/03

PhD student
Dott. Giulia Licciardi

Tutor
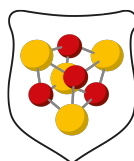Prof. Giacomo Parigi

Coordinator
Prof. Lucia Banci

November 2020 – October 2023

This thesis has been approved by the University of Florence, the University of Frankfurt and the Utrecht University

Universiteit Utrecht

All the positive things I was, am, and will be is thanks to you, Mum.
I will forever be grateful
I hope you knew
I hope I made you proud

Abstract

Nuclear Magnetic Resonance (NMR) stands as one of the most powerful techniques for offering key information on a wide variety of systems, ranging from small molecules to materials and biologically relevant macromolecules. To no surprise, it has a pivotal role in structural biology as well as in applications related to food and health sciences.

Among NMR-based methods, relaxometry emerges as the main option to explore multiscale dynamics. Fast Field Cycling (FFC) relaxometry, which exploits a wide magnetic field range from a few kHz to MHz (proton Larmor frequency), makes it possible to investigate molecular dynamics across timescales from picoseconds to microseconds. In typical situations, FFC relaxometry allows for the measurement of the longitudinal relaxation time of all protons within the sample under investigation, however the field inhomogeneity and the low detection field intrinsically limit the resolution.

At the end of the last century, to address the limitations of FFC relaxometry, Bryant and Redfield pioneered the cycling between high and low fields in commercial high-field spectrometers. Subsequent applications of the so called High Resolution Relaxometry (HRR) proved successful, allowing for high-resolution measurements of nuclear relaxation at variable fields. Recently, two prototypes carrying a new technology for HRR, called Fast Shuttle System (FSS), have been installed at ENS in Paris and at CERM in Florence. Thanks to the high-field detection, this cutting-edge shuttle system enables to perform high-resolution relaxometry measurements with resolution. The technology harnesses the stray field of a high field spectrometer as a variable relaxation field, giving a whole new flavor to relaxation measurements.

This doctoral thesis includes several projects in which I have been engaged. My primary focus has been on applying FFC relaxometry across diverse systems and objectives. Specific examples are outlined here, notably showing how relaxometry has been exploited to evaluate possible therapeutic and contrast agents (CAs) for Magnetic Resonance Imaging (MRI), to assess the supramolecular organization of a viscous diamagnetic system and to charac-

terize the multiscale dynamics of biologically relevant proteins. More recently, I had the privilege to work on both FSS prototypes, not only in terms of technique validation but also for employing them to investigate protein-ligand interactions and dynamics in a complex liquid system.

Keywords

Nuclear Magnetic Resonance · Low Field NMR · Relaxometry · Fast Field Cycling relaxometry · High Resolution Relaxometry · Contrast Agents · Magnetic Resonance Imaging · Biomolecules · Protein Cages · Paramagnetic proteins · Olive Oil · Blueberry Juice · L-AsparaginaseII · Human Transthyretin · Matrix Metalloproteinase-12

Abbreviations

Nuclear Magnetic Resonance, NMR · Fast Field Cycling, FFC · High Resolution Relaxometry, HRR · Fast Shuttle System, FSS · Field Cycling, FC · Zero-Field Splitting, ZFS · Contrast Agent, CA · Magnetic Resonance Imaging, MRI · Nuclear Magnetic Relaxation Dispersion, NMRD · Molecular weight · L-AsparaginaseII, ANSII · Human Transthyretin, TTR · Matrix Metalloproteinase-12, MMP12 · Wild Type, WT · Inductively Coupled Plasma-Atomic Emission Spectroscopy, ICP-AES · Mass Spectrometry, MS · Electron Paramagnetic Resonance, EPR · Free Induction Decay, FID · Ultrafast High Resolution Relaxometry, UHRR · Magnetic Tunnel, MT · Zero Field Coil, ZFC

6

Contents

Chapter 1

Introduction

Properties of matter are dictated not only by the atomic structure but also by its multiscale dynamics, which covers many orders of magnitude of length- and timescales. The study of the structure and the dynamics at the atomic scale is performed by spectroscopic methods, especially nuclear magnetic resonance (NMR), time-resolved crystallography and mass spectrometry (MS). These analytical techniques are invaluable tools for the understanding of the function of biologically and chemically interesting systems and their properties. Along with others techniques, like UV-visible spectroscopy, electron paramagnetic resonance (EPR), and infrared spectroscopy, high field NMR, crystallography and MS play a fundamental role in the fields of chemistry, biochemistry, and structural biology, as they allow to probe the atomic and molecular details of various systems, helping to advance our understanding of chemistry, biology, and materials science. Yet, these techniques, as well as any others, fail at bridging atomic-resolution and multiscale dynamics at long timescales.

1.1   Nuclear relaxation

The concept of "relaxation time" was introduced by Bloch in his famous equations describing the time evolution of nuclear magnetization in a magnetic field in 1946 [1]. Bloch's equations assume the magnetization component along an external magnetic field (the longitudinal magnetization) to relax exponentially to its equilibrium value, according to the Boltzmann distribution. The process by which the nuclear magnetization of a nucleus in a magnetic field returns to the thermal equilibrium state, after being perturbed (typically by the application of radiofrequency pulses in NMR experiments) is referred to as nuclear spin relaxation. This process is driven by fluctuations in the interactions of

the nuclear spins that can involve various processes, including energy exchange
with nearby nuclei, which induce spin transitions [2, 3].

The microscopic theory for nuclear spin relaxation was developed by Bloem-
bergen, Purcell, and Pound (BPP) shortly after Bloch's work [4]. They related
the relaxation rates to the transition probabilities between nuclear spin energy
levels. More specifically, they considered interactions like the dipole-dipole in-
teraction between nuclear spins and how random motions in a liquid modulate
these interactions. Since the main mechanism causing ^{1}H relaxation in solution
is the modulation of the dipole-dipole interaction between neighboring protons
due to molecular motions, the BPP theory laid the foundation for much of the
subsequent theoretical work in the field of NMR.

There are two main spin relaxation processes and corresponding relaxation
times: longitudinal or spin-lattice relaxation, denoted as T_1 or R_1 relaxation,
and transverse or spin-spin relaxation, denoted as T_2 or R_2 relaxation, where
R_1 and R_2 are the rate constants resulting from the reciprocal of the relaxation
times. Spin-lattice relaxation characterizes the relaxation of the longitudinal
magnetization component, which is the component of nuclear magnetization
aligned with the external magnetic field, and is the one connected with the
movement of spin populations back to their Boltzmann distribution values.
The spin-spin relaxation characterizes the relaxation of the transverse mag-
netization component, which is the component of nuclear magnetization per-
pendicular to the external magnetic field, and it involves the coherences of the
spins. These relaxation times play a crucial role in understanding the behav-
ior of nuclear spins in a magnetic field, characterize the NMR signals intensity
and line width, and therefore are important for the interpretation of NMR
spectra. As the relaxation times modulating the relaxation process can vary
depending on the specific nuclear species, the local chemical environment, and
the conditions of the experiment (temperature, solvent viscosity, presence of
paramagnetic species, etc), their determination is essential to gain insights into
the molecular dynamics, structure, and interactions in various systems.
In this thesis, we will be mainly focused on the longitudinal relaxation process.

1.1.1   The Solomon Theory

The mathematical theory for nuclear spin relaxation underlying dipole-dipole
interactions developed by Bloembergen, Purcell, and Pound was then gener-
alized by Solomon in the 1950s and extended by Bloembergen and Morgan to

give a more complete expression for relaxation in paramagnetic solutions in 1961. Together this body of work is referred to as the Solomon-Bloembergen-Morgan (SBM) theory of relaxation.

Solomon provided a set of modified Bloch's equations of motion, taking into account the perturbations among like and unlike coupled spins, for both T_1 and T_2 relaxation [5].
We will focus here on the case of a diamagnetic dipole-dipole coupled like spins system, such as two protons interacting with each other. Solomon's equation for longitudinal relaxation rate for the nuclear spin I can be written as:

$$
\begin{aligned}
R_1^{DD} = {} & \frac{1}{10}\Big(\frac{\mu_0}{4\pi}\frac{\hbar\gamma_I^2}{r^3}\Big)^2 I(I+1)\big[J(\omega_I) + 4J(2\omega_I)\big] = \\
& \frac{2}{5}\Big(\frac{\mu_0}{4\pi}\frac{\hbar\gamma_I^2}{r^3}\Big)^2 I(I+1)\Big(\frac{\tau_c}{1+\omega_I^2\tau_c^2} + \frac{4\tau_c}{1+4\omega_I^2\tau_c^2}\Big)
\end{aligned}
\tag{1.1}
$$

where μ_0 is the permeability in vacuum, γ_I is the nuclear magnetogyric ratio, r is the proton-proton distance, ω_I is the angular frequency and can be written as $-\gamma_I B_0$, with B_0 as the external magnetic field.
In this equation, and in the following, the function $J(\omega)$, called spectral density function, and τ_c, the correlation time, are present; their concepts will be addressed in *Section 1.1.3*.

In the case of unlike spins, and we will consider a particular case of interest, i. e. the case of an electron spin, S, interacting with the nuclear spin, Solomon's equation can be written as:

$$
R_1 = \frac{2}{15}\Big(\frac{\mu_0}{4\pi}\Big)^2 \frac{\hbar^2\gamma_I^2\gamma_S^2}{r^6} S(S+1)\Big(\frac{3\tau_c}{1+\omega_I^2\tau_c^2} + \frac{\tau_c}{1+(\omega_I-\omega_S)^2\tau_c^2} + \frac{6\tau_c}{1+(\omega_I+\omega_S)^2\tau_c^2}\Big)
\tag{1.2}
$$

where γ_S is the nuclear magnetogyric ratio of the electron and the spectral density functions refer to the single, zero, and double quantum transitions.

1.1.2 SBM theory and contrast agents for MRI

As anticipated in *Section 1.1.1*, the general theory of solvent nuclear relaxation in the presence of paramagnetic substances (chemical compounds with unpaired electrons) was developed by Solomon, Bloembergen, and Morgan's groups [4, 5, 6, 7, 8].
SBM theory is applied to the relaxation processes of nuclear spins that are in

close proximity to an electron spin, as in the case of contrast agents (CAs) solutions, employed in magnetic resonance imaging for their ability to increase nuclear relaxation rates of water protons, thus increasing contrast and improving image quality. In this thesis, potential CAs (typically containing transition metal ions and lanthanides, such as gadolinium) are studied, and the obtained results are interpreted through the SBM theory, as reported in the following equations.

Longitudinal relaxation rate in diluted solutions of paramagnetic systems, R_{1para} in 1.3, can be considered as the sum of the relaxation caused by the presence of the paramagnetic species (here indicated as CA), and the diamagnetic contribution, as the relaxation rate in the absence of the paramagnetic species:

$$R_{1para} = [CA]r_1 + R_{1dia} \qquad (1.3)$$

where r_1 indicates the longitudinal relaxivity of the paramagnetic complex. Relaxivity is defined as the paramagnetic enhancement of the water proton relaxation rates in the presence of 1 mM concentration of the paramagnetic complex. Relaxivity is how the effectiveness of a paramagnetic complex as a T_1 contrast agent is usually described. The total paramagnetic enhancement on the solvent proton relaxation rate can be expressed as in 1.4, where, respectively, the two term report: 1) on the inner sphere relaxivity, which depends on the chemical exchanging solvent molecules coordinated, at a fixed distance (r, see *Equation 1.5*), to the paramagnetic metal or nearby; and 2) on the outer sphere relaxivity (see *Equation 1.6*), due to random translational diffusion of the solvent around the paramagnetic metal:

$$r_1 = \frac{[CA]q}{55.6} \frac{1}{T_{1M} + \tau_M} + r_{1OS} \qquad (1.4)$$

In the first term: the concentration of the contrast agent containing the paramagnetic ion is expressed in mM units, q indicates the number of water molecules coordinating the paramagnetic center, T_{1M} is the longitudinal proton relaxation rate in the bound water and τ_M is the exchange correlation time (or lifetime of first and second sphere water molecules of the complex). The second term, r_{1OS}, is the outer sphere relaxivity.

From the SBM model we have that the relaxation of the bound water is gov-

erned by the dipole-dipole and the scalar or contact interactions:

$$
\begin{aligned}
\frac{1}{T_{1M}} = \frac{2}{15}\left(\frac{\mu_0}{4\pi}\right)^2 \frac{\gamma_I^2 g_e^2 \mu_B^2 S(S+1)}{r^6} \left[\frac{7\tau_c}{1+\omega_S^2\tau_c^2} + \frac{3\tau_c}{1+\omega_I^2\tau_c^2}\right] \\
+ \frac{2}{3}S(S+1)\left(\frac{A_C}{\hbar}\right)^2 \frac{\tau_{con}}{1+\omega_S^2\tau_{con}}
\end{aligned}
\tag{1.5}
$$

where the γ_S is given by $-\frac{g_e\mu_B}{\hbar}$, with g_e as the electron g-factor and μ_B as the Bohr magneton. The first term is the Solomon's relaxation for two unlike spins interacting, where we considered $\omega_S \ll \omega_I$, and the second term takes into account the contact contribution (usually negligible in lanthanoids due to the absence of sizable unpaired electron delocalization and spin polarization on the water protons). $\frac{A_C}{\hbar}$ is the hyperfine or contact coupling constant between the electron of the paramagnetic center and the proton of the coordinated water, while $\tau_{con}^{-1} = \tau_M^{-1} + \tau_e^{-1}$, where τ_e is the electronic relaxation correlation time.

The outer sphere contribution is

$$
r_{1OS} = \frac{32}{405}\pi\left(\frac{\mu_0}{4\pi}\right)^2 \frac{N_A\gamma_H^2 g_e^2 \mu_B^2 S(S+1)}{d(D_{metal}+D_{ligand})}\left[7J^{tr}(\omega_S) + 3J^{tr}(\omega_I)\right]
\tag{1.6}
$$

where N_A is Avogadro's constant, d is the distance of closest approach between the paramagnetic ion and the water protons (the shortest possible distance between the two species), D_{metal} and D_{ligand} are, respectively, the diffusion coefficients of paramagnetic complexes and water molecules, and

$$
\begin{aligned}
J^{tr}(\omega) &= \frac{1+5z/8+z^2/8}{1+z+z^2/2+z^3/64z^4/81+z^5/81+z^6/648} \\
z &= \sqrt{2\left(\omega\tau_D + \frac{\tau_D}{\tau_e}\right)} \\
\tau_D &= \frac{d^2}{D}
\end{aligned}
\tag{1.7}
$$

where τ_D, the diffusional correlation time and D is the diffusion coefficients of the solvent molecules. The collisions between solute and solvent molecules may induce instantaneous distortions of the metal coordination polyhedron, producing a transient zero-field splitting (ZFS). Therefore, the electronic relaxation correlation time, τ_e, depends on the mean squared fluctuations of the transient ZFS, Δ_t^2, the correlation time for the modulation of the transient

ZFS interaction, τ_v, and the field:

$$\tau_e^{-1} = \frac{1}{25}\Delta_t^2\tau_v\big[4S(S+1)-3\big]\left(\frac{1}{1+\omega_S^2\tau_v^2}+\frac{4}{1+4\omega_S^2\tau_v^2}\right) \qquad (1.8)$$

The necessary considerations about correlation times modulating the relaxation process in paramagnetic systems will be discussed in the dedicated *Paragraph*, *"Correlation time in paramagnetic systems"*, in the following *Section 1.1.3*.

1.1.3   Spectral Density Function and Correlation Time

As mentioned above, spin transitions occur due to the presence of time-dependent interactions and, even in the case of a system in its equilibrium state, information about the occurring dynamic processes can be obtained from the correlation function. The energy of the spin transitions occurring in the system changes stochastically in time, however the energy value at a given time is in general not independent from the value at a previous time. For a short time interval (compared to the timescale of the considered processes) a correlation between two energy values is expected. Considering the perturbation as a stationary (independent of the absolute time) process, the correlation function is assumed to decay exponentially

$$C(t) = \sum_i E(t)E(t+\tau) = \sum_i E(0)E(\tau) \cong \langle E(0)^2\rangle exp(-|\tau|/\tau_c) \qquad (1.9)$$

The Fourier transform of the exponential decay in the time domain is the spectral density function, $J(\omega)$, and has the form of a Lorentzian function in the frequency domain:

$$J(\omega) = \frac{\tau_c}{1+\omega^2\tau_c{}^2} \qquad (1.10)$$

where τ_c is the time constant for which the correlation function exponentially decays to zero, and it is called correlation time. The position of the dispersion is due to the value of the correlation time.
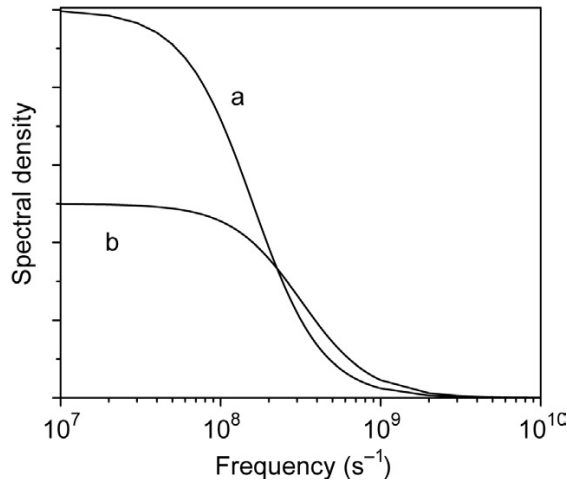
Figure 1.1: Plot of the spectral density function $J(\omega)$ in logarithmic scale. The profile a is obtained for a $\tau_c = 1 \cdot 10^{-9} s$, while the profile b is obtained for a $\tau_c = 5 \cdot 10^{-10} s$. The inflection points occurs at $\omega \tau_c = 1$ [9].

Reorientational correlation time

In the SBM model, the two spins system is assumed to be rigidly held within a molecule isotropically rotating in solution. In that case, the rotational correlation time, τ_r can be calculated, using the Stokes-Einstein equation [10], as follows:

$$\tau_r = \frac{4\pi\eta a^3}{3kT} \tag{1.11}$$

with η is the solvent viscosity, a is the radius of the molecule considered as a sphere, k is the Boltzmann constant and T is the absolute temperature.

Within this model, if a diamagnetic system is considered, and if the proton exchange rates are slower than reorientation, the correlation time of the spectral density function is the molecular reorientational correlation time, and the position of the dispersion is due to the τ_r value.

Local reorientational correlation time

If the molecule cannot be approximated as a rigid sphere, in both cases of isotropic and anisotropic overall motion, information on fast internal motions can be extracted from relaxation experiments. A general treatment for the presence of internal motions, faster than the global reorientation correlation time, is introduced through the Lipari-Szabo model-free approach [11], as shown in *Equation* 1.12:

$$R_1{}^{\text{LS}} = S^2 \langle E^2 \rangle J(\omega, \tau_r) + (1 - S^2) \langle E^2 \rangle J(\omega, \tau_f) \tag{1.12}$$

Two model-independent quantities are introduced: the correlation time for the faster local motions, indicated as τ_f, and the order parameter, S, which reports on the degree of spatial restriction of the motion. When no local motion has to be considered, and therefore only one correlation time is needed, $S^2 = 1$; in the case of completely isotropic internal motion, $S^2 = 0$.
In many cases reported in this thesis, the presence of local reorientation motions had to be taken into account.

Correlation time in paramagnetic systems

Relaxation processes occurring in paramagnetic solutions will be also considered. In these cases, the correlation times can be determined by all the processes that influence nuclear relaxation in the presence of unpaired electrons, i. e. electron spin relaxation, molecular rotation, and chemical exchange of the metal-coordinated solvent molecule(s). The reciprocal of the overall correlation time for dipolar coupling can be written as a sum of the reciprocal of each of the already mentioned correlation times:

$$\tau_c^{-1} = \tau_e^{-1} + \tau_r^{-1} + \tau_M^{-1} \tag{1.13}$$

where τ_e is the electronic relaxation correlation time, τ_r is rotational correlation time, and τ_M is the exchange correlation time. Each one of them can have a role in the modulation of the dipolar coupling energy. It usually happens that one dominates on the others.

In *Figure 1.2* the parameters that mainly contribute to the bulk water protons relaxivity are shown (see *Equations 1.5* and *1.6*). The reorientational correlation time, τ_r, modulating the overall reorientation of the molecule; the electron relaxation time, τ_e, i. e. of one gadolinium(III) ion. The exchange correlation time has different contribution depending on the distance of the water molecule involved in the exchange process: in black, the first sphere coordinated water molecule at the closest distance, r, and exchange correlation time, τ_M, is represented; in green, water molecules in the second coordination sphere, at a longer distances, r' and r'', with exchange correlation time, τ_M' and τ_M'', and τ_D, the diffusional correlation time; the distances of water molecules in the first (closest, distance r) and second coordination spheres.
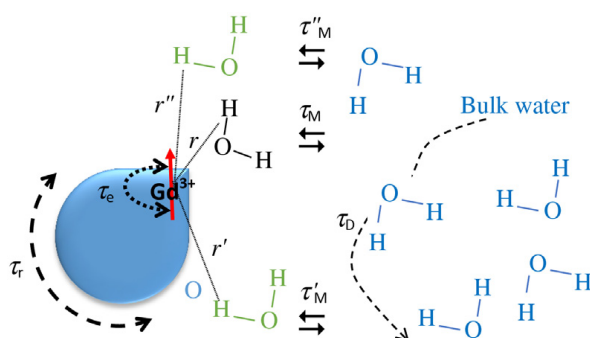
Figure 1.2: Summary of all the contribution to bulk water protons relaxivity divided in inner-sphere contribution (green) and outer-sphere contribution (blue) [9].

The nuclear magnetic relaxation dispersions

The plot representing the field dependence of the longitudinal spin relaxation rate is called the nuclear magnetic relaxation dispersion (NMRD) profile. The ^{1}H NMRD profiles reflect the superposition of multiple spectral density functions, $J(\omega)$, associated with different characteristic motional correlation times. In other words, since $J(\omega)$ depends on the time constant of the fluctuations of the nuclear spins interactions, the analysis of the NMRD profiles give direct access to the intra- and intermolecular dynamic parameters that drive magnetic relaxation. Graphic examples of NMRD profiles are shown in *Chapter 2, Figure 2.2*.

1.2 From Field Cycling to High Resolution Relaxometry

Field-cycling relaxometry is a NMR technique that exploits the systematic variation of the strength of the applied magnetic field (over a range spanning from a few kilohertz to megahertz) during an experiment to study how nuclear relaxation rates change with different field strengths. It therefore allows to obtain the NMRD profile of the system under investigation, thus providing access to the spectral density function. For this reason, field cycling techniques are exceptionally suited for studying motions and dynamical properties of molecules in different environments, such as liquids, solids, or biological systems, across a very broad range of timescales (from ps to μs). These techniques are unmatched in revealing information on slow molecular dynamics which can

only be explored at very low magnetic fields.

Since the very beginning of its development in the 1950s, field cycling (FC) relaxometry has been extensively and successfully employed for diverse applications [12, 13, 14, 15]. The first applications of relaxometry mainly revolved around the study of the inner coordination environments of paramagnetic metal aquaions and of solvent interaction with globular diamagnetic proteins. These early investigations not only provided valuable insights into these systems, but also led to advances in theory and a deeper understanding of relaxation mechanisms, and prompted refinements in the applications of this technique. As we entered the 1970s, the scope of relaxometry studies expanded significantly. Relaxometry was employed to investigate solvent nuclei, as reporters of solute structure and function, and paramagnetic macromolecular systems, including metalloproteins such as hemoglobin and its derivatives, as well as paramagnetic enzymes and their complexes. These applications marked a fundamental shift in the field, underscoring its capacity to enable the observation of dynamics and behaviors of biologically relevant systems on a molecular scale. The 1980s were characterized by the advent and significant increase of interest in magnetic resonance imaging (MRI), which led to a huge interest in new pulse sequences and in paramagnetic complexes as possible contrast agents, as ways to enhance the contrast in tissues. Measurements could be performed at any field, in a range between 10 kHz to 50 MHz, thanks to the development of the Koenig-Brown relaxometer [15].
During the last decade of the last century, improvements in the technology led to the development of Fast Field Cycling (FFC) relaxometry. Similarly to the previous version, FFC relaxometry is a non-destructive and versatile low-field magnetic resonance technique, where magnetic fields (between a few kHz up to around 100 MHz) are probed by fast (1-3 ms) switching of current in an electromagnet.

FFC relaxometry represents a precious and unique tool for designing and characterizing paramagnetic complexes and contrast or theranostic agents for MRI, of both chemical [16, 17, 18, 9, 8, 19, 20, 21] and natural origin [22, 23, 24, 25]. Furthermore, it has been used to evaluate protein structure and dynamics in solution, where water protons serve as reporters of the reorientation motions of the protein [26, 27, 28, 29, 30, 31, 32, 33, 34].
The most recent applications of FFC relaxometry include the characterization of: complex liquids in bulk and confinement [35]; solid state systems

[36, 37, 38]; nonosized paramagnetic systems [39, 40]; food products, to evaluate adulterations and to give preliminary information about quality and supramolecular organization of molecules [41, 42, 43, 44, 45].

Since the available detection field is a few MHz (proton Larmor frequency) and due to the poor homogeneity, the main downside of this technique is still the absence of resolution. Till the 1990s, no technique was available to determine dynamics from picoseconds up to microseconds with atomic resolution of complex systems in liquids.

Cycling between high and low magnetic fields using high resolution spectrometers has been simultaneously but independently experimented by Bryant and Redfield between the end of the 1900 and early 2000. Two technically different approaches were adopted and applied for studying low fields relaxation on different nuclei: Redfield used a pneumatic system to move the sample inside the high field magnet [12, 46, 47], while Bryant's group system consisted also of an electromagnet attached to the bottom of the high field magnet [48].

More recently, this approach has been redesigned and defined as high-resolution relaxometry (HRR). HRR has been shown to allow the study of: ^{15}N relaxation of proteins to gain molecular dynamics insights [49], the relaxivity of paramagnetic nanoparticles [50], weak interactions of metabolites with proteins [51]. In fact, a new method, that employs HRR, has been developed to identify and characterize interactions of small molecules and macromolecules or supramolecular assemblies in complex mixtures, namely metabolites in human blood serum. This method is based on the measurement of proton relaxation rates of small molecules in solution with macromolecules, over several orders of magnitude of magnetic field. If the small molecule is free in solution, the dispersion profile is expected to be flat. If the small molecule binds specifically to a macromolecule or supra molecular assembly, the dispersion profiles for its protons will be the weighted average between the one of the free forms and the bound form, with a dispersion appearing at low field, as a consequence of the larger correlation time of the complex. This method was firstly applied on a mixture of serum albumin and the standard TSP, and allowed not only the detection of the interaction of a small molecule to a large molecular system, but also provided quantitative information about the complex, such as its size.

1.3   Aim of the project

The aim of this project was to investigate structural and dynamic properties of a variety of systems, both in the food sciences and in the life and health sciences fields, exploiting the unique point of view of fast field cycling relaxometry and ultrafast high resolution relaxometry.

1. The relaxometry profiles of a natural oral contrast agent, i. e. blueberry juice, were acquired and characterized in order to understand the origin of the increase in relaxation rates with respect to the previously investigated pineapple juice [24], taking into account their content of manganese(II) ions;

2. The conjugation reaction of L-asparaginaseII and DOTA-NHS-ester and the addition of gadolinium(III) ions were performed, and its role as a MRI contrast agent was evaluated [20];

3. In the framework of a larger study, the behavior of gadolinium labeled protein cages, relatively large (MW in the range from 17 to 20 kDa) paramagnetic compounds proposed for magnetic resonance imaging signal amplification, were characterized [21]. For all of the diamagnetic and paramagnetic proteins involved, NMRD profiles have been acquired and fitted, and the results have been analyzed;

4. We contributed to the study of protein-drug candidates, involving human transthyretin (TTR) and a strong binder, Tafamidis. FFC relaxometry was employed to confirm that an higher tetrameric structural stability is observed in samples of wild type and mutated TTR, in the presence the ligand [34];

5. The study of molecular motions at different timescales is essential in order to define a suitable physical model for describing the supramolecular organization of complex systems, e. g. triglycerides in olive oil. This objective can be achieved taking into account all protons interactions. These have been investigated through FFC relaxometry, HRR, high resolution NMR and molecular dynamics simulations.

As a side project, taking advantage of the experience gained in carrying out the L-asparaginaseII bioconjugation reaction, I was involved in finding the best conditions for the N-terminus functionalization of the HACTR-PD-1 mutant (K131T/K135R) with N-hydroxy succinimide (NHS) activated PEG (see

Section 3.5). This reaction was preparatory for a larger study of PD-1 conjugates and it leads to the perspective of an interaction study between PD-1 and PD-L1 [52]. The study of this interaction itself could benefit from an investigation through FFC and high resolution relaxometry. Even more interestingly, a selective conjugation between a paramagnetic complex and PD-1 could in principle pave the way to the development of a paramagnetic probe specifically targeting tumor cells. FFC and high resolution relaxometry could be the ideal techniques to investigate the properties of the probe and of its adduct with PD-L1.

The last portion of my PhD project revolved around high resolution relaxometry. I employed this new technique on different systems, also addressing the problem of data analysis and interpretation. Given that HRR is performed on a prototype, validation of the results was needed and it was achieved through the comparison with FFC relaxometry data on well known samples.

A study of protein-ligand interactions has been carried out employing the prototype of the new HRR shuttle system, and the results are described. In particular, the catalytic domain of matrix metalloproteinase-12 (MMP-12) and its interaction with some small molecules, known to bound the protein in a range from μM to mM, were investigated. This new technique could be groundbreaking in the drug discovery field, since understanding the dynamics of pharmacologically-relevant proteins can lead to major improvements in the efficiency and selectivity of drugs by rational design.

In summary, during my PhD, I've worked to achieve a comprehensive understanding of the systems under investigation by coupling fast field cycling and high-resolution relaxometry with high-field NMR measurements and molecular dynamics simulations. Important molecular dynamics information which were obtained, especially through FFC relaxometry and HRR are:

- structural and dynamic properties of biomolecules, like: L-asparaginaseII, protein cages, human transthyretin, and olive oil (see *all Sections*);

- characterization of internal (e.g. rotational) dynamics of diamagnetic as well as paramagnetic compounds, such as olive oil, TTR, ANSII, and protein cages (*all Sections*);

- evaluation of promising MRI contrast agents, such as blueberry juice and paramagnetic proteins (in terms of electronic relaxation, kinetics of exchange, coordination number, correlation times of reorientation, local

mobility and diffusional dynamics) (see *Section 1.2*);

- indication of aggregation states of complex biomolecules, such as proteins like TTR (see *Section 3.2*);

- observation of the interaction between proteins and small molecules, in the case of MMP-12 interactions with ligands (see *Section 3.4*).

Chapter 2

Methodologies

2.1 Fast Field Cycling Relaxometry

Fast Field Cycling Relaxometry (FFC) harnesses the fundamental principles of Nuclear Magnetic Resonance (NMR) while introducing a dynamic discrimination through the modulation of magnetic field strengths. This unique approach is based on the measurement of nuclear spins relaxation at different field values, and yields information about molecular dynamics, besides structure and interactions. Unlike conventional NMR techniques, which use a single magnetic field, and thus probes a single frequency, FFC relaxometry can probe dynamics over the kilohertz to megahertz range. By exploiting rapid changes in magnetic field strengths, FFC relaxometry goes beyond the limitations of traditional NMR techniques, enabling the measurement of NMR relaxation times from very low (typically 0.0002 T) to high (typically 1 T) fields and thus the investigation of dynamic processes over a wide range of timescales.

To carry out FFC relaxometry measurements, the *Stelar Spinmaster FFC2000-1T* relaxometer was used. It features an electromagnet capable of generating magnetic fields ranging from 0.01 MHz to 40 MHz proton Larmor frequency.

The standardly employed sequences are displayed in *Figure 2.1* and are divided into "high field" or non-prepolarized field-cycling technique, and "low field" or prepolarized field-cycling technique. The prepolarized sequence is needed to create detectable Free Induction Decay (FID) intensity when the relaxation field is too low, i.e.: below half of the electromagnet's maximum field strength.
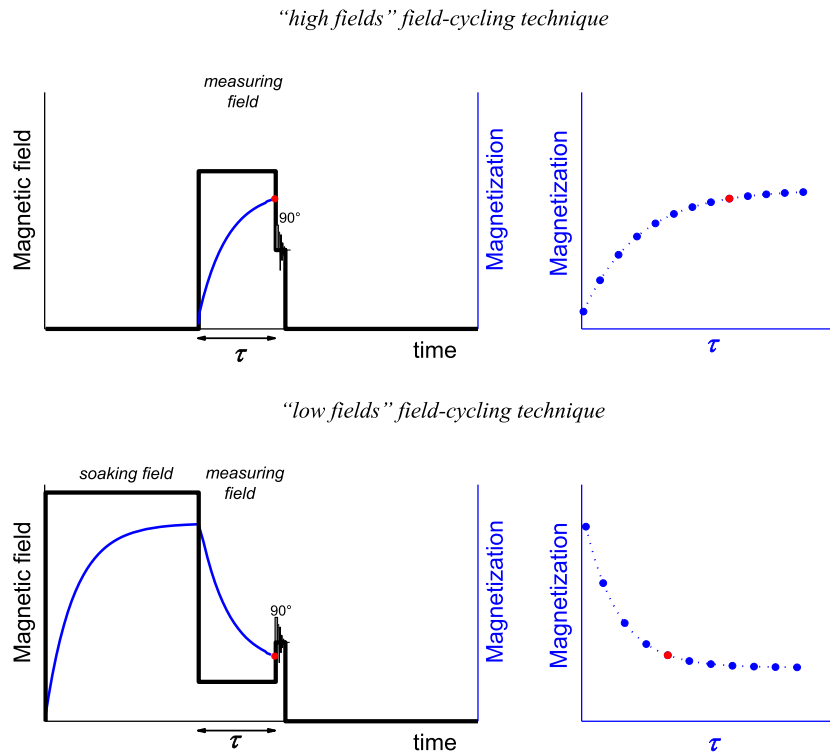
Figure 2.1: In the upper part of the figure the so called non prepolarized sequence is displayed. The bottom part shows the prepolarized sequence, employed at low fields. The reconstruction of the magnetization recovery and decay curves are also shown [33].

At low fields, the sequence consists of:

Phase 1: Application of the prepolarizing field ("soaking field" in *Figure 2.1*) for and interval of time that is five times the T_1 value estimated at that field;

Phase 2: Switch of the field to the relaxation field at which we want to measure the relaxation time ("measuring field" in *Figure 2.1*);

Phase 3: Switch of the field to the detection field, fixed value at which the receiver is tuned, and immediate application of a 90 degree radiofrequency pulse for generating the FID signal;

Phase 4: Switch the magnetic field off to allow for the complete decay of the magnetization and to avoid excessive heating of the electromagnet.

Phase 1 is not used in the case of the non-prepolarized sequence.

The switching time has a fixed value of 3 milliseconds and it is needed to change and stabilize the field value. This is a critical point of the field cycling

techniques since magnetization losses occur during these times and can prevent an accurate measurement of relaxation times smaller than the switching times.

These two sequences allow for the reconstruction of the magnetization build up and decay by measuring the magnetization of the sample at different intervals of time, indicated as τ in *Figure 2.1*. The intensity of the first 200 μs of the FID, measured in *Phase* 3 of the previous list, is indeed proportional to the magnetization at the delay τ. A fit of this curve gives the longitudinal relaxation time of the detected nuclei. Usually a monoexponential behaviour can be assumed for the relaxation process, but there are exception, which will be also discussed in this thesis.

By applying this procedure at different relaxation fields, the nuclear magnetic relaxation dispersion (NMRD) profile is obtained. This profile shows the magnetic field dependence of relaxation times (or equivalently, relaxation rates) [53]. Examples of NMRD profiles are shown in *Figure 2.2*.

(a)   (b)
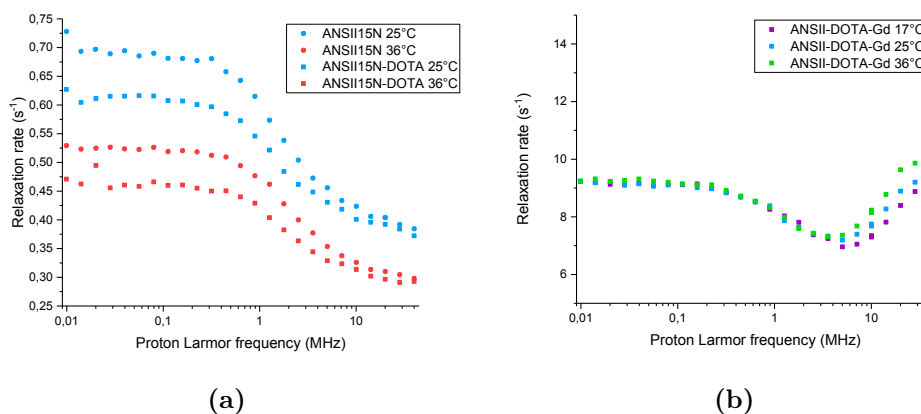
Figure 2.2: In panel (a) NMRD profiles of 0.2 mM ^{15}N labelled ANSII and conjugated system ^{15}N-ANSII-DOTA registered at 298 K and 309 K in phosphate buffer 300 mM, pH 7.5. In panel (b) NMRD profiles of ^{15}N-ANSII-DOTA-Gd (50% of DOTA concentration) registered at 290, 298 and 309 K. A small effect of temperature can be appreciated between 5 and 40 MHz.

2.2   High Resolution Relaxometry

High-resolution relaxometry (HRR) is an advanced NMR technique that combines the determination of multiscale dynamics of fast field-cycling relaxometry with the atomic-level nature and therefore the analytical power of high-resolution NMR. HRR shuttles the sample within the stray field of a commercial NMR magnet to vary the field. Currently available range spans from around 2 MHz to the high field of the employed magnet.

HRR has been recently redesigned, and two prototypes of the so called Fast Shuttle System (FSS) have been installed at ENS and at CERM. The experiments included in the present PhD thesis were carried out on both instruments. The spectrometer employed at ENS was a *Bruker Avance III HD* spectrometer operating at 600 MHz ($\sim$14.1 T), equipped with a 5mm TXI S3 (^{1}H, ^{13}C, ^{15}N) probe with xyz-gradients; BTO. The spectrometer used at CERM was a *Bruker AVANCE NEO* spectrometer operating at 700 MHz ($\sim$16.5 T) equipped with a 5mm TXI S4 (^{1}H, ^{13}C, ^{15}N) probe with z-gradient; BTO.

The FSS is an NMR accessory that is mounted on top of the dewar of the NMR magnet and that allows for the HRR measurements. It consists of 5 main components:

- The drive unit: arranges the primary motor that controls a rope, this unit moves the shuttle sample up and down;

- The sample transfer station: gives access to the pressurized FSS area for loading/removing the shuttle sample in the FSS;

- The guide tube: inserted in the standard BST within the magnet room temperature bore;

- The end stop: the interface with the NMR probe;

- The electric and pneumatic box: to control the FSS (de-/pressurize the FSS) and show the FSS operating status displayed by several leds on the front.

A continuous high pressure (4.5 bar) air flow pushes the shuttle tube inside the magnet to the high field detection position and counteracts the action of the rope.
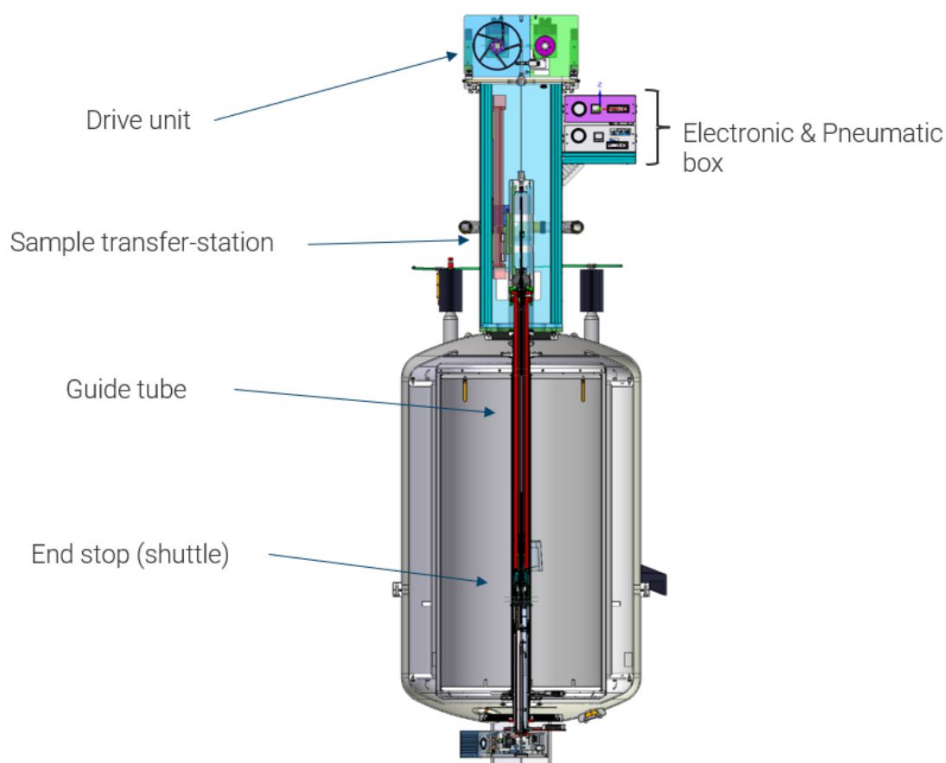
Figure 2.3: Representation of the fast shuttle system mechanism with highlighting of its main components.

The sample is contained in a 5 mm shuttle tube (see *Figure 2.4*) connected to the rope mechanism, allowing for precise positioning within the magnet. A "bubble catcher" within the tube performs dual roles: removing bubbles generated during sample preparation and preventing the formation of new ones during the movement, and serving as a seal for the liquid sample. Two rubber o-rings in contact with the tube walls keep the bubble catcher in place. A plunger screw closes the bubble catcher, runs through the entire length of the tube, and sticks out a few millimeters.

Figure 2.4: 5 mm shuttle tube employed with the fast shuttle system.

The principle of a high resolution relaxometry experiment is illustrated in *Figure 2.5*. The sample is polarized at high field, then it can be moved, with

extremely precise position control, at different heights inside the magnet. A different magnetic field value will be experienced by the sample depending on its position inside the stray field. The time required for the sample to be moved to the desired position (equal to the time required to return to the high field position) is called the travelling time and it is set to 68 milliseconds, regardless of the chosen field value. Once the shuttle container is in the high field position, a stabilization delay is needed to reduce the vibration artifacts due to its movement. With a stabilization delay of 150 milliseconds, very low vibration levels were observed on the FSS prototype at CERM.

While pulses and detection necessitate the sample to reside in the high field position, this setup allows to collect relaxation rates across a broad range of magnetic fields (from about 2 MHz, or 50 mT, to 700 MHz on the FSS prototype installed on the 700 MHz *Bruker AVANCE NEO*), and to benefit from both high sensitivity and high resolution provided by the homogeneous high field magnet.
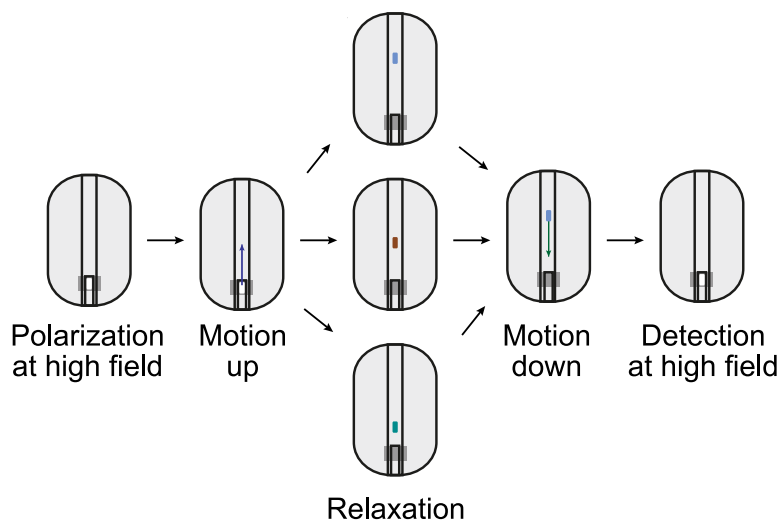
Figure 2.5: Schematic representation of the shuttle system mechanism [51].

Shuttling and relaxation at variable fields can be, in principle, integrated in every kind of pulse sequence. In *Figure 2.6*, a scheme of an inversion recovery experiment for T_1 determination is displayed. The sample is moved to the relaxation field during the variable delay times. The experiment is then repeated at different relaxation fields and variable delay times, producing, for each relaxation field, a pseudo-2D experiment that will be processed as needed. HRR

measurements can be performed to obtain the relaxation rates of all individual signal in a high-resolution spectrum. Each nucleus will show a different NMRD profile due to its relaxation mechanisms, providing precious information about the reorientational correlation time of the molecule and the internal dynamics.
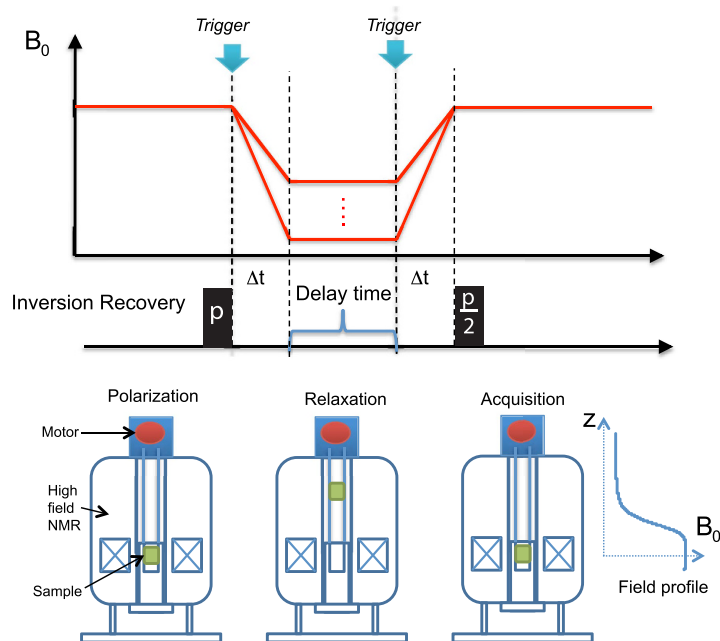
Figure 2.6: Inversion recovery experiment scheme, including the motion of the sample to the low field position during the variable delays [50].
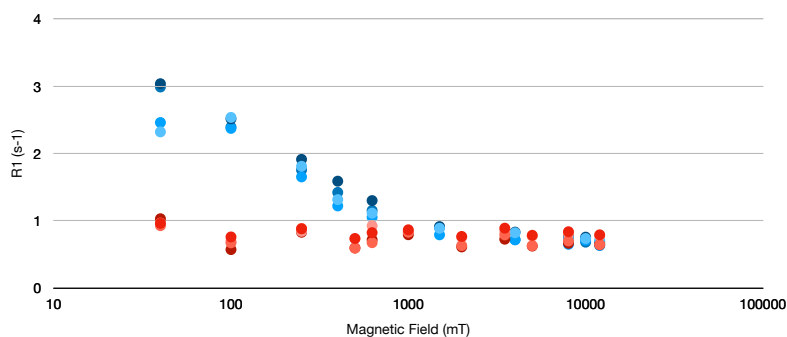
Figure 2.7: Examples of NMRD profiles obtained from the analysis of the signals of a small molecule (in red) and of the same signals when the small molecule interacts with a protein. These profiles were obtained using the FSS prototype at ENS.

2.3   HRR technique validation

Since the fast shuttle system installed on the 700 MHz *Bruker AVANCE NEO* spectrometer allows measurements between 2 and 700 MHz, there is an overlapping field zone with the *Stelar Spinmaster FFC2000-1T* relaxometer.
A comparison between the longitudinal relaxation rates of water protons measured with the two techniques was possible, and a couple of examples are displayed in the following figures.
In all the analyzed samples, we appreciated the consistency between the relaxation rates values measured between 2 and 40 MHz with the two techniques.
For the high field measurements the following sequence was employed:

$$d1- \uparrow -\tau- \downarrow -\frac{\pi}{2} - aq$$

where the $\uparrow$ and $\downarrow$ indicate the movement of the shuttle container, and τ is the variable delay.

In *Figure 2.8*, the NMRD profiles of five differently concentrated copper(II) aquaion solutions are shown. In *panel B*, the NMRD profiles of the 2.5, 5, and 10 mM copper(II) solutions, acquired at the *Stelar Spinmaster FFC2000-1T* relaxometer (black symbols) are superimposed with the values of relaxation rate measured with the FFS installed at the 700 MHz *Bruker AVANCE NEO* spectrometer (red symbols).
The NMRD profiles of the 15 and 20 mM solutions, displayed together with the others in *panel A*, show the presence of a detection limit for the shuttle system, and it occurs for rates above approximately 20 s^{-1}. This limit is imposed by the travelling time and the stabilization delay (respectively 68 and 150 ms), and make it not feasible to detect relaxation times much shorter than these times.
We can give a qualitative hypothesis for the reason why the relaxation rate values measured in these cases is nearly the same for the 15 and 20 mM samples: due to the fast relaxation times of these solutions, the sample is, partially or completely, relaxed when it returns to the high field position, so the signal we measured is the polarization resulting from the stabilization delay at 700 MHz. Unfortunately, this is the same rate maximum that Redfield and Bryant had found with their shuttling systems [48, 47].

In *Figure 2.9*, the NMRD profile of 0.25 mM solution of a self-aggregating paramagnetic complex, displayed in *panel (b)*, is shown [54]. A peak in the
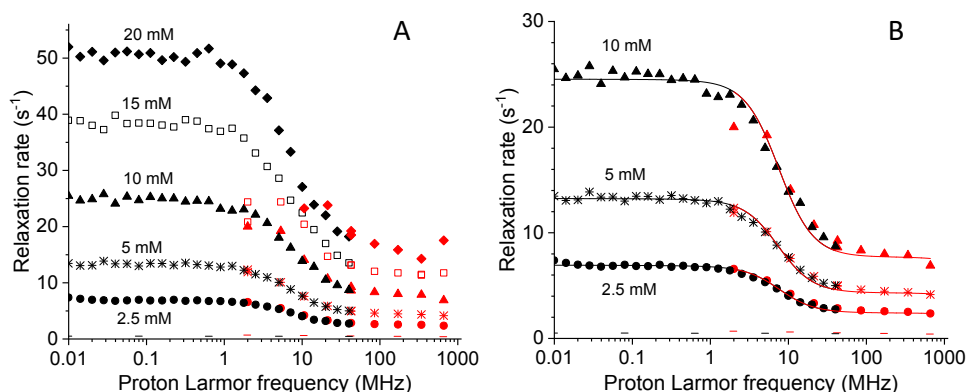
Figure 2.8: (A) Field dependence of the longitudinal relaxation rates of water protons in 2.5, 5, 10, 15, and 20 mM solutions of copper(II) aquaions. Black symbols indicate data collected with the Stelar FFC relaxometer (field between 0.01-40 MHz) and red symbols indicate data collected at the Bruker 700 MHz spectrometer equipped with the FSS. Temperature was set at 15 °C. The − symbols indicate the rates of the buffer alone. (B) Best fit profiles of the relaxation rates of water protons in 2.5, 5, and 10 mM solutions of copper(II) aquaions.

high field region appears due to the field dependence of electron relaxation, as expected for systems where the reorientational time is longer than the electron relaxation time. The overlap of the longitudinal relaxation rate values measured using the *Stelar Spinmaster FFC2000-1T* relaxometer (black symbols) with the values of relaxation rate measured with the FFS at the 700 MHz *Bruker AVANCE NEO* spectrometer (red symbols) is nearly perfect.

Additionally, HRR made it possible to extend the magnetic field range at which water protons relaxation rates could be measured and thus to probe proton relaxation rates at high fields.
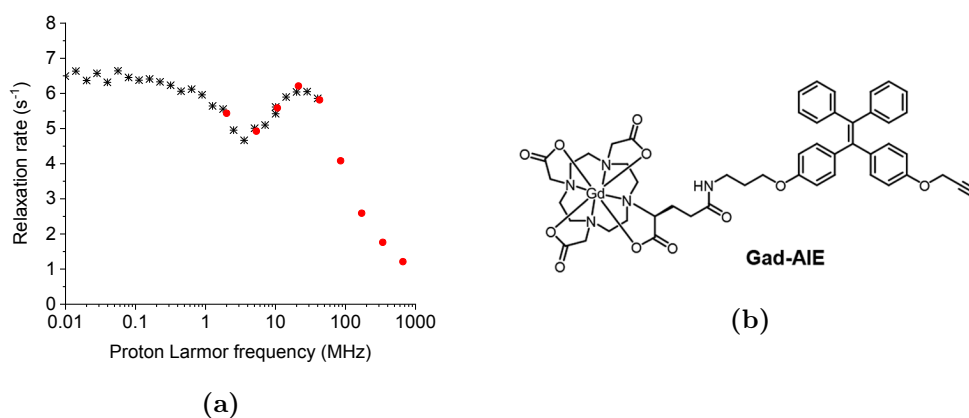
Figure 2.9: (a) Field dependence of the longitudinal relaxation rates of water protons in a 0.25 mM solution of Gd-AIE. Black symbols indicate data collected with the Stelar FFC relaxometer and red symbols indicate data collected at the Bruker 700 MHz spectrometer equipped with the FSS. Temperature was set at 15 °C. (b) Structure of the paramagnetic complex, named Gd-AIE.

2.4   Other techniques

UV-Vis Spectroscopy

Protein quantification was done by means of Uv-Visible spectroscopy at the *Varian Cary 50* spectrometer. The baseline was always acquired using the buffer solution of the protein of interest and the absorbance reading was done at 280 nm.

Inductively Coupled Plasma-Atomic Emission Spectroscopy

The *Varian ES 720* spectrometer was employed for elemental quantification of transition metals and lanthanoids in the samples.

Electrospray Ionisation Mass Spectrometry

ESI-MS spectrometry was employed to analyze the native and the conjugated form of L-asparaginaseII (see *Section 3.3.1*). The employed instrument was a TripleTOF 5600+ high-resolution mass spectrometer, equipped with a DuoSpray interface operating with an ESI probe.

Chapter 3

Results and Discussion

3.1 Dynamics in highly viscous systems: Olive Oil

Olive oil is composed of various types of lipids, including triglycerides, diglycerides, monoglycerides, and free fatty acids, as well as minor components such as antioxidants and flavor compounds. The way these components interact and arrange themselves in the oil matrix can influence its physical properties, stability, and nutritional quality.

To our knowledge, no available studies provide a precise and unambiguous description of the supramolecular organization of triglycerides (the most abundant component of olive oil), including information from different NMR-based techniques and molecular dynamics.

NMR spectroscopy is a versatile analytical technique used to study molecular structure, dynamics, and interactions at the atomic level. In the context of olive oil, NMR can provide insights into the supramolecular organization by examining the chemical shifts, coupling constants, relaxation times, and diffusion properties of different molecules within the oil.

In the present thesis, FFC relaxometry, high resolution NMR and finally HRR have been employed to measure olive oil longitudinal relaxation rates at different fields. The major scope of this study is to obtain a more accurate chemical-physical characterization and define a model for the supramolecular organization of a complex diamagnetic viscous system.

Nuclear magnetic relaxation dispersion profiles of olive oil samples have been acquired at 26 magnetic fields in the range from 0.01 to 40 MHz, at three different temperatures (288, 298, 308 K). The magnetization decay/recovery

profiles of each field were then fitted using *Origin.*
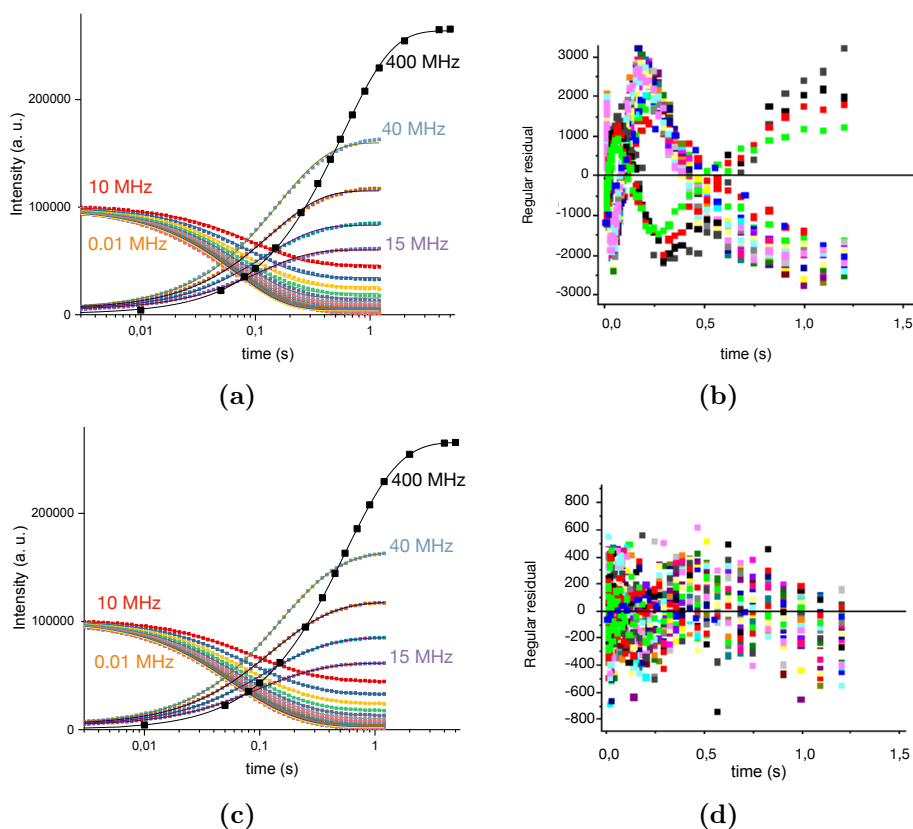
Figure 3.1: Olive oil magnetization recovery/decay curves at 298 K measured from 0.01 to 40 MHz, and at 400 MHz. Curves in *panel (a)* are the mono-exponential fit obtained using *Origin,* while *panel (b)* represents the corresponding residuals. Curves in *panel (a)* are the bi-exponential fitting, in *panel (b)* the corresponding residuals (residuals are reported in linear scale).

In *Figure 3.1(a)* all the magnetization recovery/decay curves of an olive oil sample at 298 K are represented and fitted with a monoexponential function. This fitting led to a reduced χ^2 of $2,055,893$. Residuals appear to be polarized, as shown in *panel (b)* of *Figure 3.1*, requiring at least a bi-exponential fit (see *Equation 3.1* and *Figure 3.1 panel (c)*). In this case, the reduced χ^2 was 41,658 (*panel (d)*). As it was also previously found [41, 45, 44], two different pools of protons, in approximately similar amounts, experience two different relaxation rates.

The time-dependence of the detected intensities were fitted using the equation:

$$I(t) = A\big[p \cdot exp\big(-R_1^A t\big) + (1-p) \cdot exp\big(-R_1^B t\big)\big] + B \qquad (3.1)$$

where R_1^A and R_1^B were the larger and the smaller relaxation rates, respectively,

the values of p were 0.55, 0.52, and 0.48, at 288, 298 and 308 K, respectively, and A and B are fitting constants.

From these relaxation rate values we obtained the NMRD profiles of the samples. The profiles were fitted (see *Figure 3.2*) as due to dipole-dipole relaxation, including an inner sphere contribution (using *Equation 1.1* where I is the spin of the proton, and the Lipari-Szabo approach, as in *Equation 1.12*, as a faster correlation time was needed) as well as an outer sphere one (in the case of a diamagnetic system), which takes into account the translational diffusion of molecules:

$$R_1 = R_{1dip} + R_{1diff} \tag{3.2}$$

$$R_{1dip} = \frac{3}{10}\left(\frac{\mu_0}{4\pi}\frac{\hbar\gamma_I^2}{r^3}\right)^2\left[S^2\left(J(\omega_I,\tau_c) + 4J(2\omega_I,\tau_c)\right) + (1-S^2)\left(J(\omega_I,\tau_f) + 4J(2\omega_I,\tau_f)\right)\right] \tag{3.3}$$

$$R_{1diff} = \frac{8}{45}\pi\left(\frac{\mu_0}{4\pi}\right)^2\frac{1000 N_A \gamma_I^4 \hbar^2 [H]}{2dD_T}\left[J_{diff}(\omega_I,\tau_D) + 4J_{diff}(2\omega_I,\tau_D)\right] \tag{3.4}$$

where in R_{1diff}: D_T is the diffusion coefficient of olive oil; $[H]$ is the concentration of the protons of the sample, expressed in mM; J_{diff} has the same expression as in *Equation 1.7* except for $z = \sqrt{2\omega\tau_D}$.

A structural model where proton distances within CH, CH_2, and CH_3 groups are modulated on a much shorter timescale than translational diffusion, is in fact plausible. The data collected at all the temperatures were fitted simultaneously (introducing Arrhenius relation between temperatures). The best fit parameters are reported in *Table 3.1*.

The analysis indicates that molecular tumbling times are generally in the subnanosecond range, but some protons have longer reorientation times (some nanoseconds or hundreds of nanoseconds), making them harder to approach by diffusing protons. However, FFC relaxometry does not seem to be sufficiently informative for determining the reorientation time of triglycerides and their constituent groups, because the relaxation mechanisms due to the dipole-dipole interactions within the CH_2 and CH_3 groups are almost completely averaged out by reorientational motions occurring in the subnanoseconds regime.

The small diffusion coefficients observed in olive oil samples through DOSY NMR experiments suggest slow translational diffusion ($\tau_D = d^2/2D_T$, of the order of several nanoseconds), likely due to close contacts between the fatty

$D_T{}^*$ (m^2/s)	$9.5 \cdot 10^{-12}$ exp[4160 K(1/(298 K)-1/T)]
d (Å)	3.1 ± 0.2
$[H^A]$ (mM)	109 ± 3
$[H^B]$ (mM)	30 ± 1
r* (Å)	1.75
$S_A{}^2$	0.023 ± 0.003
$\tau_c{}^A$ (ns)	(7.7 ± 0.5) exp[$(-3070 \pm 150$ K)(1/(298 K)-1/T)]
$\tau_f{}^A$ (ns)	(0.12 ± 0.02) exp[$(-3090 \pm 200$ K)(1/(298 K)-1/T)]
$S_B{}^2$	0.000082 ± 0.000020
$\tau_c{}^B$ (ns)	(380 ± 30) exp[$(-2620 \pm 150$ K)(1/(298 K)-1/T)]
$\tau_f{}^B$ (ns)	(0.092 ± 0.02) exp[$(-2010 \pm 100$ K)(1/(298 K)-1/T)]

Table 3.1: Best fit values of the parameters obtained from the fit of the relaxation profiles. Parameters followed by the symbol * were fixed: D was determined through NMR DOSY experiments (and very similar to the values reported in the literature [45, 44]), while r was set to 1.75 Å, the distance between protons in CH_2 groups, representing the large majority of the protons in triglycerides.

acid chains of the triglycerides, probably intertwined.

In order to have additional information, longitudinal relaxation rates were measured by high resolution ^{1}H-NMR at 400 MHz, on a *Bruker Avance III* spectrometer equipped with a BBO probehead, at three temperatures (288, 298 and 308 K). The sample was placed in a capillary tube, coaxial to the 5 mm NMR tube filled with D_2O in order to reduce radiation damping.

From the high resolution spectra reported in *Figure 3.3*, ten peaks can be resolved and assigned (consistently with the assignment already present in the literature [55]), and therefore ten relaxation rates can be obtained for each temperature. Nine of the signals can be related to the groups of protons in triolein (containing only monounsatured chains), which is the main component of olive oil. Therefore, a nine-exponential function (*Equation 3.5*) was employed to fit the magnetization curves measured at the relaxometer:

$$I(t) = \sum_i A\big[p_i exp\big(-R_1{}^i t\big) + B\big] \tag{3.5}$$

considering a model where only dipole-dipole interactions are modulating the relaxation rates (*Equation 3.3*). The relative populations of each group, p_i, were fixed based on the value of the integral of their signal, while the "effective distance" r was fixed, on the basis of structural considerations, to 1.75 Åfor CH_2 protons, and 1.96 Åfor CH_3 and CH protons.

Python was employed to implement a curve fitting script which allowed us to
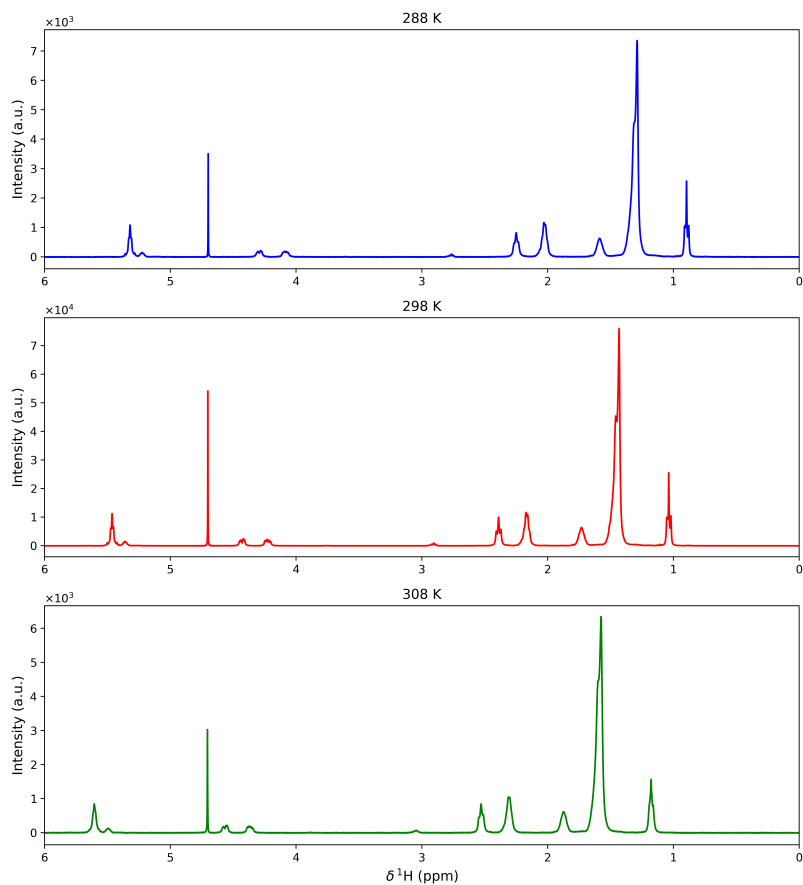
Figure 3.3: Olive oil ^{1}H NMR spectra at 288, 298 and 308 K, measured at 400 MHz.

fit collectively the FFC relaxometry and the high resolution NMR data.

(a)

(b)
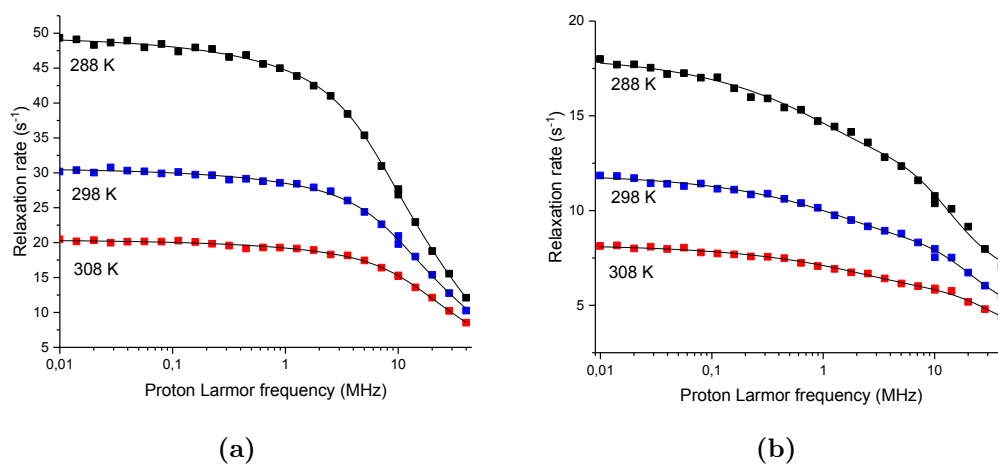
Figure 3.2: Fitting curves of the rate values obtained from biexponential fit of the magnetization curves of olive oil at 288, 298 and 308 K. The reduced χ^2 was 0.07275 for (a) and 0.0218 for (b).

	S_1^2	S_2^2	288 K			298 K			308 K		
			τ_c (ns)	τ_i (ns)	τ_f (ps)	τ_c (ns)	τ_i (ns)	τ_f (ps)	τ_c (ns)	τ_i (ns)	τ_f (ps)
$-CH_3$ p = 0.0865	0.41	0.11	0.51	2.80	88	0.40	0.95	31	0.32	0.54	9
$-(CH_2)n-$ p = 0.5768	0.13	0.44	3.86	0.48	66	2.32	0.24	31	1.62	0.14	22
$-OCO-CH_2-CH_2-$ p = 0.0577	0.0059	0.59	247	0.20	34	141	0.18	31	92.2	0.12	23
$-CH_2-CH=CH-$ p = 0.1154	0.13	0.65	16.6	0.25	34	9.21	0.17	31	5.80	0.11	28
$-OCO-CH_2-$ p = 0.0577	0.0003	0.48	1440	0.36	34	924	0.23	31	642	0.14	28
$-CH_2OCOR$ p = 0.0193	0.21	0.51	6.75	2.22	194	3.50	1.23	176	2.61	0.70	117
$-CH_2OCOR$ p = 0.0193	0.21	0.51	6.64	2.22	194	3.71	1.23	176	2.49	0.70	117
$CHOCOR$ p = 0.0096	0.091	0.80	52.8	0.28	34	24.2	0.22	31	13.3	0.18	28
$-CH=CH-$ p = 0.0577	0.091	1	50.3	0.45	-	23.2	0.10	-	14.1	0.07	-

Figure 3.4: Best fit parameters for the collective fit of low field and high field data.
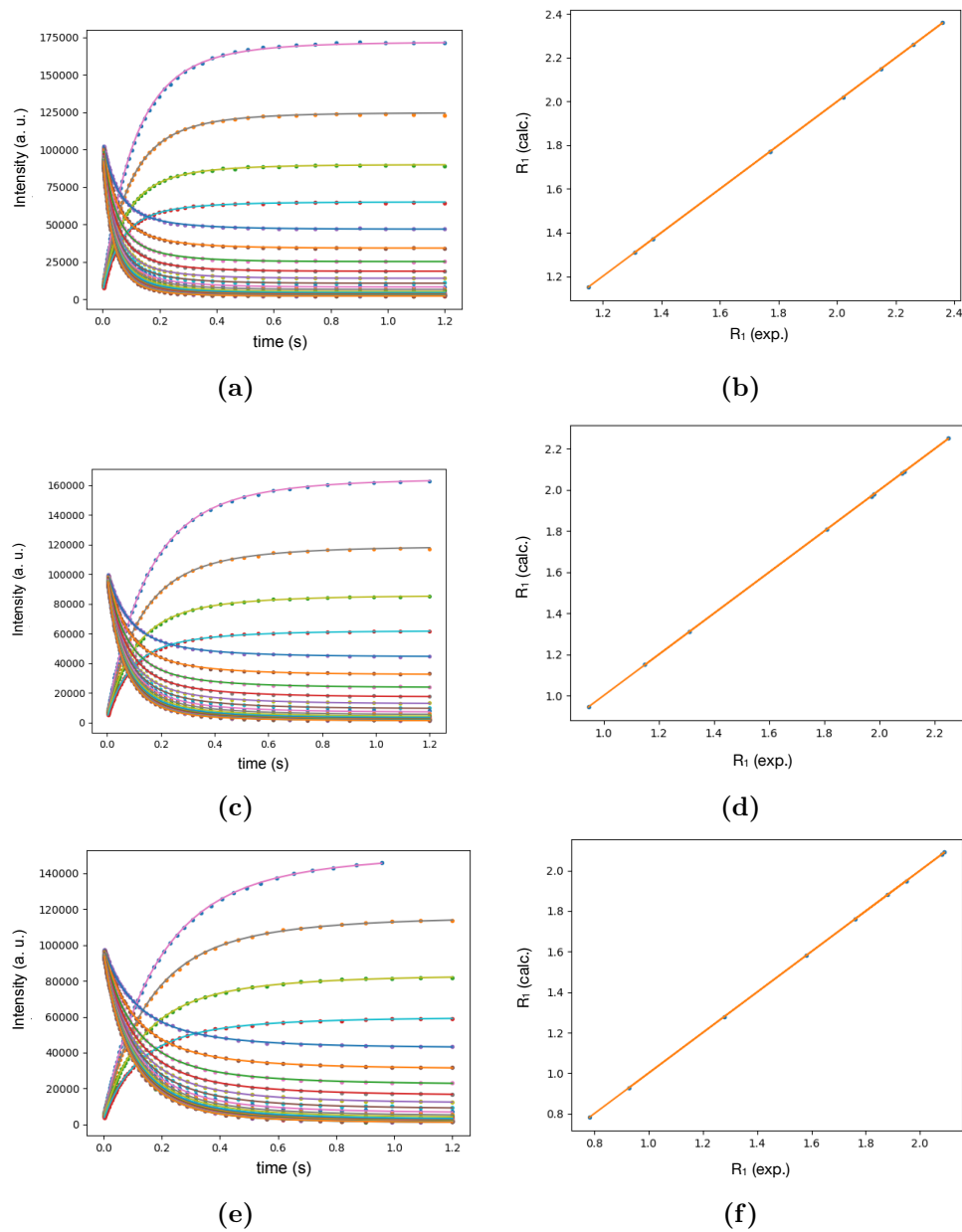
Figure 3.5: Fitting curves of the multiexponential fit (*Equations 3.5* and *3.3*) of the magnetization curves of olive oil at 288, 298 and 308 K. In *panels (b), (d) and (f)*, the extremely good agreement between the calculated rate values and the ones measured from the high resolution experiments is plotted. This is one of the fits obtained employing our customizable script.

In *Figure* 3.5, the fits obtained using this method on our customized script are plotted.

GROMACS was employed to perform a molecular dynamics simulation of a box containing 250 identical triolein molecules, including the inputs generated through *LigParGen*, and the OPLS AA force field [56]. Firstly, a quick minimization was performed. Subsequently, the equilibration was carried out using an isobaric/isothermal (NPT) ensemble, where number of particle, pressure and temperature are kept constant for the whole simulation. A high time constant for pressure coupling (10 ps) and a 0.2 fs integration time step were set.

The output configuration was employed as starting point for the first production, which was run for 200 ns. Finally, another 20 ns production started from this final configuration. The average density of the simulated system was 907.3 kg/m^3, very close to the experimental density of pure triolein, 907.8 kg/m^3. This is an indication that the force field is correctly reproducing the experimental properties of the system. Moreover, relatively small fluctuations of the four main thermodynamic properties were observed, as reported in *Figure 3.6*. The relatively small drift of the thermodynamic quantities means that the system is well equilibrated when the production is performed.
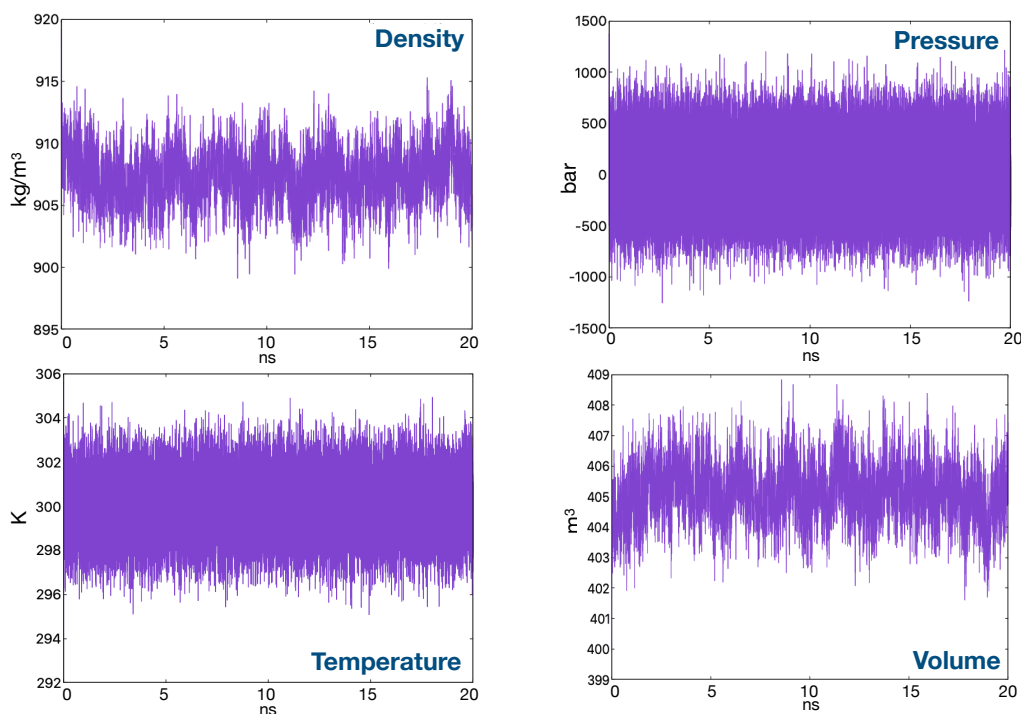
Figure 3.6: Density, pressure, temperature and volume fluctuations during the 20 ns production.
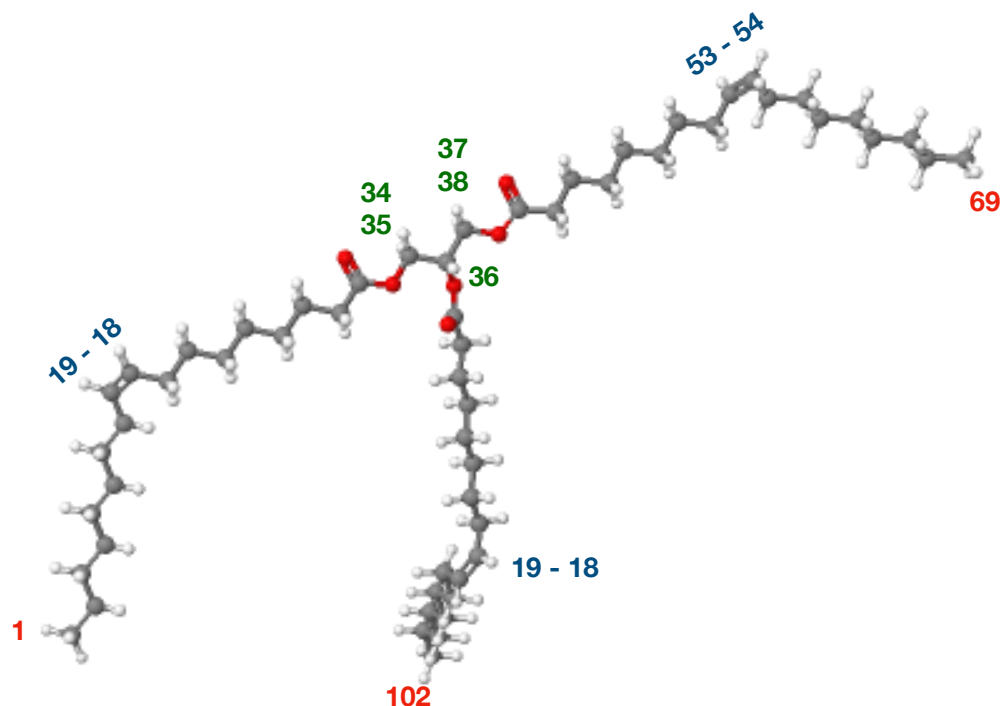
Figure 3.7: Representation of a triolein molecule with indexes of a few selected atoms. The coulor coding is the same as in *Figures 3.8*, *3.9*, and *3.10*.

The trajectory of the protons was extracted, converted into coordinates matrices and analyzed through a customized *MatLab* script. The employed script takes as input the cartesians coordinates, recursively calculates the contribution to the correlation function of the interaction between one single proton and every other proton in the simulation box and sums them up to give the correlation function of each proton. For the best fit of the proton correlation function, taking into account the inter- and intramolecular interactions, an exponential function with three correlation times and two order parameters was employed.

The obtained order parameters reflect the expected mobility of the aliphatic chains of the triglycerides. In fact, as it can be observed from *Figures 3.8*, motions that modulate the dipolar relaxation with the slower correlation time τ_1, in the order of nanoseconds, have the largest order parameters for the protons belonging to the head of the triglyceride. On the other hand, the fastest correlation time τ_3, which is in the order of picoseconds, has the highest contribution for the protons that belong to the most mobile part, which is the terminal part of the tail of the molecule (see *Figures 3.10*).
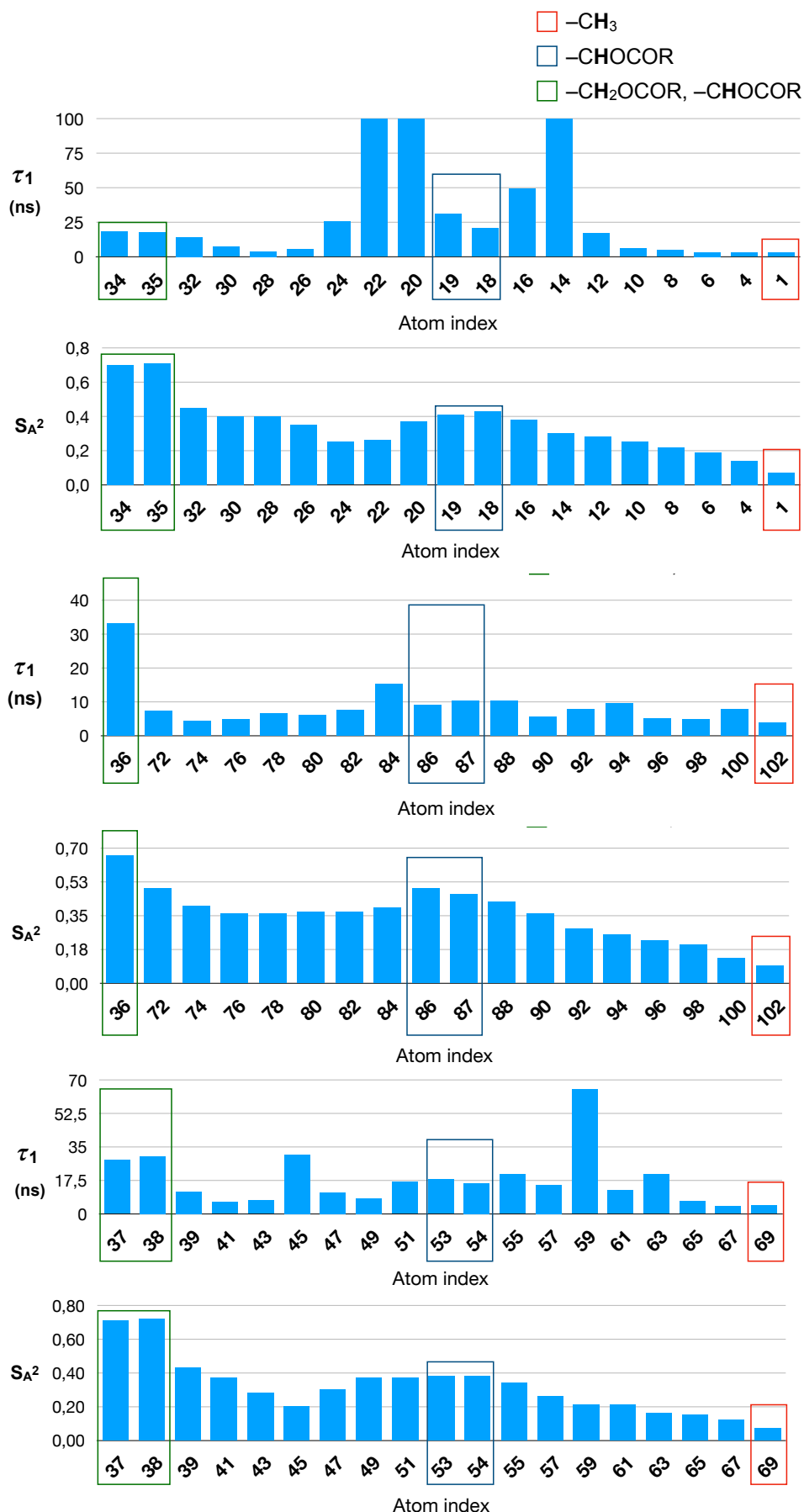
Figure 3.8: Values of τ_1 and the corresponding $S_A{}^2$ for selected protons of the triolein alchilic chains. Chain A goes from 34-35 (glycerol protons) to 1 (methyl proton), chain B goes from 36 (glycerol proton) to 102 (methyl proton), chain C goes from 37 (glycerol protons) to 69 (methyl proton), as shown in *Figures 3.7*.
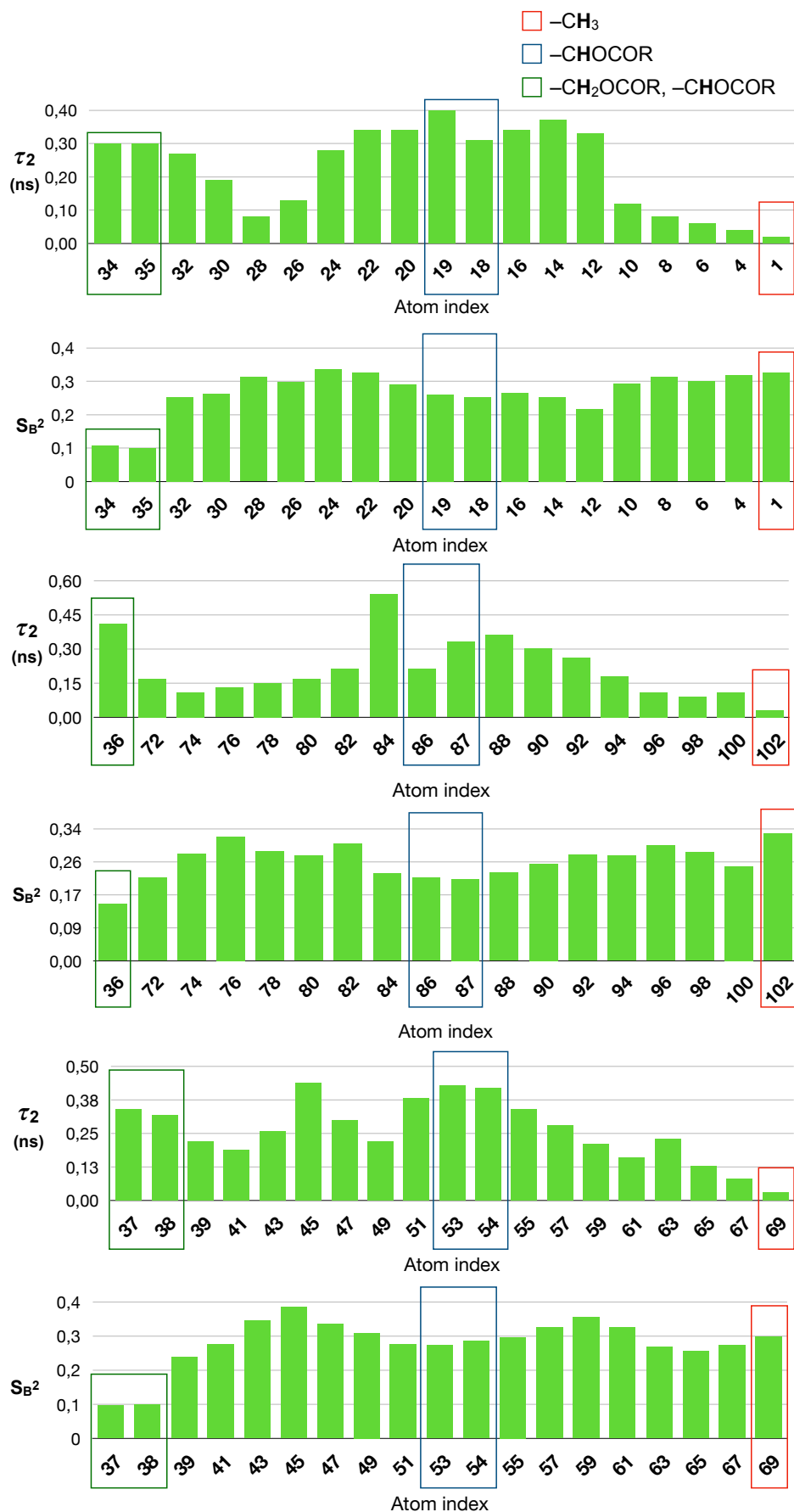
Figure 3.9: Values of τ_2 and the corresponding $S_B{}^2$ for selected protons of the triolein alchilic chains. Chain A goes from 34-35 (glycerol protons) to 1 (methyl proton), chain B goes from 36 (glycerol proton) to 102 (methyl proton), chain C goes from 37 (glycerol protons) to 69 (methyl proton), as shown in *Figures 3.7*.
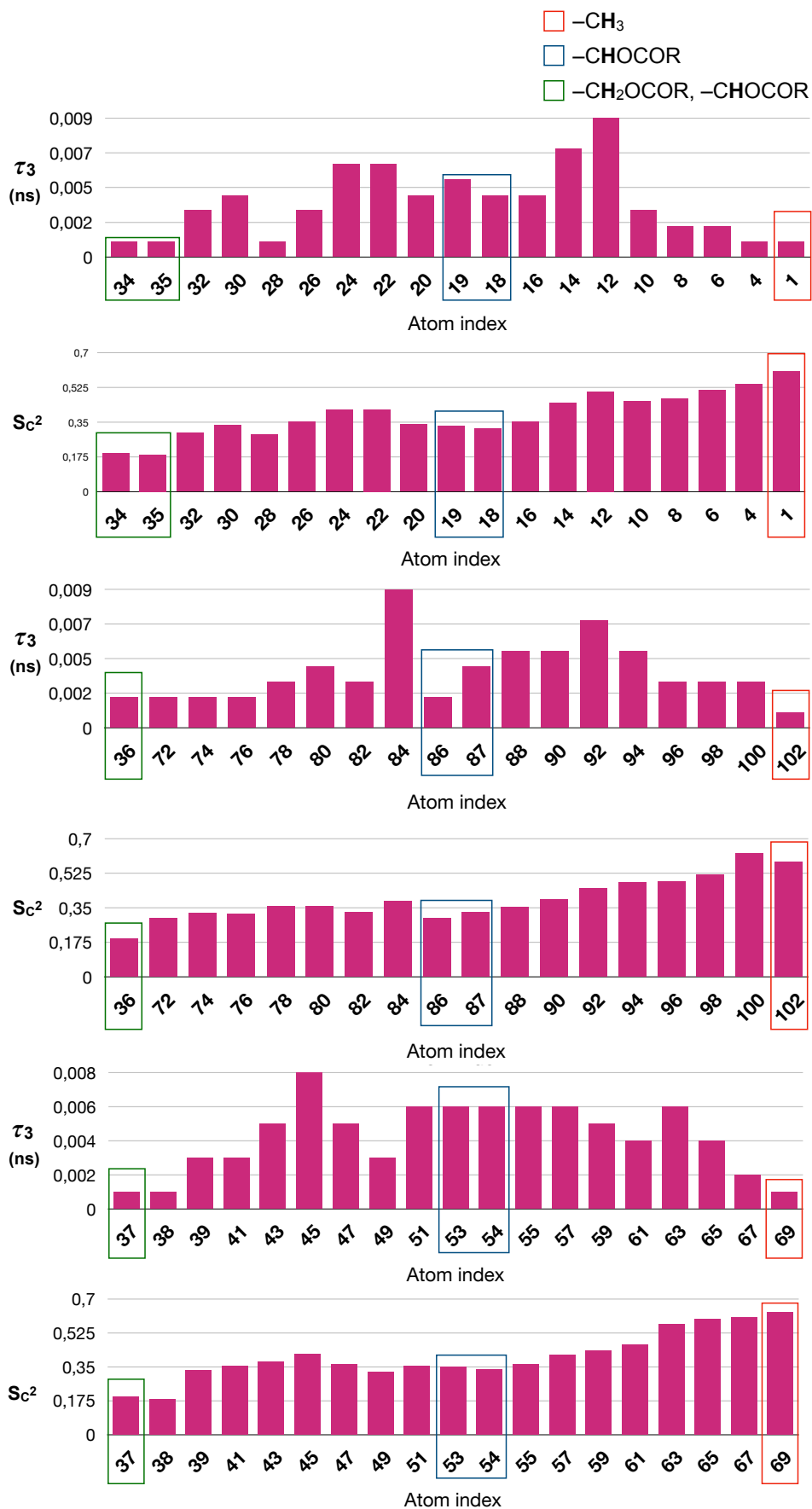
Figure 3.10: Values of τ_3 and the corresponding $S_{\mathrm{C}}{}^2$ for selected protons of the triolein alchilic chains. Chain A goes from 34-35 (glycerol protons) to 1 (methyl proton), chain B goes from 36 (glycerol proton) to 102 (methyl proton), chain C goes from 37 (glycerol protons) to 69 (methyl proton), as shown in *Figures 3.7*.

Finally, HRR measurements were performed with the first shuttle system at *Bruker* in Wissembourg, with a *Bruker Avance III* spectrometer operating at 600 MHz ($\sim$ 14.1 T), equipped with a 5mm PA TXI 600 S3 H-C/N-D probe with XYZ gradients; BTO.
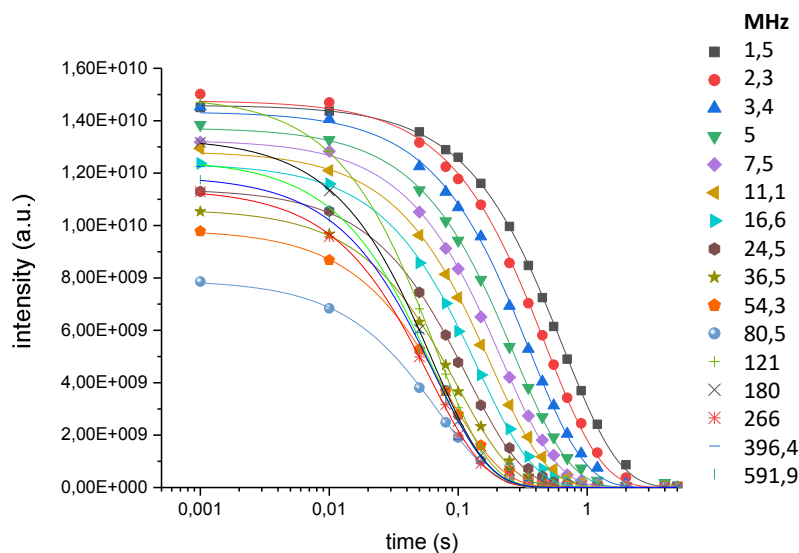
Figure 3.11: Example of time dependent magnetization decays at different relaxation fields for one NMR signal masured with the HRR shuttle system installed in Wissembourg on a *Bruker Avance III* spectrometer operating at 600 MHz.

These data were processed and analized. The integration of all the triglycerides signal was followed by the fitting of time dependent magnetization decays at 16 different relaxation fields. An example of what we obtained for each signal is displayed in *Figure 3.11*. The time dependence of the intensity of all peaks shows a mono-exponential decay, except for the CH_2 signal, which requires a bi-exponential function. It is not surprising that protons belonging to different groups of triglycerides experience different relaxation rates. This variability arises from the different motional regimes and interactions with neighboring protons at varying distances to which each proton is exposed to. To some extent, this behaviour may be seen as analogous to that of intrinsically disordered proteins, where proton relaxation rates differ due to the different distances of each CH, CH_2 and CH_3 protons from other protons, and fast local mobility occurs. However, this fast mobility is unable to completely average out the dipole-dipole interaction energy, so that longer reorientation times are effective in determining the low field relaxation rates.

The fit of the field dependence of the resulting longitudinal relaxation rates indicates the contributions of three to four correlation times, ranging from sev-

eral tens of picoseconds to few nanoseconds, with different weights (see *Figures 3.12* and *3.13*). These weights reflect the different mobility along the alchilic chain of the triglycerides.

The magnetization curves obtained through FFC relaxometry measurements are in very good agreement with the relaxation rates obtained with the HRR measurements if the slowest correlation time (τ_1) and the corresponding order parameter (S^2) were left free to adjust (*Figure 3.14*).
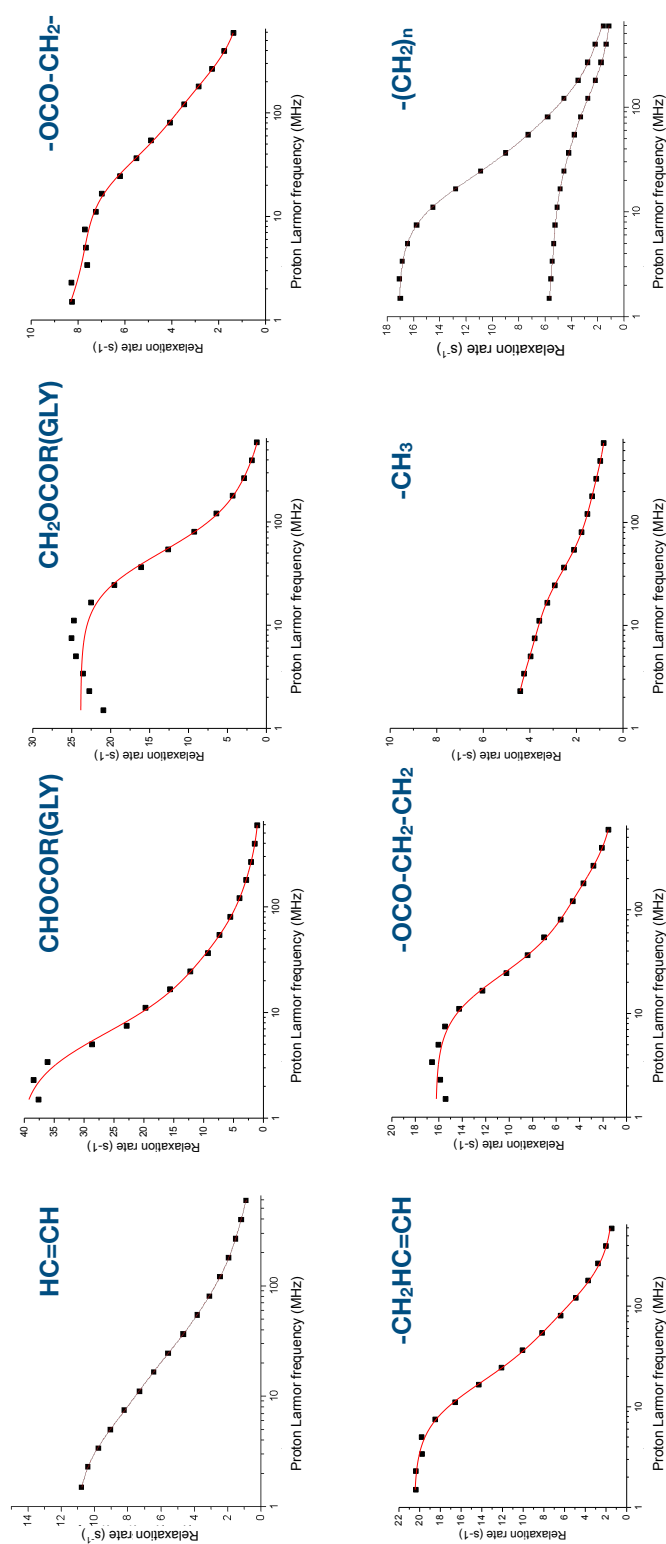
Figure 3.12: Fit of the NMRD profile for each proton signal. Each of the longitudinal relaxation rates dispersion was fitted taking into account 3 or 4 correlation times.

	S^2_1	τ_1 (ns)	p^2_2 $(1-S^2_1)$	τ_2 (ns)	p^2_3 $(1-S^2_1)(1-S^2_2)S^2_3$	τ_3 (ns)	$1-S^2$ $(1-p^2_1-p^2_2-p^2_3)$	τ_4 (ps)
-CH₃	3E-03	24,48	5,484E-02	2,63	9,33E-02	0,42	8,49E-01	70,60
-(CH₂)ₙ,high	0		7,260E-02	4,61	1,94E-01	0,88	7,34E-01	95,80
-(CH₂)ₙ,low (w=0,3)	4,90E-04	37,80	1,559E-02	3,21	1,49E-01	0,62	8,35E-01	41,90
-OCO-CH₂-CH₂	0		9,680E-02	3,85	2,99E-01	0,44	6,04E-01	70,60
-CH₂-CH=CH	1,5E-03	24,70	5,741E-02	2,99	2,23E-01	0,56	7,18E-01	71,10
-OCO-CH₂	0		7,640E-02	5,36	2,61E-01	0,85	6,62E-01	88,60
CH₂OCOR(GLY)	0		2,150E-01	2,64	3,59E-01	0,71	4,26E-01	81,10
CH₂OCOR(GLY)	0		2,170E-01	2,71	3,63E-01	0,71	4,20E-01	80,60
CHOCOR(GLY)	1,34E-01	14,20	2,719E-01	2,08	5,94E-01	0,41	0	
-CH=CH-	1,50E-02	17,50	7,388E-02	3,33	1,78E-01	0,82	7,33E-01	114,00

Figure 3.13: Best fit parameters of the NMRD profiles in *Figures 3.12.*

(a)
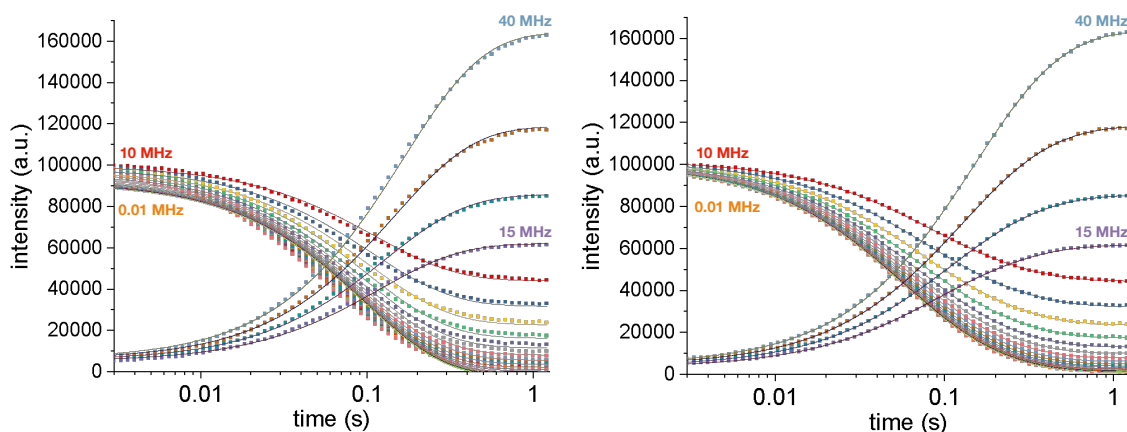
	S^2_1	τ_1 (ns)	p^2_2 $(1-S^2_1)$	τ_2 (ns)	p^2_3 $(1-S^2_1)(1-S^2_2)S^2_3$	τ_3 (ns)	$1-S^2$ $(1-p^2_1-p^2_2-p^2_3)$	τ_4 (ps)
-CH₃	5,98E-04	237,00	5,484E-02	2,63	9,33E-02	0,42	8,49E-01	70,60
-(CH₂)ₙ,high	0,00363	18,00	7,260E-02	4,61	1,94E-01	0,88	7,34E-01	95,80
-(CH₂)ₙ,low (w=0,3)	2,57E-03	3,90	1,559E-02	3,21	1,49E-01	0,62	8,35E-01	41,90
-OCO-CH₂-CH₂	0,000244	1000	9,680E-02	3,85	2,99E-01	0,44	6,04E-01	70,60
-CH₂-CH=CH	1,814E-02	17,10	5,741E-02	2,99	2,23E-01	0,56	7,18E-01	71,10
-OCO-CH₂	0		7,640E-02	5,36	2,61E-01	0,85	6,62E-01	88,60
CH₂OCOR(GLY)	0		2,150E-01	2,64	3,59E-01	0,71	4,26E-01	81,10
CH₂OCOR(GLY)	0		2,170E-01	2,71	3,63E-01	0,71	4,20E-01	80,60
CHOCOR(GLY)	1,34E-01	14,20	2,719E-01	2,08	5,94E-01	0,41	0	
-CH=CH-	3,79E-01	8,50	7,388E-02	3,33	1,78E-01	0,82	7,33E-01	114,00

(b)

Figure 3.14: (a) Left: FFC relaxometry data (dots) and curves calculated using the values of *Figure 3.12 panel (b)*. (a) Right: FFC relaxometry data (dots) and fitting curves using the values of *Figure 3.12 panel (b)* except for τ_1 and the corresponding order parameter that were not fixed. (b) Best fit parameters.

3.2 Protein dynamics insights on human TTR

Functional TTR is an assembly of four identical subunits, a dimer of dimers of D_2 symmetry, with a total molecular mass of 55 kDa. TTR is present in blood plasma and cerebrospinal fluid, where it carries the holo-retinol binding protein and the thyroxine T_4 hormone [57]. However, TTR's significance goes beyond its crucial role in hormone transport. In fact, this protein has garnered attention in the field of drug delivery for its ability to form stable complexes with various small molecules, including drugs and therapeutic compounds. This characteristic is particularly valuable in the development of targeted drug delivery systems. In fact, when a small organic drug is conjugated to a protein, specific recognition of receptors, and thus efficient targeting can be achieved. That is the reason why TTR, as well as other proteins (e.g. human serum albumin [58]), have been considered in the development of targeted drug delivery systems.

(a)

(b)
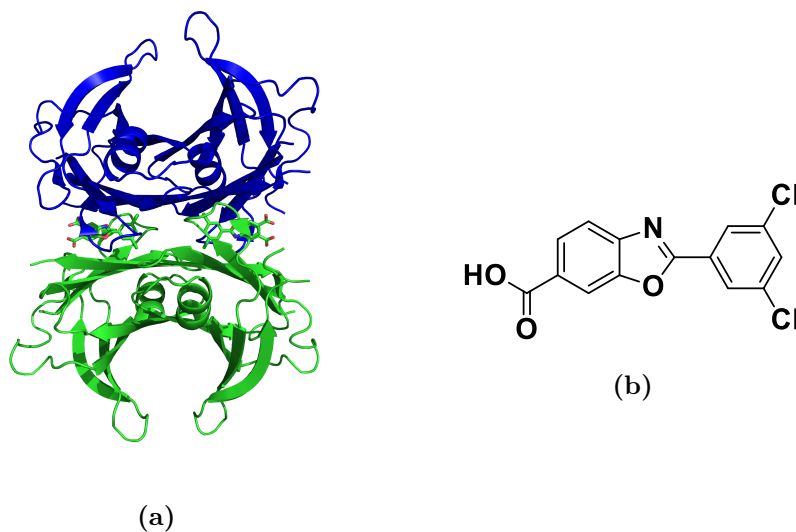
Figure 3.15: (a) Schematic representation of Human Transthyretin interacting with two molecules of Tafamidis (PDB structure 1F41). (b) Structural formula of protein ligand, Tafamidis.

Another important aspect influencing stability and activity of TTR is the presence of mutations in the gene coding for TTR [59, 57]. Some mutations offer protective effects, but unfortunately the majority are pathogenic, in many cases because they decrease the stability of the assembly leading to the dissociation of the functional tetramer into monomers that partially unfold and polymerize to form amyloid fibrils. A recent therapeutic approach to avoid monomerization relies on organic molecules, such as Tafamidis, that binds

transthyretin in a cooperative manner with low nanomolar affinity, and prevents its monomerization [60].

FFC relaxometry was employed to observe the behaviour of the protein in different conditions: in the absence and in the presence of Tafamidis, and in the presence of a stabilizing single mutation (T119M).
The ^{1}H NMRD profiles of the wild type (WT) and the mutated form of TTR, with or without Tafamidis were acquired at 288 K, 298 K, and 310 K, and are shown in *Figure 3.16*. The measurements are affected by an error of about ± 1%.

Qualitatively, the profiles report of only minor differences between the dispersion profile of the protein in presence and in absence of the ligand, Tafamidis. This occurs for both the native and mutant protein. We can therefore state that ligand binding causes no sizable changes in the dynamics of the protein.

	(a)	(b)
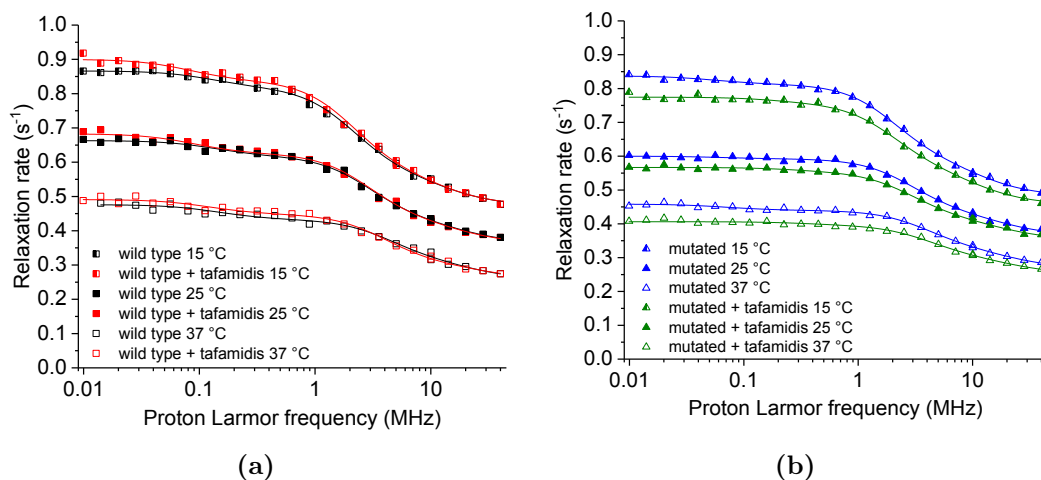
Figure 3.16: (a) ^{1}H NMRD profiles of 1.2 mM wild type TTR with and without Tafamidis at 288, 298 and 310 K. (b) ^{1}H NMRD profiles of mutated TTR with and without Tafamidis at 288, 298 and 310 K. The solution with the ligand was slightly diluted (protein concentration decreased from 1.6 mM to 1.4 mM) and that justifies the lower profile.

The observed longitudinal relaxation rates depend on the correlation times modulating the proton-proton dipole–dipole interactions. The profiles were thus fitted as a sum of multiple contributions, each modulated by a different correlation time, τ_i, according to the model-free approach (see *Section 1.1.3*):

$$R_1 = \alpha + \beta \sum_{i}^{N} c_i \left(\frac{\tau_i}{1 + \omega^2 \tau_i^2} + \frac{4\tau_i}{1 + 4\omega^2 \tau_i^2} \right) \qquad (3.6)$$

where a constant contribution, α, is added to account for water relaxation from protons with correlation times smaller than few nanoseconds (dispersion occurring beyond the highest magnetic field); β depends on the squared proton-proton dipole–dipole interaction energy and on the protein concentration; c_i are weight coefficients of each contribution arising from protons with the same correlation time, all summing to 1. The correlation times are the fastest between the proton exchange time and the reorientational times, for both the overall protein tumbling and the faster local dynamics.

All the profiles, at the different temperatures, were fitted together (in order to reduce the covariance of the parameters) and the best fit parameters are reported in *Table 3.2*. Three correlation times were employed and each of them was a shared parameter in the fit of the curves of all samples, thus allowing for monitoring the differences between the weight factors and the effect of protein mutation and of its interaction with Tafamidis. Additionally, the parameter β was constrained to be the same for the WT protein both in the presence and in the absence of Tafamidis, because of the same protein conditions and concentration.

The three correlation times, needed to fit the NMRD profiles, reported for, from slower to faster:

- The presence of molecular aggregates, with a correlation time of hundreds of nanoseconds, τ_1 and a very low weight factor, c_1. The value of c_1 decreases going from the WT protein alone to the solution of the mutated protein in the presence of the ligand, suggesting that, as expected, the WT protein has indeed a higher propensity to form aggregates;

- An intermediate correlation time of the order of tens of nanoseconds, τ_2, which is, at all temperature, consistent with the overall reorientation of the protein predicted with $HydroNMR$ [61]. The predicted values for the reorientational correlation times were 21, 28, and 37 nanoseconds at 310, 298, and 288 K, respectively. In the solution of the protein in the presence of Tafamidis, the contribution from this correlation time is slightly higher (c_2 increases from 0.28 to 0.30), and this may be due to a more rigid protein tumbling;

- The contribution to relaxation with the largest weight factor, c_3, can be addressed to the fastest local motion and/or the lifetime of proton exchange processes, with a correlation time, τ_3, of a few nanoseconds.

Although within the experimental error, from the comparison of the fitting

	WT TTR	WT TTR + Tafamidis	Mutated TTR	Mutated TTR + Tafamidis	Units
α	0.35	0.35	0.37	0.35	s^{-1}
β	2×10^7	2×10^7	1.9×10^7	1.7×10^7	s^{-2}
c_1	0.007	0.004	0.001	0.002	
τ_1		310×10^{-9}			s
c_2	0.28	0.30	0.29	0.29	
τ_2		30×10^{-9}			s
c_3	0.72	0.69	0.71	0.70	
τ_3		5×10^{-9}			s
τ_2 (15°C)	40×10^{-9}	40×10^{-9}	42×10^{-9}	42×10^{-9}	s
τ_2 (35°C)	19×10^{-9}	22×10^{-9}	21×10^{-9}	20×10^{-9}	s

Table 3.2: Best fit parameters of wild type and mutated TTR with and without Tafamidis.

parameters it results that the wild type protein without Tafamidis has an higher tendency to form aggregates and that the presence of Tafamidis results in a slight higher contribution from the overall reorientational correlation time, possibly due to a more stable protein folding. The mutation, as expected, seems to slightly stabilize the protein, preventing the monomerization and aggregate formation. In this case, the presence of Tafamidis does not produce sizable changes to the NMRD profile.

NMR Spectroscopy

Combining Solid-State NMR with Structural and Biophysical Techniques to Design Challenging Protein-Drug Conjugates

Linda Cerofolini[+], Kristian Vasa[+], Elisa Bianconi[+], Maria Salobehaj, Giulia Cappelli, Alice Bonciani, Giulia Licciardi, Anna Pérez-Ràfols, Luis Padilla-Cortés, Sabrina Antonacci, Domenico Rizzo, Enrico Ravera, Caterina Viglianisi, Vito Calderone, Giacomo Parigi, Claudio Luchinat, Antonio Macchiarulo, Stefano Menichetti,* and Marco Fragai*

Abstract: Several protein-drug conjugates are currently being used in cancer therapy. These conjugates rely on cytotoxic organic compounds that are covalently attached to the carrier proteins or that interact with them via non-covalent interactions. Human transthyretin (TTR), a physiological protein, has already been identified as a possible carrier protein for the delivery of cytotoxic drugs. Here we show the structure-guided development of a new stable cytotoxic molecule based on a known strong binder of TTR and a well-established anticancer drug. This example is used to demonstrate the importance of the integration of multiple biophysical and structural techniques, encompassing microscale thermophoresis, X-ray crystallography and NMR. In particular, we show that solid-state NMR has the ability to reveal effects caused by ligand binding which are more easily relatable to structural and dynamical alterations that impact the stability of macromolecular complexes.

Introduction

The development of a suitable drug delivery system is a crucial step in drug design to ensure extended half-lives and efficient targeting, thus achieving high therapeutic efficacy.[1,2] The conjugation of small organic drugs to protein-based biomaterials or synthetic polymers is often used to decrease renal excretion and increase their half-lives.[3] When a protein-based carrier is used, specific recognition of receptors and thus efficient targeting can be also achieved. Human serum albumin is an archetypical example of a protein used as a carrier of drugs and contrast agents.[4] It is also used as a component of nanoparticles to deliver cytotoxic molecules to cancer cells,[5,6] or fused with therapeutic peptides to prevent their fast clearance, proteolytic degradation, and to improve solubility.[7–9]

Another protein that has been considered as a drug carrier is human transthyretin (TTR hereafter), which is present in blood plasma and cerebrospinal fluid where it carries the holo-retinol binding protein and the thyroxine T_4 hormone. Functional TTR is an assembly of four identical subunits, a dimer of dimers (D_2 symmetry, total molecular mass 55 kDa). Mutations in the gene coding for TTR decrease the stability of the assembly, leading to the dissociation of the tetramer into monomers. Monomers can partially unfold and form amyloid fibrils.[10] Extracellular accumulation of TTR amyloid fibrils in different tissues and organs leads to severe disorders, and ultimately to fatal multiorgan failure. A recent therapeutic approach to treat

[*] Dr. L. Cerofolini,[+] M. Salobehaj, G. Licciardi, Dr. A. Pérez-Ràfols, L. Padilla-Cortés, S. Antonacci, Dr. D. Rizzo, Prof. Dr. E. Ravera, Prof. Dr. V. Calderone, Prof. Dr. G. Parigi, Prof. C. Luchinat, Prof. Dr. M. Fragai
Magnetic Resonance Centre (CERM), University of Florence
Via L. Sacconi 6, 50019 Sesto Fiorentino (Italy)
E-mail: fragai@cerm.unifi.it

Dr. L. Cerofolini,[+] M. Salobehaj, G. Licciardi, L. Padilla-Cortés, Dr. D. Rizzo, Prof. Dr. E. Ravera, Prof. Dr. V. Calderone, Prof. Dr. G. Parigi, Prof. C. Luchinat, Prof. Dr. M. Fragai
Consorzio Interuniversitario Risonanze Magnetiche di Metallopro-teine (CIRMMP)
Via L. Sacconi 6, 50019 Sesto Fiorentino (Italy)

Dr. L. Cerofolini,[+] K. Vasa,[+] M. Salobehaj, G. Cappelli, A. Bonciani, G. Licciardi, L. Padilla-Cortés, S. Antonacci, Dr. D. Rizzo, Prof. Dr. E. Ravera, Prof. Dr. C. Viglianisi, Prof. Dr. V. Calderone, Prof. Dr. G. Parigi, Prof. C. Luchinat, Prof. S. Menichetti,

Prof. Dr. M. Fragai
Department of Chemistry "Ugo Schiff", University of Florence
Via della Lastruccia 3-13, 50019 Sesto Fiorentino (Italy)
E-mail: stefano.menichetti@unifi.it

E. Bianconi,[+] Prof. Dr. A. Macchiarulo
Department of Pharmaceutical Sciences, University of Perugia
Via Fabretti n.48, 06123 Perugia (Italy)

Dr. A. Pérez-Ràfols, Prof. C. Luchinat
Giotto Biotech s.r.l, Sesto Fiorentino
Via della Madonna del Piano 6, 50019 Florence (Italy)

[+] These authors contributed equally to this work.

the familial amyloid polyneuropathy relies on small organic molecules that target thyroxine T$_4$ hormone binding sites.[11,12] One of these molecules, Tafamidis (2-(3,5-dichlorophenyl)benzo[*d*]oxazole-6-carboxylic acid), binds TTR at these two sites in a negative cooperative manner, but with nanomolar affinity (K$_d$s of ≈2 nM and ≈200 nM respectively), and prevents dissociation into monomers.[13] The high affinity of Tafamidis makes it an ideal anchor in the design of conjugates harboring hydrophobic cytotoxic drugs that would otherwise result poorly soluble. This strategy, but with a different high-affinity TTR ligand, has been already used to generate drug-protein conjugates with an improved selectivity against cancer cells.[14–16]

The rational design of protein-drug conjugates to maximize effectiveness, pharmacokinetics, and stability in vivo while minimizing their structural complexity is receiving more and more interest, and could benefit from highly accurate structural information from X-ray crystallography, NMR spectroscopy, and cryo-electron microscopy.[17–26] However, proteins that are covalently bound to, or that interact strongly with, relatively large drugs through long linkers can be difficult to crystallize. Furthermore, these systems are too big for NMR spectroscopy in solution, but still neither big nor rigid enough to allow for the use of cryo-electron microscopy.[27] Solid-state NMR may overcome these limitations, and it is already used to investigate non-crystalline protein samples, biologics and biomaterials.[28–39] Significant enhancements in sensitivity have been obtained by the recent achievements in the NMR probe technology and in biomolecular Dynamic Nuclear Polarization (DNP).[40–44]

We here report the design and synthesis of a new molecule that results from the conjugation of the cytotoxic Paclitaxel with Tafamidis (Scheme 1) to form a stable non-covalent protein-drug conjugate (PDC) with TTR. The design of this molecule starts with the combination of structural data from X-ray crystallography, and solution and solid-state NMR. Paclitaxel and Tafamidis are linked through a long PEGylated linker containing an easily

hydrolysable ester bond for the release of the cytotoxic agent to its pharmacological target (Taf-Ptx hereafter, Scheme 1).

The approach used for the design of this molecule, which is aimed at maintaining a high affinity for TTR, demonstrates the strength of an integrated structural biology strategy (relying upon X-ray, solution and solid-state NMR) in the structure-based design of novel PDCs.

Results and Discussion

Tafamidis was chosen to anchor Paclitaxel to TTR due to its high affinity and because it is an approved drug with minimal side effects.[45] A relaxometry analysis was carried out to investigate the stability of the tetrameric protein and the overall steadiness of protein dynamics upon ligand binding.[30,46–48] ^{1}H NMRD profiles of 1.2 mM wild-type TTR in water solutions were acquired with and without Tafamidis (shown in Figure S1). Multiple correlation times should be considered to account for many motional processes of different water protons interacting with protein (see "NMR relaxometry measurements" in the Supporting Information).[47] The analysis of the profiles indicates the major contributions from a correlation time in agreement with the overall reorientation time expected for tetrameric TTR, as calculated with HydroNMR,[49] and from a faster correlation time of few nanoseconds. In summary, the profiles indicate that i) the reorientation time is in line with that expected for a tetrameric protein assembly, ii) there are extensive internal motions, and iii) no sizable changes in the overall dynamics of the protein occur upon ligand binding.

The X-ray structure of the Tafamidis-TTR complex (PDB code: 3TCT)[13] shows the binding mode of Tafamidis (see Figure 1 and Figure S2, S3), suggesting that functionalization of the molecule on the carboxylic acid in position 6 should not affect its interaction with TTR. Therefore, a derivative of Tafamidis bearing a six carbon atoms linker in position 6 (Compound **2**) was synthesized (see Schemes 1 and S1) as a precursor of Taf-Ptx and used to soak crystals
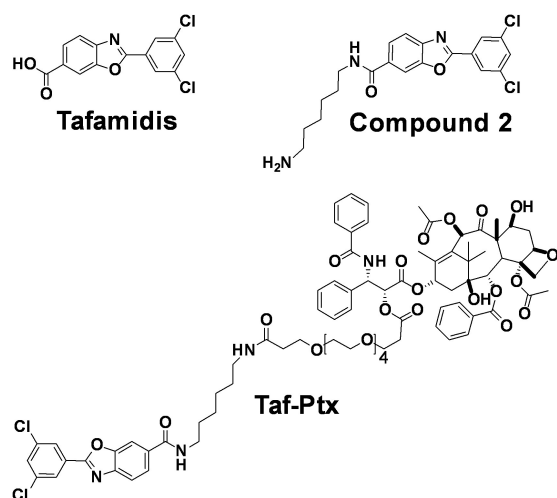
Scheme 1. Structures of Tafamidis, Compound **2**, and Taf-Ptx.
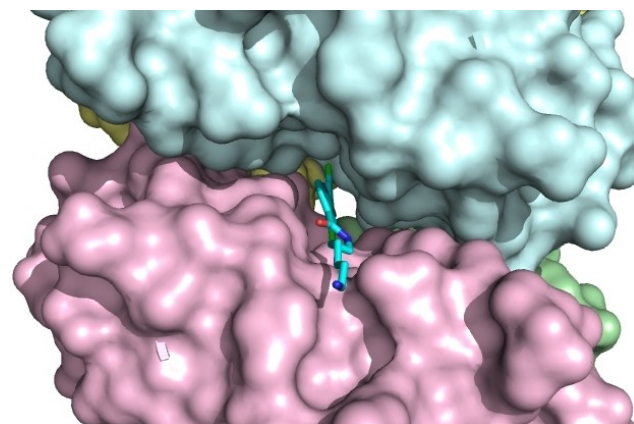
Figure 1. Detail of the surface representation of TTR interacting with compound **2** displayed as stick presented in this work (8AWW).

of TTR. The resulting X-ray structure shows that Compound **2** and Tafamidis bind TTR very similarly, and that the structure of the protein part is maintained. However, while the electron density is very well defined for all the aromatic rings in the structure of Tafamidis-bound TTR (3TCT), the Tafamidis ring that was functionalized with the hydrocarbon chain shows a weaker and less defined electron density in the structure of the adduct with Compound **2**, and this suggests a slightly higher ligand-binding heterogeneity, which in turn could be linked to a slightly lower affinity. Furthermore, the long hydrocarbon chain shows only very faint and scattered patches. This is certainly due to the mobility of this chain that is completely leaning towards the solvent. The interactions between the protein and Compound **2** are shown in Figure S4. Summarizing, the X-ray structure proves that Compound **2** preserves the binding pose of Tafamidis with the linker sticking-out from the central channel toward the solvent (see Figure 1), supporting the correct design strategy for Taf-Ptx. The X-ray structure has been deposited in the Protein Data Bank under the accession code 8AWW.

Then, the Paclitaxel molecule was conjugated to Compound **2** through an additional nineteen-atoms PEG spacer to minimize any possible steric clash with the protein and to increase the solubility. Paclitaxel is connected to the PEG spacer through an ester linkage labile in vivo,[50] which ensures its release into the cell allowing for the inhibition of tubulin polymerization.[51] As expected Taf-Ptx (Schemes 1 and S1), fails to enter the TTR crystals by soaking. Likewise, co-crystallization with TTR fails. Apparently, Taf-Ptx is too bulky, and X-ray characterization of the complex cannot be carried out. As anticipated, in cases like this, NMR could provide precious information on the structural features of the PDC, and thus validate the whole design strategy.

NMR Analysis and Assignment of Free TTR in Solution

The assignment of free tetrameric TTR in solution was obtained comparing the assignments available in the literature for the monomeric and tetrameric states of the protein,[52–55] and analyzing triple resonance spectra recorded on the perdeuterated sample of TTR. All residues (but the N-terminus, Gly-1 and Asn-98) were assigned in the spectra (Figure S5). The present assignment is the most complete and has been deposited in the bmrb under the accession code 51818.

The number of cross-peaks present in the 2D ^{1}H-^{15}N TROSY-HSQC spectrum, and the absence of signal splitting, are both consistent with the preservation of the D_2 symmetry of TTR in the tetrameric assembly. Interestingly, the signals within the same 2D spectra are characterized by different line broadening. Specifically, sharp and intense signals were observed for the residues forming loops and on the external surface of the tetramer, while broad signals were observed for the residues at the interfaces between the monomers (*i.e.*, Cys10-Lys15; His91-Phe95; Tyr105-Val121). In the 2D ^{1}H-^{15}N TROSY-HSQC spectrum recorded on the deuterated sample, these signals are also broad, suggesting

the occurrence of a conformational heterogeneity/exchange for the protein (Figure S6). These features also affect the quality of the 3D ^{1}H-^{15}N NOESY spectrum, where only few NOE correlations are visible (Figure S7). As expected for a folded protein of 55 kDa, in the 2D ^{13}C-^{15}N CON spectrum only signals of the flexible regions, which are not well-defined in most X-ray structures, can be observed (Thr3-Cy10; Ala37-Thr40; Glu51-Ser52; Asn124-Glu127; see Figure S8).

NMR Analysis and Assignment of Free TTR in the Solid-State

The solid-state NMR spectra of re-hydrated freeze-dried tetrameric TTR are of good quality and characterized by a good signal resolution (Figure S9). Nevertheless, around 20% of the expected resonances are missing and some signals are characterized by large line-broadening. Assignment of the free tetrameric protein was also obtained in the solid-state (Figure S10). The available assignment of the free protein in solution was used as starting point and complemented by the analysis of carbon-detected spectra acquired in the solid-state. The residues whose signals are missing in the spectra are mainly located at the N-terminus (up to Lys15) and in flexible regions: Asp38-Thr40, Gly57-Leu58, Phe64, Ser117-Thr119, Thr123-Asn124, Lys126. Nevertheless, as much as 80% of the spin systems of the protein could be reassigned in the solid-state NMR spectra.

NMR Analysis and Assignment of TTR-Tafamidis and TTR-Taf-Ptx in Solution

The binding-mode of Tafamidis to [U-^{13}C, ^{15}N] TTR was first analyzed by solution NMR. During the NMR titration, the cross-peaks of the free protein in the 2D ^{1}H-^{15}N TROSY-HSQC spectra decrease in intensity upon the addition of increasing concentrations of the ligand, while new cross-peaks, corresponding to the complex between TTR and Tafamidis, appear and increase in intensity. This behavior indicates that the ligand is in slow exchange regime on the NMR timescale, and confirms its expected high affinity towards the protein.[13,56] In the presence of Tafamidis at 100 μM concentration (ligand:tetramer ratio equal to 0.5:1) the cross-peaks corresponding to the free protein and to the protein bound to the ligand have similar intensities (Figure S11A), as it can be seen for the signal of Ser112 located at the interface between the dimers of the tetrameric assembly (PDB code: 3TCT).[13] During the titration the quality of spectra decreases up to a 1:1 ligand:tetramer ratio; some signals are broadened and some disappeared. The signal's line-width sharpens again at 2:1 ligand:tetramer ratio (Figure S12), in line with the lower affinity for the second binding event. The analysis of the chemical shift perturbation (CSP) was thus performed with a ligand in slight excess with respect to the 2:1 ratio. Figure S12 confirmed that the residues experiencing the largest changes (Lys15, Leu17, Ala19, Val20, Arg21, Gly22, Ser23, Ile26, Gly53, His88, Val94, Tyr105, Thr106, Ile107, Leu111,

Ser112, Ala120, Val122) are in the expected Tafamidis binding site (Figure S13). Some of the signals experiencing large perturbations (Ala19, Arg21, Gly22, Leu111) have been tentatively reassigned with some uncertainty (Figure S13A). Interestingly, the signals corresponding to residue Ser117 and Thr118, which are almost missing in the spectra of the free protein, appear with increased intensity in the spectrum of TTR in the presence of Tafamidis. This last observation is consistent with Tafamidis stabilizing the protein tetramer.

NMR titration in solution was also performed with the newly designed ligand, Taf-Ptx. The evolution of the spectra upon addition of increasing amounts of Taf-Ptx was superimposable to that previously observed for Tafamidis, with several protein resonances experiencing a slow exchange regime on the NMR timescale. After the addition of Taf-Ptx, in the presence of a ligand:tetramer ratio equal to 0.5:1, the signals of the free protein and those of the protein bound to the ligand have similar intensities (Figure S11B). As with Tafamidis, some protein signals broaden/disappear at 1:1 ligand:tetramer ratio and sharpen/reappear again in the 2:1 complex (Figure S12C and D). The analysis of CSP of the protein signals in the 2:1 complex (Figure S13B) confirmed that the residues experiencing the largest changes (Lys15, Val20, Arg21, Gly22, Ala25, Leu111, Ser112, Ala120, Val122) are in the same protein region affected by the presence of Tafamidis (Figure S13D). It is important to point out that the signals of some residues mostly affected by CSP in the spectrum of Tafamidis-TTR (Ala19, His88, Val94, Tyr105, T106) are broadened beyond detection in the spectrum of Taf-Ptx-TTR. This is probably related to the previously described slightly higher ligand-binding heterogeneity of Taf-Ptx-TTR with respect to that of Tafamidis-TTR.

NMR Analysis and Assignment of Tafamidis-TTR and Taf-Ptx-TTR in the Solid-State

Further interesting features of the complexes between TTR and Tafamidis or Taf-Ptx are revealed by solid-state NMR. The 2D solid-state NMR spectra of these complexes exhibit a higher number of cross-peaks with respect to those of the free protein. Specifically, in the 2D ^{13}C-^{13}C dipolar-assisted rotational resonance (DARR) spectrum of TTR in the presence of either Tafamidis or Taf-Ptx, several new signals appear or increase in intensity (Gly57, Arg103, Ile107, Ala108, Ser117, Thr118, Thr119, Ala120, Thr123; see Figure 2, panel A and B). This also occurs for a few signals in the 2D ^{15}N-^{13}C NCA spectra (Figure 3A and B). These signals belong to residues located at the tetramer interface, where Tafamidis binds (Figure 3, panels E and F). The increase in signal intensity can be explained by a higher rigidity of this region after the binding of Tafamidis, which is known to stabilize the tetrameric form of the protein. As shown by the high similarity of the spectra of TTR bound to one ligand or to the other, the high affinity of Tafamidis, and its stabilizing effect on the tetramer, are still present also when the Tafamidis unit is conjugated to the Paclitaxel

unit. A lower intensity of the signals corresponding to only residues S117 and T118 is observed when TTR binds to Taf-Ptx compared to when it binds to Tafamidis.

The analysis of the CSP of TTR bound to Tafamidis or Taf-Ptx with respect to the free protein indicates that the signals influenced by the ligands are largely the same. Most of the signals experiencing the largest perturbations correspond to residues at the dimer/tetramer interface (Figure 3).

To rule out the possibility that the differences, observed in the analysis of CSPs performed for solution and solid-state NMR data, are due to the comparison of different nuclei (*i.e.* ^{1}H and ^{15}N in solution, and ^{13}Cα and ^{15}N in the solid-state), the ^{15}N chemical shifts were separately compared. The analysis confirms that the largest perturbations are observed in the same areas (Figure S14).

Microscale Thermophoresis for Ligand Binding Assay

The interaction between TTR and Taf-Ptx was analyzed using a ligand binding assay with microscale thermophoresis (MST). MST detects the migration of a macromolecule in a temperature gradient, which strongly depends on size, charge, conformation and hydration shell parameters of the macromolecule. Upon a ligand binding event to the macromolecule, at least one of these parameters change, resulting in a different thermophoretic behavior.[57] In the MST experiment, 16 capillary tubes are prepared containing a fluorescent labelled protein at constant concentration and a serial titration of unlabeled ligand. An infrared laser is used to generate a temperature gradient in each tube and induce migration of the ligand-bound complex, whose fluorescence is monitored in real time. Fluorescence variations are then used to generate a binding curve as a function of ligand concentration, which is instrumental to derive the dissociation constant (K_d).[58]

MST binding experiments were performed adding Taf-Ptx to fluorescently labelled TTR (RED-TTR). A biphasic binding curve was observed, suggesting the presence of more than one Taf-Ptx binding site on RED-TTR (Figure S15A). Specifically, at low concentrations of Taf-Ptx, a first binding event is observed with the occupancy of a high affinity site by Taf-Ptx in the target protein. Then, at higher ligand concentrations, a second binding event occurs with the occupancy of a low affinity binding site. These two binding events are well separated by approximately three orders of magnitude and thus can be independently analyzed with good approximation to obtain the relative dissociation constants ($K_d1 = 0.065 \pm 0.017$ µM, Figure S15C; $K_d2 = 9.21 \pm 1.14$ µM, Figure S15B). The second dissociation constant is found lower than the first for Taf-Ptx as for Tafamidis alone, and this is consistent with the NMR observations.

Overall, these results are in agreement with the NMR measurements and with literature data,[13] supporting a high affinity interaction between Taf-Ptx and TTR with a conjugated ligand/protein stoichiometry of 2:1.
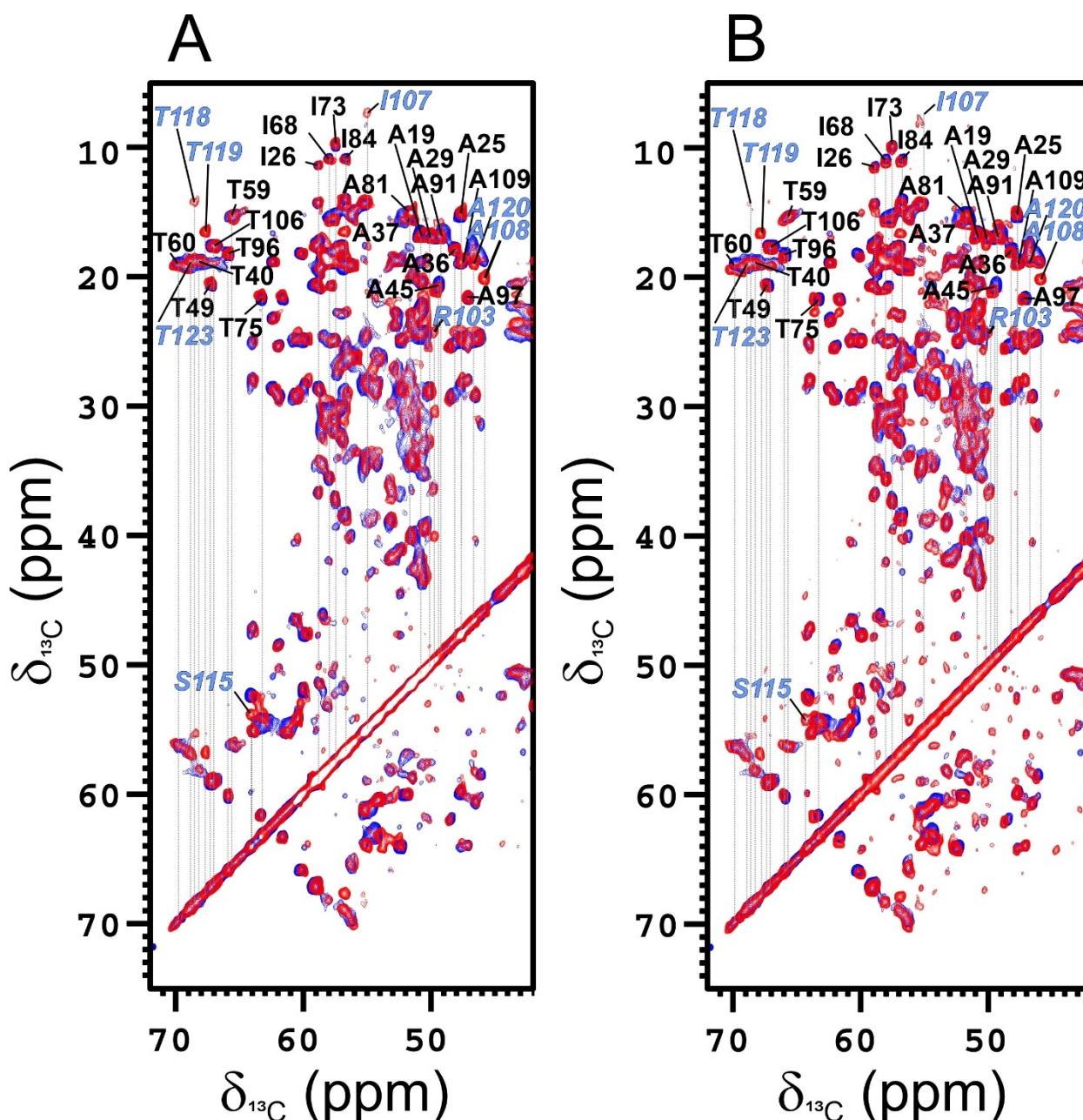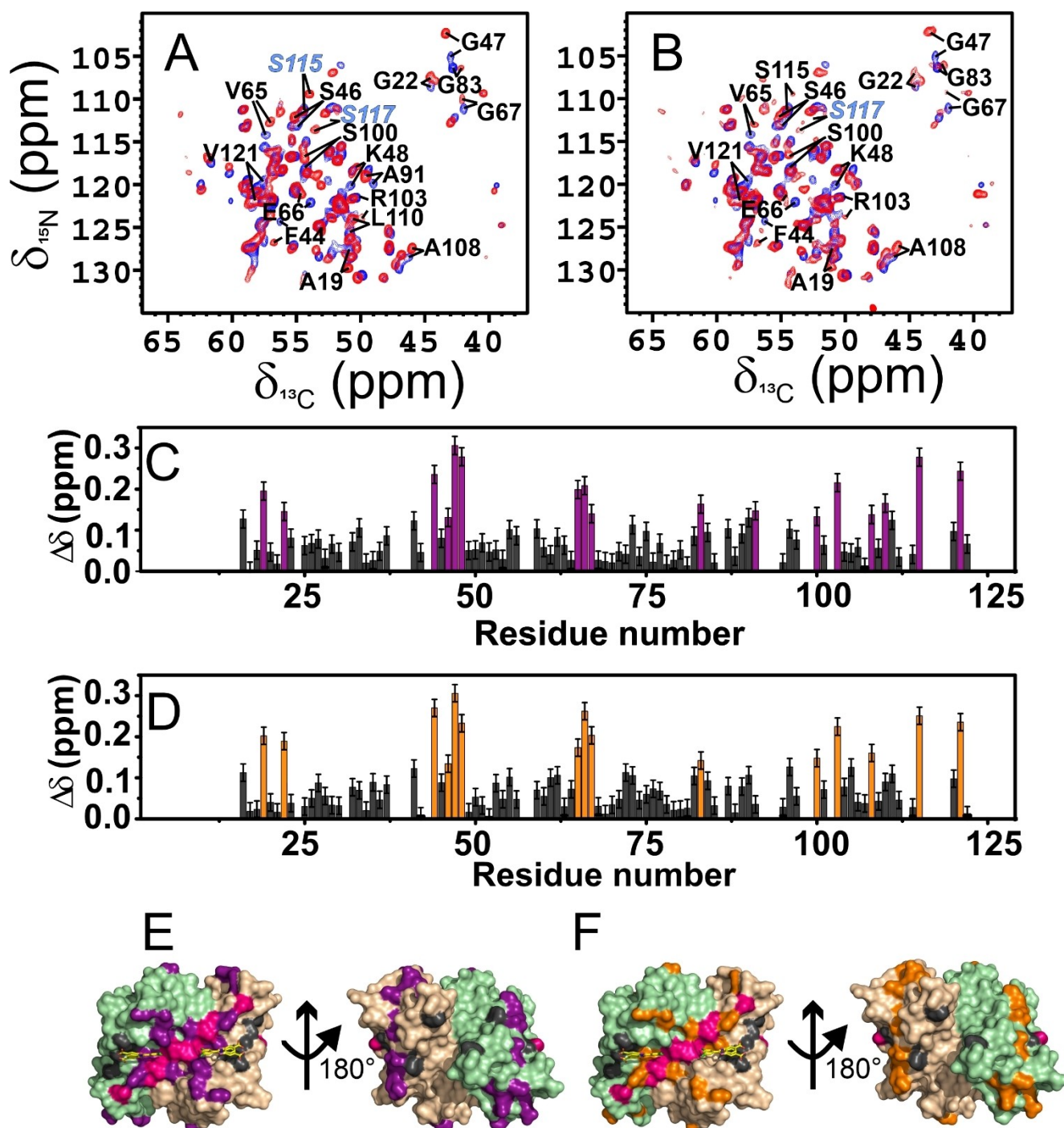
Figure 2. Comparison of a region of 2D ^{13}C-^{13}C DARR spectra (mixing time 50 ms, A, B) of free rehydrated freeze-dried TTR (blue) and TTR in the presence of the ligands (red), Tafamidis (A) or Taf-Ptx (B). The assignment of the cross-peaks related to correlations of Cβ/Cγ2 in threonine, Cα/Cδ1 in isoleucine and Cα/Cβ in alanine has been reported in the spectra. The signals with increased intensity in the spectra of TTR in complex with the ligands with respect to the free protein, have been labeled in italic font and colored in cyan. Assignment is reported also for the cross-peaks between Cβ/Cα of serine 115 and Cα/Cβ of arginine 103.

Chemical Denaturation Assay for Evaluating Taf-Ptx-Induced Stability of TTR

The impact of Taf-Ptx binding to TTR on the stability of the tetrameric protein was then evaluated using a chemical denaturation assay. Specifically, the intrinsic fluorescence of tryptophan residues (Trp41, Trp79) was monitored while denaturing the protein assembly with increasing concentrations of urea in the absence and presence of Taf-Ptx (see *Chemical denaturation assay* section in Supporting Informa-

tion). In the presence of 50 μM Taf-Ptx, the tetrameric protein complex gains stability, with the relative denaturation curve shifting rightward and not reaching an unfolding plateau (Figure S16). A ΔG value $> 47.3 \pm 2.5$ kJ mol^{-1} can be estimated in this case, suggesting a significant Taf-Ptx induced stability of TTR complex (Table S3).

Figure 3. A), B) 2D ^{15}N ^{13}C NCA spectra of free rehydrated freeze-dried TTR (blue) and TTR in the presence of the ligands (red), Tafamidis (A) or Taf-Ptx (B). Assignment has been reported for the cross-peaks experiencing the largest perturbations ($\Delta\delta \geq$ mean + std. dev.). The signals with increased intensity in the spectra of TTR in complex with the ligands with respect to the free protein, have been labeled in italic font and colored in cyan. C), D) Chemical shift perturbation (CSP) of rehydrated freeze-dried TTR in the presence of Tafamidis (C) and Taf-Ptx (D) with respect to free rehydrated freeze-dried TTR, evaluated according to the formula $\Delta\delta = \frac{1}{2}\sqrt{(\Delta\delta_{C_a}/2)^2 + (\Delta\delta_N/5)^2}$.[59] The residues experiencing the largest variations have been highlighted in violet (Ala19, Gly22, Phe44, Ser46, Gly47, Lys48, Val65, Glu66, Gly67, Gly83, Ala91, S100, Arg103, Ala108, Leu110, Ser115, Val121, for Tafamidis) and orange (Ala19, Gly22, Phe44, Ser46, Gly47, Lys48, Val65, Glu66, Gly67, Gly83, Ser100, Arg103, Ala108, Ser115, Val121, for Taf-Ptx), respectively. The error for CSP has been evaluated considering the standard deviation of the values of CSP below the mean, calculated considering all the CSP values. E), F) CSP mapping on the X-ray structure of TTR in complex with Tafamidis (PDB code: 3TCT)[13] with the residues experiencing the largest CSP in the presence of Tafamidis or Taf-Ptx colored in violet (E) and orange (F), respectively. The residues experiencing an increase in signal intensity after Tafamidis or Taf-Ptx binding have been colored in magenta. The residues missing in solid-state spectra are colored in grey. The monomers are in different colors (wheat, green) and Tafamidis is shown as yellow sticks.

Conclusion

CSP in solution are extensively used to analyze and compare the binding mode of ligands interacting with proteins or nucleic acids. For TTR the spectral changes resulting from the binding of Tafamidis or Taf-Ptx clearly point to a slow exchange regime on the NMR time scale for both ligands. Most of the residues experiencing the largest chemical shift variations on the NH resonances are placed at the interface of the two dimers and form the central channel hosting the thyroxine T4 hormone. Specifically, Lys15, Val20, Arg21, Gly22, Leu111, Ser112, Ala120, Val122 show chemical shift perturbations in the presence of both ligands, Tafamidis and Taf-Ptx. More importantly, the analysis of the X-ray structure (3TCT) of the 2:1 Tafamidis-TTR complex reveals that only Lys15, Leu17, and Thr106 appear to interact directly with the two ligand molecules among the residues experiencing the largest CSP. Therefore, the largest chemical shift perturbations appear to be mostly determined by the structural rearrangement induced by the two ligand molecules, making chemical shift mapping for the identification of the binding mode extremely challenging.

The stabilizing effect of Tafamidis was unambiguously proven in vitro and in vivo.[13,45] However, the chemical shift mapping obtained by NMR in solution provides only indirect evidence of this important structural effect, which can be inferred from the slow exchange regime on the NMR timescale of the signals corresponding to the residues where the binding occurs. In this respect, the observation of the slightly better quality of the spectra recorded on TTR in the presence of Tafamidis and Taf-Ptx is more informative.

It is important to point out that the use of solid-state NMR is critical for achieving a complete picture about the structural and dynamical features of this system. Indeed, the analysis of the data recorded on the solid-state samples of TTR in the presence and in the absence of the two ligands provides information that is out of reach for both X-ray crystallography and solution NMR. The comparative analyses on Tafamidis and Taf-Ptx were carried out using ^{15}N-^{13}C isotopically enriched samples of TTR and ^{13}C-detected experiments. The analysis of the NCA spectra shows that

TTR in complex with Tafamidis and Taf-Ptx exhibits the largest chemical shift variations on the same residues, with very few differences. This constitutes further experimental evidence of the very similar binding mode of Taf-Ptx and Tafamidis. The chemical shift variations affect several residues placed at the interface of the two dimers around the central channel as previously observed by NMR in solution. Four of these residues (Ala108, Leu110, Ser115 and Val121) are near the ligands in the X-ray structure 3TCT. The non-overlap between solution and solid-state data about the residues experiencing the largest effects is probably due to a slightly higher conformational heterogeneity of the ligand-protein complex in solution, although in both cases they are localized at the interface between the two dimers forming the assembly. This can be clearly inferred from Figure 4, where the residues experiencing the largest CSPs ($\Delta\delta \geq$ mean + std. dev.) in solution and in the solid-state are shown together.

NMRD measurements indicate that the tetrameric assembly of TTR is maintained, and possibly reinforced, in the presence of Tafamidis. However, relaxometry is not sensitive to the presence of multiple conformational states with similar reorientation time. Important information on this respect was obtained from the qualitative analysis of the signal intensity on DARR and NCA spectra. Figure 4C shows that several residues placed at the interface between the two dimers forming the assembly, including some also experiencing large chemical shift variation, increase in intensity or appear in the spectra in the presence of Tafamidis and Taf-Ptx. The increase in signal intensity or the appearance of a signal previously undetectable in the solid-state spectra is conclusive evidence of an equilibrium of the residue shifting toward a unique conformation. This is associated with the structural stabilization of the tetrameric assembly, here proven by the chemical denaturation assay, resulting from the interaction with two high affinity ligand molecules with TTR. Therefore, the analysis provides a map of the residues experiencing a decrease of the conformational heterogeneity, thus providing a different and more informative parameter to monitor the binding mode and to evaluate the effects of the interaction with the ligands. This
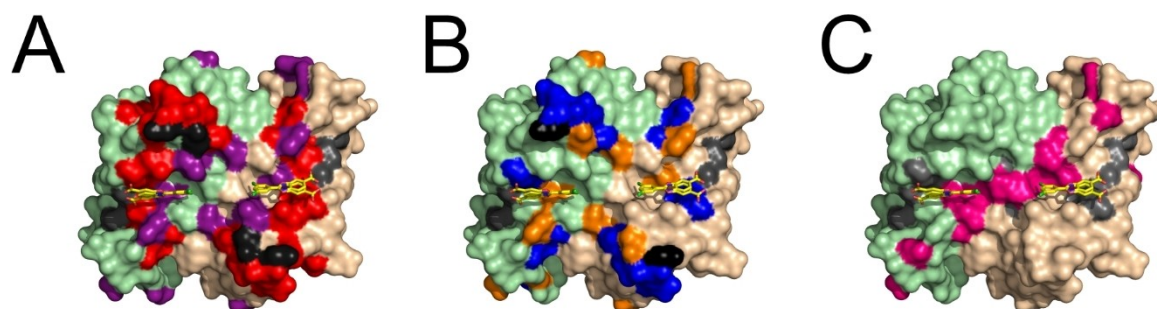
Figure 4. Comparative analysis of the NMR data collected in solution and in the solid-state of the effects of Tafamidis (A) and Taf-Ptx (B) on TTR. The residues experiencing in solution the largest CSP ($\Delta\delta \geq$ mean + std. dev.) in the presence of Tafamidis or Taf-Ptx are colored in red (A) or blue (B), respectively. The residues experiencing in the solid-state the largest CSP in the presence of Tafamidis or Taf-Ptx are colored in violet (A) or orange (B), respectively. Residues experiencing the largest CSP both in solution and in the solid state are reported in black. C) Residues experiencing in the solid-state an increase in signal intensity after the binding of Tafamidis or Taf-Ptx are colored in magenta. The residues missing in solid-state spectra are colored in grey. Monomers are in different colors (wheat, green) and Tafamidis is shown as yellow sticks.

information cannot be immediately inferred from the analysis of the CSP or from the observed improved quality of the NMR spectra recorded in solution.

When feasible, the integration of different structural biophysical methodologies is obviously the best option to develop PDCs. However, solid-state NMR can also be used on its own when the features of the investigated system prevent the use of other structural methodologies. The quality of the spectra obtained from the rehydrated freeze-dried samples, the high sensitivity of solid-state NMR to the effects of ligand binding and to small conformational heterogeneities make this technique extremely helpful to characterize the interaction of drug candidates with large monomeric/multimeric carrier proteins. In this regard, the information obtained from solid-state NMR data can be particularly important also for systems amenable to NMR characterization in solution, when the traditional chemical shift mapping based on the analysis of CSPs is not informative or resolutive.

Acknowledgements

Conflict of Interest

The authors declare no conflict of interest.

Data Availability Statement

The data that support the findings of this study are openly available in Protein Data Bank https://www.rcsb.org/ and Biological Magnetic Resonance Bank https://bmrb.io/. The raw data of the SSNMR spectra are available at https://zenodo.org under the DOI: 10.5281/zenodo.8020132.

Keywords: Drug Delivery · Drug Design · NMR Spectroscopy · Protein-Drug Conjugates · Structural Biology

[1] P. Akkapeddi, S.-A. Azizi, A. M. Freedy, P. M. S. D. Cal, P. M. P. Gois, G. J. L. Bernardes, *Chem. Sci.* **2016**, *7*, 2954–2963.

[2] R. V. J. Chari, M. L. Miller, W. C. Widdison, *Angew. Chem. Int. Ed.* **2014**, *53*, 3796–3827.

[3] J. M. Harris, R. B. Chess, *Nat. Rev. Drug Discovery* **2003**, *2*, 214–221.

[4] P. Caravan, N. J. Cloutier, M. T. Greenfield, S. A. McDermid, S. U. Dunham, J. W. M. Bulte, J. C. Amedio, R. J. Looby, R. M. Supkowski, W. D. Horrocks, T. J. McMurry, R. B. Lauffer, *J. Am. Chem. Soc.* **2002**, *124*, 3152–3162.

[5] J. Huang, B. Wu, Z. Zhou, S. Hu, H. Xu, Y. Piao, H. Zheng, J. Tang, X. Liu, Y. Shen, *Nanomedicine: Nanotechnol. Biol. Med.* **2019**, *21*, 102058.

[6] O. A. Mandrup, S. C. Ong, S. Lykkemark, A. Dinesen, I. Rudnik-Jansen, N. F. Dagnæs-Hansen, J. T. Andersen, L. Alvarez-Vallina, K. A. Howard, *Commun. Biol.* **2021**, *4*, 310.

[7] A. Zorzi, S. Linciano, A. Angelini, *MedChemComm* **2019**, *10*, 1068–1081.

[8] A. Spada, J. Emami, J. A. Tuszynski, A. Lavasanifar, *Mol. Pharmaceutics* **2021**, *18*, 1862–1894.

[9] A. D. AlQahtani, D. O'Connor, A. Domling, S. K. Goda, *Biomed. Pharmacother.* **2019**, *113*, 108750.

[10] A. W. Yee, M. Aldeghi, M. P. Blakeley, A. Ostermann, P. J. Mas, M. Moulin, D. de Sanctis, M. W. Bowler, C. Mueller-Dieckmann, E. P. Mitchell, M. Haertlein, B. L. de Groot, E. Boeri Erba, V. T. Forsyth, *Nat. Commun.* **2019**, *10*, 925.

[11] M. M. Alhamadsheh, S. Connelly, A. Cho, N. Reixach, E. T. Powers, D. W. Pan, I. A. Wilson, J. W. Kelly, I. A. Graef, *Sci. Transl. Med.* **2011**, *3*, 97ra81.

[12] M. Miller, A. Pal, W. Albusairi, H. Joo, B. Pappas, M. T. Haque Tuhin, D. Liang, R. Jampala, F. Liu, J. Khan, M. Faaij, M. Park, W. Chan, I. Graef, R. Zamboni, N. Kumar, J. Fox, U. Sinha, M. Alhamadsheh, *J. Med. Chem.* **2018**, *61*, 7862–7876.

[13] C. E. Bulawa, S. Connelly, M. DeVit, L. Wang, C. Weigel, J. A. Fleming, J. Packman, E. T. Powers, R. L. Wiseman, T. R. Foss, I. A. Wilson, J. W. Kelly, R. Labaudinière, *Proc. Natl. Acad. Sci. USA* **2012**, *109*, 9629–9634.

[14] A. Pal, W. Albusairi, F. Liu, M. T. H. Tuhin, M. Miller, D. Liang, H. Joo, T. U. Amin, E. A. Wilson, J. S. Faridi, M. Park, M. M. Alhamadsheh, *Mol. Pharmaceutics* **2019**, *16*, 3237–3252.

[15] S. C. Penchala, M. R. Miller, A. Pal, J. Dong, N. R. Madadi, J. Xie, H. Joo, J. Tsai, P. Batoon, V. Samoshin, A. Franz, T. Cox, J. Miles, W. K. Chan, M. S. Park, M. M. Alhamadsheh, *Nat. Chem. Biol.* **2015**, *11*, 793–798.

[16] F. Liu, T. Ul Amin, D. Liang, M. S. Park, M. M. Alhamadsheh, *J. Med. Chem.* **2021**, *64*, 14876–14886.

[17] J.-P. Renaud, A. Chari, C. Ciferri, W. Liu, H.-W. Rémigy, H. Stark, C. Wiesmann, *Nat. Rev. Drug Discovery* **2018**, *17*, 471–492.

[18] J. M. Lamley, D. Iuga, C. Öster, H.-J. Sass, M. Rogowski, A. Oss, J. Past, A. Reinhold, S. Grzesiek, A. Samoson, J. R. Lewandowski, *J. Am. Chem. Soc.* **2014**, *136*, 16800–16806.

[19] A. Mainz, T. L. Religa, R. Sprangers, R. Linser, L. E. Kay, B. Reif, *Angew. Chem. Int. Ed.* **2013**, *52*, 8746–8751.

[20] A. Mainz, S. Jehle, B. J. van Rossum, H. Oschkinat, B. Reif, *J. Am. Chem. Soc.* **2009**, *131*, 15968–15969.

[21] U. B. le Paige, S. Xiang, M. M. R. M. Hendrix, Y. Zhang, G. E. Folkers, M. Weingarth, A. M. J. J. Bonvin, T. G. Kutateladze,

Angew. Chem. Int. Ed. **2023**, *62*, e202303202 (8 of 9)

© 2023 The Authors. Angewandte Chemie International Edition published by Wiley-VCH GmbH

I. K. Voets, M. Baldus, H. van Ingen, *Magn. Reson.* **2021**, *2*, 187–202.

[22] L. Eshun-Wilson, R. Zhang, D. Portran, M. V. Nachury, D. B. Toso, T. Löhr, M. Vendruscolo, M. Bonomi, J. S. Fraser, E. Nogales, *Proc. Natl. Acad. Sci. USA* **2019**, *116*, 10366–10371.

[23] H. Kato, H. van Ingen, B.-R. Zhou, H. Feng, M. Bustin, L. E. Kay, Y. Bai, *Proc. Natl. Acad. Sci. USA* **2011**, *108*, 12283–12288.

[24] A. M. Gronenborn, D. R. Filpula, N. Z. Essig, A. Achari, M. Whitlow, P. T. Wingfield, G. M. Clore, *Science* **1991**, *253*, 657–661.

[25] E. Barbet-Massin, C.-T. Huang, V. Daebel, S.-T. D. Hsu, B. Reif, *Angew. Chem. Int. Ed.* **2015**, *54*, 4367–4369.

[26] D. Rizzo, L. Cerofolini, S. Giuntini, L. Iozzino, C. Pergola, F. Sacco, A. Palmese, E. Ravera, C. Luchinat, F. Baroni, M. Fragai, *J. Am. Chem. Soc.* **2022**, *144*, 10006–10016.

[27] Q. Wang, H. Yang, X. Liu, L. Dai, T. Ma, J. Qi, G. Wong, R. Peng, S. Liu, J. Li, S. Li, J. Song, J. Liu, J. He, H. Yuan, Y. Xiong, Y. Liao, J. Li, J. Yang, Z. Tong, B. D. Griffin, Y. Bi, M. Liang, X. Xu, C. Qin, G. Cheng, X. Zhang, P. Wang, X. Qiu, G. Kobinger, Y. Shi, J. Yan, G. F. Gao, *Sci. Transl. Med.* **2016**, *8*, 369ra179.

[28] S. Giuntini, L. Cerofolini, E. Ravera, M. Fragai, C. Luchinat, *Sci. Rep.* **2017**, *7*, 17934.

[29] L. Cerofolini, S. Giuntini, E. Ravera, C. Luchinat, F. Berti, M. Fragai, *npj Vaccines* **2019**, *4*, 20.

[30] L. Cerofolini, S. Giuntini, A. Carlon, E. Ravera, V. Calderone, M. Fragai, G. Parigi, C. Luchinat, *Chem. Eur. J.* **2019**, *25*, 1984–1991.

[31] E. Ravera, S. Ciambellotti, L. Cerofolini, T. Martelli, T. Kozyreva, C. Bernacchioni, S. Giuntini, M. Fragai, P. Turano, C. Luchinat, *Angew. Chem. Int. Ed.* **2016**, *55*, 2446–2449.

[32] L. Lecoq, M.-L. Fogeron, B. H. Meier, M. Nassal, A. Böckmann, *Viruses* **2020**, *12*, E1069.

[33] T. Wiegand, D. Lacabanne, A. Torosyan, J. Boudet, R. Cadalbert, F. H.-T. Allain, B. H. Meier, A. Böckmann, *Front. Mol. Biosci.* **2020**, *7*, 17.

[34] M. Lu, R. W. Russell, A. J. Bryer, C. M. Quinn, G. Hou, H. Zhang, C. D. Schwieters, J. R. Perilla, A. M. Gronenborn, T. Polenova, *Nat. Struct. Mol. Biol.* **2020**, *27*, 863–869.

[35] M. T. Eddy, T.-Y. Yu, G. Wagner, R. G. Griffin, *J. Biomol. NMR* **2019**, *73*, 451–460.

[36] M. Fragai, C. Luchinat, T. Martelli, E. Ravera, I. Sagi, I. Solomonov, Y. Udi, *Chem. Commun.* **2014**, *50*, 421–423.

[37] K. Jaudzems, A. Kirsteina, T. Schubeis, G. Casano, O. Ouari, J. Bogans, A. Kazaks, K. Tars, A. Lesage, G. Pintacuda, *Angew. Chem. Int. Ed.* **2021**, *60*, 12847–12851.

[38] D. Rizzo, L. Cerofolini, A. Pérez-Ràfols, S. Giuntini, F. Baroni, E. Ravera, C. Luchinat, M. Fragai, *Anal. Chem.* **2021**, *93*, 11208–11214.

[39] S. Gupta, R. Tycko, *J. Biomol. NMR* **2018**, *70*, 103–114.

[40] R. Gupta, H. Zhang, M. Lu, G. Hou, M. Caporini, M. Rosay, W. Maas, J. Struppe, J. Ahn, I.-J. L. Byeon, H. Oschkinat, K. Jaudzems, E. Barbet-Massin, L. Emsley, G. Pintacuda, A. Lesage, A. M. Gronenborn, T. Polenova, *J. Phys. Chem. B* **2019**, *123*, 5048–5058.

[41] T. Azaïs, S. Von Euw, W. Ajili, S. Auzoux-Bordenave, P. Bertani, D. Gajan, L. Emsley, N. Nassif, A. Lesage, *Solid State Nucl. Magn. Reson.* **2019**, *102*, 2–11.

[42] J. Viger-Gravel, F. M. Paruzzo, C. Cazaux, R. Jabbour, A. Leleu, F. Canini, P. Florian, F. Ronzon, D. Gajan, A. Lesage, *Chem. Eur. J.* **2020**, *26*, 8976–8982.

[43] A. Hassan, C. M. Quinn, J. Struppe, I. V. Sergeyev, C. Zhang, C. Guo, B. Runge, T. Theint, H. H. Dao, C. P. Jaroniec, M. Berbon, A. Lends, B. Habenstein, A. Loquet, R. Kuemmerle, B. Perrone, A. M. Gronenborn, T. Polenova, *J. Magn. Reson.* **2020**, *311*, 106680.

[44] R. Zhang, Y. Hong, T. Ravula, Y. Nishiyama, A. Ramamoorthy, *J. Magn. Reson.* **2020**, *313*, 106717.

[45] M. S. Maurer, J. H. Schwartz, B. Gundapaneni, P. M. Elliott, G. Merlini, M. Waddington-Cruz, A. V. Kristen, M. Grogan, R. Witteles, T. Damy, B. M. Drachman, S. J. Shah, M. Hanna, D. P. Judge, A. I. Barsdorf, P. Huber, T. A. Patterson, S. Riley, J. Schumacher, M. Stewart, M. B. Sultan, C. Rapezzi, *N. Engl. J. Med.* **2018**, *379*, 1007–1016.

[46] I. Bertini, M. Fragai, C. Luchinat, G. Parigi, *Magn. Reson. Chem.* **2000**, *38*, 543–550.

[47] G. Parigi, E. Ravera, M. Fragai, C. Luchinat, *Prog. Nucl. Magn. Reson. Spectrosc.* **2021**, *124–125*, 85–98.

[48] E. Ravera, G. Parigi, A. Mainz, T. L. Religa, B. Reif, C. Luchinat, *J. Phys. Chem. B* **2013**, *117*, 3548–3553.

[49] J. García de la Torre, M. L. Huertas, B. Carrasco, *J. Magn. Reson.* **2000**, *147*, 138–146.

[50] J. Brunetti, S. Piantini, M. Fragai, S. Scali, G. Cipriani, L. Depau, A. Pini, C. Falciani, S. Menichetti, L. Bracci, *Molecules* **2020**, *25*, E1088.

[51] J. Brunetti, S. Pillozzi, C. Falciani, L. Depau, E. Tenori, S. Scali, L. Lozzi, A. Pini, A. Arcangeli, S. Menichetti, L. Bracci, *Sci. Rep.* **2015**, *5*, 17736.

[52] K. Liu, J. W. Kelly, D. E. Wemmer, *J. Mol. Biol.* **2002**, *320*, 821–832.

[53] J. Oroz, J. H. Kim, B. J. Chang, M. Zweckstetter, *Nat. Struct. Mol. Biol.* **2017**, *24*, 407–413.

[54] B. I. Leach, X. Zhang, J. W. Kelly, H. J. Dyson, P. E. Wright, *Biochemistry* **2018**, *57*, 4421–4430.

[55] Y.-T. Liu, Y.-J. Yen, F. Ricardo, Y. Chang, P.-H. Wu, S.-J. Huang, K.-P. Lin, T.-Y. Yu, *Ann. Clin. Transl. Neurol.* **2019**, *6*, 1961–1970.

[56] A. Corazza, G. Verona, C. A. Waudby, P. P. Mangione, R. Bingham, I. Uings, D. Canetti, P. Nocerino, G. W. Taylor, M. B. Pepys, J. Christodoulou, V. Bellotti, *J. Med. Chem.* **2019**, *62*, 8274–8283.

[57] S. Duhr, D. Braun, *Proc. Natl. Acad. Sci. USA* **2006**, *103*, 19678–19682.

[58] M. Jerabek-Willemsen, C. J. Wienken, D. Braun, P. Baaske, S. Duhr, *Assay Drug Dev. Technol.* **2011**, *9*, 342–353.

[59] S. Grzesiek, A. Bax, G. M. Clore, A. M. Gronenborn, J. S. Hu, J. Kaufman, I. Palmer, S. J. Stahl, P. T. Wingfield, *Nat. Struct. Biol.* **1996**, *3*, 340–345.

Angewandte Chemie

Supporting Information

Combining Solid-State NMR with Structural and Biophysical Techniques to Design Challenging Protein-Drug Conjugates

L. Cerofolini, K. Vasa, E. Bianconi, M. Salobehaj, G. Cappelli, A. Bonciani, G. Licciardi, A. Pérez-Ràfols, L. Padilla-Cortés, S. Antonacci, D. Rizzo, E. Ravera, C. Viglianisi, V. Calderone, G. Parigi, C. Luchinat, A. Macchiarulo, S. Menichetti*, M. Fragai*

Table of content

EXPERIMENTAL METHODS

Expression and purification of [U-^{2}H, ^{13}C, ^{15}N] and [U- ^{13}C, ^{15}N] TTR.

Escherichia coli BL21(DE3) RIPL PLysS cells were transformed with pET-28a(+) plasmid encoding human TTR gene. For the expression of [U- ^{13}C, ^{15}N] TTR, cells were grown in M9 minimal media supplemented with ^{15}NH$_4$Cl and ^{13}C-glucose. For the expression of [U-^{2}H, ^{13}C, ^{15}N] TTR, cells were inoculated into 10 cm^3 of Silantes OD2 medium and scaled up to 1 dm^3 of the same enriched medium. The same experimental protocol was used to purify the samples of [U- ^{13}C, ^{15}N] TTR and [U-^{2}H, ^{13}C, ^{15}N] TTR. Cells were grown at 37 ºC until optical density (OD$_{600}$) reached 0.6-0.8. Expression was induced with 1 mmol·dm^{-3} of isopropyl β-D-thiogalactoside (IPTG), cells were incubated at 37 ºC overnight and harvested by centrifugation at 4 ºC, for 15 min at 7500 rpm. Cell pellet was resuspended in lysis buffer [20 mmol·dm^{-3} Tris-HCl, pH 8.6, 5 mmol·dm^{-3} DTT, 1 mmol·dm^{-3} protease inhibitors], physically disrupted by sonication and centrifugated at 30000 rpm for 35 min at 4 °C. Soluble fraction was collected and purified using an Anion exchange Q FF 16/10 column previously equilibrated in the lysis buffer. Elution was performed with increasing gradients of NaCl (60 cm^3 of 0-200 mmol·dm^{-3}, 300 cm^3 of 0.2-0.5 mol·dm^{-3}, 60 cm^3 of 0.5-1.0 mol·dm^{-3} and 60 cm^3 of 1 mol·dm^{-3}) in the buffer. An SDS-PAGE was performed to identify which fractions contained the protein. The protein was further purified by size exclusion chromatography using a Hi Load 26/60 Superdex 75 pg column previously equilibrated in the final buffer [50 mmol·dm^{-3} MES-NaOH, pH 6.5, 0.1 mol·dm^{-3} NaCl, 5 mmol·dm^{-3} DTT, 1 mmol·dm^{-3} protease inhibitors].

Synthesis of Taf-Ptx.

Taf-Ptx (**5**) was synthesized as reported in Scheme S1. In a reaction flask, HATU (190 mg, 0.50 mmol) was solubilized in 6 cm^3 of DMF, then Tafamidis (170 mg, 0.55 mmol), DIPEA (142 mg, 1.1 mmol) and a solution of tert-butyl (6-aminohexyl) carbamate (108 mg, 0.50 mmol) in DMF were added. The solution was stirred at room temperature for 12 h. Control TLC was performed (EP : AcOEt = 2 : 1). Subsequentially the mixture was diluted with H$_2$O, and NH$_4$Cl saturated solution was added until pH = 7. Extractions were performed with AcOEt (10x10 cm^3) and then washes with H$_2$O (3x20 cm^3) were carried out. The organic layer was dried under anhydrous Na$_2$SO$_4$, following filtration and evaporation of the solvent under reduced pressure to give the crude product **1** in 90% yield. Then, in a vial product **1** (50 mg, 0.1 mmol) was solubilized in 3.2 cm^3 of DCM and the solution was cooled to 0 °C. Subsequentially 0.3 cm^3 of TFA was added dropwise. The mixture was stirred at room temperature for 4 h. TLC control was performed to verify reaction completion (EP : AcOEt = 2 : 1). The mixture was diluted with 20 cm^3 of DCM and pH adjusted to 7-8 with NaHCO$_3$ saturated solution. Extractions were performed with DCM (3x20 cm^3) and the organic layer was dried over

anhydrous Na_2SO_4, following filtration and evaporation of the solvent under reduced pressure to give product **2** in 66% yield. To obtain product **4**, DMAP (1.35 mg, 0.012 mmol) was added to a solution of paclitaxel (100 mg, 0.12 mmol) in 16 cm^3 of anhydrous DCM under nitrogen flow. The solution was cooled to 0 °C and 4,7,10,13,16 - pentaoxanonadecanedioic acid (**3**) (81.20 mg, 0.24 mmol) and then DIC (19 mm^3, 0.12 mmol) were added. The reaction mixture was stirred at room temperature for 24 h. Control TLC were performed to monitor the reaction using as eluent (DCM : MeOH : AcOEt = 8 : 1 : 2). The mixture was diluted with 20 cm^3 of DCM, washed with a saturated solution of NH_4Cl (3x40 cm^3) and H_2O (6x20 cm^3). The organic layer was dried over anhydrous Na_2SO_4, following filtration and evaporation of the solvent under reduced pressure to give the crude product. After purification by silica column chromatography (DCM : MeOH : AcOEt = 8 : 1 : 4) product **4** was obtained in 65% yield. To obtain the final product **5** (Taf-Ptx), in a reaction flask, HATU (8 mg, 0.021 mmol) was solubilized in 0.25 cm^3 of DCM then **4** (27 mg, 0.023 mmol), DIPEA (6 mg, 0.046 mmol) and a solution of **2** (10 mg, 0.025 mmol) in 0.25 cm^3 of DCM were added. The reaction mixture was stirred at room temperature for 24 h. Control TLC was performed to monitor the reaction (DCM : MeOH : AcOEt = 10 : 1 : 2). The mixture was diluted with 10 cm^3 of DCM and washed with a saturated solution of NH_4Cl (3x20 cm^3), H_2O (3x20 cm^3). Solvent was dried under Na_2SO_4, following filtration and evaporation of the solvent under reduced pressure to give the crude product. After purification by silica column chromatography (DCM : MeOH : AcOEt = 6 : 1 : 2) Taf-Ptx (**5**) was obtained in 22% yield.
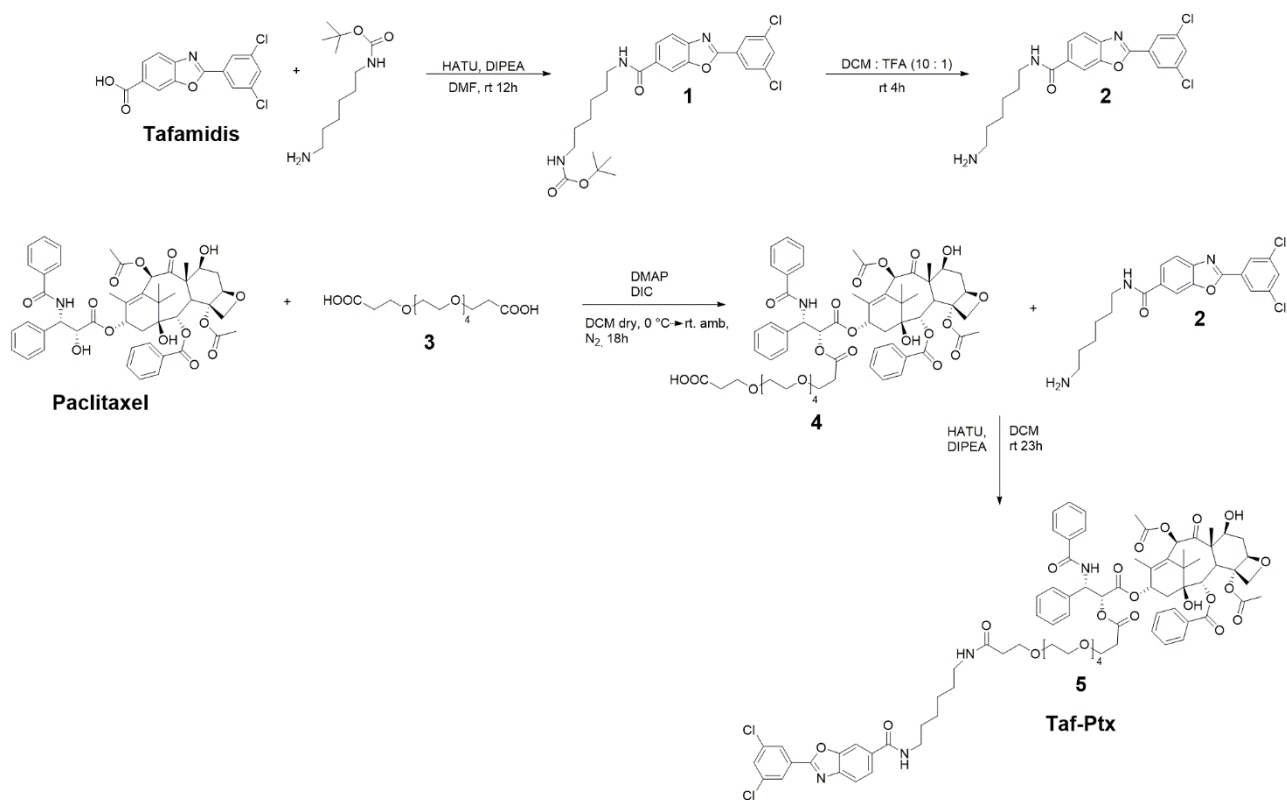
Scheme S1. Synthesis of Taf-Ptx.

Crystallization, Data Collection and Structure Solution.

Crystals of apo TTR were obtained in sitting drop by adding an aliquot of 10 mm^3 of protein solution in the final buffer [50 mmol·dm^{-3} MES-NaOH, pH 6.5, 0.1 mol·dm^{-3} NaCl, 5 mmol·dm^{-3} DTT, 1 mmol·dm^{-3} protease inhibitors] to 10 mm^3 of crystallization buffer [100 mmol·dm^{-3} HEPES – NaOH, pH 7.5, 400 mmol·dm^{-3} CaCl$_2$, 34% PEG400].[1] The reservoirs were filled with 800 mm^3 of crystallization buffer and the plates were incubated at 20 °C. The protein concentration in the sample was 10 mg·cm^{-3}. The native crystals of apo TTR were afterwards soaked in a solution containing the compound **2** with a 1 mmol·dm^{-3} concentration with respect to the protein for about some days. The dataset was collected in-house, using a BRUKER D8 Venture diffractometer equipped with a PHOTON III detector, at 100 K; the crystal used for data collection were cryo-cooled using 10% ethylene glycol in the mother liquor. The crystal diffracted up to 1.5 Å resolution but the structure was refined at 1.6 Å: it belongs to space group P2$_1$2$_1$2 with two molecules in the asymmetric unit, a solvent content of about 50%, and a mosaicity of 0.3°. The data were processed using the program XDS,[2] reduced and scaled using XSCALE[2] and amplitudes were calculated using XDSCONV.[2] The structure was solved using the molecular replacement technique; the model used was 3TCT.[3] The successful orientation hand translation of the molecule within the crystallographic unit cell was determined with MOLREP.[4] The refinement and water molecule fitting were carried out using PHENIX.[5] In between the refinement cycles, the model was subjected to manual rebuilding

S5

using COOT.[6] The quality of the refined structure was assessed using the program MOLPROBITY.[7] Data processing and refinement statistics are shown in Table S1. Coordinates and structure factors have been deposited at the PDB under the accession code 8AWW.

Figure S2 shows the superposition between the structure presented in this work and 3TCT (just one monomer for both structures is presented for clarity), with a RMSD of backbone atoms as low as 0.82 Å: it appears that the only deviations are in external loops, whereas the other regions show a negligible RMSD. As in the case of 3TCT, there is a peculiar crystallographic feature concerning the ligand: it sits with the longitudinal axis crossing the aromatic rings almost coincident with the crystallographic two-fold axis. This situation implies that the refinement has to be carried out by placing the ligand in the density at half occupancy; the application of the crystallographic symmetry itself generates a symmetry mate for the ligand, which is slightly tilted about the above mentioned two-fold axis (Figure S3).

NMR measurements

NMR relaxometry measurements. [1]H nuclear magnetic relaxation dispersion (NMRD) profiles were obtained for water solution samples of the free-TTR and of the protein in complex with Tafamidis, by measuring the water proton relaxation rates, R_1, as a function of the applied magnetic field. The profiles were recorded with a SPINMASTER2000 fast field cycling relaxometer (Stelar, Mede (PV), Italy) operating in the 0.01–40 MHz, [1]H Larmor frequency range. The measurements are affected by an error of about ±1%, as obtained in the field cycling experiment from the fit to a mono-exponential decay/recovery of the magnetization.

^{1}H NMRD profiles of 1.2 mmol·dm^{-3} wild-type TTR in water solutions were acquired with and without Tafamidis at three different temperatures (shown in Figure S1). At each temperature, the profiles are close to one another, indicating that no sizable changes in the overall dynamics of the protein occur upon addition of the ligand. The profiles report the field dependent relaxation rates of water protons, which interact with the protein protons. As expected, the observed relaxation rates increase with decreasing temperature due to their dependence on the molecular reorientation correlation time. Multiple correlation times must however be considered to account for the many motional processes of the different water protons interacting with the protein.[8] The profiles were fitted as the sum of multiple relaxation contributions arising from different correlation times τ_i, according to the model-free approach:[8,9]

$$R_1 = \alpha + \beta \sum_i^N c_i \left(\frac{\tau_i}{1+\omega^2\tau_i^2} + \frac{4\tau_i}{1+4\omega^2\tau_i^2} \right)$$

where c_i are weight coefficients summing to 1. The parameter β depends on the squared proton-proton dipole–dipole interaction energy and on the protein concentration, and the coefficients c_i report on the contributions from protons with the associated correlation times. The parameter α takes into account the contribution to water relaxation from protons with correlation times smaller than few ns (*i.e.*, with a dispersion occurring beyond the highest magnetic field). In order to reduce the covariance among the many unknown parameters, ^{1}H NMRD profiles at the same temperature were fitted simultaneously with common values of the correlation times. This allowed to better monitor differences in the values of c_i. The parameter β was also constrained to be the same because of the same protein conditions and concentration.

The analysis of the profiles indicates the major contributions from a correlation time of 30 ns at 25 °C, with a weight coefficient of ca. 0.3, and from a correlation time of few nanoseconds, with weight coefficient of ca. 0.7 (see Table S2). The correlation time of 30 ns is in nice agreement with the overall reorientation time expected for tetrameric TTR as calculated with HydroNMR.[49] The shorter correlation time reports on the internal protein mobility and it is found not to be significantly affected by ligand binding.

Solution NMR experiments on free-TTR. Solution NMR experiments for backbone resonance assignment with a TROSY scheme[10] [3D tr-HNCA, tr-HNCACB, tr-HNCO, tr-HN(CA)CO][11–16] were performed on perdeuterated [U-^{2}H, ^{13}C, ^{15}N] samples of native TTR (at the concentration of 500 μmol·dm-3 with respect to the monomer) in water buffer solution [50 mmol·dm^{-3} MES, pH 6.5, 100 mmol·dm^{-3} NaCl, 5 mmol·dm^{-3} DTT, 0.1% NaN₃, protease inhibitors (Roche)]. For 3D tr-HNCACB and tr-HN(CA)CO nonuniform random sampling at 57% and 25%, respectively, and compressed-sensing reconstruction were used.[17] A 3D [1]H-^{15}N NOESY-TROSY spectrum (mixing time 100 ms) was also acquired to help and confirm the sequential assignment. All the spectra were recorded at 310 K on Bruker AVANCE MHD and AVANCE NEO NMR spectrometers, operating at 950 and 900 MHz ([1]H Larmor frequency), respectively, and equipped with triple resonance cryo-probes. Two-dimensional carbon-detected solution ^{13}C-^{15}N CON NMR spectrum was acquired on a Bruker AVANCE NEO 700 MHz spectrometer, equipped with a triple-resonance cryo-probe optimized for ^{13}C-direct detection.[18,19]

Solution NMR experiments on TTR/Tafamidis and TTR/Taf-Ptx complexes. The titration with Tafamidis was performed using uniformly ^{13}C, ^{15}N-isotopically enriched [U-^{13}C, ^{15}N] TTR at the concentration of 800 μmol·dm^{-3} (with respect to the monomer) in 50 mmol·dm^{-3} MES buffer at pH 6.5, with 100 mmol·dm^{-3} NaCl, 5 mmol·dm^{-3} DTT, 0.1% NaN₃ and protease inhibitors (Roche). Increasing aliquots of the ligand (solubilized in DMSO-d₆), to reach the final concentrations in solution of 25, 50, 100, 200, 400 and 800 μmol·dm^{-3}, were added to TTR solution and 2D [1]H-[15]N

TROSY-HSQC acquired at 950 MHz after each addition. The binding of Taf-Ptx to TTR was also assessed by an NMR titration in solution. Increasing aliquots of the ligand (solubilized in DMSO-d_6) were added to the solution of [U-^{13}C, ^{15}N] TTR [~ 400 µmol·dm^{-3}, with respect to the monomer, in 50 mmol·dm^{-3} MES buffer at pH 6.5, with 100 mmol·dm^{-3} NaCl, 5 mmol·dm^{-3} DTT, 0.1% NaN$_3$ and protease inhibitors (Roche)] and 2D ^{1}H-^{15}N TROSY-HSQC acquired at 950 MHz after each addition. After both titrations, the excess of the ligands was removed using PD10 column and the buffer exchanged to 10 mmol·dm^{-3} MES, pH 6.5 and 20 mmol·dm^{-3} NaCl. PEG1000 (in 1:10 weight ratio with respect to the protein) was added to protect the protein during the lyophilization process. The solutions (containing ~ 6-8 mg of protein/ligand, 0.6-0.8 mg of PEG1000, 1 mg MES, 0.7 mg NaCl) were freeze-dried and the materials used to pack 3.2 mm zirconia thick wall rotors. The materials were then rehydrated by multiple additions of MilliQ H$_2$O until the resolution of the 1D {^{1}H}^{13}C CP solid-state NMR spectra stopped changing.[20] Silicon plugs (courtesy of Bruker Biospin) placed below the turbine cap were used to close the rotor and preserve hydration.

A sample of [U-^{13}C, ^{15}N] free TTR lyophilized in the presence of PEG1000 (in the same weight ratio, 25 mg TTR: 2.5 mg PEG1000) was also analyzed in 3.2 mm zirconia rotor after rehydration, as reference for solid-state NMR.

The solid-state NMR spectra of free TTR and TTR in the presence of Tafamidis or Taf-Ptx were collected on a Bruker Avance III spectrometer operating at 800 MHz (18.8 T, 201.2 MHz ^{13}C Larmor frequency) equipped with a Bruker 3.2 mm Efree NCH probe-head and on a Bruker Avance III 850 MHz wide-bore spectrometer (20 T, 213.6 MHz ^{13}C Larmor frequency), equipped with 3.2 mm DVT MAS probe head in triple-resonance mode. The spectra were recorded at 14 kHz MAS frequency and the sample temperature was kept at ~ 290 K.

Standard ^{13}C-detected solid-state NMR spectra [2D ^{15}N-^{13}C NCA, ^{15}N-^{13}C NCO and ^{13}C-^{13}C DARR; 3D NCACX and NCOCX] were acquired on the samples in 3.2 mm rotors, using the pulse sequences reported in the literature.[21–27] 3D CANCO experiment was also acquired on the sample of free TTR.

All the spectra were processed with the Bruker TopSpin 3.2 software and analyzed with the program CARA.[28]

Ligand binding assay with Microscale Thermophoresis (MST).

TTR was fluorescently labelled with RED dye NT-650-NHS of Monolith Protein Labelling Kit RED-NHS 2nd generation (NanoTemper Technologies, Munich, Germany) according to NanoTemper protocol, using 1:4 as protein:dye ratio. Therefore, 100 mm^3 of 20 µmol·dm-3 TTR in labelling buffer (130 mmol·dm-3 NaHCO$_3$, 50 mmol·dm-3 NaCl, pH 8.2) was prepared and mixed

with 100 mm³ of 80 µmol·dm-3 RED-dye in the same buffer. The labelling solution was incubated for 30 minutes in the dark at RT and then the unreached fluorophore was removed using two size-exclusion chromatography columns, equilibrated with phosphate buffer (PB, 100 mmol·dm-3 NaH₂PO₄, 100 mmol·dm-3 KCl, pH 7.6). Protein and dye concentrations were calculated by Absorption Spectroscopy (AS) using Thermo Scientific™ NanoDrop™ One spectrophotometer (Thermo Fisher Scientific Inc., Waltham Massachusetts, USA), through the equation 1 and 2 for TTR and RED dye, respectively. Where $\varepsilon_{protein} = 18575$ M-1 cm^{-1} at 280 nm, $\varepsilon_{RED-dye} = 195000$ M^{-1} cm^{-1} at 650 nm, cf = 0.04 and l is the pathlength.

$$[protein] = \frac{A_{280} - (A_{650} \times cf)}{\varepsilon_{protein} \times l} \quad (Equation\ 1)$$

$$[dye] = \frac{A_{650}}{\varepsilon_{RED\ dye} \times l} \quad (Equation\ 2)$$

Therefore, the degree of labelling (DOL) was calculated using the equation 3, yielding a value of 0.5 that falls in the recommended range (0.5 – 1).

$$DOL = \frac{[dye]}{[protein]} \quad (Equation\ 3)$$

In order to evaluate the affinity between the protein and Taf-Ptx, 16 pre-dilutions of molecule were prepared through 1:1 serial dilution with PB with 0.05% tween20 (PB-T) and 4% DMSO in PCR tubes to yield final volume of 10 mm³. RED-TTR was diluted to achieve a final protein concentration of 100 nmol·dm-3. Therefore, the labelled protein was added to each of 16 dilutions and mixed to reach a final protein concentration of 50 nmol·dm-3 and a reaction volume of 20 mm³ in PB-T, 1 mmol·dm-3 EDTA 2 % DMSO. The molecule was tested at the highest concentration of 50 µmol·dm-3. Samples were incubated at RT, in the dark for 5 minutes, loaded in Standard capillaries and inserted into the chip tray of Monolith NT.115. MST signal of each capillary was recorded at 40% LED power and Medium MST power. Raw data were analysed using in MO.Affinity Analysis software v2.3 (NanoTemper Technologies, Munich, Germany) in Manual mode, setting the hot region between 19/20 s.

Each experiment was repeated three times and the results were reported as dissociation constant (K_d) mean value ± confidence intervals, the latter defining the range where the K_d falls with a 69% of certainty. The Signal to Noise (S/N) parameter was also calculated and used to judge data quality. Specifically, $5 \leq S/N \leq 12$ suggests a good assay, whereas S/N > 12 indicates an excellent

assay. All MST experiments were carried out using a Monolith NT.115 NanoTemper instrument, yielding S/N values > 12 as indicative of excellent assay conditions.

Chemical denaturation assay

The chemical denaturation assay was performed using a label-free fluorimetric analysis using Prometheus NT.48 instrument (NanoTemper Technologies, Munich, Germany). Briefly, a protein sample of 5 $\mu mol \cdot dm^{-3}$ TTR was incubated with n.48 serial dilutions of urea (from 6 $mol \cdot dm^{-3}$ to 1.3 $mol \cdot dm^{-3}$) in the presence and absence of 50 $\mu mol \cdot dm^{-3}$ Taf-Ptx for a time of 96 h at room temperature (20°C) to reach the equilibrium of the chemical unfolding reaction. A longer time of incubation was avoided to prevent an excessive decomposition of the denaturant agent and formation of covalent adducts in the protein sample. The assays were executed in a buffer composed of 100 $mmol \cdot dm^{-3}$ NaH_2PO_4, 100 $mmol \cdot dm^{-3}$ KCl, pH 7.6, 2% DMSO. After the incubation, the samples were loaded into nanoDSF standard capillaries and the fluorescence emission was detected using PR.ChemControl software. During the denaturation process, the increasing solvent exposure of the buried tryptophan (Trp79) from the folded state to the unfolded form of TTR generates a shift of the fluorescence emission from 330 nm to 350 nm. The ratio 350 nm/330 nm was then plotted versus the concentration of the denaturant agent to obtain the denaturation curves (Figure S16).

The raw data were analyzed using PR.Stability Analysis v1.1 software applying a two-state model to calculate the free energy of protein stability (ΔG) and the concentration of denaturant to achieve 50% of protein unfolding (C_{50}). Data are reported as mean values ± standard deviations (SD) from n.3 independent measurements (Table S3).
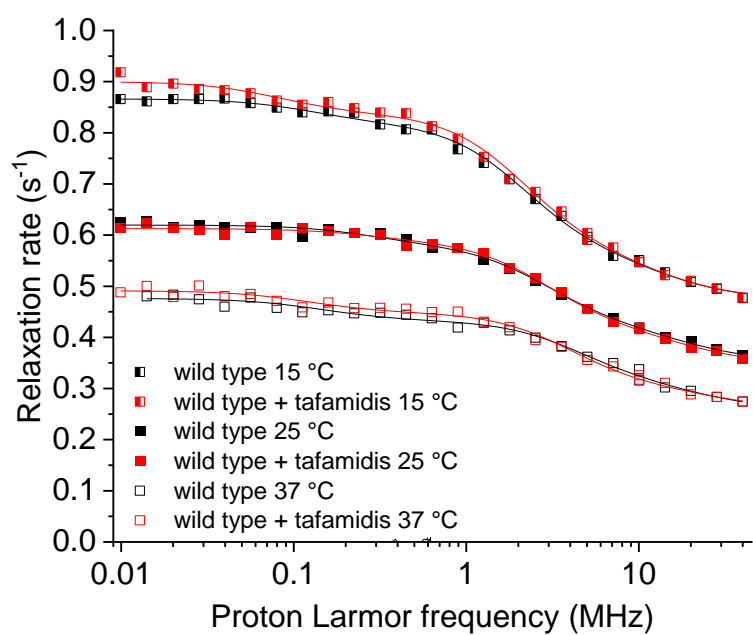
Figure S1. ^{1}H NMRD profiles of wild-type TTR, in the absence and in the presence of Tafamidis at 15, 25 and 37 °C.
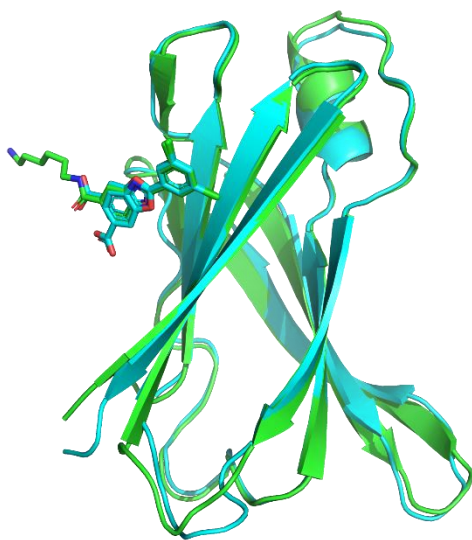
Figure S2. Superposition between the structure presented in this work, 8AWW (green), and 3TCT (cyan). One monomer for both structure is presented for clarity.
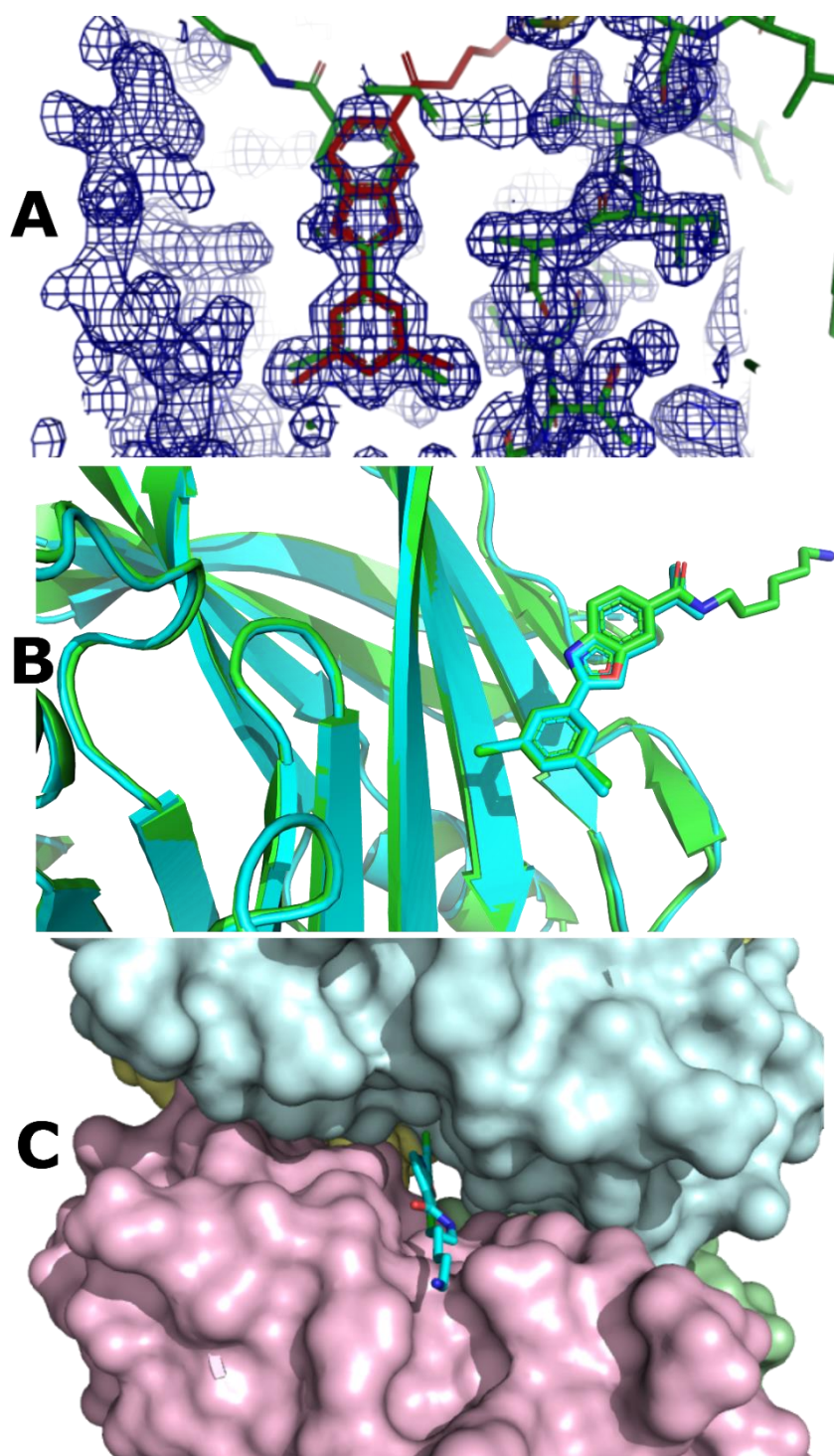
Figure S3. Detail of the protein and ligand electron density map for the complex between TTR and Compound **2** (compound 2 and the symmetry mate generated by the application of the two-fold crystallographic operation are shown) (**A**). Superposition between the structure presented in this work (8AWW, green) and 3TCT (cyan) (**B**). Surface representation of TTR interacting with one of the two possible conformations of Compound **2** displayed as stick (**C**). In all the three panels, the conformation of the aliphatic chain of Compound **2** is arbitrarily defined.
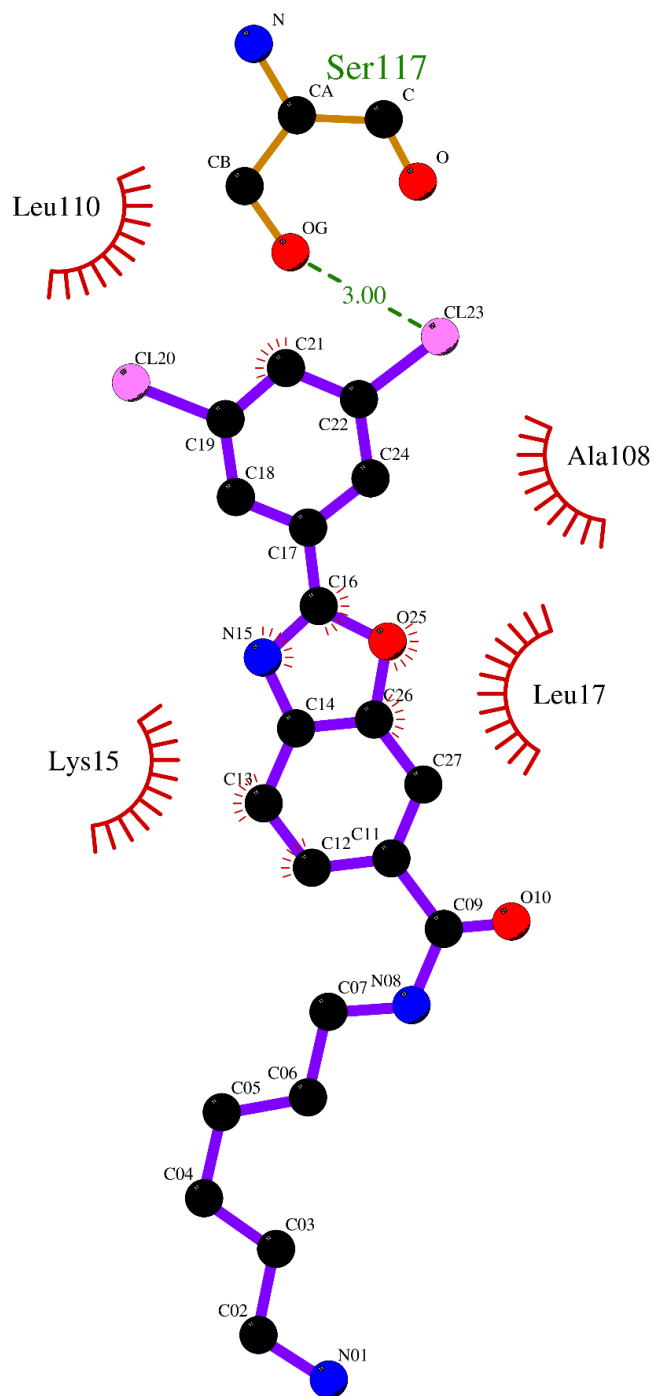
Figure S4. Interactions between the protein and Compound **2** observed in the X- ray structure solved in the present paper.
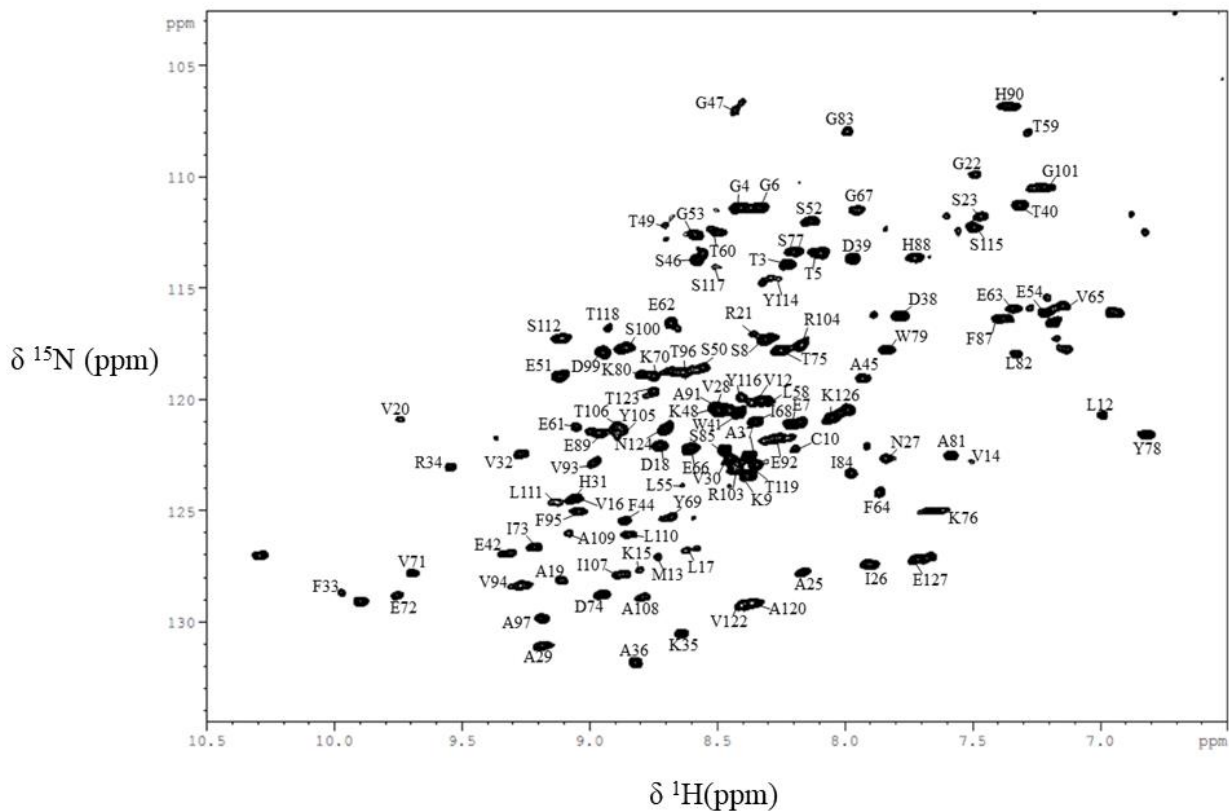
Figure S5. 2D ^{1}H ^{15}N TROSY-HSQC of [U-^{2}H-^{13}C ^{15}N] TTR with the assignment reported on the signals. The spectrum was acquired on a NMR spectrometer operating at 950 MHz (^{1}H Larmor frequency) and 310 K.
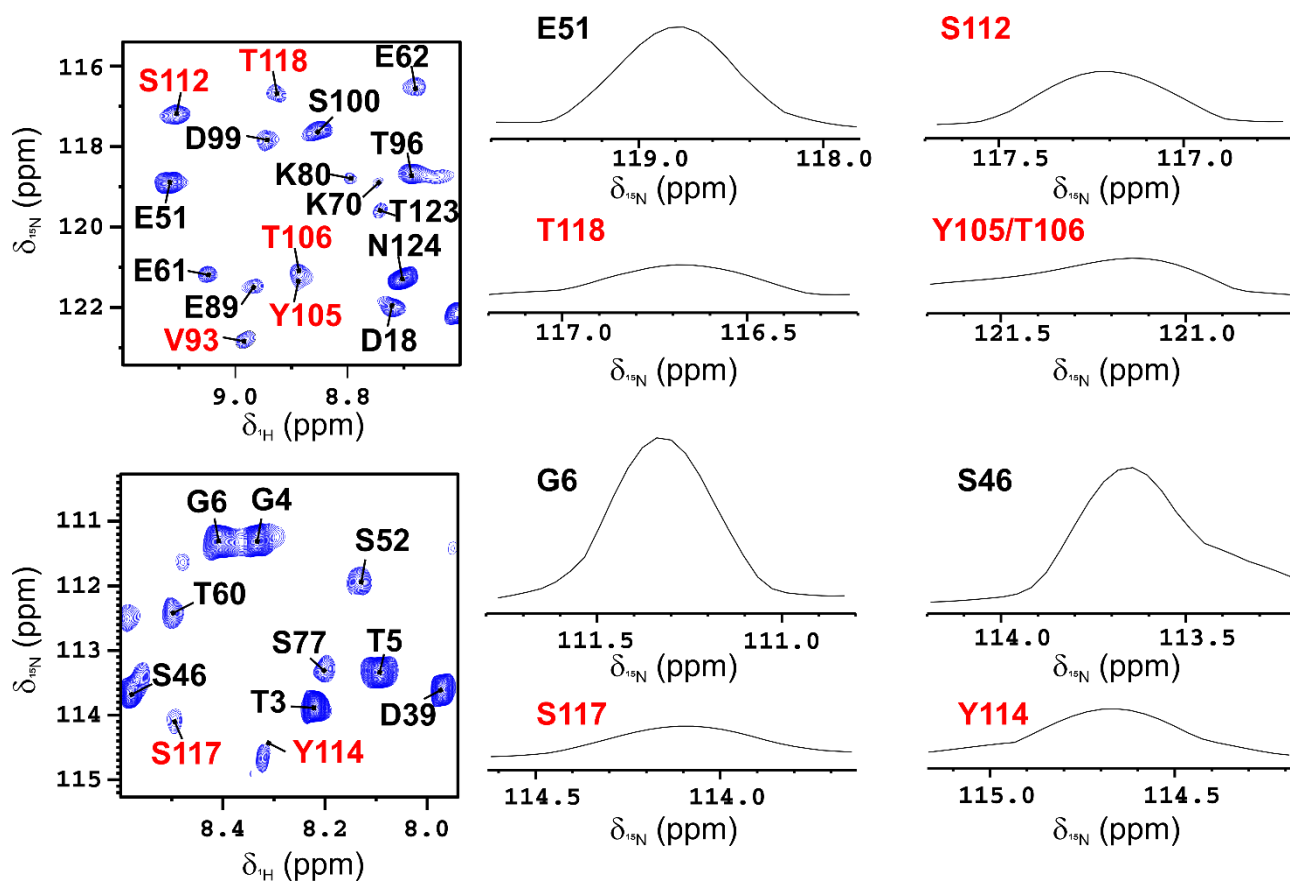
Figure S6. Portions of the 2D ^{1}H ^{15}N TROSY-HSQC of TTR with the assignment reported on the signals. The broad signals are labeled in red. The 1D projections of some signals on the ^{15}N dimension are also displayed to better highlight the difference in linewidth among different set of signals. The spectrum was acquired on a NMR spectrometer operating at 950 MHz (^{1}H Larmor frequency) and 310 K.
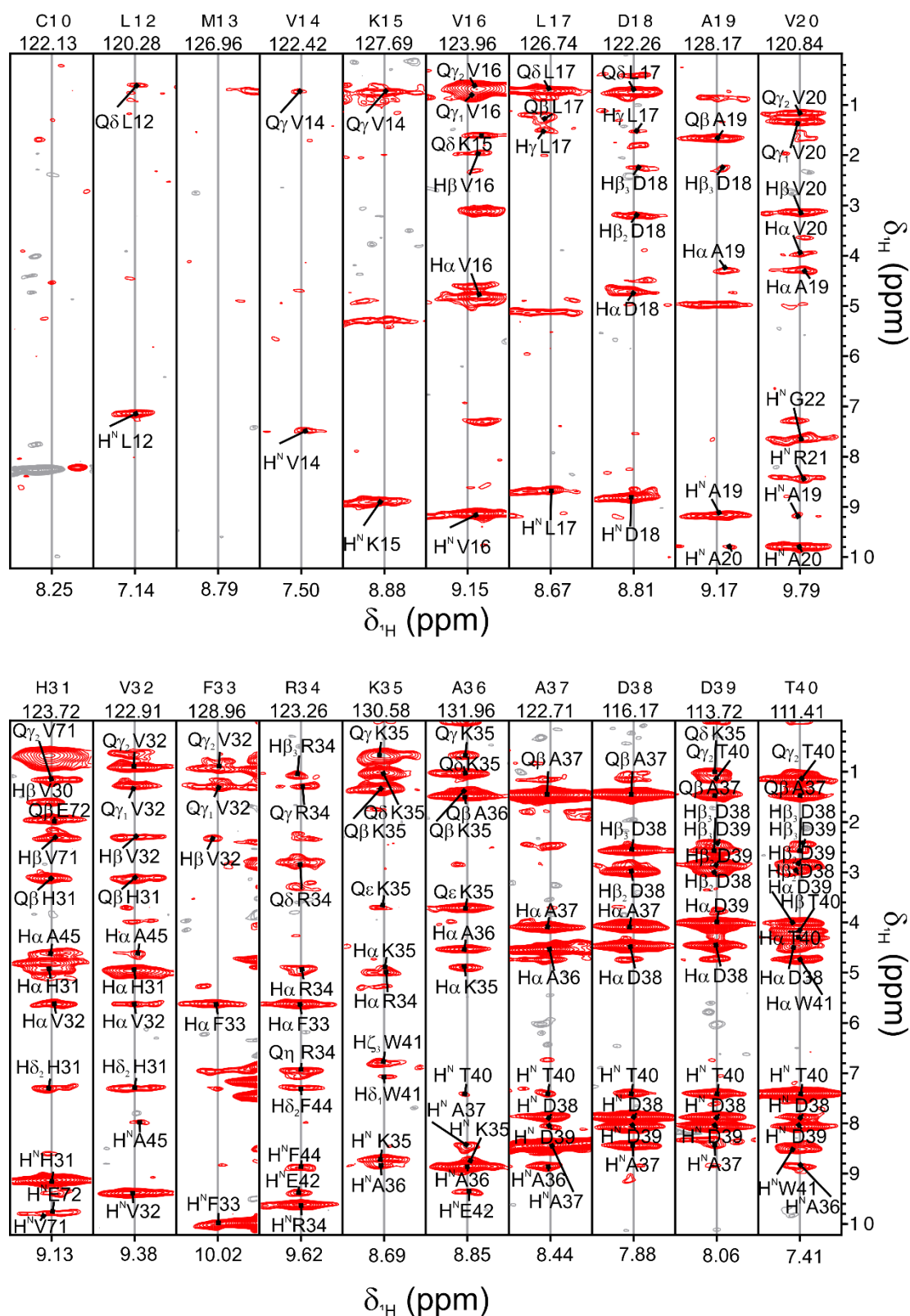
Figure S7. Selected strips of 3D ^{1}H-^{15}N NOESY spectrum (from residue C10 to residue V20 and from residue H31 to residue T40) showing the absence of cross-peaks in regions close to the inter-monomers interface (i.e. C10-V20) and the presence of the cross-peaks characteristic of β−sheet in solvent exposed regions (i.e. H31-T40).
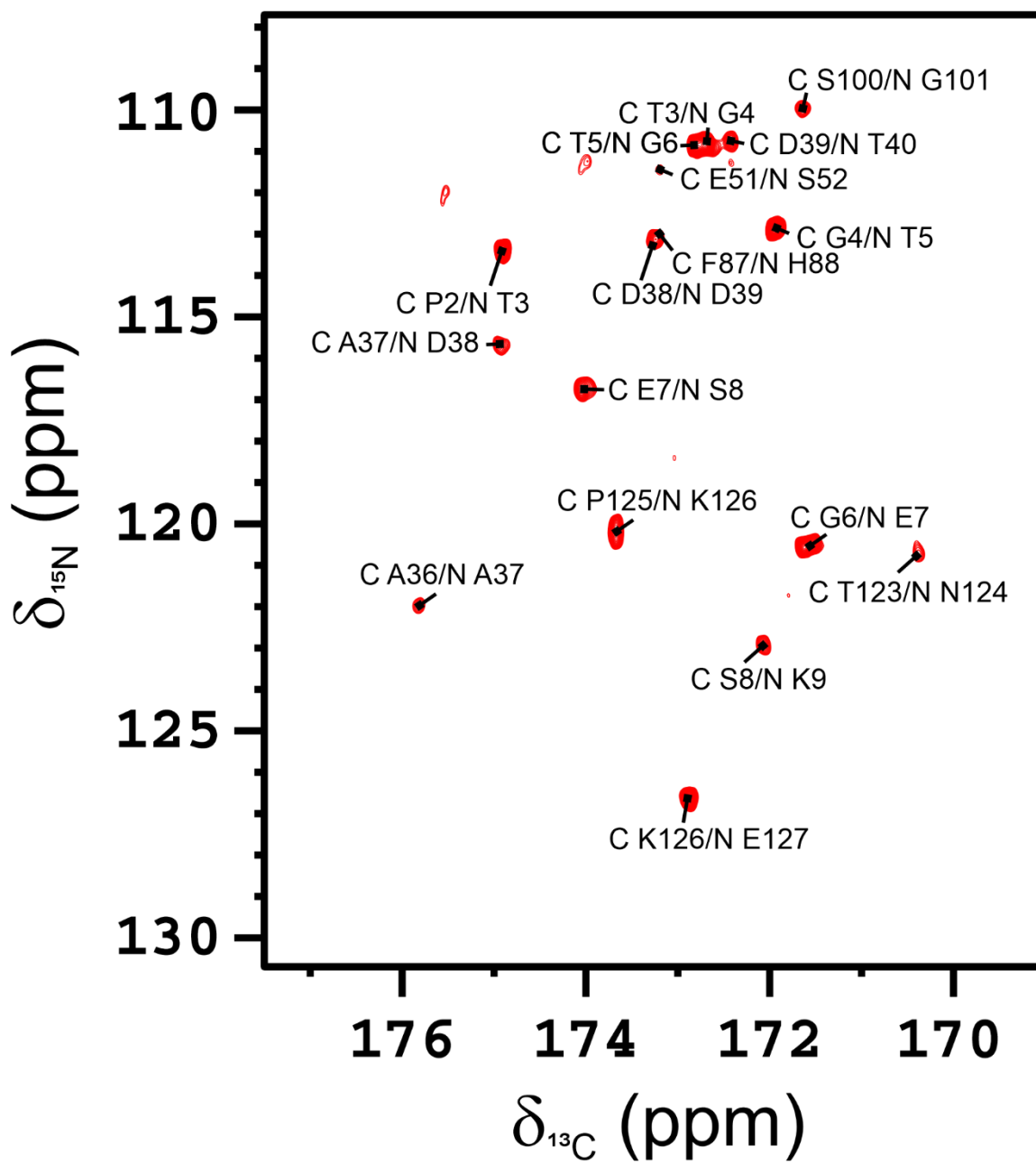
Figure S8. 2D ^{13}C ^{15}N CON spectrum of TTR with the assignment reported on the signals. The spectrum was acquired at 310 K on a Bruker AVANCE NEO 700 MHz spectrometer, equipped with a triple-resonance cryo-probe optimized for ^{13}C-direct detection.
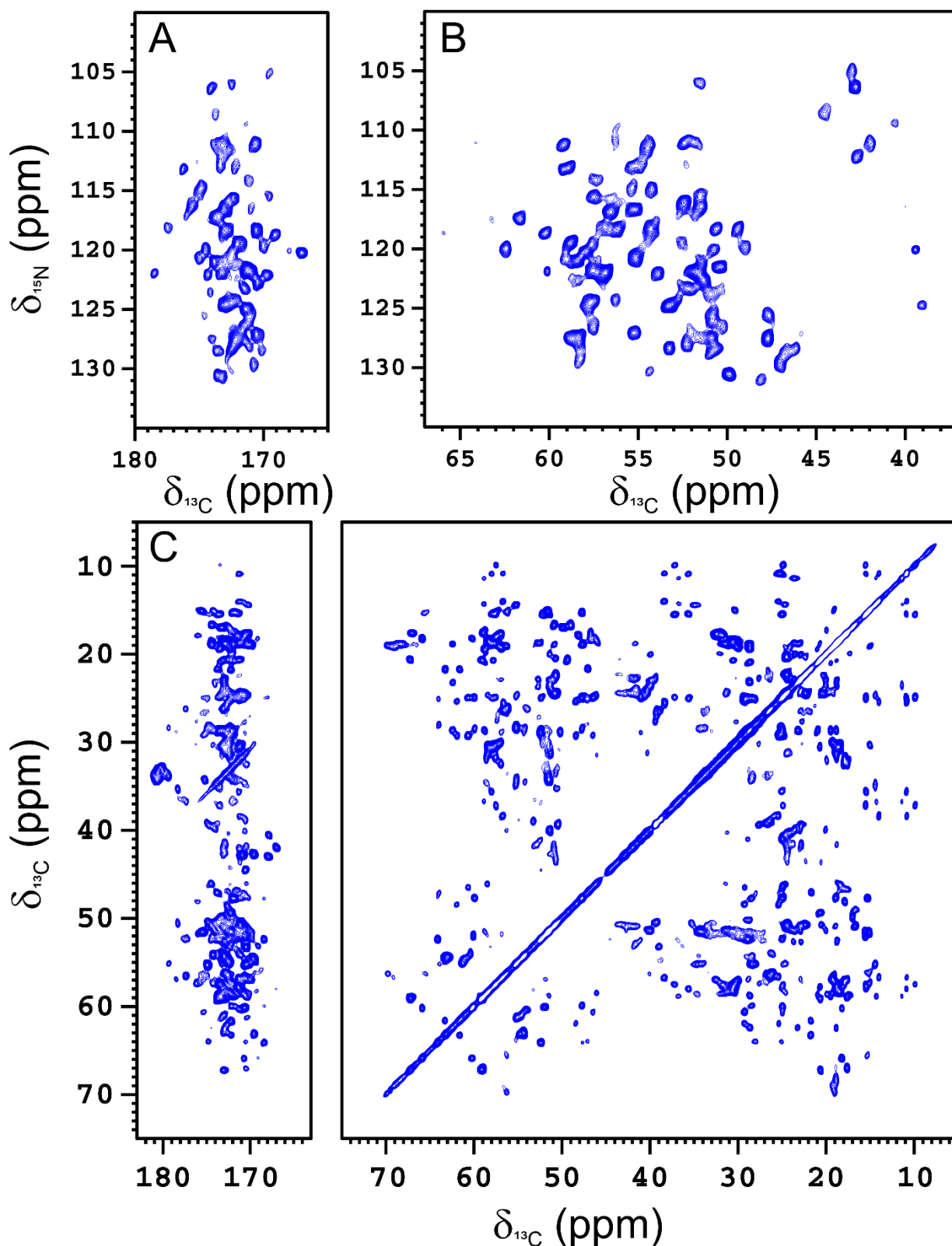
Figure S9. 2D [15]N ^{13}C NCO (A), [15]N ^{13}C NCA (B) and [13]C-^{13}C DARR (C) spectra acquired after rehydration on a sample of freeze-dried [U-^{13}C, ^{15}N] TTR. Spectra were acquired on a spectrometer operating at 800 MHz ([1]H Larmor frequency) with MAS of 14 kHz and temperature of ~ 290 K.
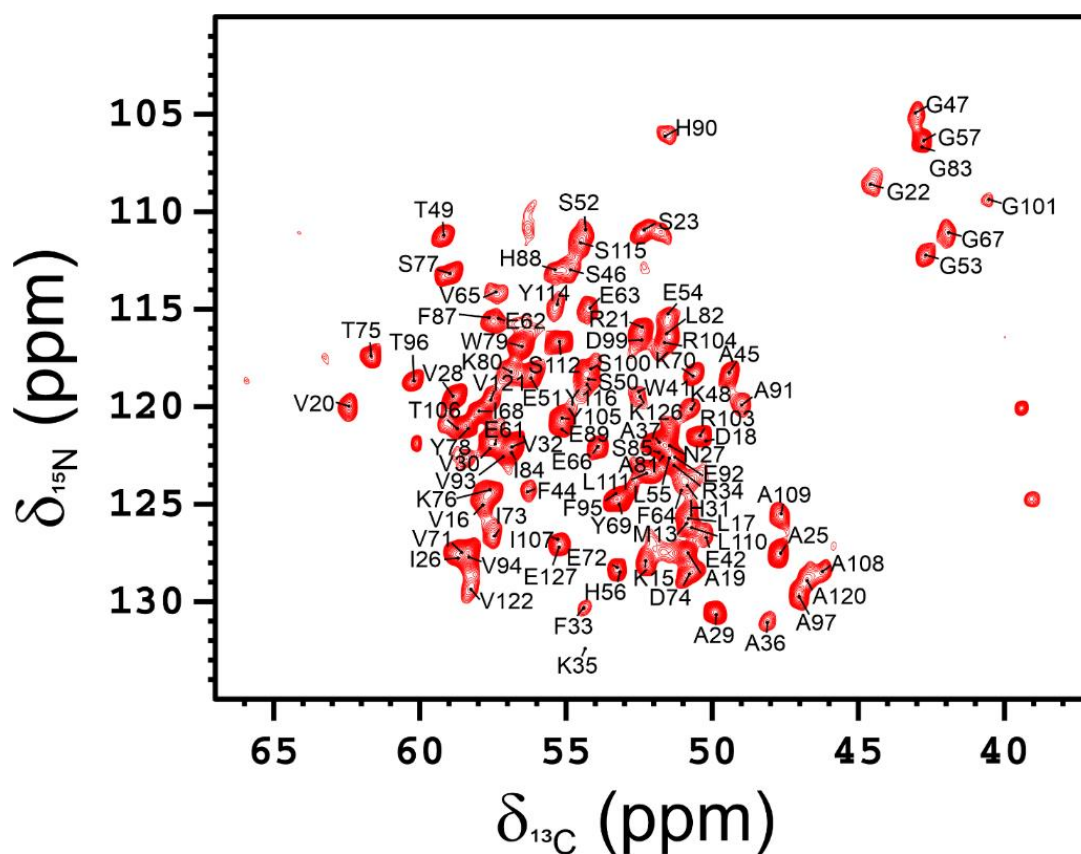
Figure S10. 2D ^{15}N ^{13}C NCA spectrum of rehydrated freeze-dried [U-^{13}C, ^{15}N] TTR with the assignment reported on the signals. The spectrum was acquired on a spectrometer operating at 800 MHz (^{1}H Larmor frequency) with MAS of 14 kHz and temperature of ~ 290 K.
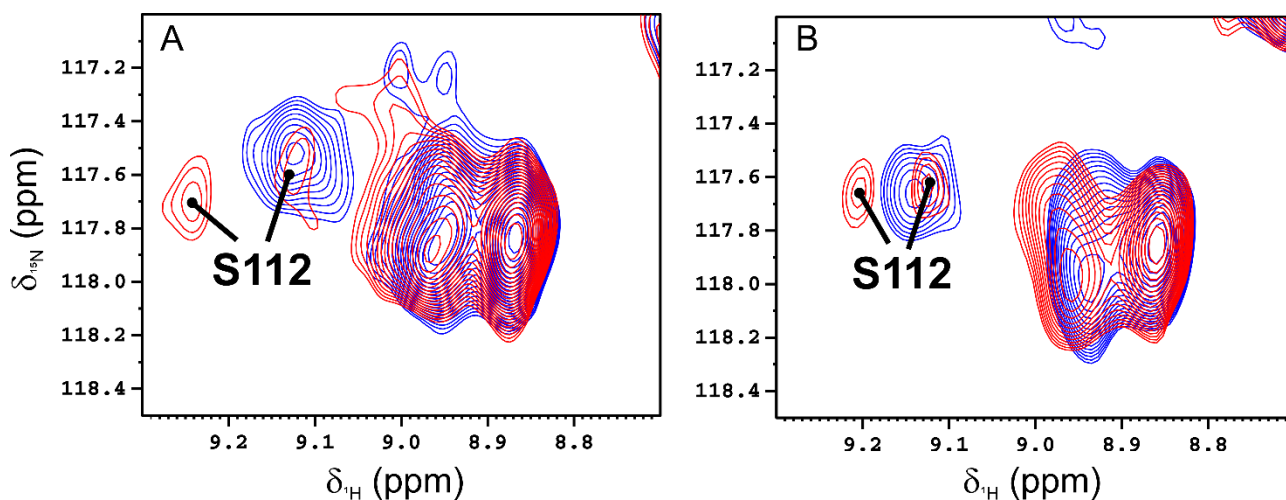
Figure S11. Region of the 2D ^{1}H-^{15}N HSQC spectra of free TTR (200 µM with respect to the tetramer, blue) and TTR in the presence of ~100 µM Tafamidis (A, red) or ~100 µM Taf-Ptx (B, red). The signals of the free and bound species display almost equal intensities as indicated by the assigned peak of Ser112.
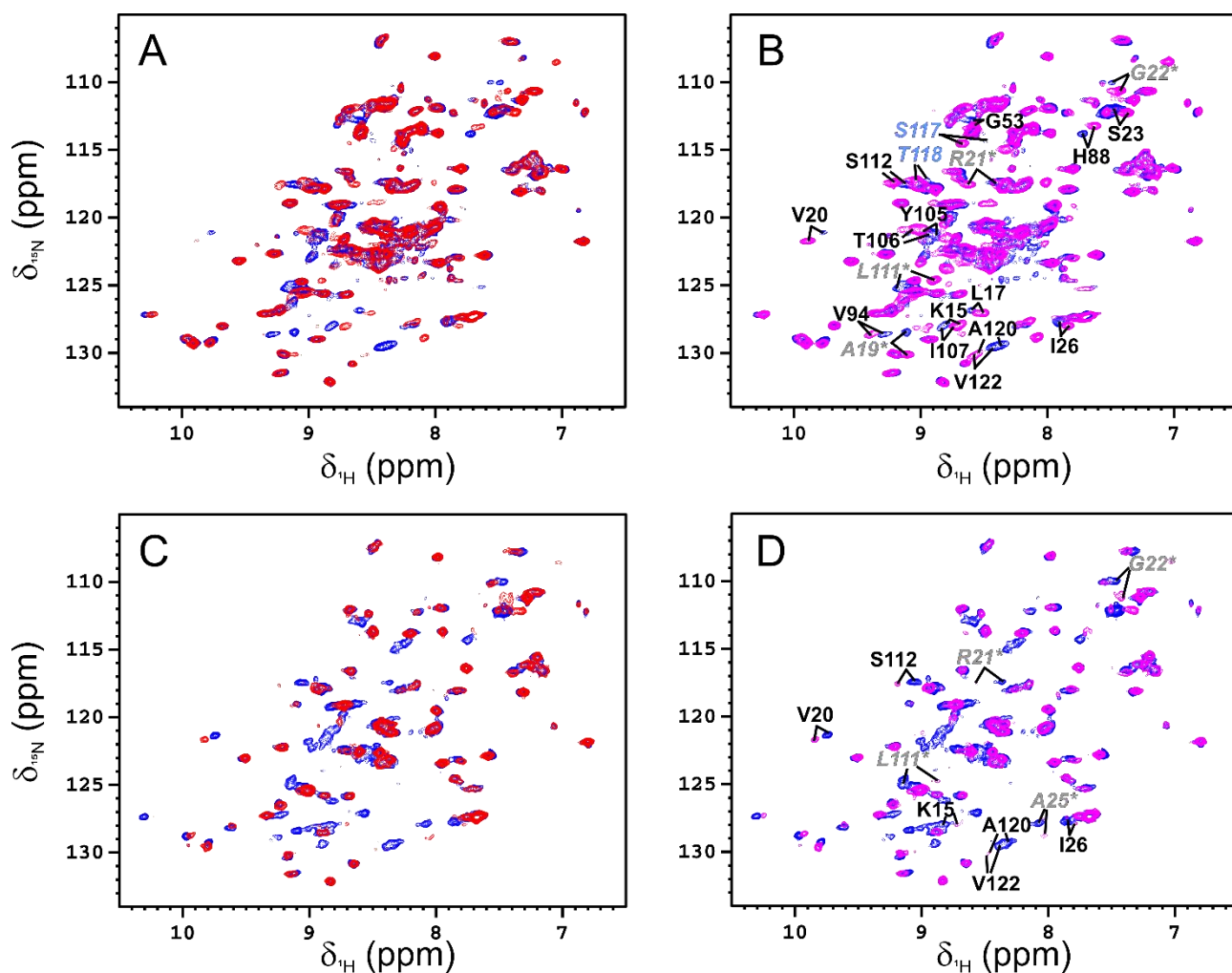
Figure S12. 2D ^{1}H ^{15}N TROSY-HSQC of free TTR (blue) and TTR in the presence of tafamidis (red, A) and Taf-Ptx (red, C) in a 1:1 ligand/tetramer ratio, and in the presence of tafamidis (magenta, B) and Taf-Ptx (magenta, D) in a 2:1 ligand/tetramer ratio. The spectra were acquired on an NMR spectrometer operating at 950 (^{1}H Larmor frequency) and 310 K. Assignment of the signals experiencing the largest CSPs are reported in the spectra with a 2:1 ligand/tetramer ratio. The residues that were tentatively reassigned with some uncertainties are labeled in italic font and colored in grey. Instead, the signals with increased intensity in the spectra of TTR in complex with tafamidis with respect to the free protein, are labeled in italic font and colored in cyan.
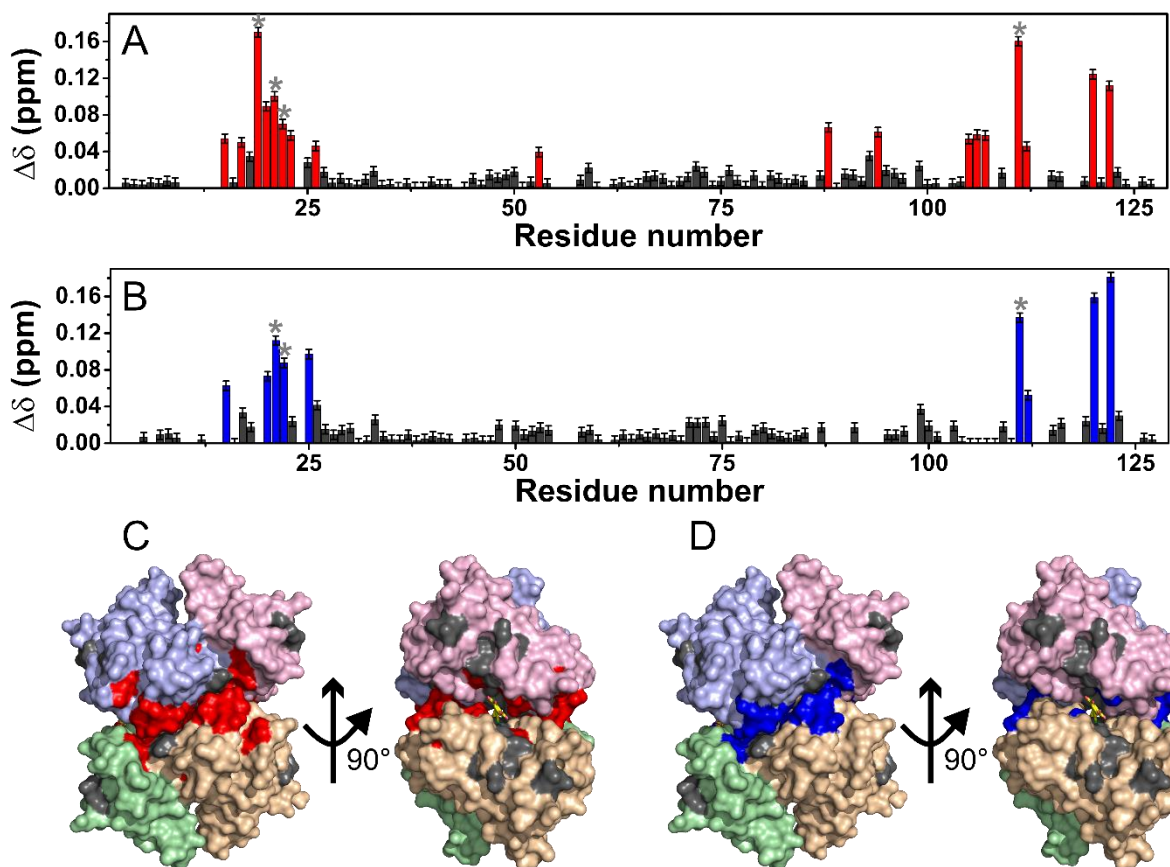
Figure S13. (A, B) Chemical shift perturbation (CSP) of TTR in the presence of Tafamidis (A) and Taf-Ptx (B) (in 2:1 ratio) with respect to free TTR, evaluated according to the formula $\Delta\delta = {}^{1}\!/_{2}\sqrt{\Delta\delta_{H}^{2} + (\Delta\delta_{N}/5)^{2}}$. The residues experiencing the largest variations ($\Delta\delta \geq$ mean + std. dev.) have been highlighted in red and blue, respectively. The residues that were tentatively assigned have been indicated by a star. The error for CSP has been evaluated considering the standard deviation of the values of CSP below the mean, calculated considering all the CSP values. (C, D) CSP mapping on the X-ray structure of TTR in complex with Tafamidis (PDB code: 3TCT)[3] with the residues experiencing the largest perturbations ($\Delta\delta \geq$ mean + std. dev.) in the presence of Tafamidis or Taf-Ptx colored in red (C) and blue (D), respectively. The residues missing in the 2D ^{1}H-^{15}N HSQC spectra are colored in grey. The monomers are in different colors (wheat, green, violet, pink) and Tafamidis as yellow sticks.
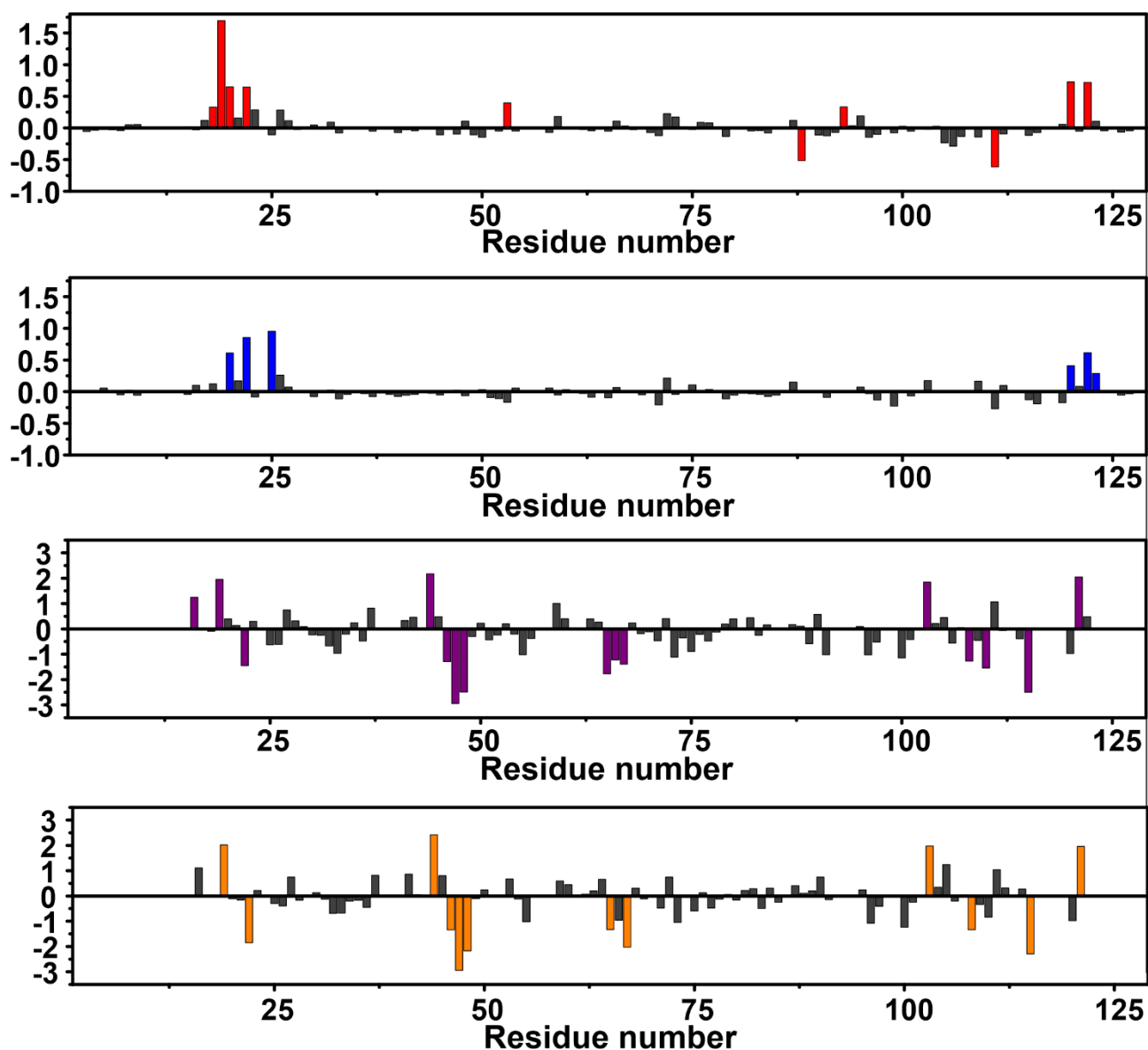
Figure S14. Difference in chemical shift of ^{15}N for TTR bound to Tafamidis (red and violet) and to Taf-PTX (blue and orange) with respect to the free protein evaluated in solution (red and blue, for Tafamidis and Taf-PTX, respectively) and at the solid-state (violet and orange, for Tafamidis and Taf-PTX, respectively).
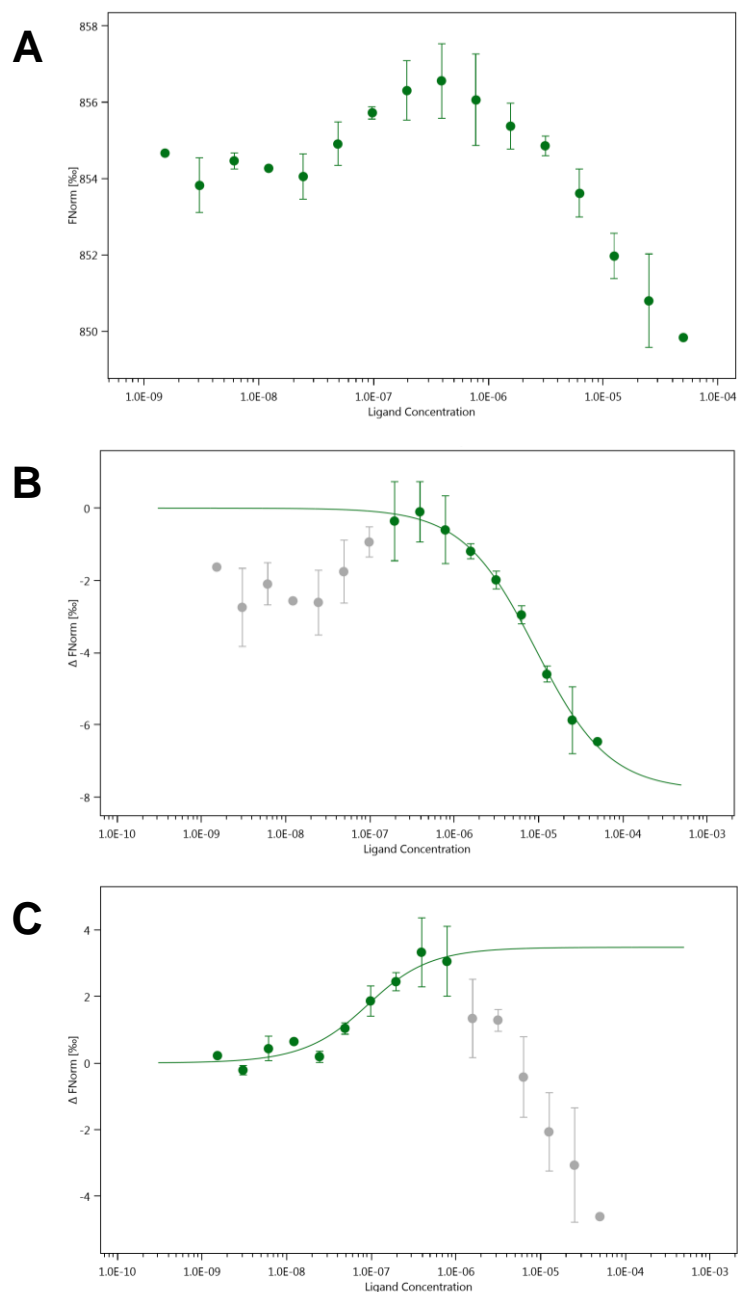
Figure S15. Biphasic binding curve obtained from TTR/Taf-Ptx interaction (A). Curve analysis from 1 to 9 samples (B) and from 7 to 16 samples (C). The difference in normalized fluorescence [‰] is plotted against ligand concentration ($mol \cdot dm^{-3}$)Data obtained from three independent measurements; error bars represent the standard deviation of the points.
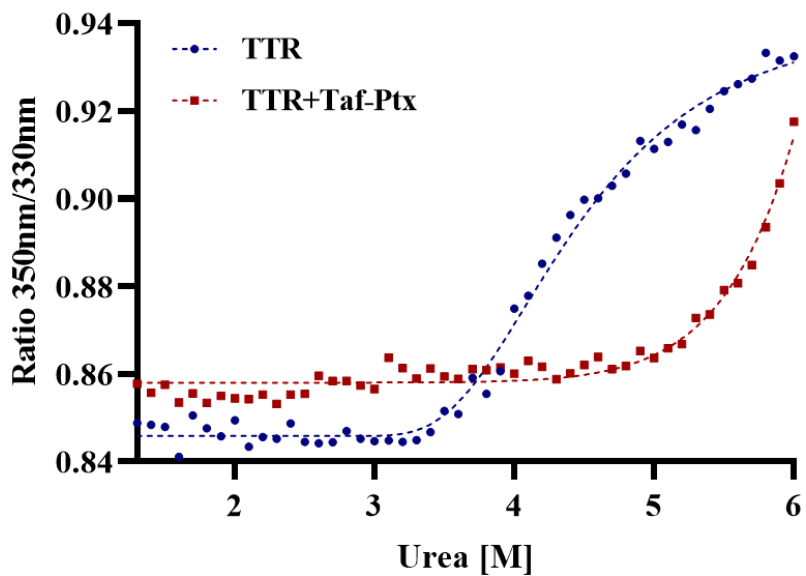
Figure S16. Denaturation curve of TTR (blue circles) and TTR in the presence of Taf-Ptx (red squares). The curves are obtained plotting the ratio 350nm/330nm versus serial dilutions of the denaturant agent (urea). Data are plotted as mean values from n.3 independent experiments.

Table S1. Data processing and refinement statistics for the X-ray structure solved in the present paper.

	TTR
Wavelength	1.541
Resolution range	35.47 - 1.6 (1.657 - 1.6)
Space group	P 21 21 2
Unit cell	43.48 85.34 63.79 90 90 90
Total reflections	384543 (15355)
Unique reflections	31504 (2783)
Multiplicity	12.2 (5.5)
Completeness (%)	98.21 (88.60)
Mean I/sigma(I)	22.29 (2.08)
Wilson B-factor	16.87
R-merge	0.08045 (0.9225)
R-meas	0.08391 (1.016)
R-pim	0.02336 (0.4066)
CC1/2	1 (0.668)
CC*	1 (0.895)
Reflections used in refinement	31492 (2783)
Reflections used for R-free	1574 (139)
R-work	0.1783 (0.2452)
R-free	0.2035 (0.2458)
CC(work)	0.968 (0.839)
CC(free)	0.977 (0.802)

Number of non-hydrogen atoms	2068
macromolecules	1785
ligands	54
solvent	229
Protein residues	231
RMS(bonds)	0.014
RMS(angles)	1.28
Ramachandran favored (%)	98.68
Ramachandran allowed (%)	1.32
Ramachandran outliers (%)	0.00
Rotamer outliers (%)	0.00
Clashscore	3.92
Average B-factor	23.91
macromolecules	22.45
ligands	31.26
solvent	33.63

Table S2. Best fit values of the ^{1}H NMRD profiles of wild-type TTR with and without tafamidis. Unless differently specified, the values refer to the profiles collected at 25 °C.

	wild type TTR	wild type TTR + tafamidis	
α	0.35 ± 0.01	0.35 ± 0.01	s^{-1}
β	2.0 ± 0.4	2.0 ± 0.4	$10^7\ s^{-2}$
c_1	0.007 ± 0.002	0.004 ± 0.002	
τ_1	310 ± 70		$10^{-9}\ s$
c_2	0.28 ± 0.04	0.30 ± 0.05	
τ_2	30 ± 2		$10^{-9}\ s$
c_3	0.72 ± 0.04	0.69 ± 0.05	
τ_3	5 ± 1		$10^{-9}\ s$
τ_2 (15 °C)	40 ± 1	40 ± 1	$10^{-9}\ s$
τ_2 (37 °C)	19 ± 1	22 ± 1	$10^{-9}\ s$

Table S3. Free energy of protein stability (ΔG) and C_{50} values obtained for TTR in the presence and absence of Taf-Ptx. Results are reported as mean $\pm$ standard deviation of n.3 independent experiments. ΔG and C_{50} values of TTR in complex with Taf-Ptx are estimated from a denaturation curve that does not reach an unfolding plateau.

Protein Sample	ΔG (kJ/mol)	C_{50} (M)
TTR	25.7 $\pm$ 2.6	3.98 $\pm$ 0.03
TTR+Taf-Ptx	> 47.3 $\pm$ 2.5	> 6.91 $\pm$ 0.13

References:

[1] T. Yokoyama, Y. Kosaka, M. Mizuguchi, *J Med Chem* **2014**, *57*, 1090–1096.

[2] W. Kabsch, *Acta Crystallogr D Biol Crystallogr* **2010**, *66*, 133–144.

[3] C. E. Bulawa, S. Connelly, M. DeVit, L. Wang, C. Weigel, J. A. Fleming, J. Packman, E. T. Powers, R. L. Wiseman, T. R. Foss, I. A. Wilson, J. W. Kelly, R. Labaudinière, *Proc Natl Acad Sci U S A* **2012**, *109*, 9629–9634.

[4] A. Vagin, A. Teplyakov, *Acta Crystallogr D Biol Crystallogr* **2000**, *56*, 1622–1624.

[5] P. D. Adams, P. V. Afonine, G. Bunkóczi, V. B. Chen, I. W. Davis, N. Echols, J. J. Headd, L.-W. Hung, G. J. Kapral, R. W. Grosse-Kunstleve, A. J. McCoy, N. W. Moriarty, R. Oeffner, R. J. Read, D. C. Richardson, J. S. Richardson, T. C. Terwilliger, P. H. Zwart, *Acta Crystallogr D Biol Crystallogr* **2010**, *66*, 213–221.

[6] P. Emsley, B. Lohkamp, W. G. Scott, K. Cowtan, *Acta Crystallogr D Biol Crystallogr* **2010**, *66*, 486–501.

[7] V. B. Chen, W. B. Arendall, J. J. Headd, D. A. Keedy, R. M. Immormino, G. J. Kapral, L. W. Murray, J. S. Richardson, D. C. Richardson, *Acta Crystallographica Section D Biological Crystallography* **2009**, *66*, 12–21.

[8] G. Parigi, E. Ravera, M. Fragai, C. Luchinat, *Progress in Nuclear Magnetic Resonance Spectroscopy* **2021**, *124–125*, 85–98.

[9] I. Bertini, M. Fragai, C. Luchinat, G. Parigi, *Magn. Reson. Chem.* **2000**, *38*, 543–550.

[10] Y. Xu, S. Matthews, *Top Curr Chem* **2013**, *335*, 97–119.

[11] S. Grzesiek, A. Bax, *Journal of Magnetic Resonance (1969)* **1992**, *96*, 432–440.

[12] J. Schleucher, M. Sattler, C. Griesinger, *Angewandte Chemie International Edition in English* **1993**, *32*, 1489–1491.

[13] L. E. Kay, G. Y. Xu, T. Yamazaki, *Journal of Magnetic Resonance, Series A* **1994**, *109*, 129–133.

[14] M. Wittekind, L. Mueller, *Journal of Magnetic Resonance, Series B* **1993**, *101*, 201–205.

[15] D. R. Muhandiram, L. E. Kay, *Journal of Magnetic Resonance, Series B* **1994**, *103*, 203–216.

[16] S. Grzesiek, A. Bax, *J Biomol NMR* **1993**, *3*, 185–204.

[17] M. Bostock, D. Nietlispach, *Concepts in Magnetic Resonance Part A* **2017**, *46A*, e21438.

[18] W. Bermel, I. Bertini, I. C. Felli, Y.-M. Lee, C. Luchinat, R. Pierattelli, *J. Am. Chem. Soc.* **2006**, *128*, 3918–3919.

[19] W. Bermel, I. Bertini, L. Duma, I. C. Felli, L. Emsley, R. Pierattelli, P. R. Vasos, *Angew. Chem. Int. Ed. Engl.* **2005**, *44*, 3089–3092.

[20] M. Fragai, C. Luchinat, G. Parigi, E. Ravera, *J Biomol NMR* **2013**, *57*, 155–166.

[21] L. B. Andreas, T. Le Marchand, K. Jaudzems, G. Pintacuda, *Journal of Magnetic Resonance* **2015**, *253*, 36–49.

[22] E. Barbet-Massin, A. J. Pell, K. Jaudzems, W. T. Franks, J. S. Retel, S. Kotelovica, I. Akopjana, K. Tars, L. Emsley, H. Oschkinat, A. Lesage, G. Pintacuda, *J. Biomol. NMR* **2013**, *56*, 379–386.

[23] E. Barbet-Massin, A. J. Pell, J. S. Retel, L. B. Andreas, K. Jaudzems, W. T. Franks, A. J. Nieuwkoop, M. Hiller, V. Higman, P. Guerry, A. Bertarello, M. J. Knight, M. Felletti, T. Le Marchand, S. Kotelovica, I. Akopjana, K. Tars, M. Stoppini, V. Bellotti, M. Bolognesi, S. Ricagno, J. J. Chou, R. G. Griffin, H. Oschkinat, A. Lesage, L. Emsley, T. Herrmann, G. Pintacuda, *J. Am. Chem. Soc.* **2014**, *136*, 12489–12497.

[24] A. Schuetz, C. Wasmer, B. Habenstein, R. Verel, J. Greenwald, R. Riek, A. Böckmann, B. H. Meier, *ChemBioChem* **2010**, *11*, 1543–1551.

[25] M. Baldus, A. Petkova, Herzfeld, Judith, R. G. Griffin, *Molecular Physics* **1998**, *95*, 1197–1207.

[26] M. Hong, R. G. Griffin, *J. Am. Chem. Soc.* **1998**, *120*, 7113–7114.

[27] K. Takegoshi, S. Nakamura, T. Terao, *Chemical Physics Letters* **2001**, *344*, 631–637.

[28] R. Keller, *The Computer Aided Resonance Assignment Tutorial (CARA)*, CANTINA Verlag, Goldau. Switzerland, **2004**.

3.3 Contrast agents: paramagnetic proteins and blueberry juice

Paramagnetic systems are widely used in MRI for their ability to enhance the nuclear relaxation rates of water protons, thus increasing the contrast and improving the quality of the images [8]. Given the widespread diffusion of this diagnostic technique, the development of more efficient and less toxic contrast agents is highly desirable. NMR relaxometry is the state of the art technique to characterize contrast agents.

The modulation of the rotational correlation time of the paramagnetic agent is an exploited strategy to increase the relaxivity at low magnetic fields, where MRI is performed (around 1 T) [9, 17]. Moreover, in order to reduce the dose of gadolinium(III) while achieving a high payload of paramagnetic ions, several types of nanoparticles have been studied as promising contrast agents [39].
In the framework of this project, with the aim of slowing down the rotational correlation time (τ_R) of the paramagnetic complex, macromolecules with attached gadolinium(III) complexes have been synthesized and characterized by relaxometry. In particular, Gd-DOTA conjugated L-asparaginaseII (ANSII), was expressed, purified and characterized. Additionally, my contribution to the characterization of two paramagnetic engineered protein cages is described. These kind of complexes can serve as candidates for theranostic platform to monitor the efficacy of therapeutic drugs non-invasively and in real time.

Similar to gadolinium(III) used in intravenous MRI contrast agents, manganese(II) is a paramagnetic ion that enhances longitudinal relaxation (R_1) of adjacent water protons, increasing signal intensity in T_1-weighted MRI images. This creates a higher contrast between tissues with and without paramagnetic ions. Manganese(II) also acts as a T_2-agent by increasing transverse relaxation (R_2), reducing signal intensity in T_2-weighted scans. While intravenous contrast is common for neurologic and musculoskeletal MRI, oral agents are prevalent for gastrointestinal and hepatobiliary MRI [23].
Promising oral contrast agents include pineapple and blueberry juices due to their manganese(II) content [62, 63, 24]. These juices have demonstrated effectiveness in MRI images. A field-cycling relaxometric analysis was conducted on pineapple juice to characterize its relaxation properties with and without hydrogels [24]. The NMRD profile analysis yielded insights into dynamic processes and structural parameters affected by the paramagnetic metal ions and

their interactions with water protons. The study included in this PhD thesis, expanded the analysis to blueberry juice. We compared its relaxation properties with those of pineapple juice and a $[Mn(H_2O)_6]^{2+}$ solution. A commercially available blueberry nectar was used to investigate the relaxation properties of a readily obtainable product, which can be both repeatable and immediately available for clinical administration.

3.3.1   GdDOTA-conjugated ANSII

L-asparaginase II (ANSII hereafter) was expressed and purified in both not labelled and ^{15}N labelled form, following the published protocol for ANSII production and purification [64]. ANSII native form consists of 4 identical units assembled as a tetramer which total weight is 138 kDa. Each monomeric subunit contains 22 lysine residues which have been already successfully functionalized in previous works [65].

(a)

(b)
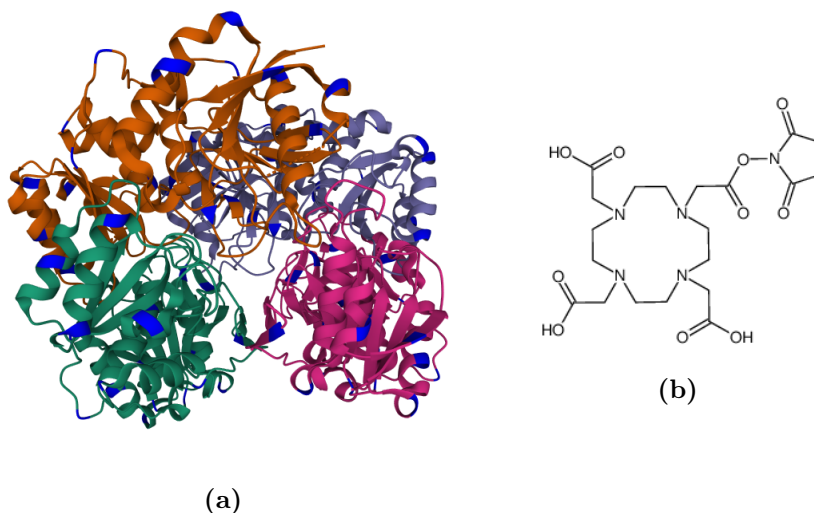
Figure 3.17: (a) L-asparaginase structure representation (PDB structure 6EOK). In blue, lysine residues are highlighted in blue. (b) DOTA-NHS-ester structure.

The conjugation reaction with DOTA-NHS-ester was performed as reported in the *experimental procedure* section of the attached article [20]. In the same section, information on the addition of gadolinium(III) ions is reported.
The exposed lysines of the ANSII undergo a nucleophilic attack from the functionalized DOTA carboxylic group. This leads to the formation of a new amide bond and leaves the other three DOTA carboxylate anions free to bind trivalent ions such as gadolinium. Considering the lower pK$_a$ of the α-amine of the

	Residue Number	pK$_a$	Buried %
N+	1	7.85	0
LYS	301	7.94	100
LYS	104	8.71	48
LYS	172	9.37	93.75
LYS	49	9.63	11.75
LYS	71	9.98	0
LYS	162	10.02	100
LYS	262	10.16	0
LYS	196	10.28	0
LYS	107	10.30	3

Table 3.3:   Most relevant results of the bioinformatic analysis conducted via *PROPKA*.

N-terminus compared to the ε-amine of lysines, at the employed mild conditions and pH, a selective acylation and alkylation of N-terminal amines was favored, although complete site specificity was not achieved. Beside the considerations on the experimental conditions of the bioconjugation reaction, we can expect that only a rather limited number of lysine groups are modified even in the presence of relatively high DOTA-NHS-ester/protein ratio as they are not equally exposed to the solvent. A bioinformatic analysis using *PROPKA* [66], allowed for an estimation of the most accessible lysines upon the reactive ones. The results reported in *Table 3.3*, suggested that the lysines that are most likely involved in the functionalization reaction are the N-terminus and lysines 104, 49, and 71. These conditions were chosen because we aimed at evaluating the paramagnetic relaxation enhancement with distant gadolinium(III) ions, to avoid possible magnetic coupling.

As can be observed in *Figure 3.18 panel (a)*, the ^{1}H NMRD profiles of DOTA-conjugated ANSII (solid symbols) and the unconjugated ANSII protein (empty symbols) are basically identical at every considered temperature. The profiles of native ANSII were consistent with the ones already reported in the literature [65]. We can therefore state that, after the bioconjugation reaction, only small structural changes occur. The NMRD profiles were fitted employing two correlation times, one for the slow overall molecular tumbling, the other to take into account the faster local molecular motion (see *Equation 3.6*). Details on the fitting procedure of the NMRD profiles are included in the attached article [20].

The value of the rotational correlation time (67 ns) is in agreement with the

one reported in literature, although in different experimental conditions (buffer and concentration) [28, 65]. We can therefore affirm that the tetrameric structure of the protein is maintained upon conjugation. The different weight of the contribution arising from global and local motion, respectively c_1 and c_2, indicate the presence of an extensive mobility in the nanoseconds timescale (below 10 ns) ascribable to the high local mobility of the many loop regions of the protein. A high mobility was previously noted through high resolution NMR [65].
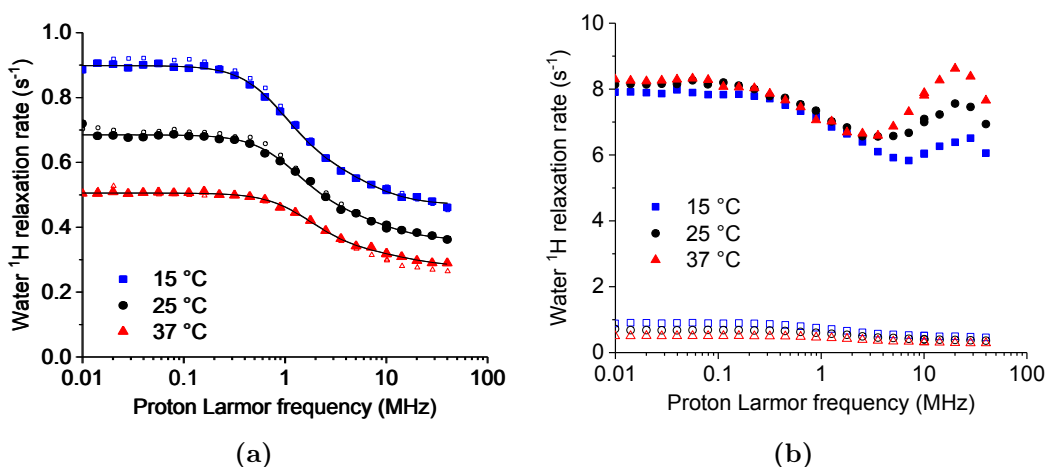
Figure 3.18: (a) ^{1}H NMRD profiles (solid symbols) of DOTA-conjugated ANSII (0.38 mM monomeric protein concentration) in 150 mM phosphate buffer, pH 7.5. Basically identical profiles were measured for the unconjugated ANSII protein (empty symbols). The profiles were collected at 288, 298 and 310 K. (b) ^{1}H NMRD profiles of GdDOTA-conjugated ANSII and of the diamagnetic DOTA-conjugated ANSII (empty symbols) that was subtracted to the paramagnetic profile. Same symbols refer to same temperature.

The relaxivity values, obtained from the difference between the relaxation rates measured from the paramagnetic bioconjugated GdDOTA-ANSII and the diamagnetic DOTA-ANSII samples, scaled to 1 mM gadolinium(III) concentration (determined through ICP-AES), are shown in *Figure 3.19*. Details on the fitting procedure of the NMRD profiles are included in the attached article [20].

As expected, we observed an increase in the relaxivity of the Gd-labeled ANSII due to the higher reorientational correlation time with respect to the free complex [67], which is in the optimal range for high field MRI, but the increase is below the theoretical limit. From the temperature dependence of the profiles, we can affirm that the slow exchange regime of the coordinated water molecules limits the relaxivity enhancement. This could be arising from

a pattern of hydrogen bonds involving the coordinated water, the carboxylic groups and the closest amino acids. This hypothesis is confirmed by the values of the lifetime of coordinated water molecules, τ_M, that lies between 0.2 and 0.5 μs, slower with respect to the value observed for the free complex in water [67].
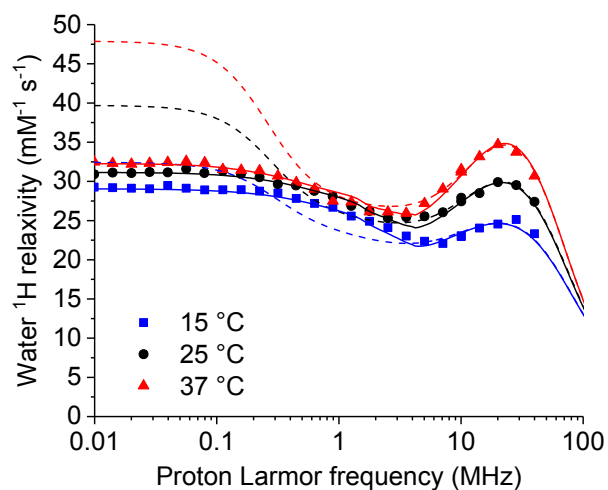
Figure 3.19: [1]H relaxivity profiles of GdDOTA-conjugated ANSII in 50mM MES pH 6.5, at 288, 298 and 310 K. The profiles were fitted with Florence and the best fit parameters are shown in *Table 2* in [20].

Article

Large Protein Assemblies for High-Relaxivity Contrast Agents: The Case of Gadolinium-Labeled Asparaginase

Giulia Licciardi, Domenico Rizzo, Maria Salobehaj, Lara Massai, Andrea Geri, Luigi Messori, Enrico Ravera, Marco Fragai, and Giacomo Parigi*

Read Online

ACCESS | Metrics & More | Article Recommendations | Supporting Information

ABSTRACT: Biologics are emerging as the most important class of drugs and are used to treat a large variety of pathologies. Most of biologics are proteins administered in large amounts, either by intramuscular injection or by intravenous infusion. Asparaginase is a large tetrameric protein assembly, currently used against acute lymphoblastic leukemia. Here, a gadolinium(III)-DOTA derivative has been conjugated to asparaginase, and its relaxation properties have been investigated to assess its efficiency as a possible theranostic agent. The field-dependent ^1H longitudinal relaxation measurements of water solutions of gadolinium(III)-labeled asparaginase indicate a very large increase in the relaxivity of this paramagnetic protein complex with respect to small gadolinium chelates, opening up the possibility of its use as an MRI contrast agent.
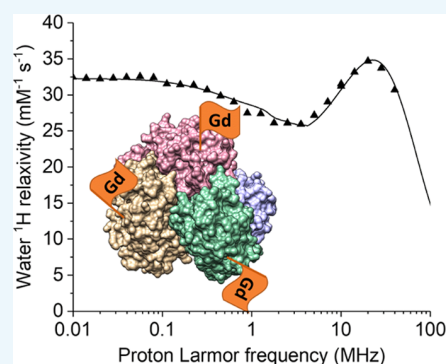
INTRODUCTION

The millions of MRI exams performed annually in the world after administration of gadolinium(III) contrast agents and the concerns about their safety continuously stimulate the efforts for the development of safer contrast agents.[1] The contrast agents used in the clinics are nowadays almost exclusively small gadolinium(III) complexes. Administration of these complexes has been shown to determine gadolinium accumulation in the tissues of the patients, thus raising concerns for their long-term consequences on health.[2,3] For instance, they have been associated with nephrogenic systemic fibrosis in patients with impaired renal clearance.[4−6]

The strategy to reduce the risks associated with the administration of contrast agents without reducing the quality, and thus the diagnostic accuracy, of the MRI images, passes through the use of molecules not containing gadolinium(III) ions but similarly able to enhance the nuclear relaxation rates of water protons,[7−10] or through the development of gadolinium complexes with higher efficiency so that the injected dose can be sizably reduced. A reduction of the injected gadolinium(III) dose can be achieved (i) by targeting the contrast agents to specifically accumulate them in the tissues of interest and (ii) by increasing the capability of the agents to enhance the water proton relaxation rates. This capability is called relaxivity and is defined as the enhancement in the water proton relaxation rate due to a gadolinium concentration of 0.001 mol dm^{-3}.

An effective way to increase relaxivity at low and intermediate magnetic fields (below ca. 1 T) is slowing down the reorientation mobility of the complex. This can be achieved by functionalizing low-molecular-weight gadolinium(III) complexes to bind noncovalently to macromolecules,[11−13] by confining them within nanosized matrices, like nanogels,[14−18] or by exploiting nanosized gadolinium(III)-based compounds.[19−24] On the other hand, an increase in the reorientation time of the contrast agent determines a decrease in relaxivity at high magnetic fields. The optimal reorientation time τ_R is related to the applied magnetic field B_0 through the relationship $\tau_R^{opt} = (\gamma_I B_0)^{-1}$, with $\tau_c^{-1} = \tau_R^{-1} + \tau_M^{-1} + R_{1e}$, where γ_I is the proton magnetogyric ratio, τ_M is the lifetime of the water molecule(s) coordinated to the gadolinium(III) ion, and R_{1e} is the electron relaxation rate.[25,26] At 1.5 T, if water exchange and electron relaxation are slower than molecular reorientation, τ_R^{opt} = 2.5 ns. Therefore, reorientation times in the nanosecond timescale are needed to achieve the highest relaxivities at the fields of MRI scanners.

Metalloprotein-based contrast agents have been considered because of the ease of preparation and the availability of engineering techniques that can allow for their functionalization and targeting.[27] The relaxivity of (either natural or metal-substituted) paramagnetic metalloproteins is however typically limited, despite their overall reorientation times of the order of nanoseconds or larger, due to the presence of paramagnetic

ions (different from gadolinium) with short electron relaxation times, and/or the long lifetime of coordinated water molecules. Proteins engineered by rational design were thus proposed by creating a gadolinium-binding site with strong metal selectivity in a stable and potentially fully functioning host protein.[28,29] Chimeric proteins were also constructed by inserting an EF-hand motif, which can bind a gadolinium ion, into a functionalized protein.[30−32] However, the application of these chimeric proteins is limited by their metal binding affinities which are much weaker than those of the chelates approved for clinical use. A high binding affinity and metal selectivity was achieved by engineering an EF-hand motif of the protein α-parvalbumin.[33]

An easier, preferable alternative is attaching a paramagnetic tag to a diamagnetic protein, like albumin and immunoglobulins.[34] Gadolinium(III) ions can be attached to proteins by bifunctional chelates, usually DOTA-like or DTPA-like complexes with an electrophilic group for conjugation to nucleophilic groups of macromolecules.[35] The possibility of genetically engineering protein polymers at multiple backbone sites allows attaching multiple paramagnetic tags per protein.[36,37] This results in multivalent, biomacromolecular contrast agents endowed with extremely high relaxivity per particle, although the relaxivity per gadolinium ion is often limited. GdDTPA-monoamide tethered to polylysine[38] or dextran,[39] for instance, shows low relaxivities because of the internal mobility which limits the relaxivity enhancement.[40] Furthermore, an increase in the water lifetime of about a factor 3 has been observed upon the replacement of one carboxylate function by an amide in both DOTA-like and DTPA-like chelates.[41]

Along these lines, we have attached a derivative of 1,4,7,10-tetraazacyclododecane-1,4,7,10-tetraacetic acid (DOTA) to the protein L-asparaginase II (ANSII), a biological drug in clinical use against leukemia. Together with the four macrocyclic nitrogen atoms, four acetate arms of the chelate coordinate the gadolinium(III) ion, and the carboxylate group on the 5-carbon arm, activated with the ester, is used for covalent attachment to the primary amine of lysine residues via amide bond formation (Figure 1).[35] Carboxylates and
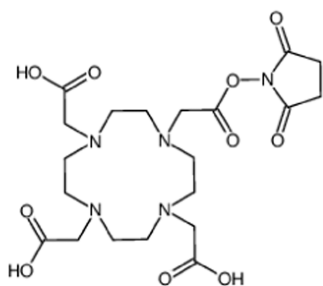
Figure 1. 1,4,7,10-Tetraazacyclododecane-1,4,7,10-tetraacetic acid mono-*N*-hydroxysuccinimide ester (DOTA-NHS-ester) chemical structure.

backbone carbonyls, and hydroxyls to a lesser extent, can also coordinate lanthanoids.[42] However, it has long been proven that in the presence of a high-affinity chelator and after thorough purification, the ions aspecifically bound to the protein surface are in negligible concentration.[43,44] Analogous paramagnetic tags were previously attached to dendrimers, silica nanoparticles, or proteins like albumin through

methanethiosulfonate anchor groups.[45] In these cases, they showed a relaxivity not exceeding 25 s^{−1} mM[−1] even at the peak magnetic field because of being limited by a subnanosecond reorientation time and a rather long lifetime of the coordinated water molecule.[45,46]

ANSII consists of four identical subunits, forming a dimer of dimers of 138 kDa with D_2 symmetry, with an extensive mobility in the nanosecond timescale.[47] The attachment of a paramagnetic tag to ANSII is thus expected to result in an MRI contrast agent of much improved relaxivity with respect to those presently used in clinics, and of the order of that of previously reported paramagnetic proteins. Here, the relaxivity properties of the Gd(III)-DOTA-NHS-ester conjugated to amine groups of ANSII have been investigated in detail to evaluate the relaxation enhancement achieved upon conjugation. Indeed, we found a relaxivity at 37 °C as large as ca. 35 s^{−1} mM[−1] at the peak magnetic field.

Most importantly, this protein represents an attractive carrier for the delivery of the paramagnetic moiety because:

(1) ANSII is one of the oldest biologics approved for clinical use as a drug against acute lymphoblastic leukemia both in its native and PEGylated forms.[48] It is currently used in humans by intramuscular injection or by intravenous infusion three times weekly. The grafting of gadolinium(III) tags is not expected to affect the therapeutic efficacy of ANSII as proved by the enzymatic activity of the clinically approved highly PEGylated form of the enzyme, where most of the surface exposed lysines are conjugated to PEG chains.[49] Therefore, this protein is a good model to develop protein-based theranostic agents and also to develop new strategies to investigate the pharmacokinetics and fate of biologics.

(2) Each of the four ANSII subunits contains 22 lysine residues, which can be largely functionalized.[50] The many solvent-exposed lysine residues can thus allow for the conjugation of a huge amount of paramagnetic chelates to the same protein. In perspective, this can allow the development of an agent carrying a high payload of paramagnetic ions.

■ RESULTS AND DISCUSSION

Preparation and Characterization of the Conjugated Protein. The functionalization of ANSII with DOTA-NHS-ester was carried out as described in the Experimental Procedures section. Considering the lower pK_a of the α-amine of the N-terminus compared to the ε-amine of lysines, as a result of the inductive effects of the nearby carbonyl group, at pH 7.5, a selective acylation and alkylation of N-terminal amines is favored, although complete site specificity is not achieved.[51,52] Under these conditions, a few amines in the protein are expected to be significantly reactive.[53,54] Mild conditions for conjugation were employed, as we aimed at evaluating the paramagnetic relaxation enhancement with distant gadolinium(III) ions, to avoid possible magnetic coupling. Gadolinium(III) was added in defect, and the addition was followed by gel filtration purification. ICP-OES was employed to determine the gadolinium(III) concentration into the sample; it was found to correspond to the presence of 3 gadolinium(III) ions per tetramer.

ESI MS Characterization of the Free and Conjugated Protein. The free and DOTA-NHS-ester conjugated protein were further characterized through ESI MS analysis according
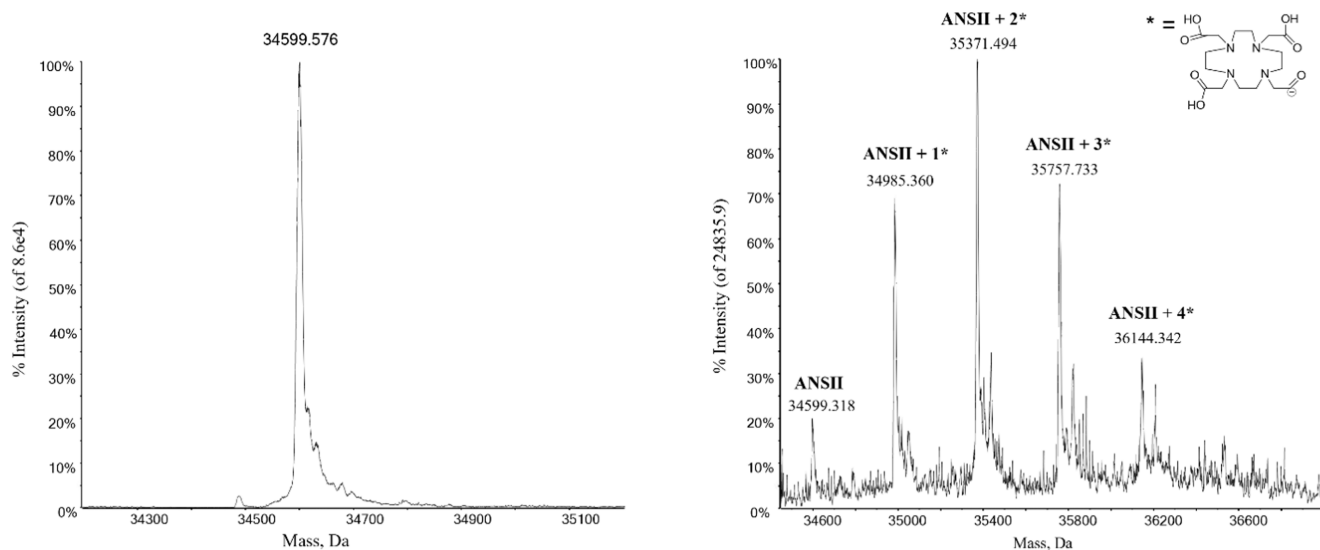
Figure 2. Deconvoluted mass spectra of ANSII 10^{-6} M (left panel) and deconvoluted mass spectra of DOTA-NHS conjugated protein 10^{-6} M (right panel).

to standard procedures.[55,56] The ESI MS spectrum of the free protein is shown in Figure 2a. The deconvoluted ESI MS spectrum shows an intense and very well resolved single peak with a mass of 34 599 Da. This value is very close—though not identical (there is an apparent difference of a few Daltons)—to the calculated value for the sequence of the protein reported in UNIPROT (P00805) being equal to 34 595 Da. Upon inspection of the ESI MS spectrum, it emerges that the ANSII protein shows a high degree of purity. The spectrum of the DOTA-NHS-ester conjugated protein, prepared as described in the Experimental Procedures section, is reported in Figure 2b. The latter spectrum shows a number of additional peaks with mass values greater than the free protein. Notably, the peaks at 34 985, 35 371, 35 757, and 36 144 Da are straightforwardly assigned to protein conjugates bearing one, two, three, and four DOTA-NHS-ester moieties, respectively. The percentage ratios between free ANSII and the various forms of ANSII conjugated with DOTA-NHS are reported in Figure S1. This means that the sample contains in comparable amounts a few species with a variable number of DOTA-NHS-ester groups. It is known that the DOTA-NHS-ester manifests a large selectivity for free amino groups, but it is difficult to identify by MS which lysine groups are actually modified. As only a rather limited number of lysine groups are modified even in the presence of relatively large DOTA-NHS-ester/protein ratios 15:1, it can be inferred that only the most accessible and reactive lysine groups will be modified. A plausible estimation of the most accessible and reactive lysines has been obtained independently through a bioinformatic analysis using the program PROPKA.[53,54] This analysis suggests that the most reactive amino groups residues are the N-terminus and lysines 104, 49, and 71 (see Table S1).

Water ¹H NMRD Profiles of ANSII-DOTA. The ¹H NMRD profiles of water solutions of diamagnetic (metal free) ANSII-DOTA at 15, 25, and 37 °C are shown in Figure 3. The concentration of the monomeric protein was 0.38 mmol dm⁻³.

The decrease in the relaxation rates measured for increasing magnetic fields reports on the dynamics of the water protons interacting with the protein.[57] Their dipole–dipole coupling energy is modulated by the shortest time between the overall
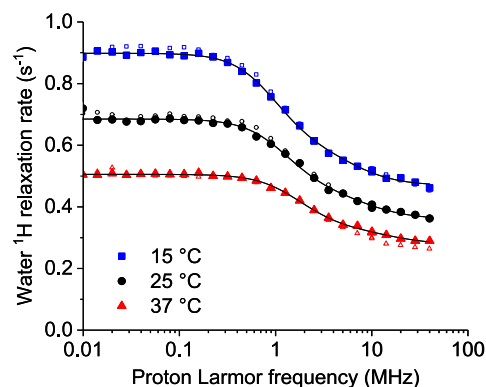
Figure 3. ¹H NMRD profiles of a water solution of DOTA-conjugated ANSII (0.38 mmol dm⁻³ monomeric protein concentration) at 15, 25, and 37 °C (solid symbols). Basically identical profiles were measured for the unconjugated ANSII protein (empty symbols).

reorientation time τ_R of the tetrameric protein assembly, the local internal mobility times τ_f, and the lifetime τ_M of the water molecule on the protein surface. Water molecules with τ_M longer than τ_R or τ_f thus provide information on the molecular tumbling time and on possible presence of faster internal mobility. The ¹H NMRD profiles were fitted using eq 1[58,59]

$$R_{1dia} = \alpha + \beta \sum_n^N c_n \left(\frac{\tau_n}{1 + \omega^2 \tau_n^2} + \frac{4\tau_n}{1 + 4\omega^2 \tau_n^2} \right) \tag{1}$$

where c_n are weight coefficients summing to 1. The profiles could not be nicely fitted with $N = 1$, whereas fits of good quality could be obtained with $N = 2$ (solid lines in Figure 3). The best-fit profiles are reported in Table 1, where the longest and shortest τ's obtained from the fit were indicated as τ_R and τ_f, respectively.[60] These values are in agreement with those previously obtained for the unconjugated ANSII protein in a different concentration and water buffer solution (20 mm sodium phosphate, pH 7.5, 0.02% NaN₃, 0.1 mg mL⁻¹ protease inhibitors (Pefabloc)), when the following values were obtained at 25 °C: $c_1 = 0.42$, $\tau_1 = 6.0 \times 10^{-8}$ s, $\tau_2 = 9 \times$

Table 1. Best-Fit Parameters of the ^1H NMRD Profiles of DOTA-Conjugated ANSII

	15 °C	25 °C	37 °C	
α	0.47	0.36	0.28	s^{-1}
β		1.2×10^7		s^{-2}
c_1		0.31		
$\tau_R = \tau_1$	8.7×10^{-8}	6.7×10^{-8}	4.9×10^{-8}	s
$\tau_f = \tau_2{}^a$	1.3×10^{-8}	9.3×10^{-9}	5.5×10^{-9}	s

$^a c_2 = 1 - c_1$.

10^{-9} s.[50] The values of τ_R confirm that indeed the protein forms tetrameric assemblies, being of the order of what expected for globular proteins with MW of ca. 140 kDa.[58] This finding represents an evidence that the tetrameric structure of the unconjugated protein is retained also upon its functionalization with DOTA-NHS-ester. The large contribution from correlation times smaller than 10 ns (at 25 °C) indicate the presence of an extensive mobility in the nanosecond timescale, probably reflecting the intrinsic flexibility related to the many loop regions present in the protein. As previously noted, this extensive internal mobility is consistent with the intensity and resolution of the solution NMR spectra of the protein.[50]

Water ^1H NMRD Profiles of Gd-DOTA-Conjugated ANSII. The NMRD profiles of the water solution of Gd-DOTA-conjugated ANSII were collected at 15, 25, and 37 °C (Figure 4). The concentration of the gadolinium(III) ions was
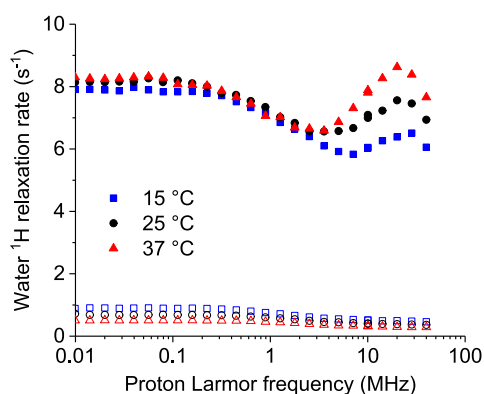
Figure 4. ^1H NMRD profiles of a water solution of Gd-DOTA-conjugated ANSII (0.24 mmol dm^{-3}) at 15, 25, and 37 °C (solid symbols). The profiles of the Gd-free protein are also shown as empty symbols.

0.24 mmol dm^{-3}, as determined from ICP-OES measurements. The relaxivity values, obtained from the difference between the relaxation rates measured from the paramagnetic and the diamagnetic samples, scaled to 1 mmol dm^{-3} gadolinium(III) concentration, are shown in Figure 5.

Interestingly, the relaxivity is quite large (although much smaller than the theoretical limit[61]) for a complex with one water molecule ($q = 1$) coordinated to the gadolinium ion, with respect to that measured for other proteins conjugated to DOTA-like or DTPA-like complexes. Nevertheless, the temperature dependence of the profiles indicates that the relaxivity is limited by the water protons exchange rate, as it increases with the temperature. The whole profiles cannot be fitted with the Solomon–Bloembergen–Morgan (SBM) model due to the presence of zero-field splitting (ZFS), which affects the energy of the electron spin states.[62,63] The
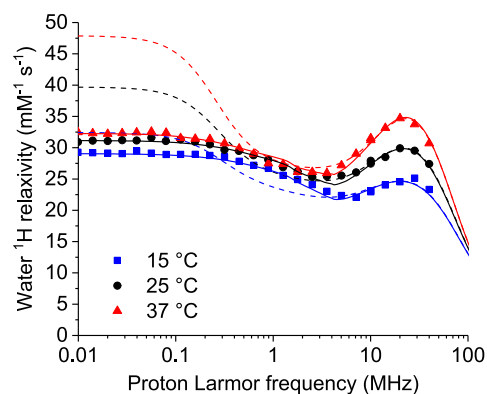
Figure 5. ^1H relaxivity profiles of GdDOTA-conjugated ANSII at 15, 25, and 37 °C. Solid lines are the best-fit profiles obtained with the Florence NMRD program, and dashed lines are calculated with the SBM model.

SBM model can however be used to reproduce the high-field regions of the profiles, when ZFS can be neglected because much smaller than the Zeeman energy. In the fit, outer-sphere contributions were also considered with typical values for the distance of closest approach and the diffusion coefficients.[64] The fit of the high-field region (proton Larmor frequencies larger than 5 MHz) shows that reorientation times τ_i of the order of nanoseconds are needed to reproduce the profiles and their temperature dependence. These times are 1 order of magnitude smaller than the tumbling times of the tetrameric protein (τ_R, see above), which implies that the dipole–dipole interactions between the unpaired electrons of the gadolinium(III) ions and the water protons are completely averaged out by internal dynamics.

The profiles were thus fitted using the modified Florence NMRD program,[63,65,66] which can reproduce the effects of the ZFS both in the electron and the nuclear relaxation rates, in the Redfield and slow rotation limits.[67] The slow rotation limit implies that reorientation is much slower than electron relaxation (determined from the parameters Δ_t and τ_v according to the pseudorotation model[68]). Contributions from even faster motions (with correlation time τ_l) were included through a Lipari-Szabo model-free approach[11,69] so as to further improve the quality of the fit. The best-fit parameters are reported in Table 2, and the corresponding profiles are

Table 2. Best-Fit Parameters of the ^1H Relaxivity Profiles of GdDOTA-Conjugated ANSII

	15 °C	25 °C	37 °C	
r^a		3.05		Å
q^a		1		
Δ_t		0.0095		cm^{-1}
τ_v	16×10^{-12}	15×10^{-12}	14×10^{-12}	s
τ_i	3.8×10^{-9}	3.6×10^{-9}	3.4×10^{-9}	s
τ_M	5.5×10^{-7}	3.6×10^{-7}	2.3×10^{-7}	s
S^2		0.71		
τ_l	1.7×10^{-10}	1.2×10^{-10}	0.8×10^{-10}	s
ZFS		0.03		cm^{-1}
θ	35	47	55	degrees

^{a}Fixed values. The outer-sphere parameters d (distance of closest approach) and D (diffusion coefficient) were fixed to 3.6 Å and to 1.8×10^{-9}, 2.3×10^{-9}, and 3.0×10^{-9} m^2 s^{-1} at 15, 25, and 37 °C, respectively.

shown in Figure 5 as solid lines. The dashed lines in Figure 5 show the relaxivity profiles calculated with the same parameters and using the SBM model.

The best-fit profiles were obtained by allowing the angle θ between the z axis of the ZFS tensor and the line passing through the positions of the gadolinium ion and the coordinated water molecule to change with changing temperature. The quality of the fit gets worse if θ is constrained to be the same at all temperatures (unless the squared order parameter S^2, τ_v, and τ_i are unrealistically allowed to increase with increasing temperature). Some inaccuracy in the calculated rates is expected because τ_i and the electron relaxation time are of the same order of magnitude for frequencies smaller than 10 MHz, and therefore the slow rotation treatment is only approximate (more general approaches than the modified Florence NMRD program have been developed[70−72] for a more accurate treatment of these cases). This is however not preventing the accuracy of all other parameters, which are mainly determined from the relaxivity data at high fields, when ZFS is negligible and the SBM model holds.

In the fit, a single conformational state was assumed to be present. However, the variability of the angle θ with temperature may also suggest the occurrence of multiple states, with a temperature-dependent equilibrium. At low temperatures, the gadolinium chelate may in fact interact to some extent with protein residues, whereas at higher temperatures, the increased mobility of the tag can favor more free and extended conformations.

The fit indicates an optimal reorientation time of few nanoseconds, and a lifetime of the coordinated water molecule of 0.2−0.5 μs, i.e., about double with respect to the values observed for the free chelates in water.[73,74] A marked increase in the lifetime of the coordinated water molecule is often observed for gadolinium chelates conjugated to other proteins and macromolecular substrates. This increase is usually ascribed to the formation of hydrogen bonds involving the coordinated water itself and/or between the carboxylic groups of the ligand and amino acid side chains on the surface of the protein, which result in a significant release of the electric charge on the complex that, in turn, yields slower dissociation kinetics.[75] Figure 6 shows the largest enhancement in relaxivity, which can be achieved for an optimal lifetime of the
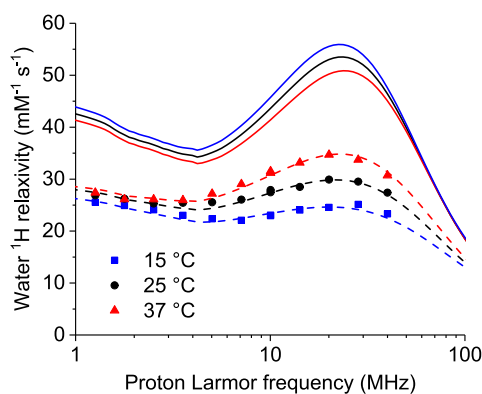
coordinated water molecule of 20−30 ns. The profiles show that, for an optimized water exchange, at 1.5 T (ca. 60 MHz proton Larmor frequency), the relaxivity could increase from 25 to 34 s^{-1} mM^{-1}. An even larger enhancement can be obtained at lower fields. An increase in the reorientation time, on the contrary, would produce a decrease in water relaxivity for fields higher than 1 T.

CONCLUSIONS

The relaxometric profiles of the Gd-labeled ANSII indicate a relaxivity at about 1 T more than 5 times higher than that of clinically used contrast agents and quite high for a gadolinium-labeled protein. The analysis of the profiles sheds light on the origin of the observed relaxivity enhancement. The main contribution arises from the increased reorientational correlation time, amounting to few nanoseconds, i.e., only 1 order of magnitude larger than that of the unbound paramagnetic complex, but optimal for high-field MRI (1.5 T). Conversely, the observed slow exchange regime of the coordinated water molecules limits the relaxivity enhancement. It has been hypothesized that slow exchange arises from a pattern of hydrogen bonds involving the coordinated water itself, the carboxylic groups, and the amino acids at the protein surface. This view is supported by the short length of the linker connecting the paramagnetic core to the protein residues. We can speculate that the use of a longer linker may on the other hand decrease the reorientation time, leading to a decrease in relaxivity. A more interesting solution could be the use of a different gadolinium chelate, characterized by a faster exchange of the coordinated water, as, for instance, some DO3A derivatives,[19] which are sufficiently stable and inert for biological use.[76] The tetrameric assembly of the protein and the high relaxivity of the gadolinium chelates are key factors that make Gd(III)-labeled asparaginase an interesting model to develop new theranostic agents.

EXPERIMENTAL PROCEDURES

Protein Expression and Purification. ANSII was expressed and purified in both nonlabeled and ^{15}N-labeled forms, following the published protocol for ANSII production and purification.[77]

Conjugation Reaction. DOTA-NHS-ester solution was prepared by dissolving the reagent in a volume of dry DMF so that the percentage of organic solvent in the final 12 mL reaction volume was less than 1%. An excess of DOTA-NHS-ester (15 times the monomer concentration) with respect to a 0.152 mmol dm^{-3} protein solution was employed for the conjugation. The reaction occurred overnight in 150 mmol dm^{-3} phosphate buffer, pH 7.5, at room temperature.

A desalting column (Hi prep 26/10) was performed to eliminate the unreacted DOTA-NHS-ester and to change the buffer to 50 mmol dm^{-3} MES−NaOH 100 mmol dm^{-3} NaCl, pH 6.5.

Chelation Reaction. A 10 mmol dm^{-3} solution of GdCl$_3$ was added to the conjugated protein solution, to have a concentration of gadolinium(III) equal to 80% of the estimated DOTA-NHS-ester bound to the protein. The solution was incubated at 309 K and under stirring for 3 days overall.

Size exclusion chromatography using a HiLoad 16/60 Superdex 75 pg column was performed to remove the nonreacted gadolinium(III) ions.

Figure 6. ^{1}H relaxivity profiles calculated for optimized water exchange ($\tau_M \approx 2-3 \times 10^{-8}$ s) and all other parameters equal to the values reported in Table 2 (solid lines). The experimental data for GdDOTA-conjugated ANSII are also reported.

ICP-OES. Inductively coupled plasma coupled with optical emission spectrometry was employed to determine gadolinium(III) concentration into the conjugated ANSII-DOTA sample.

ESI MS Spectrometry. The ESI MS investigations were performed using a TripleTOF 5600+ high-resolution mass spectrometer (Sciex, Framingham, MA), equipped with a DuoSpray interface operating with an ESI probe. All of the ESI mass spectra were acquired through direct infusion at 7 μL min^{-1} flow rate.

The ESI source parameters optimized for the protein are the following:

Positive polarity, ionspray voltage floating (ISFV) 5500 V, temperature (TEM) 25 °C, ion source gas 1 (GS1) 25 L min^{-1}; ion source gas 2 (GS2) 0 L min^{-1}; curtain gas (CUR) 20 L min^{-1}, collision energy (CE) 10 V; declustering potential (DP) 30 V, acquisition range 500−3400 m/z.

For acquisition, Analyst TF software 1.7.1 (Sciex) was used and deconvoluted spectra were obtained using the Bio Tool Kit micro-application v.2.2 embedded in PeakView software v.2.2 (Sciex).

Both samples were diluted to a final protein concentration of 10^{-6} M using LC-MS water, pH 5.5, and the 0.5% v/v of formic acid was added just before the infusion in the mass spectrometer to enhance the ionization process.

The percentages of free ANSII and of its conjugates in the final sample has been calculated according to the relative intensity of each MS peak.

^{1}H NMRD. Nuclear magnetic relaxation dispersion (NMRD) profiles were acquired with a fast-field-cycling Stelar relaxometer. They provided the field dependence of the longitudinal relaxation rate of water protons in samples with ANSII-DOTA solutions, from 0.01 to 40 MHz proton Larmor frequency.[57]

ASSOCIATED CONTENT

Supporting Information

The Supporting Information is available free of charge at https://pubs.acs.org/doi/10.1021/acs.bioconjchem.2c00506.

Percentages of free and conjugated ANSII (Figure S1) and pKa and buried surface of amines of ANSII (Table S1) (PDF)

AUTHOR INFORMATION

Corresponding Author

Giacomo Parigi − *Magnetic Resonance Center (CERM), University of Florence, Sesto Fiorentino 50019, Italy; Department of Chemistry "Ugo Schiff", University of Florence, Sesto Fiorentino 50019, Italy; Consorzio Interuniversitario Risonanze Magnetiche Metallo Proteine (CIRMMP), Sesto Fiorentino 50019, Italy;* orcid.org/0000-0002-1989-4644; Email: parigi@cerm.unifi.it

Authors

Giulia Licciardi − *Magnetic Resonance Center (CERM), University of Florence, Sesto Fiorentino 50019, Italy; Department of Chemistry "Ugo Schiff", University of Florence, Sesto Fiorentino 50019, Italy; Consorzio Interuniversitario Risonanze Magnetiche Metallo Proteine (CIRMMP), Sesto Fiorentino 50019, Italy*

Domenico Rizzo − *Magnetic Resonance Center (CERM), University of Florence, Sesto Fiorentino 50019, Italy;*

Department of Chemistry "Ugo Schiff", University of Florence, Sesto Fiorentino 50019, Italy; Consorzio Interuniversitario Risonanze Magnetiche Metallo Proteine (CIRMMP), Sesto Fiorentino 50019, Italy

Maria Salobehaj − *Magnetic Resonance Center (CERM), University of Florence, Sesto Fiorentino 50019, Italy; Department of Chemistry "Ugo Schiff", University of Florence, Sesto Fiorentino 50019, Italy; Consorzio Interuniversitario Risonanze Magnetiche Metallo Proteine (CIRMMP), Sesto Fiorentino 50019, Italy*

Lara Massai − *Department of Chemistry "Ugo Schiff", University of Florence, Sesto Fiorentino 50019, Italy*

Andrea Geri − *Department of Chemistry "Ugo Schiff", University of Florence, Sesto Fiorentino 50019, Italy*

Luigi Messori − *Department of Chemistry "Ugo Schiff", University of Florence, Sesto Fiorentino 50019, Italy;* orcid.org/0000-0002-9490-8014

Enrico Ravera − *Magnetic Resonance Center (CERM), University of Florence, Sesto Fiorentino 50019, Italy; Department of Chemistry "Ugo Schiff", University of Florence, Sesto Fiorentino 50019, Italy; Consorzio Interuniversitario Risonanze Magnetiche Metallo Proteine (CIRMMP), Sesto Fiorentino 50019, Italy;* orcid.org/0000-0001-7708-9208

Marco Fragai − *Magnetic Resonance Center (CERM), University of Florence, Sesto Fiorentino 50019, Italy; Department of Chemistry "Ugo Schiff", University of Florence, Sesto Fiorentino 50019, Italy; Consorzio Interuniversitario Risonanze Magnetiche Metallo Proteine (CIRMMP), Sesto Fiorentino 50019, Italy;* orcid.org/0000-0002-8440-1690

Complete contact information is available at:
https://pubs.acs.org/10.1021/acs.bioconjchem.2c00506

Notes

The authors declare no competing financial interest.

ACKNOWLEDGMENTS

REFERENCES

(1) Wahsner, J.; Gale, E. M.; Rodríguez-Rodríguez, A.; Caravan, P. Chemistry of MRI Contrast Agents: Current Challenges and New Frontiers. *Chem. Rev.* **2019**, *119*, 957−1057.

(2) Gianolio, E.; Bardini, P.; Arena, F.; Stefania, R.; Di Gregorio, E.; Iani, R.; Aime, S. Gadolinium Retention in the Rat Brain: Assessment of the Amounts of Insoluble Gadolinium-Containing Species and Intact Gadolinium Complexes after Repeated Administration of Gadolinium-Based Contrast Agents. *Radiology* **2017**, *285*, 839−849.

(3) McDonald, R. J.; McDonald, J. S.; Kallmes, D. F.; Jentoft, M. E.; Murray, D. L.; Thielen, K. R.; Williamson, E. E.; Eckel, L. J. Intracranial Gadolinium Deposition after Contrast-Enhanced MR Imaging. *Radiology* **2015**, *275*, 772−782.

(4) Idée, J.-M.; Port, M.; Robic, C.; Medina, C.; Sabatou, M.; Corot, C. Role of Thermodynamic and Kinetic Parameters in Gadolinium Chelate Stability. *J. Magn. Reson. Imaging* **2009**, *30*, 1249−1258.

(5) Di Gregorio, E.; Gianolio, E.; Stefania, R.; Barutello, G.; Digilio, G.; Aime, S. On the Fate of MRI Gd-Based Contrast Agents in Cells. Evidence for Extensive Degradation of Linear Complexes upon Endosomal Internalization. *Anal. Chem.* **2013**, *85*, 5627−5631.

(6) Marckmann, P.; Skov, L.; Rossen, K.; Dupont, A.; Damholt, M. B.; Heaf, J. G.; Thomsen, H. S. Nephrogenic Systemic Fibrosis: Suspected Causative Role of Gadodiamide Used for Contrast-Enhanced Magnetic Resonance Imaging. *J. Am. Soc. Nephrol.* **2006**, *17*, 2359−2362.

(7) Uzal-Varela, R.; Rodríguez-Rodríguez, A.; Martínez-Calvo, M.; Carniato, F.; Lalli, D.; Esteban-Gómez, D.; Brandariz, I.; Pérez-Lourido, P.; Botta, M.; Platas-Iglesias, C. Mn2+ Complexes Containing Sulfonamide Groups with PH-Responsive Relaxivity. *Inorg. Chem.* **2020**, *59*, 14306−14317.

(8) Rizzo, D.; Ravera, E.; Fragai, M.; Parigi, G.; Luchinat, C. Origin of the MRI Contrast in Natural and Hydrogel Formulation of Pineapple Juice. *Bioinorg. Chem. Appl.* **2021**, *2021*, 1−12.

(9) Licciardi, G.; Rizzo, D.; Ravera, E.; Fragai, M.; Parigi, G.; Luchinat, C. Not Only Manganese, but Fruit Component Effects Dictate the Efficiency of Fruit Juice as an Oral Magnetic Resonance Imaging Contrast Agent. *NMR Biomed.* **2022**, *35*, No. e4623.

(10) Wu, Y.; Zhou, I. Y.; Igarashi, T.; Longo, D. L.; Aime, S.; Sun, P. Z. A Generalized Ratiometric Chemical Exchange Saturation Transfer (CEST) MRI Approach for Mapping Renal PH Using Iopamidol. *Magn. Reson. Med.* **2018**, *79*, 1553−1558.

(11) Caravan, P.; Cloutier, N. J.; McDermid, S. A.; Ellison, J. J.; Chasse, J. M.; Lauffer, R. B.; Luchinat, C.; McMurry, T. J.; Parigi, G.; Spiller, M. Albumin Binding, Relaxivity and Water Exchange Kinetics of the Diastereoisomers of MS-325 a Gadolinium(III) Based Magnetic Resonance Angiography Contrast Agent. *Inorg. Chem.* **2007**, *46*, 6632−6639.

(12) Anelli, P. L.; Bertini, I.; Fragai, M.; Lattuada, L.; Luchinat, C.; Parigi, G. Sulfonamide-Functionalized Gadolinium DTPA Complexes as Possible Contrast Agents for MRI: A Relaxometric Investigation. *Eur. J. Inorg. Chem.* **2000**, *2000*, 625−630.

(13) Li, H.; Parigi, G.; Luchinat, C.; Meade, T. J. Bimodal Fluorescence-Magnetic Resonance Contrast Agent for Apoptosis Imaging. *J. Am. Chem. Soc.* **2019**, *141*, 6224−6233.

(14) Carniato, F.; Tei, L.; Botta, M.; Ravera, E.; Fragai, M.; Parigi, G.; Luchinat, C. 1H NMR Relaxometric Study of Chitosan-Based Nanogels Containing Mono- and Bis-Hydrated Gd(III) Chelates: Clues for MRI Probes of Improved Sensitivity. *ACS Appl. Bio Mater.* **2020**, *3*, 9065−9072.

(15) Fragai, M.; Ravera, E.; Tedoldi, F.; Luchinat, C.; Parigi, G. Relaxivity of Gd-Based MRI Contrast Agents in Crosslinked Hyaluronic Acid as a Model for Tissues. *ChemPhysChem* **2019**, *20*, 2204−2209.

(16) Courant, T.; Roullin, V. G.; Cadiou, C.; Callewaert, M.; Andry, M. C.; Portefaix, C.; Hoeffel, C.; de Goltstein, M. C.; Port, M.; Laurent, S.; Elst, L. V.; Muller, R.; Molinari, M.; Chuburu, F. Hydrogels Incorporating GdDOTA: Towards Highly Efficient Dual T1/T2 MRI Contrast Agents. *Angew. Chem., Int. Ed.* **2012**, *51*, 9119−9122.

(17) Yon, M.; Gineste, S.; Parigi, G.; Lonetti, B.; Gibot, L.; Talham, D. R.; Marty, J.-D.; Mingotaud, C. Hybrid Polymeric Nanostructures Stabilized by Zirconium and Gadolinium Ions for Use as Magnetic Resonance Imaging Contrast Agents. *ACS Appl. Nano Mater.* **2021**, *4*, 4974−4982.

(18) Aime, S.; Frullano, L.; Geninatti Crich, S. Compartmentalization of a Gadolinium Complex in the Apoferritin Cavity: A Route To Obtain High Relaxivity Contrast Agents for Magnetic Resonance Imaging. *Angew. Chem., Int. Ed.* **2002**, *41*, 1017−1019.

(19) Rotz, M. W.; Culver, K. S. B.; Parigi, G.; MacRenaris, K. W.; Luchinat, C.; Odom, T. W.; Meade, T. J. High Relaxivity Gd(III)−DNA Gold Nanostars: Investigation of Shape Effects on Proton Relaxation. *ACS Nano* **2015**, *9*, 3385−3396.

(20) Carniato, F.; Tei, L.; Botta, M. Gd-Based Mesoporous Silica Nanoparticles as MRI Probes. *Eur. J. Inorg. Chem.* **2018**, *2018*, 4936−4954.

(21) Carniato, F.; Tei, L.; Martinelli, J.; Botta, M. Relaxivity Enhancement of Ditopic Bishydrated Gadolinium(III) Complexes Conjugated to Mesoporous Silica Nanoparticles. *Eur. J. Inorg. Chem.* **2018**, *2018*, 2363−2368.

(22) Tei, L.; Gugliotta, G.; Gambino, G.; Fekete, M.; Botta, M. Developing High Field MRI Contrast Agents by Tuning the Rotational Dynamics: Bisaqua GdAAZTA-Based Dendrimers. *Isr. J. Chem.* **2017**, *57*, 887−895.

(23) Alhaique, F.; Bertini, I.; Fragai, M.; Carafa, M.; Luchinat, C.; Parigi, G. Solvent 1H NMRD Study of Biotinylated Paramagnetic Liposomes Containing Gd-Bis-SDA-DTPA or Gd-DMPE-DTPA. *Inorg. Chim. Acta* **2002**, *331*, 151−157.

(24) Datta, A.; Hooker, J. M.; Botta, M.; Francis, M. B.; Aime, S.; Raymond, K. N. High Relaxivity Gadolinium Hydroxypyridonate−Viral Capsid Conjugates: Nanosized MRI Contrast Agents1. *J. Am. Chem. Soc.* **2008**, *130*, 2546−2552.

(25) Mastarone, D. J.; Harrison, V. S. R.; Eckermann, A. L.; Parigi, G.; Luchinat, C.; Meade, T. J. A Modular System for the Synthesis of Multiplexed Magnetic Resonance Probes. *J. Am. Chem. Soc.* **2011**, *133*, 5329−5337.

(26) Caravan, P.; Farrar, C. T.; Frullano, L.; Uppal, R. Influence of Molecular Parameters and Increasing Magnetic Field Strength on Relaxivity of Gadolinium- and Manganese-Based T1 Contrast Agents. *Contrast Media Mol. Imaging* **2009**, *4*, 89−100.

(27) Matsumoto, Y.; Jasanoff, A. Metalloprotein-Based MRI Probes. *FEBS Lett.* **2013**, *587*, 1021−1029.

(28) Yang, J. J.; Yang, J.; Wei, L.; Zurkiya, O.; Yang, W.; Li, S.; Zou, J.; Zhou, Y.; Maniccia, A. L. W.; Mao, H.; Zhao, F.; Malchow, R.; Zhao, S.; Johnson, J.; Hu, X.; Krogstad, E.; Liu, Z.-R. Rational Design of Protein-Based MRI Contrast Agents. *J. Am. Chem. Soc.* **2008**, *130*, 9260−9267.

(29) Xue, S.; Qiao, J.; Pu, F.; Cameron, M.; Yang, J. J. Design of a Novel Class of Protein-Based Magnetic Resonance Imaging Contrast Agents for the Molecular Imaging of Cancer Biomarkers. *Wiley Interdiscip. Rev.: Nanomed. Nanobiotechnol.* **2013**, *5*, 163−179.

(30) Caravan, P.; Greenwood, J. M.; Welch, J. T.; Franklin, S. J. Gadolinium-Binding Helix−Turn−Helix Peptides: DNA-Dependent MRI Contrast Agents. *Chem. Commun.* **2003**, 2574−2575.

(31) Daughtry, K. D.; Martin, L. J.; Sarraju, A.; Imperiali, B.; Allen, K. N. Tailoring Encodable Lanthanide-Binding Tags as MRI Contrast Agents. *ChemBioChem* **2012**, *13*, 2567−2574.

(32) Grum, D.; Franke, S.; Kraff, O.; Heider, D.; Schramm, A.; Hoffmann, D.; Bayer, P. Design of a Modular Protein-Based MRI Contrast Agent for Targeted Application. *PLoS One* **2013**, *8*, No. e65346.

(33) Xue, S.; Yang, H.; Qiao, J.; Pu, F.; Jiang, J.; Hubbard, K.; Hekmatyar, K.; Langley, J.; Salarian, M.; Long, R. C.; Bryant, R. G.; Hu, X. P.; Grossniklaus, H. E.; Liu, Z.-R.; Yang, J. J. Protein MRI Contrast Agent with Unprecedented Metal Selectivity and Sensitivity for Liver Cancer Imaging. *Proc. Natl. Acad. Sci. U.S.A.* **2015**, *112*, 6607−6612.

(34) Lauffer, R. B.; Brady, T. J. Preparation and Water Relaxation Properties of Proteins Labeled with Paramagnetic Metal Chelates. *Magn. Reson. Imaging* **1985**, *3*, 11−16.

(35) Frullano, L.; Caravan, P. Strategies for the Preparation of Bifunctional Gadolinium(III) Chelators. *Curr. Org. Synth.* **2011**, *8*, 535−565.

(36) Karfeld, L. S.; Bull, S. R.; Davis, N. E.; Meade, T. J.; Barron, A. E. Use of a Genetically Engineered Protein for the Design of a Multivalent MRI Contrast Agent. *Bioconjugate Chem.* **2007**, *18*, 1697−1700.

(37) Karfeld-Sulzer, L. S.; Waters, E. A.; Davis, N. E.; Meade, T. J.; Barron, A. E. Multivalent Protein Polymer MRI Contrast Agents: Controlling Relaxivity via Modulation of Amino Acid Sequence. *Biomacromolecules* **2010**, *11*, 1429−1436.

(38) Spanoghe, M.; Lanens, D.; Dommisse, R.; Van der Linden, A.; Alderweireldt, F. Proton Relaxation Enhancement by Means of Serum Albumin and Poly-l-Lysine Labeled with DTPA-Gd3+: Relaxivities as

a Function of Molecular Weight and Conjugation Efficiency. *Magn. Reson. Imaging* **1992**, *10*, 913−917.

(39) Rebizak, R.; Schaefer, M.; Dellacherie, É. Polymeric Conjugates of Gd3+−Diethylenetriaminepentaacetic Acid and Dextran. 2. Influence of Spacer Arm Length and Conjugate Molecular Mass on the Paramagnetic Properties and Some Biological Parameters. *Bioconjugate Chem.* **1998**, *9*, 94−99.

(40) Zhang, Z.; Greenfield, M. T.; Spiller, M.; McMurry, T. J.; Lauffer, R. B.; Caravan, P. Multilocus Binding Increases the Relaxivity of Protein-Bound MRI Contrast Agents. *Angew. Chem., Int. Ed.* **2005**, *44*, 6766−6769.

(41) Tircsó, G.; Tircsóné Benyó, E.; Garda, Z.; Singh, J.; Trokowski, R.; Brücher, E.; Sherry, A. D.; Tóth, É.; Kovács, Z. Comparison of the Equilibrium, Kinetic and Water Exchange Properties of Some Metal Ion-DOTA and DOTA-Bis(Amide) Complexes. *J. Inorg. Biochem.* **2020**, *206*, No. 111042.

(42) Geraldes, C. F. G. C.; Luchinat, C. Lanthanides as Shift and Relaxation Agents in Elucidating the Structure of Proteins and Nucleic Acids. *Met. Ions Biol. Syst.* **2003**, *40*, 513−588.

(43) Keizers, P. H. J.; Ubbink, M. Paramagnetic Tagging for Protein Structure and Dynamics Analysis. *Prog. Nucl. Magn. Reson. Spectrosc.* **2011**, *58*, 88−96.

(44) Nitsche, C.; Otting, G.Chapter 2: Intrinsic and Extrinsic Paramagnetic Probes. In *Paramagnetism in Experimental Biomolecular NMR*; Royal Society of Chemistry, 2018; pp 42−84 DOI: 10.1039/9781788013291-00042.

(45) Thonon, D.; Jacques, V.; Desreux, J. F. A Gadolinium Triacetic Monoamide DOTA Derivative with a Methanethiosulfonate Anchor Group. Relaxivity Properties and Conjugation with Albumin and Thiolated Particles. *Contrast Media Mol. Imaging* **2007**, *2*, 24−34.

(46) Tóth, É.; Pubanz, D.; Vauthey, S.; Helm, L.; Merbach, A. E. The Role of Water Exchange in Attaining Maximum Relaxivities for Dendrimeric MRI Contrast Agents. *Chem. - Eur. J.* **1996**, *2*, 1607−1615.

(47) Swain, A. L.; Jaskólski, M.; Housset, D.; Rao, J. K.; Wlodawer, A. Crystal Structure of Escherichia Coli L-Asparaginase, an Enzyme Used in Cancer Therapy. *Proc. Natl. Acad. Sci. U.S.A.* **1993**, *90*, 1474−1478.

(48) Hill, J. M.; Roberts, J.; Loeb, E.; Khan, A.; MacLellan, A.; Hill, R. W. L-Asparaginase Therapy for Leukemia and Other Malignant Neoplasms. Remission in Human Leukemia. *JAMA* **1967**, *202*, 882−888.

(49) Heo, Y.-A.; Syed, Y. Y.; Keam, S. J. Pegaspargase: A Review in Acute Lymphoblastic Leukaemia. *Drugs* **2019**, *79*, 767−777.

(50) Cerofolini, L.; Giuntini, S.; Carlon, A.; Ravera, E.; Calderone, V.; Fragai, M.; Parigi, G.; Luchinat, C. Characterization of PEGylated Asparaginase: New Opportunities from NMR Analysis of Large PEGylated Therapeutics. *Chem. - Eur. J.* **2019**, *25*, 1984−1991.

(51) Rosen, C. B.; Francis, M. B. Targeting the N Terminus for Site-Selective Protein Modification. *Nat. Chem. Biol.* **2017**, *13*, 697−705.

(52) Jiang, H.; D'Agostino, G. D.; Cole, P. A.; Dempsey, D. R. Selective Protein N-Terminal Labeling with N-Hydroxysuccinimide Esters. *Methods Enzymol.* **2020**, *639*, 333−353.

(53) Rostkowski, M.; Olsson, M. H.; Søndergaard, C. R.; Jensen, J. H. Graphical Analysis of PH-Dependent Properties of Proteins Predicted Using PROPKA. *BMC Struct. Biol.* **2011**, *11*, No. 6.

(54) Cutiño-Avila, B.; Gil, D.; González-Bacerio, J.; Mokarzel-Falcón, L.; Chavez, M.; Díaz, J.; del Monte-Martínez, A. In *Algorithm Development for Protein Ionizable Group's Reactivity on Covalent Immobilization*; Rational Design of Immobilized Derivatives, 2010. DOI: 10.13140/2.1.1755.7769.

(55) Massai, L.; Zoppi, C.; Cirri, D.; Pratesi, A.; Messori, L. Reactions of Medicinal Gold(III) Compounds With Proteins and Peptides Explored by Electrospray Ionization Mass Spectrometry and Complementary Biophysical Methods. *Front. Chem.* **2020**, *8*, No. 581648.

(56) Cirri, D.; Massai, L.; Giacomelli, C.; Trincavelli, M. L.; Guerri, A.; Gabbiani, C.; Messori, L.; Pratesi, A. Synthesis, Chemical Characterization, and Biological Evaluation of a Novel Auranofin Derivative as an Anticancer Agent. *Dalton Trans.* **2022**, *51*, 13527−13539.

(57) Parigi, G.; Ravera, E.; Fragai, M.; Luchinat, C. Unveiling Protein Dynamics in Solution with Field-Cycling NMR Relaxometry. *Prog. Nucl. Magn. Reson. Spectrosc.* **2021**, *124−125*, 85−98.

(58) Bertini, I.; Fragai, M.; Luchinat, C.; Parigi, G. ^{1}H NMRD Profiles of Diamagnetic Proteins: A Model-Free Analysis. *Magn. Reson. Chem.* **2000**, *38*, 543−550.

(59) Halle, B.; J¢hannesson, H.; Venu, K. Model-Free Analysis of Stretched Relaxation Dispersions. *J. Magn. Reson.* **1998**, *135*, 1−13.

(60) Ravera, E.; Parigi, G.; Mainz, A.; Religa, T.; Reif, B.; Luchinat, C. Experimental Determination of Microsecond Reorientation Correlation Times in Protein Solutions. *J. Phys. Chem. B* **2013**, *117*, 3548−3553.

(61) Aime, S.; Botta, M.; Fasano, M.; Terreno, E. Lanthanide(II) Chelates for NMR Biomedical Applications. *Chem. Soc. Rev.* **1998**, *27*, 19−29.

(62) Parigi, G.; Ravera, E.; Luchinat, C. Magnetic Susceptibility and Paramagnetism-Based NMR. *Prog. Nucl. Magn. Reson. Spectrosc.* **2019**, *114−115*, 211−236.

(63) Bertini, I.; Galas, O.; Luchinat, C.; Parigi, G. A Computer Program for the Calculation of Paramagnetic Enhancements of Nuclear Relaxation Rates in Slowly Rotating Systems. *J. Magn. Reson. A* **1995**, *113*, 151−158.

(64) Freed, J. H. Dynamic Effects of Pair Correlation Functions on Spin Relaxation by Translational Diffusion in Liquids. II. Finite Jumps and Independent T_1 Processes. *J. Chem. Phys.* **1978**, *68*, 4034−4037.

(65) Bertini, I.; Kowalewski, J.; Luchinat, C.; Nilsson, T.; Parigi, G. Nuclear Spin Relaxation in Paramagnetic Complexes of S = 1: Electron Spin Relaxation Effects. *J. Chem. Phys.* **1999**, *111*, 5795−5807.

(66) Kruk, D.; Nilsson, T.; Kowalewski, J. Nuclear Spin Relaxation in Paramagnetic Systems with Zero-Field Splitting and Arbitrary Electron Spin. *Phys. Chem. Chem. Phys.* **2001**, *3*, 4907−4917.

(67) Kowalewski, J.; Luchinat, C.; Nilsson, T.; Parigi, G. Nuclear Spin Relaxation in Paramagnetic Systems: Electron Spin Relaxation Effects under Near-Redfield Limit Conditions and Beyond. *J. Phys. Chem. A* **2002**, *106*, 7376−7382.

(68) Bloembergen, N.; Morgan, L. O. Proton Relaxation Times in Paramagnetic Solutions. Effects of Electron Spin Relaxation. *J. Chem. Phys.* **1961**, *34*, 842−850.

(69) Lipari, G.; Szabo, A. Model-Free Approach to the Interpretation of Nuclear Magnetic Resonance Relaxation in Macromolecules. 1. Theory and Range of Validity. *J. Am. Chem. Soc.* **1982**, *104*, 4546−4559.

(70) Fries, P. H. Computing Electronic Spin Relaxation for Gd3+-Based Contrast Agents − Practical Implementation. *Eur. J. Inorg. Chem.* **2012**, *2012*, 2156−2166.

(71) Kowalewski, J.; Kruk, D.; Parigi, G. NMR Relaxation in Solution of Paramagnetic Complexes: Recent Theoretical Progress for S > 1. *Adv. Inorg. Chem.* **2005**, *57*, 41−104.

(72) Belorizky, E.; Fries, P. H.; Helm, L.; Kowalewski, J.; Kruk, D.; Sharp, R. R.; Westlund, P.-O. Comparison of Different Methods for Calculating the Paramagnetic Relaxation Enhancement of Nuclear Spins as a Function of the Magnetic Field. *J. Chem. Phys.* **2008**, *128*, No. 052315.

(73) Powell, D. H.; Dhubhghaill, O. M. N.; Pubanz, D.; Helm, L.; Lebedev, Y. S.; Schlaepfer, W.; Merbach, A. E. Structural and Dynamic Parameters Obtained from 17O NMR, EPR, and NMRD Studies of Monomeric and Dimeric Gd3+ Complexes of Interest in Magnetic Resonance Imaging: An Integrated and Theoretically Self-Consistent Approach1. *J. Am. Chem. Soc.* **1996**, *118*, 9333−9346.

(74) Laurent, S.; Elst, L. V.; Muller, R. N. Comparative Study of the Physicochemical Properties of Six Clinical Low Molecular Weight Gadolinium Contrast Agents. *Contrast Media Mol. Imaging* **2006**, *1*, 128−137.

(75) Aime, S.; Castelli, D. D.; Crich, S. G.; Gianolio, E.; Terreno, E. Pushing the Sensitivity Envelope of Lanthanide-Based Magnetic

Resonance Imaging (MRI) Contrast Agents for Molecular Imaging Applications. *Acc. Chem. Res.* **2009**, *42*, 822−831.

(76) Takács, A.; Napolitano, R.; Purgel, M.; Bényei, A. C.; Zékány, L.; Brücher, E.; Tóth, I.; Baranyai, Z.; Aime, S. Solution Structures, Stabilities, Kinetics, and Dynamics of DO3A and DO3A− Sulphonamide Complexes. *Inorg. Chem.* **2014**, *53*, 2858−2872.

(77) Ravera, E.; Ciambellotti, S.; Cerofolini, L.; Martelli, T.; Kozyreva, T.; Bernacchioni, C.; Giuntini, S.; Fragai, M.; Turano, P.; Luchinat, C. Solid-State NMR of PEGylated Proteins. *Angew. Chem., Int. Ed.* **2016**, *55*, 2446−2449.

📖 Recommended by ACS

Molecular Engineering of Self-Immolative Bioresponsive MR Probes

Jian-Hong Tang, Thomas J. Meade, *et al.*

APRIL 28, 2023
JOURNAL OF THE AMERICAN CHEMICAL SOCIETY   READ 🔗

The Application of Bio-orthogonality for In Vivo Animal Imaging

Jun Yang, Chongzhao Ran, *et al.*

JULY 07, 2023
CHEMICAL & BIOMEDICAL IMAGING   READ 🔗

Rational Design of Gd-DOTA-Type Contrast Agents for Hepatobiliary Magnetic Resonance Imaging

Weiyuan Xu, Lixiong Dai, *et al.*

JUNE 27, 2023
JOURNAL OF MEDICINAL CHEMISTRY   READ 🔗

Rapid In Vitro Quantification of a Sensitized Gadolinium Chelate via Photoinduced Triplet Harvesting

James A. Tranos, Youssef Z. Wadghiri, *et al.*

JANUARY 09, 2023
ACS OMEGA   READ 🔗

Get More Suggestions >

Large protein assemblies for high relaxivity contrast agents: the case of gadolinium-labeled asparaginase

Giulia Licciardi,[a,b,c] Domenico Rizzo,[a,b,c] Maria Salobehaj,[a,b,c] Lara Massai,[b] Andrea Geri,[b] Luigi Messori,[b] Enrico Ravera,[a,b,c] Marco Fragai,[a,b,c] Giacomo Parigi[a,b,c] *

[a]Magnetic Resonance Center (CERM), University of Florence, via Luigi Sacconi 6, Sesto Fiorentino, 50019 Italy; [b]Department of Chemistry "Ugo Schiff", University of Florence, via della Lastruccia 3, Sesto Fiorentino, 50019 Italy; and [c]Consorzio Interuniversitario Risonanze Magnetiche Metallo Proteine (CIRMMP), via Luigi Sacconi 6, Sesto Fiorentino, 50019 Italy

Supporting information
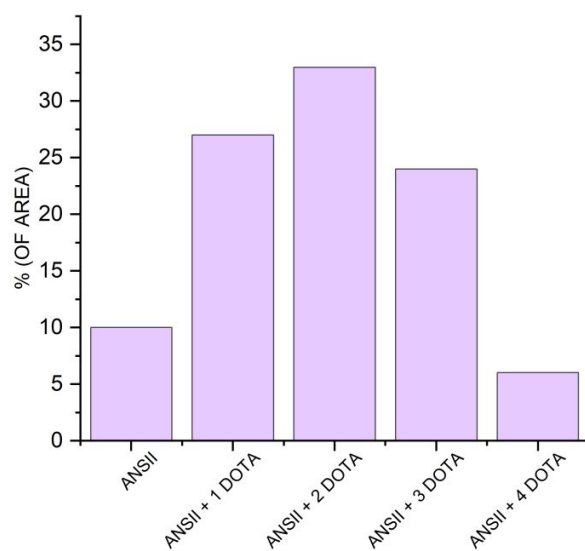
Figure S1. The percentages of free and conjugated ANSII in the sample has been calculated according to the relative intensity of each peak.

Table S1. pK$_a$ and buried surface of amines of ANSII

	RESIDUE NUMBER	pK$_a$	BURIED %
N+	1	7.85	0
LYS	301	7.94	100
LYS	104	8.71	48
LYS	172	9.37	93.75
LYS	49	9.63	11.75
LYS	71	9.98	0
LYS	162	10.02	100
LYS	262	10.16	0
LYS	196	10.28	0
LYS	107	10.30	3
LYS	43	10.36	0
LYS	186	10.41	10.25
LYS	314	10.46	7.75
LYS	139	10.48	0
LYS	213	10.50	2.5
LYS	207	10.51	0
LYS	79	10.89	0
LYS	251	10.92	0
LYS	288	10.94	0
LYS	229	11.47	0
LYS	72	12.33	3.5

3.3.2 Gd-Labeled Protein Cages

A relaxometric study was carried out on two structurally distinct engineered protein cages, called AaLS-13 and OP, that could serve as excellent candidates for the development of molecular delivery vehicle and nanoparticle platforms for MRI.

AaLS-13 is an evolved variant of the cage-forming enzyme lumazine synthase from Aquifex aeolicus. AaLS-13 self-assembles from 360 monomer proteins into 38 nm icosahedrally symmetric cages (*Figure 3.20 a*). OP, in contrast, is a smaller (~13 nm diameter), 24-subunit, octahedrally symmetric cage, computationally designed (*Figure 3.20 b*).
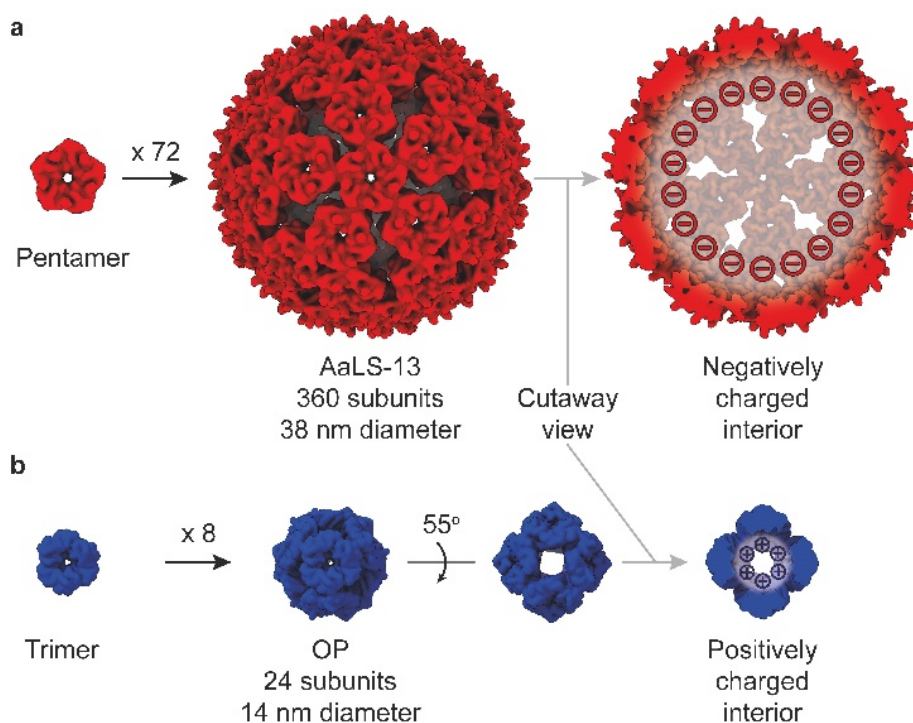
Figure 3.20: Representation of the engineered AaLS-13 (a) and OP (b) protein cages [21].

The ^{1}H NMRD profiles of diamagnetic AaLS-13 and OP, acquired at 298 and 310 K, are shown in figure (*Figure 3.21*). These were subtracted to the paramagnetic profiles of the corresponding species. Details on the analysis of the NMRD profiles are reported in the *Supporting Information* of the attached article [21].

(a)

(b)
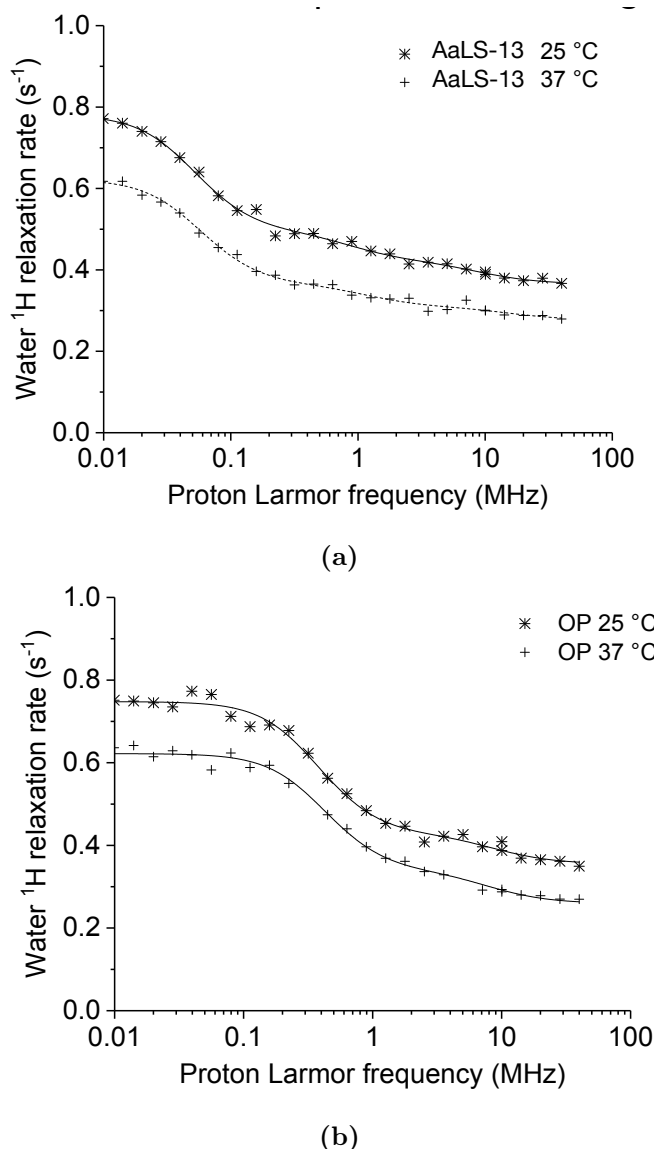
Figure 3.21: (a) ^{1}H NMRD profiles of diamagnetic AaLS-13 protein in sodium phosphate buffer at 298 K (∗ symbols) and at 310 K (+ symbols). (b) ^{1}H NMRD profiles of OP in TRIS buffer at 298 K (∗ symbols) and at 310 K (+ symbols).

In order to evaluate possible nonviral theranostic platforms, AaLS-13 and OP cages functionalized with a DOTA-based gadolinium(III) complex (shown in *Figure 3.22*) were studied through FFC relaxometry. AaLS-13 has one functionalization, located on the lumenal surface of the cage; in the case of the OP cage, four variants having one to four functionalizations (on residues mutated to cysteine) were studied. These are called: OP-1intC (S38C), OP-2intC (S38C, R103C), and OP-3intC (S38C, R66C, R103C), and OP-1extC (K93C). The first three carrying 24, 48, and 72 reactive sites per multimeric assembly on the lumenal surface, respectively; the last presenting 24 cysteines on the outer surface.

The ^{1}H NMRD profiles of the functionalized protein cages were acquired at 298 and 310 K, and the calculated relaxivity values are shown in figure (*Figure 3.23*). Details on the analysis of the NMRD profiles are reported in the *Supporting Information* of the attached article [21].

Gd-C4-IA
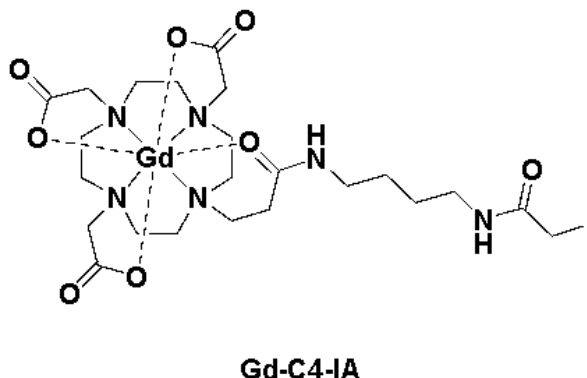
Figure 3.22: Structure of the DOTA-based gadolinium(III) complex employed for AaLS-13 and OP protein cages functionalization [21].

The expected signal amplification has been achieved by all the gadolinium(III)-labeled protein cages, reaching the maximum relaxivity at 298 K at around 0.5 T in the case of Gd-OP-3intC (almost 50 $s^{-1}mM^{-1}$). The enhancement of the relaxivity when the gadolinium complex is bound to the protein cage is, as expected, large and it is due to the increase in the correlation times that modulate the dipole-dipole interactions. We hypothesized the presence of transient interactions in the nanoseconds timescale between the complex and the numerous charged residues at the lumenal surface, which are taken into account by the τ_i correlation time. Additionally, the increase in relaxivity value is the result of an increasing crowding of the internal space, which causes a decrease in the local mobility of the ligand and therefore an increasing in the τ_l value. In this case, water exchange rate did not limit relaxation since the temperature dependence indicates that the coordinated water molecule is in the fast exchange regime.

	Gd-AaLS-13	Gd-OP-3intC	Gd-OP-2intC	Gd-OP-1intC	Gd-OP-1extC	Units
τ_i (298 K)	5.2	3.7	4.0	4.3	1.8	ns
τ_i (310 K)	3.5	3.3	3.2	3.3	1.1	ns
τ_l (298 K)	540	1800	320	68	78	ps
τ_l (310 K)	250	480	98	38	28	ps
S^2	0.28	0.46	0.39	0.36	0.36	

Table 3.4: Comparison of the two reorientational correlation times obtained from the fit of the NMRD profiles of the Gd-AaLS-13 and Gd-OP-like cages.

(a)

(b)
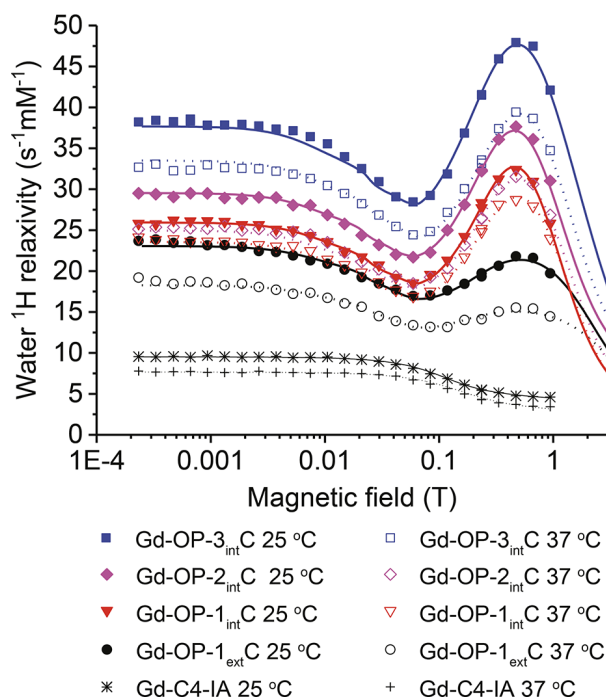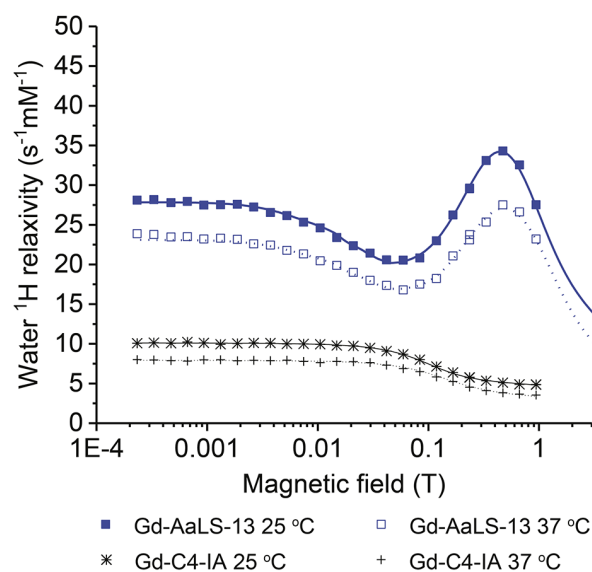
Figure 3.23: The grey symbols and lines refer to the ^{1}H NMRD profiles of Gd-C4-IA complex ($*$ for 298 K, $+$ for 310 K) in the corresponding protein buffer. In panel (a) the ^{1}H NMRD profiles of Gd-AaLS-13 protein in sodium phosphate buffer at 298 K (solid symbols) and at 310 K (empty symbols). Panel (b) reports the ^{1}H NMRD profiles of Gd-OP-3intC in blue, Gd-OP-2intC in pink, Gd-OP-1intC in red, and Gd-OP-1extC in black at 298 K (solid symbols) and 310 K (empty symbols). All this samples were dissolved in TRIS buffer. Solid and dotted lines are the best fit profiles at 298 K and 310 K, respectively.

Article

Engineered Nonviral Protein Cages Modified for MR Imaging

Megan A. Kaster, Mikail D. Levasseur, Thomas G. W. Edwardson, Michael A. Caldwell,
Daniela Hofmann, Giulia Licciardi, Giacomo Parigi, Claudio Luchinat, Donald Hilvert,*
and Thomas J. Meade*

Cite This: *ACS Appl. Bio Mater.* 2023, 6, 591−602

Read Online

ACCESS | Metrics & More | Article Recommendations | Supporting Information

ABSTRACT: Diagnostic medical imaging utilizes magnetic resonance (MR) to provide anatomical, functional, and molecular information in a single scan. Nanoparticles are often labeled with Gd(III) complexes to amplify the MR signal of contrast agents (CAs) with large payloads and high proton relaxation efficiencies (relaxivity, r_1). This study examined the MR performance of two structurally unique cages, AaLS-13 and OP, labeled with Gd(III). The cages have characteristics relevant for the development of theranostic platforms, including (i) well-defined structure, symmetry, and size; (ii) the amenability to extensive engineering; (iii) the adjustable loading of therapeutically relevant cargo molecules; (iv) high physical stability; and (v) facile manufacturing by microbial fermentation. The resulting conjugates showed significantly enhanced proton relaxivity ($r_1 = 11−18$ mM^{-1} s^{-1} at 1.4 T) compared to the Gd(III) complex alone ($r_1 = 4$ mM^{-1} s^{-1}). Serum phantom images revealed 107% and 57% contrast enhancements for Gd(III)-labeled AaLS-13 and OP cages, respectively. Moreover, proton nuclear magnetic relaxation dispersion (^{1}H NMRD) profiles showed maximum relaxivity values of 50 mM^{-1} s^{-1}. Best-fit analyses of the ^{1}H NMRD profiles attributed the high relaxivity of the Gd(III)-labeled cages to the slow molecular tumbling of the conjugates and restricted local motion of the conjugated Gd(III) complex.

KEYWORDS: *nonviral protein cages, magnetic resonance imaging, gadolinium, magnetism, NMRD*

Chemical modification of protein cages

Gd(III) complex
Fast molecular reorientation

Gd-protein conjugate
Increased relaxivity
Long molecular reorientation
High contrast enhancement
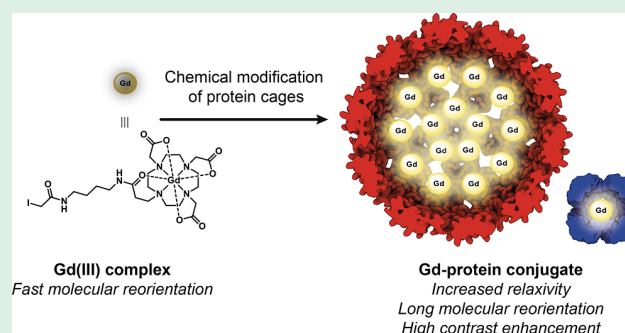
1. INTRODUCTION

Magnetic resonance (MR) imaging is an attractive modality for medical diagnostic imaging because of its unlimited depth penetration, excellent spatiotemporal resolution, and safety profile that does not require ionizing radiation or radiotracers. Furthermore, MR provides unparalleled native soft tissue contrast with highly detailed anatomical information based on inherent tissue differences arising from proton density, perfusion and diffusion, and biomolecule content.[1,2] Administration of contrast agents (CAs) with paramagnetic metal ions greatly enhances tissue contrast by shortening the longitudinal (T_1) and transverse (T_2) relaxation times of protons on local water molecules. In addition, CAs can be designed to report on biomarkers for molecular imaging applications, enabling the correlation of molecular information with tissue structures in a single scan.

Clinical MR imaging often utilizes trivalent gadolinium (Gd(III)) based CAs for T_1-weighted images, where short T_1 values correspond to a bright MR signal.[3] The efficiency with which a CA influences the water proton T_1 is the relaxivity (r_1), defined by eq 1. The observed longitudinal relaxation rate constant in the presence of CA ($1/T_1^{obs}$) comprises a background diamagnetic component (T_1^0) and a paramagnetic component consisting of r_1 and the concentration of Gd(III) in the CA ([Gd(III)]).

$$\frac{1}{T_1^{obs}} = \frac{1}{T_1^0} + r_1[\text{Gd(III)}] \tag{1}$$

Clinically approved small molecule Gd(III) CAs typically have $r_1 \sim 4$ mM^{-1} s^{-1} at clinical MR field strengths (0.2−3 T), where a local concentration of over 100 μM CA is required to induce a detectable change in T_1 over a biological background.[4−6] However, it is difficult for small molecule CAs to reach these local concentrations through biomarker targeting because most biomarkers of interest are expressed at micromolar to picomolar concentrations.[7] Thus, signal amplification strategies are needed to bridge the gap between biomarker expression and the MR detection limit.
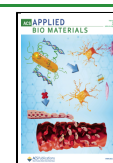
Nanoparticles (NPs) provide an attractive platform for MR imaging with several advantages over their small molecule counterparts, as they can (1) carry a high Gd(III) payload; (2) improve relaxivity per Gd(III) at clinically relevant field strengths; (3) incorporate targeting groups and therapeutic cargo; and (4) extend circulation lifetimes, offering a means to tune biodistribution. The first two points are signal amplification strategies that increase the paramagnetic contribution to the observed MR signal (eq 1). The second, increasing relaxivity, also enhances the safety profile by requiring lower dosing concentrations of Gd(III).[8] Concerns about toxicity related to Gd(III)-based CAs, such as nephrogenic systemic fibrosis (NSF) and Gd(III) deposition in organs, arise primarily from free Gd(III) ions that dissociate from their ligand due to poor kinetic stability. Thus, kinetically stable Gd(III) complexes with macrocyclic ligands have been used clinically in over 500 million MR scans worldwide with only 1 severe adverse event per 40,000 injections.[3,8] Gd(III)-labeled NPs further mitigate toxicity issues by having lower dosing concentrations than required for molecular Gd(III) complexes.

Several types of NPs have been investigated for MR signal amplification as Gd(III)-labeled conjugates,[9] including gold NPs,[10−17] carbon nanodiamonds,[18] metal−organic frameworks,[19] liposomes,[20,21] dendrimers,[22−28] polymers,[29−31] micelles,[32−35] and hydrogels.[36,37] Of the parameters that govern r_1 (eqs 1 and 2), conjugating Gd(III) complexes to NPs most strongly influences the rotational correlation time (τ_R, eq 3) to achieve what is called a "τ_R boost" in relaxivity at clinical field strengths. A brief discussion of MR physics is required to understand the origin of this τ_R boost.

The relaxation processes of nuclear spins (i.e., T_1 of water protons) can be enhanced through magnetic dipole−dipole interactions with unpaired electrons in paramagnetic metals. The strength of this interaction depends on the spin of the paramagnetic metal, the distance between nuclear and electronic spins, and the precession frequencies of nuclear and electronic spins. The high spin state ($S = 7/2$) and long electronic relaxation time ($T_{1e} \sim 10^{-9}$ s at clinical field strengths) of Gd(III) make it an excellent candidate to influence water protons for MR imaging. The highest contribution to r_1 comes from water molecules directly coordinated to Gd(III) with a mean residence time τ_m and exchange with bulk water (eq 2). While r_1 is directly proportional to the number of water molecules bound to Gd(III) (q), increasing q can lead to poor kinetic ligand stability, which would lead to the release of Gd(III) ions from the ligand.[4]

The dipolar longitudinal relaxation time (T_{1m}) originates from the modulation of the magnetic dipole−dipole interaction between electron and proton spins. The time constant of this modulation known as the rotational correlation time (τ_c), is determined by the fastest parameter among T_{1e}, τ_R, and τ_m (eq 3). Relaxivity approaches the theoretical maximum value when the inverse correlation time (τ_c^{-1}) matches the Larmor frequency (ω_I) of water protons. This is when the coupling of the electronic and nuclear spins is most efficient. At clinically relevant field strengths, the fast τ_R values (10^{-10} s to 10^{-12} s) of small molecule Gd(III) CAs determine τ_c and limit relaxivity. Tethering Gd(III) complexes to macromolecules results in a slower τ_R that does not determine τ_c, allowing relaxivity to approach theoretical maximum values (the τ_R boost).

$$r_1 = \frac{q/[\mathrm{H_2O}]}{T_{1m} + \tau_m} \tag{2}$$

$$\frac{1}{\tau_c} = \frac{1}{\tau_R} + \frac{1}{\tau_m} + \frac{1}{T_{1e}} \tag{3}$$

The extended circulation lifetimes of NPs and their amenability to modification also make them attractive cargo delivery vehicles. Many NPs can also serve as theranostic agents, carrying both diagnostic agents and therapeutic drugs, to monitor the drug's efficacy noninvasively and in real time.[38−41] NPs can be further modified to control their biodistribution and for targeted delivery of a therapeutic drug or molecular imaging of a biomarker, depending on the nature of the cargo. Finally, the extended circulation lifetimes of Gd(III)-labeled NPs compared to small molecule Gd(III) complexes increases bioavailability and potential for cellular uptake.[3,4,42] Although NPs provide many benefits for Gd(III)-based MR CAs, concerns with the safety profile of synthetic and inorganic NPs have motivated the search for platforms made from biocompatible materials.

Nanoscale compartments formed by self-assembling proteins are a promising class of NP for achieving MR signal amplification. These protein cages are biodegradable and readily produced recombinantly from bacterial or mammalian cell cultures. Furthermore, the cages assemble with high efficiency and fidelity into monodisperse particles amenable to characterization at the molecular scale not afforded by many other NP materials.[43] Protein cages have been investigated as high-relaxivity agents due to their diversity in terms of shape, size, valency, and the ability to modify both the exterior and interior surfaces.[43] These high relaxivity agents can be broadly grouped into three main categories based on design: (1) binding of Gd(III) ion at endogenous[44] or genetically engineered[45,46] metal binding sites, (2) noncovalent loading of Gd(III) complexes as cargo, and (3) covalent conjugation of Gd(III) complexes to protein cages.[45,47−58] The third approach is attractive for developing theranostic platforms as it allows the cage to be optimized for therapeutic cargo while maintaining an ability to covalently bind Gd(III) complexes.

Two structurally distinct engineered protein cages, AaLS-13 and OP, are excellent candidates for the development of NP platforms for MR imaging. AaLS-13 is an evolved variant of the cage-forming enzyme lumazine synthase from *Aquifex aeolicus.* AaLS-13 self-assembles from 360 monomer proteins into 38 nm icosahedrally symmetric cages (Figure 1a).[59−61] Owing to its negatively supercharged interior and large keyhole-shaped surface pores, AaLS-13 encapsulates positively charged cargo at rates approaching the diffusion limit.[62,63] Additionally, the surface-exposed termini of AaLS-13 offer further functionalization opportunities, which have already been exploited to display antibodies[64] or for enzymatic labeling.[65−67]

OP, in contrast, is a smaller (~13 nm diameter), 24-subunit, octahedrally symmetric cage, which derives from the computationally designed O3−33 cage (Figure 1b).[68] Positive charges were introduced by mutating six lumenal residues in the starting scaffold to arginine, enabling efficient encapsulation of negatively charged cargo, such as oligonucleotides[69] and anionic surfactants.[70] Therapeutically relevant guests, like siRNA and drug-loaded micelles, have been successfully delivered to cells using OP, substantially improving the potency of the active ingredients. These properties make it a promising molecular delivery vehicle.[71]

a

Assembled cages — Cutaway view

Pentamer ×72

AaLS-13
360 subunits
38 nm diameter

Negatively charged interior

b

Trimer ×8 → 55°

OP
24 subunits
~13 nm diameter

Positively charged interior
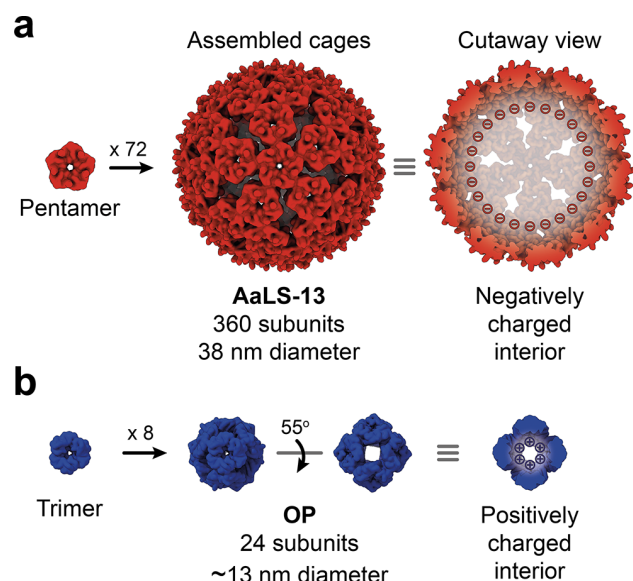
Figure 1. Engineered AaLS-13 and OP protein cages. Surface representation of (a) AaLS-13 (PDB 5MQ7) and (b) OP (PDB 6FDB) cages. AaLS-13 assembles into 38 nm spherical cages, possessing a negatively supercharged interior, from 72 pentameric subunits. OP forms ~13 nm positively supercharged cubic cages from eight trimeric capsomers.

AaLS-13 and OP cages have been applied as delivery vehicles for proteins, oligonucleotides, and small molecules. Conjugating DOTA-based Gd(III) complexes to these tunable cages provides an opportunity to develop nonviral theranostic platforms. To this end, we have covalently linked Gd(III) complexes to the interior and exterior of AaLS-13 and OP cages and assessed how these modifications influence the MR signal. Relaxivity measurements of Gd(III)-labeled proteins show substantial signal amplification with high Gd(III) payloads per cage as well as high relaxivity. In addition to the τ_R boost, the highly charged cage interior appears to restrict Gd(III) complex mobility. Notably, because of the

significant signal amplification, these Gd(III)-protein conjugates provide detectable contrast enhancement at concentrations below those of common small molecule Gd(III) complexes used in the clinic.

2. RESULTS AND DISCUSSION

2.1. Synthesis and Characterization of Gd-C4-IA. The Gd(III) complex Gd-C4-IA was designed using the macrocyclic cyclen scaffold of clinically approved CAs that exhibits good kinetic stability. Gd-C4-IA was synthesized as described in Figure 2, with characterization data for compounds **1**−**4** (Scheme S1) provided in Figures S1−S23. Literature conditions were followed to prepare tri-^{t}Bu 2,2′,2″-(1,4,7,10-tetraazacyclododecane-1,4,7-triyl)triacetate (^{t}BuDO3A) and benzyl acrylate.[51,72,73] Benzyl acrylate served as the foundation for the functional arm that was later used to covalently link Gd-C4-IA to the protein cages. ^{t}BuDO3A and benzyl acrylate were reacted via an aza-Michael addition. The functional arm was deprotected by Pd/C hydrogenation and reacted with ^{t}Bu-(4-aminobutyl)carbamate. Acidic conditions were used to perform a global deprotection of all ^{t}Bu groups, followed by metalation with GdCl$_3$. The Gd-C4-NH$_2$ intermediate was purified by high-performance liquid chromatography (HPLC) (Figure S24a), and then reacted with iodoacetic anhydride to give Gd-C4-IA, which was purified by HPLC (Figure S24b).

2.2. Preparation of Protein Variants. Wild-type (wt) AaLS possesses one buried cysteine (Cys37) per monomer with negligible reactivity.[62] Functionalization of wt AaLS using thiol-reactive species requires introducing additional surface exposed cysteine residues.[74] In contrast, AaLS-13 contains two additional cysteine residues (Cys52 and Cys127) per monomer that were introduced during evolution. Although Cys52 is buried, Cys127 is located on the lumenal surface and can be exploited for thiol-mediated labeling (Figure 3a, left).

OP possesses two cysteines per monomer (Cys108 and Cys136) that form a buried disulfide. To provide specific reactive handles for Gd-C4-IA conjugation, cysteine mutations were introduced at surface exposed, inner loop positions that
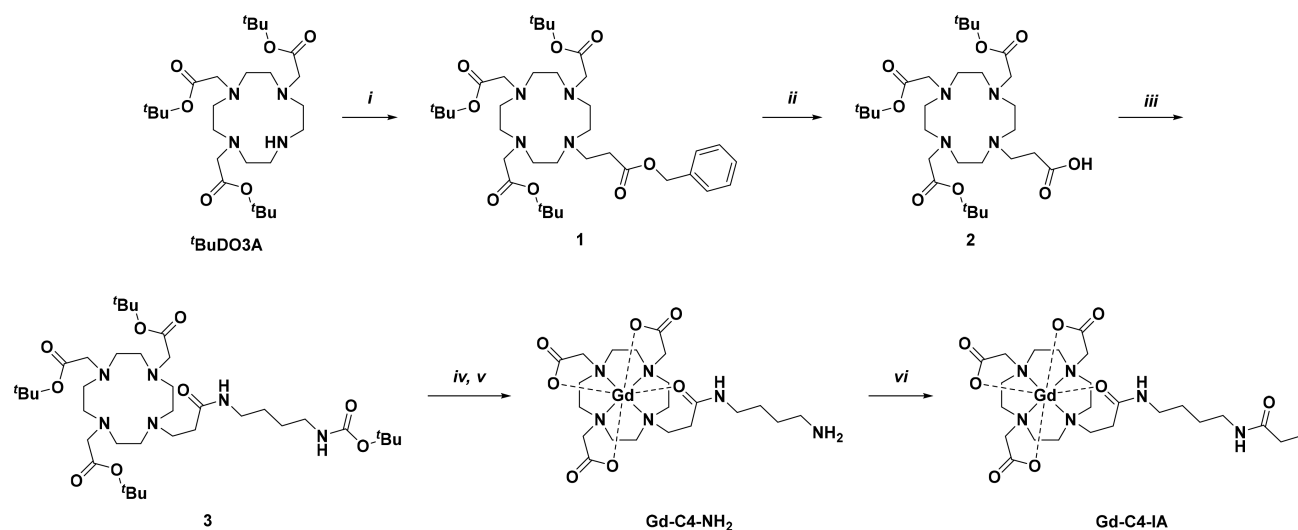
Figure 2. Synthetic scheme for Gd-C4-IA. (*i*) ^{t}BuDO3A (1 equiv), benzyl acrylate (2 equiv), DIEA (5.9 equiv), MeCN, N$_2$ (g), RT, 47%; (*ii*) **1** (1 equiv), Pd/C (catalyst), MeOH, H$_2$ (g), RT, 27%; (*iii*) **2** (1 equiv), ^{t}Bu (4-aminobutyl)carbamate (1.5 equiv), NHS (3 equiv), DIEA (5 equiv), DIC (5 equiv), DMF, N$_2$ (g), RT, quantitative yield; (*iv*) **3** (1 equiv), TFA, CH$_2$Cl$_2$, N$_2$ (g), RT, crude; (*v*) **4** (1 equiv), GdCl$_3$·6H$_2$O (1.3 equiv), H$_2$O, N$_2$ (g), RT, 34% over 2 steps; (*vi*) Gd-C4−NH$_2$ (1 equiv), iodoacetic anhydride (3 equiv), K$_2$CO$_3$ (3 equiv), DMF, N$_2$ (g), 0 °C, 20%.
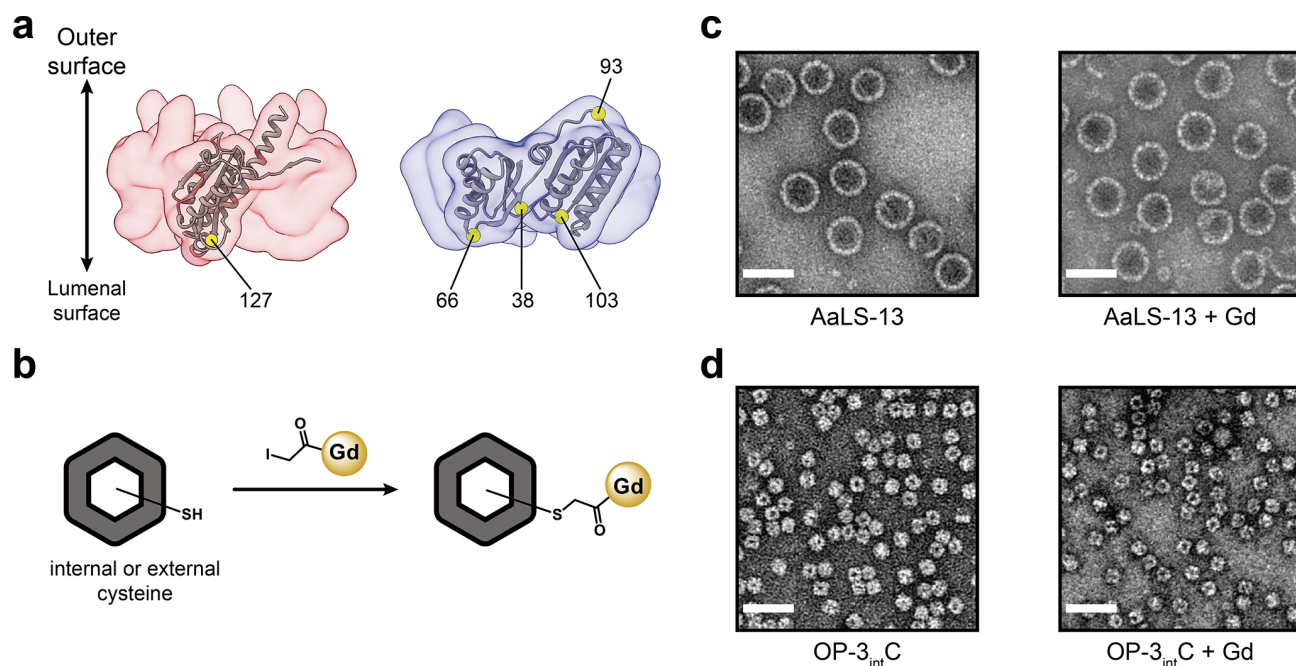
Figure 3. Thiol-mediated functionalization of AaLS-13 and OP and transmission electron microscopy (TEM) images of AaLS-13 and OP-3$_{int}$C. (a) Transparent surface of a pentamer used to construct an AaLS-13 cage (left) and a trimer used to construct OP (right). Monomers are shown as gray ribbons. Targeted cysteine residue on AaLS-13 (Cys127) and positions on OP targeted for cysteine mutations (Ser38, Arg66, and Arg103) are highlighted as yellow spheres. (b) Representations of Gd(III) labeling the cysteine reactive sites. TEM images of (c) AaLS-13 and (d) OP-3$_{int}$C cages, unmodified (left) or labeled with Gd-complexes (right). Scale bar is equal to 50 nm.

were previously shown to be mutable.[69] The three variants, OP-1$_{int}$C (S38C), OP-2$_{int}$C (S38C, R103C), and OP-3$_{int}$C (S38C, R66C, R103C), provide 24, 48, or 72 reactive sites per multimeric assembly on the lumenal surface, respectively. An additional variant, OP-1$_{ext}$C, which presents 24 cysteine residues on the exterior surface of each cage, was designed by mutating the surface exposed lysine at position 93 to cysteine (K93C) (Figure 3a, right).

2.3. Conjugation of Gd(III) Complex with Protein Cages. The Gd-C4-IA complex was conjugated to the protein cages by alkylation of the cysteine thiols in the protein cages with the iodoacetamide group in Gd-C4-IA (Figure 3b). Modification was performed by mixing AaLS-13 or the OP cages with 2 equiv of Gd-C4-IA per reactive thiol and incubating for 4.5 h at room temperature in the dark. Unreacted Gd-C4-IA was removed through desalting columns and the Gd-C4-protein conjugates were isolated by size exclusion chromatography (SEC, Figure S27). The AaLS-13 and OP cages remain intact after labeling with Gd-C4-IA (Figure 3c,d).

The concentration of Gd-C4-IA and protein in the purified samples was determined by ICP-MS and UV−vis measurements, respectively (Table S1, Figure S30). Labeling efficiency, defined as the number of reactive sites per cage successfully labeled with Gd-C4-IA, was measured to evaluate the ability of the cages to carry a high payload of Gd(III) complex for MR imaging (Table 1).

The porous nature of the cages enables efficient labeling of reactive sites positioned on the lumenal surface (41−47% for AaLS-13, OP-3$_{int}$C, OP-2$_{int}$C, and OP-1$_{int}$C). Labeling efficiency is even higher for reactive sites positioned on the exterior surface (60% for OP-1$_{ext}$C). These labeling efficiencies are in the range of previously reported values.[62,74]

Table 1. Labeling of Protein Cages with Gd(III) Complexes

sample name	labeling[a] (complexes/cage)	reactive sites	labeling efficiency (%)
Gd-AaLS-13	149 ± 12	360	41
Gd-OP-3$_{int}$C	33 ± 7	72	46
Gd-OP-2$_{int}$C	23 ± 1	48	47
Gd-OP-1$_{int}$C	11 ± 1	24	46
Gd-OP-1$_{ext}$C	14 ± 2	24	60

[a]Standard deviation accounts for variations across biological replicates.

Furthermore, the Gd(III)-labeled cages were shown to be stable for several months by MS analysis (Figures S28, S29).

2.4. MR Signal Amplification Revealed through Relaxivity Measurements. Relaxivity measurements for Gd-C4-IA and the Gd-C4-protein conjugates were performed at a clinically relevant low field strength (1.4 T, Figure S31) and at a higher field strength (7 T, Figures S31−S38) used for high-resolution imaging. The results are reported in Table 2 and Table S2. Increasing the field strength of MR instruments improves the signal-to-noise ratio (SNR) and spatial resolution, and also shortens acquisition times.[75,76] The ionic relaxivity ($r_{1,ionic}$) values are normalized per millimolar Gd(III) to identify the structure that imparts the best MR physics properties, whereas the particle relaxivity ($r_{1,particle}$, Eq. S1) accounts for the number of Gd(III) complexes per particle as well as $r_{1,ionic}$.

Gd-C4-IA was studied in sodium phosphate buffer (50 mM sodium phosphate (pH 8.0), 200 mM NaCl, 5 mM EDTA) and Tris buffer (25 mM Tris (pH 7.6), 200 mM NaCl, 5 mM EDTA). The ionic relaxivity of Gd-C4-IA behaved as expected for a small molecule Gd(III) complex, with values of 4.1−4.2 mM^{-1} s^{-1} at 1.4 T and 37 °C, and decreased to 2.6 and 3.2

Table 2. Relaxivity Measurements of Gd-C4-IA and Gd(III)-Labeled Protein Cages at 1.4 and 7 T[a]

| | 1.4 T at 37 °C | | 7 T at 25 °C | |
sample name	$r_{1,\text{ionic}}$ (mM^{-1} s^{-1})	$r_{1,\text{particle}}$ (mM^{-1} s^{-1})	$r_{1,\text{ionic}}$ (mM^{-1} s^{-1})	$r_{1,\text{particle}}$ (mM^{-1} s^{-1})
Gd-C4-IA[b]	4.2	N/A	2.6	N/A
Gd-C4-IA[c]	4.1	N/A	3.2	N/A
Gd-AaLS-13[b]	18.3	2727	8.0	1192
Gd-OP-3$_{\text{int}}$C[c]	15.9	525	5.3	175
Gd-OP-2$_{\text{int}}$C[c]	18.0	419	5.4	124
Gd-OP-1$_{\text{int}}$C[c]	15.0	165	4.6	51
Gd-OP-1$_{\text{ext}}$C[c]	11.2	157	4.9	69

[a]Relaxation times (T_1) were measured with error of <5%, while standard deviations of [Gd(III)] were determined by ICP-MS of triplicate samples. [b]Relaxivity data in 50 mM sodium phosphate (pH 8.0), 200 mM NaCl, 5 mM EDTA. [c]Relaxivity data in 25 mM Tris (pH 7.6), 200 mM NaCl, 5 mM EDTA.

mM^{-1} s^{-1} at 7 T and 25 °C (Table 2). These values are consistent those observed for q = 1 Gd(III) complexes.

As expected, higher $r_{1,\text{ionic}}$ values were measured for the Gd-C4-protein conjugates compared to Gd-C4-IA at both field strengths due to the τ_R boost (Table 2), with a stronger τ_R boost observed at the lower field strength (1.4 T, 37 °C). For Gd-AaLS-13, $r_{1,\text{ionic}}$ increased from ∼4 to 18.3 mM^{-1} s^{-1}, while conjugation to the OP cages increased $r_{1,\text{ionic}}$ to 11−18 mM^{-1} s^{-1}. At 7 T and 25 °C, a smaller τ_R boost was also observed, with $r_{1,\text{ionic}}$ increasing from ∼3 mM^{-1} s^{-1} to 5−8 mM^{-1} s^{-1} for the Gd(III)-C4-protein conjugates. Interestingly, the protein cages labeled with Gd(III) on the lumenal surface (Gd-AaLS-13, Gd-OP-3$_{\text{int}}$C, Gd-OP-2$_{\text{int}}$C, and Gd-OP-1$_{\text{int}}$C) showed higher $r_{1,\text{ionic}}$ values than Gd-OP-1$_{\text{ext}}$C with Gd(III) labeled on the external surface at the low field strength conditions (1.4 T and 37 °C). This trend is also observed under the high field strength conditions (7 T and 25 °C), except for Gd-OP-1$_{\text{int}}$C, which shows an $r_{1,\text{ionic}}$ lower than but comparable to that of Gd-OP-1$_{\text{ext}}$C.

The ionic relaxivities measured here are comparable to other Gd(III)-labeled protein cages, which show relaxivities of 10−60 mM^{-1} s^{-1}, depending on experimental conditions, particle size, and location of the Gd(III) complex.[47,48,50−55,57,58] Notably, previous studies of Gd(III)-labeled wt AaLS cages showed ionic relaxivities of 30−60 mM^{-1} s^{-1} at 1.4 T and 37 °C and 16 mM^{-1} s^{-1} at 7 T and 25 °C.[52,58] Gd(III) complexes in the interior of MS viral capsids similarly had higher ionic relaxivities than Gd(III) complexes on the cage exterior,[48] likely due to the restricted flexibility of Gd(III) complexes at the cage interior compared to their counterparts at the exterior surface.[49]

In order to determine the cause of the differences in $r_{1,\text{ionic}}$ between the small molecule Gd-C4-IA and the Gd-C4-protein conjugates, and among the Gd(III)-labeled cages, the relaxation mechanisms were investigated with nuclear magnetic relaxation dispersion (NMRD) profiles.

2.5. Relaxation Mechanistic Details Obtained from ^{1}H Nuclear Magnetic Relaxation Dispersion Profiles. *General Description of Methodology.* ^{1}H NMRD profiles are routinely used to study relaxation mechanisms of paramagnetic complexes and nanomaterials.[77] This technique measures the relaxation rate constants of water protons across a range of magnetic field strengths (0.0002−1 T). Fitting NMRD data to relaxation theory models reveals mechanistic information

about paramagnetic complexes.[77] The low field portion of the NMRD profiles (0.0001−0.1 T) are fit using a modified Florence NMRD program,[78−80] which accounts for the presence of static zero-field splitting (ZFS) of Gd(III) which primarily affects low field relaxivity. The high field region of the profile (0.1−1 T) is not affected by static ZFS and can thus be interpreted using the so-called SBM model requiring fewer parameters.[81]

Water ^{1}H NMRD profiles for Gd-C4-IA and the Gd-C4-protein conjugates were collected at 25 and 37 °C in sodium phosphate (Gd-C4-IA and Gd-AaLS-13) and Tris (Gd-C4-IA and OP) buffers, and the normalized relaxivities per millimolar Gd(III) ($r_{1,\text{ionic}}$) are shown in Figure 4. These best fit profiles (Figure 4, solid versus dotted lines) were obtained using the parameters reported in Table 5 and Tables S4−S6.

τ_R Boost of the Gd-C4-Protein Conjugates Yields High Relaxivity. The profiles of Gd-C4-IA in both buffers look as expected for a small molecule Gd(III) complex with q = 1 (Figure 4).[77] The relaxivities of the Gd(III)-labeled protein cages are much larger than that of Gd-C4-IA, showcasing successful signal amplification with a maximum $r_{1,\text{ionic}}$ of 20−50 mM^{-1} s^{-1} (Table 3). In the case of the Gd(III)-labeled OP cages, the ionic relaxivities of cages with Gd(III) on the lumenal surface (Gd-OP-3$_{\text{int}}$C, Gd-OP-2$_{\text{int}}$C, and Gd-OP-1$_{\text{int}}$C) are higher than cages with Gd(III) on the external surface (Gd-OP-1$_{\text{ext}}$C) (Figure 4b). Furthermore, the ionic relaxivity of the lumenally labeled cages progressively increases with increasing number of Gd(III) complexes per cage from Gd-OP-1$_{\text{int}}$C to Gd-OP-2$_{\text{int}}$C to Gd- OP-3$_{\text{int}}$C. These results are consistent with the ionic relaxivity at 1.4 and 7 T (Table 2).

The shapes of the Gd(III)-labeled cage profiles (Figure 4) are relatively similar, with the appearance of peaks in the high field region (∼0.5 T) indicating a field dependence of τ_c that originates from the field dependence of T_{1e}. Thus, the other field independent parameters in eq 3 (τ_R and τ_m) must be longer than T_{1e}. On the other hand, the absence of this peak for the Gd-C4-IA profiles (Figure 4) demonstrates that relaxivity of the Gd(III) complex is limited by a τ_c determined by a fast τ_R.

Very few Gd(III)-labeled protein cages have been studied by ^{1}H NMRD, including Gd(III)-polymer covalently attached to the interior of protein cages[50,55] and Gd(III)-labeled MS2 viral capsids.[49] The Gd(III)-labeled MS2 system is comparable to Gd(III)-labeled AaLS-13 and OP cages studied here, with a peak appearing in the high field region (∼0.7 T) with maximum relaxivity values of 30−40 mM^{-1} s^{-1}.[49]

Water Exchange Rate Does Not Limit the τ_R Boost. The profiles in Figure 4 show a significant decrease in ionic relaxivity with increasing temperature across the whole range of field strengths. This temperature dependence indicates that $\tau_m < T_{1m}$ (eq 2), i.e., that the coordinated water molecule is in the fast exchange regime. Under these conditions, the water lifetime (τ_m) is in the range of 10^{-8} to 10^{-7} s (Tables S5 and S6) and does not limit the correlation time ($\tau_m > T_{1e}$). Gd(III)-labeled MS2 capsids have also been reported to possess water molecules in the fast exchange regime, observed by the temperature dependence of ^{1}H NMRD profiles.[43] A long τ_R, and a lifetime τ_m longer than T_{1e} but shorter than T_{1m} ($\tau_R > T_{1m} > \tau_m > T_{1e}$) represent ideal conditions for maximizing relaxivity.

Two Correlation Times Contribute to the Relaxation Mechanism. The best fit analysis of the profiles indicates that two different correlation times must contribute to the

a

Gd-AaLS-13 25 °C   □ Gd-AaLS-13 37 °C
* Gd-C4-IA 25 °C   + Gd-C4-IA 37 °C

b

■ Gd-OP-3$_{int}$C 25 °C   □ Gd-OP-3$_{int}$C 37 °C
◆ Gd-OP-2$_{int}$C 25 °C   ◇ Gd-OP-2$_{int}$C 37 °C
▼ Gd-OP-1$_{int}$C 25 °C   ▽ Gd-OP-1$_{int}$C 37 °C
● Gd-OP-1$_{ext}$C 25 °C   ○ Gd-OP-1$_{ext}$C 37 °C
* Gd-C4-IA 25 °C   + Gd-C4-IA 37 °C
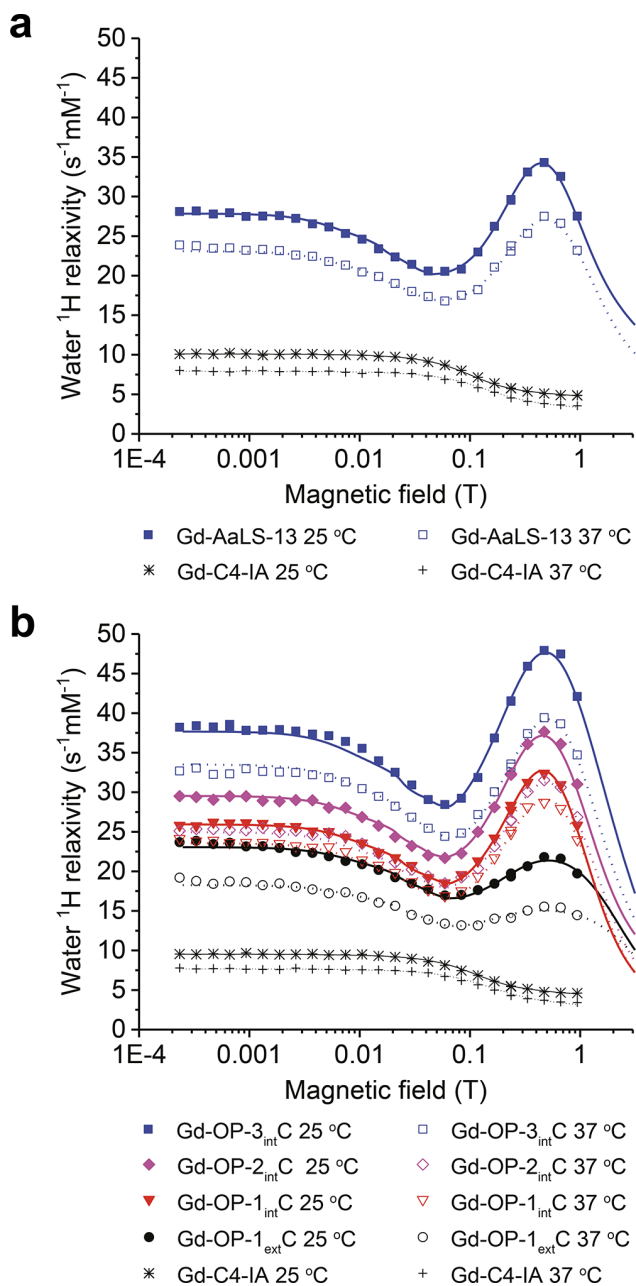
Figure 4. ^{1}H relaxivity profiles of Gd-C4-IA and Gd(III)-labeled protein cages. (a) Gd-C4-IA and Gd-AaLS-13 in sodium phosphate (pH 8.0) buffer at 25 °C and 37 °C. (b) Gd-C4-IA, Gd-OP-3$_{int}$C, Gd-OP-2$_{int}$C, Gd-OP-1$_{int}$C, and Gd-OP-1$_{ext}$C in Tris (pH 7.6) buffer at 25 °C and 37 °C. Solid and dotted lines are the best fit profiles at 25 and 37 °C, respectively, obtained with the parameters reported in Table 3 and Tables S4—S6.

modulation of the dipole—dipole interaction between Gd(III) and water proton spins for all Gd(III)-labeled protein cages. These two correlation times are modeled using the Lipari-Szabo model-free approach,[82] with an S^2 parameter providing the weight of the slower correlation time (τ_{c1} from eq 4 and 1 − S^2 as the weight for the faster correlation time (τ_{c2} from eq 5), where τ_l is the correlation time of the faster local mobility (Table 4).

$$\frac{1}{\tau_{c1}} = \frac{1}{\tau_R} + \frac{1}{\tau_m} + \frac{1}{T_{1e}} + \frac{1}{\tau_i} \tag{4}$$

Table 3. Maximum Ionic Relaxivity for Gd-C4-IA and the Gd-C4-Protein Conjugates

sample name	Max $r_{1,ionic}$ at 25 °C	Max $r_{1,ionic}$ at 37 °C
Gd-C4-IA[a,c]	10	7.5
Gd-C4-IA[b,c]	10	7.5
Gd-AaLS-13[a,d]	35	27.5
Gd-OP-3$_{int}$C[b,d]	48	40
Gd-OP-2$_{int}$C[b,d]	37.5	30
Gd-OP-1$_{int}$C[b,d]	32.5	28
Gd-OP-1$_{ext}$C[b,d]	20	15

[a]Relaxivity data in 50 mM sodium phosphate (pH 8.0), 200 mM NaCl, 5 mM EDTA. [b]Relaxivity data in 25 mM Tris (pH 7.6), 200 mM NaCl, 5 mM EDTA. [c]Relaxivity values at <0.02 T. [d]Relaxivity values at 0.5 T.

$$\frac{1}{\tau_{c2}} = \frac{1}{\tau_R} + \frac{1}{\tau_m} + \frac{1}{T_{1e}} + \frac{1}{\tau_i} + \frac{1}{\tau_l} \tag{5}$$

In both buffers, Gd-C4-IA exhibits τ_R values of tens of picoseconds (Table S4), as expected for a fast-tumbling small molecule.[77,83] On the other hand, both Gd(III)-labeled AaLS-13 and OP proteins show similar high-field τ_{c1} values on the nanosecond time scale, despite their different sizes (Table 4). These values are orders of magnitude smaller than the overall tumbling times of the protein cages (τ_R) as indicated by the relaxation profiles of the diamagnetic proteins (Table S3, Figure S39), and are also smaller than τ_m (10^{-8} to 10^{-7} s, Tables S5 and S6). Thus, this time value should be determined by an intermediate correlation time (τ_i) that is slower than the fast local mobility correlation time (τ_l) and faster than the global correlation time (τ_R). The τ_l values on the picosecond to nanosecond time scale (Table 4) suggest that considerable flexibility of the Gd(III) tag allows for extensive reorientation of the Gd(III) complex.

The different ionic relaxivity values among the Gd-C4-protein conjugates are ascribed to the different values of the τ_i and τ_l parameters. The lower relaxivity of Gd-OP-1$_{ext}$C compared toGd-OP-1$_{int}$C can be ascribed to somewhat smaller τ_i values than those observed for Gd-OP-2$_{int}$C, Gd-OP-3$_{int}$C, and Gd-AaLS-13. For the protein cages with Gd(III) complexes on the lumenal surface, the ionic relaxivity increases with increasing number of Gd(III) complexes from Gd-OP-1$_{int}$C to Gd-OP-2$_{int}$C to Gd-OP-3$_{int}$C. This is due to a τ_l that increases with the number of Gd(III) complexes in the interior of the protein cage from tens of picoseconds for Gd-OP-1$_{int}$C to a few nanoseconds for Gd-OP-3$_{int}$C. This effect cannot be related to magnetic coupling between Gd(III) ions, which would rather decrease relaxivity. A relatively long τ_l of a few nanoseconds is also obtained for Gd-AaLS-13.

As previously mentioned, a study of Gd(III) complexes conjugated to either the interior or exterior surface of an MS2 viral capsid showed higher relaxivities for the interior conjugation strategy.[43] A best fit analysis of the ^{1}H NMRD profiles also used the Liparis Szabo model-free approach to model the anisotropic molecular reorientation time. In this case, the Gd(III) complexes on the exterior surface showed higher local flexibility than for those on the interior surface with τ_l values of 310 and 400 ps, respectively. The different flexibility was attributed to the amino acid side chains used for exterior (lysine) or interior (tyrosine) conjugation.[49]

Transient coordination of Gd(III) to nearby charged protein residues may explain τ_i and τ_m time scales in the AaLS-13 and

Table 4. Selected ^{1}H NMRD Parameters to Describe Molecular Reorientation

	Gd-AaLS-13[a]		Gd-OP-3$_{int}$C[b]		Gd-OP-2$_{int}$C[b]		Gd-OP-1$_{int}$C[b]		Gd-OP-1$_{ext}$C[b]	
	25 °C	37 °C	25 °C	37 °C	25 °C	37 °C	25 °C	37 °C	25 °C	37 °C
τ_i (ns)	5.2	3.5	3.7	3.3	4.0	3.2	4.3	3.3	1.8	1.1
τ_l (ns)	540	250	1800	480	320	98	68	38	78	28
S^2	0.28		0.46		0.39		0.36		0.36	

[a]Relaxivity data in 50 mM sodium phosphate (pH 8.0), 200 mM NaCl, 5 mM EDTA. [b]Relaxivity data in 25 mM Tris (pH 7.6), 200 mM NaCl, 5 mM EDTA.
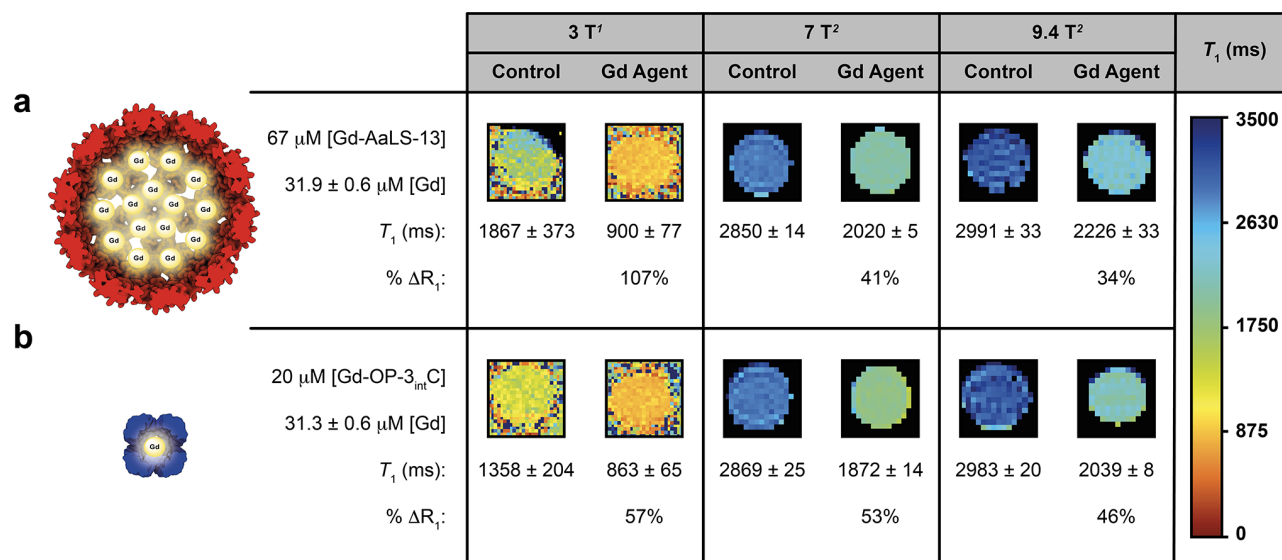
Figure 5. T_1-weighted MR solution phantom images of (a) Gd-AaLS-13 and (b) Gd-OP-3$_{int}$C at 3, 7, and 9.4 T. (a) Control sample of 10% FBS in 50 mM sodium phosphate (pH 8.0), 200 mM NaCl, 5 mM EDTA. The Gd-AaLS-13 sample was prepared at 67 μM with respect to monomer, and Gd(III) concentration was measured by ICP-MS. (b) Control sample of 10% FBS in 25 mM Tris-HCl (pH 7.6), 200 mM NaCl, 5 mM EDTA. The Gd-OP-3$_{int}$C sample was prepared at 20 μM with respect to monomer, and Gd(III) concentration was measured by ICP-MS. [1]Values at 3 T were measured using a dual gradient echo method with two different flip angles. [2]Values at 7 and 9.4 T were obtained using a saturation recovery method.

OP cages. Although the nature of the obtained τ_i values and the origin of the long τ_l values are not fully clear, the overall lengthening of the correlation times to values in the nanosecond time scale make these systems interesting as MR CAs. Correlation times of a few nanoseconds are in fact optimal for maximizing the relaxivity at clinical field strengths.

The time scale of τ_i corresponds to conformational flexibility of protein regions that substantially reorient the dipole—dipole interaction between Gd(III) and water protons. However, this seems unlikely due to the relatively rigid nature of the multimeric assembly. Rather, we speculate that the high flexibility of the Gd(III) complexes may allow for transient coordination of the Gd(III) ion by nearby protein residues on the nanosecond time scale. The OP cages have several negatively charged residues (Asp and Glu) near the Gd(III) binding sites that could interact with Gd(III) (Figure S26). Furthermore, increasing the number of Gd(III) complexes inside the OP cage replaces positively charged Arg residues with Cys residues that are covalently linked to Gd-C4-IA, decreasing the overall positive charge of the capsid interior and resulting in increased crowding that potentially favors the bending of the complexes toward these residues. This would explain the unexpected increase of τ_l from Gd-OP-1$_{int}$C to Gd-OP-2$_{int}$C to Gd-OP-3$_{int}$C such that τ_l approaches the longer correlation time τ_i as interior space for mobility is reduced.

Similarly, for Gd-AaLS-13, the large number of negatively charged residues (Asp and Glu) that line the interior capsid surface could favor transient coordination of protein residues to Gd(III) ions (Figure S26), reducing the tag mobility (τ_l) to a value similar to Gd-OP-2$_{int}$C despite the larger interior space (Table 4). The proposed transient coordination might also facilitate exchange of coordinated water molecules on a time scale that is typical for small Gd(III) complexes ($\tau_m = 10^{-7}$ to 10^{-8} s, Tables S5 and S6), but is a remarkable result for Gd(III)-labeled proteins.

2.6. Solution Phantom Images. MR phantom images were used to quantify the ability of Gd-C4-protein conjugates to increase MR image contrast under mock biological conditions. Based on particle relaxivity (Table 2) and ^{1}H NMRD profiles (Figure 4), Gd-AaLS-13 and Gd-OP-3$_{int}$C were chosen for study at clinically relevant 3 T as well as high fields 7 and 9.4 T. The Gd-C4-protein conjugates were incubated in 10% fetal bovine serum (FBS) in sodium phosphate (pH 8.0) or Tris (pH 7.6) buffers. The stability of the AaLS-13 and OP cages was previously demonstrated in both human serum and FBS,[64,69] allowing the phantom image measurements to be performed in FBS.

The longitudinal relaxation rate constant ($R_1 = 1/T_1$) was measured for each sample (Figures S41−S43) and compared to a control solution to determine contrast enhancement (Eq. S3). Samples were prepared at 67 μM Gd-AaLS-13 and 20 μM

Gd-OP-3$_{int}$C with respect to the monomer, with Gd(III) concentrations measured by ICP-MS as 31.9 μM and 31.3 μM Gd(III), respectively. At 3 T, Gd-AaLS-13 increased R_1 by 107%, while Gd-OP-3$_{int}$C increased R_1 by 57%. At high field strengths of 7 and 9.4 T, Gd-AaLS-13 increased R_1 by 41% and 34%, respectively, whereas Gd-OP-3$_{int}$C increased R_1 by 53% and 46%, respectively (Figure 5).

In clinical MR exams, a detectable change in contrast requires an approximately 20% increase in R_1.[4,5] At all field strengths, the Gd-C4-protein conjugates show appreciable contrast enhancement (%ΔR_1) relative to control conditions with 30 μM Gd(III). Considering that clinically approved Gd(III) agents require a local concentration of 125 μM of Gd(III) for detectable contrast enhancement, both Gd-AaLS-13 and Gd-OP-3$_{int}$C show excellent contrast enhancement at four times lower Gd(III) concentration at all field strengths, but most notably at clinically relevant 3 T with 107% and 57% for Gd-AaLS-13 and Gd-OP-3$_{int}$C, respectively. Lower concentrations of Gd-OP-3$_{int}$C (12.5 μM monomer, 23.2 μM Gd(III)) still showed detectable contrast enhancement at 7 and 9.4 T at 32% and 27%, respectively (Figures S44, S45).

These results show that Gd-AaLS-13 and Gd-OP-3$_{int}$C are promising candidates for *in vivo* MR imaging. However, the immunogenicity of protein-based delivery systems presents a potential limitation for biological applications, especially if multiple administrations are required. Since MR imaging would likely require only a single injection of a contrast agent, there is less concern about immunogenicity. Moreover, appending antibody binding domains to the surface of AaLS-13 was shown to mitigate the immune response.[64] Other strategies to passivate the surface of protein scaffolds and extend the circulation times of the resulting cages have been described.[43]

3. CONCLUSIONS

Our results demonstrate the ability of Gd(III)-labeled AaLS-13 and OP protein cages to function as highly effective MR contrast agents. We have investigated these newly labeled cages by ^{1}H NMRD to elucidate the parameters governing relaxivity. The MR performance of the protein cages can be summarized in four key results. (i) MR signal amplification was achieved through both a high payload of Gd(III) in each protein cage and increased relaxivity over the Gd(III) complex Gd-C4-IA. The Gd-C4-protein conjugates were labeled with 150 or 33 Gd(III) complexes for Gd-AaLS-13 and Gd-OP-3$_{int}$C, respectively. The ionic relaxivity of the Gd(III)-labeled cages was increased 2.5- to 4.5-fold from Gd-C4-IA.

(ii) The increase in ionic relaxivity resulted from the τ_R boost common for Gd(III)-labeled NPs. Furthermore, this increase was not limited by the water exchange rate, which is in the fast exchange regime. (iii) The long τ_l values of tens to thousands of picoseconds and τ_m of 10−100 ns likely result from transient coordination of Gd(III) to charged protein residues near the covalently bound Gd(III) complex. This would also explain the increase in ionic relaxivity in the series Gd-OP-1$_{int}$C to Gd-OP-2$_{int}$C to Gd-OP-3$_{int}$C. Steric crowding slows τ_l and favors transient Gd(III) interactions with nearby charged residues.

Finally, (iv) the parameters responsible for nuclear relaxation are optimized for high relaxivity at clinical field strengths, with coordinated water molecules in the fast exchange regime and correlation times on the nanosecond time scale. The serum phantom images at 3 T showcase this

result with contrast enhancements of 57% or 107% for only 30 μM Gd(III) of Gd-AaLS-13 and Gd-OP-3$_{int}$C, respectively.

The MR performance of Gd(III)-labeled AaLS-13 and OP cages is comparable to other previously studied Gd(III)-labeled proteins. The ionic relaxivity values at 1.4 and 7 T for Gd(III)-labeled AaLS-13 and OP compared with previously studied Gd(III)-labeled protein cages (10−18 mM^{-1} s^{-1} vs 10−60 mM^{-1} s^{-1}).[45,47−55,57,58] Only two previously studied protein cages report higher ionic relaxivity values than what is reported here (e.g., 60 mM^{-1} s^{-1}).[52,54] The differences in relaxivities reported for the Gd(III)-labeled cages likely arise from the different sizes and structures of the protein cages and the flexibility of the Gd(III) complex that is covalently bound to the protein cage.[53]

The high relaxivity of Gd(III)-protein conjugates results from the low flexibility of the covalently bound Gd(III) complex (τ_l), so decreasing τ_l could result in even higher ionic relaxivity. This could be accomplished through a Gd(III) complex that employs a shorter, more rigid connecting arm,[53] or by further increasing steric hindrance in the Gd(III)-labeled protein cages as seen in the OP variants. For example, a new variant OP-4$_{int}$C would presumably show even higher relaxivity than Gd-OP-1$_{int}$C, Gd-OP-2$_{int}$C, and Gd-OP-3$_{int}$C. Alternatively, the long correlation time (τ_i) could be slowed to approach expected values for τ_R, even though the nature of τ_i is currently not fully understood.

Gd(III)-labeled AaLS-13 and OP protein cages represent excellent platforms for a variety of MR imaging applications. The pharmacokinetics of Gd(III)-labeled cages can be studied by *in vivo* MR fate mapping or *ex vivo* biodistribution. Alternatively, these versatile cages can be modified to incorporate surface modifications that alter biodistribution and/or bind specific cell surface receptors for targeted molecular imaging and theranostic platforms.

4. EXPERIMENTAL METHODS

Details of experimental methods are included in the Supporting Information. No unexpected or unusually high safety hazards were encountered.

■ ASSOCIATED CONTENT

Ⓢ Supporting Information

The Supporting Information is available free of charge at https://pubs.acs.org/doi/10.1021/acsabm.2c00892.

■ AUTHOR INFORMATION

Corresponding Authors

Thomas J. Meade − *Departments of Chemistry, Molecular Biosciences, Neurobiology and Radiology, Northwestern University, Evanston, Illinois 60208, United States;* ⓞ orcid.org/0000-0001-6202-1155; Email: tmeade@northwestern.edu

Donald Hilvert − *Laboratory of Organic Chemistry, ETH Zurich, Zürich 8093, Switzerland;* ⓞ orcid.org/0000-0002-3941-621X; Email: hilvert@org.chem.ethz.ch

Authors

Megan A. Kaster − *Departments of Chemistry, Molecular Biosciences, Neurobiology and Radiology, Northwestern*

University, Evanston, Illinois 60208, United States;
orcid.org/0000-0001-5550-4028

Mikail D. Levasseur − *Laboratory of Organic Chemistry, ETH Zurich, Zürich 8093, Switzerland;* orcid.org/0000-0003-4228-0875

Thomas G. W. Edwardson − *Laboratory of Organic Chemistry, ETH Zurich, Zürich 8093, Switzerland;* orcid.org/0000-0001-8661-8036

Michael A. Caldwell − *Departments of Chemistry, Molecular Biosciences, Neurobiology and Radiology, Northwestern University, Evanston, Illinois 60208, United States;* orcid.org/0000-0002-8636-0706

Daniela Hofmann − *Laboratory of Organic Chemistry, ETH Zurich, Zürich 8093, Switzerland*

Giulia Licciardi − *Magnetic Resonance Center (CERM), University of Florence, Sesto Fiorentino 50019, Italy; Department of Chemistry "Ugo Schiff", University of Florence, Sesto Fiorentino 50019, Italy; Consorzio Interuniversitario Risonanze Magnetiche Metallo Proteine (CIRMMP), Sesto Fiorentino 50019, Italy*

Giacomo Parigi − *Magnetic Resonance Center (CERM), University of Florence, Sesto Fiorentino 50019, Italy; Department of Chemistry "Ugo Schiff", University of Florence, Sesto Fiorentino 50019, Italy; Consorzio Interuniversitario Risonanze Magnetiche Metallo Proteine (CIRMMP), Sesto Fiorentino 50019, Italy;* orcid.org/0000-0002-1989-4644

Claudio Luchinat − *Magnetic Resonance Center (CERM), University of Florence, Sesto Fiorentino 50019, Italy; Department of Chemistry "Ugo Schiff", University of Florence, Sesto Fiorentino 50019, Italy; Consorzio Interuniversitario Risonanze Magnetiche Metallo Proteine (CIRMMP), Sesto Fiorentino 50019, Italy*

Complete contact information is available at:
https://pubs.acs.org/10.1021/acsabm.2c00892

Author Contributions

All authors have given approval to the final version of the manuscript.

Notes

The authors declare no competing financial interest.

ABBREVIATIONS

CAs, contrast agents; CH_2Cl_2, dichloromethane; DIC, diisopropylcarbodiimide; DIEA, diisopropylethylamine; DMF, dimethylformamide; DOTA, 1,4,7,11-tetraazacyclododecane; EDTA, ethylenediaminetetraacetic acid; equiv, equivalent; FBS, fetal bovine serum; $GdCl_3\cdot6H_2O$, gadolinium(III) chloride hexahydrate; ^1H, proton; H_2, dihydrogen gas; H_2O, water; K_2CO_3, potassium carbonate; MeCN, acetonitrile; MR, magnetic resonance; MQ, miili-Q direct water purification system; NaCl, sodium chloride; NHS, *N*-hydroxysuccinimide; NMRD, nuclear magnetic relaxation dispersion; N_2, dinitrogen gas; NP, nanoparticle; Pd/C, palladium on carbon catalyst; RT, room temperature; SBM, Solomon-Bloembergen-Morgan; SNR, signal-to-noise ratio; tBu, tertiary butyl; Tris, tris-(hydroxymethyl)aminomethane; $^tBuDO3A$, tri-^tBu 2,2′,2″-(1,4,7,10-tetraazacyclododecane-1,4,7-triyl)triacetate; TFA, tri-fluoroacetic acid; wt, wild type; ZFS, zero-field splitting

REFERENCES

(1) Currie, S.; Hoggard, N.; Craven, I. J.; Hadjivassiliou, M.; Wilkinson, I. D. Understanding MRI: basic MR physics for physicians. *Postgrad Med. J.* **2013**, *89* (1050), 209−223.

(2) Jaffer, F. A.; Weissleder, R. Molecular imaging in the clinical arena. *JAMA* **2005**, *293* (7), 855−862.

(3) Wahsner, J.; Gale, E. M.; Rodriguez-Rodriguez, A.; Caravan, P. Chemistry of MRI Contrast Agents: Current Challenges and New Frontiers. *Chem. Rev.* **2019**, *119* (2), 957−1057.

(4) Caravan, P.; Ellison, J. J.; McMurry, T. J.; Lauffer, R. B. Gadolinium(III) Chelates as MRI Contrast Agents: Structure, Dynamics, and Applications. *Chem. Rev.* **1999**, *99* (9), 2293−2352.

(5) Caravan, P. Strategies for increasing the sensitivity of gadolinium based MRI contrast agents. *Chem. Soc. Rev.* **2006**, *35* (6), 512−523.

(6) James, M. L.; Gambhir, S. S. A molecular imaging primer: modalities, imaging agents, and applications. *Physiol Rev.* **2012**, *92* (2), 897−965.

(7) Xue, S.; Qiao, J.; Jiang, J.; Hubbard, K.; White, N.; Wei, L.; Li, S.; Liu, Z. R.; Yang, J. J. Design of ProCAs (protein-based Gd(3+) MRI contrast agents) with high dose efficiency and capability for molecular imaging of cancer biomarkers. *Med. Res. Rev.* **2014**, *34* (5), 1070−1099.

(8) Runge, V. M. Critical Questions Regarding Gadolinium Deposition in the Brain and Body After Injections of the Gadolinium-Based Contrast Agents, Safety, and Clinical Recommen-dations in Consideration of the EMA's Pharmacovigilance and Risk Assessment Committee Recommendation for Suspension of the Marketing Authorizations for 4 Linear Agents. *Invest Radiol* **2017**, *52* (6), 317−323.

(9) Botta, M.; Tei, L. Relaxivity Enhancement in Macromolecular and Nanosized GdIII-Based MRI Contrast Agents. *Eur. J. Inorg. Chem.* **2012**, *2012*, 1945−1960.

(10) Vistain, L. F.; Rotz, M. W.; Rathore, R.; Preslar, A. T.; Meade, T. J. Targeted delivery of gold nanoparticle contrast agents for reporting gene detection by magnetic resonance imaging. *Chem. Commun.* **2016**, *52* (1), 160−163.

(11) Bruckman, M. A.; Yu, X.; Steinmetz, N. F. Engineering Gd-loaded nanoparticles to enhance MRI sensitivity via T(1) shortening. *Nanotechnology* **2013**, *24* (46), 462001.

(12) Holbrook, R. J.; Rammohan, N.; Rotz, M. W.; MacRenaris, K. W.; Preslar, A. T.; Meade, T. J. Gd(III)-Dithiolane Gold Nanoparticles for T1-Weighted Magnetic Resonance Imaging of the Pancreas. *Nano Lett.* **2016**, *16* (5), 3202−3209.

(13) Nicholls, F. J.; Rotz, M. W.; Ghuman, H.; MacRenaris, K. W.; Meade, T. J.; Modo, M. DNA-gadolinium-gold nanoparticles for in vivo T1MR imaging of transplanted human neural stem cells. *Biomaterials* **2016**, *77*, 291−306.

(14) Rammohan, N.; Holbrook, R. J.; Rotz, M. W.; MacRenaris, K. W.; Preslar, A. T.; Carney, C. E.; Reichova, V.; Meade, T. J. Gd(III)-Gold Nanoconjugates Provide Remarkable Cell Labeling for High Field Magnetic Resonance Imaging. *Bioconjug Chem.* **2017**, *28* (1), 153−160.

(15) Rotz, M. W.; Culver, K. S.; Parigi, G.; MacRenaris, K. W.; Luchinat, C.; Odom, T. W.; Meade, T. J. High relaxivity Gd(III)-DNA gold nanostars: investigation of shape effects on proton relaxation. *ACS Nano* **2015**, *9* (3), 3385−3396.

(16) Song, Y.; Xu, X.; MacRenaris, K. W.; Zhang, X. Q.; Mirkin, C. A.; Meade, T. J. Multimodal gadolinium-enriched DNA-gold nanoparticle conjugates for cellular imaging. *Angew. Chem., Int. Ed. Engl.* **2009**, *48* (48), 9143−9147.

(17) Rotz, M. W.; Holbrook, R. J.; MacRenaris, K. W.; Meade, T. J. A Markedly Improved Synthetic Approach for the Preparation of Multifunctional Au-DNA Nanoparticle Conjugates Modified with Optical and MR Imaging Probes. *Bioconjug Chem.* **2018**, *29* (11), 3544−3549.

(18) Rammohan, N.; MacRenaris, K. W.; Moore, L. K.; Parigi, G.; Mastarone, D. J.; Manus, L. M.; Lilley, L. M.; Preslar, A. T.; Waters, E. A.; Filicko, A.; et al. Nanodiamond-Gadolinium(III) Aggregates for Tracking Cancer Growth In Vivo at High Field. *Nano Lett.* **2016**, *16* (12), 7551−7564.

(19) McLeod, S. M.; Robison, L.; Parigi, G.; Olszewski, A.; Drout, R. J.; Gong, X.; Islamoglu, T.; Luchinat, C.; Farha, O. K.; Meade, T. J. Maximizing Magnetic Resonance Contrast in Gd(III) Nanoconjugates: Investigation of Proton Relaxation in Zirconium Metal-Organic Frameworks. *ACS Appl. Mater. Interfaces* **2020**, *12* (37), 41157−41166.

(20) Strijkers, G. J.; Mulder, W. J.; van Heeswijk, R. B.; Frederik, P. M.; Bomans, P.; Magusin, P. C.; Nicolay, K. Relaxivity of liposomal paramagnetic MRI contrast agents. *MAGMA* **2005**, *18* (4), 186−192.

(21) Gambino, G.; Tei, L.; Carniato, F.; Botta, M. Amphiphilic Ditopic Bis-Aqua Gd-AAZTA-like Complexes Enhance Relaxivity of Lipidic MRI Nanoprobes. *Chem. Asian J.* **2016**, *11* (15), 2139−2143.

(22) Kobayashi, H.; Brechbiel, M. W. Nano-sized MRI contrast agents with dendrimer cores. *Adv. Drug Deliv Rev.* **2005**, *57* (15), 2271−2286.

(23) Barrett, T.; Kobayashi, H.; Brechbiel, M.; Choyke, P. L. Macromolecular MRI contrast agents for imaging tumor angiogenesis. *Eur. J. Radiol* **2006**, *60* (3), 353−366.

(24) Pierre, V. C.; Botta, M.; Raymond, K. N. Dendrimeric gadolinium chelate with fast water exchange and high relaxivity at high magnetic field strength. *J. Am. Chem. Soc.* **2005**, *127* (2), 504−505.

(25) Nazemi, A.; Gillies, E. R. Dendritic surface functionlization of nanomaterials: controlling properties and functions for biomedical applications. *Braz J. Pharm. Sci.* **2013**, *49*, 15−32.

(26) Klemm, P. J.; Floyd, W. C., 3rd; Andolina, C. M.; Frechet, J. M.; Raymond, K. N. Conjugation to Biocompatible Dendrimers Increases Lanthanide T2 Relaxivity of Hydroxypyridinone (HOPO) Complexes for Magnetic Resonance Imaging (MRI). *Eur. J. Inorg. Chem.* **2012**, *2012* (12), 2108−2114.

(27) Klemm, P. J.; Floyd, W. C., 3rd; Smiles, D. E.; Frechet, J. M.; Raymond, K. N. Improving T(1) and T(2) magnetic resonance imaging contrast agents through the conjugation of an esteramide dendrimer to high-water-coordination Gd(III) hydroxypyridinone complexes. *Contrast Media Mol. Imaging* **2012**, *7* (1), 95−99.

(28) Nicolle, G. M.; Toth, E.; Schmitt-Willich, H.; Raduchel, B.; Merbach, A. E. The impact of rigidity and water exchange on the relaxivity of a dendritic MRI contrast agent. *Chem.—Eur. J.* **2002**, *8* (5), 1040−1048.

(29) Matthews, S. E.; Pouton, C. W.; Threadgill, M. D. Macromolecular systems for chemotherapy and magnetic resonance imaging. *Adv. Drug Deliver Rev.* **1996**, *18* (2), 219−267.

(30) Allen, M. J.; Raines, R. T.; Kiessling, L. L. Contrast agents for magnetic resonance imaging synthesized with ring-opening metathesis polymerization. *J. Am. Chem. Soc.* **2006**, *128* (20), 6534−6535.

(31) Soleimani, A.; Martinez, F.; Economopoulos, V.; Foster, P. J.; Scholl, T. J.; Gillies, E. R. Polymer cross-linking: a nanogel approach to enhancing the relaxivity of MRI contrast agents. *J. Mater. Chem. B* **2013**, *1* (7), 1027−1034.

(32) Nicolle, G. M.; Toth, E.; Eisenwiener, K. P.; Macke, H. R.; Merbach, A. E. From monomers to micelles: investigation of the parameters influencing proton relaxivity. *J. Biol. Inorg. Chem.* **2002**, *7* (7−8), 757−769.

(33) Millan, J. G.; Brasch, M.; Anaya-Plaza, E.; de la Escosura, A.; Velders, A. H.; Reinhoudt, D. N.; Torres, T.; Koay, M. S.; Cornelissen, J. J. Self-assembly triggered by self-assembly: optically active, paramagnetic micelles encapsulated in protein cage nanoparticles. *J. Inorg. Biochem* **2014**, *136*, 140−146.

(34) Briley-Saebo, K. C.; Geninatti-Crich, S.; Cormode, D. P.; Barazza, A.; Mulder, W. J. M.; Chen, W.; Giovenzana, G. B.; Fisher, E. A.; Aime, S.; Fayad, Z. A. High-Relaxivity Gadolinium-Modified High-Density Lipoproteins as Magnetic Resonance Imaging Contrast Agents. *J. Phys. Chem. B* **2009**, *113*, 6283−6289.

(35) Babič, A.; Vorobiev, V.; Trefalt, G.; Crowe, L. A.; Helm, L.; Vallée, J.-P.; Allémann, E. MRI micelles self-assembled from synthetic gadolinium-based nano building blocks. *Chem. Commun.* **2019**, *55* (7), 945−948.

(36) Carniato, F.; Ricci, M.; Tei, L.; Garello, F.; Terreno, E.; Ravera, E.; Parigi, G.; Luchinat, C.; Botta, M. High Relaxivity with No Coordinated Waters: A Seemingly Paradoxical Behavior of [Gd-(DOTP)](5-) Embedded in Nanogels. *Inorg. Chem.* **2022**, *61* (13), 5380−5387.

(37) Carniato, F.; Tei, L.; Botta, M.; Ravera, E.; Fragai, M.; Parigi, G.; Luchinat, C. (1)H NMR Relaxometric Study of Chitosan-Based Nanogels Containing Mono- and Bis-Hydrated Gd(III) Chelates: Clues for MRI Probes of Improved Sensitivity. *ACS Appl. Bio Mater.* **2020**, *3* (12), 9065−9072.

(38) Janib, S. M.; Moses, A. S.; MacKay, J. A. Imaging and drug delivery using theranostic nanoparticles. *Adv. Drug Deliver Rev.* **2010**, *62*, 1052−1063.

(39) Jokerst, J. V.; Gambhir, S. S. Molecular imaging with theranostic nanoparticles. *Acc. Chem. Res.* **2011**, *44* (10), 1050−1060.

(40) Ma, X.; Zhao, Y.; Liang, X. J. Theranostic nanoparticles engineered for clinic and pharmaceutics. *Acc. Chem. Res.* **2011**, *44* (10), 1114−1122.

(41) Ryu, J. H.; Lee, S.; Son, S.; Kim, S. H.; Leary, J. F.; Choi, K.; Kwon, I. C. Theranostic nanoparticles for future personalized medicine. *J. Controlled Release* **2014**, *190*, 477−484.

(42) Soo Choi, H.; Liu, W.; Misra, P.; Tanaka, E.; Zimmer, J. P; Itty Ipe, B.; Bawendi, M. G; Frangioni, J. V Renal clearance of quantum dots. *Nat. Biotechnol.* **2007**, *25* (10), 1165−1170.

(43) Edwardson, T. G. W.; Levasseur, M. D.; Tetter, S.; Steinauer, A.; Hori, M.; Hilvert, D. Protein Cages: From Fundamentals to Advanced Applications. *Chem. Rev.* **2022**, *122* (9), 9145−9197.

(44) Allen, M.; Bulte, J. W.; Liepold, L.; Basu, G.; Zywicke, H. A.; Frank, J. A.; Young, M.; Douglas, T. Paramagnetic viral nanoparticles as potential high-relaxivity magnetic resonance contrast agents. *Magn Reson Med.* **2005**, *54* (4), 807−812.

(45) Liepold, L.; Anderson, S.; Willits, D.; Oltrogge, L.; Frank, J. A.; Douglas, T.; Young, M. Viral capsids as MRI contrast agents. *Magn Reson Med.* **2007**, *58* (5), 871−879.

(46) Xue, S.; Yang, H.; Qiao, J.; Pu, F.; Jiang, J.; Hubbard, K.; Hekmatyar, K.; Langley, J.; Salarian, M.; Long, R. C.; et al. Protein MRI contrast agent with unprecedented metal selectivity and sensitivity for liver cancer imaging. *Proc. Natl. Acad. Sci. U. S. A.* **2015**, *112* (21), 6607–6612.

(47) Anderson, E. A.; Isaacman, S.; Peabody, D. S.; Wang, E. Y.; Canary, J. W.; Kirshenbaum, K. Viral nanoparticles donning a paramagnetic coat: conjugation of MRI contrast agents to the MS2 capsid. *Nano Lett.* **2006**, *6* (6), 1160–1164.

(48) Hooker, J. M.; Datta, A.; Botta, M.; Raymond, K. N.; Francis, M. B. Magnetic resonance contrast agents from viral capsid shells: a comparison of exterior and interior cargo strategies. *Nano Lett.* **2007**, *7* (8), 2207–2210.

(49) Datta, A.; Hooker, J. M.; Botta, M.; Francis, M. B.; Aime, S.; Raymond, K. N. High relaxivity gadolinium hydroxypyridonate-viral capsid conjugates: nanosized MRI contrast agents. *J. Am. Chem. Soc.* **2008**, *130* (8), 2546–2552.

(50) Liepold, L. O.; Abedin, M. J.; Buckhouse, E. D.; Frank, J. A.; Young, M. J.; Douglas, T. Supramolecular protein cage composite MR contrast agents with extremely efficient relaxivity properties. *Nano Lett.* **2009**, *9* (12), 4520–4526.

(51) Prasuhn, D. E., Jr; Yeh, R. M.; Obenaus, A.; Manchester, M.; Finn, M. G. Viral MRI contrast agents: coordination of Gd by native virions and attachment of Gd complexes by azide-alkyne cyclo-addition. *Chem. Commun.* **2007**, No. 12, 1269–1271.

(52) Kim, H.; Jin, S.; Choi, H.; Kang, M.; Park, S. G.; Jun, H.; Cho, H.; Kang, S. Target-switchable Gd(III)-DOTA/protein cage nano-particle conjugates with multiple targeting affibody molecules as target selective T1 contrast agents for high-field MRI. *J. Controlled Release* **2021**, *335*, 269–280.

(53) Garimella, P. D.; Datta, A.; Romanini, D. W.; Raymond, K. N.; Francis, M. B. Multivalent, high-relaxivity MRI contrast agents using rigid cysteine-reactive gadolinium complexes. *J. Am. Chem. Soc.* **2011**, *133* (37), 14704–14709.

(54) Min, J.; Jung, H.; Shin, H. H.; Cho, G.; Cho, H.; Kang, S. Implementation of P22 viral capsids as intravascular magnetic resonance T1 contrast conjugates via site-selective attachment of Gd(III)-chelating agents. *Biomacromolecules* **2013**, *14* (7), 2332–2339.

(55) Qazi, S.; Liepold, L. O.; Abedin, M. J.; Johnson, B.; Prevelige, P.; Frank, J. A.; Douglas, T. P22 viral capsids as nanocomposite high-relaxivity MRI contrast agents. *Mol. Pharmaceutics* **2013**, *10* (1), 11–17.

(56) Lucon, J.; Qazi, S.; Uchida, M.; Bedwell, G. J.; LaFrance, B.; Prevelige, P. E., Jr; Douglas, T. Use of the interior cavity of the P22 capsid for site-specific initiation of atom-transfer radical polymer-ization with high-density cargo loading. *Nat. Chem.* **2012**, *4* (10), 781–788.

(57) Usselman, R. J.; Qazi, S.; Aggarwal, P.; Eaton, S. S.; Eaton, G. R.; Russek, S.; Douglas, T. Gadolinium-Loaded Viral Capsids as Magnetic Resonance Imaging Contrast Agents. *Appl. Magn. Reson.* **2015**, *46* (3), 349–355.

(58) Song, Y.; Kang, Y. J.; Jung, H.; Kim, H.; Kang, S.; Cho, H. Lumazine Synthase Protein Nanoparticle-Gd(III)-DOTA Conjugate as a T1 contrast agent for high-field MRI. *Sci. Rep* **2015**, *5*, 15656.

(59) Seebeck, F. P.; Woycechowsky, K. J.; Zhuang, W.; Rabe, J. P.; Hilvert, D. A simple tagging system for protein encapsulation. *J. Am. Chem. Soc.* **2006**, *128* (14), 4516–4517.

(60) Worsdorfer, B.; Woycechowsky, K. J.; Hilvert, D. Directed evolution of a protein container. *Science* **2011**, *331* (6017), 589–592.

(61) Sasaki, E.; Bohringer, D.; van de Waterbeemd, M.; Leibundgut, M.; Zschoche, R.; Heck, A. J.; Ban, N.; Hilvert, D. Structure and assembly of scalable porous protein cages. *Nat. Commun.* **2017**, *8*, 14663.

(62) Zschoche, R.; Hilvert, D. Diffusion-Limited Cargo Loading of an Engineered Protein Container. *J. Am. Chem. Soc.* **2015**, *137* (51), 16121–16132.

(63) Azuma, Y.; Zschoche, R.; Tinzl, M.; Hilvert, D. Quantitative Packaging of Active Enzymes into a Protein Cage. *Angew. Chem., Int. Ed. Engl.* **2016**, *55* (4), 1531–1534.

(64) Levasseur, M. D.; Mantri, S.; Hayashi, T.; Reichenbach, M.; Hehn, S.; Waeckerle-Men, Y.; Johansen, P.; Hilvert, D. Cell-Specific Delivery Using an Engineered Protein Nanocage. *ACS Chem. Biol.* **2021**, *16* (5), 838–843.

(65) Tytgat, H. L. P.; Lin, C. W.; Levasseur, M. D.; Tomek, M. B.; Rutschmann, C.; Mock, J.; Liebscher, N.; Terasaka, N.; Azuma, Y.; Wetter, M.; et al. Cytoplasmic glycoengineering enables biosynthesis of nanoscale glycoprotein assemblies. *Nat. Commun.* **2019**, *10* (1), 5403.

(66) Tang, T. M. S.; Cardella, D.; Lander, A. J.; Li, X.; Escudero, J. S.; Tsai, Y. H.; Luk, L. Y. P. Use of an asparaginyl endopeptidase for chemo-enzymatic peptide and protein labeling. *Chem. Sci.* **2020**, *11* (23), 5881–5888.

(67) Levasseur, M. D.; Hofmann, R.; Edwardson, T. G. W.; Hehn, S.; Thanaburakorn, M.; Bode, J. W.; Hilvert, D. Post-Assembly Modification of Protein Cages by Ubc9-Mediated Lysine Acylation. *Chembiochem* **2022**, *23*, e202200332.

(68) King, N. P.; Sheffler, W.; Sawaya, M. R.; Vollmar, B. S.; Sumida, J. P.; Andre, I.; Gonen, T.; Yeates, T. O.; Baker, D. Computational design of self-assembling protein nanomaterials with atomic level accuracy. *Science* **2012**, *336* (6085), 1171–1174.

(69) Edwardson, T. G. W.; Mori, T.; Hilvert, D. Rational Engineering of a Designed Protein Cage for siRNA Delivery. *J. Am. Chem. Soc.* **2018**, *140* (33), 10439–10442.

(70) Edwardson, T. G. W.; Tetter, S.; Hilvert, D. Two-tier supramolecular encapsulation of small molecules in a protein cage. *Nat. Commun.* **2020**, *11* (1), 5410.

(71) Edwardson, T. G. W.; Levasseur, M. D.; Hilvert, D. The OP Protein Cage: A Versatile Molecular Delivery Platform. *Chimia* **2021**, *75* (4), 323–328.

(72) Machitani, K.; Sakamoto, H.; Nakahara, Y.; Kimura, K. Molecular design of tetraazamacrocyclic derivatives bearing a spirobenzopyran and three carboxymethyl moieties and their metal-ion complexing behavior. *Anal. Sci.* **2008**, *24*, 463–469.

(73) Chanthamath, S.; Takaki, S.; Shibatomi, K.; Iwasa, S. Highly stereoselective cyclopropanation of alpha,beta-unsaturated carbonyl compounds with methyl (diazoacetoxy)acetate catalyzed by a chiral ruthenium(II) complex. *Angew. Chem., Int. Ed. Engl.* **2013**, *52* (22), 5818–5821.

(74) Min, J.; Kim, S.; Lee, J.; Kang, S. Lumazine synthase protein cage nanoparticles as modular delivery platforms for targeted drug delivery. *RSC Adv.* **2014**, *4* (89), 48596–48600.

(75) Caravan, P.; Farrar, C. T.; Frullano, L.; Uppal, R. Influence of molecular parameters and increasing magnetic field strength on relaxivity of gadolinium- and manganese-based T1 contrast agents. *Contrast Media Mol. Imaging* **2009**, *4* (2), 89–100.

(76) Vaughan, T.; DelaBarre, L.; Snyder, C.; Tian, J.; Akgun, C.; Shrivastava, D.; Liu, W.; Olson, C.; Adriany, G.; Strupp, J.; et al. 9.4T human MRI: preliminary results. *Magn Reson Med.* **2006**, *56* (6), 1274–1282.

(77) Bertini, I.; Luchinat, C.; Parigi, G.; Ravera, E. Chapter 10 - Relaxometry and contrast agents for MRI. In *NMR of Paramagnetic Molecules*, second ed.; Bertini, I., Luchinat, C., Parigi, G., Ravera, E., Eds.; Elsevier, 2017; pp 313–345.

(78) Bertini, I.; Galas, O.; Luchinat, C.; Parigi, G. A Computer Program for the Calculation of Paramagnetic Enhancements of Nuclear-Relaxation Rates in Slowly Rotating Systems. *J. Magn Reson Ser. A* **1995**, *113*, 151–158.

(79) Bertini, I.; Kowalewski, J.; Luchinat, C.; Nilsson, T.; Parigi, G. Nuclear spin relaxation in paramagnetic complexes of S = 1: Electron spin relaxation effects. *J. Chem. Phys.* **1999**, *111*, 5795–5807.

(80) Kowalewski, J.; Kruk, D.; Parigi, G.NMR Relaxation in Solution of Paramagnetic Complexes: Recent Theoretical Progress for S ≥ 1. In *Advances in Inorganic Chemistry*; Academic Press, 2005; Vol. *57*, pp 41–104.

(81) Parigi, G.; Ravera, E.; Fragai, M.; Luchinat, C. Unveiling protein dynamics in solution with field-cycling NMR relaxometry. *Prog. Nucl. Magn. Reson. Spectrosc.* **2021**, *124−125*, 85−98.

(82) Lipari, G.; Szabo, A. Model-free approach to the interpretation of nuclear magnetic resonance relaxation in macromolecules. 1. Theory and range of validity. *J. Am. Chem. Soc.* **1982**, *104* (17), 4546−4559.

(83) Merbach, A. E.; Helm, L.; Tóth, É. *The Chemisty of Contrast Agents in Medical Magnetic Resonance Imaging*; John Wiley and Sons, 2013.

📖 **Recommended by ACS**

Molecular Engineering of Self-Immolative Bioresponsive MR Probes

Jian-Hong Tang, Thomas J. Meade, *et al.*

APRIL 28, 2023
JOURNAL OF THE AMERICAN CHEMICAL SOCIETY

READ 🗗

Large Protein Assemblies for High-Relaxivity Contrast Agents: The Case of Gadolinium-Labeled Asparaginase

Giulia Licciardi, Giacomo Parigi, *et al.*

DECEMBER 02, 2022
BIOCONJUGATE CHEMISTRY

READ 🗗

Rational Design of Gd-DOTA-Type Contrast Agents for Hepatobiliary Magnetic Resonance Imaging

Weiyuan Xu, Lixiong Dai, *et al.*

JUNE 27, 2023
JOURNAL OF MEDICINAL CHEMISTRY

READ 🗗

Label-Free Chemically and Molecularly Selective Magnetic Resonance Imaging

Tianhe Wu, Hui Mao, *et al.*

APRIL 12, 2023
CHEMICAL & BIOMEDICAL IMAGING

READ 🗗

Get More Suggestions >

Supporting Information

Title: Engineered Nonviral Protein Cages Modified for MR Imaging

Authors: Megan A. Kaster,[†] Mikail D. Levasseur,[‡] Thomas G. W. Edwardson,[‡] Michael A. Caldwell,[†] Daniela Hofmann,[‡] Giulia Licciardi,[§,‖,⊥] Giacomo Parigi,[§,‖,⊥] Claudio Luchinat,[§,‖,⊥] Donald Hilvert,[*,‡] and Thomas J. Meade[*,†]

[†]Departments of Chemistry, Molecular Biosceinces, Neurobiology and Radiology, Northwestern University, 2145 N. Sheridan Road, Evanston, IL 60208, United States

[‡]Laboratory of Organic Chemistry, ETH Zurich, Vladimir-Prelog-Weg 1-5/10, 8093 Zürich, Switzerland

[§]Magnetic Resonance Center (CERM), University of Florence, via Luigi Sacconi 6, Sesto Fiorentino, 50019 Italy

[‖]Department of Chemistry "Ugo Schiff", University of Florence, via della Lastruccia 3, Sesto Fiorentino, 50019 Italy

[⊥]Consorzio Interuniversitario Risonanze Magnetiche Metallo Proteine (CIRMMP), via Luigi Sacconi 6, Sesto Fiorentino, 50019 Italy

*Email: tmeade@northwestern.edu; hilvert@org.chem.ethz.ch

Table of Contents

1. General Methods

Unless otherwise indicated, all reactions were performed under a nitrogen atmosphere using oven-dried glassware. Anhydrous solvents were used in all reactions and obtained from a J.C. Meyer solvent system (Laguna Beach, CA). Thin-layer chromatography (TLC) was performed on EMD 60 F254 silica gel plates. Standard grade 60 Å 230–400 mesh silica gel was used for normal-phase column chromatography. Unless otherwise stated, all silica gel columns were flashed with air. ^{1}H and ^{13}C NMR spectra were obtained on a Bruker 500 MHz Avance III NMR spectrometer with DCH cryoprobe. ESI-MS was performed on a Bruker AmaZon-SL spectrometer.

Cyclen was purchased from Strem Chemical. Ethylenediaminetetraacetic acid (EDTA) was purchased from AppliChem GmbH. All other buffer components, salts, and reagents were purchased from Sigma Aldrich, Merck KGaA, Fisher Scientific, Acros Organics, or TCI and used without purification.

Analytical HPLC-MS was performed on an Agilent 1260 Infinity II HPLC system with an in-line Agilent 6120 Quad mass spectrometer. Semi-preparative HPLC was performed on an Agilent PrepStar 218 equipped with an Agilent 1260 Infinity diode array detector. HPLC purifications utilized deionized water (18.2 MΩ·cm) obtained from a Millipore Q-Guard System and HPLC grade MeCN, formic acid, and ammonium hydroxide (all obtained from Fisher Scientific). Analytical HPLC-MS used an Atlantis C18 column (4.6 × 250 mm, 5 µm). Semipreparative HPLC used an Atlantis T3 C18 column (19 x 250 mm, 10 µm). **Gd-C4-NH$_2$** and **Gd-C4-IA** were purified using the following method: MeCN held at 0% for 5 min followed by a 20 min ramp to 100%.

All restriction enzymes, T4 polynucleotide kinase (PNK), Phusion® High-Fidelity DNA polymerase, and T4 DNA ligase were obtained from New England BioLabs. Oligonucleotides were synthesized by Microsynth AG. Isopropyl β-D-1-thiogalactopyranoside (IPTG) was purchased from Fluorochem. Kanamycin sulfate was obtained from AppliChem GmbH. Ni-NTA agarose resin was obtained from Qiagen GmbH. Amicon® Ultra centrifugal filters were purchased from Merck and PD Mini-/MidiTrap desalting columns from GE Healthcare. Millipore purification system was used to obtain Milli-Q water. All buffers were prepared using Milli-Q (MQ) water, pH adjusted for the temperature at which the buffer was used, and sterile-filtered (0.2 µm membrane filter).

DNA and protein quantification were carried out using a NanoDrop 2000c spectrophotometer from ThermoFisher Scientific Inc. Size-exclusion chromatography (SEC) was carried out on an NGC^{TM} Medium-Pressure Chromatography System from Bio-Rad Laboratories, Inc., unless otherwise

mentioned. Transmission electron microscopy (TEM) images were obtained on a Morgagni 268 from FEI.

UV-vis spectroscopy was performed on an Agilent Technologies Cary 60 spectrophotometer.

2. Synthetic Route of **Gd-C4-IA**

Scheme S1. Synthetic preparation of **Gd-C4-IA** from starting components **benzyl acrylate** and *t*BuDO3A.
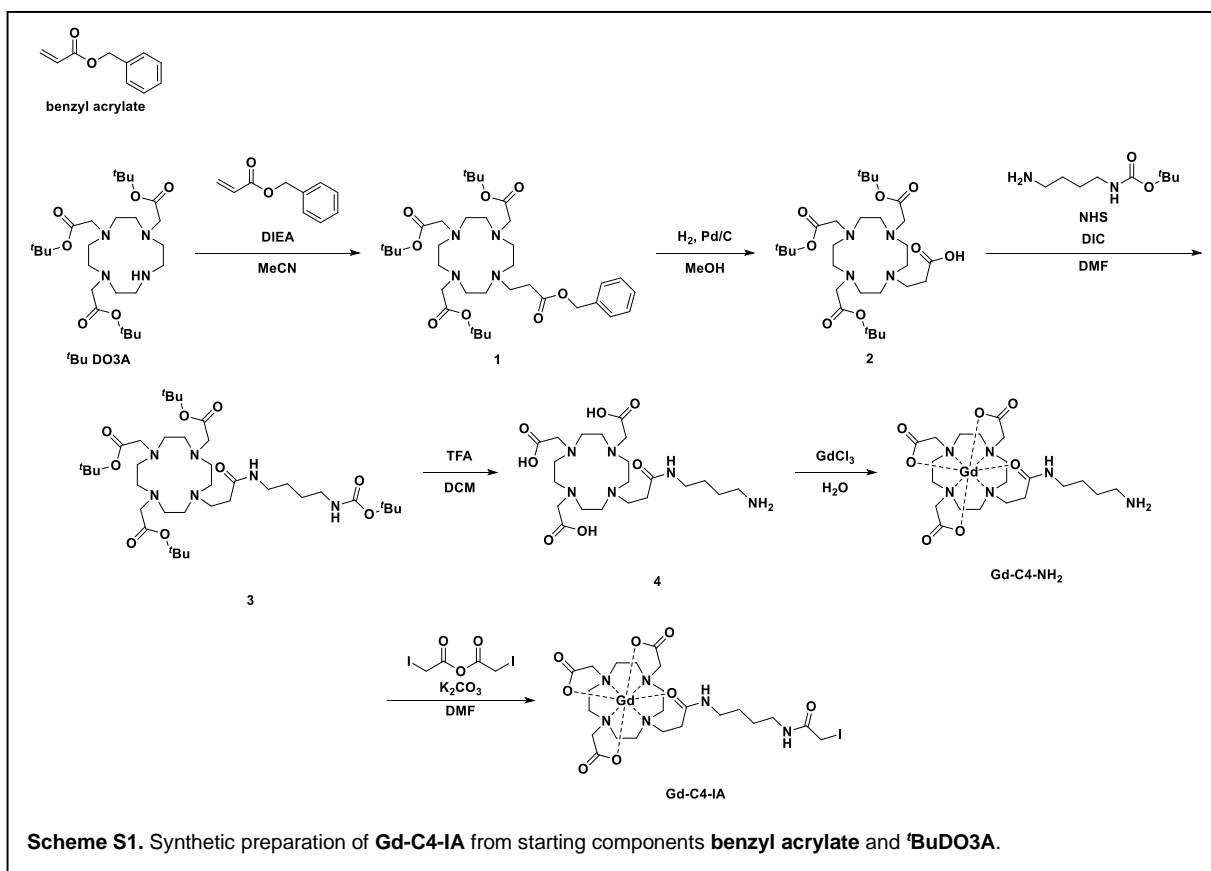
Synthesis of benzyl acrylate

Benzyl acrylate was synthesized following literature procedure.[1]

Synthesis of tri-tert-butyl 2,2',2''-(1,4,7,10-tetraazacyclododecane-1,4,7-triyl)triacetate (*t*Bu DO3A)

*t*Bu DO3A was synthesized following literature procedure.[2, 3]

Structure of **1**
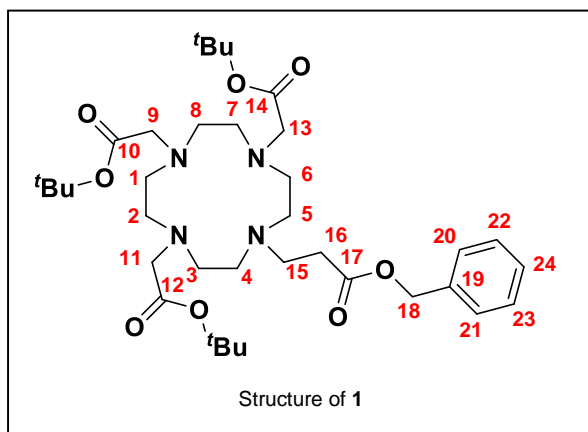
Synthesis of tri-tert-butyl 2,2',2''-(10-(3-(benzyloxy)-3-oxopropyl)-1,4,7,10-tetraazacyclododecane-1,4,7-triyl)triacetate (1)

To a stirred solution of *t*Bu DO3A (500 mg, 0.971 mmol, 1 equiv.) and **benzyl acrylate** (217.9 mg, 1.94 mmol, 2 equiv.) in anhydrous MeCN (30 mL) was slowly added DIPEA (1 mL, 5.74 mmol, 5.9 equiv.) at room temperature under N_2 (g). The mixture was stirred for 72 hours at room temperature until starting material was consumed (monitored by TLC). The reaction mixture was dried by reduced pressure and the clear residue brought up in 50 mL CH_2Cl_2. The organic layer was washed with saturated $NaHCO_3$ aq. (3 x 20 mL) and saturated NaCl aq. (1 x 20 mL). The organic layer was dried over Na_2SO_4 and concentrated under reduced pressure. The off-white solid was purified by flash chromatography in 1:20 MeOH:CH_2Cl_2 (Rf = 0.25, stained by Pt) to yield **1** as a pale yellow oil (353.7 mg, 47.3% yield). ^{1}H NMR (500 MHz, CDCl$_3$): δ = 7.35 (m, 3 Hs, 22-24), 7.30 (m, 2 Hs, 20-21), 5.09 (s, 2Hs, 18), 3.48 (d, *J* = 4.9 Hz, 4 H, 9, 11, 13), 2.77 – 3.37 (br overlapping signals), 2.55 (t, *J* = 7.2 Hz, 2 H, 16), 2.32 (br s), 1.73 (br s, 5 Hs), 1.43 – 1.46 (br s, 27 Hs, C(CH$_3$)$_3$); ^{13}C NMR (500 MHz, CDCl$_3$): δ = 172.9 (10), 172.6 (12), 172.2 (13), 135.3 (19), 128.4 (22-23), 128.2 (24), 127.8 (20-21), 82.3 (C(CH$_3$)$_3$), 82.1 (C(CH$_3$)$_3$), 66.2 (18), 56.3, 55.5, 49.8 (9, 11, 13), 30.8 (16), 27.7 (trans pair of C(CH$_3$)$_3$), 27.6 (single C(CH$_3$)$_3$); ESI/MS$^+$ m/z = 677.638 [M+H]$^+$, 699.621 [M+Na]$^+$.

Structure of **2**
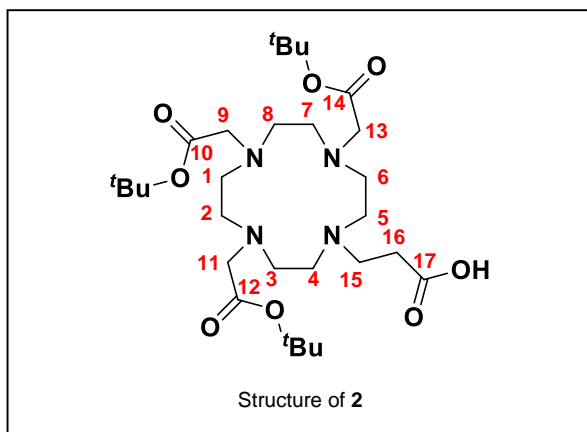
Synthesis of 3-(4,7,10-tris(2-(tert-butoxy)-2-oxoethyl)-1,4,7,10-tetraazacyclododecan-1-yl)propanoic acid (2)

A stirring solution of **1** (452.3 mg, 0.668 mmol, 1 equiv.) and Pd/C (approximately 1 g) in 10 mL MeOH was purged with H_2 (g) (3 x 100 mL) and then stirred under H_2 (g) for 24 hours The solution was filtered through celite and washed with MeOH (3 x 20 mL). Analysis by MS and TLC suggested the reaction was not complete, so the organic layer was concentrated under reduced pressure. Again, the stirring solution of **1** and Pd/C in 20mL MeOH was purged with H_2 (g) (3 x 100 mL) and then stirred under H_2 (g) for 18 hours The solution was filtered through celite and washed with MeOH (3 x 20 mL). The organic layer was concentrated under reduced pressure, and the resulting yellow oil purified by flash chromatography in 1:19 MeOH:CH_2Cl_2 to 1:9 MeOH:CH_2Cl_2 to 1:9:40 NH_4OH:MeOH:CH_2Cl_2 (Rf$_{1:9\ MeOH:CH2Cl2}$ = 0.31, stained by Pt) to yield **2** as a pale yellow oil (107.0 mg, 27.3% yield). ^{1}H NMR (500 MHz, CD$_3$OD): δ = 3.39 (br s, 0.5 Hs, 9, 11, 13), 2.56 – 3.39 (br overlapping signals, 16 Hs), 2.53 (t, *J* = 7.4 Hz, 2 Hs, 16), 1.45-1.46 (overlapping s, 27 Hs , C(C$\underline{H}_3$)$_3$); ^{13}C NMR (500 MHz, CD$_3$OD): δ = 83.0 ($\underline{C}$(CH$_3$)$_3$), 57.3 (11, 13), 56.6 (9), 51.5, 49.9, 32.4 (16), 28.4 (trans pair of C($\underline{C}$H$_3$)$_3$), 28.4 (single C($\underline{C}$H$_3$)$_3$); ESI/MS$^+$ m/z = 587.604 [M+H]$^+$, 609.574 [M+Na]$^+$, 1218.422 [2M+H+Na]$^+$.

Structure of **3**
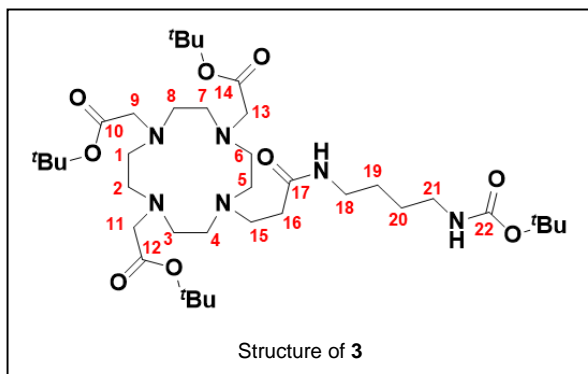
Synthesis of tri-tert-butyl 2,2',2''-(10-(3-((4-((tert-butoxycarbonyl)amino)butyl)amino)-3-oxopropyl)-1,4,7,10-tetraazacyclododecane-1,4,7-triyl)triacetate (3)

To a stirring solution of **2** (107.0 mg, 0.182 mmol, 1 equiv.) and NHS (62.96 mg, 0.547 mmol, 3 equiv.) in 10 mL anhydrous DMF was added DIEA (160 µL, 0.912 mmol, 5 equiv.) and DIC (150 µL, 0.912 mmol, 5 equiv.). To this stirring solution was dropwise added t-butyl (4-aminobutyl)carbamate (136.2 mg, 0.279 mmol, 1.5 equiv.) in 10 mL DMF over the course of 40 min and the solution stirred under N_2 (g) for 24 hours The solvent was concentrated under reduced pressure, and the resulting yellow oil dissolved in CH_2Cl_2 and washed with saturated $NaHCO_3$ (3 x 20 mL) and saturated NaCl aq. (3 x 20 mL). The organic layer was dried over Na_2SO_4 and concentrated under reduced pressure. The pale yellow oil was purified by flash chromatography in 1:20 MeOH:CH_2Cl_2 to 1:10 MeOH:CH_2Cl_2 (Rf$_{1:9}$ $_{MeOH:CH2Cl2}$ = 0.5, stained by Pt) to yield **3** as a pale yellow oil (150.1 mg, quantitative yield). ^{1}H NMR (500 MHz, CD$_3$OD): δ = 3.34 (t, J = 6.5 Hz, 2 Hs, 15), 3.16 (m, 2Hs, 21), 3.08 (m, 2 Hs, 18), 3.02 (m, 4 Hs, 3-6), 2.33 (t, J = 6.6 Hz, 2 Hs, 16), 1.44 – 1.49 (m, 12 Hs, C(CH$_3$)$_3$), 1.41 (s, 17Hs, C(CH$_3$)$_3$); ^{13}C NMR (500 MHz, CD$_3$OD): δ = 174.1 (10, 12, 14), 161.0 (17), 158.5 (22), 79.9 (C(CH$_3$)$_3$), 79.8 (C(CH$_3$)$_3$), 41.0 (overlapping s, 3, 4, 5, 6), 40.7 (18), 40.0 (21), 37.7 (16), 37.6 (15), 28.8 (NCH$_3$COOC(CH$_3$)$_3$), 28.6 (20), 28.3 (NHCOOC(CH$_3$)$_3$), 27.7 (19); ESI/MS$^+$ m/z = 757.803 [M+H]$^+$.
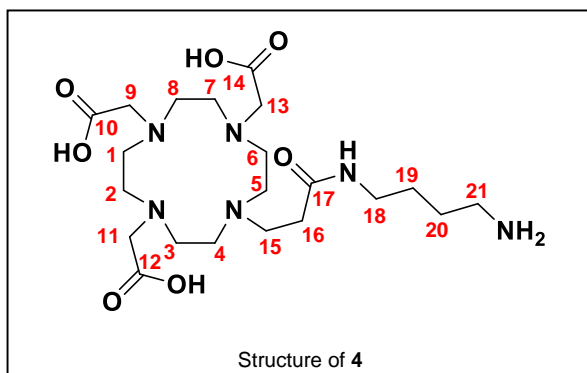
Structure of **4**

Synthesis of 2,2',2''-(10-(3-((4-aminobutyl)amino)-3-oxopropyl)-1,4,7,10-tetraazacyclododecane-1,4,7-triyl)triacetic acid (4)

A solution of **3** (10.8083 mg, 14.3 mmol) in 4:1 TFA:CH_2Cl_2 (100 mL) was stirred under N_2 (g) for 18 hours The solvent was concentrated under reduced pressure, and the resulting brown oil (crude **4**) was carried on crude to the next reaction. ESI/MS$^+$ m/z = 489.394 [M+H]$^+$.
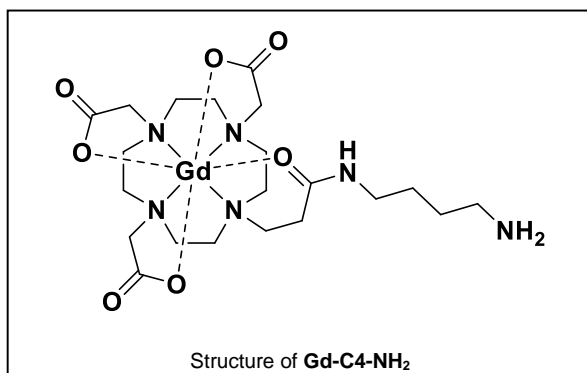
Structure of **Gd-C4-NH₂**

Synthesis of 2,2',2''-(10-(3-((4-aminobutyl)amino)-3-oxopropyl)-1,4,7,10-tetraazacyclododecane-1,4,7-triyl)triacetate gadolinium(III) (Gd-C4-NH₂)

A crude solution of **4** (7 g, 14.3 mmol, 1 equiv.) in H_2O (100 mL) was adjusted to pH 6.5 with 0.5 M HCl. To this stirring solution, a solution of $GdCl_3$ hexahydrate (6.9763 g, 18.8 mmol, 1.3 equiv.) in H_2O (15 mL) was added. The pH was maintained at 6.5. The reaction was stirred at room temperature under N_2 (g) overnight. The solution was adjusted to neutral pH with 0.5 M NaOH and filtered for HPLC. **Gd-C4-NH₂** was collected from the HPLC at 12.1 min. as a yellow oil (3.3685 g, 34 % yield over 2 steps). ESI/MS$^+$ m/z = 644.314 [M+ H]$^+$; HRMS (ESI) m/z = 644.2057 (calcd. 644.2038) [M+H]$^+$

Structure of **Gd-C4-IA**
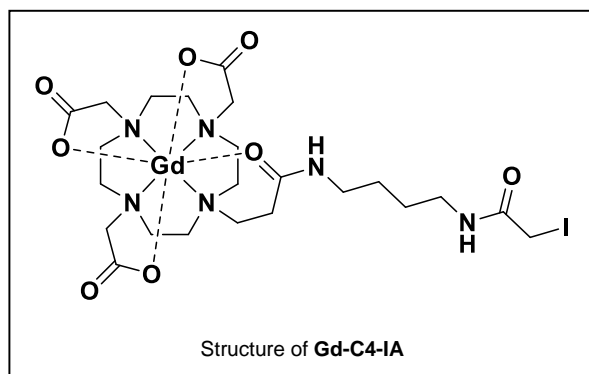
Synthesis of 2,2',2''-(10-(3-((4-(2-iodoacetamido)butyl)amino)-3-oxopropyl)-1,4,7,10-tetraazacyclododecane-1,4,7-triyl)triacetate gadolinium(III) (Gd-C4-IA)

The materials **Gd-C4-NH₂** (187.4 mg, 0.235 mmol, 1 equiv.), iodoacetic anhydride (321.3 mg, 0.706 mmol, 3 equiv.), and K_2CO_3 (99.01 mg, 0.706 mmol, 3 equiv.) were combined and placed under vacuum for 30 min. The materials were then dissolved in 10 mL DMF at 0 °C and stirred under N_2 (g) for 24 hours, allowing the solution to warm to room temperature. The solvent was concentrated by reduced pressure, and the pale yellow residue dissolved in H_2O and adjusted to pH 7. The solution was filtered for HPLC, and **Gd-C4-IA** was collected from the HPLC at 13.5 min. as a white fluffy powder (46.3 mg, 19.6% yield). ESI/MS⁺ m/z = 811.278 [M]⁺, 833.257 [M+Na]⁺, 849.218 [M+K]⁺; HRMS (ESI) m/z = 812.1113 (calcd. 812.1110) [M+H]⁺

3. NMR Spectra of **Gd-C4-IA** Synthons

Figure S1. ^{1}H NMR Spectrum of **1** in CDCl$_3$ at 500 MHz.

Figure S2. ^{13}C NMR Spectrum of **1** in CDCl$_3$ at 500 MHz.

Figure S3. ^{1}H-^{1}H COSY Spectrum of **1** in CDCl$_3$ at 500 MHz.

Figure S4. ^{1}H-^{13}C HSQC Spectrum of **1** in CDCl₃ at 500 MHz.

Figure S5. [1]H-^{1}H TOCSY Spectrum of **1** in CDCl$_3$ at 500 MHz.

Figure S6. ^{1}H Spectrum of **2** in CD$_3$OD at 500 MHz.

Figure S7. ^{13}C Spectrum of **2** in CD$_3$OD at 500 MHz.
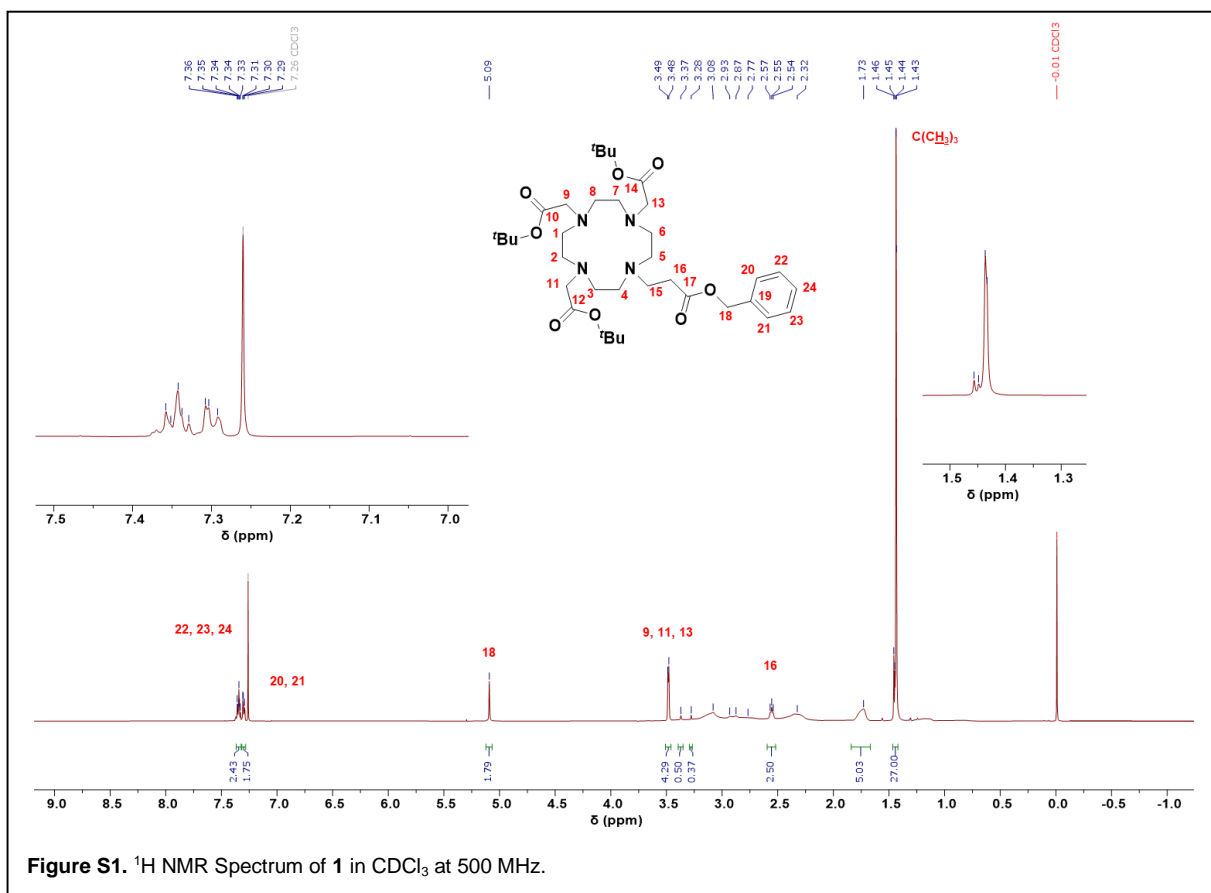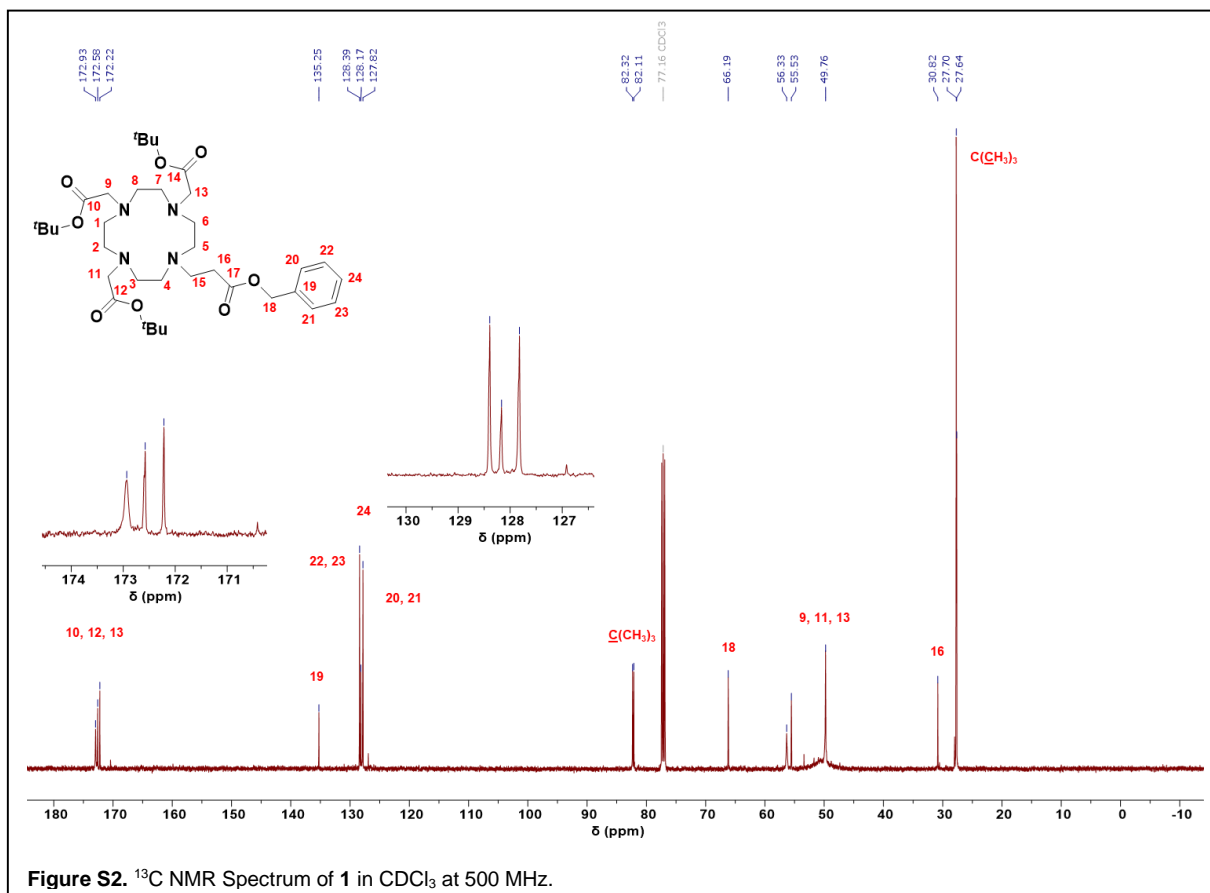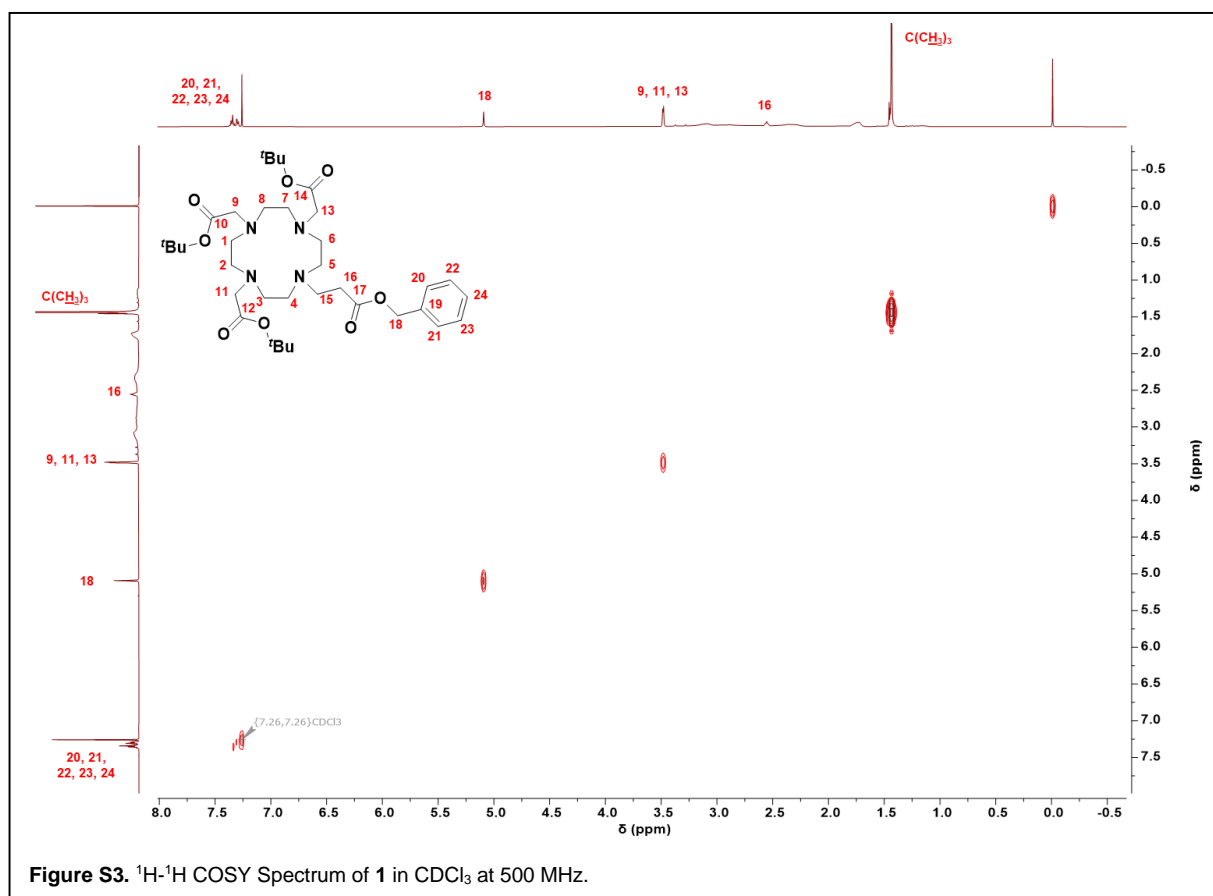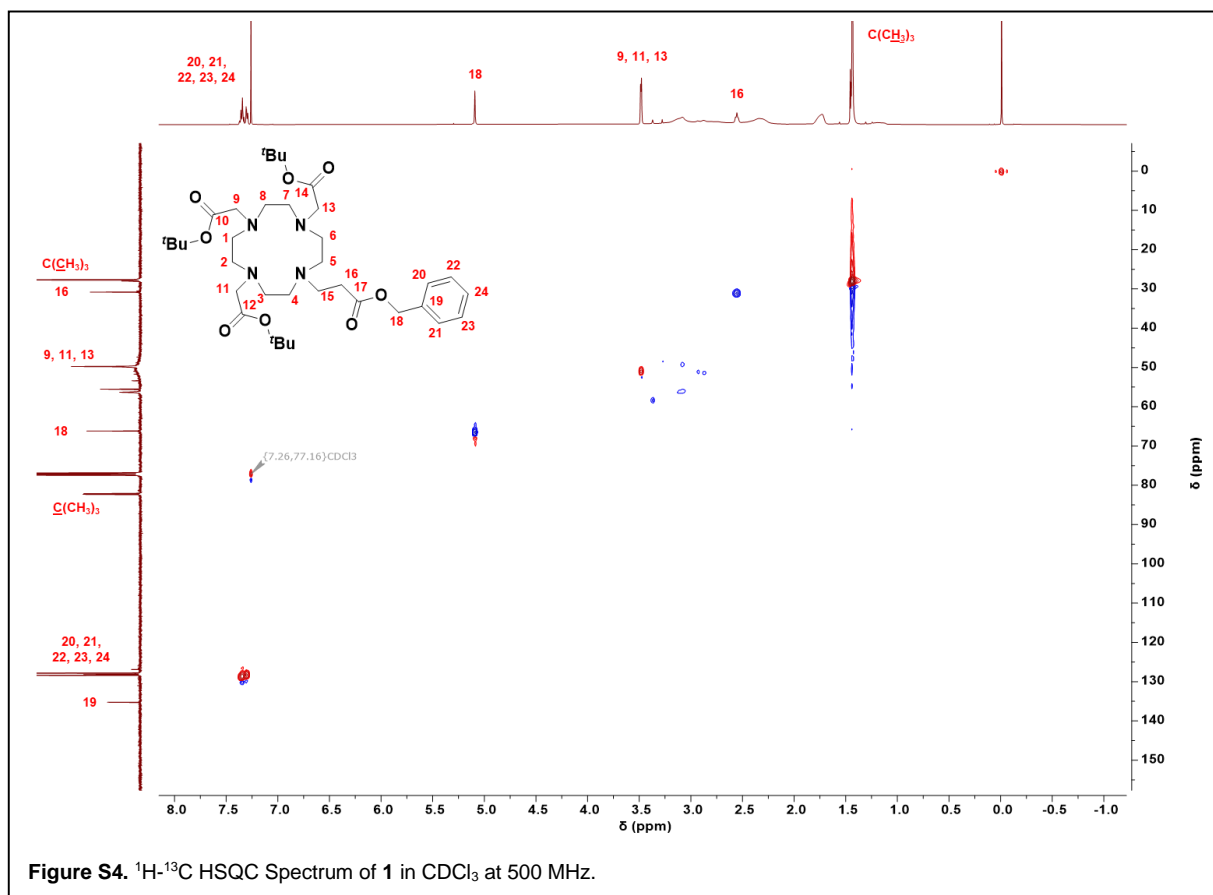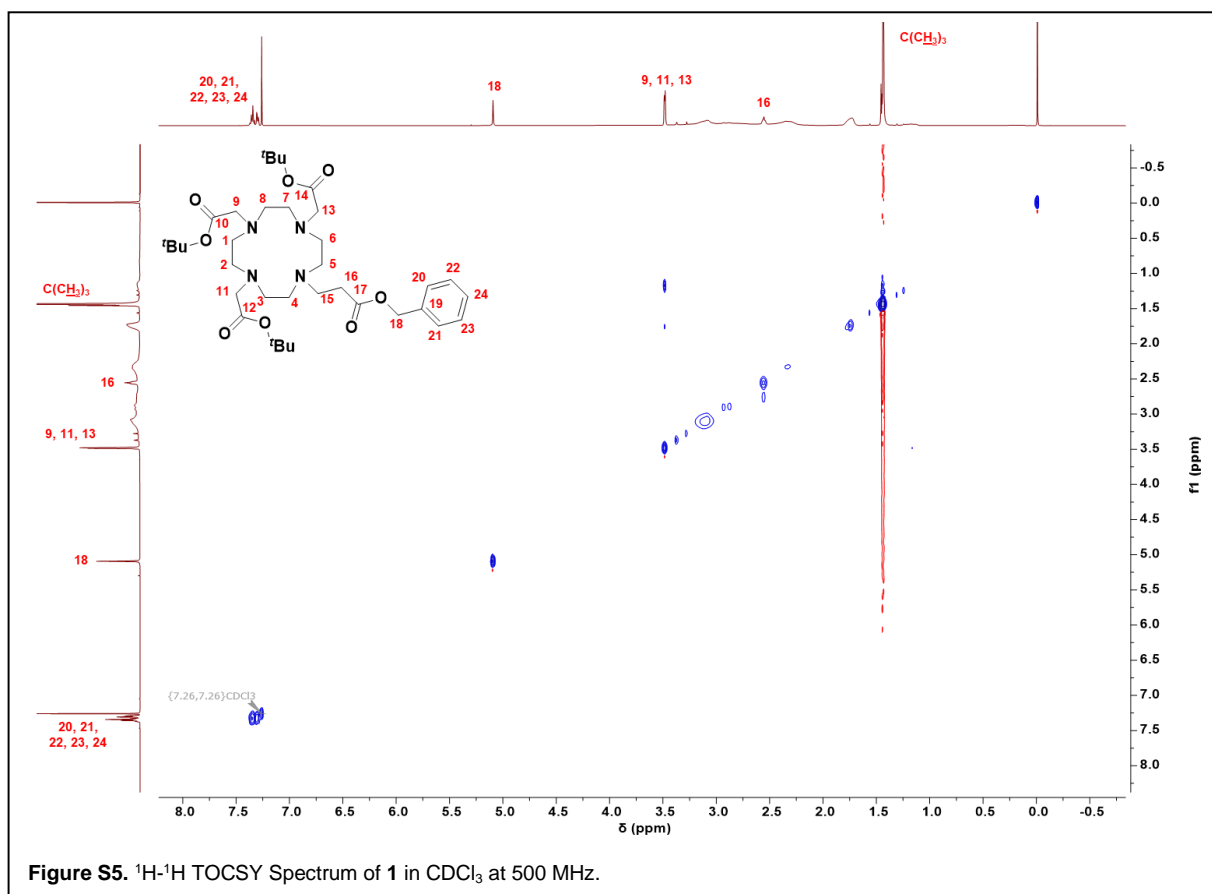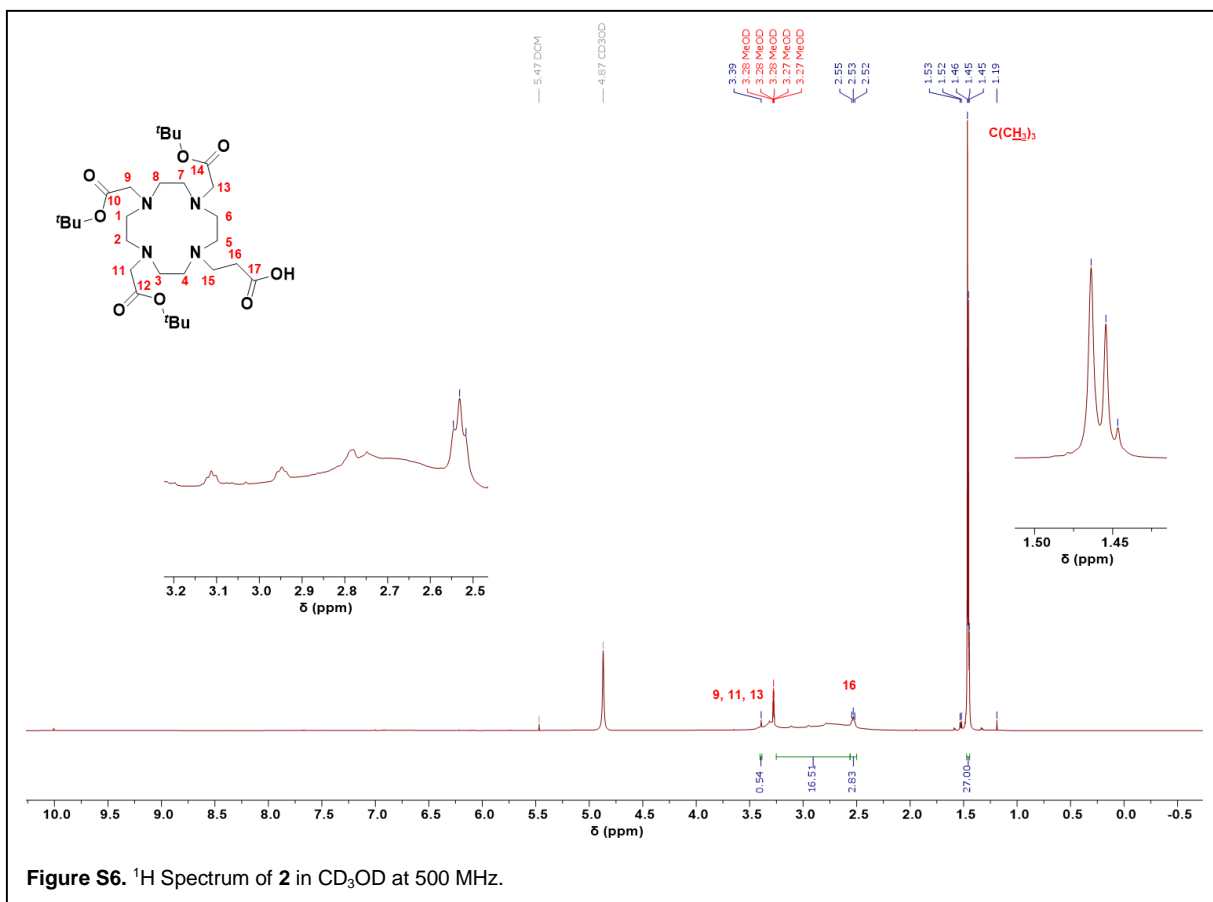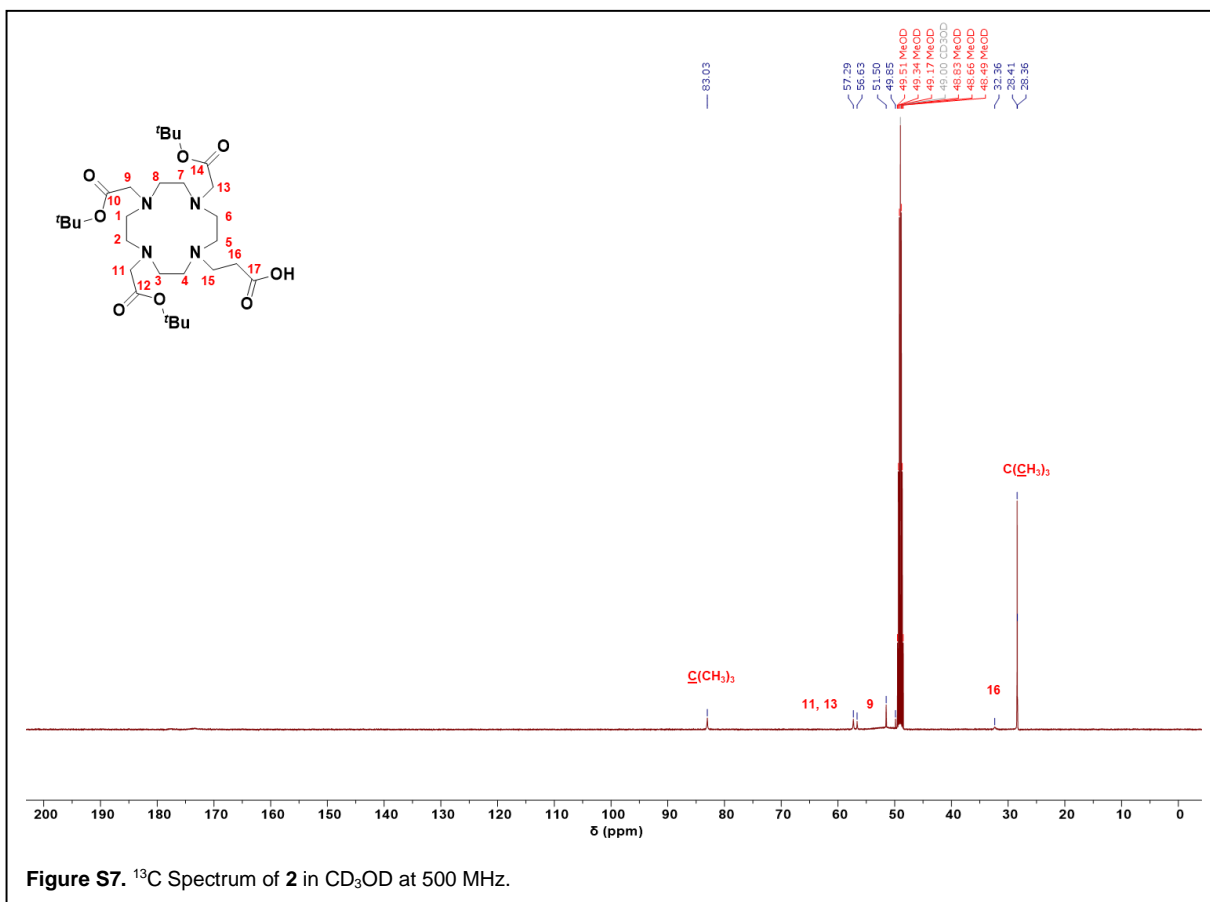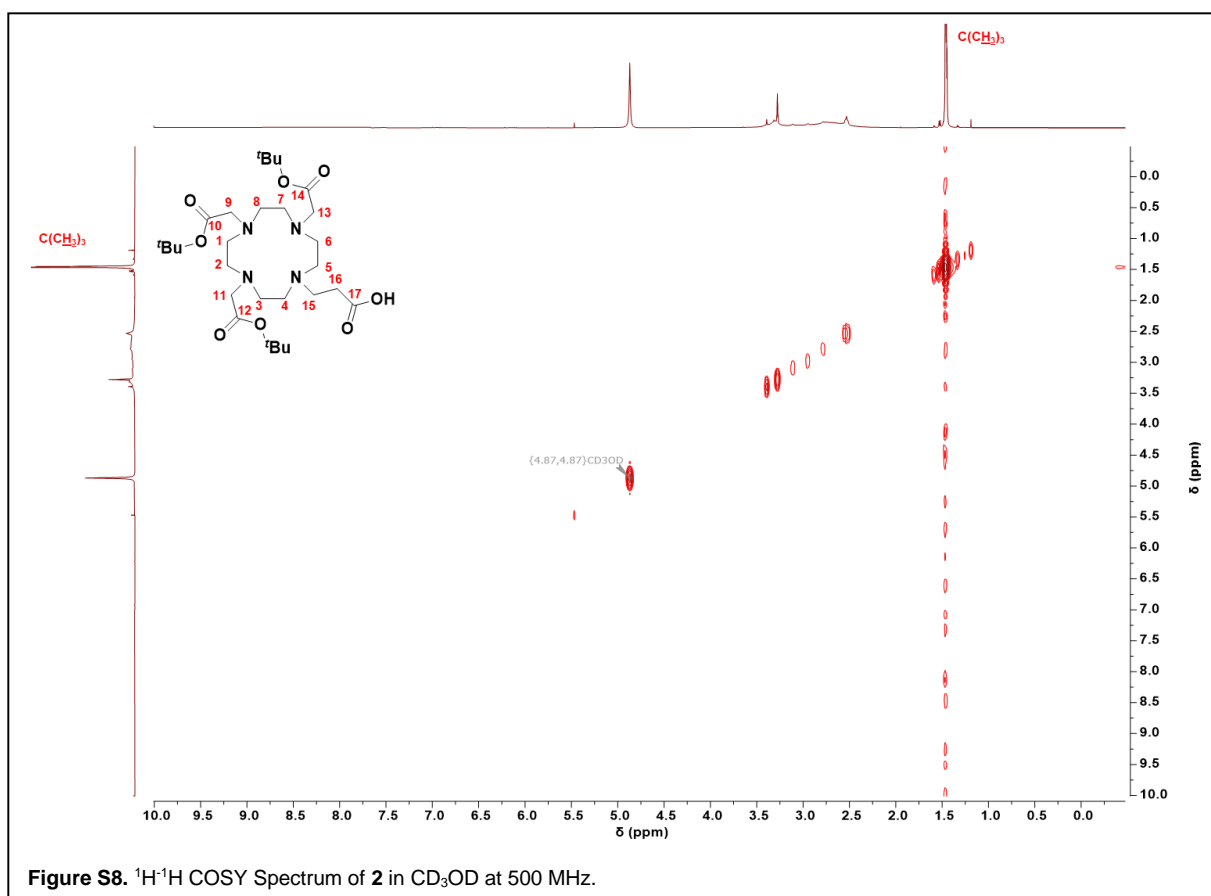
Figure S8. ^{1}H-^{1}H COSY Spectrum of **2** in CD$_3$OD at 500 MHz.

Figure S9. ^{1}H-^{13}C HSQC Spectrum of **2** in CD$_3$OD at 500 MHz.

Figure S10. ^{1}H-^{1}H TOCSY Spectrum of **2** in CD$_3$OD at 500 MHz.

Figure S11. ^{1}H Spectrum of **3** in CD$_3$OD at 500 MHz.

Figure S12. ^{13}C Spectrum of **3** in CD$_3$OD at 500 MHz.

Figure S13. ^{1}H-^{1}H COSY Spectrum of **3** in CD$_3$OD at 500 MHz.

Figure S14. $^1H-^{13}C$ HSQC Spectrum of **3** in CD$_3$OD at 500 MHz.
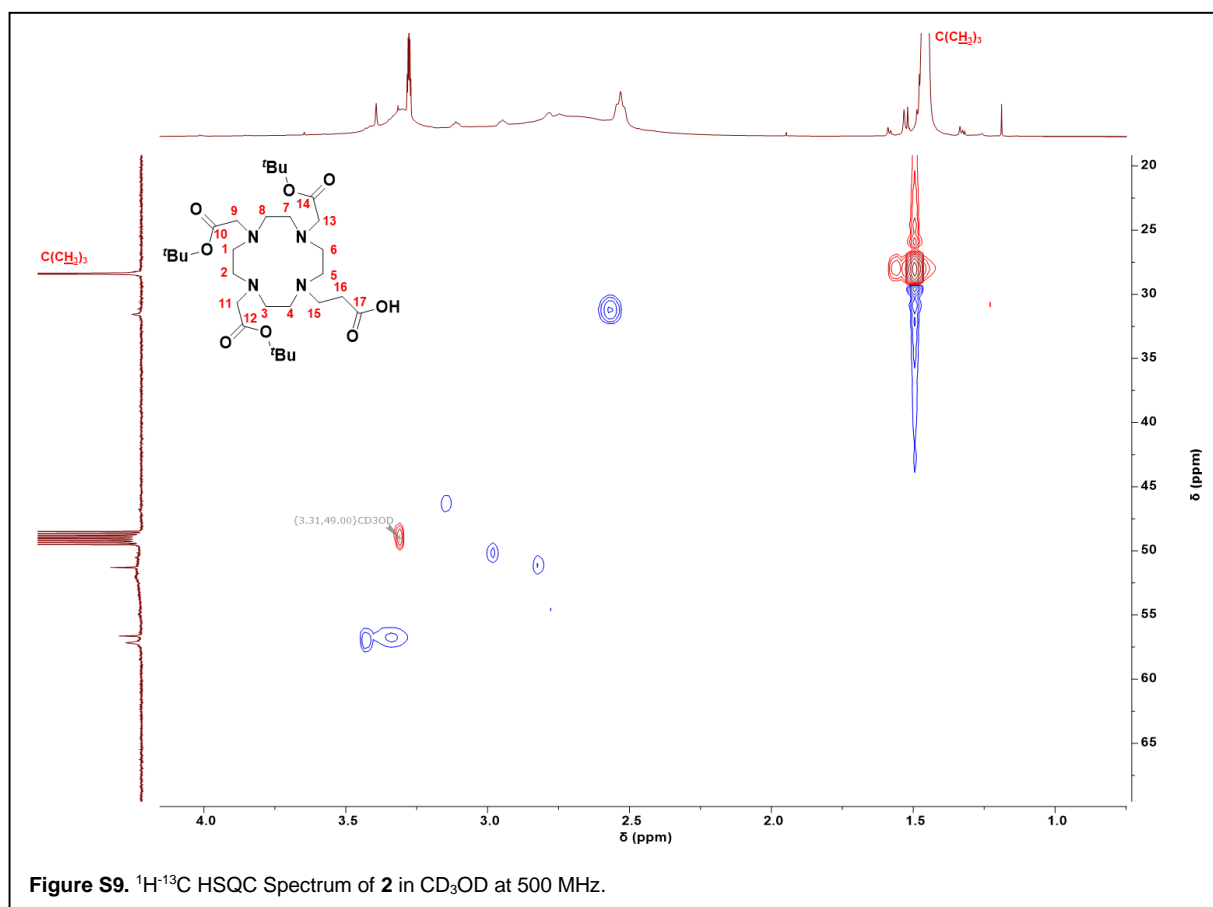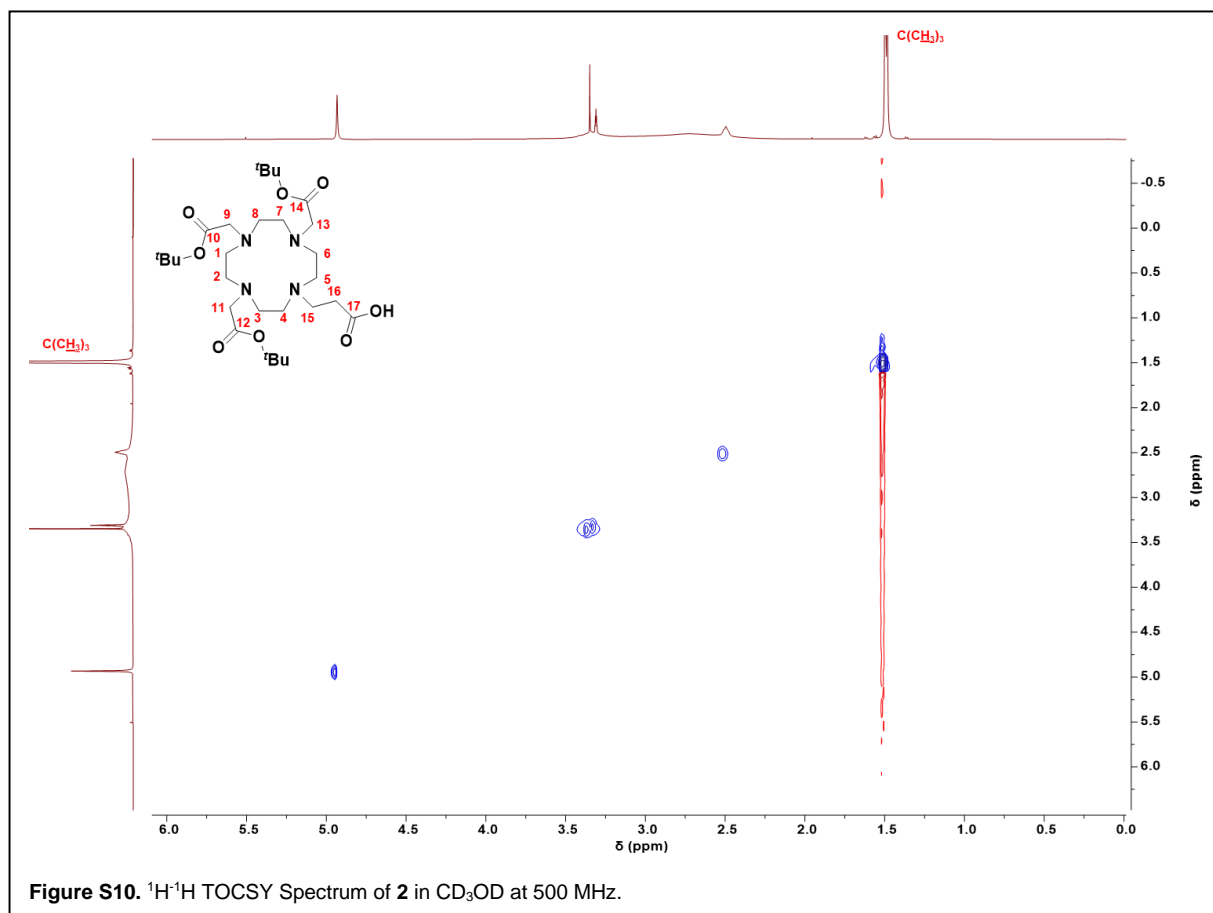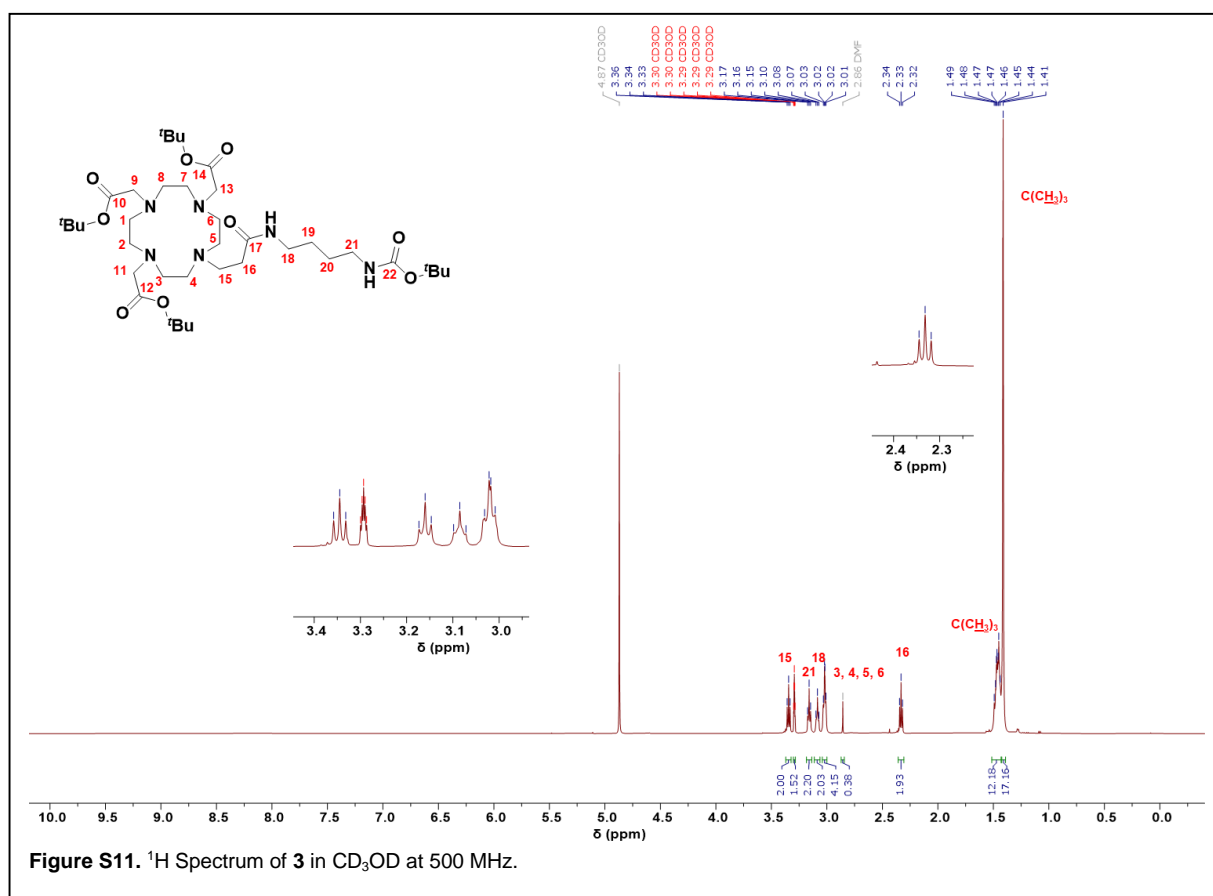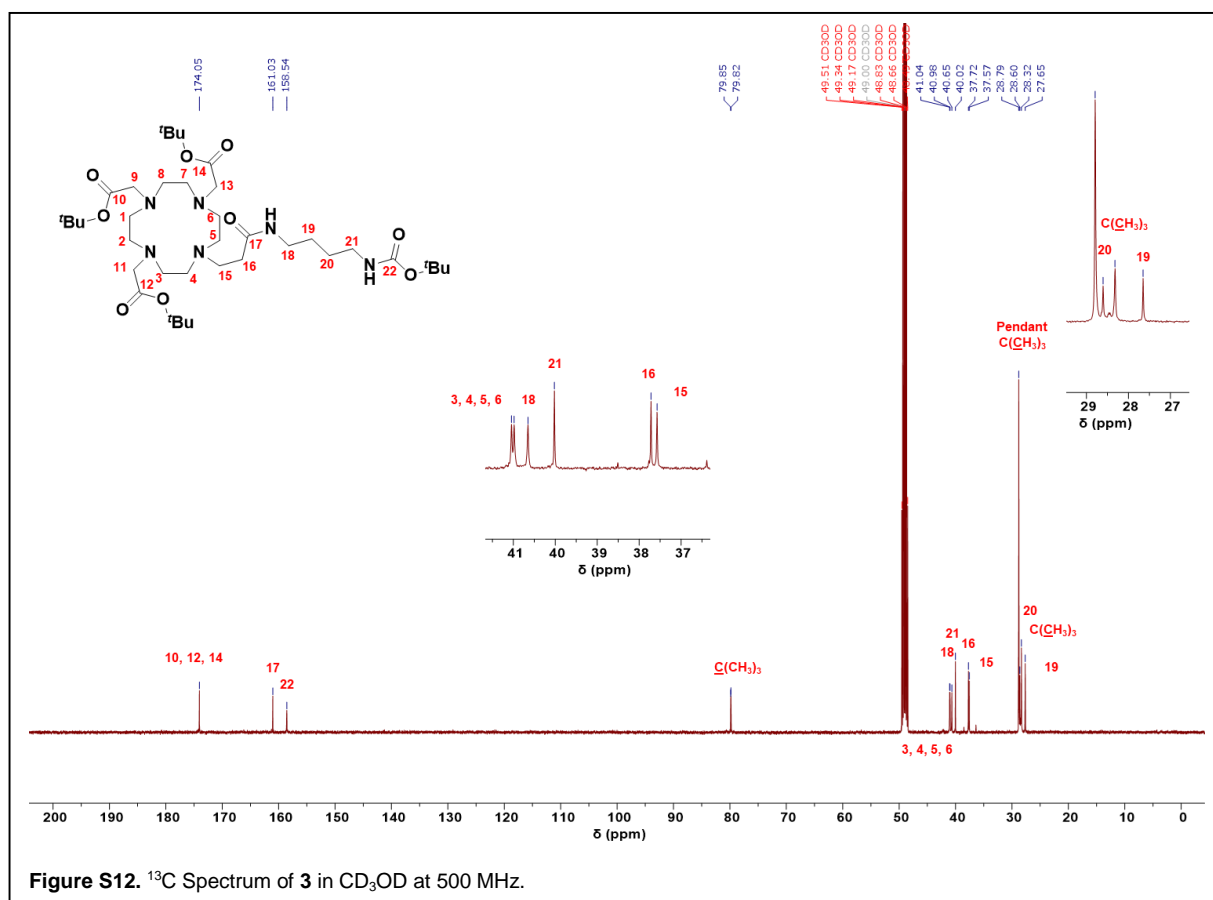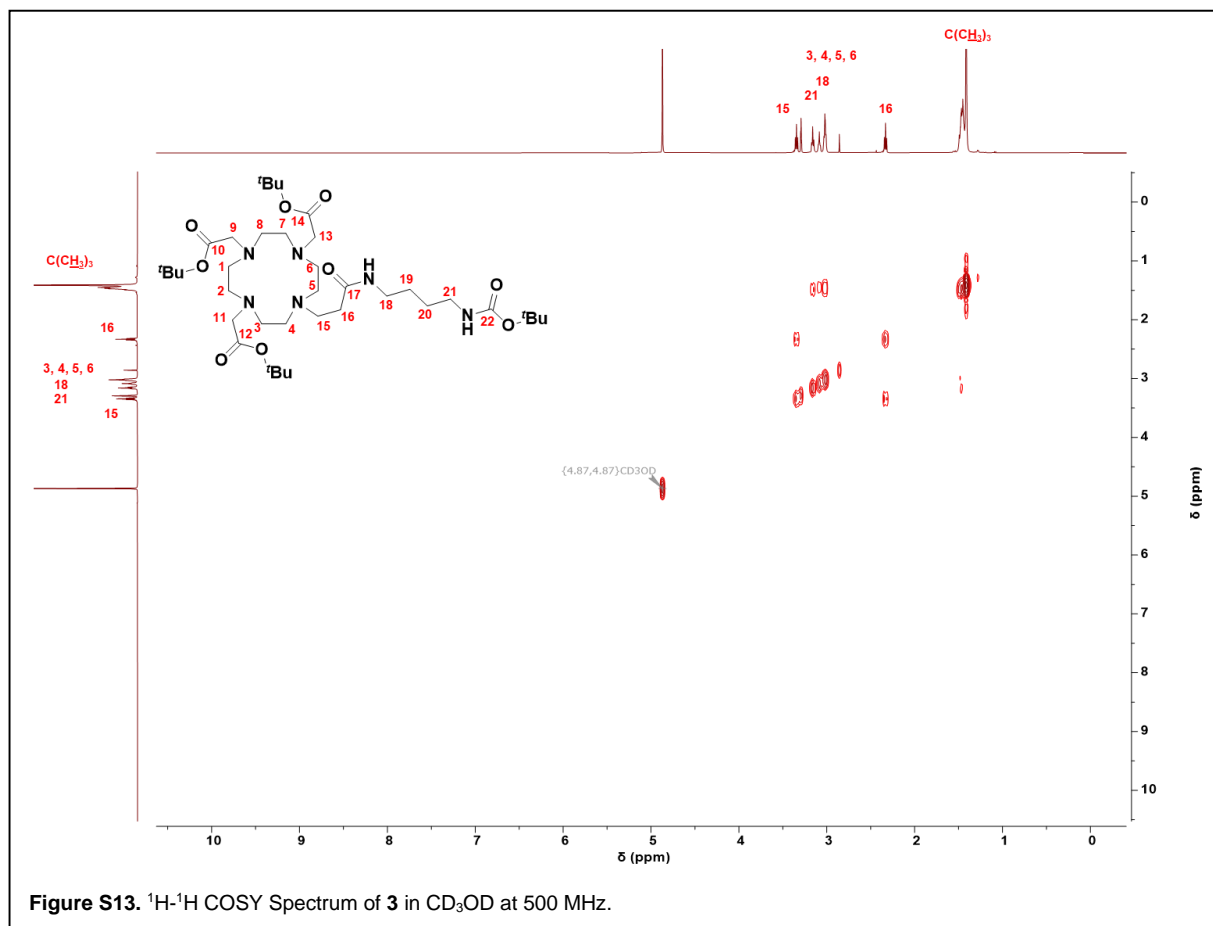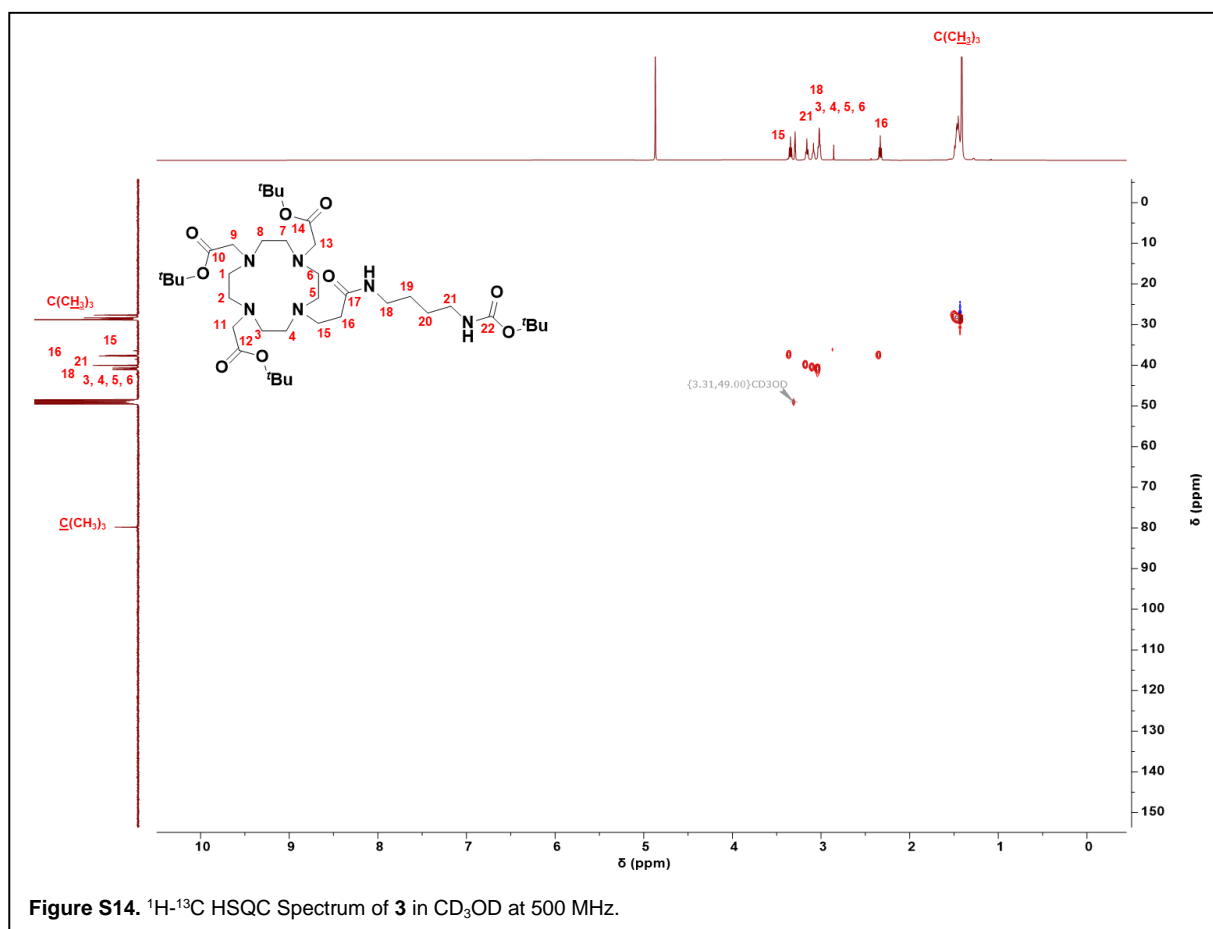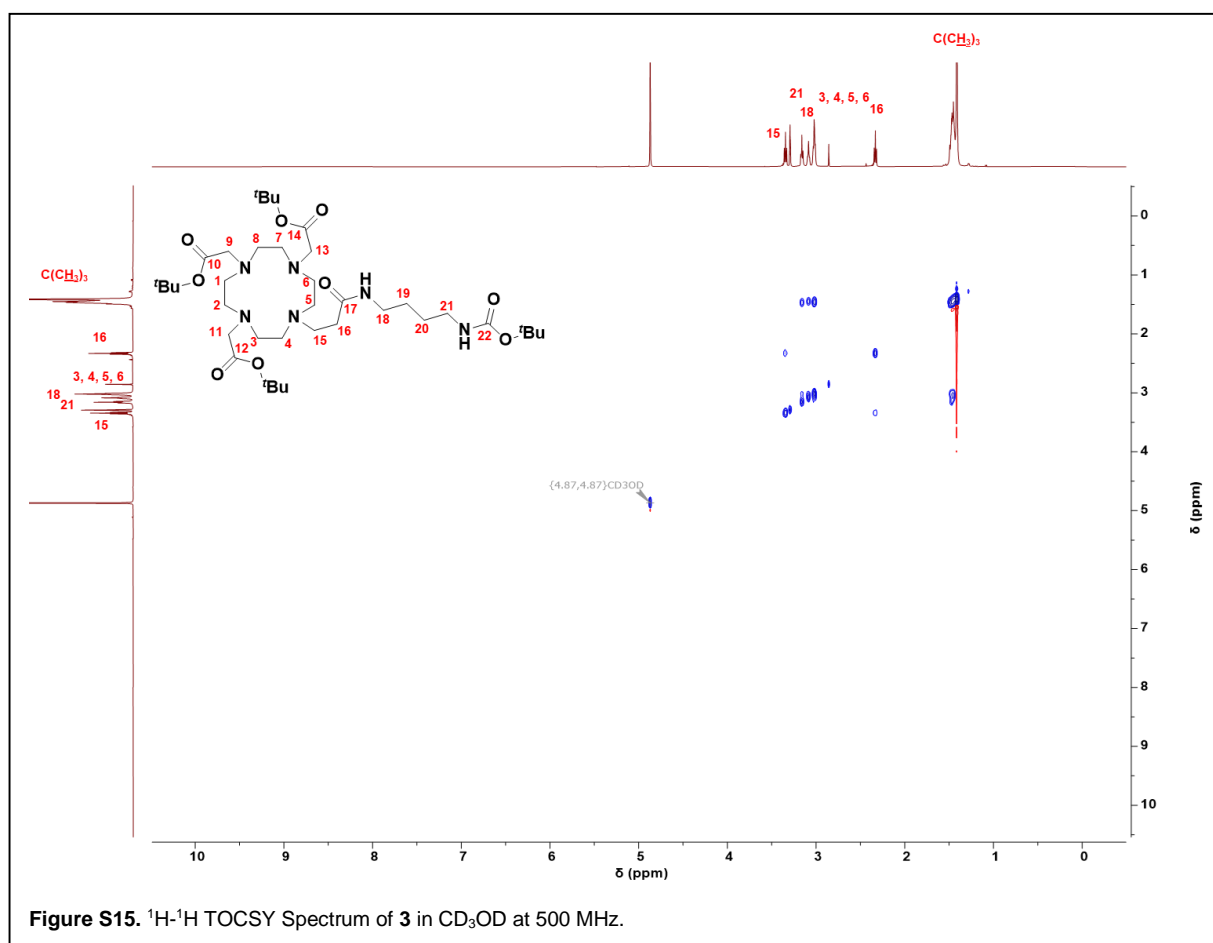
Figure S15. ^{1}H-^{1}H TOCSY Spectrum of **3** in CD$_3$OD at 500 MHz.

4. MS Spectra of **Gd-C4-IA** Synthons

Figure S16. ESI-MS+ Spectrum of **1**.

Figure S17. ESI-MS⁺ Spectrum of **2**.

Figure S18. ESI-MS+ Spectrum of **3**.

Figure S19. ESI-MS⁺ Spectrum of crude **4**.

Figure S20. ESI-MS+ Spectrum of **Gd-C4-NH₂**.

Figure S21. ESI-MS⁺ Spectrum of **Gd-C4-IA**.
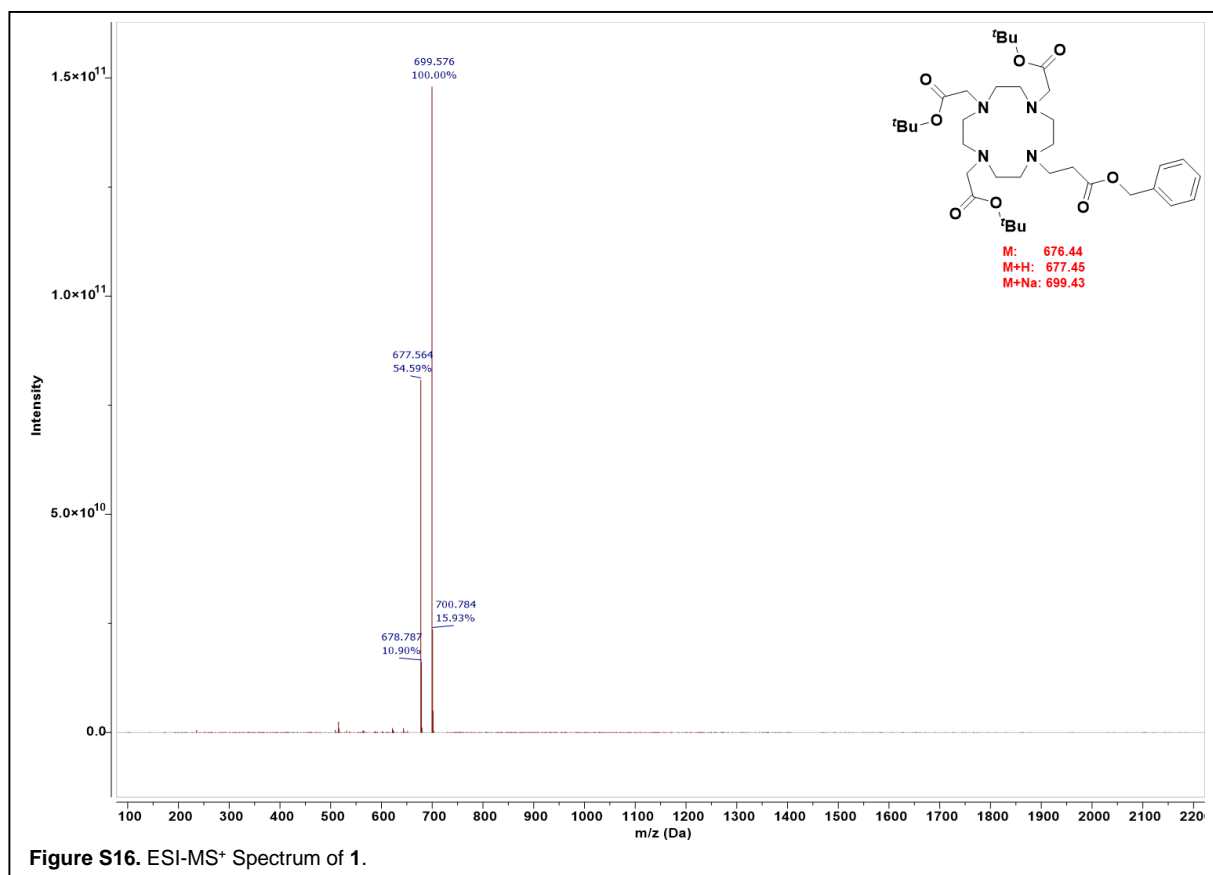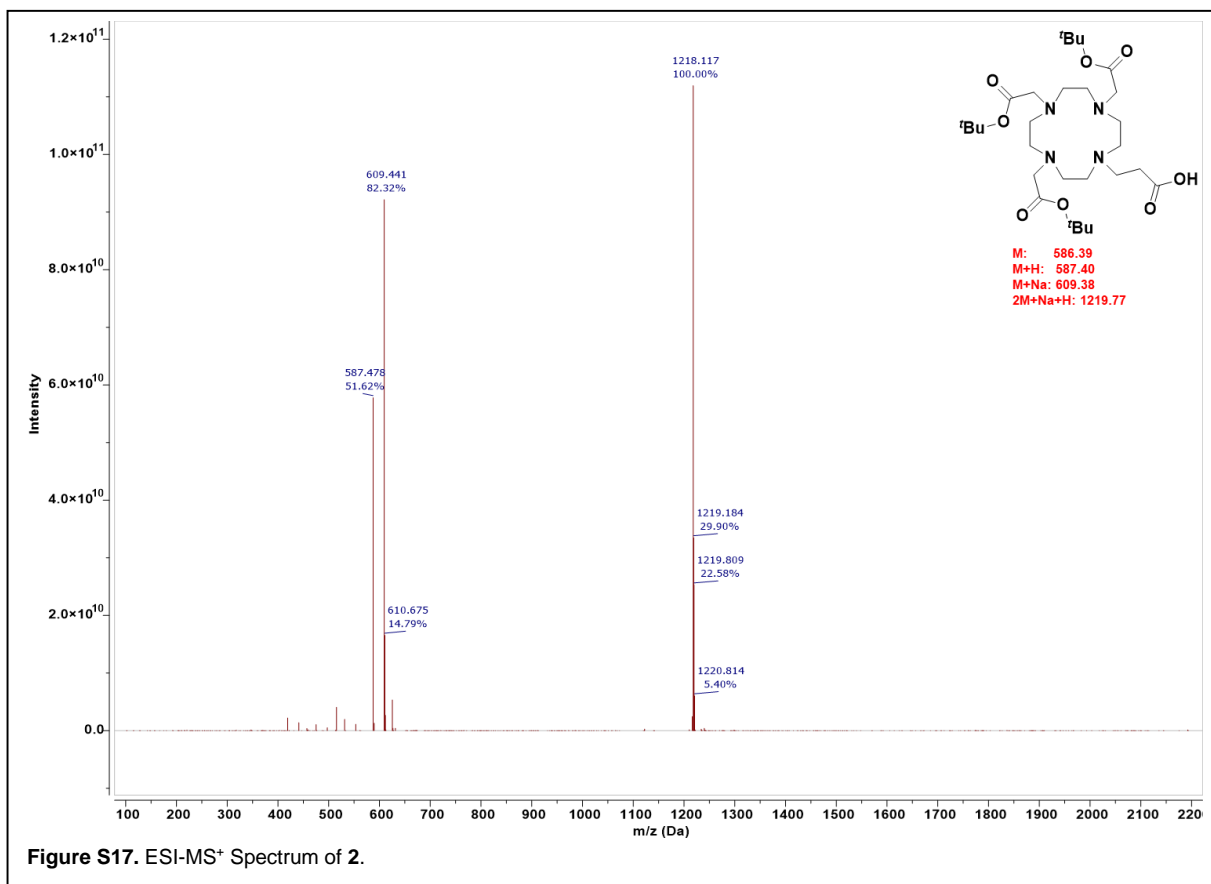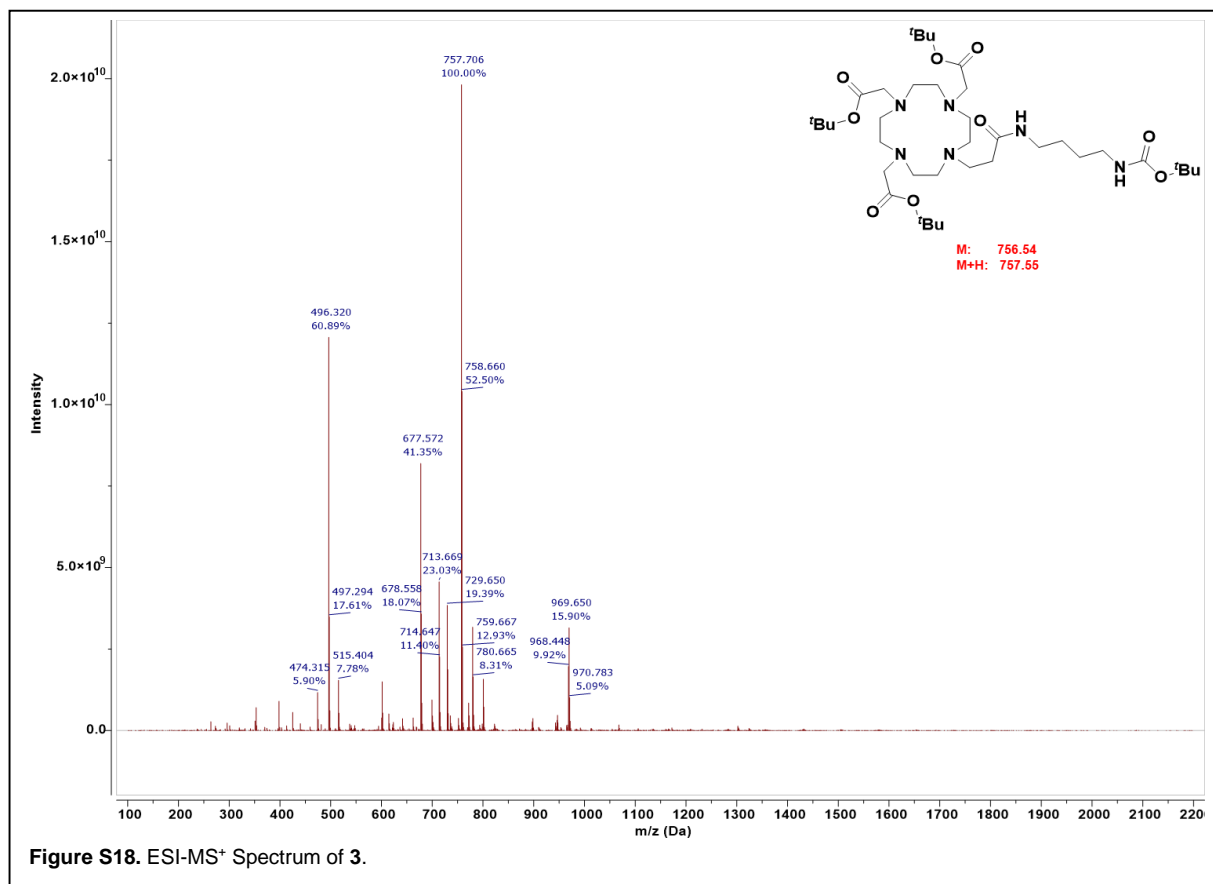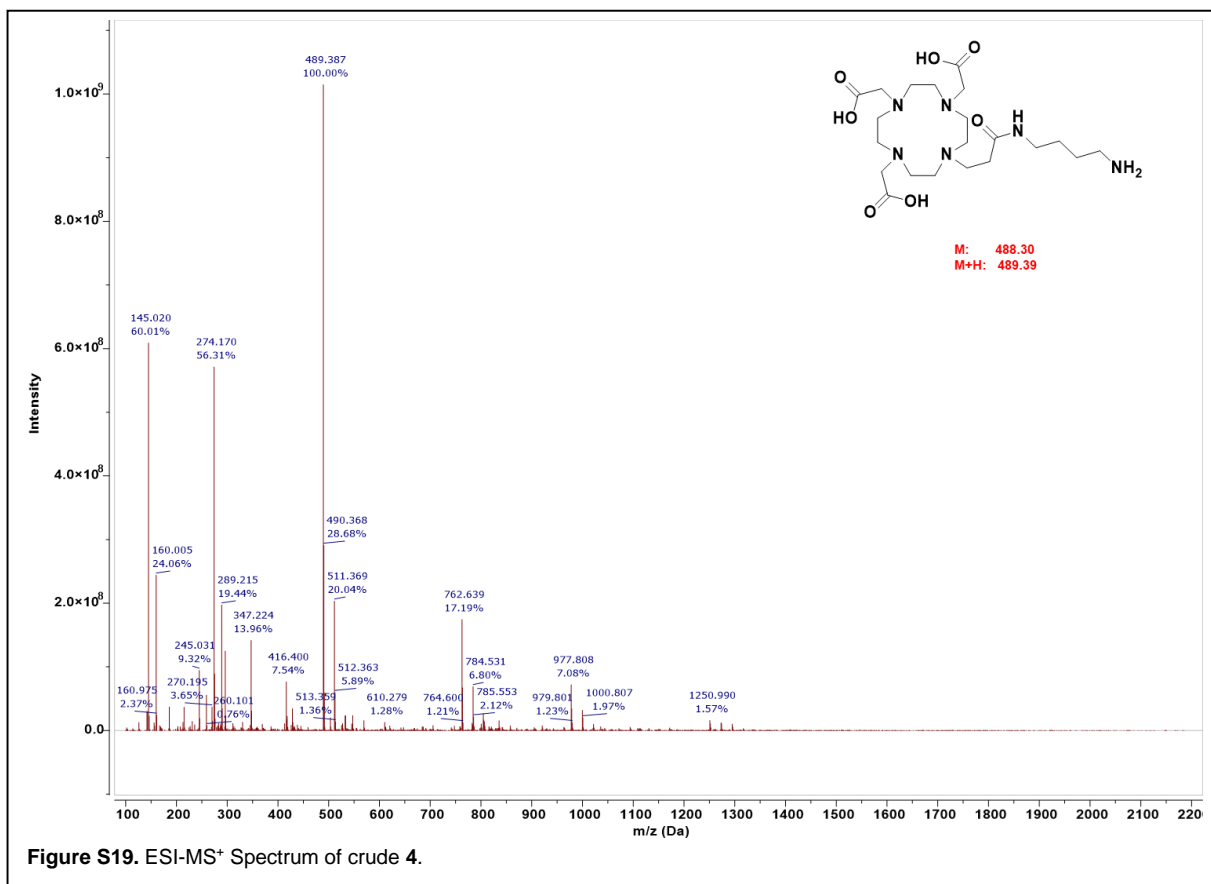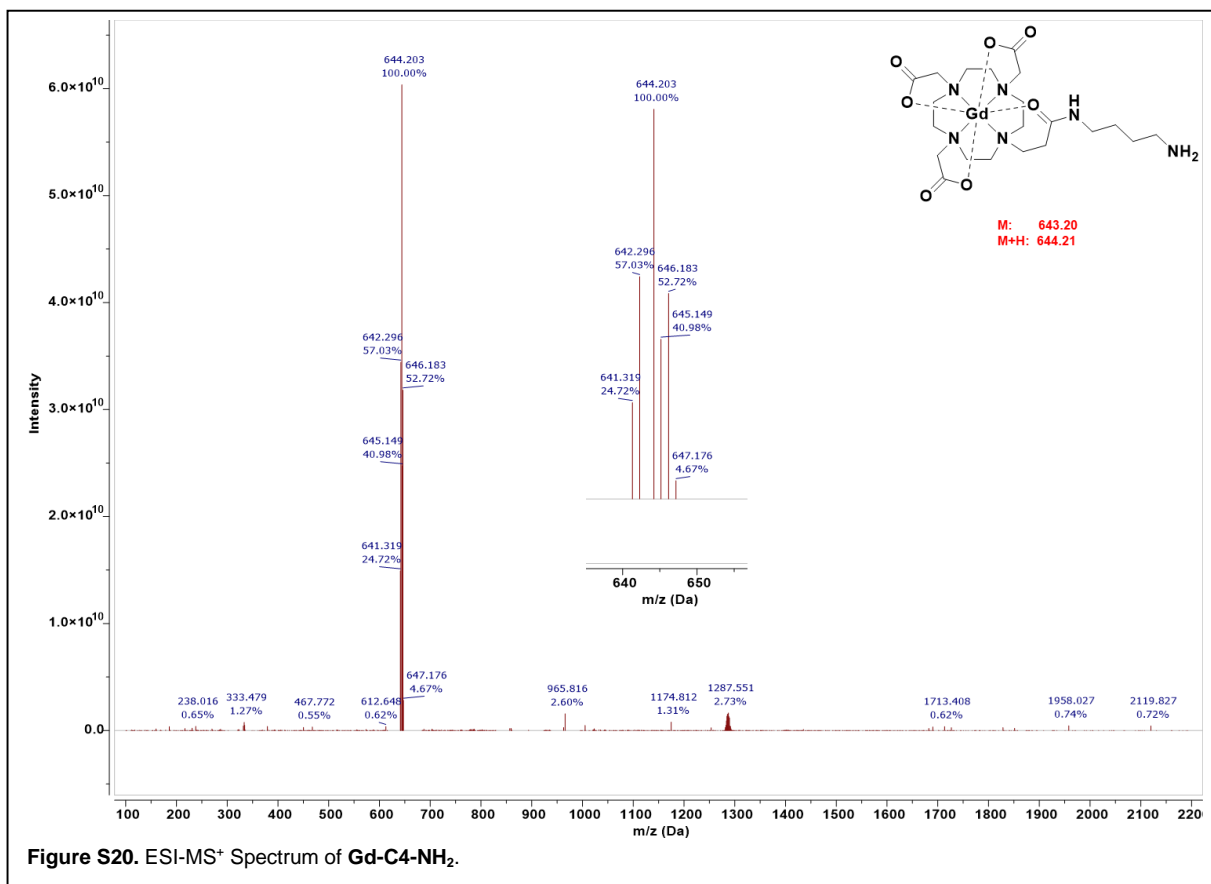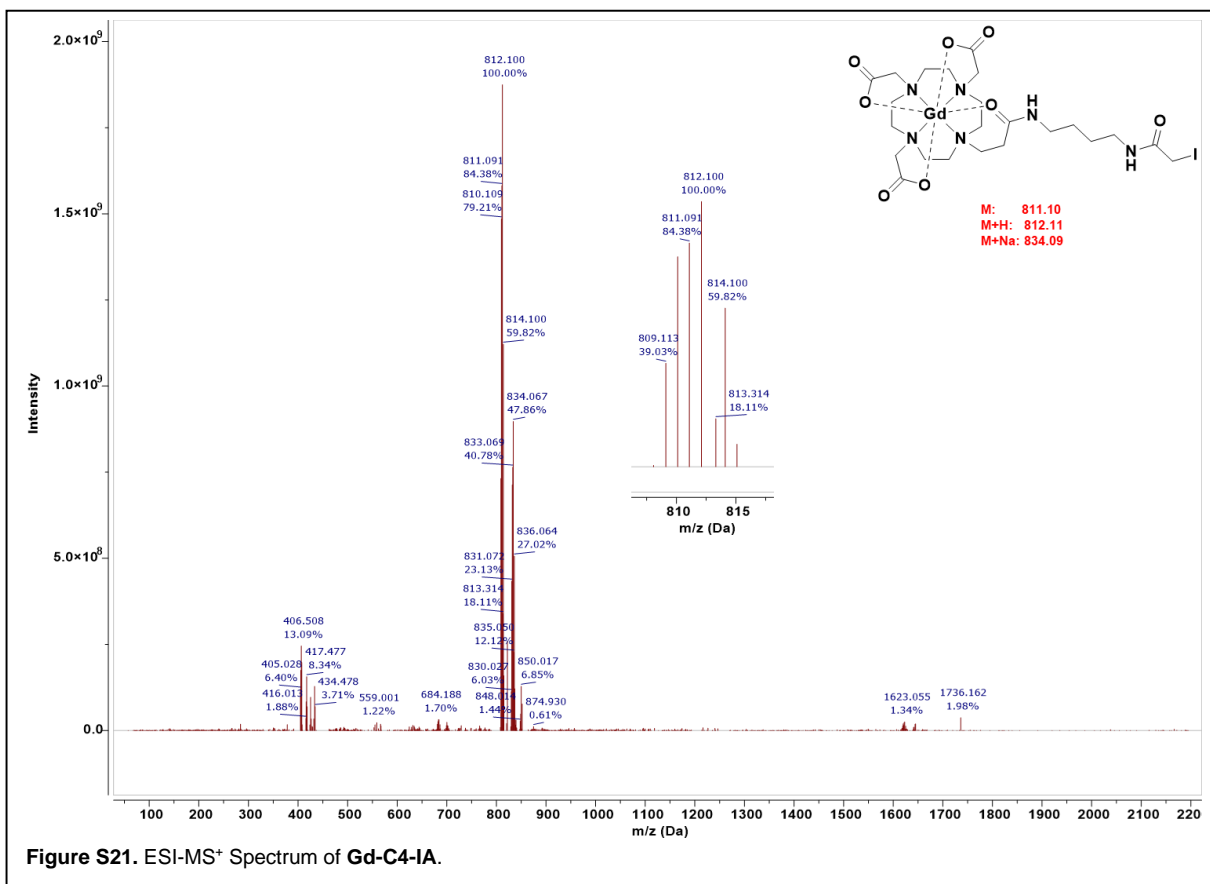
5. HR-MS Spectrum of **Gd-C4-IA**

Samples were prepared at 1 mg/mL in MQ H_2O, and were analyzed using an Agilent 6230 Time of Flight (TOF) mass spectrometer with an electrospray ionization (ESI) source, attached to an Agilent 1200 series HPLC stack. Data was acquired on Agilent Mass Hunter Acquisition software and analyzed on Agilent Mass Hunter Qualitative Analysis software.
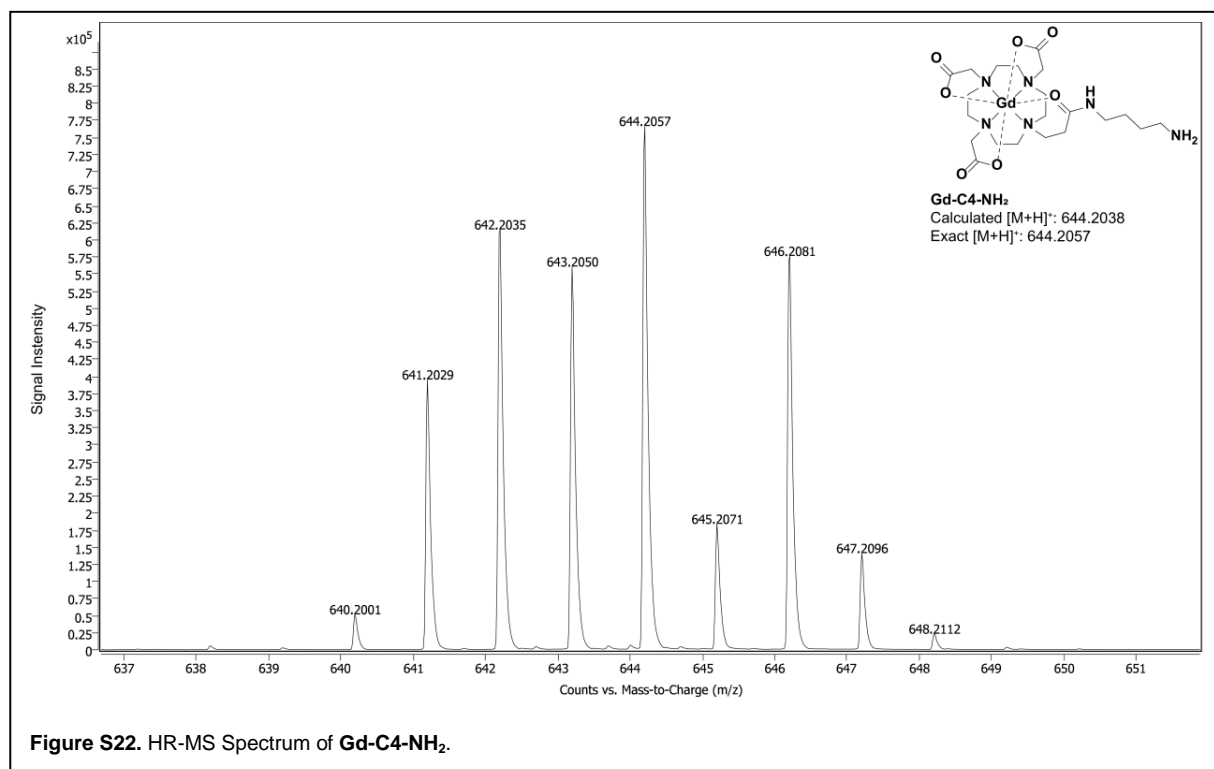
Figure S22. HR-MS Spectrum of **Gd-C4-NH$_2$**.

Figure S23. HR-MS Spectrum of **Gd-C4-IA**.

6. HPLC Traces of Gd(III) Complexes

Figure S24. Analytical HPLC chromatogram traces of Gd(III) complexes. (a) **Gd-C4-NH₂** and (b) **Gd-C4-IA** HPLC chromatogram traces at 210 nm (blue), 230 nm (red), 254 nm (black), 270 nm (purple), and either 290 nm (b, green) or 300 nm (a, green).
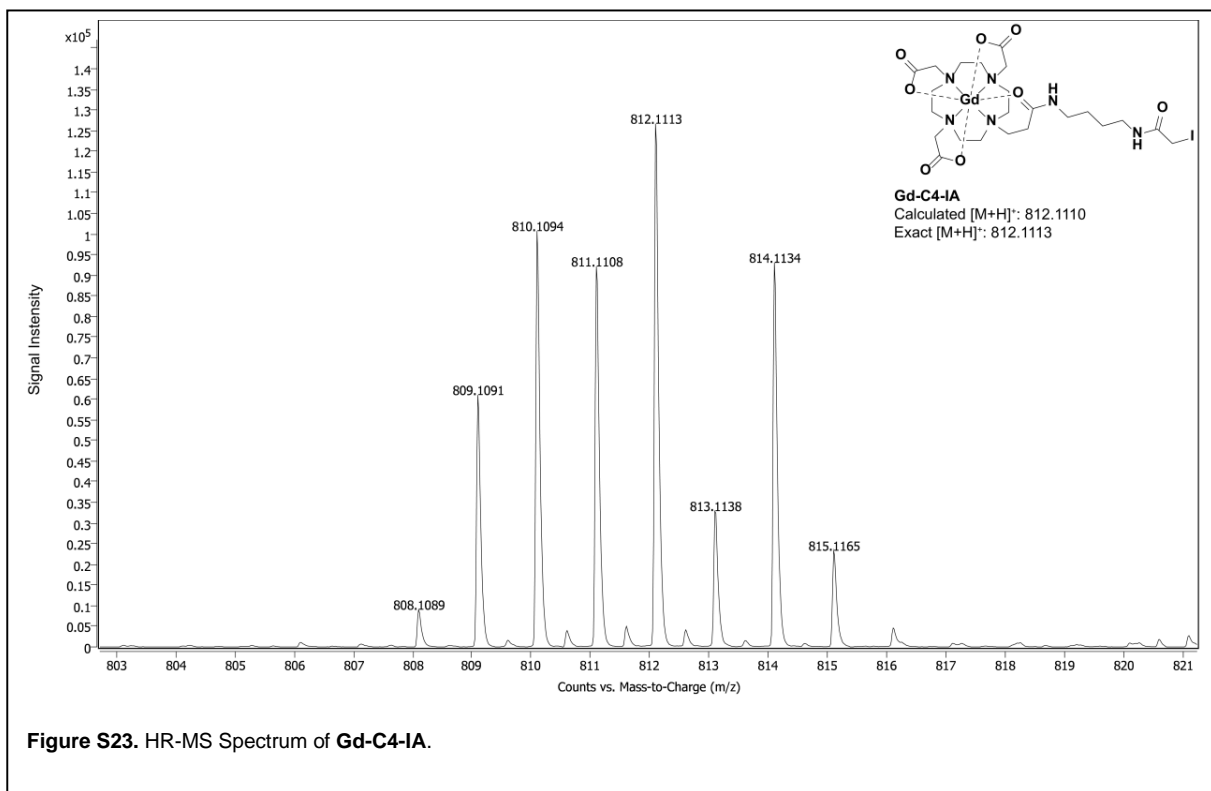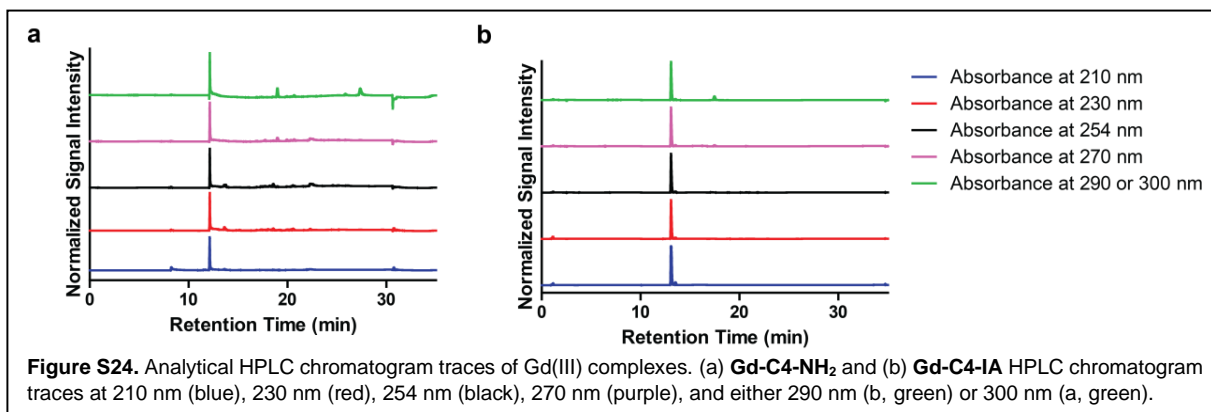
7. Preparation and Characterization of Protein Cages

Protein sequences

Molecular weights (MW), isoelectropoints (pI), and extinction coefficients at 280 nm (ε_{280}, $M^{-1}cm^{-1}$) of proteins were calculated using the SIB Bioinformatics Resource Portal tool (http://web.expasy.org/protparam/).

AaLS-13 (162 residues, MW = 17,684.01 Da, pI = 4.96, ε_{280} = 13,980 $M^{-1}cm^{-1}$)

MEIYEGKLTAEGLRFGIVASRFNHALVGRLVEGAIDCIVRHGGREEDITLVCVPGSWEIPVAAGE
LARKEDIDAVIAIGVLIEGAEPHFDYIASEVSKGLANLSLELRKPISFGDITDDELEEAIECAGTEH
GNKGWEAALSAIEMANLFKSLRLEHHHHHH

OP (192 residues, MW = 20,107.35 Da, pI = 8.67, ε_{280} = 9,970 $M^{-1}cm^{-1}$)

MSQAIGILELRSIAAGMELGDAMLKSANVDLLVSKTISRGKFLLMLGGDIGAIQQAIETGTSQAG
RLLVDSLVLANIHPSVLPAISGLNSVDKRQAVGIVETRSVAACISAADRAVKGSNVTLVRVHMAR
GIGGKCYMVVAGDVSDVALAVTVASSSAGAYGRLVYASLIPRPHEAMWRQMVEGLEHHHHHH

OP-1intC (192 residues, MW = 20,123.41 Da, pI = 8.53, ε_{280} = 9,970 $M^{-1}cm^{-1}$)

MSQAIGILELRSIAAGMELGDAMLKSANVDLLVSKTICRGKFLLMLGGDIGAIQQAIETGTSQAG
RLLVDSLVLANIHPSVLPAISGLNSVDKRQAVGIVETRSVAACISAADRAVKGSNVTLVRVHMAR
GIGGKCYMVVAGDVSDVALAVTVASSSAGAYGRLVYASLIPRPHEAMWRQMVEGLEHHHHHH

OP-2intC (192 residues, MW = 20,070.36 Da, pI = 7.78, ε_{280} = 9,970 $M^{-1}cm^{-1}$)

MSQAIGILELRSIAAGMELGDAMLKSANVDLLVSKTICRGKFLLMLGGDIGAIQQAIETGTSQAG
RLLVDSLVLANIHPSVLPAISGLNSVDKRQAVGIVETCSVAACISAADRAVKGSNVTLVRVHMAR
GIGGKCYMVVAGDVSDVALAVTVASSSAGAYGRLVYASLIPRPHEAMWRQMVEGLEHHHHHH

OP-3intC (192 residues, MW = 20,017.31 Da, pI = 7.11, ε_{280} = 9,970 $M^{-1}cm^{-1}$)

MSQAIGILELRSIAAGMELGDAMLKSANVDLLVSKTICRGKFLLMLGGDIGAIQQAIETGTSQAG
CLLVDSLVLANIHPSVLPAISGLNSVDKRQAVGIVETCSVAACISAADRAVKGSNVTLVRVHMAR
GIGGKCYMVVAGDVSDVALAVTVASSSAGAYGRLVYASLIPRPHEAMWRQMVEGLEHHHHHH

OP-1extC (192 residues, MW = 20,082.32 Da, pI = 7.84, ε_{280} = 9,970 $M^{-1}cm^{-1}$)

MSQAIGILELRSIAAGMELGDAMLKSANVDLLVSKTISRGKFLLMLGGDIGAIQQAIETGTSQAG
RLLVDSLVLANIHPSVLPAISGLNSVDCRQAVGIVETRSVAACISAADRAVKGSNVTLVRVHMAR
GIGGKCYMVVAGDVSDVALAVTVASSSAGAYGRLVYASLIPRPHEAMWRQMVEGLEHHHHHH

Cloning of OP variants

To provide specific handles for conjugation, one, two or three cysteine mutations were introduced per OP protein monomer, affording variants OP-1$_{int}$C, OP-2$_{int}$C, and OP-3$_{int}$C, respectively. The residues targeted from mutation were Ser38, Arg66 and Arg103. The variant OP-1$_{int}$C, which contains the S38C mutation, has been previously described.[4] As such, plasmid pET29b(+)_OPS38C was used as a basis for generation of the OP-2$_{int}$C (S38C, R103C), and OP-3$_{int}$C (S38C, R66C, R103C) variants. The genes for these variants were generated by "QuikChange" (Agilent) site-directed mutagenesis. The primers used for OP-2$_{int}$C were: OP_R103Cfw; GTATTGTGGAAACCTGTAGCGTGGCGGCG and OP_R103Crv; CGCCGCCACGCTACAGGTTTCCACAATAC, affording plasmid pET29b(+)_OP-2$_{int}$C, which was used for the next mutagenesis step with primers OP_R66Cfw; AGCCAGGCGGGTTGTCTGCTGGTGG and OP_R66Crv; CCACCAGCAGACAACCCGCCTGGCT. To provide a specific handle for external surface conjugation, a single cysteine mutation was introduced at residue Lys93 to generate the variant OP-1$_{ext}$C. Using the previously reported pET29b(+)_OP plasmid[5] as a starting point, primers OP_K93Cfw; GGTCTGAATAGCGTGGATTGCCGTCAGGCGGTGGGTATTG, and OP_K93Crv; CAATACCCACCGCCTGACGGCAATCCACGCTATTCAGACC were used for the QuikChange mutagenesis to afford plasmid pET29b(+)_OP. Successful molecular cloning was confirmed by Sanger sequencing (Microsynth AG, Switzerland) of the pET29b(+) plasmids used for protein expression.

Protein expression of AaLS-13 and OP cysteine mutants

AaLS-13 and OP cages were expressed in *E. coli* strain BL21-Gold (DE3) which was transformed with either pMG211-AaLS-13 or the appropriate pET29b(+)-OP. Cells were grown at 37 °C in selective LB medium until the OD_{600} reached ~0.6-0.8, at which point protein production was induced by adding IPTG to a final concentration of 0.1 mM. After culturing at 25 °C for 22 hours, cells were harvested by centrifugation at 5,000 *g* and 4 °C for 10 min. The cell pellet was stored at -20 °C until purification.

Cell lysis and Ni-NTA purification of AaLS-13

The cell pellet from a 400 mL culture was re-suspended in 20 mL lysis buffer (50 mM sodium phosphate (pH 8.0), 300 mM NaCl, 10 mM imidazole) supplemented with lysozyme (0.1 mg/mL), DNase I (5 µg/mL), RNase A (5 µg/mL), and a protease inhibitor cocktail (Sigma). The lysate was incubated for 1 hour at room temperature. After lysis by sonication (using a 50% duty cycle and 80% amplitude setting on ice for 2 min, followed by cooling on ice for 2 min, repeated 5 times) and clearance by centrifugation at 9,500 *g* and 25 °C for 25 min, the supernatants were loaded

onto 1.5 mL Ni(II)-NTA Sepharose resin (50% v/v, Qiagen) pre-equilibrated with 30 mL lysis buffer in a gravity flow column. After washing with 40 mL wash buffer (50 mM sodium phosphate (pH 8.0), 800 mM NaCl) containing 20 mM and 40 mM imidazole, AaLS-13 was eluted with 15 mL lysis buffer containing 500 mM imidazole. The buffer was exchanged to AaLS storage buffer (50 mM sodium phosphate buffer (pH 8.0), 200 mM NaCl, 5 mM EDTA) using an Amicon Ultra-15 centrifugal filter unit (30 kDa MWCO) (Merck Millipore). After the buffer was exchanged, a 5 M NaCl solution was added (10% by volume) to the concentrated AaLS-13 sample to give a final NaCl concentration of 600 mM, the mixture was incubated at room temperature for 3 days to complete cage formation. The AaLS-13 cages were then purified by size-exclusion chromatography (SEC) using a Superose 6 increase column (GE Healthcare). The purified AaLS-13 cages were stored at room temperature. The concentration of AaLS-13 was determined by absorbance at 280 nm (ε_{280} = 13,980 $M^{-1}cm^{-1}$).

Cell lysis and Ni-NTA purification of OP variants

Each cell pellet from 800 mL of culture was resuspended in 10 mL of lysis buffer (50 mM sodium phosphate buffer (pH 7.4), 1 M NaCl, 20 mM imidazole) supplemented with lysozyme (0.1 mg/mL), DNase I (5 µg/mL), RNase A (5 µg/mL), 2 mM DTT, and protease inhibitor cocktail (Sigma), and incubated at 37 °C for 1.5 h. After lysis, sonication and centrifugation (10,000 g) at 25 °C for 25 min, the supernatant was loaded onto 5 mL of Ni-NTA resin in a gravity flow column and incubated for 15 min. After multiple washes with lysis buffer containing 20 mM and 40 mM imidazole, the target protein was eluted with elution buffer (50 mM sodium phosphate buffer (pH 7.4), 300 mM NaCl, 500 mM imidazole). Typically, between 10-20 mL were collected and supplemented with 2 U/mL RNase A, 5 mM EDTA and protease inhibitor cocktail and incubated overnight at 37 °C to digest any contaminant *E. coli* RNA which was not removed during the Ni-NTA purification. The protein was then purified by SEC using a Superose 6 increase column. After this point, the storage of the protein and all experiments were carried out at room temperature unless specified otherwise. The concentration of OP-3$_{int}$C was determined by absorbance at 280 nm (ε_{280} = 9,970 $M^{-1}cm^{-1}$).

Sulfhydryl groups on protein cages

a

b

c

Figure S25. Position of the cysteine residues on AaLS-13 and OP. Cysteines residues for each of the cage variants, (a) AaLS-13 (Cys127), (b) OP-3$_{int}$C (Cys38, Cys66, and Cys103), and (c) OP-1$_{ext}$C (Cys93) are highlighted as yellow spheres, with (left) or without (right) surface representation.
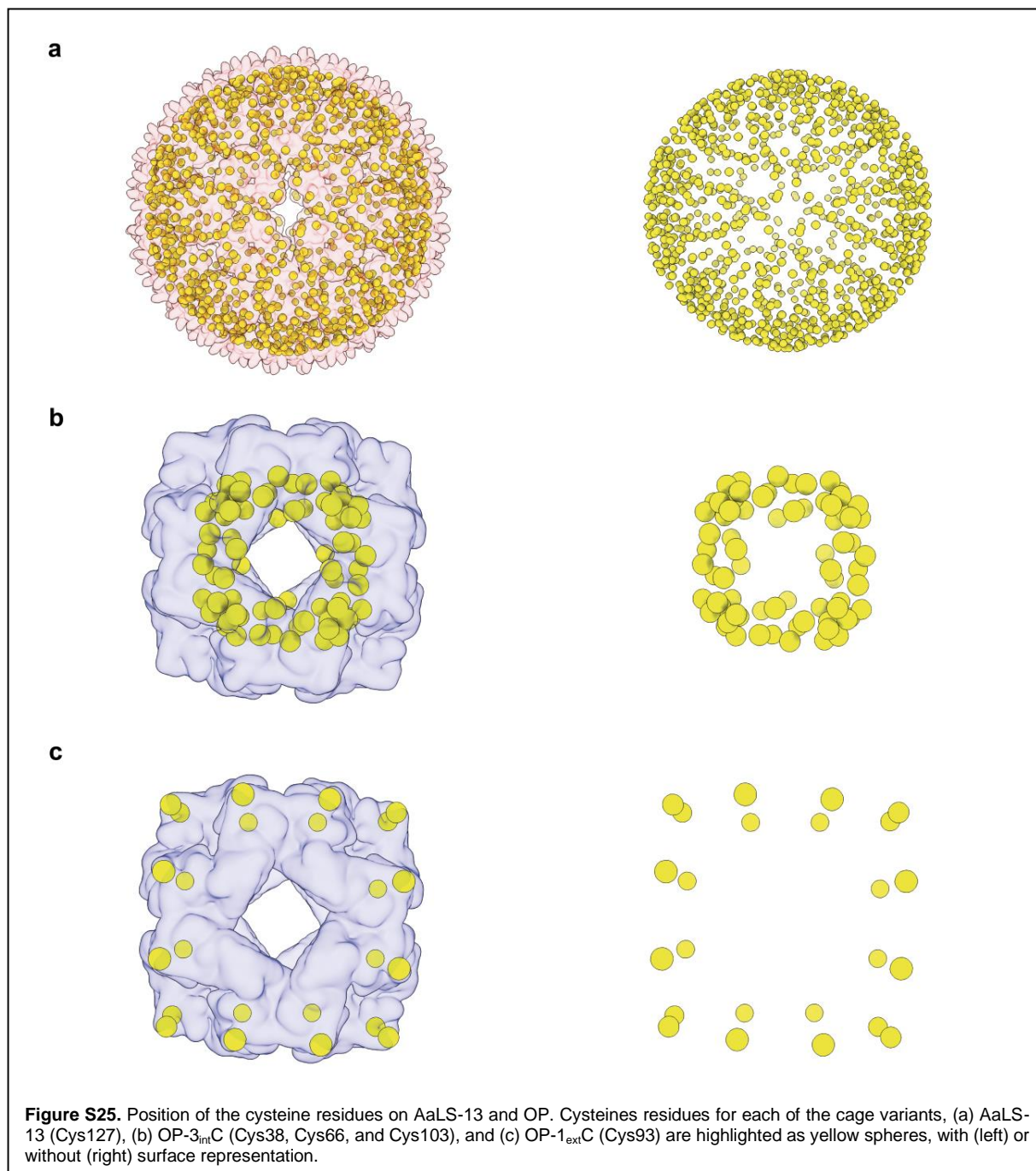
Selected residues in close proximity to reactive sites

Figure S26. Charged residues in close proximity to the reactive sites. Transparent surface of a pentamer used to construct an AaLS-13 cage (top) and a trimer used to construct OP (bottom). Monomers are shown as gray ribbons. Negatively charged residues close to Cys127 on AaLS-13 (yellow sphere) are shown as red spheres (Asp118, Asp119, Glu122, Glu123, Glu126, and Glu131), while positively charged residues are shown as blue spheres (Arg29 and Lys135). Positively and negatively charged residues near the positions targeted for cysteine mutations (Ser38, Arg66, and Arg103, represented as yellow spheres) on OP are shown as blue spheres (Arg11, Arg39, Arg130, Lys135, Arg163) and red spheres (Glu9, Asp70, and Glu101).

8. Protein Conjugation with **Gd-C4-IA**

Protein labeling with Gd-C4-IA

AaLS-13 (820 μM) was mixed with 5 equivalents of **Gd-C4-IA** per monomer in a final volume of 500 μL. OP constructs (520 μM) were mixed with 4 equivalents of **Gd-C4-IA** per reactive cysteine residue, also in a final volume of 500 μL. After 4.5 h incubation at room temperature in the dark, the samples were loaded onto a PD-10 minitrap desalting column to remove unbound Gd complexes. The samples were subjected to a further round of purification by size-exclusion chromatography using a Superose 6 increase column, pre-equilibrated in the appropriate protein storage buffer: 50 mM sodium phosphate (pH 8.0), 200 mM NaCl, 5 mM EDTA for AaLS-13 and 25 mM Tris-HCl (pH 7.6), 200 mM NaCl, 5 mM EDTA for OP cages.

Size exclusion chromatography of Gd-protein conjugates

Figure S27. Size-exclusion chromatography (SEC) of AaLS-13 and OP cages. SEC chromatograms of the crude mixtures after Ni-NTA affinity purification are shown (top blue curves) for (a) OP-1extC, (b) OP-1intC, (c) OP-2intC, (d) OP-3intC, and (e) AaLS-13. The elution traces of Gd-labeled cages are shown in orange (bottom curves).
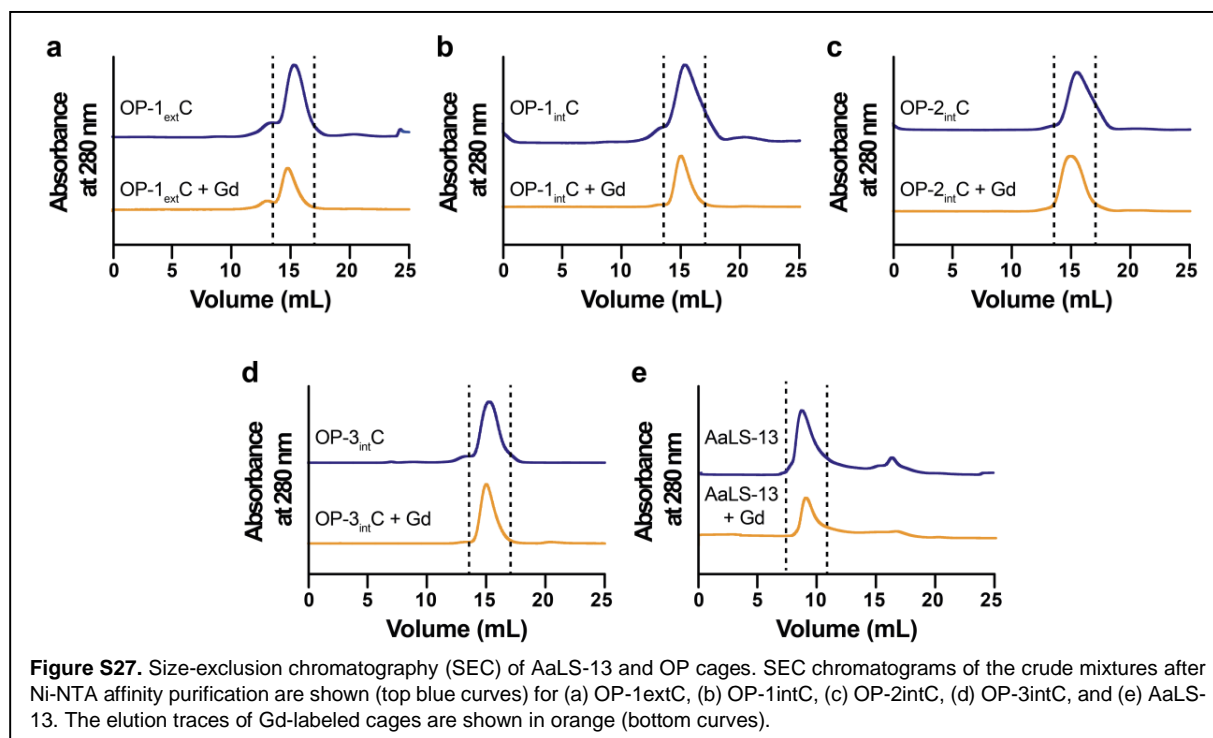
MS Spectra of Gd-Protein Conjugates

The stability of Gd(III)-labeled protein cages was evaluated by MS. AaLS-13 as studied in 50 mM sodium phosphate (pH 8.0), 200 mM NaCl, 5 mM EDTA; while the OP cages were studied in 25 mM Tris (pH 7.6), 200 mM NaCl, 5 mM EDTA. MS samples were prepared at 1 mg/mL in appropriate buffers. After the first MS, AaLS-13 and OP-3intC were left in their respective buffers at room temperature at 50 µM for 4 months and 500 µM for 7 months, respectively, and MS spectra prepared again. Ions were detected by Bruker Impact II o-TOF High Resolution Time of Flight Mass Spectrometer connected to a Bruker Elute UHPLC. Samples were injected onto a Waters Acquity UPLC Protein BEH C4 column (300 A, 1.7 µM, 2.1 mm x 50 mm) using a gradient separation flowing at 0.3 mL/min of Water with 0.1% formic acid (A) and acetonitrile with 0.1% formic acid (B) programmed as follows: 0 minutes 95%A:5%B to 10 minutes 5%A:95%B. Two column washes were performed with each injection using the same gradient percentages described above before re-equilibration was performed to eliminate any carryover. Compass HyStar 4.1 Data Acquisition software was used for instrument operation, and Compass DataAnalysis was used for data analysis and processing. All proteins were deconvoluted using MaxEntropy deconvolution.

AaLS-13 calc.	17,684.0 Da	
Gd-C4-IA	+ 683.0 Da	
	18,367.0 Da	
Gd-C4-IA	+ 683.0 Da	
	19,050.0 Da	

Figure S28. MS Traces of Gd-AaLS-13 at (a) 0 and (b) 4 months. Masses correspond to AaLS-13 monomer.

OP-3$_{int}$C calc.	20,017.0 Da
Met	− 131.2 Da
	19,886.1 Da
Gd-C4-IA	+ 683.0 Da
	20,569.1 Da
Gd-C4-IA	+ 683.0 Da
	21,252.1 Da
Gd-C4	
	21,935.1 Da

Figure S29. MS Traces of Gd-OP-3$_{int}$C at (a) 0 and (b) 7 months. Masses correspond to OP-3$_{int}$C monomer.
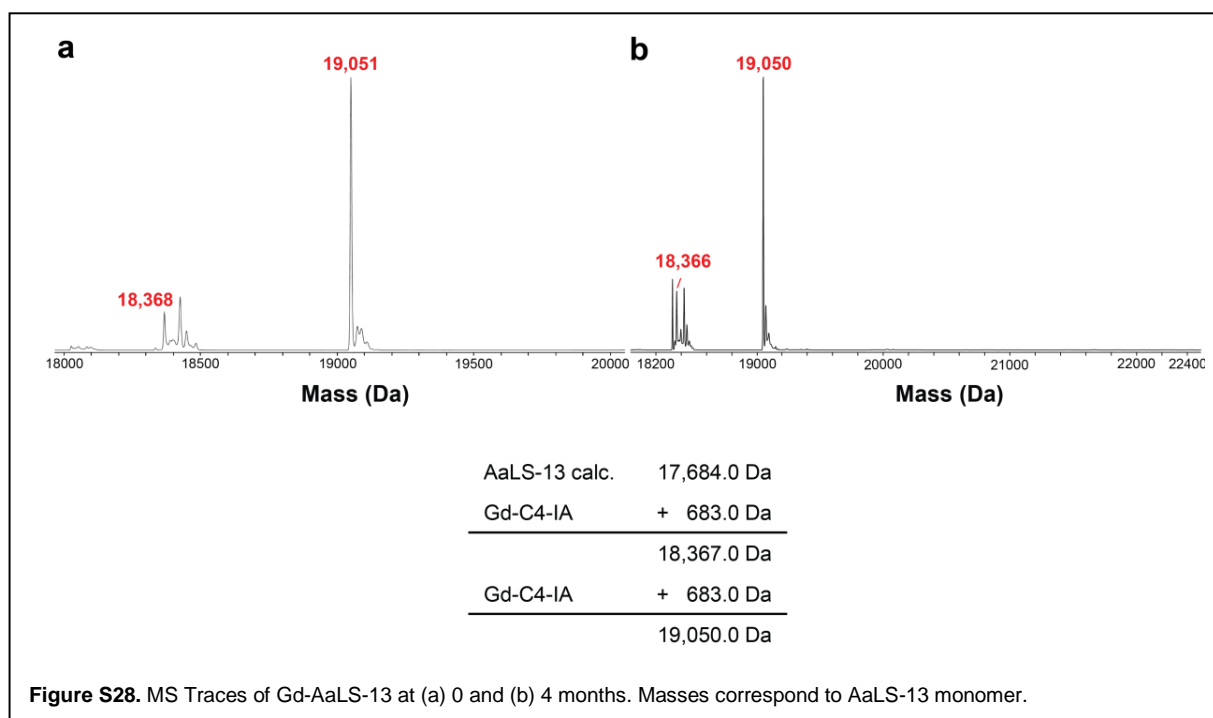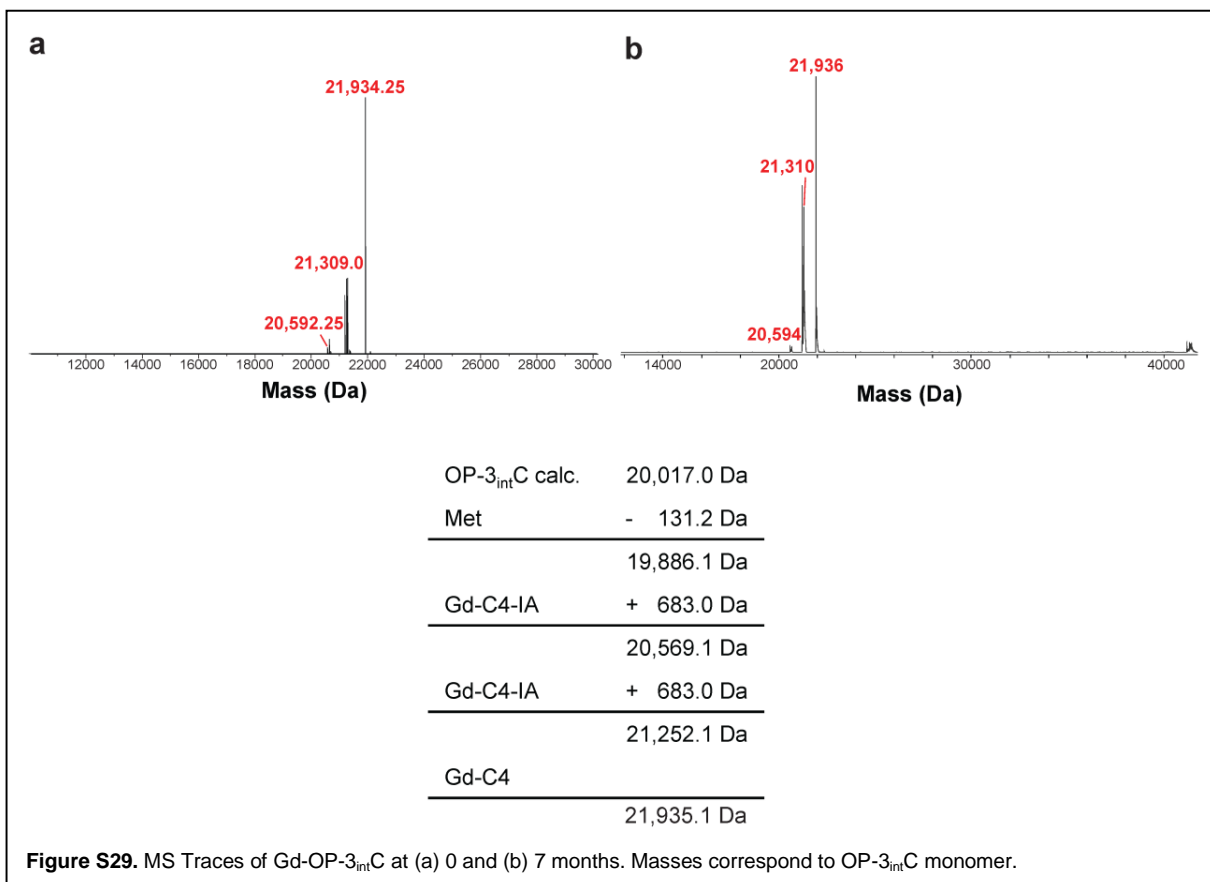
Analysis of Gd(III) content by ICP-MS

Quantification of Gd in relaxivity samples was accomplished using inductively coupled plasma mass spectrometry (ICP-MS) of acid digested samples. Specifically, 10 µL of each sample was digested in 300 µL concentrated trace nitric acid (> 69%, Thermo Fisher Scientific, Waltham, MA, USA) and placed at 65 °C for at least 3 hours to allow for complete sample digestion. Ultrapure H_2O (18.2 MΩ·cm) was then added to produce a final solution of 3.0% nitric acid in a total sample volume of 10 mL. Quantitative standards were made using a 1,000 µg/mL Gd elemental standard (Inorganic Ventures, Christiansburg, VA, USA) which were used to create a 200 ng Gd / g solvent element standard in 3.0% nitric acid (v/v) in a total sample volume of 50 mL. A second quantitative standard was made by performing a 100x dilution of the 200 ng/g Gd standard, to create a 2 ng/g element standard in 3.0% nitric acid (v/v) in a total sample volume of 50 mL. A solution of 3.0% nitric acid (v/v) was used as the calibration blank.

ICP-MS was performed on a computer-controlled (QTEGRA software) Thermo iCapQ ICP-MS (Thermo Fisher Scientific, Waltham, MA, USA) operating in STD mode and equipped with an ESI SC-2DX PrepFAST autosampler (Omaha, NE, USA). Internal standard was added inline using the prepFAST system and consisted of 1 ng/mL of a mixed element solution containing Li, Sc, Y, In, Tb, Bi (IV-ICPMS-71D from Inorganic Ventures). Online dilution was also carried out by the prepFAST system and used to generate a calibration curve consisting of 200, 100, 50, 10, 2, 1, 0.5, 0.1, 0.01, and 0.01 ppb Gd. Each sample was acquired using 1 survey run (10 sweeps) and 3 main (peak jumping) runs (40 sweeps). The isotopes selected for analysis were ^{156,157}Gd, and ^{115}In, ^{159}Tb (chosen as internal standards for data interpolation and machine stability). Instrument performance is optimized daily through autotuning followed by verification via a performance report (passing manufacturer specifications).

UV-vis spectroscopy of Gd(III) complexes

Figure S30. UV-vis spectra of Gd(III) complexes in MQ H$_2$O. Molar extinction coefficient of (a) **Gd-C4-NH$_2$** and (b) **Gd-C4-IA**.
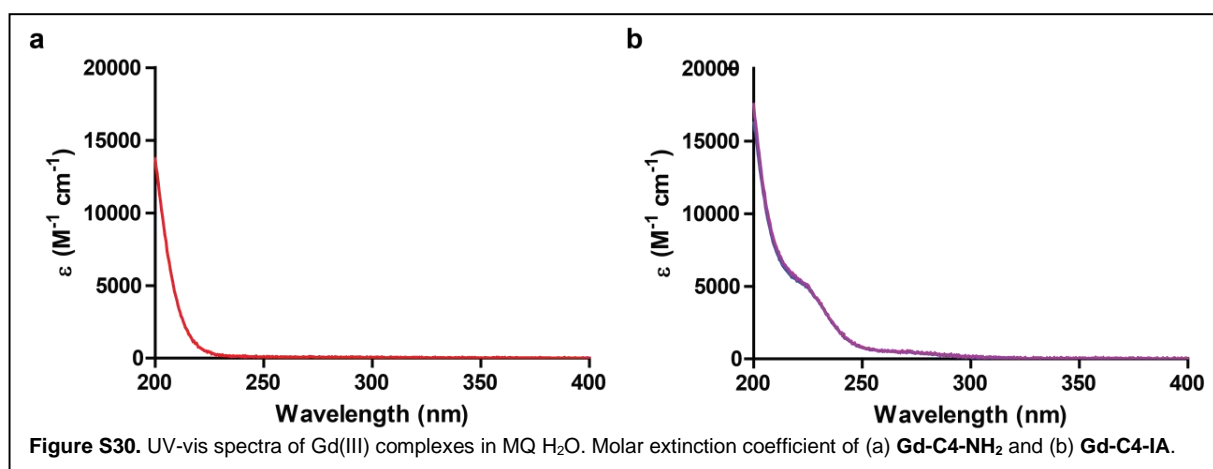
Gd-C4-NH$_2$ and **Gd-C4-IA** were dissolved in MQ H$_2$O at 1 mM and the UV-vis spectra obtained to confirm the lack of absorption at 280 nm, the wavelength used to quantify protein concentration.

The absorption at 280 nm was measured for Gd-protein conjugates in 50 mM sodium phosphate (pH 8.0), 200 mM NaCl, 5 mM EDTA for AaLS-13 and 25 mM Tris (pH 7.6), 200 mM NaCl, 5 mM EDTA for the OP variants. The molar extinction coefficient at 280 nm is 13,980 M^{-1} cm^{-1} and 10,095 M^{-1} cm^{-1} for AaLS-13 and OP variants, respectively.

Quantification of protein cage labeling with Gd(III)

Loading of Gd-C4-IA was quantified by UV-vis measurement of protein concentration and ICP measurement of Gd concentration. The loading for each sample was measured in triplicate and averaged to give the loading value.

Batch Number	[Gd] (uM)	[monomer] (uM)	[Cage] (uM)	Avg Gd/cage	Reactive Sites	Total Avg Gd/cage	Labeling Efficiency
Table S1. Gd-protein Conjugate Labeling Calculation							
Gd-AaLS-13[a]							
1	146 ± 2	365 ± 6	1.01	144 ± 2			
2	116 ± 2	310 ± 11	0.860	135 ± 3	360	149 ± 12	0.41
3	207 ± 4	450 ± 10	1.25	166 ± 3			
4	112 ± 5	266 ± 5	0.740	152 ± 7			
Gd-OP-3$_{int}$C[b]							
1	368 ± 16	286 ± 7	12.0	31 ± 1			
2	312 ± 11	334 ± 6	13.9	22.4 ± 0.8			
3	360 ± 19	301 ± 11	12.5	29 ± 2	72	33 ± 7	0.46
4	903 ± 5	502	20.9	43.2 ± 0.2			
5	738 ± 7	509 ± 4	21.2	34.8 ± 0.3			
6	300 ± 4	179 ± 4	7.48	40.1 ± 0.5			
Gd-OP-2$_{int}$C[b]							
1	335 ± 8	380	15.8	21.8 ± 0.5			
2	349 ± 3	380	15.8	22.0 ± 0.2	48	23 ± 1	0.47
3	466 ± 18	490 ± 4	20.4	22.8 ± 0.9			
4	194 ± 6	190 ± 4	7.93	24.4 ± 0.7			
Gd-OP-1$_{int}$C[b]							
1	244 ± 3	459	19.1	12.7 ± 0.1			
2	169 ± 7	402 ± 2	16.7	10.1 ± 0.4	24	11 ± 1	0.46
3	57 ± 1	133 ± 2	5.55	10.2 ± 0.2			
Gd-OP-1$_{ext}$C[b]							
1	785 ± 31	1132	47.2	16.6 ± 0.7			
2	652 ± 2	1034 ± 7	43.1	15.13 ± 0.06	24	14 ± 2	0.60
3	101 ± 3	211 ± 2	8.81	11.5 ± 0.4			

[a]Measurements in 50 mM sodium phosphate (pH 8.0), 200 mM NaCl, 5 mM EDTA

[b]Measurements in 25 mM Tris (pH 7.6), 200 mM NaCl, 5 mM EDTA

9. Relaxivity Measurements

Relaxivity measurements at 1.4 T

Gd-AaLS-13 was studied in sodium phosphate buffer (50 mM sodium phosphate (pH 8.0), 200 mM NaCl, 5 mM EDTA) while the OP proteins were studied in Tris buffer (25 mM Tris (pH 7.6), 200 mM NaCl, 5 mM EDTA). **Gd-C4-IA** was studied in sodium phosphate buffer and Tris buffer.

For each material, a stock sample was prepared at the following concentrations: 784 µM **Gd-AaLS-13**, 440 µM **Gd-OP-1$_{int}$C**, 360 µM **Gd-OP-2$_{int}$C**, 453 µM **Gd-OP-3$_{int}$C**, 1169 µM **Gd-OP-1$_{ext}$C**, and 4.5 mM (sodium phosphate buffer) or 3.5 mM (Tris buffer) **Gd-C4-IA**. The stock sample was serially diluted four times, generating 5 samples of 400 µL or 500 µL each (as material allowed), and heated to 37 °C. Relaxation times were measured on a Bruker mq60 NMR analyzer equipped with Minispec v 2.51 Rev.00/NT software (Bruker Biospin, Billerica, MA, USA) operating at 1.41 T (60 MHz) and 37 °C. Measurement of T_1 relaxation times were made using an inversion recovery pulse sequence using the following parameters: 4 scans per point, 10 data points, mono-exponential curve fitting, phase cycling, 10 ms first pulse separation, and a recycle delay and final pulse separation ≥ 5 T_1. Measurement of T_2 relaxation times were made using the Carr-Purcell-Meiboom-Gill (CPMG) pulse sequence using the following parameters: 10 scans per point, 5000 data points, mono-exponential curve fitting, phase cycling, a recycle delay of 10 sec, and τ of 1 sec. The inverse of the relaxation time ($1/T_1$ or $1/T_2$, s^{-1}) was plotted against the Gd(III) concentration (mM) determined by ICP-MS for each of the five samples. By applying a linear fit to this data, the slope generated was defined as the relaxivity (r_1, r_2) of the agent in units of mM^{-1} s^{-1}.

Relaxivity measurements at 7 T

A 60 µL aliquot of each sample from 1.4 T measurements was pipetted into flame sealed Pasteur pipettes. The pipette tips containing solution were scored, separated, and sealed with parafilm to make small capillaries containing solution. These capillaries were imaged using a Bruker PharmaScan 7 T MR imaging spectrometer (Bruker BioSpin, Billerca, MA, USA). T_1 relaxation times were measured using a rapid-acquisition rapid-echo (RARE-VTR) T_1-map pulse sequence with static TE (10 ms) and variable TR (100, 200, 400, 500, 750, 1000, 2500, 7500, 10000 ms) values. Imaging parameters were as follows: field of view, 25 x 25 mm^2; matrix size, 256 x 256; number of axial slices, 5; slice thickness, 1.0 mm; and averages, 4. T_2 relaxation times were measured using a multislice multiecho (MSME) T_2-map pulse sequence, with static TR (5000 ms) and 32 fitted echoes in 11 ms intervals (11, 22, ..., 352 ms). Imaging parameters were as follows: field of view, 25 × 25 mm2; matrix size, 256 × 256; number of axial slices, 4; slice thickness, 1.0

mm; and averages, 3. T_1 and T_2 analysis was carried out using the image sequence analysis tool in Paravision 6.0 software (Bruker) with mono-exponential curve-fitting of image intensities of selected ROIs for each axial slice. The relaxation rates ($1/T_1$ or $1/T_2$, s^{-1}) was plotted against the Gd(III) concentration (mM) determined by ICP-MS for each of the five samples. By applying a linear fit to this data, the generated was defined as the relaxivity (r_1, r_2) of the agent in units of mM^{-1} s^{-1}.

Figure S31. Longitudinal (r_1) and transverse (r_2) relaxivity measurements of Gd(III) complexes and Gd(III)-labeled protein cages. Longitudinal relaxation rates ($1/T_1$) at 3 T and 7 T. Transverse relaxation rates ($1/T_2$) at 3 T and 7 T. Relaxivity of **Gd-C4-IA** in (a) 50 mM sodium phosphate (pH = 8.0), 200 mM NaCl, 5 mM EDTA, and (b) 25 mM Tris (pH = 7.6), 200 mM NaCl, 5 mM EDTA. Relaxivity of (c) **Gd-AaLS-13** in 50 mM sodium phosphate (pH = 8.0), 200 mM NaCl, 5 mM EDTA. Relaxivity of (d) **Gd-OP-3intC**, (e) **Gd-OP-2intC**, (f) **Gd-OP-1intC**, and (g) **Gd-OP-1extC** in 25 mM Tris (pH = 7.6), 200 mM NaCl, 5 mM EDTA.

Solution phantom images at 7 T for relaxivity

Figure S32. Solution phantom images of **Gd-C4-IA** in 50 mM sodium phosphate (pH 8.0), 200 mM NaCl, 5 mM EDTA at 7 T. (a) T_1 and (b) T_2 relaxation measurements.

Figure S33. Solution phantom images of **Gd-C4-IA** in 25 mM Tris (pH 7.6), 200 mM NaCl, 5 mM EDTA at 7 T. (a) T_1 and (b) T_2 relaxation measurements.
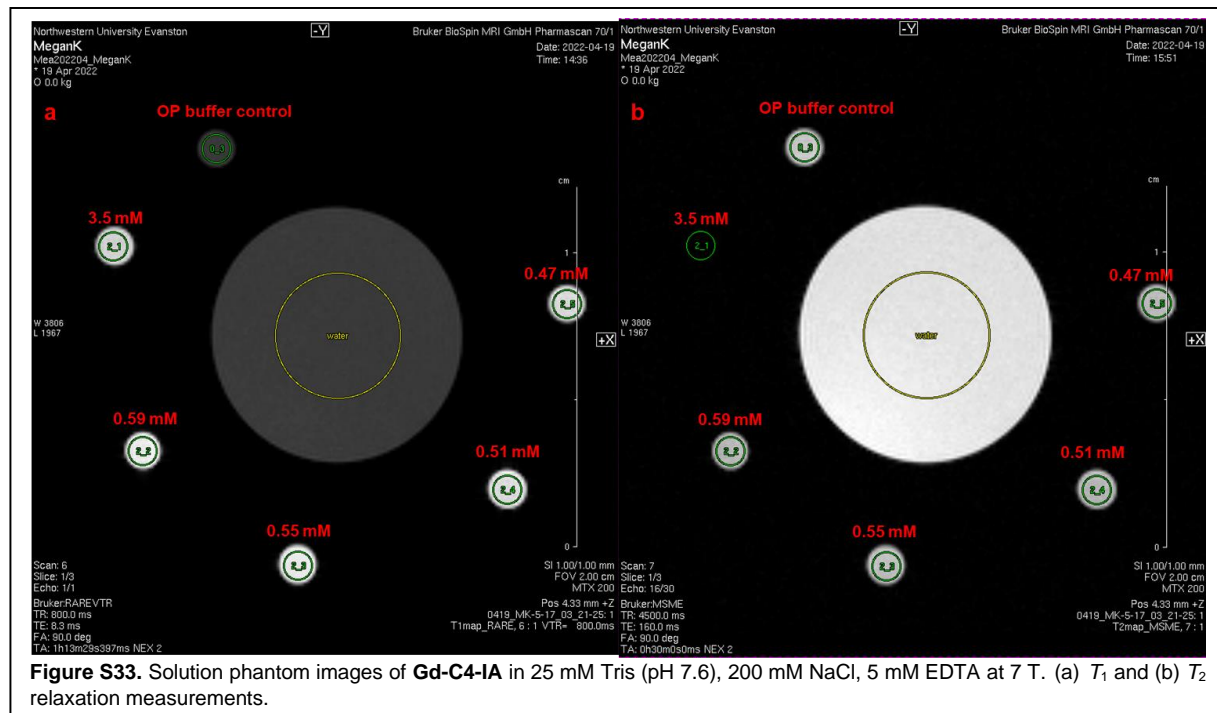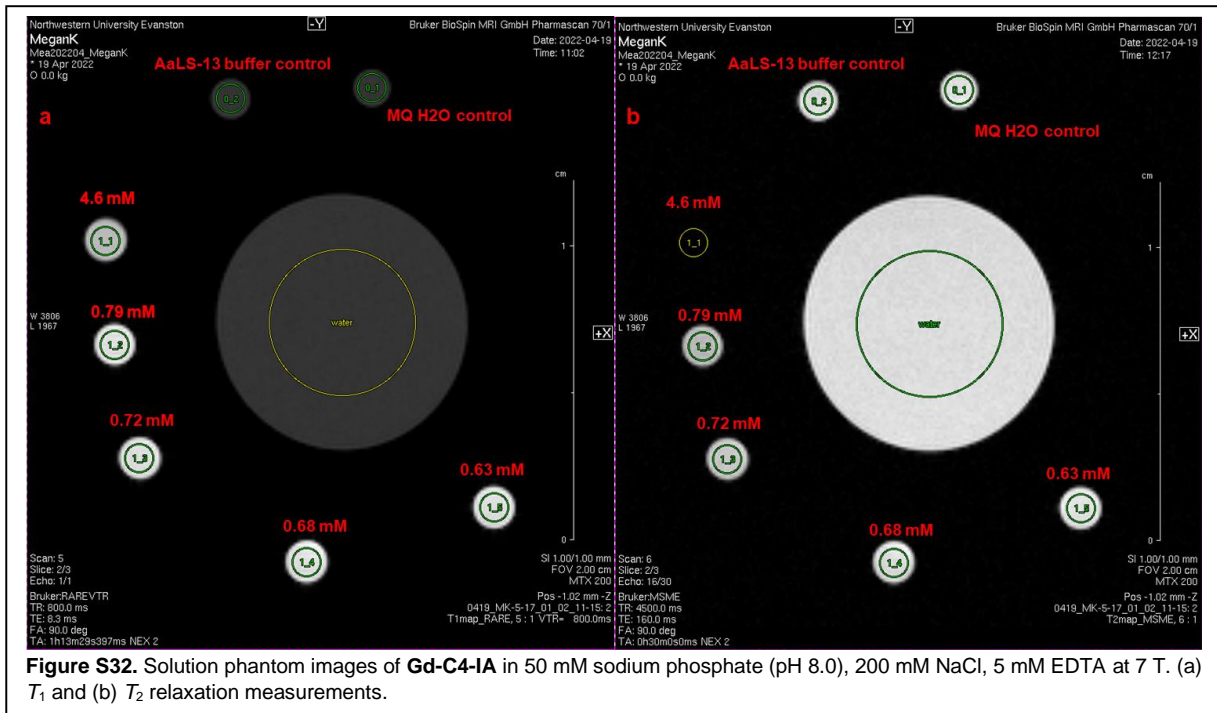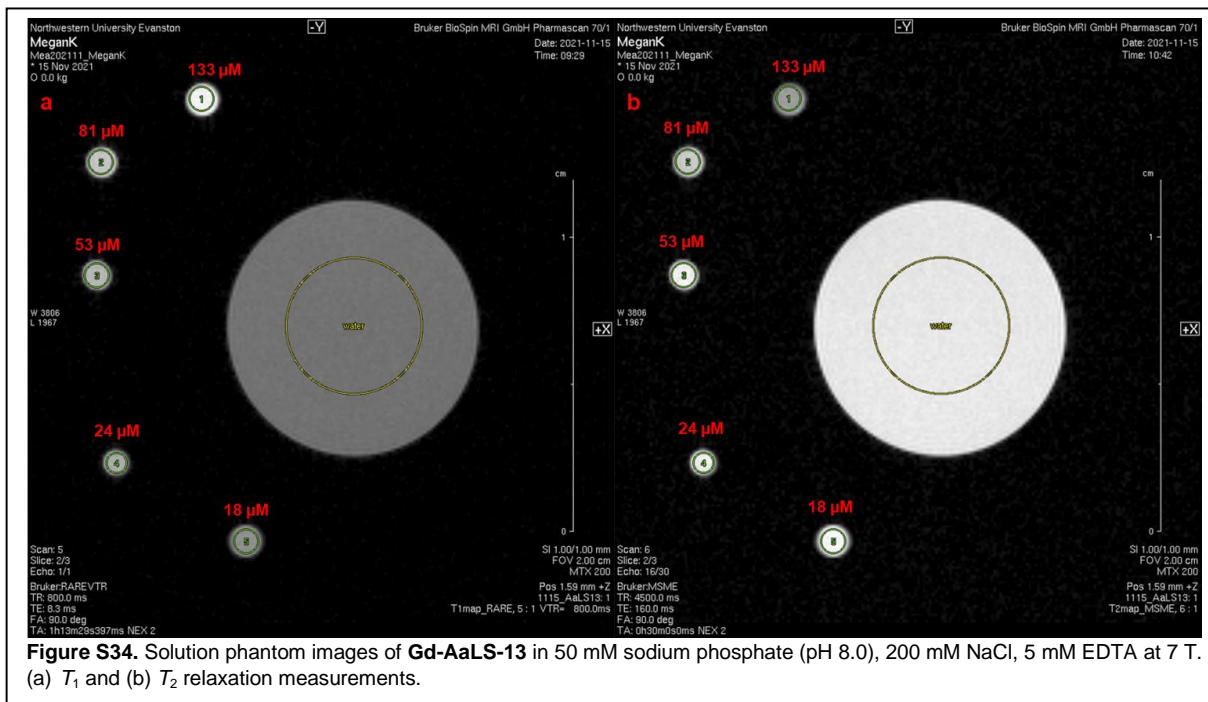
Figure S34. Solution phantom images of **Gd-AaLS-13** in 50 mM sodium phosphate (pH 8.0), 200 mM NaCl, 5 mM EDTA at 7 T. (a) T_1 and (b) T_2 relaxation measurements.
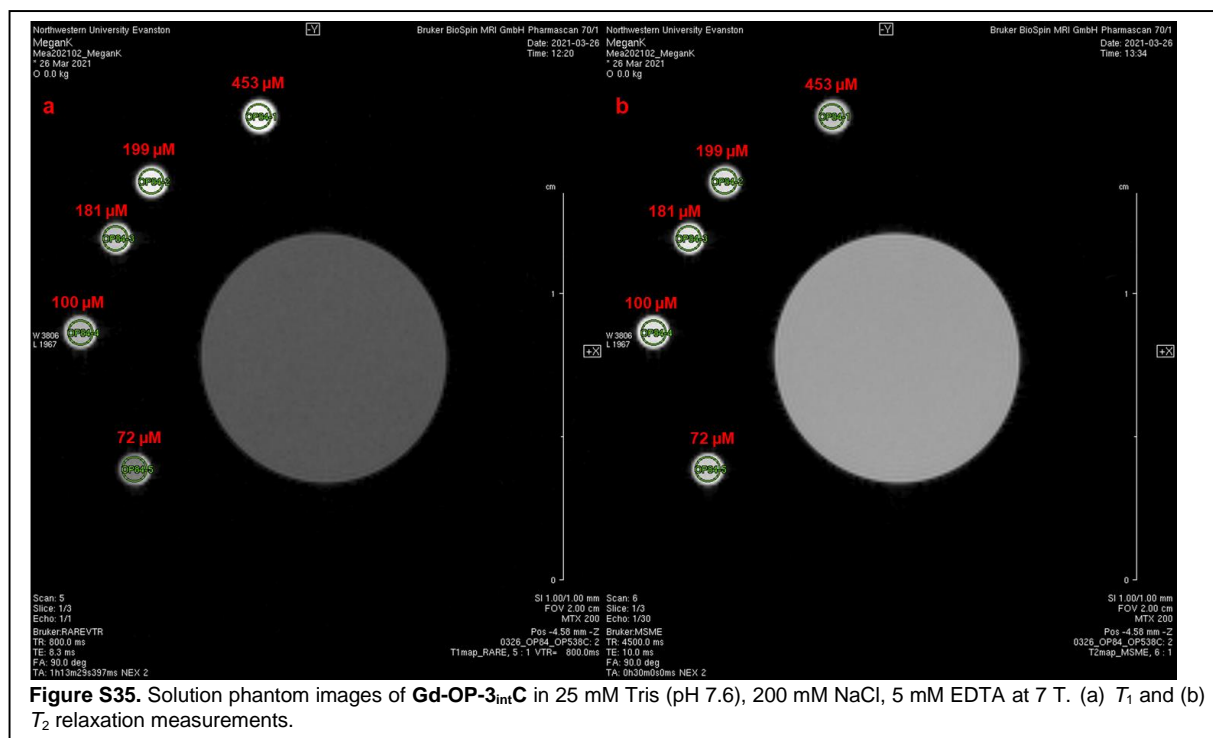
Figure S35. Solution phantom images of **Gd-OP-3$_{int}$C** in 25 mM Tris (pH 7.6), 200 mM NaCl, 5 mM EDTA at 7 T. (a) T_1 and (b) T_2 relaxation measurements.
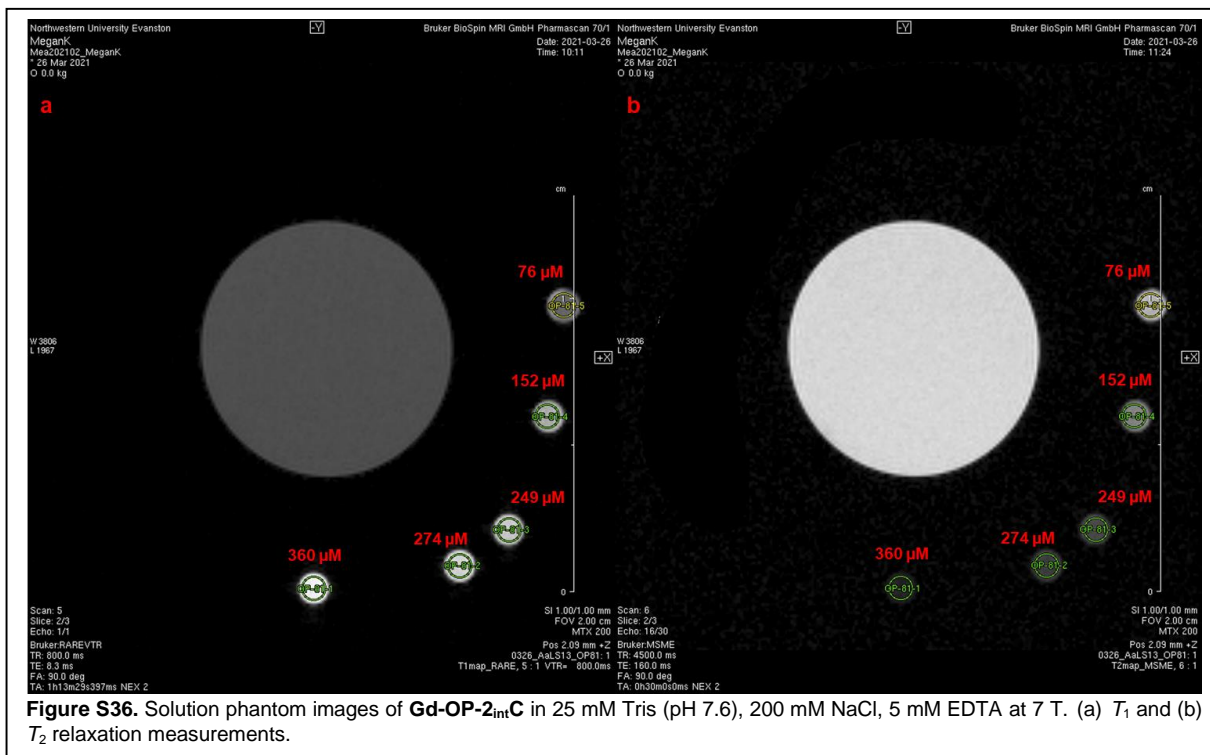
Figure S36. Solution phantom images of **Gd-OP-2$_{int}$C** in 25 mM Tris (pH 7.6), 200 mM NaCl, 5 mM EDTA at 7 T. (a) T_1 and (b) T_2 relaxation measurements.
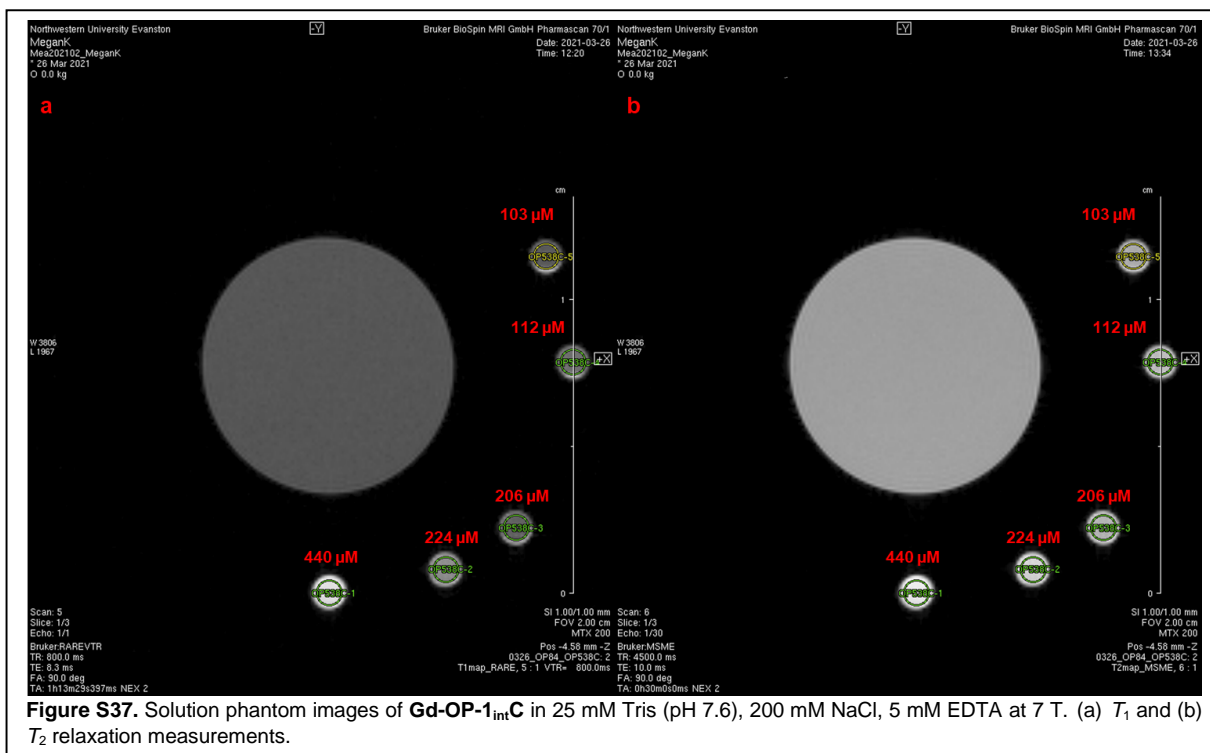
Figure S37. Solution phantom images of **Gd-OP-1$_{int}$C** in 25 mM Tris (pH 7.6), 200 mM NaCl, 5 mM EDTA at 7 T. (a) T_1 and (b) T_2 relaxation measurements.

Figure S38. Solution phantom images of **Gd-OP-1_{ext}C** in 25 mM Tris (pH 7.6), 200 mM NaCl, 5 mM EDTA at 7 T. (a) T_1 and (b) T_2 relaxation measurements.
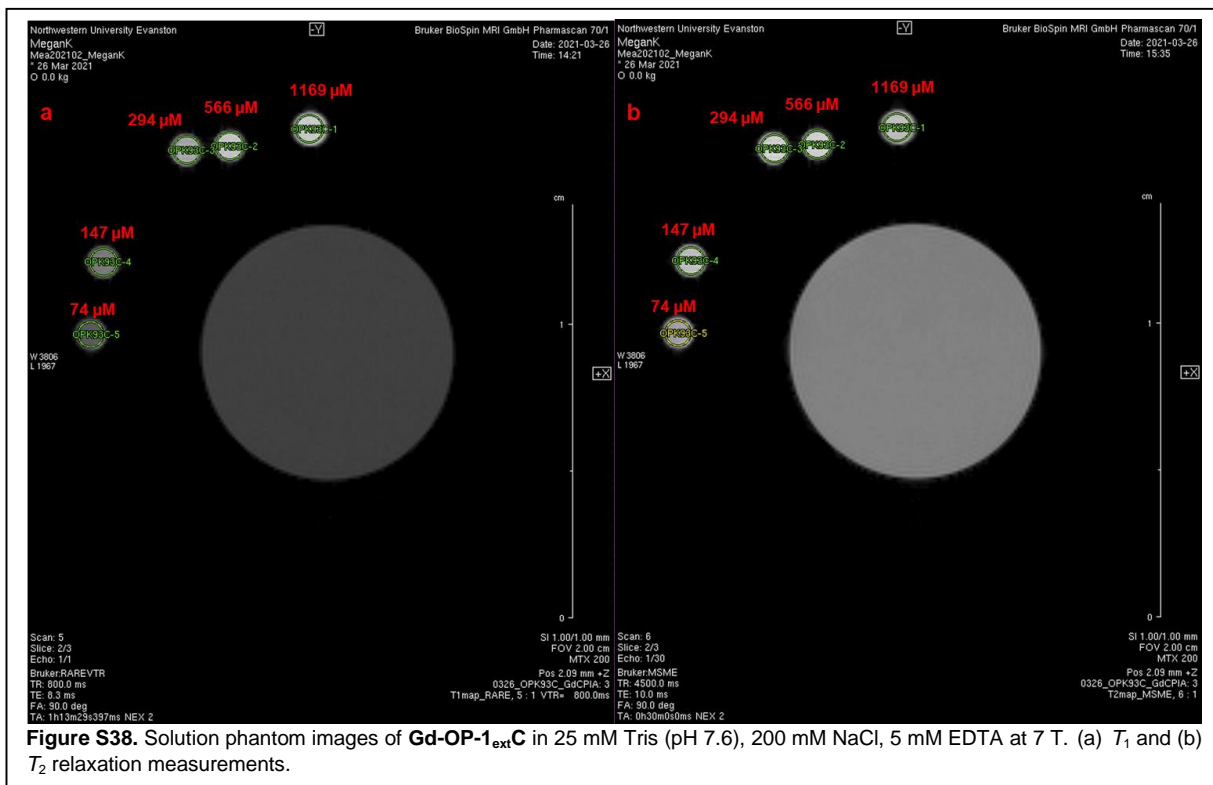
Determination of relaxivity values

The ionic relaxivity values ($r_{1,ionic}$ and $r_{2,ionic}$) obtained from the linear fit of relaxation rates versus concentration of Gd(III) at 1.4 T and 3 T using GraphPad Prism software. The reported error in ionic relaxivity measurements associated in each measurement was propagated through the linear regression analysis. Particle relaxivity values ($r_{1,particle}$ and $r_{2,particle}$) are calculated by multiplying the ionic relaxivity (per Gd relaxivity, $r_{1,ionic}$ and $r_{2,ionic}$) by the number of Gd(III) complexes per particle (**Eq. S1**).

$$r_{i,particle} = (r_{i,ionic}) \times (Avg\ Gd\ per\ cage);\ i = 1,2 \quad \textbf{Eq. S1}$$

Table S2. Transverse Relaxivity Measurements				
Sample Name	1.4 T at 37 °C		7 T at 25 °C	
	$r_{2,ionic}$ (mM^{-1} s^{-1})	$r_{2,particle}$ (mM^{-1} s^{-1})	$r_{2,ionic}$ (mM^{-1} s^{-1})	$r_{2,particle}$ (mM^{-1} s^{-1})
Gd-C4-IA[a]	4.90 ± 0.01	N/A	7.72 ± 0.05	N/A
Gd-C4-IA[b]	4.758 ± 0.008	N/A	7.58 ± 0.08	N/A
Gd-AaLS-13[a]	36.3 ± 0.9	5409	77 ± 9	11473
Gd-OP-3$_{int}$C[b]	28 ± 1	924	42 ± 7	1386
Gd-OP-2$_{int}$C[b]	34 ± 4	782	46 ± 7	1058
Gd-OP-1$_{int}$C[b]	32 ± 2	352	39 ± 6	429
Gd-OP-1$_{ext}$C[b]	17.5 ± 0.1	245	27 ± 1	378
Relaxation times (T_2) were measured with error of < 1%, while standard deviations of [Gd(III)] were determined by ICP-MS of triplicate samples.				
[a]Relaxivity data in 50 mM sodium phosphate buffer (pH 8.0), 200 mM NaCl, 5 mM EDTA.				
[b]Relaxivity data in 5 mM Tris (pH 7.6), 200 mM NaCl, 5 mM EDTA.				

10. ¹H NMRD Measurements

¹H NMRD measurements of AaLS-13 and OP

Figure S39. ¹H NMRD profiles of a water solution of unlabeled AaLS-13 and OP protein cages. Profiles of (a) **AaLS-13** and (b) **OP** at 0.222 and 0.442 mmol/dm³ monomeric protein concentrations, respectively, at 25 and 37°C. The solid and dotted lines are the best fit profiles corresponding to the parameters reported in Table S3.
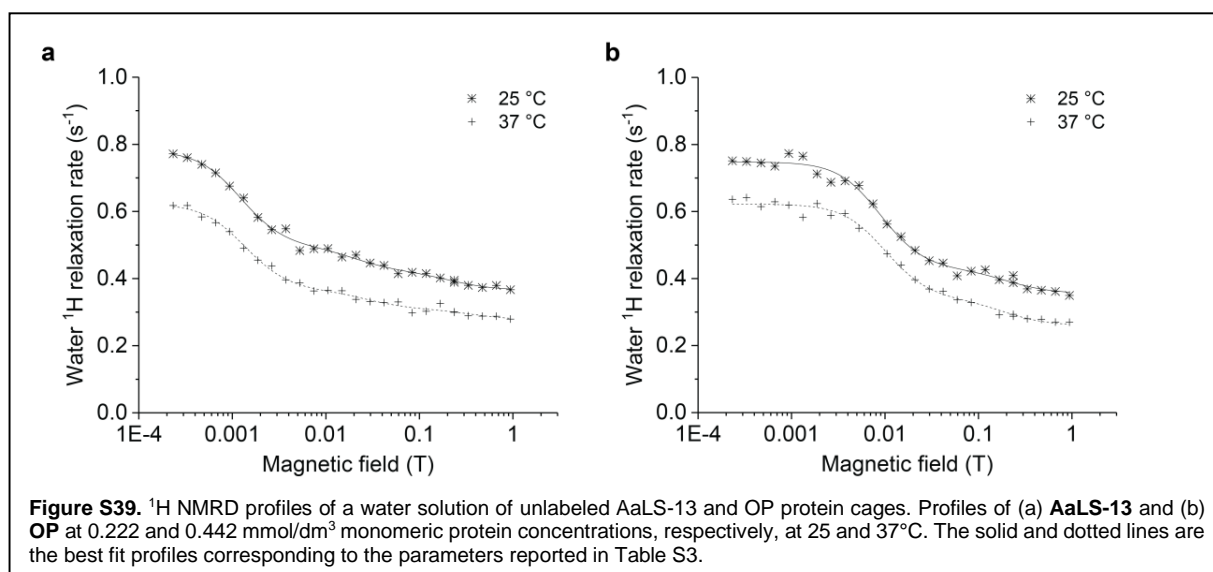
Proton Nuclear magnetic relaxation dispersion (¹H NMRD) profiles were acquired with a fast-field-cycling Stelar relaxometer. They provide the field dependence of the longitudinal relaxation rate of water protons in samples from 0.0002 to 1 T. Relaxation rates were measured with an error below 1%. Protein and Gd concentrations were 0.232 and 0.0979 mmol/dm³, respectively, in the **Gd-AaLS-13** sample; 0.357 and 0.517 mmol/dm³ in the **Gd-OP-3$_{int}$C** sample; 0.466 and 0.443 mmol/dm³ in the **Gd-OP-2$_{int}$C** sample; 0.416 and 0.175 mmol/dm³ in the **Gd-OP-1$_{int}$C** sample; 0.941 and 0.593 mmol/dm³ in the **Gd-OP-1$_{ext}$C** sample. The relaxation profiles were calculated with **Eq. S2** and the best fit parameters are reported in Table S3 – S6.

$$R_1 = \alpha + \beta \sum_{i=1}^{3} c_i \left(\frac{0.2\,\tau_i}{1 + \omega^2\tau_i^2} + \frac{0.8\,\tau_i}{1 + 4\omega^2\tau_i^2} \right) \qquad \textbf{Eq. S2}$$

Table S3. Diamagnetic Parameters from Best Fit Profiles				
Parameters	AaLS-13[a]		OP[b]	
	25 °C	37 °C	25 °C	37 °C
α (s^{-1})	0.37	0.28	0.36	0.26
β (s^{-2})	6.6×10^6		8.4×10^6	
c_1	0.03		0.16	
τ_1 (s)	1.7×10^{-6}	1.5×10^{-6}	2.3×10^{-7}	2.1×10^{-7}
c_2	0.11		0.84	
τ_2 (s)	9.9×10^{-8}	7.4×10^{-8}	1.0×10^{-8}	1.1×10^{-8}
τ_3 (s)	9.6×10^{-9}	5.6×10^{-9}	N/A	N/A
*$c_3 = 1 - c_1 - c_2$				

Parameters from best fit profiles of Gd-C4-IA

Table S4. Gd-C4-IA Parameters from Best Fit Profiles				
Parameters	Gd-C4-IA[a]		Gd-C4-IA[b]	
	25 °C	37 °C	25 °C	37 °C
r^* (Å)	3.05			
q^*	1			
Δ_t (cm^{-1})	0.030		0.030	
τ_v (s)	17×10^{-12}	13×10^{-12}	17×10^{-12}	10×10^{-12}
τ_R (s)	86×10^{-12}	51×10^{-12}	77×10^{-12}	45×10^{-12}
τ_m (s)	≈10^{-7}			
*fixed values.				
[a]NMRD measurements in 50 mM sodium phosphate (pH 8.0), 200 mM NaCl, 5 mM EDTA				
[b]NMRD measurements in 25 mM Tris (pH 7.6), 200 mM NaCl, 5 mM EDTA				
The outer-sphere parameters d (distance of closest approach) and D (diffusion coefficient) were fixed to 3.6 Å and to 2.3×10^{-9} and 3.0×10^{-9} m^2/s at 25 and 37 °C, respectively.				

Parameters from best fit profiles of Gd-labeled proteins

Table S5. Gd-AaLS-13 Parameters from Best Fit Profiles		
Parameters	Gd-AaLS-13[a]	
	25 °C	37 °C
r^* (Å)	3.05	
q^*	1	
Δ_t (cm^{-1})	0.010	
τ_v (s)	32×10^{-12}	31×10^{-12}
τ_i (s)	5.2×10^{-9}	3.5×10^{-9}
τ_m (s)	1.3×10^{-7}	1.0×10^{-7}
S^2	0.28	
τ_l (s)	5.4×10^{-10}	2.5×10^{-10}
ZFS (cm^{-1})	0.013	
θ (°)	42	

*fixed values.

[a]NMRD measurements in 50 mM sodium phosphate (pH 8.0), 200 mM NaCl, 5 mM EDTA

[b]NMRD measurements in 25 mM Tris (pH 7.6), 200 mM NaCl, 5 mM EDTA

The outer-sphere parameters d (distance of closest approach) and D (diffusion coefficient) were fixed to 3.6 Å and to 2.3×10^{-9} and 3.0×10^{-9} m^2/s at 25 and 37 °C, respectively.

Table S6. Gd-labeled OP Cages Parameters from Best Fit Profiles								
Parameters	Gd-OP-3$_{int}$C[b]		Gd-OP-2$_{int}$C[b]		Gd-OP-1$_{int}$C[b]		Gd-OP-1$_{ext}$C[b]	
	25 °C	37 °C	25 °C	37 °C	25 °C	37 °C	25 °C	37 °C
r^* (Å)	3.05		3.05		3.05		3.05	
q^*	1		1		1		1	
Δ_t (cm^{-1})	0.0095		0.0098		0.0097		0.0097	
τ_v (s)	28×10^{-12}	23×10^{-12}	32×10^{-12}	28×10^{-12}	28×10^{-12}	26×10^{-12}	28×10^{-12}	26×10^{-12}
τ_i (s)	3.7×10^{-9}	3.3×10^{-9}	4.0×10^{-9}	3.2×10^{-9}	4.3×10^{-9}	3.3×10^{-9}	1.8×10^{-9}	1.1×10^{-9}
τ_m (s)	1.0×10^{-7}	7.4×10^{-8}	1.0×10^{-7}	7.4×10^{-8}	1.0×10^{-7}	7.4×10^{-8}	1.0×10^{-7}	7.4×10^{-8}
S^2	0.46		0.39		0.36		0.36	
τ_l (s)	1.8×10^{-9}	4.8×10^{-10}	3.2×10^{-10}	9.8×10^{-11}	6.8×10^{-11}	3.8×10^{-11}	7.8×10^{-11}	2.8×10^{-11}
ZFS (cm^{-1})	0.020		0.018		0.020		0.018	
θ (°)	47		43		41		40	

*fixed values.

[a]NMRD measurements in 50 mM sodium phosphate (pH 8.0), 200 mM NaCl, 5 mM EDTA

[b]NMRD measurements in 25 mM Tris (pH 7.6), 200 mM NaCl, 5 mM EDTA

The outer-sphere parameters d (distance of closest approach) and D (diffusion coefficient) were fixed to 3.6 Å and to 2.3×10^{-9} and 3.0×10^{-9} m^2/s at 25 and 37 °C, respectively.

Best fit analysis of the profiles indicates that the parameters describing electron relaxation (Δ_t and τ_v) are very similar for all Gd-labeled protein cages. This finding shows that the electron relaxation mechanisms do not change significantly depending on the attachment point of the Gd(III) complex to the protein cages, as also suggested by the similar frequencies at which the relaxometry peaks are centered. A similar electron relaxation for **Gd-OP-3$_{int}$C**, **Gd-OP-2$_{int}$C** and **Gd-OP-1$_{int}$C** also confirms that magnetic coupling between different Gd ions is negligible even when multiple Gd-tags are attached to each protein monomer, because it would have the effect of decreasing the electron relaxation time. We note that the electron relaxation parameters are largely determined by the relaxivity at high fields (1 to 100 MHz), which is not influenced by the presence of static ZFS and can be analyzed with the SBM model, pointing out to the robustness of these parameters.

11. Solution Phantom Images

Solution phantom image sample preparation

Gd-AaLS-13 was studied in 50 mM sodium phosphate (pH 8.0), 200 mM NaCl, 5 mM EDTA, while **Gd-OP-3$_{int}$C** was studied in 25 mM Tris (pH 7.6), 200 mM NaCl, 5 mM EDTA. Samples were prepared at 90% target concentration in specific buffer and diluted with 10% FBS to achieve final concentration.

Trial 1: stock samples were prepared at 403 ± 2 µM **Gd-AaLS-13** and 351 ± 2 µM **Gd-OP-3$_{int}$C**. The stock samples were diluted to obtain 0.5 µM, 5 µM, 20 µM, and 67 µM for **Gd-AaLS-13**; and 0.5 µM, 5 µM, 20 µM, and 200 µM for **Gd-OP-3$_{int}$C**. A 1.5 mL aliquot of each solution was pipetted into a protein low-bind Eppendorf tube. Control samples were prepared at 10% FBS with the appropriate buffer. These Eppendorf tubes were imaged using a Bruker PharmaScan 7 T MR imaging spectrometer

Trial 2: stock samples were prepared at 279.1 ± 0.8 µM **Gd-AaLS-13** and 177 ± 2 µM **Gd-OP-3$_{int}$C**. These stock samples were diluted to obtain 67 µM **Gd-AaLS-13**; and 12.5 µM and 20 µM **Gd-OP-3$_{int}$C**. Control samples were prepared at 10% FBS with the appropriate buffer. A 60 µL aliquot of each sample was pipetted into flame sealed Pasteur pipettes. The pipette tips containing solution were scored, separated, and sealed with parafilm to make small capillaries containing solution. These capillaries were imaged using a Bruker PharmaScan 7 T MR imaging spectrometer and Bruker BioSpec 9.4 T MR imaging spectrometer. A 1.5 mL aliquot of each sample was pipetted into a protein low-bind Eppendorf tube. These Eppendorf tubes were imaged using a Siemens Prisma 3 T MR imaging spectrometer.

Phantom image measurements at 3 T

The Eppendorf tubes from experiment 2 were imaged using a Siemens 3 T Prisma MR imaging spectrometer. T_1 relaxation times were measured using a dual gradient echo method (StaGE) with two different flip angles. T_1 analysis was carried out using the image sequence analysis tool in Paravision 6.0 software (Bruker) to selected ROIs for each axial slice.

Phantom image measurements at 7 T

These eppendorfs were imaged using a Bruker PharmaScan 7 T MR imaging spectrometer (Bruker BioSpin, Billerca, MA, USA). T_1 relaxation times were measured using a rapid-acquisition rapid-echo (RARE-VTR) T1-map pulse sequence with static TE (10 ms) and variable TR (100, 200, 400, 500, 750, 1000, 2500, 7500, 10000 ms) values. Imaging parameters were as follows: field of view, 25 x 25 mm^2; matrix size, 256 x 256; number of axial slices, 5; slice thickness, 1.0 mm; and averages, 4. T_2 relaxation times were measured using a multislice multiecho (MSME)

T_2-map pulse sequence, with static TR (5000 ms) and 32 fitted echoes in 11 ms intervals (11, 22, ..., 352 ms). Imaging parameters were as follows: field of view, 25 × 25 mm; matrix size, 256 × 256; number of axial slices, 4; slice thickness, 1.0 mm; and averages, 3. T_1 and T_2 analysis was carried out using the image sequence analysis tool in Paravision 6.0 software (Bruker) with mono-exponential curve-fitting of image intensities of selected ROIs for each axial slice.

Phantom image measurements at 9.4 T

These eppendorfs were imaged using a Bruker PharmaScan 7 T MR imaging spectrometer (Bruker BioSpin, Billerca, MA, USA). T_1 relaxation times were measured using a rapid-acquisition rapid-echo (RARE-VTR) T_1-map pulse sequence with static TE (10 ms) and variable TR (100, 200, 400, 500, 750, 1000, 2500, 7500, 10000 ms) values. Imaging parameters were as follows: field of view, 25 x 25 mm^2; matrix size, 256 x 256; number of axial slices, 5; slice thickness, 1.0 mm; and averages, 4. T_2 relaxation times were measured using a multislice multiecho (MSME) T_2-map pulse sequence, with static TR (5000 ms) and 32 fitted echoes in 11 ms intervals (11, 22, ..., 352 ms). Imaging parameters were as follows: field of view, 25 × 25 mm; matrix size, 256 × 256; number of axial slices, 4; slice thickness, 1.0 mm; and averages, 3. T_1 and T_2 analysis was carried out using the image sequence analysis tool in Paravision 6.0 software (Bruker) with mono-exponential curve-fitting of image intensities of selected ROIs for each axial slice.

Equation for ΔR₁

Percent change in relaxation rate is determined by **Eq. S3**.[6]

$$\%\Delta R_1 = \frac{(R_{1,sample} - R_{1,control})}{R_{1,control}} \cdot 100\% \qquad \textbf{Eq. S3}$$

Phantom image data

Figure S40. Trial 1 (a) T_1 and (b) T_2 serum phantom images of **Gd-AaLS-13** and **Gd-OP-3$_{int}$C** at 7 T. Imaged samples are (1.1) 67 µM **Gd-AaLS-13** in 10% FBS in 50 mM sodium phosphate (pH 8.0), 200 mM NaCl, 5 mM EDTA; (1.2) 20 µM **Gd-AaLS-13** in 10% FBS in 50 mM sodium phosphate (pH 8.0), 200 mM NaCl, 5 mM EDTA; (1.3) 5 µM **Gd-AaLS-13** in 10% FBS in 50 mM sodium phosphate (pH 8.0), 200 mM NaCl, 5 mM EDTA; (1.4) 0.5 µM **Gd-AaLS-13** in 10% FBS in 50 mM sodium phosphate (pH 8.0), 200 mM NaCl, 5 mM EDTA; (1.5) 10% FBS in 50 mM sodium phosphate (pH 8.0), 200 mM NaCl, 5 mM EDTA; (2.1) 200 µM **Gd-OP-3$_{int}$C** in 10% FBS in 25 mM Tris (pH 7.6), 200 mM NaCl, 5 mM EDTA; (2.2) 20 µM **Gd-OP-3$_{int}$C** in 10% FBS in 25 mM Tris (pH 7.6), 200 mM NaCl, 5 mM EDTA; (2.3) 5 µM **Gd-OP-3$_{int}$C** in 10% FBS in 25 mM Tris (pH 7.6), 200 mM NaCl, 5 mM EDTA; (2.4) 0.5 µM **Gd-OP-3$_{int}$C** in 10% FBS in 25 mM Tris (pH 7.6), 200 mM NaCl, 5 mM EDTA; and (2.5) 10% FBS in 25 mM Tris (pH 7.6), 200 mM NaCl, 5 mM EDTA.

Figure S41. Trial 2 T_1 serum phantom image of **Gd-AaLS-13** and **Gd-OP-3$_{int}$C** at 3 T. Imaged samples are (1) 10% FBS in 50 mM sodium phosphate (pH 8.0), 200 mM NaCl, 5 mM EDTA; (2) 67 µM **Gd-AaLS-13** in 10% FBS in 50 mM sodium phosphate (pH 8.0), 200 mM NaCl, 5 mM EDTA; (3) 10% FBS in 25 mM Tris (pH 7.6), 200 mM NaCl, 5 mM EDTA; (4) 20 µM **Gd-OP-3$_{int}$C** in 10% FBS in 25 mM Tris (pH 7.6), 200 mM NaCl, 5 mM EDTA; and (5) 12.5 µM **Gd-OP-3$_{int}$C** in 10% FBS in 25 mM Tris (pH 7.6), 200 mM NaCl, 5 mM EDTA.

Figure S42. Trial 2 (a) T_1 and (b) T_2 serum phantom images of **Gd-AaLS-13** and **Gd-OP-3$_{int}$C** at 7 T. Imaged samples are (1) 10% FBS in 50 mM sodium phosphate (pH 8.0), 200 mM NaCl, 5 mM EDTA; (2) 67 µM **Gd-AaLS-13** in 10% FBS in 50 mM sodium phosphate (pH 8.0), 200 mM NaCl, 5 mM EDTA; (3) 10% FBS in 25 mM Tris (pH 7.6), 200 mM NaCl, 5 mM EDTA; (4) 20 µM **Gd-OP-3$_{int}$C** in 10% FBS in 25 mM Tris (pH 7.6), 200 mM NaCl, 5 mM EDTA; and (5) 12.5 µM **Gd-OP-3$_{int}$C** in 10% FBS in 25 mM Tris (pH 7.6), 200 mM NaCl, 5 mM EDTA.

Figure S43. Trial 2 (a) T_1 and (b) T_2 serum phantom images of **Gd-AaLS-13** and **Gd-OP-3$_{int}$C** at 9.4 T. Imaged samples are (1) 10% FBS in 50 mM sodium phosphate (pH 8.0), 200 mM NaCl, 5 mM EDTA; (2) 67 µM **Gd-AaLS-13** in 10% FBS in 50 mM sodium phosphate (pH 8.0), 200 mM NaCl, 5 mM EDTA; (3) 10% FBS in 25 mM Tris (pH 7.6), 200 mM NaCl, 5 mM EDTA; (4) 20 µM **Gd-OP-3$_{int}$C** in 10% FBS in 25 mM Tris (pH 7.6), 200 mM NaCl, 5 mM EDTA; and (5) 12.5 µM **Gd-OP-3$_{int}$C** in 10% FBS in 25 mM Tris (pH 7.6), 200 mM NaCl, 5 mM EDTA.

Phantom image analysis

Determined contrast enhancement as percent change in relaxation rate (**Eq. S3**) with serum phantom image data from Trial 1 and Trial 2 T_1 and T_2 measurements (**Figures S40**-**S43**).

Figure S44. Trial 1 (a, b) T_1-weighted and (c, d) T_2-weighted MR solution phantom images of (a, c) **Gd-AaLS-13** and (b, d) **Gd-OP-3intC** at 7 T. (a) and (c) Control sample of 10% FBS in 50 mM sodium phosphate (pH 8.0), 200 mM NaCl, 5 mM EDTA. **Gd-AaLS-13** samples were prepared at 0.5 µM, 5 µM, 20 µM, and 67 µM monomer. (b) and (d) Control sample of 10% FBS in 25 mM Tris (pH 7.6), 200 mM NaCl, 5 mM EDTA. **Gd-OP-3intC** samples were prepared at 0.5 µM, 5 µM, 20 µM, 200 µM monomer.
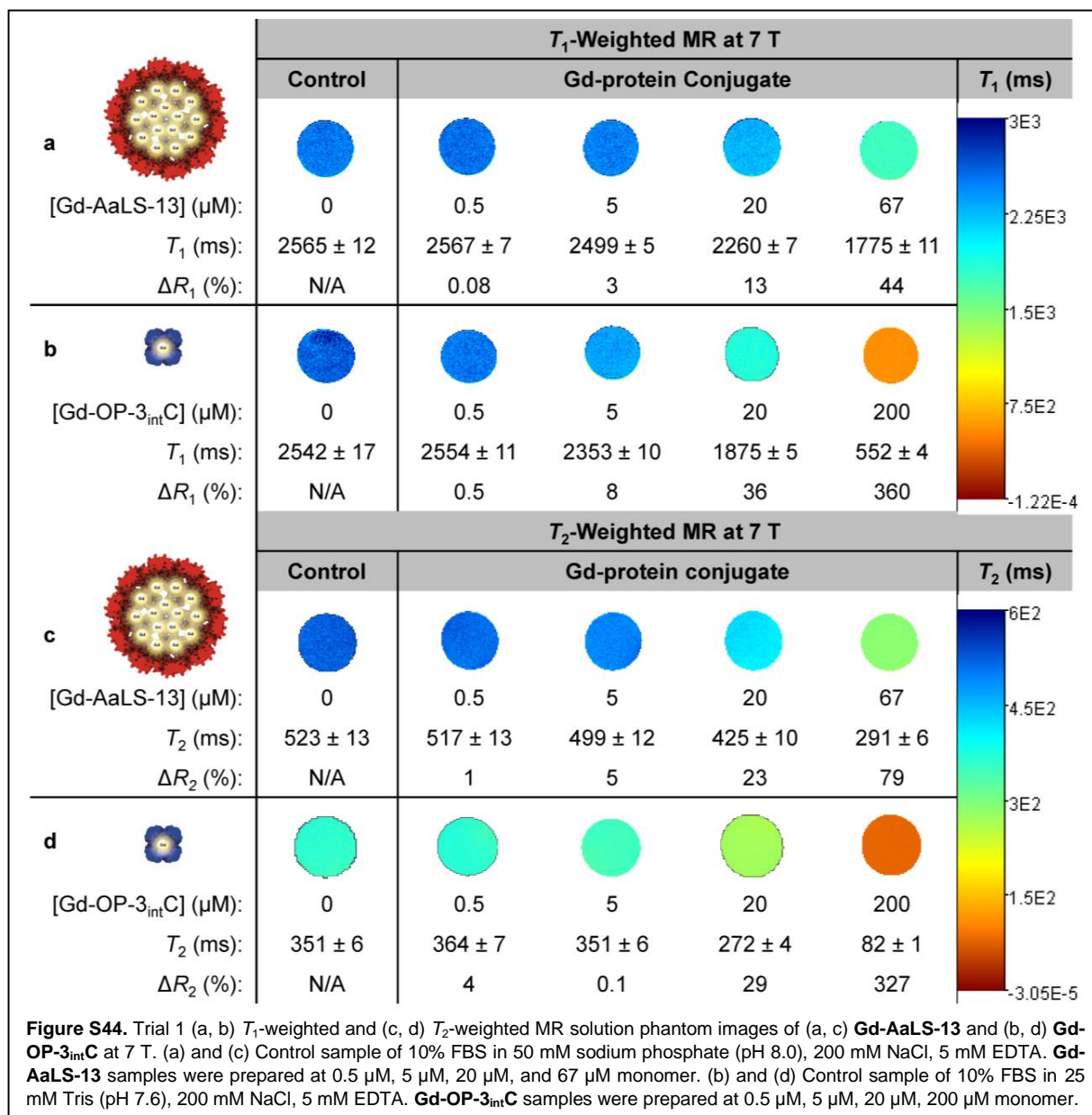
At 7 T, 20 µM **Gd-AaLS-13** with respect to monomer increased R_1 by 13%, while 67 µM **Gd-AaLS-13** with respect to monomer increased R_1 by 44%. However, 20 µM **Gd-OP-3intC** with respect to monomer increased R_1 by 36%, while 200 µM **Gd-OP-3intC** with respect to monomer increased R_1 by 360%. The T_2-weighted MR images also show relaxation enhancement at the same concentrations. 20 µM **Gd-AaLS-13** with respect to monomer increased R_2 by 23%, while

67 µM **Gd-AaLS-13** with respect to monomer increased R_2 by 79%. However, 20 µM **Gd-OP-3$_{int}$C** with respect to monomer increased R_2 by 29%, while 200 µM **Gd-OP-3$_{int}$C** with respect to monomer increased R_2 by 327%.

Figure S45 includes 12.5 µM **Gd-OP-3$_{int}$C** with respect to monomer data, which increased R_1 by 4% at 3 T, 32% at 7 T, and 27% at 9.4 T.

	Control	Gd Agent		T_1 (ms)
[Gd-OP-3$_{int}$C] (µM):	0	12.5	20	
[Gd] (µM):	0	23.2 ± 0.9	31.3 ± 0.6	
T_1 at 3 T (ms):	1358 ± 204	1409 ± 185	863 ± 65	3.5E3
% ΔR_1 at 3 T:	N/A	4%	57%	2.63E3
T_1 at 7 T (ms):	2869 ± 25	2167 ± 10	1872 ± 14	1.75E3
% ΔR_1 at 7 T:	N/A	32%	53%	8.75E2
T_1 at 9.4 T (ms):	2983 ± 20	2356 ± 30	2039 ± 8	
% ΔR_1 at 9.4 T:	N/A	27%	46%	1.22E-4

Figure S45. Trial 2 T_1-weighted MR solution phantom images of **Gd-OP-3$_{int}$C** at 3 T, 7 T, and 9.4 T. Control sample of 10% FBS in 25 mM Tris (pH 7.6), 200 mM NaCl, 5 mM EDTA; while **Gd-OP-3$_{int}$C** samples were prepared at 12.5 µM and 20 µM with respect to monomer.

12. References

(1) Chanthamath, S.; Takaki, S.; Shibatomi, K.; Iwasa, S. Highly stereoselective cyclopropanation of alpha,beta-unsaturated carbonyl compounds with methyl (diazoacetoxy)acetate catalyzed by a chiral ruthenium(II) complex. *Angew Chem Int Ed Engl* **2013**, *52* (22), 5818-5821. DOI: 10.1002/anie.201300468 From NLM Medline.

(2) Prasuhn, D. E., Jr.; Yeh, R. M.; Obenaus, A.; Manchester, M.; Finn, M. G. Viral MRI contrast agents: coordination of Gd by native virions and attachment of Gd complexes by azide-alkyne cycloaddition. *Chem Commun (Camb)* **2007**, (12), 1269-1271. DOI: 10.1039/b615084e From NLM Medline.

(3) Machitani, K.; Sakamoto, H.; Nakahara, Y.; Kimura, K. Molecular design of tetraazamacrocyclic derivatives bearing a spirobenzopyran and three carboxymethyl moeities and their metal-ion complexing behavior. *Anal. Sci* **2008**, *24*, 463-469.

(4) Edwardson, T. G. W.; Tetter, S.; Hilvert, D. Two-tier supramolecular encapsulation of small molecules in a protein cage. *Nat Commun* **2020**, *11* (1), 5410. DOI: 10.1038/s41467-020-19112-1 From NLM Medline.

(5) Edwardson, T. G. W.; Mori, T.; Hilvert, D. Rational Engineering of a Designed Protein Cage for siRNA Delivery. *J Am Chem Soc* **2018**, *140* (33), 10439-10442. DOI: 10.1021/jacs.8b06442 From NLM Medline.

(6) Elster, A. D. Field-Strength Dependence of Gadolinium Enhancement - Theory and Implications. *American Journal of Neuroradiology* **1994**, *15* (8), 1420-1423.

3.3.3   Blueberry juice

A untreated sample of *Viviverde Coop organic blueberry nectar* was analyzed, with ingredients being water, blueberry puree (40%), brown sugar and citric acid. The centrifuged sample was also examined. It was prepared by ultracentrifugation at 20000 rpm at 277 K for 15 minutes. The supernatant was subsequently used for the measurements.

High resolution measurements of the longitudinal and transverse relaxation rates, at 298 and 310 K, were performed on a *Bruker Avance III* spectrometer operating at 400 MHz ^{1}H Larmor frequency ($\sim$9.4 T), equipped with a BBO probehead. The sample was placed in a capillary tube, coaxial to the 5 mm NMR tube filled with D_2O in order to reduce radiation damping.

In order to evaluate the contribution to the relaxation rates due to the manganese(II) ions, the diamagnetic relaxation rates, as well as the contributions from other paramagnetic ions present in the blueberry juice, had to be estimated.

The slight difference in the NMRD profiles of blueberry juice and centrifuged blueberry juice is particularly relevant at lower fields, and is ascribable to the increasing of the diamagnetic relaxation rate due to the presence of aggregated material. To remove the higher molecular weight components possibly present in the juice, the sample was ultracentrifuged.

ICP-AES was employed to determine the paramagnetic ion concentrations in blueberry juice. As reported in *Table 3.5*, the paramagnetic contribution is mainly due to the concentration of manganese(II), although (unlike the one of the other ions) the concentration of iron ions is negligible and can contribute non trivially to the relaxation rates.

	Blueberry juice	**Centrifuged blueberry juice**
Mn	0.116 mM	0.109 mM
Fe	0.040 mM	0.040 mM
Cu	d. l.	0.002 mM

Table 3.5: Metals concentrations in blueberry juice and centrifuged blueberry juice estimated through ICP-AES.

Two different approaches were employed in order to evaluate it. A 0.04 mM solution of $Fe(NO_3)_3$ in citrate buffer at the same pH of blueberry juice (3.2) was prepared and its relaxation profile was recorded, and then subtracted to the centrifuged fruit juice profile (red symbols in *Figure 3.24*. For the second approach, $Fe(NO_3)_3$ was directly added to the centrifuged fruit juice to increase iron concentration by 50%, 100% and 300%, allowing for the extrapolation of the relaxation rates in the absence of iron (blue symbols in *Figure 3.24*). The two obtained profiles were subtracted to the NMRD profile of the centrifuged fruit juice, giving basically the same relaxivity profiles due to the manganese(II) ion contribution in centrifuged fruit juice (*Figure 3.24*).

The NMRD of blueberry juice and centrifuged blueberry juice, recorded at 298 and 310 K, are shown in *Figure 3.25 panel (a)*.
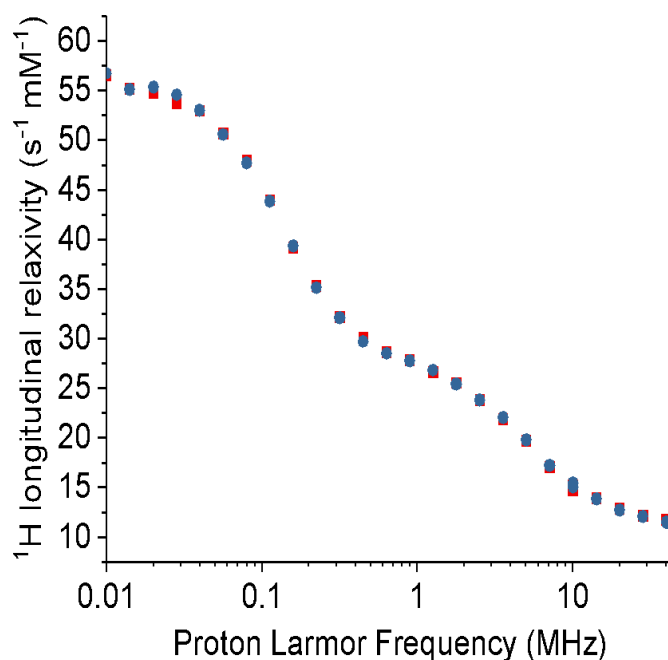
Figure 3.24: Relaxivity profiles due to manganese(II) ions contribution in centrifuged blueberry juice. Blue symbols correspond to the profile calculated extrapolating the rate values in the absence of iron, while red symbols correspond to the profile obtained subtracting the rates of $Fe(NO_3)_3$ in citrate buffer from the rates of the centrifuged juice.
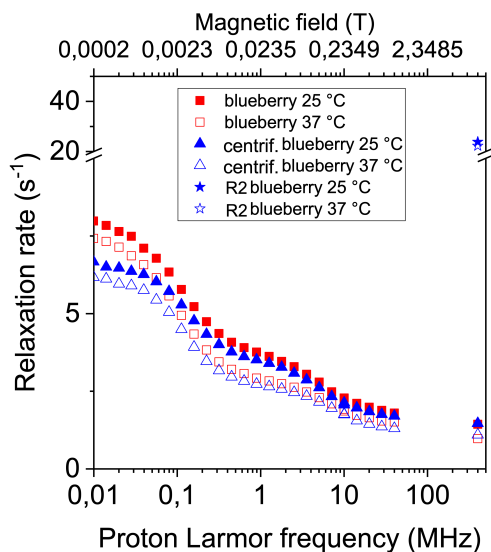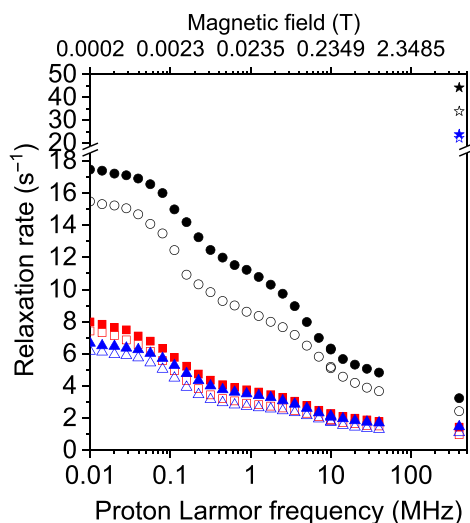
Figure 3.25: (a) NMRD profiles of blueberry juice (red squares and blue stars) and centrifuged blueberry juice (blue triangles), registered at 298 and 310 K. The value of R_2 of the centrifuged blueberry juice at 400 MHz is also included. Same symbols are used for the same sample. (b) The same NMRD profiles at 298 K of panel (a) compared to the ones of pineapple juice (black symbols) previously collected and reported in literature [24].

The relaxometric analysis of blueberry juice compared to pineapple juice [24] revealed that blueberry juice contains manganese ions with higher relaxivity, leading to greater water proton relaxation rate increases in blueberry juice when manganese(II) ions are present in the same concentration (see *Figure 4* in [25]). This means that a smaller quantity of manganese(II) in blueberry juice can achieve the same MRI image contrast as the larger quantity in pineap-

ple juice. Moreover, blueberry juice exhibited almost double the transverse relaxation rate at high magnetic fields compared to pineapple juice with the same manganese(II) concentration, indicating higher efficiency as a T2-agent. This enhanced efficiency is attributed to a larger Fermi-contact contribution to relaxation. The fitted profiles and the best fit parameters are included in the following article [25]. In summary, while manganese(II) is responsible for MRI contrast enhancements in these juices, its interaction with other juice components significantly impacts its efficiency as an MRI contrast agent.

RESEARCH ARTICLE

Not only manganese, but fruit component effects dictate the efficiency of fruit juice as an oral magnetic resonance imaging contrast agent

Giulia Licciardi[1,2] | Domenico Rizzo[1,2] | Enrico Ravera[1,2] | Marco Fragai[1,2] | Giacomo Parigi[1,2] | Claudio Luchinat[1,2]

[1]Magnetic Resonance Center (CERM), Department of Chemistry "Ugo Schiff", University of Florence, Sesto Fiorentino, Italy

[2]Consorzio Interuniversitario Risonanze Magnetiche Metallo Proteine (CIRMMP), Sesto Fiorentino, Italy

Correspondence
Marco Fragai and Giacomo Parigi, Magnetic Resonance Center (CERM), Department of Chemistry "Ugo Schiff", University of Florence, via Sacconi 6, Sesto Fiorentino, 50019, Italy.
Email: fragai@cerm.unifi.it; parigi@cerm.unifi.it

Several fruit juices are used as oral contrast agents to improve the quality of images in magnetic resonance cholangiopancreatography. They are often preferred to conventional synthetic contrast agents because of their very low cost, natural origin, intrinsic safety, and comparable image qualities. Pineapple and blueberry juices are the most employed in clinical practice due to their higher content of manganese(II) ions. The interest of pharmaceutical companies in these products is testified by the appearance in the market of fruit juice derivatives with improved contrast efficacy. Here, we investigate the origin of the contrast of blueberry juice, analyze the parameters that can effect it, and elucidate the differences with pineapple juice and manganese(II) solutions. It appears that, although manganese(II) is the paramagnetic ion responsible for the contrast, it is the interaction of manganese(II) with other juice components that modulates the efficiency of the juice as a magnetic resonance contrast agent. On these grounds, we conclude that blueberry juice concentrated to the same manganese concentration of pineapple juice would prove a more efficient contrast agent than pineapple juice.

KEYWORDS
manganese in fruit juice, nuclear magnetic relaxation dispersion, paramagnetic molecules, relaxometry

1 | INTRODUCTION

Oral contrast agents are used in magnetic resonance cholangiopancreatography because they can greatly improve the visualization of biliary tree and pancreatic ducts, the images of which are frequently degraded by the high signal due to the fluid collecting in stomach and duodenum.[1] Ideal oral contrast agents must increase the contrast homogeneously through the gastrointestinal tract, must be nontoxic and easily digestible, palatable, not stimulate peristalsis, with no side effects, and with a low cost.[2] Fruit juices that are rich in manganese ions fulfill most of the above requirements, and therefore they are conveniently used in magnetic resonance cholangiopancreatography.[3–7] Similar to gadolinium(III), whose complexes with multidentate ligands are used as intravenous MRI contrast agents, manganese(II) is a paramagnetic ion that can increase the longitudinal relaxation rate (R_1) of the neighboring water protons, thus increasing their signal intensity in T1-weighted MRI images.[3,8–10] This causes a

---

Abbreviations used: ICP-AES, inductively coupled plasma-atomic emission spectroscopy; NMRD, nuclear magnetic relaxation dispersion.

higher contrast between tissues where the paramagnetic ions are absorbed and those where they are not present. Manganese (II) is also a T2-agent because, similar to iron oxides, it can increase the transverse relaxation rate (R_2) of the neighboring water protons, thus decreasing their signal intensity in T2-weighted MRI scans. Intravenous administration of contrast agents is a routine method in neurologic and musculoskeletal T1-weighted MRI images; oral contrast agents are mostly used for gastrointestinal and hepatobiliary T2-weighted MRI images.[7] Because manganese(II) ions can largely increase both R_1 and R_2, manganese oral contrast agents can be used either as a T2-agent to suppress the signal from bowel fluid, or as a T1-agent to better delineate the gut.[11]

The most promising and clinically employed juices are pineapple and blueberry juices, due to their relatively high content of manganese (II) ions.[12] These fruit juices have been shown to be effective as oral contrast agents in magnetic resonance images. More recently, concentrated juices added with hydrogels,[13] and semiliquid preparations of concentrates from pineapple, organic agave syrup, blackcurrant, guar gum (thickening agent), and defoamers,[14,15] have been proposed to further enhance the contrast.

A field-cycling relaxometric analysis of pineapple juice was recently performed to characterize its relaxation properties in detail, with and without the addition of hydrogels.[16] The field-cycling relaxometric characterization is based on the analysis of the magnetic field dependence of water proton relaxation rates, called the nuclear magnetic relaxation dispersion (NMRD) profile.[17,18] Water ^{1}H longitudinal relaxation rates are measured with a fast-field cycling relaxometer, ranging from $\sim$ 0.0002 to 1 T.[19] Longitudinal and transverse relaxation rates can then be measured at higher magnetic fields using high-resolution NMR spectrometers. The decrease in the relaxation rates with increasing magnetic fields, called dispersion, informs on the timescales of the dynamic processes occurring in the system and causing nuclear relaxation,[18,20–22] whereas the magnitude of the rates can provide information on structural parameters, such as the number and distance of water molecules coordinated to the paramagnetic metal ions, and on the unpaired electron spin density delocalized onto the water protons.[17] The analysis of the NMRD profiles of pineapple juice permitted evaluating the contributions to relaxation arising from the modulation of different types of metal-proton interactions, and to analyze the effects of the addition of alginate, a natural food able to slow down the dynamics of the paramagnetic ions present in the juice and thus to increase the relaxation rates.

In this paper, we analyze the NMRD profiles of blueberry juice, the second most employed fruit juice in oral MRI, and compare its relaxation properties with those of pineapple juice and of a solution containing $[Mn(H_2O)_6]^{2+}$. A commercially available blueberry nectar was used to investigate the relaxation properties of a readily obtainable product, which can be both repeatable and immediately available for clinical administration.

2 | MATERIALS AND METHODS

2.1 | Sample preparation

The analyzed juice was Viviverde Coop organic blueberry nectar (fruit, 40% minimum), with ingredients of water, blueberry puree (40%), brown sugar, and citric acid. The centrifuged blueberry juice was prepared by collecting the supernatant after centrifugation of the blueberry nectar at 20,000 rpm at 4°C for 15 min.

2.2 | ^{1}H NMRD measurements

Water ^{1}H NMRD profiles were acquired with a Stelar Spinmaster FFC2000-1 T relaxometer by measuring the water proton relaxation rates as a function of the applied magnetic field (0.01–40 MHz proton Larmor frequency). The relaxation measurements, obtained from the fit of the magnetization decay/recovery curves against a monoexponential function, were affected by an error of about ±1%.

2.3 | High field NMR measurements

R_1 and R_2 at high field were measured on a Bruker Avance III spectrometer operating at 400 MHz ^{1}H Larmor frequency (9.4 T), using a 5-mm, BBO probehead. To mitigate the effect of radiation damping, the samples were placed into a capillary tube, coaxial to the 5-mm NMR tube filled with D_2O.

3 | RESULTS AND DISCUSSION

The ^{1}H NMRD profiles of the blueberry juice were collected at 25 and 37°C. The profiles, reported in Figure 1 as red symbols, show two dispersions, as is typical of solutions containing manganese(II) aqua ions.[23] Figure 1 also shows the relaxation rates measured for pineapple juice (black
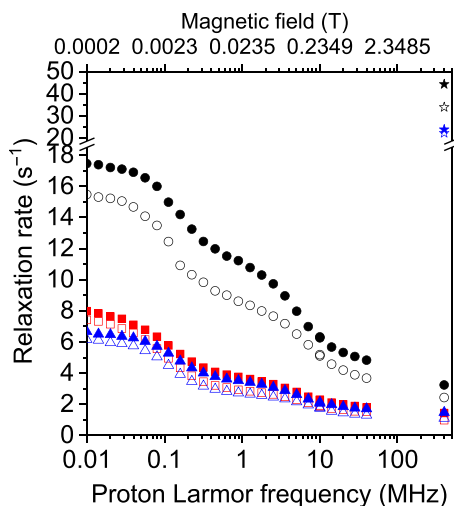
FIGURE 1 Experimental ^{1}H R_1 profiles of intact blueberry juice (red squares) and of centrifuged blueberry juice (blue triangles) at 25°C (solid symbols) and 37°C (empty symbols). The profiles previously collected for pineapple juice are also reported.[16] ^{1}H R_2 profiles at 400 MHz in the centrifuged blueberry juice (blue stars) and pineapple juice (black stars) are also shown

symbols), which was determined to contain 0.45 mmol/dm^3 of manganese.[16] The shape of the profiles for the two fruit juices are similar, as a result of the leading contribution from this paramagnetic ion. The lower relaxation rates measured for blueberry juice are in agreement with the lower manganese concentration expected in this juice,[11] where water was added to the blueberry puree, with respect to that of the pineapple juice.

The amounts of paramagnetic metals present in the juice were evaluated through ICP-AES. The concentration of manganese in the blueberry juice was measured as equal to 0.116 mmol/dm^3. The relaxation efficiency of a paramagnetic metal is expressed by its longitudinal and transverse relaxivities, r_1 and r_2, defined as the longitudinal and transverse relaxation enhancements, respectively, due to the presence of 1 mmol/dm^3 of paramagnetic metal ions in the system under investigation. Therefore, because the manganese concentration in blueberry juice is four times smaller than that in pineapple juice, whereas the relaxation rates at low fields are only about two-thirds smaller, the relaxivities of manganese in blueberry juice are expected to be significantly larger than in pineapple juice.

To evaluate the contribution to the relaxation rates from the manganese (II) ions, the diamagnetic relaxation rates, as well as the contributions from other paramagnetic ions present in the blueberry juice, should be estimated. The appearance of the juice was not that of a clear solution, but rather a fine suspension, so that the presence of some aggregated material is expected. This may largely affect the diamagnetic contribution to the observed relaxation rates, especially at low fields. The juice was thus centrifuged and the NMRD profiles of the centrifuged juice were acquired (shown in Figure 1 as blue symbols). Water ^{1}H longitudinal and transverse relaxation rates were also measured at 400 MHz. The concentration of manganese in the centrifuged blueberry juice was measured as equal to 0.109 mmol/dm^3 (very close to that of the intact juice, 0.116 mmol/dm^3). Consistently, the rates measured for the centrifuged juice are only slightly smaller than those measured for the intact juice at all frequencies larger than 0.1 MHz. However, at lower frequencies the disagreement becomes relevant. This expected disagreement increases with decreasing magnetic field, and is thus ascribable to the increasing diamagnetic relaxation rates, because of the presence of aggregated material, which yields a typical power-law dependence.

The concentration of iron in both intact and centrifuged blueberry juice was 0.040 mmol/dm^3. The concentrations of copper, nickel, and cobalt were below 0.002 mmol/dm^3. The concentration of manganese is thus substantially higher than that of the other paramagnetic metals, so that this metal ion is largely responsible for determining the relaxation profile of the juice. The concentration of iron is, however, not negligible with respect to that of manganese, and therefore this metal ion may also contribute significantly to the relaxation rates observed. The contribution from iron ions largely depends on the oxidation state of this metal and on the pH. In fact, the relaxivity of high spin iron(III) is expected to be large at very low pH (close to 0), and to decrease markedly above pH 3 as a result of the formation and precipitation of a variety of hydroxides.[24] On the other hand, the relaxivity of iron(II) is very low, even at very low pH.[17] The pH of the investigated blueberry juice was measured as 3.2. Thus, it is not easy to predict the contributions to relaxation from iron ions at this pH, and experimental information is needed.

To separate the contribution of manganese(II) species to the paramagnetic relaxivity from those of iron species, the contribution from iron ions was estimated using two different approaches. In the first approach, Fe (NO$_3$)$_3$ was dissolved at a concentration of 0.040 mmol/dm^3 in a citrate buffer solution (pH 3.2) containing 0.1 mmol/dm^3 oxalate. Citrate buffer was used because the investigated juice contains citric acid (see the Materials and Methods section), and oxalate was added because the juice was estimated to contain it in the concentration used.[25] Basically,

identical profiles were also obtained in the absence of oxalate (Figure S1). The relaxation rates have very little dependence on the magnetic field, ranging from 0.50 to 0.43 s^{-1} on passing from low fields to 1 T, at 25°C. The water proton relaxivity due to manganese(II) ions in the centrifuged blueberry juice was then calculated from the differences between the relaxation rates of the juice and those of the Fe (NO$_3$)$_3$ solution, normalized to a manganese concentration of 1 mmol/dm^3 (Figure 2). In the second approach, Fe (NO$_3$)$_3$ was added in known concentrations (0.020, 0.040, and 0.120 mmol/dm^3, corresponding to 50%, 100%, and 300% of the amount of iron concentration originally present in the juice, respectively) to the centrifuged blueberry juice, so that the relaxation rates in the absence of iron could be extrapolated (Figure S2B). Both approaches provided basically the same relaxivity profiles (Figure S2B) for manganese in the centrifuged blueberry juice.

Figure 2 shows the longitudinal and transverse relaxivity data for manganese in the centrifuged blueberry juice and in the pineapple juice, as well as the relaxivity data of the manganese(II) aqua ion at pH 3.6. As expected, the relaxivity of the blueberry juice is much higher than that of the pineapple juice. Interestingly, at intermediate fields (around 1 MHz), the relaxivity is smallest for the manganese aqua ion, and increases on passing to the pineapple juice, and then to the blueberry juice. This suggests that the reorientation correlation times should increase on passing from the aqua ion to the juices, and thus that the manganese ions partially interact with other molecules in the pineapple juice, and possibly even more in the blueberry juice; a larger relaxivity in blueberry than in pineapple juice may also be due to a higher number of water molecules coordinated to the manganese(II) ion and/or to a slightly higher fraction of manganese(II) bound to macromolecules.

The low field relaxivity is largely determined by the Fermi-contact relaxation. The low field relaxivity in the blueberry juice, similar to that of the manganese aqua ion, indicates a greater fraction of manganese aqua ions, or a larger Fermi-contact coupling constant, than that in pineapple juice (the difference in relaxivity before and after the first dispersion being, however, significantly smaller in the blueberry juice than in the manganese aqua ions). Together with a higher (low field) Fermi-contact longitudinal relaxivity, the transverse relaxivity at high field is also consistently higher in the blueberry than in the pineapple juice.

The relaxivity profiles were fitted using the Solomon–Bloembergen–Morgan model[26–29] (see the supporting information) and the best fit parameters are reported in Table 1 together with those previously obtained for the pineapple juice and the manganese aqua ion.[16] The best fit profiles are shown in Figure 2, and the different contributions to the relaxivity (inner-sphere dipole–dipole relaxation modulated by slow mobility and by fast mobility, Fermi-contact relaxation, and outer-sphere relaxation) in Figure 3. Clearly, Fermi-contact relaxation provides a very large contribution to the longitudinal relaxivity at low fields, whereas at high fields the longitudinal relaxivity is determined by dipole–dipole interactions. However, the Fermi-contact interaction represents by far the largest source for transverse relaxation at 400 MHz.

The best fit parameters indicate that, as expected from inspection of the profiles, the reorientation time increases on passing from the aqua ion to the juices (from 28 to ∼ 50 ps, at 25°C), with a minor component present only in the juices (with weight 1.4% in the blueberry juice) experiencing reorientation times of a few nanoseconds. This points to the presence of some large manganese complexes in the juices, with a molecular weight of at least 5000 Da.[30] The best fit value of hydration water molecules can result from the averaging between those in aqua ions and in other complexes. This value in blueberry juice is higher than that of in pineapple juice, possibly due to a lower concentration of polydentate ligands, which occur naturally in the juice.[31]

The higher r_1 relaxivity and, most importantly, the higher r_2 relaxivity, of blueberry than of pineapple juice suggests a higher efficiency of the former, if concentrated in such a way that the manganese ions have the same concentration than as in the pineapple juice. This assumes that by
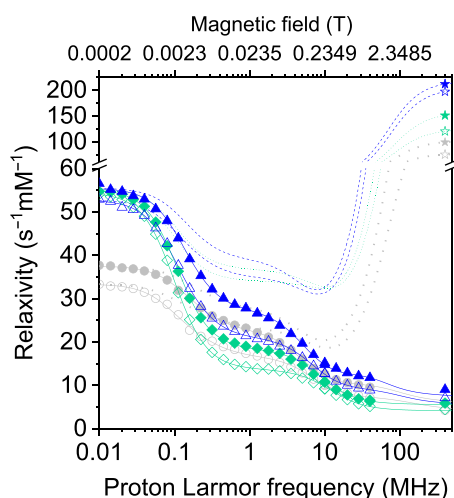
FIGURE 2 ^{1}H longitudinal relaxivity profiles (blue triangles) and transverse relaxivity at 400 MHz (blue stars) of Mn^{2+} ions in centrifuged blueberry juice at 25°C (solid symbols) and 37°C (empty symbols). The same data for pineapple juice (gray symbols) and Mn^{2+} aqua ions (green symbols) are also shown. The solid and dotted lines represent the best fit profiles of the longitudinal and transverse relaxivities, respectively

TABLE 1   Best fit parameters for the centrifuged blueberry juice, pineapple juice and the Mn^{2+} solution. The corresponding best fit profiles are shown in Figures 2 and 3

	Blueberry juice		Pineapple juice		Mn^{2+} aqua ion		
	25°C	37°C	25°C	37°C	25°C	37°C	
$r^{(*)}$	2.85						Å
q	5.2 ± 0.2		4.0 ± 0.1		6 $^{(*)}$		
$\Delta_t^{(*)}$	0.015				0.018		cm^{-1}
w	0.014 ± 0.003		0.021 ± 0.003		1		
τ_r	2800 ± 900	1600 ± 600	1700 ± 300	1000 ± 200	28 ± 1	20 ± 1	ps
τ_v	9 ± 1	8 ± 1	9 ± 1	7 ± 1	5.3 ± 0.1	4.5 ± 0.1	ps
τ_M	38 ± 2	36 ± 2	39 ± 3	29 ± 2	18 ± 1	14 ± 1	ns
τ_I	48 ± 2	36 ± 1	51 ± 2	36 ± 2	-	-	ps
A^{FC}/h	0.74 ± 0.02		0.55 ± 0.02		0.82 ± 0.01		MHz

Outer-sphere relaxation was also included with d = 3.6 Å and D = 3.0 and 3.9 × 10^{-5} cm^2/s at 25°C and 37°C, respectively.
$^{(*)}$fixed.
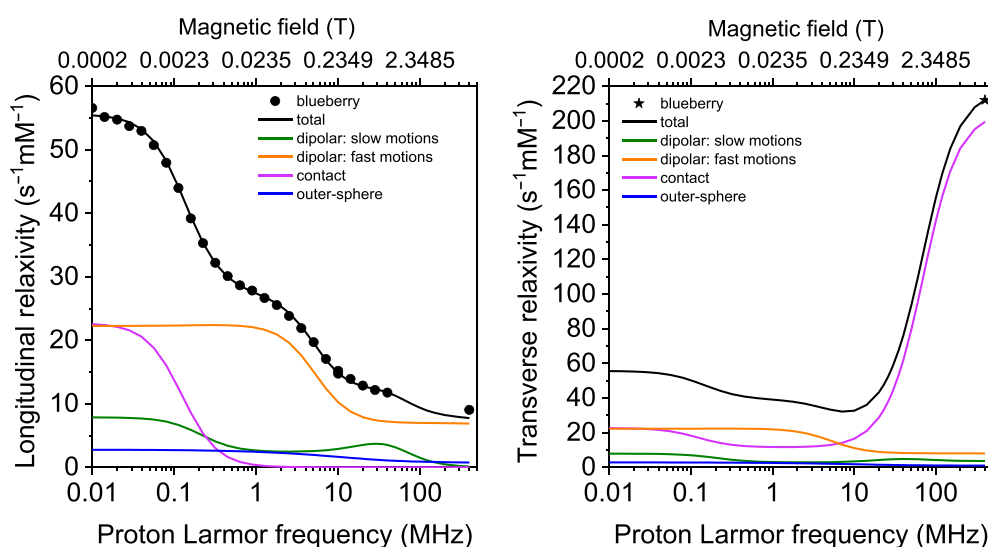
FIGURE 3 ^1H longitudinal relaxivity (left) and transverse relaxivity (right) of Mn^{2+} ions at 25°C and their dipolar, Fermi-contact, and outer-sphere contributions in the centrifuged blueberry juice

concentrating the blueberry juice there are no significant changes in the parameters upon which its relaxation properties depend (aggregation, lifetimes of water molecules coordinated to manganese(II), tumbling times, and metal ion coordination environment). To verify this higher efficiency of the concentrated blueberry juice, 10.0 mL of the juice was freeze-dried then redissolved in 2.50 mL of H_2O to achieve a manganese(II) concentration of 0.45 mmol/dm^3 (i.e. the same concentration of the pineapple juice). The acquired NMRD profiles are shown in Figure 4 as pink triangles, whereas the profiles calculated from the original blueberry juice (rescaled to account for the increased metal ions concentrations) are shown as red squares. Interestingly, there is very good agreement at the intermediate magnetic fields, whereas the longitudinal relaxation rates are smaller than expected at low magnetic fields and higher at high magnetic fields. These effects were also observed for pineapple juice upon the addition of alginate, and are ascribed to the larger viscosity of the solution resulting from juice concentration and to transient interactions of manganese(II) ions, with possible confinement in a restricted environment, in such a way as to reduce their mobility.[16] This is confirmed by the appearance of a small relaxivity peak at about 25 MHz. The increase in the tumbling time is paralleled by a reduction of Fermi-contact relaxation (due to a smaller fraction of manganese aqua ions, a smaller electron relaxation time at low fields and/or a smaller contact coupling constant), which is also causing a decrease in the observed transverse relaxation rate at 400 MHz with respect to the prediction from the intact blueberry juice data. Nevertheless, both the longitudinal and transverse relaxation rates of the concentrated blueberry juice are substantially larger than those of the pineapple juice, despite having the same Mn^{2+} concentration.
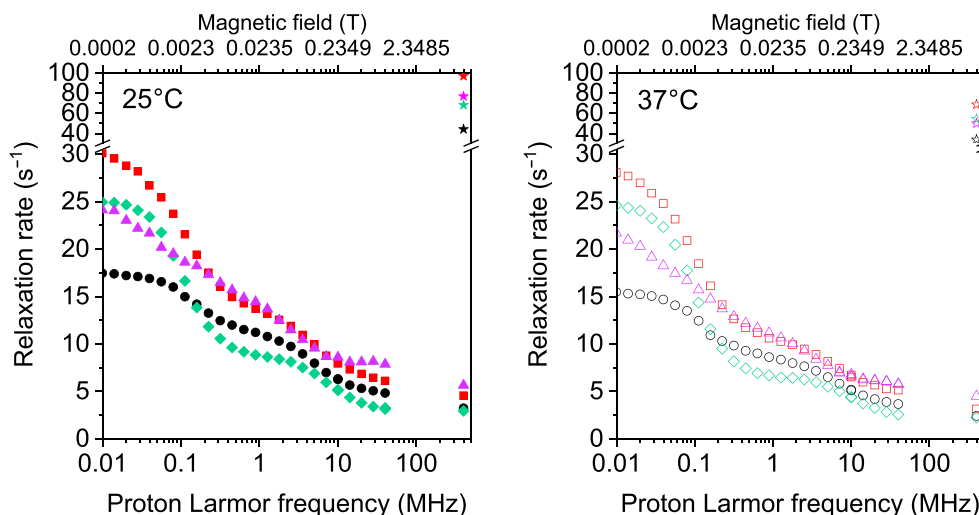
FIGURE 4   Longitudinal relaxation rates (triangles and circles) and transverse relaxation rates at 400 MHz (stars) of the blueberry juice concentrated 4.1 times (pink symbols) and of the pineapple juice (black symbols). The relaxation rates of these samples, containing Mn^{2+} with concentration 0.45 mmol/dm^3, are also compared with those of Mn^{2+} aqua ions (green symbols) and those obtained by rescaling the data collected for intact blueberry juice (red symbols) at the same Mn^{2+} concentration. Solid symbols indicate data at 25°C (left), while empty symbols indicate data at 37°C (right)

4 | CONCLUSIONS

The relaxometric analysis performed for blueberry juice indicates that the manganese ions in this juice have a higher relaxivity than those in pineapple juice. Therefore, the water proton relaxation rates in the blueberry juice are increased to a larger extent than in pineapple juice when manganese(II) ions are contained in the same concentration (Figure 4). On the other hand, this implies that a lower quantity of manganese(II) contained in blueberry juice is sufficient to achieve the same relaxation enhancement, and thus the same contrast in the MRI images, obtainable with a larger quantity of manganese(II) contained in pineapple juice.

Very importantly, the transverse relaxation rate at high fields is substantially larger (almost double) in blueberry juice than in pineapple juice when both juices contain the same concentration of manganese(II). This points to a higher efficiency as T2-agent of the concentrated blueberry juice, similar to that of Mn^{2+} aqua ions, than of pineapple juice. Analysis of the relaxivity profiles shows that this higher efficacy is determined by a larger Fermi-contact contribution to relaxation. This larger transverse relaxation rate is, however, somewhat smaller than expected without considering in the concentrated solution the presence of a larger fraction of metal ions interacting with other molecules/macromolecules contained in the juice. In conclusion, although manganese(II) is the paramagnetic ion responsible for the relaxation enhancements caused by the juices, its interaction with other molecules present in the juices can substantially affect its efficiency as an MRI contrast agent.

DATA AVAILABILITY STATEMENT

The data that support the findings of this study are available from the corresponding author upon reasonable request.

ORCID

Giacomo Parigi 🔘 https://orcid.org/0000-0002-1989-4644

REFERENCES

1. Frisch A, Walter TC, Hamm B, Denecke T. Efficacy of oral contrast agents for upper gastrointestinal signal suppression in MRCP: a systematic review of the literature. *Acta Radiol Open.* 2017;6(9):1-7.

2. Giovagnoni A, Fabbri A, Maccioni F. Oral contrast agents in MRI of the gastrointestinal tract. *Abdom Imaging.* 2002;27(4):367-375.

3. Wahsner J, Gale EM, Rodríguez-Rodríguez A, Caravan P. Chemistry of MRI contrast agents: current challenges and new frontiers. *Chem Rev.* 2019; 119(2):957-1057.

4. Karantanas AH, Papanikolaou N, Kalef-Ezra J, Challa A, Gourtsoyiannis N. Blueberry juice used per os in upper abdominal MR imaging: composition and initial clinical data. *Eur Radiol.* 2000;10(6):909-913.

5. Riordan RD, Khonsari M, Jeffries J, Maskell GF, Cook PG. Pineapple juice as a negative oral contrast agent in magnetic resonance cholangiopancreatography: a preliminary evaluation. *Br J Radiol.* 2004;77(924):991-999.

6. Hiraishi K, Narabayashi I, Fujita O, et al. Blueberry juice: preliminary evaluation as an oral contrast agent in gastrointestinal MR imaging. *Radiology.* 1995;194(1):119-123.

7. Zarrini M, Seilanian Toosi F, Davachi B, Nekooei S. Natural oral contrast agents for gastrointestinal magnetic resonance imaging. *Rev Clin Med.* 2015; 2(4):200-204.

8. Uzal-Varela R, Rodríguez-Rodríguez A, Martínez-Calvo M, et al. Mn2+ complexes containing sulfonamide groups with PH-responsive relaxivity. *Inorg Chem.* 2020;59(19):14306-14317.

9. Terreno E, Castelli DD, Viale A, Aime S. Challenges for molecular magnetic resonance imaging. *Chem Rev.* 2010;110(5):3019-3042.

10. Li H, Parigi G, Luchinat C, Meade TJ. Bimodal fluorescence-magnetic resonance contrast agent for apoptosis imaging. *J Am Chem Soc.* 2019;141(15): 6224-6233.

11. Arthurs OJ, Graves MJ, Edwards AD, Joubert I, Set PA, Lomas DJ. Interactive neonatal gastrointestinal magnetic resonance imaging using fruit juice as an oral contrast media. *BMC Med Imaging.* 2014;14(1):1-8.

12. Renzulli M, Biselli M, Fabbri E, et al. What is the best fruit juice to use as a negative oral contrast agent in magnetic resonance cholangio-pancreatography? *Clin Radiol.* 2019;74(3):220-227.

13. Faletti R, Gatti M, Di Chio A, et al. Concentrated pineapple juice for visualisation of the oesophagus during magnetic resonance angiography before atrial fibrillation radiofrequency catheter ablation. *Eur Radiol Exp.* 2018;2(1):1-6.

14. Kulinna-Cosentini C, Arnoldner MA, Schima W, et al. Performance of a new natural oral contrast agent (LumiVision®) in dynamic MR swallowing. *Eur Radiol.* 2021;1-8.

15. Frisch A, Walter TC, Grieser C, Geisel D, Hamm B, Denecke T. Performance survey on a new standardized formula for oral signal suppression in MRCP. *Eur J Radiol Open.* 2018;5:1-5.

16. Rizzo D, Ravera E, Fragai M, Parigi G, Luchinat C. Origin of the MRI contrast in natural and hydrogel formulation of pineapple juice. *Bioinorg Chem Appl.* 2021;2021:1-12.

17. Bertini I, Luchinat C, Parigi G, Ravera E. *NMR of paramagnetic molecules: Applications to Metallobiomolecules and Models.* 2017;1-508.

18. Parigi G, Ravera E, Fragai M, Luchinat C. Unveiling protein dynamics in solution with field-cycling NMR relaxometry. *Prog Nucl Magn Reson Spectrosc.* 2021;124–125:85-98.

19. Ferrante G, Sykora S. Technical aspects of fast field cycling. *Adv Inorg Chem.* 2005;57:405-470.

20. Bertini I, Luchinat C, Parigi G. 1H NMRD profiles of paramagnetic complexes and metalloproteins. *Adv Inorg Chem.* 2005;57:105-172.

21. Ravera E, Takis PG, Fragai M, Parigi G, Luchinat C. NMR spectroscopy and metal ions in life sciences: NMR spectroscopy and metal ions in life sciences. *Eur J Inorg Chem.* 2018;2018(44):4752-4770.

22. Fragai M, Ravera E, Tedoldi F, Luchinat C, Parigi G. Relaxivity of Gd-based MRI contrast agents in crosslinked hyaluronic acid as a model for tissues. *Chem Phys Chem.* 2019;20(17):2204-2209.

23. Esteban-Gómez D, Cassino C, Botta M, Platas-Iglesias C. ^{17}O and ^{1}H relaxometric and DFT study of hyperfine coupling constants in $[Mn(H_2O)_6]^{2+}$. *RSC Adv.* 2014;4(14):7094-7103.

24. Bertini I, Capozzi F, Luchinat C, Xia Z. Nuclear and electron relaxation of Fe (OH2)63+. *J Phys Chem.* 1993;97:1134-1137.

25. Nguyễn HVH, Savage GP. Oxalate content of New Zealand grown and imported fruits. *J Food Compos Anal.* 2013;31(2):180-184.

26. Bloembergen N, Morgan L. O. proton relaxation times in paramagnetic solutions. Effects of electron spin relaxation. *J Chem Phys.* 1961;34:842-850.

27. Solomon I. Relaxation processes in a system of two spins. *Phys Rev.* 1955;99(2):559-565.

28. Bloembergen N. Proton relaxation times in paramagnetic solutions. *J Chem Phys.* 1957;27:572-573.

29. Parigi G, Ravera E, Luchinat C. Magnetic susceptibility and paramagnetism-based NMR. *Prog Nucl Magn Reson Spectrosc.* 2019;114–115:211-236.

30. Bertini I, Fragai M, Luchinat C, Parigi G. 1H NMRD profiles of diamagnetic proteins: a model-free analysis. *Magn Reson Chem.* 2000;38:543-550.

31. Wojcieszek J, Kwiatkowski P, Ruzik L. Speciation analysis and bioaccessibility evaluation of trace elements in Goji berries (Lycium Barbarum, L.). *J Chromatogr A.* 2017;1492:70-78.

SUPPORTING INFORMATION

Additional supporting information may be found in the online version of the article at the publisher's website.

Theoretical model used for the fit of the relaxivity data

The relaxivity profiles were fitted using the Solomon-Bloembergen-Morgan model[1–4], considering the contributions from Fermi-contact and dipole-dipole relaxation, and the presence of two components, with weights w and $(1-w)$, with a fast (τ_l) and a slow (τ_r) reorientation correlation times, respectively:

$$r_i = \frac{q\left[\text{Mn}^{2+}\right]}{55.5}\left(R_{iM}^{-1} + \tau_M\right)^{-1} + R_{i\text{out}} \qquad (1)$$

$$R_{1M} = \frac{2S(S+1)}{3}\left(\frac{A^{FC}}{\hbar}\right)^2\left[\frac{\tau_{FC}}{1+\omega_S^2\tau_{FC}^2}\right] + \frac{2}{15}\left(\frac{\mu_0}{4\pi}\frac{\gamma_I g_{\text{iso}}\mu_B}{r^3}\right)^2 S(S+1)\left\{w\left[\frac{7\tau_c}{1+\omega_s^2\tau_c^2}+\frac{3\tau_c}{1+\omega_I^2\tau_c^2}\right] + (1-w)\left[\frac{7\tau_f}{1+\omega_s^2\tau_f^2}+\frac{3\tau_f}{1+\omega_I^2\tau_f^2}\right]\right\}$$

$$(2)$$

$$R_{2M} = \frac{S(S+1)}{3}\left(\frac{A^{FC}}{\hbar}\right)^2\left[\tau_{c1}^{FC} + \frac{\tau_{c2}^{FC}}{1+\omega_S^2\left(\tau_{c2}^{FC}\right)^2}\right] +$$

$$\frac{1}{15}\left(\frac{\mu_0}{4\pi}\frac{\gamma_I g_{\text{iso}}\mu_B}{r^3}\right)^2 S(S+1)\left\{w\left[4\tau_c + \frac{13\tau_c}{1+\omega_s^2\tau_c^2}+\frac{3\tau_c}{1+\omega_I^2\tau_c^2}\right] + (1-w)\left[4\tau_f + \frac{13\tau_f}{1+\omega_s^2\tau_f^2}+\frac{3\tau_f}{1+\omega_I^2\tau_f^2}\right]\right\}$$

$$(3)$$

where $i = 1$ or 2, q is the number of water molecules coordinated to the manganese ion, τ_M is their lifetimes, $\dfrac{A^{FC}}{h}$ is the Fermi-contact coupling constant, r the distance between metal ion and coordinated protons, S the electron spin quantum number (5/2 in the case of Mn^{2+}), τ_{FC} the correlation time for the Fermi-contact interaction

$$\tau_{FC}^{-1} = \tau_e^{-1} + \tau_M^{-1} \qquad (4)$$

1

τ_c and τ_f are the correlation times for the dipole-dipole interaction

$$\tau_c^{-1} = \tau_r^{-1} + \tau_e^{-1} + \tau_M^{-1} \qquad (5)$$

$$\tau_f^{-1} = \tau_l^{-1} + \tau_e^{-1} + \tau_M^{-1} \qquad (6)$$

and τ_e is the electron relaxation time,

$$\tau_e^{-1} = \frac{2\Delta_t^2}{50}\left[4S(S+1) - 3\right]\left[\frac{\tau_v}{1 + \omega_S^2\tau_v^2} + \frac{4\tau_v}{1 + 4\omega_S^2\tau_v^2}\right] \qquad (7)$$

described in the pseudorotation model by the parameters Δ_t and τ_v, which correspond to the transient zero-field splitting and to the correlation time for electron relaxation, respectively. $R_{i\text{out}}$ (in Eq. 1) indicate the paramagnetic relaxation enhancements due to the dipole-dipole interaction between the manganese ion and the water molecules freely diffusing around. This contribution has been described using the Freed model[5] and standard parameters. Other symbols have their usual meaning[6].

A fit of the longitudinal relaxivity profiles of the blueberry juice was first tried using a single reorientation correlation time ($w = 1$). After checking that the best fit profiles thus obtained were unsatisfactory, the fit was performed by allowing w to be smaller than 1; the best fit parameters are reported in Table 1 together with those previously obtained for the pineapple juice and the manganese aqua ion[7]. In the fit, the distance r of the protons in the q fast exchanging water molecules coordinated to the manganese ion was fixed to 2.85 Å, and Δ_t was fixed to the value obtained from the fit of the relaxivity of pineapple juice with addition of alginate[7], to

remove the strong covariance of this parameter with τ_v, and facilitate the comparison of the obtained parameters.

The number of hydration water molecules (5.2 ± 0.2) in the blueberry juice is somewhat smaller than 6, but significantly larger than in the pineapple juice. Also the constant of Fermi-contact interaction is somewhat smaller than for the manganese aqua ion, but significantly larger than in pineapple juice, likely because water coordination is less hampered by interactions between the metal and other molecules/macromolecules contained in the juice. This significantly larger constant of the Fermi-contact interaction, causing a high low-field longitudinal relaxivity, is also responsible of a transverse relaxivity at 400 MHz much larger for the blueberry juice than for the pineapple juice.

Figure S1. NMRD profiles of Fe(NO$_3$)$_3$ at a concentration of 0.040 mmol/dm^3 in a citrate buffer

solution (pH 3.2) without (blue symbols) and with (black symbols) oxalate (0.1 mmol/dm^3).
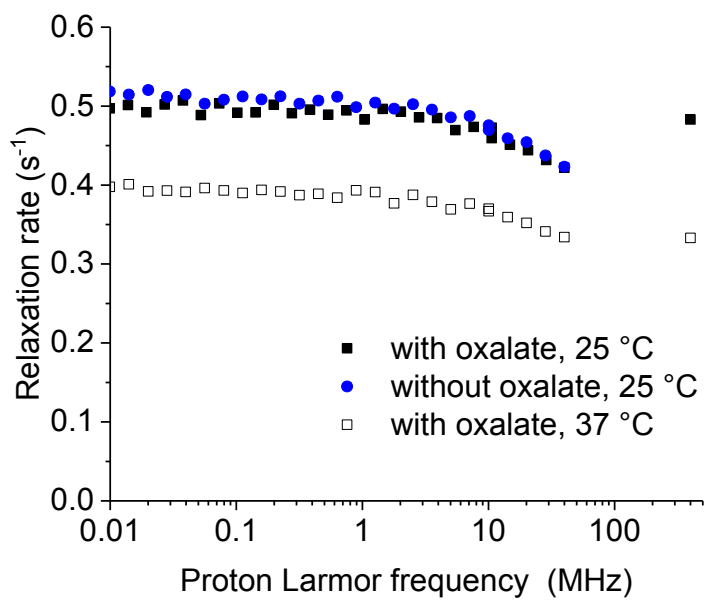
Figure S2. (A) Relaxation rates of centrifuged blueberry juice with addition of 0.020, 0.040 and 0.120 mmol/dm³ Fe(NO₃)₃ (corresponding to 50%, 100% and 300% of the iron originally present in the juice), at 25 °C. The relaxation rates in the absence of iron could be extrapolated from a linear ft. The different lines correspond to the fits obtained for the data collected at the different proton Larmor frequencies. (B) ^1H longitudinal relaxivity of manganese(II) ions in the centrifuged blueberry juice, calculated from extrapolation of the rates in the absence of iron (blue symbols), and by subtracting the rates of Fe(NO₃)₃ reported in Fig. S1 (red symbols).
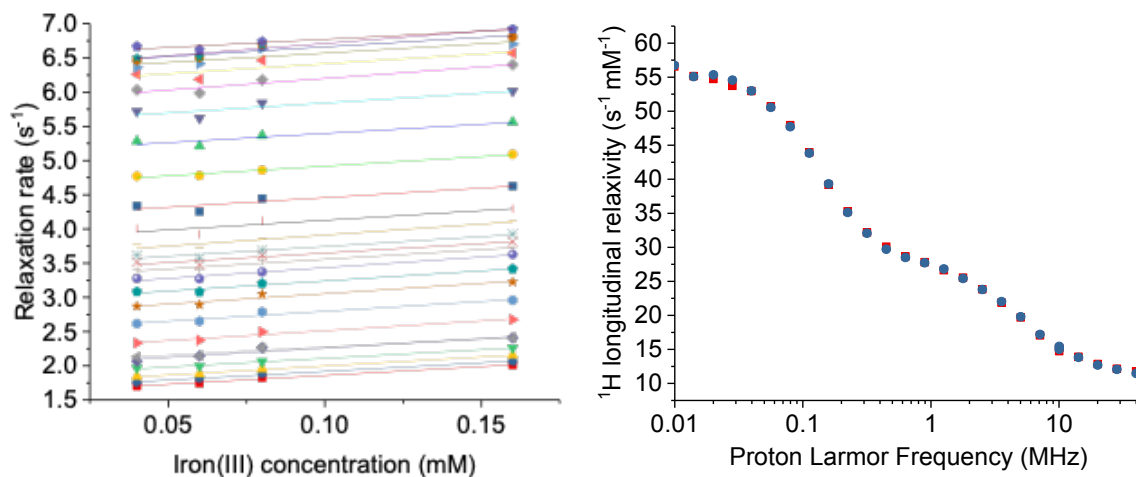
(1) Bloembergen, N.; Morgan, L. O. Proton Relaxation Times in Paramagnetic Solutions. Effects of Electron Spin Relaxation. *J.Chem.Phys.* **1961**, *34*, 842–850.

(2) Solomon, I. Relaxation Processes in a System of Two Spins. *Phys. Rev.* **1955**, *99* (2), 559–565. https://doi.org/10.1103/PhysRev.99.559.

(3) Bloembergen, N. Proton Relaxation Times in Paramagnetic Solutions. *J.Chem.Phys.* **1957**, *27*, 572–573.

(4) Parigi, G.; Ravera, E.; Luchinat, C. Magnetic Susceptibility and Paramagnetism-Based NMR. *Prog. Nucl. Magn. Reson. Spectrosc.* **2019**, *114–115*, 211–236. https://doi.org/10.1016/j.pnmrs.2019.06.003.

(5) Freed, J. H. Dynamic Effects of Pair Correlation Functions on Spin Relaxation by Translational Diffusion in Liquids. II. Finite Jumps and Independent T1 Processes. *J.Chem.Phys.* **1978**, *68*, 4034–4037.

(6) Bertini, I.; Luchinat, C.; Parigi, G.; Ravera, E. *NMR of Paramagnetic Molecules: Applications to Metallobiomolecules and Models*; 2017.

(7) Rizzo, D.; Ravera, E.; Fragai, M.; Parigi, G.; Luchinat, C. Origin of the MRI Contrast in Natural and Hydrogel Formulation of Pineapple Juice https://www.hindawi.com/journals/bca/2021/6666018/ (accessed 2021 -03 -09). https://doi.org/https://doi.org/10.1155/2021/6666018.

3.4 Protein-ligand interaction: the case of MMP-12

Human matrix metalloproteinases (MMPs) are a well known class of proteolytic enzymes that regulate the metabolism of extracellular matrix proteins. These multidomain enzymes are crucial in a number of physiological processes, such as embryonic development, tissue remodeling and repairing, angiogenesis and wound healing, but also in the control of cellular activity by releasing biologically active peptides and growth factors [68]. Alterations in the level of these proteases, namely their overexpression, are implicated in a wide range of pathological states, so that the development of inhibitors has been, and still is, an attractive research field.

One of them, the protein matrix metalloproteinase-12 (MMP12) has been selected for the first ligand-protein interaction study using HRR. An adapted NOESY sequence with water suppression, and with shuttling up and down during the mixing time, was employed to record the ligand signal loss as the delay increased. The ^{1}H NMRD profiles of the ligands (see *Figure 3.26 panel (b)*) 4,4-biphenol (BPN), 2-phenylpyrimidine (PPyr), 4-methoxybenzenesulfonamide glycine (MLC), 4-methoxybenzenesulfonamide (MBS), known to bind MMP-12 with different binding constants, in the range from few μM to mM, were collected.

The samples were prepared with a large excess of one of the ligands with respect to the protein, in order to have both bound and unbound forms in solution. The majority of the ligand is expected to be in the unbound state, but the fraction in exchange with the protein can be used as a reporter in their interaction. The buffer was 20 mM Tris pH 7.2, 10 mM $CaCl_2$, 0.1 mM $ZnCl_2$, 0.3 M NaCl, 0.2 M hydroxamic acid AHA.

Hydroxamic acid protects the enzyme against self-proteolysis, so it is used in high concentrations in the protein buffer. We can thus plan, use HRR to investigate the interactions of the protein in the presence of the different ligands, and also to monitor the competition for the binding site between hydroxamic acid and the other ligands.

	Ligand concentration	Protein concentration
BPN	200 mM	2 μM
PPyr	200 mM	4 μM
MCL	200 mM	10 μM
MBS	800 mM	20 μM

Table 3.6: Employed ligand and protein concentrations.

(a)

(b)
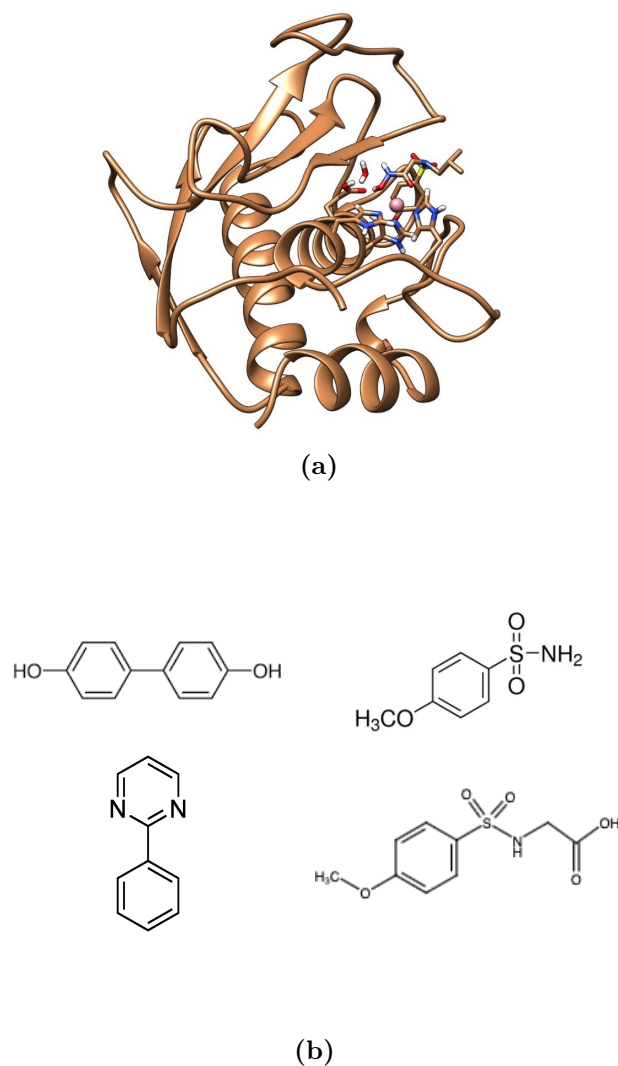
Figure 3.26: (a) Representation of MMP12 catalytic domain. (b) Structures of the ligands observed during the protein-ligand interaction study: on the left, 4.4-Biphenol and 2-phenylpyrimidine; on the right, 4-methoxybenzenesulfonamide glycine and 4-methoxybenzenesulfonamide.

The experiments were acquired at ten relaxation magnetic fields (ranging from about 2 MHz to 600 MHz) and six delays. The spectra were processed and the signals of each ligand at every delay were fitted with a *Python* script in order to obtain the longitudinal relaxation time. Preliminary results on three

ligands are reported here.

The signals of the ligands MLC and MBS in the presence of the protein (K_d of $(4.3 \pm 0.6) \cdot 10^{-4}$ M and $(3.3 \pm 0.2) \cdot 10^{-4}$ M, respectively), appeared only slightly shifted with respect to the ones of the ligands alone. We can therefore affirm that the ligands MLC and MBS and are in fast exchange with the protein. Since biphenol has an higher affinity with the protein (K_d of $(2 \pm 1) \cdot 10^{-6}$ M), its signals appeared both shifted and broadened, due to a slightly slower exchange with the protein.

As expected different NMRD profiles were obtained for the ligand signals in the presence and in the absence of the protein. Examples of this data are reported in *Figures 3.28, 3.29*, and *3.30*.
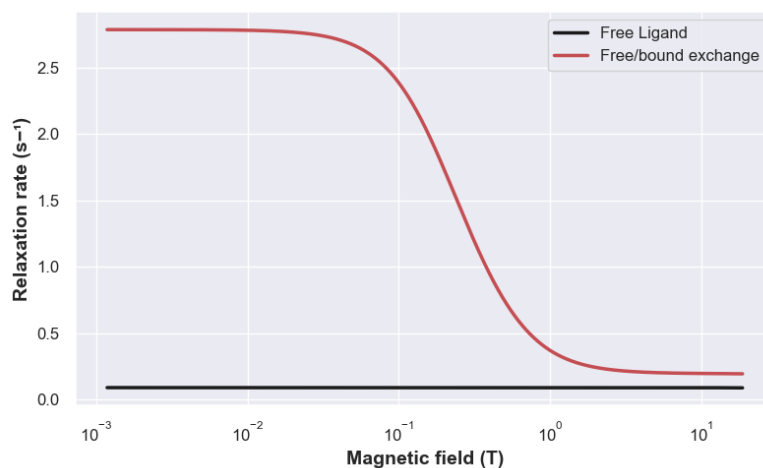
Figure 3.27: What is expected from the HRR study are these kind of NMRD profiles: in red the profile of the small molecule in the presence of the protein, in black the flat profile of the small molecule alone. The dispersion depends on the binding constants (and therefore on the populations of the bound and unbound forms of the ligand) and on two reorientational correlation times.

| (a) | (b) |
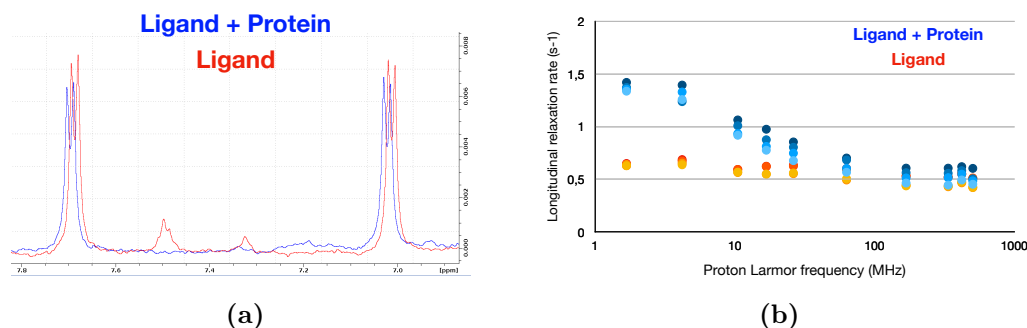
Figure 3.28: (a) NMR signals of 4-Methoxybenzenesulfonamide glycine (MLC) with (in blue) and without the protein (in red). (b) NMRD profiles of the signals of a MLC (in blue) and of the same signals when the small molecule interacts with a protein (in red). These profiles were obtained using the HRR prototype in ENS.

(a)

(b)
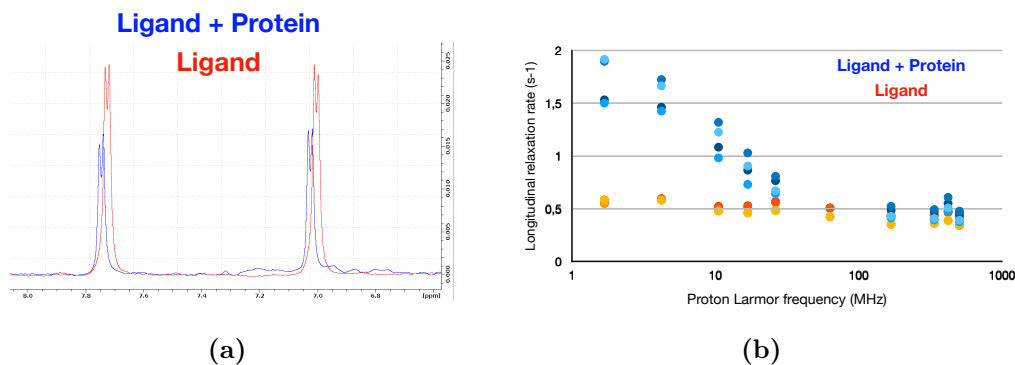
Figure 3.29: (a) NMR signals of 4-4-Methoxybenzenesulfonamide (MBS) with (in blue) and without the protein (in red). (b) NMRD profiles of the signals of a MBS (in blue) and of the same signals when the small molecule interacts with a protein (in red). These profiles were obtained using the HRR prototype in ENS.

(a)

(b)
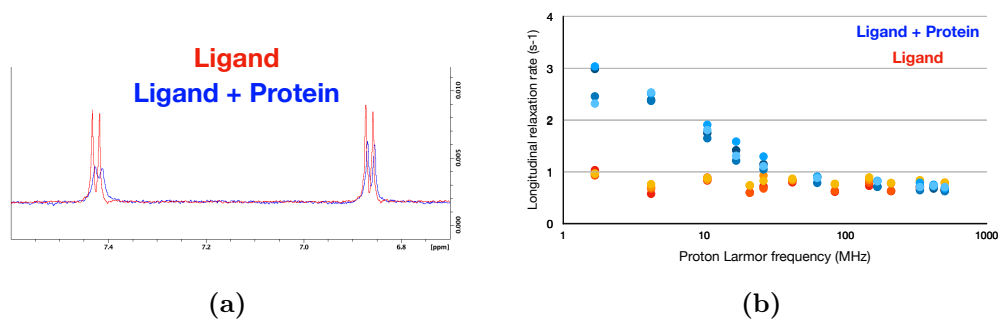
Figure 3.30: (a) NMR signals of biphenol with (in blue) and without the protein (in red). (b) NMRD profiles of the signals of a biphenol (in blue) and of the same signals when the small molecule interacts with a protein (in red). These profiles were obtained using the HRR prototype in ENS.

Although further analysis are currently being preformed to obtain quantitative information about the interactions, including the implementation of a more complete method for the analysis of the spectra, these data show that HRR allows us to monitor changes in the NMRD profile of the small molecule and therefore makes it possible to use it as a reporter of its interaction with the macromolecule.

3.5 PD-1 bioconjugation with activated PEG

Protein functionalization is a relevant process in various fields, especially in biotechnology, materials science, and, more recently, medicine. The importance of protein functionalization lies in its ability to modify proteins, either chemically or genetically, to tailor their properties and functions to meet specific requirements in various applications. Among these, functionalized proteins have a key role in the development of biosensors and biomaterials, biocatalysis, and as therapeutic agents in the treatment of various diseases.
HACTR-PD-1 mutant (K131T/K135R) has been designed for selective bioconjugation reactions involving immunogenic ligands and paramagnetic complexes, such as DOTA derivatives carrying a N-hydroxy succinimide (NHS), as in the case of L-asparaginase II (*Section 3.3.1*). It would be possible to design a selective MRI contrast agent candidate, formed by HACTR-PD-1 mutant carrying a Gd-DOTA ligand, for tumor cells overexpressing PD-L1. FFC and high resolution relaxometry could be useful in designing and characterizing such promising CAs by monitoring the relaxation enhencement occurring upon the binding of the PD-1 derivative to the PD-L1. The NMRD profile, obtained by FFC relaxometry, of a solution of the conjugated protein could provide extremely useful insights into the interaction between PD1 and PD-L1.

On the down side, proteins functionalization can lead to an undesired loss of affinity for the partner, thus it is important, in the framework of affinity studies, to evaluate the effect of bioconjugation on the reactivity and stability of the protein [52].
I was involved in finding the best conditions for the N-terminus functionalization of the HACTR-PD-1 mutant (K131T/K135R) with N-hydroxy succinimide (NHS) activated PEG. PEG conjugates of the HACTR-PD-1 mutant were obtained by bioconjugation reaction between the protein and NHS ester derivatives of PEG-1000, PEG-5000 (weight of 1 and 5 kDa, respectively). Protein concentration during the reaction was ~ 1 mg/mL in 150 mM sodium phosphate buffer at pH 7.5, and a large excess of NHS ester activated PEG was employed (reactive PEG to protein molar ratio of 15:1). After overnight incubation at room temperature under gentle stirring, the conjugates were purified from the unreacted fraction by size exclusion chromatography using a *HiLoad Superdex 16/60 200 pg* column and then dialyzed on 10 MW cut-off membrane against 150 mM sodium phosphate buffer at pH 7.5.

BioMACROMOLECULES

Article

Site-Selective Functionalized PD-1 Mutant for a Modular Immunological Activity against Cancer Cells

Silvia Fallarini, Linda Cerofolini, Maria Salobehaj, Domenico Rizzo, Giulia Roxana Gheorghita, Giulia Licciardi, Daniela Eloisa Capialbi, Valerio Zullo, Andrea Sodini, Cristina Nativi,* and Marco Fragai*

Cite This: https://doi.org/10.1021/acs.biomac.3c00893

Read Online

ACCESS | lıl Metrics & More | 📖 Article Recommendations | ⓈⒾ Supporting Information

ABSTRACT: Targeting immune checkpoints is a well-established strategy in cancer therapy, and antibodies blocking PD-1/PD-L1 interactions to restore the immunological activity against cancer cells have been clinically validated. High-affinity mutants of the PD-1 ectodomain have recently been proposed as an alternative to antibodies to target PD-L1 on cancer cells, shedding new light on this research area. In this dynamic scenario, the PD-1 mutant, here reported, largely expands the chemical space of nonantibody and nonsmall-molecule inhibitor therapeutics that can be used to target cancer cells overexpressing PD-L1 receptors. The polyethylene glycol moieties and the immune response-stimulating carbohydrates, used as site-selective tags, represent the proof of concept for future applications.
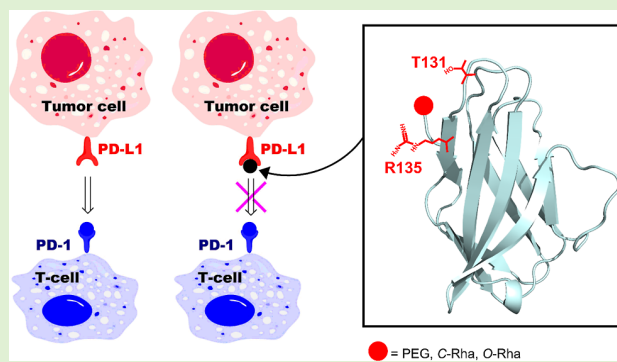
INTRODUCTION

T-cells are crucial components of the immune system involved in the adaptive response against pathogens and unhealthy cells, including cancer cells.[1-5] Unfortunately, immune selection pressure often enables abnormal cells to deceive the immune system and escape immune surveillance. For example, many immunogenic tumors can bypass immune destruction by exploiting checkpoints that are naturally deputed to regulate the immune system and suppress autoimmunity.[6]

One of these checkpoints modulates T-cell function through the activation of programmed cell death protein 1 (PD-1) and its physiological programmed cell death ligands PD-L1 and PD-L2.[7,8] Cancer cells overexpressing PD-L1 transmembrane protein neutralize the cytotoxic activity of T-cells, becoming free to replicate and metastasize.[9] Currently, PD-L1 is a target for cancer therapy, and several monoclonal antibodies designed to bind the ectodomain of this transmembrane protein have been approved for clinical use.[10-13] Thanks to recent advances in the characterization of PD-L1 biology, numerous small-molecule inhibitors have also been developed.[14,15]

An additional recent approach to inhibit the PD-1/PD-L1 axis relies on the use of the recombinant PD-1 ectodomain to address the PD-L1 protein on the surface of cancer cells.[16] In fact, the formation of a complex between recombinant PD-1 and PD-L1 on cancer cells hampers the interaction of the latter with PD-1 exposed on T-cells and circumvents the main issue of the immune system suppression.[17,18]

It is noteworthy that recombinant PD-1 can also be used as a vector to target cancer cells overexpressing PD-L1 with probes, toxins, or therapeutic molecules. An advantage of this approach over the monoclonal antibodies is related to the possibility of using *Escherichia coli* as an expression system where this protein can be easily produced using straightforward manufacturing procedures. This strategy is also advantageous over using small molecules that are often difficult to modify without altering the affinity for the target. Particularly intriguing is the possibility of employing recombinant PD-1 as a carrier to address cancer cells with immune-stimulating agents. For example, the administration of L-rhamnose conjugated to proteins or peptides is known to induce an immune response through the generation of antirhamnose antibodies.[19,20] These antibodies may be effective in activating macrophages and lymphocytes, thus, eliciting an immune response cascade.

For this purpose, a vast literature exists on the functionalization of endogenous or biocompatible macromolecules with *N*-hydroxysuccinimide (NHS)-activated rhamnosides as donors.[21,22] Bioconjugation with NHS-activated molecules is

A

67 indeed one of the most effective strategies to decorate or
68 functionalize peptides or proteins under physiological con-
69 ditions to modulate their solubility, bioavailability, or
70 immunogenicity.

71 Recently, the high-affinity mutant of the N-terminal domain
72 of PD-1, termed high-affinity consensus PD-1 (HAC-PD-1,
73 hereafter), has been developed and successfully investigated for
74 immunotherapy and PET imaging of cancers overexpressing
75 PD-L1.[16] A limitation of this effective mutant is, however, its
76 limited versatility in terms of bioconjugation. As a matter of
77 fact, conjugation of HAC-PD-1 with amine-reactively activated
78 molecules is not feasible because two residues of lysine are
79 located in the binding site for PD-L1. The functionalization of
80 one or both of these residues would interfere with the binding
81 properties of the mutant, likely preventing the interaction with
82 PD-L1.

83 Here, we report on the design, biophysical characterization,
84 and site-selective glycosylation of a new mutant of PD-1,
85 namely, HACTR-PD-1. The HACTR-PD-1 mutant presents
86 (i) a nanomolar affinity vs PD-L1, (ii) the N-terminal moiety
87 as a unique amino group reacting with NHS-reagents, and (iii)
88 suitable features for the development of new anti-PD-L1
89 proteins endowed with modular immunological activity. The
90 site-selective functionalization of HACTR-PD-1 with polymers
91 or rhamnosides as model glycans is herein described. The
92 monofunctionalization of the mutant did not dampen its
93 affinity vs PD-L1 and the immunomodulating properties of the
94 derivatives obtained were investigated in vitro vs two different
95 types of breast cancer (BC) cell lines. The HACTR-PD-1
96 rhamnosyl derivatives successfully prepared, namely, **1**-
97 HACTR-PD-1 and **2**-HACTR-PD-1, are characterized by
98 two different spacers and different types of glycosidic bonds
99 used to link the rhamnosyl moiety to the mutant.

■ EXPERIMENTAL SECTION

101 **Expression and Purification of the Human HACTR-PD-1**
102 **Mutant.** E. coli BL21 (DE3) cells were transformed with the pET-28a
103 (+) plasmid encoding the HACTR-PD-1 mutant (residues D26−
104 R147, with the following mutations: V64H, L65 V, N66 V, Y68H,
105 M70E, N74G, K78T, C93A, L122 V, A125 V, K131T, A132I, and
106 K135R). In order to obtain uniformly isotopically enriched PD-1
107 [U−^{15}N] and [U−^{13}C, ^{15}N], the cells were cultured in M9 minimal
108 medium supplied with 1.1 g of ^{15}N−NH$_4$Cl or 1.1 g of ^{15}N−NH$_4$Cl
109 and 3 g of ^{13}C-glucose, respectively, 1 mL of 0.1 mg/mL solution of
110 ampicillin, 1 mL of 1 mg/mL solution of thiamine, 1 mL of 1 mg/mL
111 solution of biotin, 1 mmol·dm^{-3} MgSO$_4$, and 0.3 mmol·dm^{-3} CaCl$_2$;
112 they were allowed to grow at 37 °C until OD600 reached 0.8 and then
113 overexpression was induced with 1 mmol·dm^{-3} isopropyl β-D-1-
114 thiogalactopyranoside. They were further incubated at 37 °C
115 overnight and then harvested by centrifugation at 6500 rpm (JA-10
116 Beckman Coulter) for 15 min at 4 °C. In all instances, the pellet was
117 suspended at first in 50 mmol·dm^{-3} Tris-HCl, pH 8.0, 200 mmol·
118 dm^{-3} NaCl, 10 mmol·dm-3 β-mercaptoethanol, and 10 mmol·dm^{-3}
119 EDTA (50 mL per liter of culture) and sonicated for 30 s 10 times on
120 ice at 4 °C. The suspension was centrifuged at 40,000 rpm (F15-6 ×
121 100y Thermo Scientific) for 40 min, and the supernatant was
122 discarded. The recovered pellet was resuspended in 50 mmol·dm^{-3}
123 Tris-HCl, pH 8.0, 200 mmol·dm^{-3} NaCl, 10 mmol·dm^{-3} β-
124 mercaptoethanol, and 6 mol·dm^{-3} guanidinium chloride (25 mL
125 per liter of culture) and newly incubated at 4 °C overnight under
126 magnetic stirring. Again, the suspension was centrifuged at 40,000
127 rpm (F15-6 × 100y Thermo Scientific) for 40 min. The pellet was
128 discarded, whereas the supernatant containing the denatured protein
129 solution was diluted in a refolding buffer containing 0.1 mol·dm^{-3}
130 Tris-HCl, pH 8.5, 1 mol·dm^{-3} arginine, 0.25 mmol·dm^{-3} reduced
131 glutathione, and 0.25 mmol·dm^{-3} oxidized glutathione. The solution

132 was incubated at 4 °C under stirring for 12−18 h, clarified by passing
133 through a 0.45 μm filter, and then dialyzed extensively against 10
134 mmol·dm^{-3} Tris, pH 8.0, and 20 mmol·dm^{-3} NaCl. The protein
135 solution was concentrated with an Amicon Stirred Cell and then
136 purified by size exclusion chromatography (SEC) using a HiLoad
137 Superdex 26/60 75 pg (GE Healthcare) column previously
138 equilibrated in 10 mmol·dm^{-3} Tris-HCl at pH 8.0 and 20 mmol·
139 dm^{-3} NaCl.

140 **Functionalization of the HACTR-PD-1 Mutant with NHS-**
141 **Activated PEG and Activated Rhamnose Derivatives 1 and 2.**
142 Polyethylene glycol (PEG) conjugates of the HACTR-PD-1 mutant
143 were obtained by reacting the protein with NHS ester derivatives of
144 PEG-1000, PEG-5000 (Creative PEG Works), and rhamnosides
145 (protein concentration around ∼1 mg/mL in 0.15 mol·dm^{-3} sodium
146 phosphate buffer, pH 7.5, and reactive to a protein molar ratio of
147 15:1). After overnight incubation at room temperature with gentle
148 stirring, the conjugates were purified from the unreacted fraction by
149 SEC using a HiLoad Superdex 16/60 200 pg column and dialyzed on
150 a 10 MW cutoff membrane against 0.15 mol·dm^{-3} sodium phosphate
151 pH 7.5 buffer.

■ RESULTS AND DISCUSSION

153 The interaction of PD-1 on T-cells with PD-L1 on tumor cells
154 reduces the T-cell function and dampens the antitumor
155 immune response. Although beneficial under physiological
156 conditions (autoimmunity control and modulation of harmful
157 inflammations), in a tumoral scenario, such interactions
158 promote tumor escape and progression. Impressive clinical
159 results have been obtained by blocking the PD-1/PD-L1
160 interaction with monoclonal antibodies as specific inhibitors
161 (immune checkpoint inhibitors) in advanced- and metastatic-
162 stage cancers. Even though PD-1/PD-L1-neutralizing antibod-
163 ies are considered the most promising drugs in cancer
164 immunotherapy, the use of antibodies in some solid tumors[9]
165 has raised some concerns due to potential toxicity that may
166 result from ADCC-mediated lysis of subsets of immune cells
167 that express PD-L1.[23] Therefore, current clinical trials are
168 evaluating anti-PD-1/PD-L1 drugs for use in combination with
169 other drugs or immune modulators.

170 **Design and Expression of the HACTR-PD-1 Mutant.**
171 Capitalizing on the potential of small proteins and their broad
172 applicability in the modulation of the immune system, inspired
173 by the already described HAC-PD-1 protein,[16] an original set
174 of PD-1 derivatives, where the two lysine residues K131 and
175 K135 are replaced by nonreactive amino acids toward the NHS
176 moiety, has been designed and screened in silico by performing
177 docking calculations.

178 After structural analysis of the experimental HAC-PD-1/PD-
179 L1 complex, three amino acids with different physical−
180 chemical properties were taken into consideration to replace
181 the two residual lysines present in the protein binding site: (i)
182 a charged amino acid (Arg), (ii) a polar uncharged amino acid
183 with a long side-chain (Gln), and (iii) a polar uncharged amino
184 acid with a short side-chain (Thr). A computational study was
185 performed by using the HADDOCK 2.2 web-portal[24] to screen
186 in silico the mutations on the stability of the complex with PD-
187 L1. The complexes of PD-L1 with the two HAC-PD-1 mutants
188 K131T/K135R and K131R/K135R showed the most favorable
189 docking energies expressed in terms of HADDOCK-scores
190 (see Table S1, Supporting Information). It is noteworthy that
191 the stability of the two complexes is like that of the parent
192 HAC-PD-1/PD-L1 adduct. The analysis of the calculated
193 structural models revealed that in the K131R/K135R protein,
194 the native small β-strand bearing the two mutated residues
195 adopts a random coil shape. Conversely, this secondary
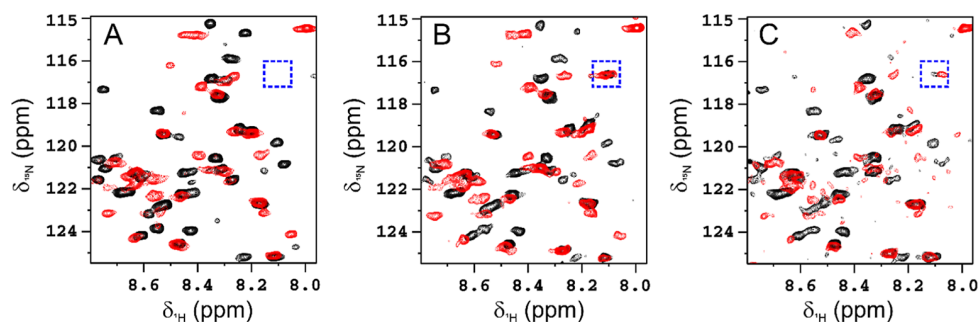
Figure 1. Region of 2D ^{1}H$-^{15}$N HSQC spectra of HACTR-PD-1/PD-L1 complexes superimposed with the corresponding references: (A) free HACTR-PD-1 (black) with respect to HACTR-PD-1 in the presence of PD-L1 (in 1:1 molar ratio, red); (B) HACTR-PD-1 conjugated with PEG 5 kDa (black) with respect to HACTR-PD-1 conjugated with PEG 5 kDa in the presence of PD-L1 (in 1:1 molar ratio, red); and (C) HACTR-PD-1 conjugated with L-rhamnose (black) with respect to HACTR-PD-1 conjugated with L-rhamnose in the presence of PD-L1 (in 1:1 molar ratio, red). The spectra were acquired on spectrometers operating at 900 (A), 950 (B), and 700 (C) MHz, ^{1}H Larmor frequency, and 298 K. The spectra of the complexes were acquired with a higher number of scans than the reference spectra. The signal surrounded by the blue square is related to the new amide formed by conjugation with PEG5000 or the L-rhamnose derivative.
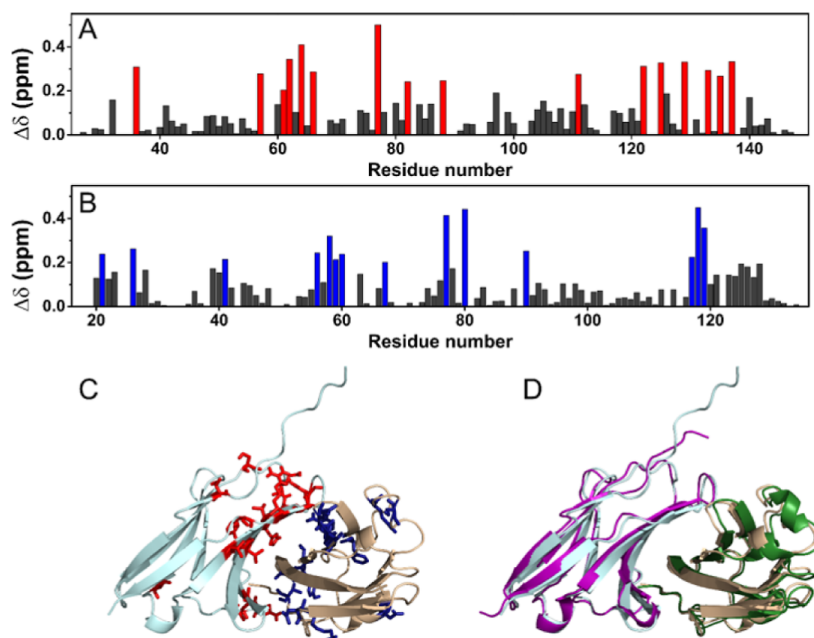
Figure 2. Chemical shift perturbation of HACTR-PD-1 in the presence of PD-L1 (A) and of PD-L1 in the presence of HACTR-PD-1 (B) (in a 1:1 molar ratio) evaluated using the Picasso Web server. The residues experiencing the largest perturbations have been highlighted in red and blue, respectively, and used as "active residues" in the HADDOCK calculation. (C) Model of the complex between HACTR-PD-1 (light cyan) and PD-L1 (wheat) with the lowest HADDOCK-score. The active residues have been highlighted as red and blue sticks, respectively. (D) Superimposition of the model of the complex evaluated with HADDOCK, where HACTR-PD-1 is in light cyan and PD-L1 is in wheat, with the X-ray structure (PDB code: 1IUS), where HAC-PD-1 is in purple and PD-L1 in green.

structure element is well preserved in the K131*T*/K135R mutant (HACTR-PD-1). Therefore, this last mutant was selected for expression in *E. coli* to evaluate the correct folding and PD-L1-binding properties.

The spreading of the signals in the 1D ^{1}H NMR and 2D ^{1}H$-^{15}$N HSQC spectra recorded on the HACTR-PD-1 protein is consistent with that of a well-structured protein. The 2D ^{1}H$-^{15}$N HSQC spectrum shows sharp and well-resolved signals. The backbone assignment of the protein, obtained from the analysis of triple-resonance spectra recorded on samples of [U$-^{13}$C, ^{15}N] HACTR-PD-1, allowed us to identify and characterize 114 spin systems over 122 total residues. The predictions of the secondary structure elements, obtained by TALOS+ analysis using the resonances of

HACTR-PD-1 as input (Figure S1), indicate that the HACTR-PD-1 mutant has the same folding as the HAC-PD-1 protein. Concerning the protein partner, PD-L1, the assignment was already available in the BMRB (accession code 51169).[25]

Epitope mapping and qualitative information on the binding affinity were achieved by monitoring the evolution of the resonances of the ^{15}N isotopically enriched HACTR-PD-1 in a 2D ^{1}H$-^{15}$N HSQC NMR spectrum upon the addition of increasing amounts of PD-L1 in natural abundance (Figure 1A and S2). In the spectra of HACTR-PD-1, the intensity of several signals decreases progressively, while new signals appear by increasing the concentration of PD-L1. These spectral changes fit with an interaction in the slow exchange

regime on the NMR time scale. Complementary information was obtained by monitoring the evolution of the signals of the ^{15}N isotopically enriched PD-L1 in a 2D ^{1}H−^{15}N HSQC NMR spectrum upon the addition of HACTR-PD-1 in natural abundance (Figure S3). This set of NMR data is consistent with a slow exchange regime on the NMR time scale previously observed and provides complementary information on the residues involved in the binding. To obtain the experimental restraints for the docking calculation of the adduct between HACTR-PD-1 and PD-L1, a prediction of the assignment of the resonances observed in the 2D ^{1}H−^{15}N HSQC NMR spectra of the complex and the related chemical shift perturbation set (Figure 2A,B) were generated by using the PICASSO Web server.[26] In the program, the 2D ^{1}H−^{15}N HSQC reference spectra of free [U−^{15}N] HACTR-PD-1 and free [U−^{15}N] PD-L1 were compared to the spectra of [U−^{15}N] HACTR-PD-1/PD-L1 and [U−^{15}N] PD-L1/ HACTR-PD-1 (in 1:1 molar ratio), respectively, to provide the assignment and the chemical shift perturbations on the two proteins in the complex. The residues experiencing the largest effects were imposed as "active residues" in the HADDOCK calculations (Figure 2C). The structural models of the mostly populated cluster (53 structures over 200) were also endowed with the lowest HADDOCK-score and were superimposable with the experimental X-ray structure of the complex (PDB code: 5IUS) available for the HAC-PD-1 protein (PyMOL rmsd of 0.875, Figure 2D). Then, the affinity of HACTR-PD-1 for PD-L1 was investigated by isothermal titration micro-calorimetry (Figure 3). The titration was performed by adding HACTR-PD-1 to PD-L1 and provided a dissociation constant of 59 nmol·dm^{-3}, which is in the good range for a drug candidate.

Site-Selective Functionalization of the HACTR-PD-1 Mutant. Since the functionalization or bioconjugation of proteins involved in protein−protein complexes can lead to an undesired loss of affinity for the partner as functionalization can potentially mask the interaction surface, the effect of HACTR-PD-1 conjugation at the N-terminus was investigated by using two PEG chains of different sizes (1 and 5 kDa). These bulky polar chains have been chosen because they are often used to increase protein solubility, half-life in vivo, and renal clearance.[27−29] Solutions of HACTR-PD-1 were thus reacted with a 15-fold molar excess of the two linear PEG chains properly activated as NHS ester derivatives. After chromatographic purification (see Supporting Information), samples of the two PEG-HACTR-PD-1 conjugates, obtained starting from ^{15}N isotopically enriched proteins, were characterized by 2D ^{1}H−^{15}N HSQC NMR spectra.

The analysis of the spectra showed that the native folding is well preserved in the PEGylated proteins with only three residues at the N-terminus experiencing a large chemical shift variation. Also, the interaction between the two PEG-HACTR-PD-1 derivatives and PD-L1 is not negatively affected by the PEG hindering chains since the slow exchange regime and the distribution of the resonances observed in the 2D ^{1}H−^{15}N HSQC NMR spectra of the complexes are largely similar to those of the HACTR-PD-1 protein in complex with PD-L1 (Figure 1B and S4).

In keeping with this, to evaluate the potential of HACTR-PD-1 as an immunomodulating vector (see above), the mutant protein was conjugated to two selected rhamnopyranosides characterized by two different glycosidic linkages: the non-native, physiologically stable *C*- and the native *O*-glycosidic linkages.
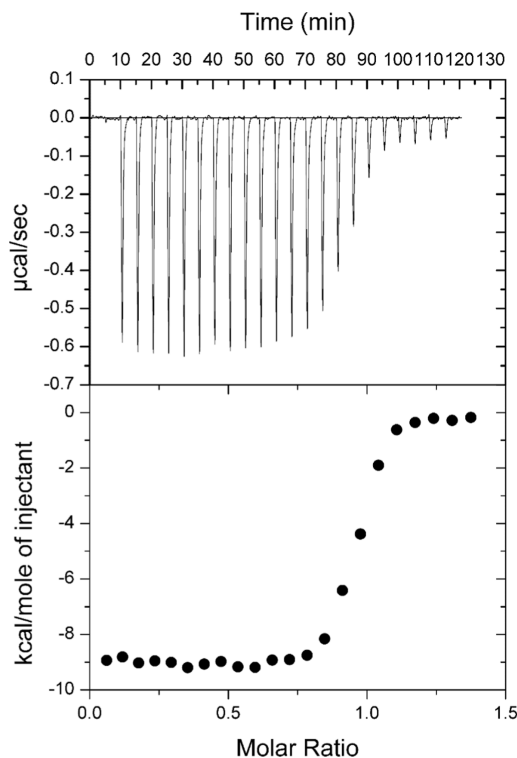
Figure 3. ITC data for the binding of the N-terminal domain of PD-L1 to HACTR-PD-1 in Tris buffer at pH 8.0 and 298 K. The thermogram is reported at the top, and the plot of the heat-released vs molar ratio is at the bottom of the panel. The data were fitted using a single binding site model.

Synthesis of Activated Rhamnosides 1 and 2. α-*C*-L-rhamnoside **1** and α-*O*-L-rhamnoside **2** were synthesized as displayed in Schemes 1 and 2.

In detail, *C*-rhamnoside **1** was obtained from the peracetylated C-allyl rhamnoside **3** as starting material, which was prepared as previously described.[30] Upon oxidation with an excess of NaIO$_4$ in the presence of RuCl$_4$ as catalyst, compound **3** was transformed into carboxylic acid **4** (70% of conversion) which, in turn, was coupled with glycine ^{13}C benzyl ester **5**. The coupling reaction was performed by using EDAC and HOBT as coupling reagents in the presence of NMM as a base and dry DMF as a solvent. The rhamnoside **6** so obtained (74%) was first transformed into the free carboxylic acid **7** (Pd/C, H$_2$, THF, 2 h) and then reacted with the mono Boc-protected ethylenediamine **8** (with TBTU and NMM in dry DMF) to afford rhamnoside **9** (52%).

After the removal of the acetyl residues (NH$_3$, 4 mol·dm^{-3} in MeOH, rt, overnight) and of the Boc protecting group (TFA, dry DCM, rt, 2 h), the crude **10** isolated as trifluoroacetic salt was reacted with **11** in the presence of NMM and dry DMF as the solvent. The desired rhamnosyl derivative **1** was thus obtained (75% over three steps), ready for the glycosylation of the PD-1 mutant (see Scheme 1 and Supporting Information).

Triacetyl rhamnoside **12**[31] was the starting material for the synthesis of rhamnoside **2**, which presents an *O*-glycosidic linkage and a shorted linker with respect to **1** (Scheme 2). Glycosylation of **12** with N-Boc protected ethanolamine **14**

Scheme 1. Synthesis of the α-C-L-rhamnoside 1
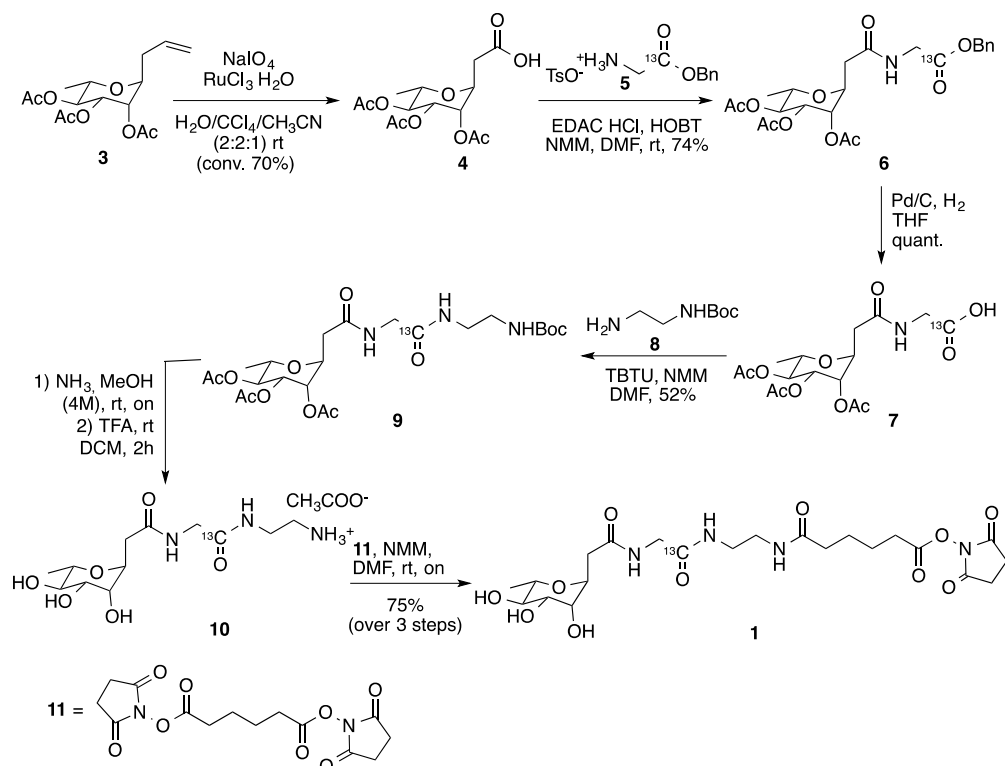
Scheme 2. Synthesis of α-O-L-rhamnoside 2
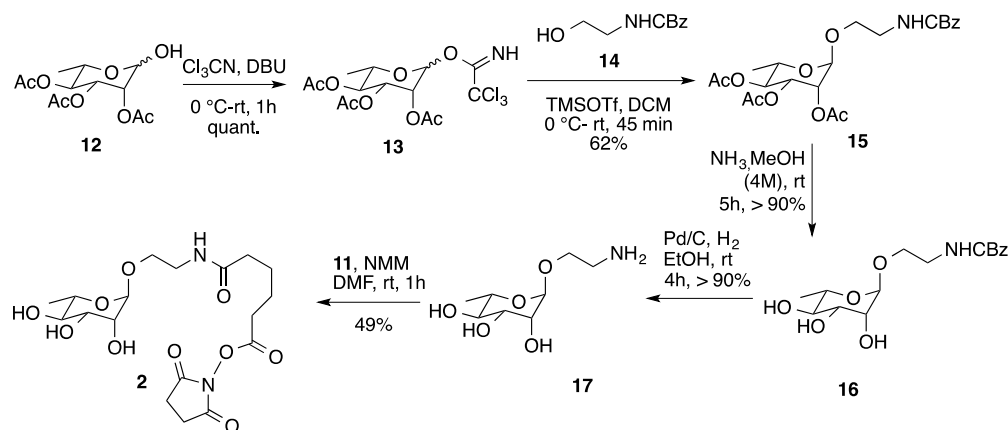
was performed relying on the trichloroacetimidate strategy by using trimethylsilyl triflate as a glycosidic promoter in dry DCM as a solvent. O-rhamnoside **15**, obtained as the α isomer (62%), was deacetylated with NH_3 in MeOH (4 mol·dm^{-3}, rt, 5 h, **16**, >90%) and the benzyl protecting group removed by treatment with H_2, catalytic Pd/C, and EtOH as a solvent (rt, 4 h, >90%) to afford the fully deprotected rhamnoside **17**. Compound **17** was finally reacted with linker **11** (see Scheme 1) to form the desired α-O-rhamnoside **2** suitably armed to glycosylate HACTR-PD-1 (Scheme 2 and Supporting Information).

The HACTR-PD-1 glycosylation was performed through two different linkers, properly activated as NHS-ester derivatives (Schemes 1 and 2), to afford the rhamnosyl mutants **1**-HACTR-PD1 and **2**-HACTR-PD1 (Figure 4). Both glycosylations proceeded smoothly at room temperature in buffer phosphate, and the two rhamnosyl mutants were obtained quantitatively after dialysis.

To confirm the data obtained for PEG-HACTR-PD-1, the rhamnosyl mutant **1**-HACTR-PD1 was screened by NMR for its binding properties vs those of PD-L1. A new signal corresponding to the functionalized N-terminus appeared in the 2D $^1H-^{15}N$ HSQC NMR spectrum, with a few signals corresponding to residues structurally closed to the N-terminus experiencing a sizable chemical shift variation. As previously observed for the PEGylated derivatives, the presence of L-rhamnose at the N-terminus of HACTR-PD-1 did not affect the interaction with PD-L1, which is still in the slow exchange regime on the NMR time scale (see Figure 1C and S6). This was indeed expected due to the smaller size of the rhamnoside with respect to the PEG. NMR analysis was used to verify that all the compounds were pure (>95% pure).
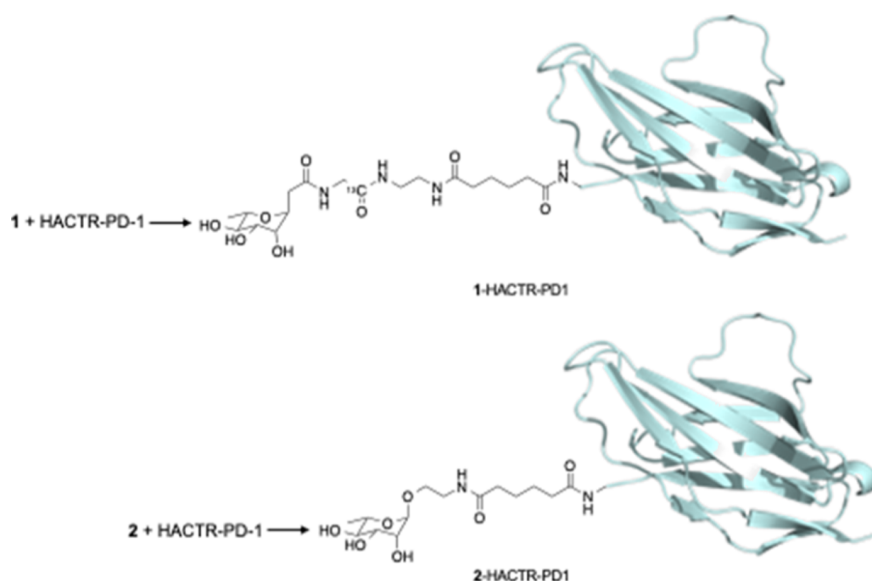
Figure 4. Rhamnosylated mutants **1**-HACTR-PD-1 and **2**-HACTR-PD-1.
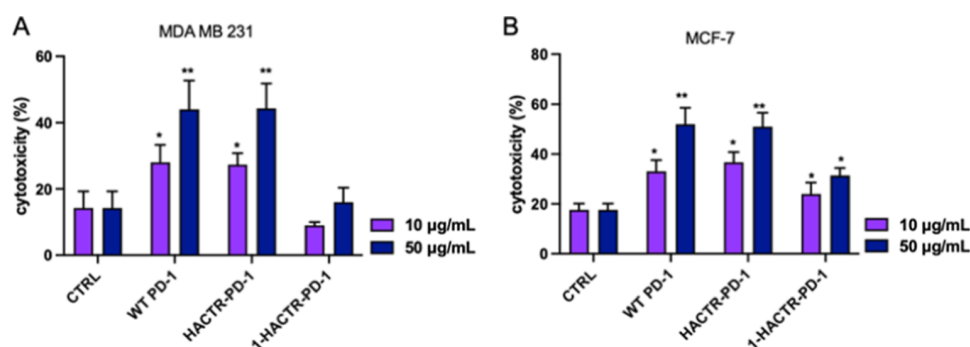
Figure 5. Effects of WT PD-1, HACTR-PD-1, and **1**-HACTR-PD-1 on T-cell-mediated BC cell cytotoxicity. CAM-labeled cancer cells were treated with 10 or 50 μg/mL of PD-1, HACTR-PD-1, or **1**-HACTR-PD-1 for 1 h and then incubated with PHA-stimulated PBMC. After 24 h of coculture, BC cells were harvested, and the level intensity of CAM was analyzed by FACS. (A) PBMC-mediated cytotoxicity against the MDA MB 231 cell line in the presence or absence of WT PD-1, HACTR-PD-1, or **1**-HACTR-PD-1; (B) PBMC-mediated cytotoxicity against the MCF-7 cell line in the presence or absence of WT PD-1, HACTR-PD-1, or **1**-HACTR-PD-1. Results are expressed as the mean ± SEM of at least three independent experiments run in triplicate using PBMCs from three different donors. *$p \leq 0.05$ natural/recombinant protein treated vs untreated cocultures; **$p \leq 0.01$ natural/recombinant protein treated vs untreated cocultures. For data on **2**-HACTR-PD-1, see Figure S12.

Biological Tests. Finally, to investigate the biological profile of the new PD-1 mutant and of its L-rhamnosyl derivatives, a set of cell-based assays were carried out on wild-type (natural) PD-1, HACTR-PD-1, **1**-HACTR-PD-1, and **2**-HACTR-PD-1. The two rhamnosyl derivatives were screened to investigate the possible effects of the linker's length and the glycosidic bond on cell tests.

PD-L1 has been established as a valuable biomarker for different types of cancer, and several studies have demonstrated that PD-L1 expression may be used to predict the outcome of the disease: patients with high PD-L1 expression have a significantly worse prognosis.[32]

BC is one of the most common tumors in women, and triple-negative breast cancer (TNBC) is the most aggressive BC, is difficult to treat, and has a poor prognosis. Antibodies targeting PD-1 or PD-L1 are currently considered a promising therapeutic strategy in TNBC.

MDA-MB-231 and MCF-7 cell lines represent valid study models for the evaluation of the activities of new compounds for BC therapy. In fact, these two cell lines embody a wide range of characteristics that are typically found in BC. MCF-7 is an ER-, PR-, and HER2-positive type of adenocarcinoma, while MDA-MB-231 cells stand for a triple-negative type of metastatic adenocarcinoma and are more aggressive than MCF-7 cells. Before testing the PD-1 variants' activity on the selected tumor cell lines, we evaluated the expression of PD-L1 in each line. Flow cytometry analysis was thus performed, showing that PD-L1 is expressed on both cell lines (Figure S7). This result clearly confirms that both cell lines can be used to study the effect of the newly synthesized recombinant PD-1 proteins on restoring and/or modulating antitumor immune activity.

First, wild type PD-1, HACTR-PD-1, and **1**- and **2**-HACTR-PD-1 were tested to evaluate their immunomodulatory activity in a macrophage model. All proteins were active (see Figures S8−S10); glycosylated (**1**- and **2**-HACTR-PD-1) and not glycosylated (HACTR-PD-1) mutants displayed similar immunomodulatory activities in inducing M1 differentiation and TNF-α release, with a moderate but significant higher activity for glycosylated derivatives (Figure S10). M1 macro-
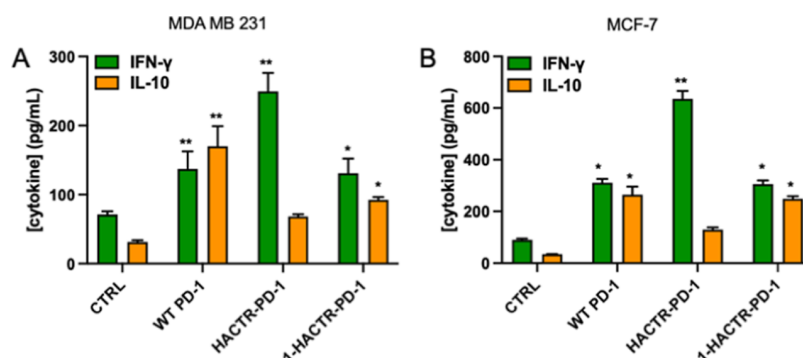
Figure 6. Effects of WT PD-1, HACTR-PD-1, and **1**-HACTR-PD-1 on T helper or Treg cytokine release. Cancer cells were treated with 10 μg/mL WT PD-1, HACTR-PD-1, or **1**-HACTR-PD-1 for 1 h and then incubated with PHA-stimulated PBMCs. After 48 h of cell culture, media were collected, and IFN-γ and IL-10 were measured by ELISA. (A) IFN-γ and IL-10 released by PBMCs cocultured with the MDA MB 231 cell line in the presence/absence of WT PD-1, HACTR-PD-1, or **1**-HACTR-PD-1; (B) IFN-γ and IL-10 released by PBMCs cocultured with the MCF-7 cell line in the presence or absence of WT PD-1, HACTR-PD-1, or **1**-HACTR-PD-1. Results are expressed as the mean ± SEM of at least three independent experiments run in triplicate using PBMCs from different donors. *$p \leq 0.05$ natural/recombinant protein treated vs untreated cocultures; **$p \leq 0.01$ natural or recombinant protein treated vs untreated cocultures. For data on **2**-HACTR-PD-1, see Figure S12.

phages are pro-inflammatory cells involved in the recruitment and differentiation of other immune cells toward an antitumor phenotype. Of note, immune checkpoint inhibitors evoke a higher response when they are associated with other drugs able to stimulate the locked immune system.[33] In this view, the ability of mutants (in particular of **1**- and **2**-HACTR-PD-1) to induce M1 differentiation can represent a valuable opportunity to educate macrophages toward a pro-inflammatory, antitumoral phenotype.

Afterward, the ability to overcome T cell inhibition mediated by PD-L1/PD-1 interaction was also investigated, starting from inhibited T cells' regulatory and cytotoxic functions.[34] Since both CD8 T and NK cells show cytotoxic activity against tumor cells and literature data suggest that both are affected by PD-L1/PD-1 binding, we performed a cytotoxic assay using peripheral blood mononuclear cells (PBMCs) that contain both populations. Cytotoxicity experiments were thus performed to verify the ability of PD-1 mutants to restore T and NK cell cytotoxic activity against tumor cells. Phytohemagglutinin (PHA)-stimulated PBMC were cocultured with CAM-stained tumor cells for 24 h, and the tumor cells' death was analyzed by FACS.

As shown in Figure 5, WT PD-1 and HACTR-PD-1 were able to re-establish the CD8 T and NK cells' cytotoxic activity in a concentration-dependent manner. As far as WT PD-1 and HACTR-PD-1 are concerned, similar data were collected for both MDA-MB-231 and MCF-7 cell line cocultures. Differently, for **1**-HACTR-PD-1, significant results were obtained in coculture with MCF-7 tumor cells. Comparable data were registered for **2**-HACTR-PD-1 (see Figure S11).

T helper cell functions are also affected by the PD-L1/PD-1 pathway.[35] CD4 T helper cells are plastic cells that can differentiate toward the Th1 or Th2 phenotype depending on the milieu composition. In particular, Th1-polarized cells are pro-inflammatory cells defined by the production of interferon-γ (IFN-γ). These cells mediate cellular immunity through activation of pro-inflammatory macrophages and recruitment and promotion of the cytolytic activity of NK and CD8⁺ T cells, the main cells involved in the elimination of tumor cells. Moreover, IFN-γ can directly induce cell death through the binding of the IFN receptor and the induction of apoptosis. Another class of cells affected by the PD-L1/PD-1 pathway is

represented by T regulatory (Treg) cells (CD4⁺CD25⁺). Tregs are a specialized T cell subpopulation involved in homeostasis and self-tolerance maintenance through immune response suppression. As is known, Tregs inhibit T cell proliferation and cytokine production.[36] Treg population is recruited to the tumor site and promotes the immune-suppressive microenvironment through different pathways mediated by both cellular and soluble components (i.e., CTLA-4/B7, TGF-β, and IL-10). IL-10 is an immunoregulatory cytokine that inhibits innate and acquired immune responses and has important immune-inhibitory activity. In the tumor context, the PD-L1/PD-1 pathway induces CD4⁺ conversion in highly suppressive T cells. In detail, PD-L1 engagement results in downregulation of PI3K/Akt/mTOR signaling that switches CD4 differentiation toward regulatory T cells (Treg), which in the tumor context take part in immunosuppression.[37] Moreover, PD-1 signaling in CD4⁺ T cells reduces the PKC activation essential for the activation of NF-κB transcription factors responsible for the production of pro-inflammatory antitumoral cytokines like IFN-γ.[38]

Starting from these observations, we screened the ability of PD-1 mutants to restore IFN-γ production and inhibit the IL-10 release.

PHA-stimulated PBMCs were cocultured with tumor cells for 48 h, and the levels of IFN-γ and IL-10 were assessed by ELISA. The presence of both tumor cell lines affected PBMC cytokine production with a reduction of the IFN-γ concentration and an increase in IL-10. In both MDA-MB-231 and MCF-7 cell line cocultures, WT PD-1, HACTR-PD-1, and **1**-HACTR-PD-1 were effective in increasing the IFN-γ levels (Figure 6). The highest IFN-γ release was observed upon HACTR-PD-1 treatment. In fact, HACTR-PD-1 in MDA-MB-231/PBMC coculture induces an increase in IFN-γ production of 250%, while WT PD-1 and **1**-HACTR-PD-1 induce an increase of 92 and 84%, respectively. When tested on MCF-7/PBMC coculture, all recombinant proteins induced higher IFN-γ production when compared with MDA-MB-231/PBMC-treated cells, even if the rates between the different treatments remained very similar. In all compound-treated cocultures, a significant increase in IL-10 production was observed (Figure 6), but this result was expected since with recombinant protein treatment, we have eliminated the PD-1/

G
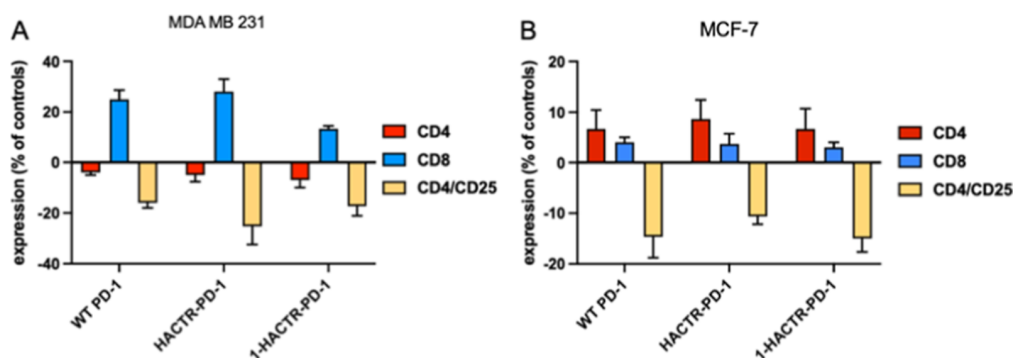
Figure 7. Effects of WT PD-1, HACTR-PD-1, and **1**-HACTR-PD-1 on the T subset percentage. Cancer cells were treated with 10 μg/mL PD-1, HACTR-PD-1, or **1**-HACTR-PD-1 for 1 h and then incubated with PHA-stimulated PBMCs. After 72 h of coculture, PBMCs were harvested, labeled with CD3, CD4, CD8, and CD25 monoclonal antibodies, and the percentage of CD4-, CD8-, and CD4−CD25-positive cells was evaluated by FACS. (A) CD4, CD8, and CD4−CD25 percentage after coculture with the MDA MB 231 cell line in the presence or absence of WT PD-1, HACTR-PD-1, or **1**-HACTR-PD-1; (B) CD4, CD8, and CD4−CD25 after coculture with the MCF-7 cell line in the presence or absence of WT PD-1, HACTR-PD-1, or **1**-HACTR-PD-1. Results are expressed as the mean ± SEM of at least three independent experiments run in triplicate using PBMCs from different donors. For data on **2**-HACTR-PD-1, see Figure S13.

PD-L1 inhibitory effect on PHA-stimulated PBMCs. WT PD-1 and **1**-HACTR-PD-1 induced a higher level of IL-10, while HACTR-PD-1 induced a lower level in both coculture systems. Of note, when we analyzed the ratio between these cytokines that can be used as a rate of protumoral or antitumoral microenvironments, we observed that both HACTR-PD-1 and **1**-HACTR-PD-1 induced a clear increase in the IFN-γ/IL-10 ratio in both cell lines. These results suggest that both mutants participate in the establishment of an antitumor microenvironment able to sustain the antitumor immune responses.

To evaluate whether the tested mutants can induce changes in the lymphocyte subtype percentage after 72 h of tumor cell/PBMC coculture in the presence or absence of natural or recombinant proteins, PBMCs were harvested and labeled with anti-CD3, CD4, CD8, and CD25 antibodies and analyzed by FACS (Figure 7).

Although to a different extent, an increase in CD8 T cell percentage and a significant decrease in CD4/CD25 percentage (Figure 7) were detected for all mutants in PBMCs cocultured with both MDA-MB-231 and MCF-7 cell lines. An increase in CD4 was observed when PBMCs were cocultured with MCF-7 in the presence of recombinant proteins; conversely, when PBMCs were cocultured with MDA-MB-231, a slight but significant increase was observed for both CD4 and CD8 lymphocytes. All together, these data corroborate the properties of the compounds tested in mediating a desired antitumoral environment at the cellular level.

■ CONCLUSIONS

In conclusion, in this article, we describe the design, expression, biophysical characterization, and site-selective glycosylation of the HACTR-PD-1 protein, a new mutant of the PD-1 ectodomain. The preservation of the folding state of the protein was proved by the minimal alteration of the 2D ^{1}H−^{15}N HSQC spectra and by the nanomolar affinity vs PD-L1 that was assessed by NMR spectroscopy and isothermal titration microcalorimetry as independent techniques. This new mutant, featuring the N-terminal moiety as a unique free amino group, was selectively functionalized with biocompatible moieties relevant for modulation of the PD-1 mutant in terms of solubility, clearance, and immunostimulant properties. The

investigation of the biological profile of the new PD-1 mutant and of its L-rhamnosyl derivatives was carried out, and a set of cell-based assays was discussed. Rhamnoside tags have been selected as examples of known immunomodulators.[17−19]

The data collected clearly suggested that the HACTR-PD-1 mutant and its rhamnosyl derivatives reduced the anergy for all components of the T cells, with a resultant increase in proliferative and functional responses. Both HACTR-PD-1 and the rhamnosyl derivatives possess the ability to stimulate the innate immune system (in particular, macrophages) to set a pro-inflammatory environment essential to sustain an anti-tumoral immune response and to promote an antitumoral *milieu*, switching the IFN-γ/IL-10 ratio.

Rhamnosyl derivatives **1**-HACTR-PD-1 and **2**-HACTR-PD-1 showed similar activity in all tests, independent of the linker and glycosidic bond. Endowed with immunomodulating properties similar to, or in some cases, only slightly lower with respect to HACTR-PD-1, the site-selectively function-alized mutants **1**-HACTR-PD-1 and **2**-HACTR-PD-1, thanks to the antigenic properties of rhamnose, represent the proof of concept for an unprecedented application of a PD-1 mutant as a ligand and also as a carrier with a panel of immunological activities. In perspective, the novel functionalized mutants herein described may pave the way for the development of new biologics to target the cancer cells overexpressing the PD-L1 receptor, not only by inhibiting the PD-1/PD-L1 interaction but also by exerting a more direct cytotoxic and immunological activity. On this forecast generation of molecules, a more in-depth investigation into ADME and immunological properties will be conducted.

■ ASSOCIATED CONTENT

🆂�📄 Supporting Information

The Supporting Information is available free of charge at https://pubs.acs.org/doi/10.1021/acs.biomac.3c00893.

Methods and materials, synthesis of rhamnosyl deriva-tives **1** and **2**, NMR measurements, and ITC titration (PDF)

■ AUTHOR INFORMATION

Corresponding Authors

Cristina Nativi − *Department of Chemistry, DICUS, University of Florence, Sesto Fiorentino (FI) 50019, Italy;* ⓘ orcid.org/0000-0002-6312-3230;
Email: cristina.nativi@unifi.it

Marco Fragai − *Department of Chemistry, DICUS, University of Florence, Sesto Fiorentino (FI) 50019, Italy; CeRM/CIRMMP, University of Florence, Sesto Fiorentino (FI) 50019, Italy;* ⓘ orcid.org/0000-0002-8440-1690;
Email: fragai@cerm.unifi.it

Authors

Silvia Fallarini − *Department of Pharmaceutical Sciences, DSF, University of Piemonte Orientale, Novara (NO) 28100, Italy*

Linda Cerofolini − *Department of Chemistry, DICUS, University of Florence, Sesto Fiorentino (FI) 50019, Italy; CeRM/CIRMMP, University of Florence, Sesto Fiorentino (FI) 50019, Italy*

Maria Salobehaj − *Department of Chemistry, DICUS, University of Florence, Sesto Fiorentino (FI) 50019, Italy; CeRM/CIRMMP, University of Florence, Sesto Fiorentino (FI) 50019, Italy*

Domenico Rizzo − *Department of Chemistry, DICUS, University of Florence, Sesto Fiorentino (FI) 50019, Italy; CeRM/CIRMMP, University of Florence, Sesto Fiorentino (FI) 50019, Italy*

Giulia Roxana Gheorghita − *Department of Chemistry, DICUS, University of Florence, Sesto Fiorentino (FI) 50019, Italy; CeRM/CIRMMP, University of Florence, Sesto Fiorentino (FI) 50019, Italy; Giotto Biotech, S.R.L, Sesto Fiorentino (FI) 50019, Italy*

Giulia Licciardi − *Department of Chemistry, DICUS, University of Florence, Sesto Fiorentino (FI) 50019, Italy; CeRM/CIRMMP, University of Florence, Sesto Fiorentino (FI) 50019, Italy*

Daniela Eloisa Capialbi − *Department of Chemistry, DICUS, University of Florence, Sesto Fiorentino (FI) 50019, Italy*

Valerio Zullo − *Department of Chemistry, DICUS, University of Florence, Sesto Fiorentino (FI) 50019, Italy*

Andrea Sodini − *Department of Chemistry, DICUS, University of Florence, Sesto Fiorentino (FI) 50019, Italy*

Complete contact information is available at:
https://pubs.acs.org/10.1021/acs.biomac.3c00893

Notes

The authors declare no competing financial interest.

■ REFERENCES

(1) Booth, J. S.; Toapanta, F. R. B and T Cell Immunity in Tissues and Across the Ages. *Vaccines* **2021**, *9* (1), 24.

(2) Freud, A. G.; Caligiuri, M. A. Human Natural Killer Cell Development. *Immunol. Rev.* **2006**, *214*, 56−72.

(3) Huntington, N. D.; Cursons, J.; Rautela, J. The Cancer-Natural Killer Cell Immunity Cycle. *Nat. Rev. Cancer* **2020**, *20* (8), 437−454.

(4) Ouyang, Z.; Gao, Y.; Yang, R.; Shen, M.; Shi, X. Genetic Engineering of Dendritic Cells Using Partially Zwitterionic Dendrimer-Entrapped Gold Nanoparticles Boosts Efficient Tumor Immunotherapy. *Biomacromolecules* **2022**, *23* (3), 1326−1336.

(5) Chen, X.; Jiang, Z.; Lin, Y.; Yu, C.; Nie, X.; Xu, G.; Xu, W.; Jiang, Y.; Luan, Y. Tumor Lysates-Constructed Hydrogel to Potentiate Tumor Immunotherapy. *J. Controlled Release* **2023**, *358*, 345−357.

(6) Schreiber, R. D.; Old, L. J.; Smyth, M. J. Cancer Immunoediting: Integrating Immunity's Roles in Cancer Suppression and Promotion. *Science* **2011**, *331* (6024), 1565−1570.

(7) Francisco, L. M.; Sage, P. T.; Sharpe, A. H. The PD-1 Pathway in Tolerance and Autoimmunity. *Immunol. Rev.* **2010**, *236*, 219−242.

(8) Freeman, G. J.; Long, A. J.; Iwai, Y.; Bourque, K.; Chernova, T.; Nishimura, H.; Fitz, L. J.; Malenkovich, N.; Okazaki, T.; Byrne, M. C.; Horton, H. F.; Fouser, L.; Carter, L.; Ling, V.; Bowman, M. R.; Carreno, B. M.; Collins, M.; Wood, C. R.; Honjo, T. Engagement of the PD-1 Immunoinhibitory Receptor by a Novel B7 Family Member Leads to Negative Regulation of Lymphocyte Activation. *J. Exp. Med.* **2000**, *192* (7), 1027−1034.

(9) Iwai, Y.; Ishida, M.; Tanaka, Y.; Okazaki, T.; Honjo, T.; Minato, N. Involvement of PD-L1 on Tumor Cells in the Escape from Host Immune System and Tumor Immunotherapy by PD-L1 Blockade. *Proc. Natl. Acad. Sci. U.S.A.* **2002**, *99* (19), 12293−12297.

(10) Topalian, S. L.; Hodi, F. S.; Brahmer, J. R.; Gettinger, S. N.; Smith, D. C.; McDermott, D. F.; Powderly, J. D.; Carvajal, R. D.; Sosman, J. A.; Atkins, M. B.; Leming, P. D.; Spigel, D. R.; Antonia, S. J.; Horn, L.; Drake, C. G.; Pardoll, D. M.; Chen, L.; Sharfman, W. H.; Anders, R. A.; Taube, J. M.; McMiller, T. L.; Xu, H.; Korman, A. J.; Jure-Kunkel, M.; Agrawal, S.; McDonald, D.; Kollia, G. D.; Gupta, A.; Wigginton, J. M.; Sznol, M. Safety, Activity, and Immune Correlates of Anti-PD-1 Antibody in Cancer. *N. Engl. J. Med.* **2012**, *366* (26), 2443−2454.

(11) Brahmer, J.; Reckamp, K. L.; Baas, P.; Crinò, L.; Eberhardt, W. E. E.; Poddubskaya, E.; Antonia, S.; Pluzanski, A.; Vokes, E. E.; Holgado, E.; Waterhouse, D.; Ready, N.; Gainor, J.; Arén Frontera, O.; Havel, L.; Steins, M.; Garassino, M. C.; Aerts, J. G.; Domine, M.; Paz-Ares, L.; Reck, M.; Baudelet, C.; Harbison, C. T.; Lestini, B.; Spigel, D. R. Nivolumab versus Docetaxel in Advanced Squamous-Cell Non-Small-Cell Lung Cancer. *N. Engl. J. Med.* **2015**, *373* (2), 123−135.

(12) Liu, K.; Tan, S.; Chai, Y.; Chen, D.; Song, H.; Zhang, C. W.-H.; Shi, Y.; Liu, J.; Tan, W.; Lyu, J.; Gao, S.; Yan, J.; Qi, J.; Gao, G. F. Structural Basis of Anti-PD-L1 Monoclonal Antibody Avelumab for Tumor Therapy. *Cell Res.* **2017**, *27* (1), 151−153.

(13) Collins, J. M.; Gulley, J. L. Product Review: Avelumab, an Anti-PD-L1 Antibody. *Hum. Vaccines Immunother.* **2019**, *15* (4), 891−908.

(14) Boisgerault, N.; Bertrand, P. Inside PD-1/PD-L1,2 with Their Inhibitors. *Eur. J. Med. Chem.* **2023**, *256*, 115465.

(15) Zwergel, C.; Fioravanti, R.; Mai, A. PD-L1 Small-Molecule Modulators: A New Hope in Epigenetic-Based Multidrug Cancer Therapy? *Drug Discovery Today* **2023**, *28* (2), 103435.

(16) Maute, R. L.; Gordon, S. R.; Mayer, A. T.; McCracken, M. N.; Natarajan, A.; Ring, N. G.; Kimura, R.; Tsai, J. M.; Manglik, A.; Kruse, A. C.; Gambhir, S. S.; Weissman, I. L.; Ring, A. M. Engineering High-Affinity PD-1 Variants for Optimized Immunotherapy and Immuno-PET Imaging. *Proc. Natl. Acad. Sci. U.S.A.* **2015**, *112* (47), E6506−E6514.

(17) Zak, K. M.; Kitel, R.; Przetocka, S.; Golik, P.; Guzik, K.; Musielak, B.; Dömling, A.; Dubin, G.; Holak, T. A. Structure of the Complex of Human Programmed Death 1, PD-1, and Its Ligand PD-L1. *Structure* **2015**, *23* (12), 2341−2348.

(18) Pascolutti, R.; Sun, X.; Kao, J.; Maute, R. L.; Ring, A. M.; Bowman, G. R.; Kruse, A. C. Structure and Dynamics of PD-L1 and an Ultra-High-Affinity PD-1 Receptor Mutant. *Structure* **2016**, *24* (10), 1719−1728.

(19) Lin, H.; Hong, H.; Wang, J.; Li, C.; Zhou, Z.; Wu, Z. Rhamnose Modified Bovine Serum Albumin as a Carrier Protein Promotes the Immune Response against sTn Antigen. *Chem. Commun.* **2020**, *56* (90), 13959−13962.

(20) Hossain, M. K.; Vartak, A.; Karmakar, P.; Sucheck, S. J.; Wall, K. A. Augmenting Vaccine Immunogenicity through the Use of Natural Human Anti-Rhamnose Antibodies. *ACS Chem. Biol.* **2018**, *13* (8), 2130−2142.

(21) Kuhaudomlarp, S.; Cerofolini, L.; Santarsia, S.; Gillon, E.; Fallarini, S.; Lombardi, G.; Denis, M.; Giuntini, S.; Valori, C.; Fragai, M.; Imberty, A.; Dondoni, A.; Nativi, C. Fucosylated Ubiquitin and Orthogonally Glycosylated Mutant A28C: Conceptually New Ligands for Burkholderia Ambifaria Lectin (BambL). *Chem. Sci.* **2020**, *11* (47), 12662−12670.

(22) Zhang, H.; Wang, B.; Ma, Z.; Wei, M.; Liu, J.; Li, D.; Zhang, H.; Wang, P. G.; Chen, M. L-Rhamnose Enhances the Immunogenicity of Melanoma-Associated Antigen A3 for Stimulating Antitumor Immune Responses. *Bioconjugate Chem.* **2016**, *27* (4), 1112−1118.

(23) Boyerinas, B.; Jochems, C.; Fantini, M.; Heery, C. R.; Gulley, J. L.; Tsang, K. Y.; Schlom, J. Antibody-Dependent Cellular Cytotoxicity Activity of a Novel Anti-PD-L1 Antibody Avelumab (MSB0010718C) on Human Tumor Cells. *Cancer Immunol. Res.* **2015**, *3* (10), 1148−1157.

(24) van Zundert, G. C. P.; Rodrigues, J. P. G. L. M.; Trellet, M.; Schmitz, C.; Kastritis, P. L.; Karaca, E.; Melquiond, A. S. J.; van Dijk, M.; de Vries, S. J.; Bonvin, A. M. J. J. The HADDOCK2.2 Web Server: User-Friendly Integrative Modeling of Biomolecular Complexes. *J. Mol. Biol.* **2016**, *428* (4), 720−725.

(25) Rizzo, D.; Cerofolini, L.; Giuntini, S.; Iozzino, L.; Pergola, C.; Sacco, F.; Palmese, A.; Ravera, E.; Luchinat, C.; Baroni, F.; Fragai, M. Epitope Mapping and Binding Assessment by Solid-State NMR Provide a Way for the Development of Biologics under the Quality by Design Paradigm. *J. Am. Chem. Soc.* **2022**, *144* (22), 10006−10016.

(26) Laveglia, V.; Giachetti, A.; Cerofolini, L.; Haubrich, K.; Fragai, M.; Ciulli, A.; Rosato, A. Automated Determination of Nuclear Magnetic Resonance Chemical Shift Perturbations in Ligand Screening Experiments: The PICASSO Web Server. *J. Chem. Inf. Model.* **2021**, *61* (12), 5726−5733.

(27) Holz, E.; Darwish, M.; Tesar, D. B.; Shatz-Binder, W. A Review of Protein- and Peptide-Based Chemical Conjugates: Past, Present, and Future. *Pharmaceutics* **2023**, *15* (2), 600.

(28) Zaman, R.; Islam, R. A.; Ibnat, N.; Othman, I.; Zaini, A.; Lee, C. Y.; Chowdhury, E. H. Current Strategies in Extending Half-Lives of Therapeutic Proteins. *J. Controlled Release* **2019**, *301*, 176−189.

(29) Ginn, C.; Khalili, H.; Lever, R.; Brocchini, S. PEGylation and Its Impact on the Design of New Protein-Based Medicines. *Future Med. Chem.* **2014**, *6* (16), 1829−1846.

(30) Johansson, E. M. V.; Crusz, S. A.; Kolomiets, E.; Buts, L.; Kadam, R. U.; Cacciarini, M.; Bartels, K.-M.; Diggle, S. P.; Cámara, M.; Williams, P.; Loris, R.; Nativi, C.; Rosenau, F.; Jaeger, K.-E.; Darbre, T.; Reymond, J.-L. Inhibition and Dispersion of Pseudomonas Aeruginosa Biofilms by Glycopeptide Dendrimers Targeting the Fucose-Specific Lectin LecB. *Chem. Biol.* **2008**, *15* (12), 1249−1257.

(31) Larson, D. P.; Heathcock, C. H. Total Synthesis of Tricolorin A. *J. Org. Chem.* **1997**, *62* (24), 8406−8418.

(32) Passariello, M.; D'Alise, A. M.; Esposito, A.; Vetrei, C.; Froechlich, G.; Scarselli, E.; Nicosia, A.; De Lorenzo, C. Novel Human Anti-PD-L1 mAbs Inhibit Immune-Independent Tumor Cell Growth and PD-L1 Associated Intracellular Signalling. *Sci. Rep.* **2019**, *9* (1), 13125.

(33) Wang, Y.; Han, H.; Zhang, F.; Lv, T.; Zhan, P.; Ye, M.; Song, Y.; Liu, H. Immune Checkpoint Inhibitors Alone vs Immune Checkpoint Inhibitors-Combined Chemotherapy for NSCLC Patients with High PD-L1 Expression: A Network Meta-Analysis. *Br. J. Cancer* **2022**, *127* (5), 948−956.

(34) Shi, L.; Chen, S.; Yang, L.; Li, Y. The Role of PD-1 and PD-L1 in T-Cell Immune Suppression in Patients with Hematological Malignancies. *J. Hematol. Oncol.* **2013**, *6*, 74.

(35) Liu, C.; Lu, Z.; Xie, Y.; Guo, Q.; Geng, F.; Sun, B.; Wu, H.; Yu, B.; Wu, J.; Zhang, H.; Yu, X.; Kong, W. Soluble PD-1-Based Vaccine Targeting MUC1 VNTR and Survivin Improves Anti-Tumor Effect. *Immunol. Lett.* **2018**, *200*, 33−42.

(36) Kondělková, K.; Vokurková, D.; Krejsek, J.; Borská, L.; Fiala, Z.; Andrýs, C. Regulatory T Cells (TREG) and Their Roles in Immune System with Respect to Immunopathological Disorders. *Acta Med.* **2010**, *53* (2), 73−77.

(37) Han, J. M.; Patterson, S.; Levings, M. The Role of the PI3K Signaling Pathway in CD4+ T Cell Differentiation and Function. *Front. Immunol.* **2012**, *3*, 245.

(38) Sheppard, K.-A.; Fitz, L. J.; Lee, J. M.; Benander, C.; George, J. A.; Wooters, J.; Qiu, Y.; Jussif, J. M.; Carter, L. L.; Wood, C. R.; Chaudhary, D. PD-1 inhibits T-cell receptor induced phosphorylation of the ZAP70/CD3ζ signalosome and downstream signaling to PKCθ. *FEBS Lett.* **2004**, *574* (1−3), 37−41.

Supplementary Information

Site-selective functionalized PD-1 mutant for a modular immunological activity against cancer cells.

Silvia Fallarini,[†] Linda Cerofolini,[‡,#] Maria Salobehaj, [‡,#] Domenico Rizzo, [‡,#] Giulia Roxana Gheorghita, [‡,#,§] Giulia Licciardi,[‡,#] Daniela Eloisa Capialbi,[‡] Valerio Zullo,[‡] Andrea Sodini,[‡] Cristina Nativi* [‡] and Marco Fragai* [‡,#].

[†] Department of Pharmaceutical Sciences, DSF, University of Piemonte Orientale, Largo Donegani 2 – 28100 Novara (NO), Italy

[‡] Department of Chemistry, DICUS, University of Florence, via della Lastruccia 3,13 – 50019 Sesto F.no (FI), Italy

[#] CeRM/CIRMMP, University of Florence, via L. Sacconi,6 – 50019 Sesto F.no (FI), Italy

[§] Giotto Biotech, S.R.L, Via Madonna del piano 6, Sesto Fiorentino, Florence 50019, Italy.

Table of Content

Synthesis of compound 3:

Allyl-TMS (690 µL, 4.34 mmol), BF$_3$ · Et$_2$O (1.2 mL, 4.34 mmol) and TMSOTf (20 µL, 0.11 mmol) were added to a solution of peracetylated L-rhamnose (720 mg, 2.17 mmol) in dry CH$_3$CN (4 mL) at 0°C. The reaction mixture was stirred at 0°C for 5 hours, then neutralized with Et$_2$O (5 mL) and NaHCO$_3$ (s.s., 10 mL), diluted with EtOAc, washed with H$_2$O (2x) and brine (2x). The organic layer was dried over anhydrous Na$_2$SO$_4$ and the solvent removed under vacuum. The crude mixture was purified by flash chromatography on silica gel (PE/EtOAc : 8/2) to yield **3** as a colourless oil (450 mg, 66 % yield).

MW: (C$_{15}$H$_{22}$O$_7$) 314.33 g/mol.

ESI-MS: *m/z* (%) 337 (100) [M+Na]$^+$.

¹H NMR: (500 MHz, CDCl$_3$) δ: 5.79 (ddt, *J* $_{b-c\ trans}$ = 17.1 Hz, *J* $_{b-c\ cis}$ = 10.1 Hz, *J* $_{b-a}$ = 6.95 Hz, 1H, H-b), 5.16 – 5.12 (m, 4H, H-3 + H-2 + H-c), 5.06 – 5.01 (m, 1H, H-4), 3.99 – 3.93 (m, 1H, H-1), 3.78 (dq, *J* $_{5-4}$ = 8.5 Hz, *J* $_{5-6}$ = 6.3 Hz 1H, H-5), 2.58 – 2.51 (m, 1H, 1H of H-a) 2.45 – 2.38 (m, 1H, 1H of H-a), 2.12 (s, 3H, Ac), 2.06 (s, 3H, Ac), 2.01 (s, 3H, Ac), 1.23 (d, *J* $_{6-5}$ = 6.3 Hz, 3H, H-6) ppm.

¹³C NMR: (125 MHz, CDCl$_3$) δ: 170.3 (C$_q$, CO), 170.1 (C$_q$, CO), 169.9 (C$_q$, CO), 132.9 (CH, C-b), 118.2 (CH$_2$, C-c), 74.4 (CH, C-1), 71.5 (CH, C-4), 70.4 (CH, C-3), 69.1 (CH, C-2), 68.2 (CH, C-5), 33.7 (CH$_2$, C-a), 20.9 (CH$_3$, Ac), 20.8 (CH$_3$, Ac), 20.7 (CH$_3$, Ac), 17.6 (CH$_3$, C-6) ppm.

Synthesis of compound 4:
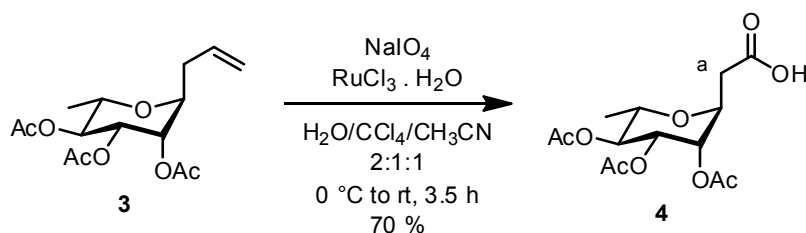
NaIO$_4$ (1.14 g, 5.34 mmol) and RuCl$_3$·H$_2$O (12 mg, 0.053 mmol) were added to a solution of **3** (420 mg, 1.33 mmol) in the mixture of solvents H$_2$O:CCl$_4$:CH$_3$CN = 2:1:1 (14 mL) at 0°C. The reaction mixture was stirred at room temperature for 3.5 hours, after which it was filtered on #4 frit filtered on a Celite® pad, washing with H$_2$O (2x) and NaHCO$_3$ (s.s. 2x). The mixture of solvents was transferred in a separating funnel and the aqueous layer was washed with DCM (3 times). The combined organic phases were extracted with H$_2$O (2x) and NaHCO$_3$ (s.s. 2x). The aqueous layers were pulled together, acidified to pH=4 by addition of conc. HCl, then reextracted with DCM (3x). The organic phase was dried over Na$_2$SO$_4$ and solvents were removed in vacuo to obtain 300 mg of crude **4** that was progressed to the next step without further purification.

MW: (C$_{14}$H$_{20}$O$_9$) 332.31 g/mol.

ESI-MS: *m/z* (%) 331 (100) [M - H]$^-$.

¹H NMR: (500 MHz, CDCl$_3$) δ: 5.23 (dd, 1H, *J* $_{2-3}$ = 3.4 Hz, *J* $_{3-4}$ = 7.5 Hz, H-3), 5.17 (dd, 1H, *J* $_{1-2}$ = 4.9 Hz, *J* $_{2-3}$ = 3.4 Hz, H-2), 5.00 (dd, 1H, *J* $_{4-3}$ = 7.5 Hz, *J* $_{4-5}$ = 6.5 Hz, H-4), 4.48 – 4.42 (m, 1H, H-1), 3.96 – 3.89

(aquint, 1H, J = 6.5 Hz, H-5), 2.82 – 2.76 (A part of an ABX system, J_{a-b} = 15.5 Hz, J_{a-x} = 9.6 Hz, 1H, 1H of H-a), 2.70 – 2.66 (B part of an ABX system, 1H, J_{b-a} = 15.5 Hz, J_{b-x} = 4.6 Hz, one H of H-a), 2.12 (s, 3H, Ac), 2.11 (s, 3H, Ac), 2.08 (s, 3H, Ac), 1.35 (d, J_{6-5} = 6.6 Hz, 3H, C-6) ppm.

¹³C NMR: (125 MHz, CDCl₃) δ: 174.5 (C_q, CO), 170.1 (C_q, CO), 169.9 (C_q, CO), 169.9 (C_q, CO), 71.4 (CH, C-4), 69.8 (CH, C-5), 69.7 (CH, C-2), 69.3 (CH, C-1), 68.5 (CH, C-3), 35.3 (CH_2, C-a), 20.9 (CH_3, Ac), 20.8 (CH_3, Ac), 20.7 (CH_3, Ac), 16.9 (CH_3, C-6) ppm.

Synthesis of compound 6:
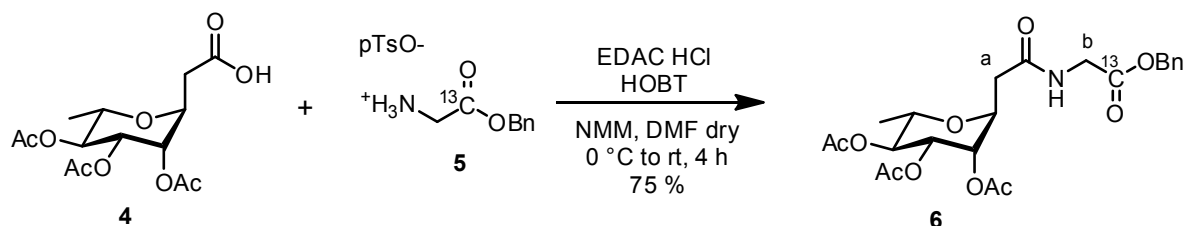
To a solution of **4** (280 mg, 0.84 mmol) in dry DMF (3.8 mL), EDAC·HCl (315 mg, 2.02 mmol) and HOBT (250 mg, 1.85 mmol) were added at 0 °C (solution A). The solution was stirred at 0 °C for 30 minutes. To a solution of **5** (345 mg, 1.01 mmol) in dry DMF (6.6 mL), NMM (333 µL, 3.03 mmol) was added at 0 °C (solution B). The solution was stirred at 0 °C for 20 minutes. Solution B was then added to solution A and the reaction mixture stirred at 0 °C for 40 minutes and at room temperature for 3 hours. The mixture was then diluted with EtOAc and washed with HCl 3% (3x), NaHCO₃ (s.s., 3x) and brine (3x). The organic layer was dried over anhydrous Na₂SO₄ and the organic solvent removed under vacuum. The crude was purified by flash chromatography on silica gel (PE/EtOAc : 45/55) to yield compound **6** as a colourless oil (360 mg, 75 % yield).

MW: (C_{22}¹³$CH_{29}NO_{10}$) 480.46 g/mol.
ESI-MS: *m/z* (%) 480 (100) [M +Na]⁺.
¹H NMR: (500 MHz, CDCl₃) δ: 7.42 – 7.33 (m, 5H, Ph), 6.74 (bs, 1H, NH), 5.24 (dd, J_{3-4} = 6.6 Hz, J_{3-2} = 3.4 Hz, 1H, H-3), 5.20 (d, J = 3.2 Hz, 2H, CH₂-Ph) 5.11 (dd, J_{2-1} = 6.1 Hz, J_{2-3} = 3.4 Hz, 1H, H-2), 4.95 (dd, J_{4-3} = 6.6 Hz, J_{4-5} = 5.3 Hz, 1H, H-4), 4.41 (ddd, J_{1-Ha} = 9.8 Hz, J_{1-2} = 6.1 Hz, J_{1-Ha} = 3.7 Hz, 1H, H-1), 4.14 – 4.05 (m, 2H, H-b), 3.99 – 3.93 (m, 1H, H-5), 2.66 – 2.60 (A part of ABX system, J_{a-b} = 15.5 Hz, J_{a-x} = 9.8 Hz, 1H, 1H of H-a), 2.58 – 2.53 (B part of ABX system, J_{b-a} = 15.5 Hz, J_{b-x} = 3.7 Hz, 1H, 1H of H-a), 2.10 (s, 3H, Ac), 2.08 (s, 3H, Ac), 2.08 (s, 3H, Ac), 1.38 (d, J_{6-5} = 6.6 Hz, 3H, H-6) ppm.

¹³C NMR: (125 MHz, CDCl₃) δ: 169.9 (C_q, CO), 169.8 (C_q, CO), 169.7 (C_q, CO), 169.7 (¹³C_q, CO), 169.4 (C_q, CO), 135.1, 128.7, 128.6, 128.4, 71.5 (CH, C-4), 70.3 (CH, C-5), 69.5 (CH, C-2), 68.7 (CH, C-3), 68.2 (CH, C-1), 67.2 (CH₂, OBn), 41.5 (d, J_{c-c} = 61.8 Hz, CH₂, C-b), 36.8 (CH₂, C-a), 20.9 (CH_3, Ac), 20.8 (CH_3, Ac), 20.8 (CH_3, Ac), 16.7 (CH_3, C-6) ppm.

Synthesis of compound 9:
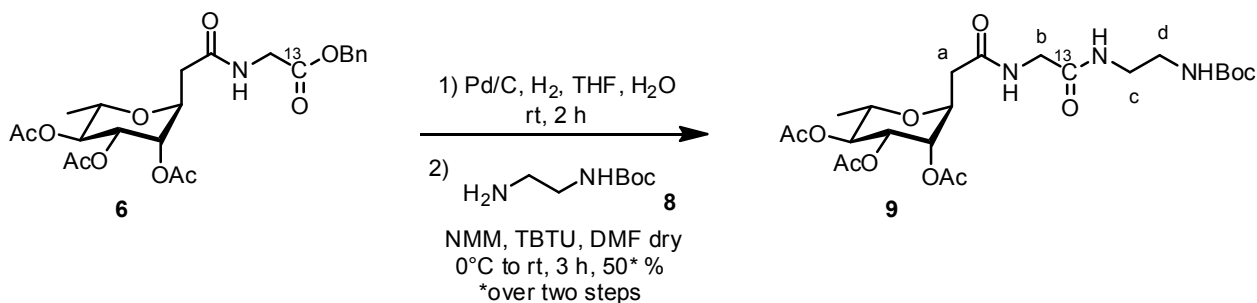
Pd/C (66 mg, 106.42 mmol) was added to a solution of **6** (270 mg, 0.56 mmol) in THF (7 mL) and H_2O (30 µL). The suspension was stirred at room temperature under H_2 atmosphere for 2 hours. The mixture was then filtered on a Celite® pad, washing with THF and the solvent was removed under vacuo. The crude compound was then resolubilized in DMF (2.7 mL), then TBTU (328 mg, 1.02 mmol), NMM (156 mg, 1.53 mmol) and compound **8** (106 mg, 0.66 mmol) were added at 0°C. The mixture was stirred at room temperature for 3 hours then diluted with EtOAc and washed with HCl 3% (3x), $NaHCO_3$ (s.s. 3x) and brine (3x). The organic layer was dried over Na_2SO_4 and the organic solvent evaporated to dryness. The crude was purified via flash chromatography on silica gel (CH_2Cl_2:CH_3OH / 95:5), to yield compound **9** as a pale yellow oil (140 mg, 50 % yield over two steps).

MW: ($C_{22}{}^{13}CH_{37}N_3O_{11}$) 532.55 g/mol.

ESI-MS: *m/z* (%) 555 (100) [M + Na]$^+$.

^{1}H NMR: (500 MHz, CDCl$_3$) δ: 7.34 (bs, 1H, NH), 7.16-7.10 (m, 1H, NH), 5.28 (bs, 1H, NH), 5.19 (dd, J_{3-4} = 6.6 Hz, J_{3-2} = 3.4 Hz, 1H, H-3), 5.14 (dd, J_{2-1} = 6.1 Hz, J_{2-3} = 3.4 Hz, 1H, H-2), 4.97 (dd, J_{4-3} = 6.6 Hz, J_{4-5} = 5.3 Hz, 1H, H-4), 4.43 – 4.37 (m, 1H, H-1), 3.95 – 3.88 (m, 3H, H-5 + H-b), 3.39 – 3.32 (m, 2H, H-c), 3.27 – 3.21 (m, 2H, H-d), 2.74 – 2.67 (A part of an ABX system, J_{a-b} = 15.0 Hz, J_{a-x} = 9.6 Hz, 1H, 1H of H-a), 2.61 – 2.53 (B part of ABX system, J_{b-a} = 15.0 Hz, J_{b-x} = 4.7 Hz, 1H, 1H of H-a), 2.08 (s, 3H, Ac), 2.07 (s, 3H, Ac), 2.03 (s, 3H, Ac), 1.41 (s, 9H, tBu), 1.31 (d, J_{6-5} = 6.6 Hz, 3H, H-6) ppm.

^{13}C NMR: (125 MHz, CDCl$_3$) δ: 170.4 (C$_q$, CO), 170.1 (C$_q$, CO), 169.9 (C$_q$, CO), 169.9 (C$_q$, CO), 169.8 (C$_q$, CO), 169.3 (^{13}C$_q$, CO), 79.7 (C$_q$), 71.4 (CH, C-4), 69.9 (CH, C-1), 69.7 (CH, C-5), 68.7 (CH, C-2), 68.5 (CH, C-3), 43.15 (d, J_{c-c} = 52.3 Hz, CH$_2$, C-b), 40.6 (CH$_2$, C-c), 40.2 (CH$_2$, C-d), 36.7 (CH$_2$, C-a), 28.4 (3CH$_3$, tBu), 20.9 (CH$_3$, Ac), 20.8 (CH$_3$, Ac), 20.7 (CH$_3$, Ac), 17.0 (CH$_3$, C-6) ppm.

Synthesis of compound 10:
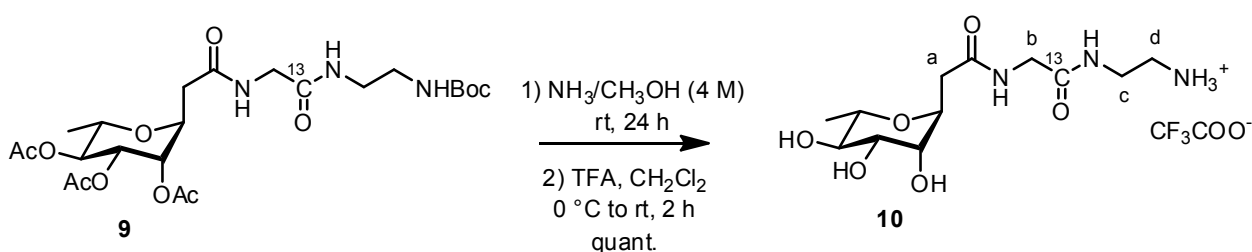
Compound **9** (120 mg, 0.22 mmol) was dissolved in 0.5 mL of a 4 M solution of NH$_3$ in CH$_3$OH. The reaction mixture was stirred at room temperature for 24 hours then evaporated to dryness. The crude compound was then resuspended in anhydrous CH$_2$Cl$_2$ (1.6 mL) and TFA (120 µL, 1.56 mmol) was added dropwise at 0 °C. The solution was stirred at room temperature for 2 hours then it was evaporated to dryness to give crude **10** (140 mg) which was used without further purification.

MW: ($C_{13}{}^{13}CH_{24}F_3N_3O_8$) 420.35 g/mol.

ESI-MS: *m/z* (%) 307 (100) [M + H]$^+$.

^{1}H NMR: (500 MHz, CD$_3$OD) δ: 4.31 (ddd, J_{1-Ha} = 9.1 Hz, J_{1-2} = 5.4 Hz, J_{1-Ha} = 3.7 Hz, 1H, H-1), 3.90 – 3.85 (m, 2H, H-b), 3.80 (at, J_{2-H} = 3.6 Hz, 1H, H-2), 3.69 (dd, 1H, J_{3-4} = 6.6 Hz, J_{3-2} = 3.4 Hz, H-3), 3.67 – 3.61 (m, 1H, H-5), 3.53 – 3.47 (m, 3H, H-4+H-c), 3.08 (t, J_{d-c} = 5.8 Hz, 2H, H-d), 2.75 – 2.69 (A part of an ABX system, J_{a-b} = 14.5 Hz, J_{a-x} = 9.1 Hz, 1H, 1H of H-a), 2.60 – 2.54 (B part of an ABX system, J_{b-a} = 14.5 Hz, J_{b-x} = 5.4 Hz, 1H, 1H of H-a), 1.30 (d, J_{6-5} = 6.3 Hz, 3H, H-6) ppm.

13C NMR: (125 MHz, CD$_3$OD) δ: 172.3 (C$_q$, CO), 170.4 (¹³C$_q$, CO), 72.7 (CH, C-1), 71.1 (CH, C-4), 71.1 (CH, C-5), 71.1 (CH, C-3), 70.8 (CH, C-2), 42.4 (d, $J_{c\text{-}c}$ = 52.6 Hz, CH$_2$, C-b), 39.6 (CH$_2$, C-d), 36.6 (CH$_2$, C-c), 36.2 (CH$_2$, C-a), 16.7 (CH$_3$, C-6) ppm.

Synthesis of compound 1:
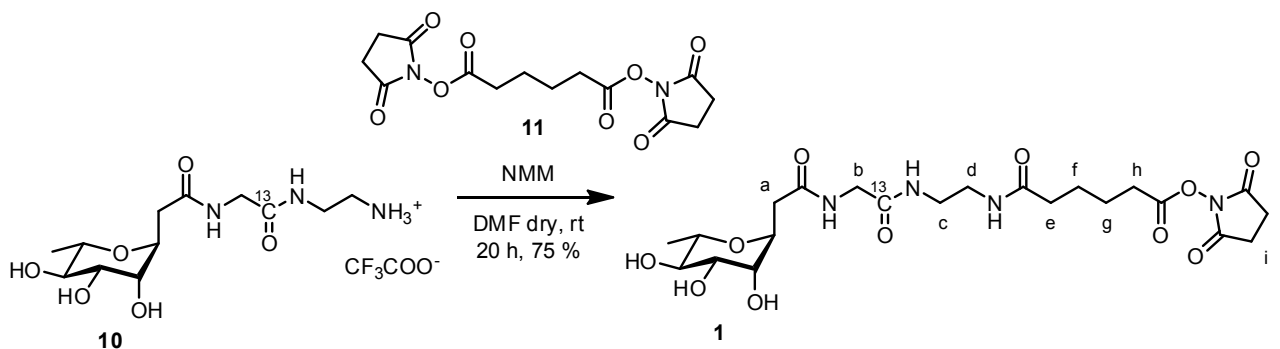
NMM (58 mg, 0.58 mmol) was added to a solution of **10** (115 mg, 0.15 mmol) in dry DMF (1.6 mL). After 20 minutes, compound **11** (220 mg, 0.64 mmol) [1] was added. The reaction mixture was stirred at room temperature for 20 hours then the suspension obtained was filtered on #4 frit and washed with DMF (2x). The solid (unreacted linker **11**) was discarded, while the organic phase was evaporated to dryness. The crude was purified by precipitation with EtOAc, the precipitate was filtered on #4 frit, washed with EtOAc (2x) and dried under vacuum affording the desired compound **1** (65 mg, 70 % yield over three steps).

MW: (C$_{21}$¹³CH$_{34}$N$_4$O$_{11}$) 531.52 g/mol.

ESI-MS: *m/z* (%) 554 (100) [M + Na]$^+$, 570 (100) [M + K]$^+$.

[α]$_D^{22}$ = +2.9 (c=0.1 in CH$_3$OH).

1H NMR: (500 MHz, CD$_3$OD) δ: 4.31 (ddd, $J_{1\text{-}Ha}$ 9.1 Hz, $J_{1\text{-}2}$ 5.3 Hz, $J_{1\text{-}Ha}$ 3.7 Hz, 1H, H-1), 3.88 – 3.82 (m, 2H, H-b), 3.79 (at, $J_{2\text{-}H}$ = 3.6 Hz, 1H, H-2) 3.69 (dd, 1H, $J_{3\text{-}2}$ = 3.4 Hz, $J_{3\text{-}4}$ = 6.6 Hz, H-3), 3.67 – 3.61 (m, 1H, H-5) 3.49 (t, $J_{4\text{-}3}$ = 6.6 Hz, 1H, H-4), 3.31 (m, 4H, H-c, H-d), 2.86 (s, 4H, H-i+H-l), 2.71 – 2.76 (m, 3H, H-e + 1H of H-a), 2.60 – 2.54 (B part of an ABX system, $J_{b\text{-}a}$ 14.5 Hz, $J_{b\text{-}x}$ 5.5 Hz, 1H, H-a) 2.28 – 2.24 (m, 2H, H-h), 1.81 – 1.69 (m, 4H, H-f + H-g), 1.30 (d, $J_{6\text{-}5}$ = 6.3 Hz, 3H, CH$_3$-6) ppm.

13C NMR: (125 MHz, CD$_3$OD) δ: 174.6 (C$_q$, CO), 172.3 (C$_q$, CO), 170.6 (C$_q$, CO), 170.5 (¹³C$_q$, CO), 168.7 (C$_q$, CO), 72.7 (CH, C-1), 71.0 (CH, C-4), 71.0 (CH, C-5), 71.0 (CH, C-3), 70.7 (CH, C-2), 42.5 (d, $J_{c\text{-}c}$ = 52.6 Hz, CH$_2$, C-b), 38.8 (CH$_2$, C-d), 38.4 (CH$_2$, C-c), 36.30 (CH$_2$, C-a), 35.0 (CH$_2$, C-h), 29.8 (CH$_2$, C-e), 24.8 (CH$_2$, C-i + C-l), 24.5 (CH$_2$, C-f), 23.8 (CH$_2$, C-g), 16.6 (CH$_3$, C-6) ppm.

Synthesis of compound 12:
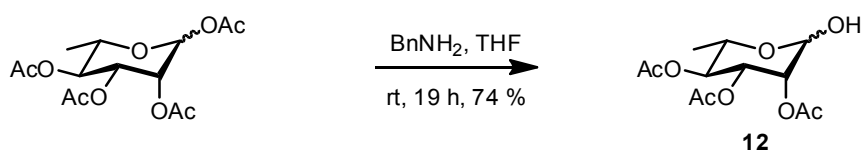
Benzylamine (1.6 mL, 14.5 mmol) was added to a solution of peracetylated rhamnose (969 mg, 2.9 mmol) in THF (16 mL). The mixture was stirred at room temperature for 19 hours after which a 1 M solution of HCl (60 mL) was added and stirred for 30 minutes. The water phase was then extracted with CH$_2$Cl$_2$ (x4), the

organic layer was dried over anhydrous Na_2SO_4 and concentrated under vacuum. The crude mixture (1.15 g) was purified by flash chromatography on silica gel (PE/EtOAc : 6/4), yielding **12** as a white solid (623 mg, 74 % yield, α anomer 90 % - β anomer 10 %).

Characterization of α anomer:

M.W.: ($C_{26}H_{38}O_{17}$) 622.57 g/mol.

^{1}H NMR: (α anomer) (500 MHz, $CDCl_3$) δ: 5.35 (dd, J_{3-4} = 10.0 Hz, J_{3-2} = 3.4 Hz, 1H, H-3), 5.25 (dd, J_{2-3} = 3.4 Hz, J_{2-1} = 1.8 Hz, 1H, H-2), 5.14 (dd, J_{1-OH} = 3.9 Hz, J_{1-2} = 1.8 Hz, 1H, H-1), 5.06 (t, J = 9.9 Hz, 1H, H-4), 4.12 (dq, J_{5-4} = 9.9 Hz, J_{5-6} = 6.3 Hz, 1H, H-5), 3.56 (d, J_{OH-1} = 3.9 Hz, 1H, OH), 2.14 (s, 3H, Ac), 2.04 (s, 3H, Ac), 1.98 (s, 3H, Ac), 1.20 (d, J_{6-5} = 6.3 Hz, 3H, H-6) ppm.

^{13}C NMR: (α anomer) (125 MHz, $CDCl_3$) δ: 170.5 (C_q, CO), 170.3 (C_q, CO), 170.3 (C_q, CO), 92.2 (CH, C-1), 71.3 (CH, C-4), 70.4 (CH, C-2), 69.0 (CH, C-3), 66.5 (CH, C-5), 21.1 (CH_3, Ac), 20.9 (CH_3, Ac), 20.9 (CH_3, Ac), 17.6 (CH_3, C-6) ppm.

Synthesis of compound 13:
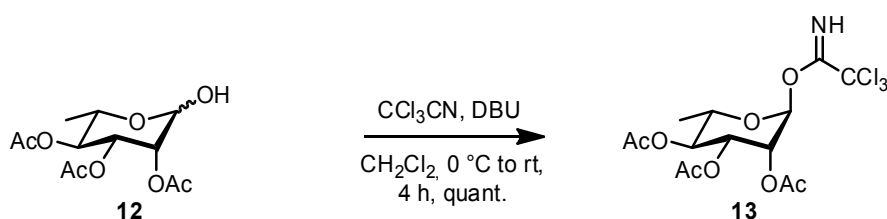
To a solution of **12** (393 mg, 1.35 mmol) in dry CH_2Cl_2 (15 mL), trichloroacetonitrile (1.0 mL, 10.0 mmol) and DBU (100 µL, 0.67 mmol) were added at 0 °C under N_2 atmosphere. The mixture was stirred at room temperature for 4 hours, then the mixture was diluted with CH_2Cl_2 (30 mL) and washed with NH_4Cl (s.s. x3), H_2O (x2) and eventually brine (x1). The organic phase was dried over Na_2SO_4 and concentrated *in vacuo* to give the crude **13** as a brown foam (679 mg, quant. yield) which was used without further purification.

M.W.: ($C_{14}H_{18}Cl_3NO_8$) 434.65 g/mol.

^{1}H NMR: (500 MHz, $CDCl_3$) δ: 8.72 (s, 1H, NH), 6.20 (d, J_{1-2} = 1.9 Hz, 1H, H-1), 5.45 (dd, J_{2-3} = 3.5 Hz, J_{2-1} = 2.0 Hz, 1H, H-2), 5.36 (dd, J_{3-4} = 10.2 Hz, J_{3-2} = 3.5 Hz, 1H, H-3), 5.17 (t, J_{4-H} = 10.0 Hz, 1H, H-4), 4.09 (dq, J_{5-4} = 10.0 Hz, J_{5-6} = 6.2 Hz, 1H, H-5), 2.18 (s, 3H, Ac), 2.07 (s, 3H, Ac), 2.00 (s, 3H, Ac), 1.27 (d, J_{6-5} = 6.2 Hz, 3H, H-6) ppm.

Synthesis of compound 15:
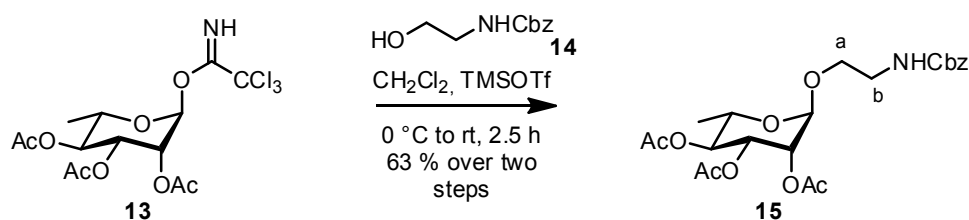
To a solution of **13** (679 mg, 1.35 mmol) and Z-ethanolamine **14** (401 mg, 2.05 mmol) in dry CH_2Cl_2 (10 mL), TMSOTf (60 µL, 0.33 mmol) was added at 0 °C under a N_2 atmosphere. The mixture was stirred at room temperature for 2.5 hours, then the reaction mixture was diluted with CH_2Cl_2 (30 mL) and washed with

H$_2$O (x3) and brine (x1). The organic phase was dried over anhydrous Na$_2$SO$_4$ and concentrated under vacuum to give the crude (995 mg), which was purified by flash chromatography on silica gel (PE/EtOAc : 6/4 to 5/5) to give **15** as a yellow oil (396 mg, 63 % yield over two steps).

M.W.: (C$_{22}$H$_{29}$NO$_{10}$) 467.47 g/mol.
ESI-MS: *m/z* (%): 490.33 (100) [M+Na]$^+$, 506.33 (35) [M+K]$^+$, 956.58 (6) [2M+Na]$^+$, 972.00 (3) [2M+K]$^+$.
[α]$_D$$^{26°C}$ = -42° (c = 0.873 g/100 mL, CHCl$_3$).

^{1}H NMR: (500 MHz, CDCl$_3$) δ: 7.39 – 7.35 (m, 4H, Ar), 7.34 – 7.28 (m, 1H, Ar), 5.28 – 5.22 (m, 2H, H-2 + H-3), 5.19 – 5.15 (m, 1H, NH), 5.11 (d, *J* = 3.4 Hz, 2H, CH$_2$-Ph), 5.06 (t, *J*$_{4-H}$ = 9.7 Hz, 1H, H-4), 4.73 (d, *J*$_{1-2}$ = 1.6 Hz, 1H, H-1), 3.83 (dq, *J*$_{5-4}$ = 9.8 Hz, *J*$_{5-6}$ = 6.3 Hz, 1H, H-5), 3.79 – 3.72 (m, 1H, 1H of H-a), 3.55 – 3.49 (m, 1H, 1H of H-a), 3.48 – 3.42 (m, 1H, 1H of H-b), 3.42 – 3.35 (m, 1H, 1H of H-b), 2.14 (s, 3H, Ac), 2.03 (s, 3H, Ac), 1.98 (s, 3H, Ac) 1.20 (d, *J*$_{6-5}$ = 6.4 Hz, 3H, H-6) ppm.
^{13}C NMR: (125 MHz, CDCl$_3$) δ: 170.3 (C$_q$, CO), 170.2 (C$_q$, CO), 170.1 (C$_q$, CO), 156.5 (C$_q$, CO), 136 (C$_q$, Ph), 128.7 (CH, Ph), 128.3 (CH, Ph), 97.7 (CH, C-1), 71.1 (CH, C-4), 69.8 (CH, C-3), 69.2 (CH, C-2), 67.4 (CH$_2$, C-a), 67.0 (CH$_2$, CH$_2$-Ph), 66.7 (CH, C-5) 40.8 (CH$_2$, C-b), 21.0 (CH$_3$, Ac), 20.9 (CH$_3$, Ac), 20.9 (CH$_3$, Ac), 17.5 (CH$_3$, C-6) ppm.

Synthesis of compound 16:

Compound **15** (393 mg, 0.85 mmol) was dissolved in 13 mL of a 4 M solution of NH$_3$ in CH$_3$OH. The mixture was stirred at room temperature for 4 hours after which the reaction mixture was evaporated to dryness and purified by flash chromatography on silica gel (CH$_2$Cl$_2$/CH$_3$OH : 9/1) to afford **16** (249 mg, 86 % yield) as a cerous solid.

M.W.: (C$_{16}$H$_{23}$NO$_7$) 341.36 g/mol.
ESI-MS: *m/z* (%): 364.33 (100) [M+Na]$^+$, 380.25 (39) [M+K]$^+$, 704.92 (29) [2M+Na]$^+$, 720.58 (4) [2M+K]$^+$.
[α]$_D$$^{26°C}$ = -43° (c = 0.913 g/100 m in CH$_3$OH).
^{1}H NMR: (500 MHz, CD$_3$OD) δ: 7.37 – 7.33 (m, 4H, Ar), 7.32 – 7.26 (m, 1H, Ar), 5.08 (s, 2H, CH$_2$-Ph), 4.68 (d, *J*$_{1-2}$ = 1.8 Hz, 1H, H-1), 4.58 (s, 1H, NH), 3.81 (dd, *J*$_{2-3}$ = 3.5 Hz, *J*$_{1-2}$ = 1.8 Hz, 1H, H-2), 3.75 – 3.69 (m, 1H, one H of H-a), 3.65 (dd, *J*$_{3-4}$ = 9.5 Hz, *J*$_{3-2}$ = 3.5, 1H, H-3), 3.58 (dq, *J*$_{5-4}$ = 9.5 Hz, *J*$_{5-6}$ = 6.3 Hz, 1H, H-5), 3.52 – 3.44 (m, 1H, one H of H-a), 3.37 (at, *J*$_{4-H}$ = 9.4 Hz, 1H, H-4), 3.35 – 3.28 (m, 2H, H-b), 1.24 (d, *J*$_{6-5}$ = 6.3 Hz, 3H, H-6) ppm.
^{13}C NMR: (125 MHz, CD$_3$OD) δ: 158.9 (C$_q$, CO), 138.3 (C$_q$, Ph), 129.5 (CH, Ph), 129.0 (CH, Ph), 128.8 (CH, Ph), 101.7 (CH, C-1), 74.0 (CH, C-4), 72.3 (CH, C-2), 69.9 (CH, C-5), 67.5 (CH$_2$, CH$_2$-Ph), 67.3 (CH2, C-a), 41.7 (CH2, C-b), 18.0 (CH$_3$, C-6) ppm.
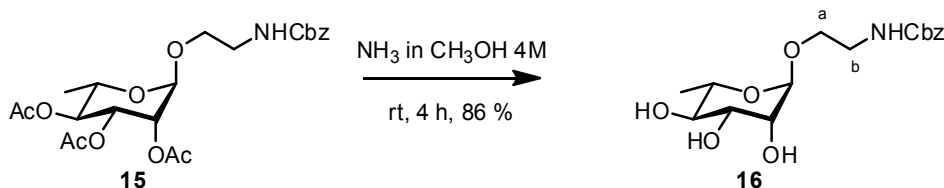
Synthesis of compound 17:
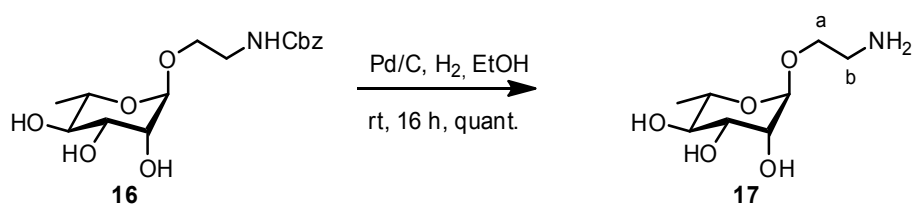
To a solution of **16** (249 mg, 0.73 mmol) in ethanol (10 mL), Pd/C (10 % wt, 189 mg) was added under a N_2 atmosphere. The reaction was stirred at room temperature, under H_2 atmosphere. After 16 h the suspension was filtered through a pad of Celite®, the solvent was removed under vacuum to give pure **17** (150 mg, quant. yield) as a cerous solid.

M.W.: ($C_8H_{17}NO_5$) 207.23 g/mol.
ESI-MS: *m/z* (%): 208.17 (100) [M+H]⁺, 230.17 (23) [M+Na]⁺.
**[α]$_D^{26°C}$ = -52° (c = 0.355 g/100 mL in CH_3OH).

¹H NMR: (500 MHz, CD_3OD) δ: 4.70 (d, J_{1-2} = 1.8 Hz, 1H, H-1), 3.83 (dd, J_{2-3} = 3.4 Hz, J_{2-1} = 1.8 Hz, 1H, H-2), 3.72 (ddd, $J_{a-a'}$ = 10.4 Hz, J_{a-b} = 6.1 Hz, $J_{a-b'}$ = 4.6 Hz, 1H, one H of H-a), 3.66 (dd J = 9.5, 3.4 Hz, 1H, H-3), 3.58 (dq, J = 9.5, 6.3 Hz, H-5), 3.45 (ddd, $J_{a-a'}$ = 10.4 Hz, J_{a-b} = 6.4 Hz, $J_{a-b'}$ = 4.6 Hz, 1H, one H of H-a), 3.38 (at, J_{4-H} = 9.5 Hz, 1H, H-4), 2.89 – 2.76 (m, 2H, H-b), 1.27 (d, J_{6-5} = 6.3 Hz, 3H, H-6) ppm.
¹³C NMR: (125 MHz, CD_3OD) δ: 101.9 (CH, C-1), 74.0 (CH, C-4), 72.4 (CH, C-3), 72.2 (CH, C-2), 69.9 (CH, C-5), 69.8 (CH_2, C-a), 42.1 (CH_2, C-b), 18.0 (CH_3, C-6) ppm.

Synthesis of compound 2:
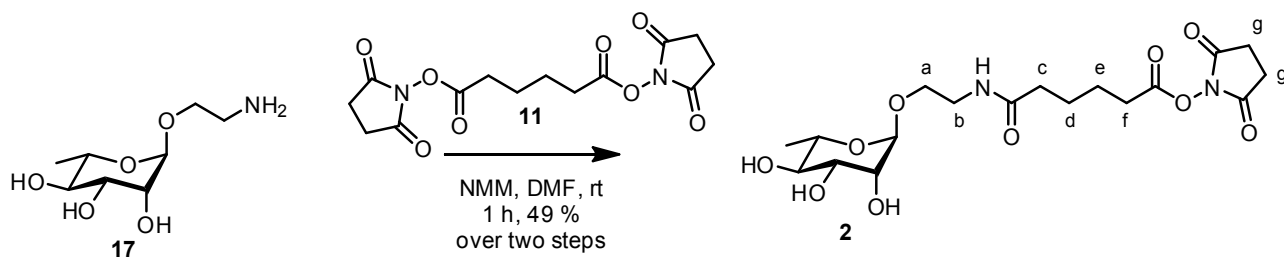
NMM (380 μL, 3.46 mmol) was added to a solution of **17** (150 mg, 0.72 mmol) in dry DMF (15 mL). After 20 minutes, **11** (695 mg, 2 mmol) was added. The mixture was stirred at room temperature for 1 hour after which the mixture was evaporated to dryness and purified via flash chromatography on silica gel (CHCl₃/ CH₃OH : 80/20) to afford **2** (153 mg, 49 % yield over two steps) as a white foam.

M.W.: ($C_{18}H_{28}N_2O_{10}$) 432.43 g/mol.
ESI-MS: *m/z* (%): 455.42 (100) [M+Na]⁺, 471.33 (8) [M+K]⁺.
**[α]$_D^{26°C}$ = -31° (c = 0.605 g/100 mL in CH_3OH).

¹H NMR: (500 MHz, CD$_3$OD) δ: 4.68 (d, J_{1-2} = 1.7 Hz, 1H, H-1), 3.81 (dd, J_{2-3} = 3.5 Hz, J_{2-1} = 1.7 Hz, 1H, H-2), 3.72 (ddd, $J_{a-a'}$ = 10.2 Hz, J_{a-b} = 6.5 Hz, $J_{a-b'}$ = 4.7 Hz, 1H, one H of H-a), 3.69 – 3.62 (m, 1H, H-3), 3.56 (dq, J_{5-4} = 9.4 Hz, J_{5-6} = 6.2 Hz, 1H, H-5), 3.45 (ddd, $J_{a-a'}$ = 10.2 Hz, J_{a-b} = 6.5 Hz, $J_{a-b'}$ = 4.6 Hz, 1H, one H of H-a), 3.44 – 3.33 (m, 3H, H-4 + H-b), 2.83 (s, 4H, H-g), 2.69 – 2.65 (m, 2H, H-c), 2.28 – 2.21 (m, 2H, H-f), 1.79 – 1.70 (m, 3H, H-d + H-e), 1.25 (d, J_{6-5} = 6.3 Hz, 3H, H-6) ppm.

¹³C NMR: (125 MHz, CD$_3$OD) δ: 175.7 (C$_q$, CO), 171.9 (C$_q$, CO), 170.1 (C$_q$, CO), 101.6 (CH, C-1), 73.9 (CH, C-4), 72.3 (CH, C-3), 72.1 (CH, C-2), 69.8 (CH, C-5), 66.9 (CH$_2$, C-a), 36.4 (CH$_2$, C-c), 31.2 (CH$_2$, C-f), 26.5 (CH$_2$, C-g), 26.0 (CH$_2$, C-d), 25.1 (CH$_2$, C-e), 18.0 (CH$_3$, C-6) ppm.

Material and Methods

Cell culture

The MDA-MB-231 is a highly aggressive, invasive, and poorly differentiated triple-negative breast cancer (TNBC) cell line as it lacks estrogen receptor (ER), and progesterone receptor (PR) expression, as well as human epidermal growth factor receptor 2 (HER2). MDA-MB-231 cells were cultivated in DMEM medium complete with inactivated 10% fetal bovine serum (FBS), 1% penicillin/streptomycin and 1% L-glutamine. MCF-7 represents an ER-positive breast cancer model expressing both ERα and Erβ, PR as well as HER2 receptors. MCF-7 cells were cultivated in EMEM medium supplemented with 10% FBS, 1% penicillin/ streptomycin, 1% L-glutamine, 1% non-essential amino acids, 1% sodium pyruvate and 1% insulin. Both cell cultures were kept in an incubator at 37°C in a humidified atmosphere with a CO$_2$ pressure of 5%. Human Peripheral Blood Mononuclear Cells (PBMC), were isolated from the buffy coat of healthy volunteers after their informed consent. PBMC were separated from whole blood by density gradient (ficoll) centrifugation. Isolated PBMC were cultivated in RPMI medium, completed with 10% FBS, 1% Kanamycin solution, 1% L-glutamine, 1% non-essential amino acids and 1% sodium pyruvate. To evaluate the expression of PD-L1 on cell lines, MDA MB 231 and MCF-7 cells were harvested labelled with PE-conjugated anti-PD-L1 antibody and the level of PD-L1 expression analysed by flow cytometry.

Cell co-culture

For co-culture experiments, each cell line was plated in a 96 well tissue culture-treated plate at a concentration of 30000 cells/well. Cells were kept in a humidified incubator at 37°C in 5% CO$_2$ for 24 h to allow the cell to adhere. PBMC were activated or not activated by PHA 10 μg/mL overnight treatment. To establish co-culture cell lines were treated with 10 μg/mL or 50 μg/mL of WT PD-1, HACTR-PD-1, **1**- or **2**-HACTR-PD-1-L-rhamnose for 1 hour, followed by the addition of inactivated/activated PBMCs (3 x 10^5 cells/well). To distinguish the effects of co-culturing PBMCs with breast cancer cells from PBMC activation, two controls were used; activated PBMCs cultured alone (negative control) or co-cultured with breast cancer cells from each cell line, in the absence of recombinant or natural proteins.

Proliferation assay

To evaluate the effect of WT PD-1, HACTR-PD-1 or HACTR-PD-1-L-rhamnose on T cell proliferation PBMC were labelled with 0.25 mM carboxyfluorescein succinimidyl ester (CFSE) in serum-free PBS for 30 min at 37°C. FBS was then added to stop the reaction, and cells were washed several times with completed RPMI-1640. CFSE-labelled PBMC were added to pleated MDA-MB-231 or MCF-7 (untreated/treated 1h with WT PD-1, HACTR-PD-1, **1**- or **2**-HACTR-PD-1-L-rhamnose) and stimulated with 10 μg/mL of PHA. After 6 days of co-culture, PBMC were harvested, and T cell proliferation analyzed by FACS.

Cytotoxicity assay

The effect of WT PD-1, HACTR-PD-1 or HACTR-PD-1-L-rhamnose on T cell cytotoxic activity was analyzed using Calcein-AM cytotoxicity assay. MDA-MB-231 and MCF-7 cells were labelled with 1 mM CAM at 37°C for 15 min, washed, and seeded in a 96-well plate at a density of 3 x 10^4 cells in 50 μL per well. The following day, labelled target cells were treated with 10 μg/mL or 50 μg/mL of WT PD-1, HACTR-PD-1, **1**- or **2**-HACTR-PD-1 for 1 hour and incubated at a 1:10 ratio with overnight stimulated PBMC

(PBMC stimulation was performed as described in paragraph Cell Co-Culture). Each plate included target cells alone, as controls, for spontaneous cell death measurements. Plates were incubated at 37°C in a humidified atmosphere with 5% CO_2 for 24h. After incubation, the cells of each well were harvested, washed and labelled with propidium iodide (PI), and the cytotoxicity was measured by flow cytometry (FACS). Live target cells were identified as CAM^{high}/PI^- population, whereas killed target cells were CAM^{low}/PI^+ and the effector cells were CAM^- (at least 10-fold less fluorescent than killed target cells). After gating on target cells, cytotoxicity was calculated as the % increase in CAM^{low}/PI^+ population relative to target cells alone [cytotoxicity, % = (CAM^{low}/PI^+ in experimental wells – CAM^{low}/PI^+ in control wells)/CAM^{high}/PI^- in control well x 100]. The mean cytotoxicity % SEM for each condition was calculated from three replicate experimental wells.

THP1 cell culture and differentiation

THP1 cell line was obtained from ATCC and maintained in RPMI 1640 medium supplemented with 10% of foetal bovine serum (FBS), 2 mmol/L L-glutamine (Immunological Sciences, Rome, Italy) and 1 mg/mL kanamycin (Sigma-Aldrich Milan, Italy). THP1 cells (2×10^5 cells/mL) were seeded in 6 multiwell and differentiated into macrophages (M0) by 24h incubation with 150 nM phorbol 12-mystrate-13-acetate (PMA) (Sigma-Aldrich) followed by 24h incubation in RMPI medium. Macrophages were polarized into M1 macrophages by incubation with 0.5 mg/mL lipopolysaccharide (LPS) (Sigma Aldrich, Milan Italy).

Flow cytometry

Flow cytometry analyses were performed using the Accuri C6 (Thermo Fisher Scientific, Italy). Forward (FCS) and side (SSC) scatters were used to identify cell populations and measure size and granularity of the cells. Auto-fluorescence was recorded by analyzing unstained cells in the FL-1 channel (blue laser; excitation 488, emission 530/30). For detection of cell surface markers 1 mg/mL of monoclonal mouse anti-human antibodies CD14-FITC, CD86-PE, CD11b- PeCy7 were used for each sample. THP1 cells (2×10^5 cells/mL) were seeded in 6 MW and differentiated into macrophages as described. Differentiate macrophages (M0) were treated with increasing concentrations (0.1 – 10 mg/mL) of tested compounds or with 0.5 mg/mL (LPS). After 24h incubation, cells were harvested, washed, incubated with the antibodies for 30 minutes on ice in the dark. Labelled samples were washed, resuspended in PBS and analyzed by FACS, for each sample 10000 events were recorded. All data was analyzed using FCS express 7 (Flow cytometry software, DeNovo software).

ELISA assay

To evaluate the effect of new PD-1 mutants on T helper/reg cell activity co-culture experiments were performed as described previously. After 48h of co-culture, plates were centrifuged at 1500 rpm for 5 minutes and cell supernatants collected and stored at -80°C until the analysis. IFN-γ and IL-10 quantification in the culture media was performed by ELISA, following the manufacturer's instructions. Absorbance at 450 nm was monitored with a microplate reader. THP1 cells (2×10^5 cells/mL) were seeded in 6 MW and differentiated into macrophages as described. Differentiate macrophages (M0) were treated with increasing concentrations (0.1 – 10 mg/mL) of tested compounds or with 0.5 mg/mL (LPS). After 24h incubation culture media were collected and stored in –80°C until analysis. Levels of IL-8, TNF-a and IL-10 were measured by ELISA assay according to manufacturer's guidelines (Biolegend® San Diego, CA, USA).

Cell subset characterization
To evaluate the effect of WT PD-1, HACTR-PD-1, **1**- or **2**-HACTR-PD-1 on T cell subset frequency co-culture experiments were performed as described previously. After 72 h of co-culture PBMC were harvested

labelled for 30 min on ice with anti-human CD3, CD4, CD8 and CD25 and washed 2 times with PBS. CD3, CD4, CD8, and CD25 frequency were analyzed by FACS.

Statistical analysis
Results are expressed as means ± SEM of at least three independent experiments. Independent experiments were conducted using PBMC from at least 3 different donors. Statistical significance was evaluated by the one-way ANOVA followed by the Student's t test for unpaired populations, using Graph Pad Prism 9 (Graph Pad Software, Inc., San Diego, CA, USA). Differences were considered statistically significant when $p < 0.05$.

Expression and purification of human wild-type PD-L1
Escherichia coli BL21 (DE3) cells were transformed with pET-21a (+) plasmid encoding PD-L1 gene. In order to obtain uniformly isotopically enriched PD-L1 [U-^{15}N], the cells were cultured in M9 Minimal Medium supplied with 1.1 g ^{15}N- NH$_4$Cl, 1 mL of 0.1 mg/mL solution of ampicillin, 1 mL of 1 mg/mL of thiamine, 1 mL of 1 mg/mL of biotin, 1 mmol·dm^{-3} MgSO$_4$, 0.3 mmol·dm^{-3} CaCl$_2$; they were allowed to grown at 37 °C until OD$_{600}$ reached 0.8 and then overexpression was induced with 1 mmol·dm^{-3} isopropyl β-D-1-thiogalactopyranoside. The cultures were further incubated in agitation at 37 °C, overnight, and then harvested by centrifugation at 6500 rpm (JA-10 Beckman Coulter) for 15 min at 4°C. In all instances the pellet was suspended, at first, in 50 mmol·dm^{-3} Tris-HCl pH 8.0, 200 mmol·dm^{-3} NaCl, 10 mmol·dm^{-3} β-mercaptoethanol, 10 mmol·dm^{-3} EDTA, (50 mL per litre of culture) and sonicated for 30 seconds 10 times on ice at 4 °C. The suspension was centrifuged at 40,000 rpm (F15-6x100y Thermo Scientific) for 40 min and the supernatant was discarded. The recovered pellet was resuspended in 50 mmol·dm^{-3} Tris-HCl pH 8.0, 200 mmol·dm^{-3} NaCl, 10 mmol·dm^{-3} β-mercaptoethanol, 6 mol·dm^{-3} Guanidinium Chloride (25 mL per litre of culture) and newly incubated at 4 °C overnight under magnetic stirring. Again, the suspension was centrifuged at 40,000 rpm (F15-6x100y Thermo Scientific) for 40 min. The pellet was discarded, whereas the supernatant containing the denatured protein solution was diluted in a refolding buffer containing 0.1 mol·dm^{-3} Tris–HCl, pH 8.5, 1 mol·dm^{-3} arginine, 0.25 mmol·dm^{-3} reduced glutathione and 0.25 mmol·dm^{-3} oxidised glutathione. The solution was incubated at 4 °C under stirring, for 12-18 h, clarified by passing a 0.45-µm filter and then dialyzed extensively against 10 mmol·dm^{-3} Tris, pH 8.0, 20 mmol·dm^{-3} NaCl. The protein solution was concentrated with an Amicon® Stirred Cell and then purified by size exclusion chromatography using a HiLoad Superdex 26/60 75pg (GE Healthcare) column previously equilibrated in 10 mmol·dm^{-3} Tris-HCl pH 8.0 and 20 mmol·dm^{-3} NaCl.

NMR measurements
Solution NMR experiments for backbone resonance assignment [3D HNCA, HNCACB, CBCA(CO)NH, HNCO, HN(CA)CO][1–3] were performed on [U-^{13}C, ^{15}N] samples of the HACTR-PD-1 mutant (at the concentration of 350 µmol·dm^{-3}) in the same water buffer solution used for PD-L1 resonance assignment[4] [10 mmol·dm^{-3} Tris, pH 8, 20 mmol·dm^{-3} NaCl]. For 3D HNCACB non-uniform random sampling at 62% and compressed-sensing reconstruction was used.[5] A 3D HNCA was also recorded at a lower pH [buffer: 20 mmol·dm^{-3} HEPES, pH 6.8, 20 mmol·dm^{-3} NaCl, 0.1% NaN$_3$] to identify a higher number of spin systems. All solution spectra were recorded at 298 K on Bruker AVANCE III and AVANCE NEO NMR spectrometers, operating at 950 and 500 MHz, ^{1}H Larmor frequency, (22.3 T and 11.7 T), respectively, equipped with triple resonance cryo-probes. Secondary structure prediction was performed with TALOS+[6] by using the chemical shifts of HN, N, C', Cα, and Cβ as input data.

NMR Titrations of the functionalized HACTR-PD-1 mutant with PD-L1
The interactions of the free and functionalized HACTR-PD-1 mutant with PD-L1 have been investigated through solution NMR titrations. During the NMR titration, increasing aliquot of PD-L1 [to reach the concentrations of 12.5, 25, 50 µmol·dm^{-3} in solution] were added to the solution of free [U-^{15}N] HACTR-PD-1 mutant or [U-^{15}N] HACTR-PD-1 mutant functionalized with PEG1000, PEG5000 and rhamnose-derivative [at protein concentration of 50 µmol·dm^{-3} in 10 mmol·dm^{-3} Tris, pH 8, 20 mmol·dm^{-3} NaCl]. 2D ^{1}H-^{15}N HSQC NMR spectra were recorded after each addition on Bruker AVANCE III and AVANCE NEO

NMR spectrometers, operating at 950 and 900 or 700 MHz, [1]H Larmor frequency, (22.3 T, 21.1 T and 16.4 T) respectively, equipped with triple resonance cryo-probes. An NMR titration of [U-^{15}N] PD-L1 [50 µmol·dm^{-3} in 10 mmol·dm^{-3} Tris, pH 8, 20 mmol·dm^{-3} NaCl] with free HACTR-PD-1 mutant was also performed on Bruker AVANCE III spectrometer, operating at 950 MHz, [1]H Larmor frequency (22.3 T); equivalent aliquots of HACTR-PD-1 [to reach the concentrations of 12.5, 25, 50 µmol·dm^{-3} in solution] were added to [U-^{15}N] PD-L1 solution.

HADDOCK calculations

The PDB structure of the complex between the HAC-PD-1 mutant and PD-L1 (PDB code: 5IUS)[7] was used as a starting input to generate the structures of the different mutants (K131T/K135R, K131R/K135R, K131Q/K135Q, K131T/K135Q) with PyMOL. The residue K135 is at the interface between the two proteins in the complex and faces an aspartate (D61) on the PD-L1 side. For this reason, in most of the complexes we kept the positive charge in this position by mutating the lysine to an arginine. Then, the obtained complexes were minimized through MODELLER[8] and finally water refined using the HADDOCK web-portal on the WeNMR GRID (http://www.wenmr.eu), using the refinement interface.[9,10] Reference calculations were also performed for the 5IUS and 4ZQK[11] PDB structures, which were refined and scored in the same way. The interacting energy of the complexes was also analyzed on the PRODIGY server[12,13] after MODELLER and HADDOCK minimization. The model of the HACTR-PD-1/PD-L1 complex was obtained by performing docking calculations with the software HADDOCK 2.4 on the WeNMR GRID (http://www.wenmr.eu).[9,10] In all calculations, during the rigid-body docking, 1000 complexes were generated, then 200 structures were selected for the semi-flexible simulated annealing in torsion angle space, and finally refined in Cartesian space with explicit solvent. The model structure of HACTR-PD-1 and PD-L1, obtained with the previous calculations, provided the input coordinates for the proteins. The NMR titrations of [U-^{15}N] HACTR-PD-1 with PD-L1 and [U-^{15}N] PD-L1 with HACTR-PD-1, analyzed with the PICASSO web server,[14] provided experimental ambiguous restraints ("active residues") to drive the docking calculation.

ITC Titration of the HACTR-PD-1 mutant with PD-L1

Isothermal titration microcalorimetry experiments were performed at 298 K with a VP-ITC microcalorimeter (MicroCal, Inc., Northampton, MA). After an initial injection of 1 µL, aliquots of 13 µL of 300 µmol·dm^{-3} HACTR-PD-1 were stepwise injected into the sample cell containing a 30 µmol·dm^{-3} solution of PD-L1 until complete saturation was obtained. All experiments were performed in 10 mmol·dm^{-3} Tris-HCl at pH 8.0 with 20 mmol·dm^{-3} NaCl. Heats of dilution were measured by injecting the ligand solution into the buffer, and the obtained values were subtracted from the binding heats. The thermodynamic parameters and K_A values were calculated by fitting the data to a single binding site model with the Origin 7.0 software (MicroCal, Inc.).

Table S1. HADDOCK-scores evaluated on the best four structures of the complexes for the mutants considered in the study.

Complex	HADDOCK-score
4ZQK	-112 ± 2
5IUS	-119 ± 3
5IUS RR	-114 ± 2
5IUS TR	-113 ± 1
5IUS TQ	-108 ± 2
5IUS QQ	-96 ± 2
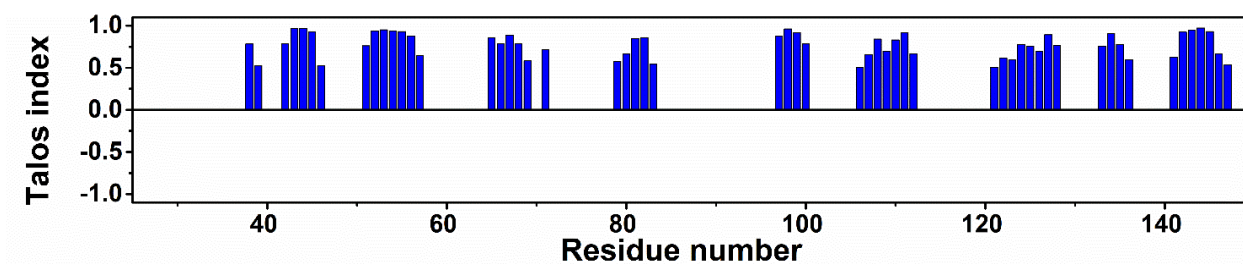
Figure S1. Secondary structure prediction obtained by the program TALOS+ using the experimental values of chemical shifts of HN, N, C', Cα, and Cβ atoms as input data. The blue bars indicate the β-strand propensity.
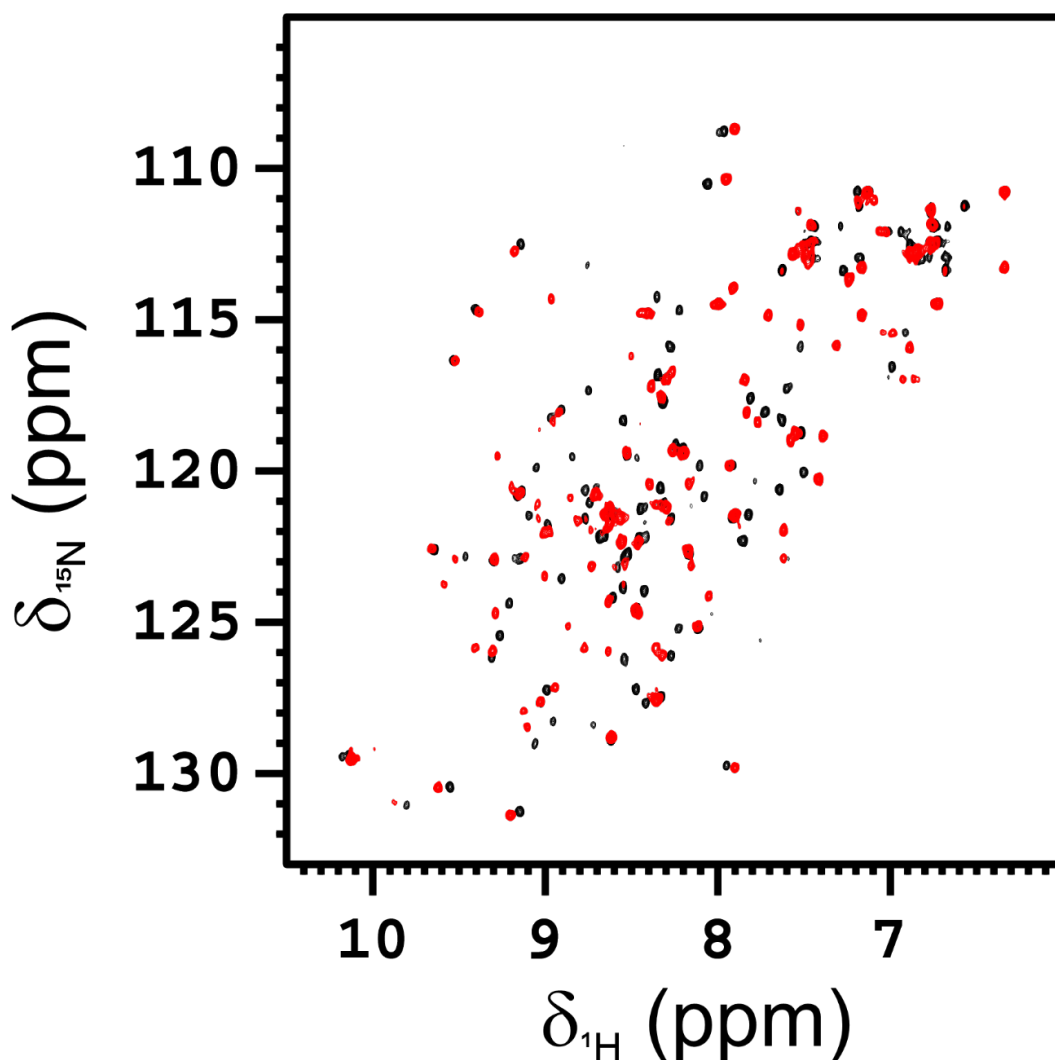
Figure S2. 2D ^{1}H-^{15}N HSQC overlaid spectra of free HACTR-PD-1 (black) with respect to HACTR-PD-1 in the presence of PD-L1 (in 1:1 molar ratio, red). The spectra were acquired on a spectrometer operating at 900 MHz, ^{1}H Larmor frequency, and 298 K. The spectrum of the complex was acquired with a higher number of scans than the reference spectrum.
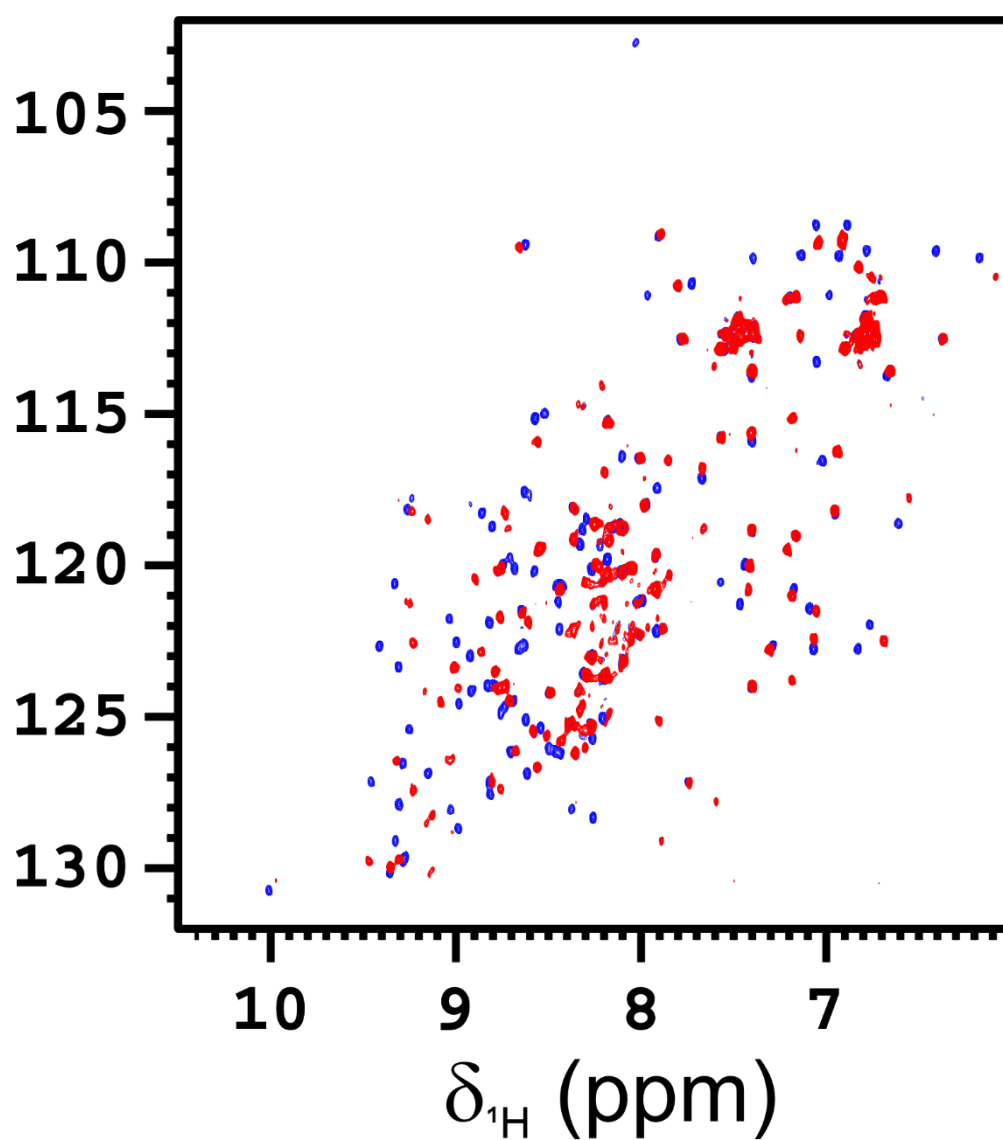
Figure S3. 2D ^{1}H-^{15}N HSQC overlaid spectra of free PD-L1 (blue) and PD-L1 in the presence of HACTR-PD-1 (in 1:1 molar ratio, red. The spectra were acquired on a spectrometer operating at 900 MHz, ^{1}H Larmor frequency, and 298 K. The spectrum of the complex was acquired with a higher number of scans than the reference spectrum.
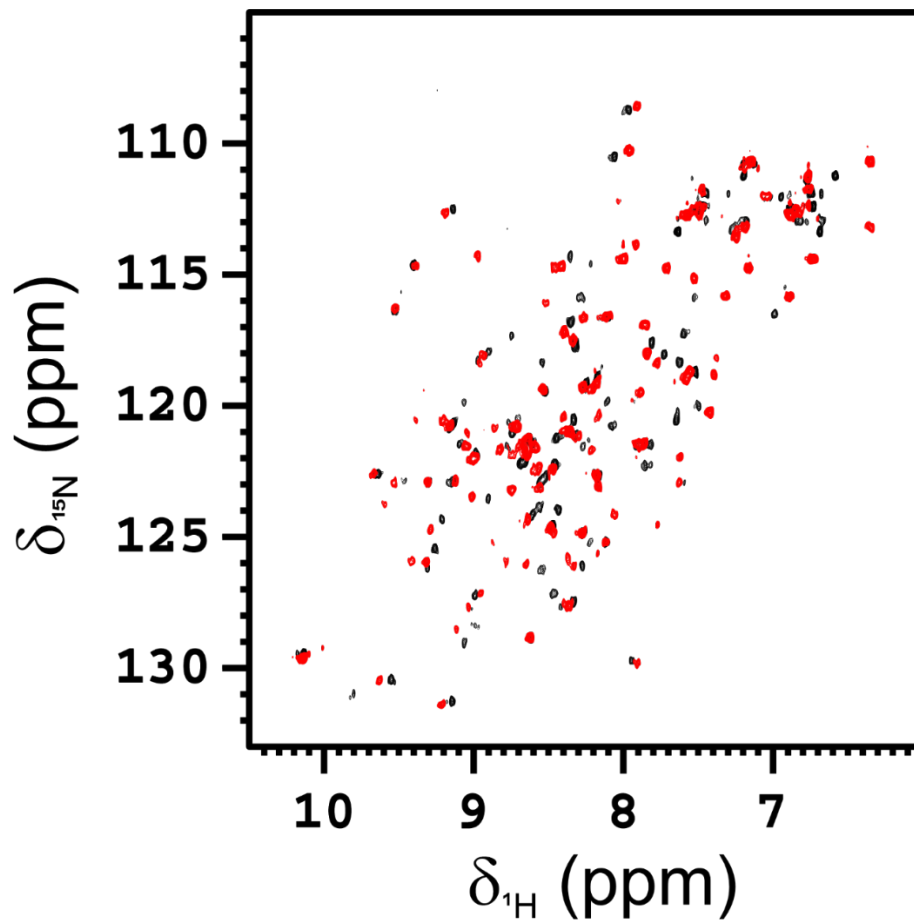
Figure S4. 2D ^{1}H-^{15}N HSQC overlaid spectra of HACTR-PD-1 conjugated with PEG 5 kDa (black) and HACTR-PD-1 conjugated with PEG 5 kDa in the presence of PD-L1 (in 1:1 molar ratio, red). The spectra were acquired on a spectrometer operating at 950 MHz, ^{1}H Larmor frequency, and 298 K. The spectrum of the complex was acquired with a higher number of scans than the reference spectrum.
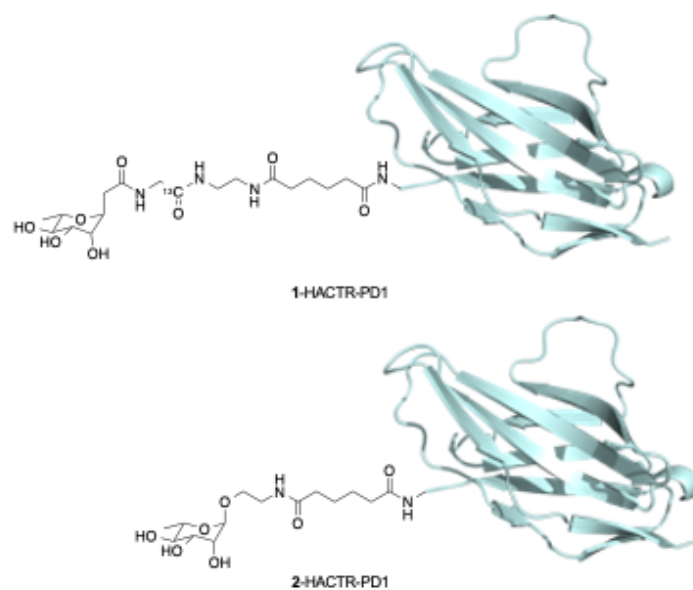
Figure S5. Rhamnosylated mutants **1**- HACTR-PD-1 and **2**- HACTR-PD-1
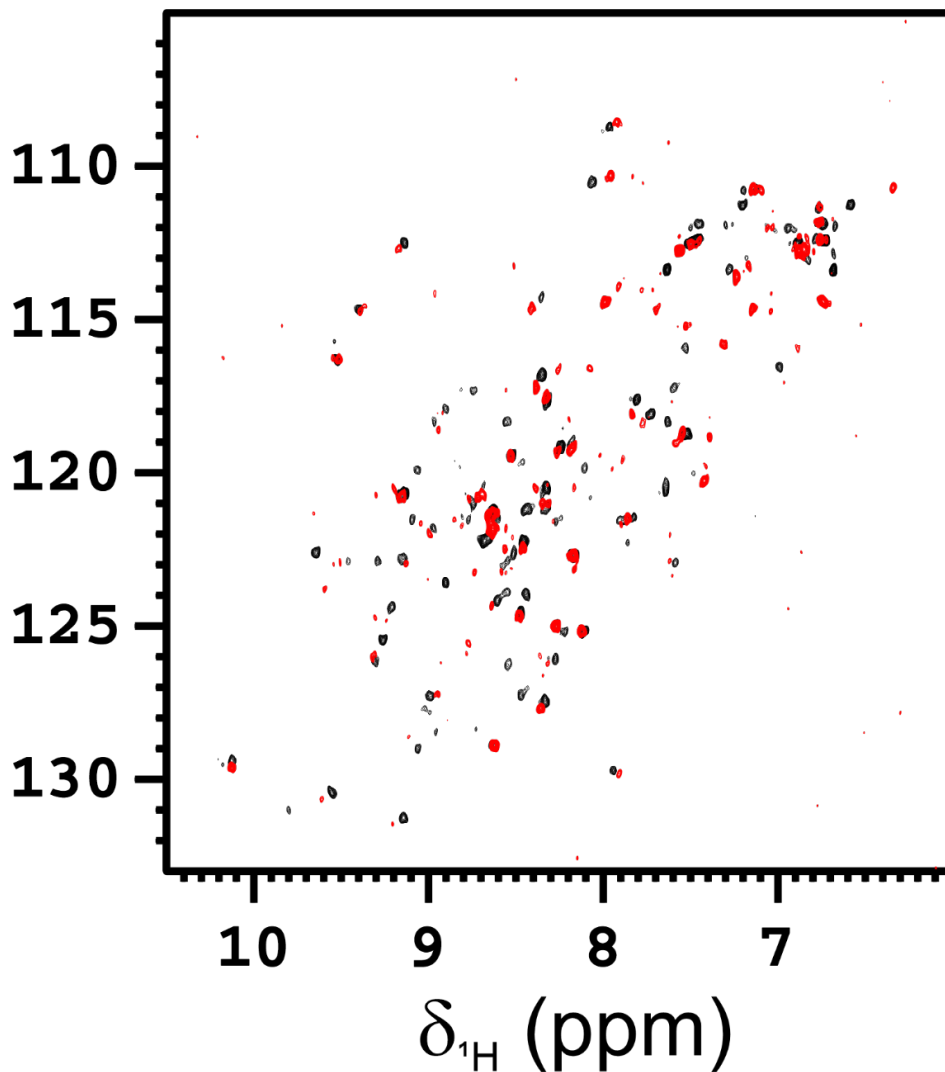
Figure S6. 2D ^{1}H-^{15}N HSQC overlaid spectra of HACTR-PD-1 conjugated with L-rhamnose, **1**- HACTR-PD-1 (black) and HACTR-PD-1 conjugated with L-rhamnose in the presence of PD-L1 (in 1:1 molar ratio, red). The spectra were acquired on a spectrometer operating at 700 MHz, ^{1}H Larmor frequency, and 298 K. The spectrum of the complex was acquired with a higher number of scans than the reference spectrum.
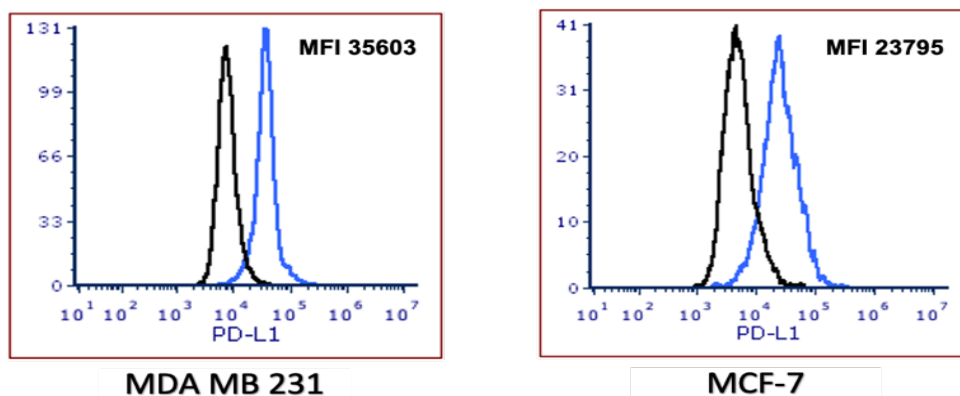
Figure S7. PD-L1 level expression on MDA MB 231 and MCF-7 breast cancer cell lines. Representative overlapping histogram plots of PD-L1 level of expression on MDA MB 231 and MCF-7 cells analysed by FACS; isotype control black; PD-L1 l blue. Data represent one of at least three independent experiments.
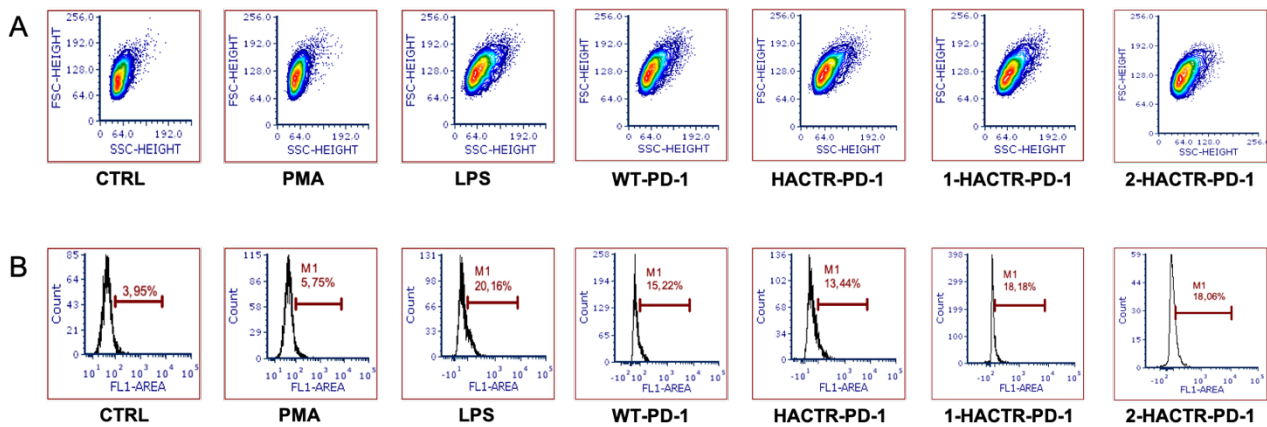
Figure S8. Effects of test compounds on THP1 cells morphological changes. (A) Representative forward light scatter and side light scatter plots of THP1 cells treated 24 h with 150 nM of PMA and of M0 treated (24 h) with 0.5 μg/mL of LPS or 1 μg/mL of tested compounds. (B) Representative histograms of autofluorescence of THP1 cells treated 24h with 150 nM of PMA and of M0 treated (24 h) with 0.5 μg/mL of LPS or 1 μg/mL of tested compounds. Data are representative of at least three experiments
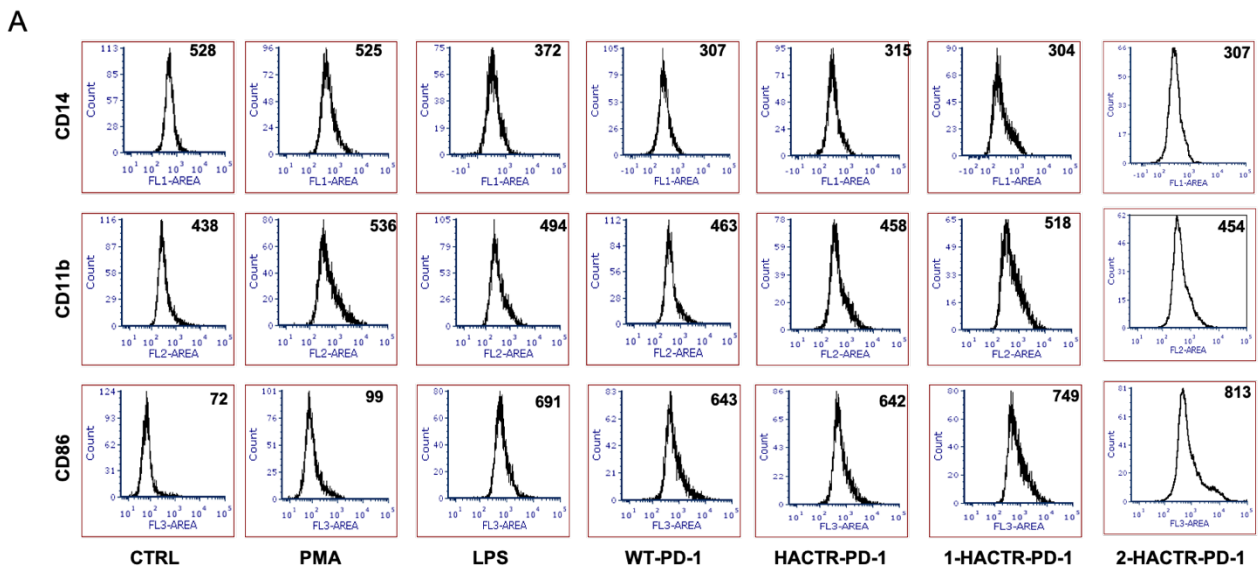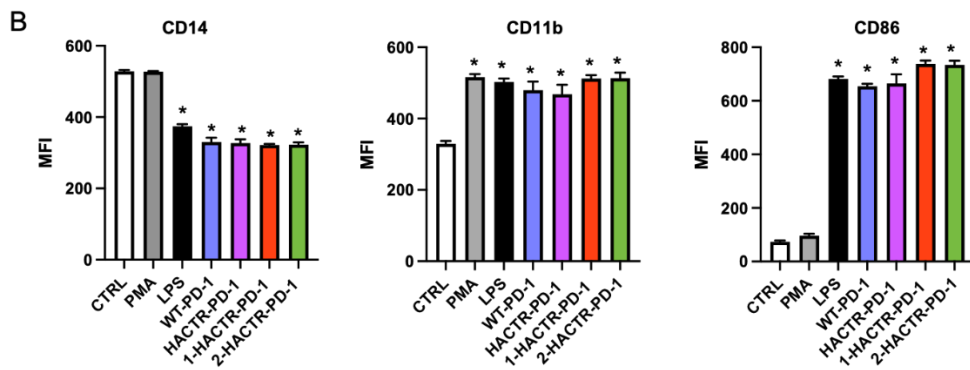
Figure S9. Effects of compounds on marker surface expression on differentiated THP1 cells. (A) Representative flow cytometry histograms showing CD14, CD11b, and CD86 expression on M0 treated (24h) with WT-PD-1, HACTR-PD-1, **1**-HACTR-PD-1-L-rhamnose or **2**-HACTR-PD-1-L-rhamnose. Level of expression of CD14 (B), CD11b (C), and CD86 (D) on M0 treated (24 h) with WT-PD-1, HACTR-PD-1, **1**-HACTR-PD-1-L-rhamnose or **2**-HACTR-PD-1-L-rhamnose. Results represent mean ± SEM of at least three independent experiments. * ≤0.05 treated *vs.* control (CTRL).
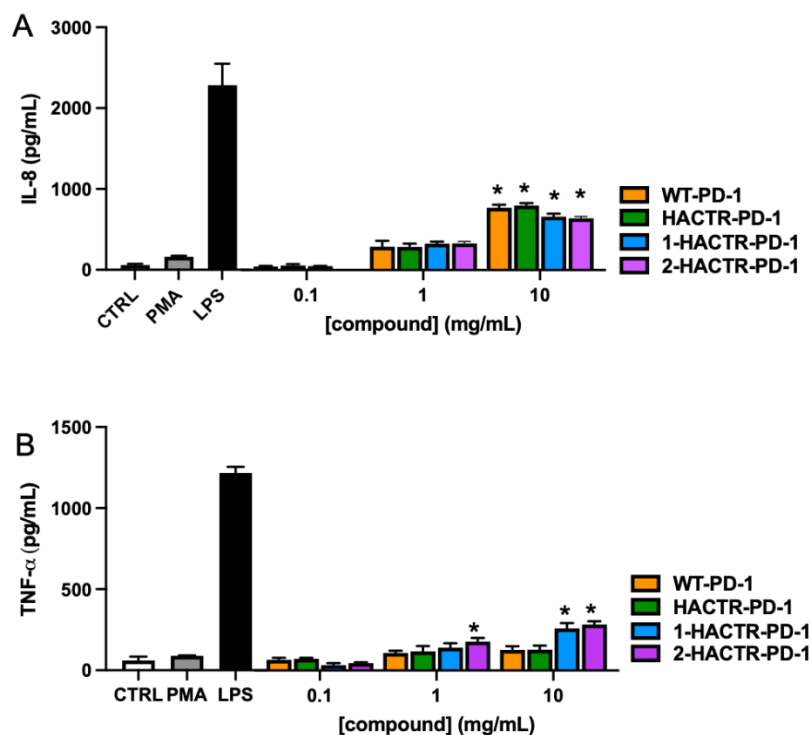
Figure S10. Effects of tested compound on cytokines secretion in differentiated THP1 cells. PMA differentiated THP1 cells were treated with 0.5 μg/mL of LPS or 1 μg/mL of tested compounds for 48h, cells culture medium harvested and IL-8 (A) and TNF-α (B) levels measured by ELISA assay. Results represent mean ± SEM of at least three independent experiments. * ≤0.05 treated *vs.* control (CTRL).
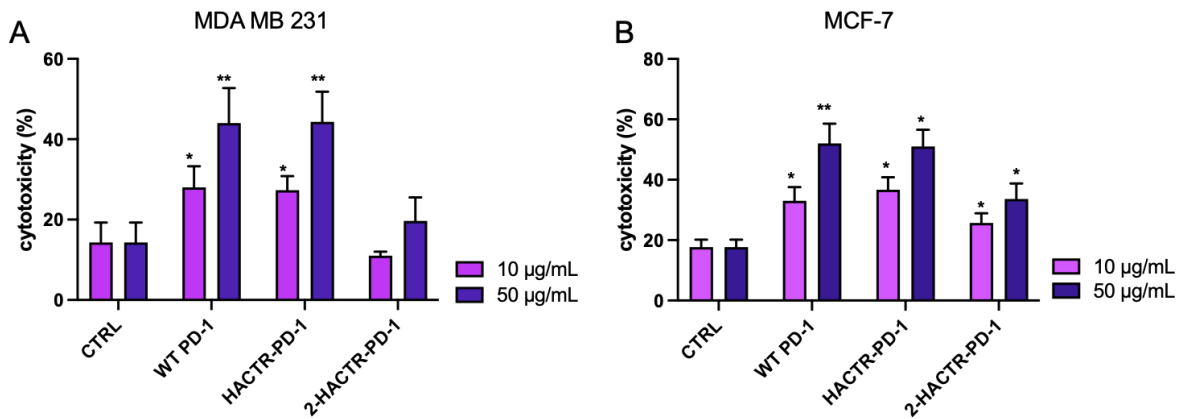
Figure S11. Effects of WT PD-1, HACTR-PD-1 and **2**-HACTR-PD-1 on T cell-mediated breast cancer cell cytotoxicity. CAM labelled cancer cells were treated with 10 or 50 μg/mL of PD-1, HACTR-PD-1 or **2**-HACTR-PD-1 for 1h and then incubated with PHA-stimulated PBMC. After 24h of co-culture breast cancer cells were harvested and the level intensity of CAM was analysed by FACS. A. PBMC mediated cytotoxicity against MDA MB 231 cell line in presence/absence of WT PD-1, HACTR-PD-1 or **2**-HACTR-PD-1; B. PBMC mediated cytotoxicity against MCF-7 cell line in presence/absence of WT PD-1, HACTR-PD-1 or **2**-HACTR-PD-1. Results are expressed as the mean ± SEM of at least three independent experiments run in triplicate using PBMC from three different donors. *p≤0.05 natural/recombinant protein treated vs untreated co-cultures; **p≤0.01 natural/recombinant protein treated vs untreated co-cultures.
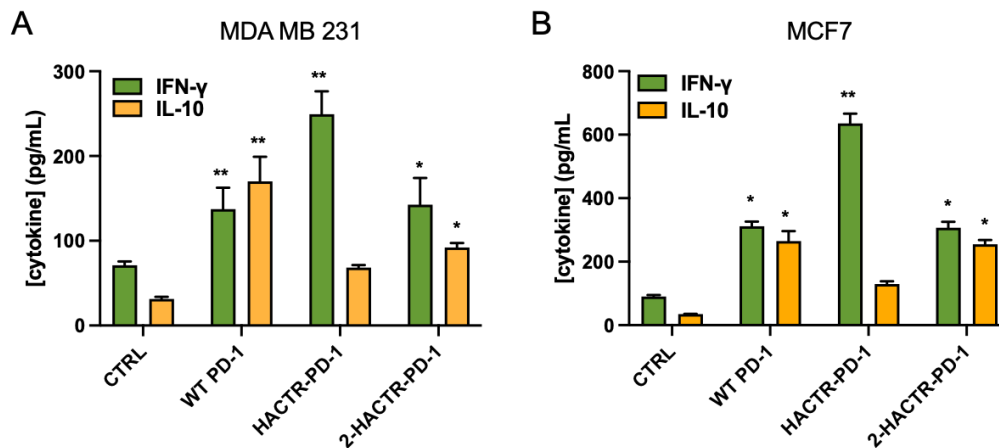
Figure S12. Effects of WT PD-1, HACTR-PD-1 and **2**-HACTR-PD-1 on T helper or Treg cytokine release. Cancer cells were treated with 10 μg/mL of WT PD-1, HACTR-PD-1 or **2**-HACTR-PD-1 for 1h and then incubated with PHA-stimulated PBMC. After 48h of cell culture media were collected and IFN- and IL-10 measured by ELISA. A. IFN- and IL-10 released by PBMC co-cultured with MDA MB 231 cell line in presence/absence of WT PD-1, HACTR-PD-1 or **2**-HACTR-PD-1; B. IFN-γ and IL-10 released by PBMC co-cultured with MCF-7 cell line in presence/absence of WT PD-1, HACTR-PD-1 or **2**-HACTR-PD-1. Results are expressed as the mean ± SEM of at least three independent experiments run in triplicate using PBMC from different donors. * p≤0.05 natural/recombinant protein treated vs untreated co-cultures; **p≤0.01 natural/recombinant protein treated vs untreated co-cultures
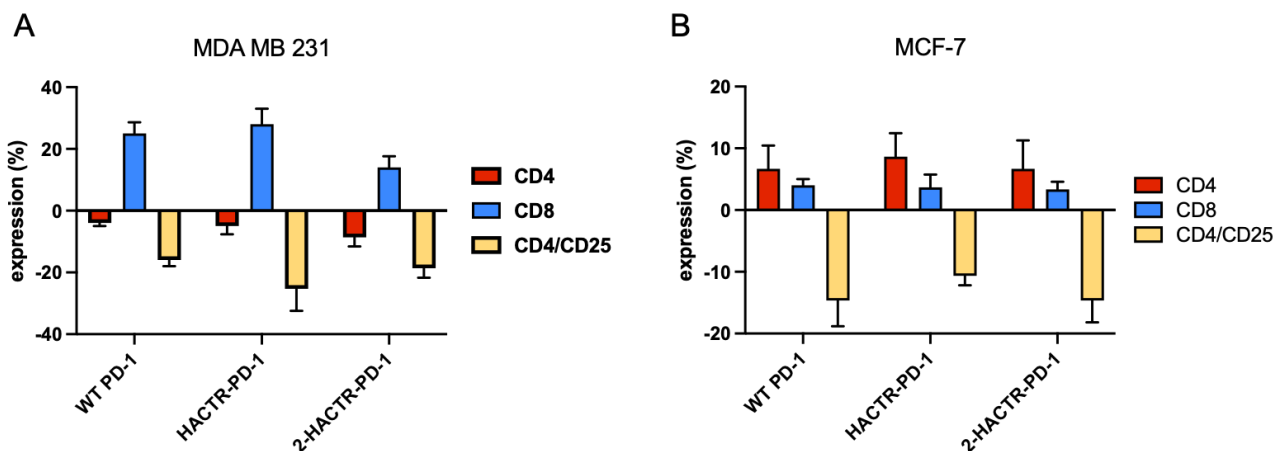
Figure S13. Effects of WT PD-1, HACTR-PD-1 and **2**-HACTR-PD-1 on T subset percentage. Cancer cells were treated with 10 μg/mL of PD-1, HACTR-PD-1 or **2**-HACTR-PD-1 for 1h and then incubated with PHA-stimulated PBMC. After 72h of co-culture, PBMC were harvested, labelled with CD3, CD4, CD8, and CD25 monoclonal antibodies and the percentage of CD4, CD8 and CD4-CD25 positive cells evaluated by FACS. A. CD4, CD8 and CD4CD25 percentage after co-cultured with MDA MB 231 cell line in presence/absence of WT PD-1, HACTR-PD-1 or **2**-HACTR-PD-1; B. CD4, CD8 and CD4CD25 after co-cultured with MCF-7 cell line in presence/absence of WT PD-1, HACTR-PD-1 or **2**-HACTR-PD-1. Results are expressed as mean ± SEM of at least three independent experiments run in triplicate using PBMC from different donors

References

(1)   Grzesiek, S.; Bax, A. Improved 3D Triple-Resonance NMR Techniques Applied to a 31 KDa Protein. *Journal of Magnetic Resonance (1969)* **1992**, *96* (2), 432–440. https://doi.org/10.1016/0022-2364(92)90099-S.

(2)   Schleucher, J.; Sattler, M.; Griesinger, C. Coherence Selection by Gradients without Signal Attenuation: Application to the Three-Dimensional HNCO Experiment. *Angewandte Chemie International Edition in English* **1993**, *32* (10), 1489–1491. https://doi.org/10.1002/anie.199314891.

(3)   Kay, L. E.; Xu, G. Y.; Yamazaki, T. Enhanced-Sensitivity Triple-Resonance Spectroscopy with Minimal H2O Saturation. *Journal of Magnetic Resonance, Series A* **1994**, *109* (1), 129–133. https://doi.org/10.1006/jmra.1994.1145.

(4)   Rizzo, D.; Cerofolini, L.; Giuntini, S.; Iozzino, L.; Pergola, C.; Sacco, F.; Palmese, A.; Ravera, E.; Luchinat, C.; Baroni, F.; Fragai, M. Epitope Mapping and Binding Assessment by Solid-State NMR Provide a Way for the Development of Biologics under the Quality by Design Paradigm. *J. Am. Chem. Soc.* **2022**, *144* (22), 10006–10016. https://doi.org/10.1021/jacs.2c03232.

(5)   Bostock, M.; Nietlispach, D. Compressed Sensing: Reconstruction of Non-Uniformly Sampled Multidimensional NMR Data. *Concepts in Magnetic Resonance Part A* **2017**, *46A* (2), e21438. https://doi.org/10.1002/cmr.a.21438.

(6)   Shen, Y.; Delaglio, F.; Cornilescu, G.; Bax, A. TALOS+: A Hybrid Method for Predicting Protein Backbone Torsion Angles from NMR Chemical Shifts. *J. Biomol. NMR* **2009**, *44* (4), 213–223. https://doi.org/10.1007/s10858-009-9333-z.

(7)   Pascolutti, R.; Sun, X.; Kao, J.; Maute, R. L.; Ring, A. M.; Bowman, G. R.; Kruse, A. C. Structure and Dynamics of PD-L1 and an Ultra-High-Affinity PD-1 Receptor Mutant. *Structure* **2016**, *24* (10), 1719–1728. https://doi.org/10.1016/j.str.2016.06.026.

(8)   Fiser, A.; Šali, A. Modeller: Generation and Refinement of Homology-Based Protein Structure Models. In *Methods in Enzymology*; Charles W. Carter, Jr. and R. M. S., Ed.; Macromolecular Crystallography, Part D; Academic Press, 2003; Vol. Volume 374, pp 461–491.

(9)   van Zundert, G. C. P.; Rodrigues, J. P. G. L. M.; Trellet, M.; Schmitz, C.; Kastritis, P. L.; Karaca, E.; Melquiond, A. S. J.; van Dijk, M.; de Vries, S. J.; Bonvin, A. M. J. J. The HADDOCK2.2 Web Server: User-Friendly Integrative Modeling of Biomolecular Complexes. *Journal of Molecular Biology* **2016**, *428* (4), 720–725. https://doi.org/10.1016/j.jmb.2015.09.014.

(10)   Honorato, R. V.; Koukos, P. I.; Jiménez-García, B.; Tsaregorodtsev, A.; Verlato, M.; Giachetti, A.; Rosato, A.; Bonvin, A. M. J. J. Structural Biology in the Clouds: The WeNMR-EOSC Ecosystem. *Frontiers in Molecular Biosciences* **2021**, *8*.

(11)   Zak, K. M.; Kitel, R.; Przetocka, S.; Golik, P.; Guzik, K.; Musielak, B.; Dömling, A.; Dubin, G.; Holak, T. A. Structure of the Complex of Human Programmed Death 1, PD-1, and Its Ligand PD-L1. *Structure* **2015**, *23* (12), 2341–2348. https://doi.org/10.1016/j.str.2015.09.010.

(12)   Xue, L. C.; Rodrigues, J. P.; Kastritis, P. L.; Bonvin, A. M.; Vangone, A. PRODIGY: A Web Server for Predicting the Binding Affinity of Protein-Protein Complexes. *Bioinformatics* **2016**, *32* (23), 3676–3678. https://doi.org/10.1093/bioinformatics/btw514.

(13)   Vangone, A.; Bonvin, A. M. Contacts-Based Prediction of Binding Affinity in Protein–Protein Complexes. *eLife 4*. https://doi.org/10.7554/eLife.07454.

(14)   Laveglia, V.; Giachetti, A.; Cerofolini, L.; Haubrich, K.; Fragai, M.; Ciulli, A.; Rosato, A. Automated Determination of Nuclear Magnetic Resonance Chemical Shift Perturbations in Ligand Screening Experiments: The PICASSO Web Server. *J. Chem. Inf. Model.* **2021**, *61* (12), 5726–5733. https://doi.org/10.1021/acs.jcim.1c00871.

Chapter 4

Conclusions and Perspectives

In the context of this PhD thesis different NMR techniques have been used for various purposes: from the physicochemical characterization of complex systems to the study of potential MRI contrast agents, and from the study of protein dynamics to that of protein-ligand interactions.

FFC relaxometry was applied to assess possible theranostic and MRI contrast agents (of both synthetic and natural origin), measuring their relaxivity at the fields of interest for MRI, and to discriminate the different contributions to the relaxation of water protons through the models that were used to fit the NMRD profiles. FFC has been extremely useful for the characterization of motions in diamagnetic systems, and it allowed an estimation of local and reorientational correlation times, as well as the presence of aggregate forms, of biologically relevant proteins.

The new approach, offered by HRR, combines the high sensitivity and exquisite qualitative nature of high-resolution NMR with the determination of multiscale dynamics typical of fast field-cycling relaxometry. Therefore, this technique constitutes an unprecedented investigation tool for interrogating both structure and dynamics of molecules with atomic resolution, over a very wide range of time scales, from picoseconds up to microseconds and on different kinds of systems.

Since HRR is based on a new technology, it required the development of new classes of experiments, both from the point of view of the field of applicability and of the experimental setup. An optimization of the pulse sequence, that features the shuttling of the sample at the different fields, has been crucial in order to achieve the highest sensitivity and the determination of the observable of interest. A fast and reliable method for the analysis of the large amount of data that arise from these measurements has been implemented and is currently under testing.

In principle, HRR has a broad applicability: small complexes, biomolecules, such as diamagnetic proteins and their interactions with small molecules, paramagnetic proteins, contrast agents, food related systems, biological fluids etc. The two main targets on which we plan to focus on are: the study of the interaction of small molecules and metabolites in biological fluids, extending the study that was already performed in blood serum [51]; the study of intrinsically disordered domains and proteins with fast internal mobility [32]. HRR has the potential to give unprecedented information on the mobility of these systems, that have a central role in many biological processes and diseases.

Some upgrades of the instrumentation are also expected in order to improve the performances of HRR and to unblock very low relaxation fields, crucial for many applications: first a magnetic tunnel (MT), which will sustain moderate and low fields till 0.5 T during the transfer of the sample, in order to avoid loss of magnetization, and also a Zero Field Coil (ZFC), a fast field-cycling system of shielded coils that can generated a field of 0.5 T and change it down to 100 μT and back up in 1 ms. As a consequence of the shorter delays in the switching of the field, this new system will open the way for exploring other timescales and make it possible to perform Ultrafast High Resolution Relaxometry (UHRR) measurements.

(a)

(b)
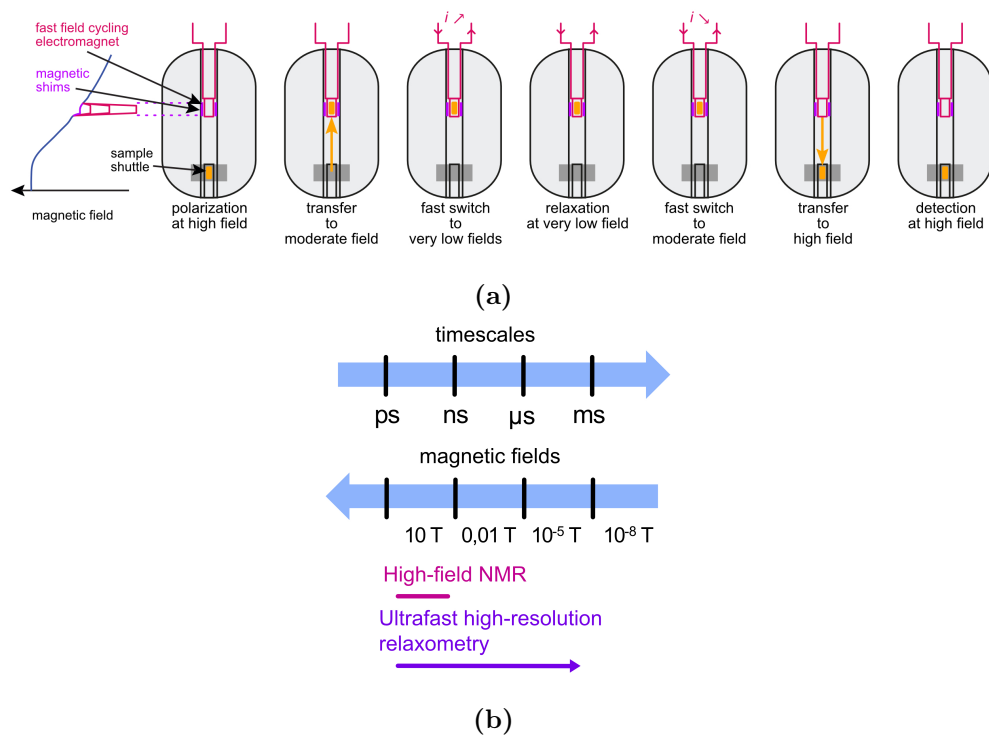
Figure 4.1: (a) Schematic representation of the Ultrafast High Resolution Relaxometry system mechanism. (b) UHRR will widen the accessible molecular motions timescales.

Bibliography

[1] F. Bloch, "Nuclear induction," *Physical review*, vol. 70, no. 7-8, p. 460, 1946.

[2] J. Kowalewski, "Nuclear spin relaxation in diamagnetic fluids: Part 1. general aspects and inorganic applications," *Annual Reports on NMR Spectroscopy*, vol. 22, pp. 307–414, 1990.

[3] M. H. Levitt, *Spin dynamics: basics of nuclear magnetic resonance*. John Wiley & Sons, 2013.

[4] N. Bloembergen, E. M. Purcell, and R. V. Pound, "Relaxation effects in nuclear magnetic resonance absorption," *Physical review*, vol. 73, no. 7, p. 679, 1948.

[5] I. Solomon, "Relaxation processes in a system of two spins," *Physical Review*, vol. 99, no. 2, p. 559, 1955.

[6] N. Bloembergen and L. Morgan, "Proton relaxation times in paramagnetic solutions. effects of electron spin relaxation," *The Journal of Chemical Physics*, vol. 34, no. 3, pp. 842–850, 1961.

[7] A. S. Merbach, L. Helm, and E. Toth, *The chemistry of contrast agents in medical magnetic resonance imaging*. John Wiley & Sons, 2013.

[8] J. Wahsner, E. M. Gale, A. Rodríguez-Rodríguez, and P. Caravan, "Chemistry of mri contrast agents: current challenges and new frontiers," *Chemical reviews*, vol. 119, no. 2, pp. 957–1057, 2018.

[9] I. Bertini, C. Luchinat, G. Parigi, and E. Ravera, *NMR of paramagnetic molecules: applications to metallobiomolecules and models*. Elsevier, 2016.

[10] A. Einstein, *Investigations on the Theory of the Brownian Movement*. Courier Corporation, 1956.

[11] G. Lipari and A. Szabo, "Model-free approach to the interpretation of nuclear magnetic resonance relaxation in macromolecules. 1. theory and range of validity," *Journal of the American Chemical Society*, vol. 104, no. 17, pp. 4546–4559, 1982.

[12] A. Anderson and A. Redfield, "Nuclear spin-lattice relaxation in metals," *Physical Review*, vol. 116, no. 3, p. 583, 1959.

[13] R. Kimmich, "Field cycling in nmr relaxation spectroscopy: Applications in biological, chemical and polymer physics," *Bull. Magn. Reson*, vol. 1, no. 4, pp. 195–218, 1980.

[14] F. Noack, "Nmr field-cycling spectroscopy: principles and applications," *Progress in nuclear magnetic resonance Spectroscopy*, vol. 18, no. 3, pp. 171–276, 1986.

[15] S. H. Koenig and R. D. Brown III, "Field-cycling relaxometry of protein solutions and tissue: implications for mri," *Progress in Nuclear Magnetic Resonance Spectroscopy*, vol. 22, no. 6, pp. 487–567, 1990.

[16] S. Aime, M. Botta, M. Fasano, and E. Terreno, "Lanthanide (iii) chelates for nmr biomedical applications," *Chemical Society Reviews*, vol. 27, no. 1, pp. 19–29, 1998.

[17] P. Caravan, J. J. Ellison, T. J. McMurry, and R. B. Lauffer, "Gadolinium (iii) chelates as mri contrast agents: structure, dynamics, and applications," *Chemical reviews*, vol. 99, no. 9, pp. 2293–2352, 1999.

[18] P. Caravan, "Strategies for increasing the sensitivity of gadolinium based mri contrast agents," *Chemical Society Reviews*, vol. 35, no. 6, pp. 512–523, 2006.

[19] F. Carniato, L. Tei, M. Botta, E. Ravera, M. Fragai, G. Parigi, and C. Luchinat, "1h nmr relaxometric study of chitosan-based nanogels containing mono-and bis-hydrated gd (iii) chelates: Clues for mri probes of improved sensitivity," *ACS Applied Bio Materials*, vol. 3, no. 12, pp. 9065–9072, 2020.

[20] G. Licciardi, D. Rizzo, M. Salobehaj, L. Massai, A. Geri, L. Messori, E. Ravera, M. Fragai, and G. Parigi, "Large protein assemblies for high-relaxivity contrast agents: The case of gadolinium-labeled asparaginase," *Bioconjugate Chemistry*, vol. 33, no. 12, pp. 2411–2419, 2022.

[21] M. A. Kaster, M. D. Levasseur, T. G. Edwardson, M. A. Caldwell, D. Hofmann, G. Licciardi, G. Parigi, C. Luchinat, D. Hilvert, and T. J. Meade, "Engineered nonviral protein cages modified for mr imaging," *ACS Applied Bio Materials*, 2023.

[22] R. Riordan, M. Khonsari, J. Jeffries, G. Maskell, and P. Cook, "Pineapple juice as a negative oral contrast agent in magnetic resonance cholangiopancreatography: a preliminary evaluation," *The British journal of radiology*, vol. 77, no. 924, pp. 991–999, 2004.

[23] M. Zarrini, F. Seilanian Toosi, B. Davachi, and S. Nekooei, "Natural oral contrast agents for gastrointestinal magnetic resonance imaging," *Reviews in Clinical Medicine*, vol. 2, no. 4, pp. 200–204, 2015.

[24] D. Rizzo, E. Ravera, M. Fragai, G. Parigi, and C. Luchinat, "Origin of the mri contrast in natural and hydrogel formulation of pineapple juice," *Bioinorganic chemistry and applications*, 2021.

[25] G. Licciardi, D. Rizzo, E. Ravera, M. Fragai, G. Parigi, and C. Luchinat, "Not only manganese, but fruit component effects dictate the efficiency of fruit juice as an oral magnetic resonance imaging contrast agent," *NMR in Biomedicine*, vol. 35, no. 2, p. e4623, 2021.

[26] K. Venu, V. P. Denisov, and B. Halle, "Water 1h magnetic relaxation dispersion in protein solutions. a quantitative assessment of internal hydration, proton exchange, and cross-relaxation," *Journal of the American Chemical Society*, vol. 119, no. 13, pp. 3122–3134, 1997.

[27] B. Halle, H. Jóhannesson, and K. Venu, "Model-free analysis of stretched relaxation dispersions," *Journal of Magnetic Resonance*, vol. 135, no. 1, pp. 1–13, 1998.

[28] I. Bertini, M. Fragai, C. Luchinat, and G. Parigi, "1h nmrd profiles of diamagnetic proteins: a model-free analysis," *Magnetic Resonance in Chemistry*, vol. 38, no. 7, pp. 543–550, 2000.

[29] C. Luchinat and G. Parigi, "Collective relaxation of protein protons at very low magnetic field: a new window on protein dynamics and aggregation," *Journal of the American Chemical Society*, vol. 129, no. 5, pp. 1055–1064, 2007.

[30] G. Diakova, Y. A. Goddard, J.-P. Korb, and R. G. Bryant, "Water and backbone dynamics in a hydrated protein," *Biophysical journal*, vol. 98, no. 1, pp. 138–146, 2010.

[31] E. Ravera, G. Parigi, A. Mainz, T. L. Religa, B. Reif, and C. Luchinat, "Experimental determination of microsecond reorientation correlation times in protein solutions," *The Journal of Physical Chemistry B*, vol. 117, no. 13, pp. 3548–3553, 2013.

[32] G. Parigi, N. Rezaei-Ghaleh, A. Giachetti, S. Becker, C. Fernandez, M. Blackledge, C. Griesinger, M. Zweckstetter, and C. Luchinat, "Long-range correlated dynamics in intrinsically disordered proteins," *Journal of the American Chemical Society*, vol. 136, no. 46, pp. 16201–16209, 2014.

[33] G. Parigi, E. Ravera, M. Fragai, and C. Luchinat, "Unveiling protein dynamics in solution with field-cycling nmr relaxometry," *Progress in Nuclear Magnetic Resonance Spectroscopy*, vol. 124, pp. 85–98, 2021.

[34] L. Cerofolini, K. Vasa, E. Bianconi, M. Salobehaj, G. Cappelli, A. Bonciani, G. Licciardi, A. Pérez-Ràfols, L. Padilla-Cortés, S. Antonacci, *et al.*, "Combining solid-state nmr with structural and biophysical techniques to design challenging protein-drug conjugates," *Angewandte Chemie International Edition*, p. e202303202, 2023.

[35] J.-P. Korb, "Multiscale nuclear magnetic relaxation dispersion of complex liquids in bulk and confinement," *Progress in Nuclear Magnetic Resonance Spectroscopy*, vol. 104, pp. 12–55, 2018.

[36] C. Luchinat, G. Parigi, and E. Ravera, "Water and protein dynamics in sedimented systems: a relaxometric investigation," *ChemPhysChem*, vol. 14, no. 13, pp. 3156–3161, 2013.

[37] F. Fujara, D. Kruk, and A. F. Privalov, "Solid state field-cycling nmr relaxometry: Instrumental improvements and new applications," *Progress in Nuclear Magnetic Resonance Spectroscopy*, vol. 82, pp. 39–69, 2014.

[38] D. Kruk, E. Masiewicz, A. M. Borkowska, P. Rochowski, P. H. Fries, L. M. Broche, and D. J. Lurie, "Dynamics of solid proteins by means of nuclear magnetic resonance relaxometry," *Biomolecules*, vol. 9, no. 11, p. 652, 2019.

[39] M. Botta and L. Tei, "Relaxivity enhancement in macromolecular and nanosized gdiii-based mri contrast agents," *European Journal of Inorganic Chemistry*, vol. 2012, no. 12, pp. 1945–1960, 2012.

[40] M. Yon, S. Gineste, G. Parigi, B. Lonetti, L. Gibot, D. R. Talham, J.-D. Marty, and C. Mingotaud, "Hybrid polymeric nanostructures stabilized by zirconium and gadolinium ions for use as magnetic resonance imaging contrast agents," *ACS Applied Nano Materials*, vol. 4, no. 5, pp. 4974–4982, 2021.

[41] P. Conte, A. Maccotta, C. De Pasquale, and G. Alonzo, "Supramolecular organization of triglycerides in extra-virgin olive oils as assessed by nmr relaxometry," *Fresenius Environ Bull*, vol. 19, no. 9b, pp. 2077–2082, 2010.

[42] P. Conte, V. Mineo, S. Bubici, C. De Pasquale, F. Aboud, A. Maccotta, D. Planeta, and G. Alonzo, "Dynamics of pistachio oils by proton nuclear magnetic resonance relaxation dispersion," *Analytical and bioanalytical chemistry*, vol. 400, pp. 1443–1450, 2011.

[43] E. G. Ates, V. Domenici, M. Florek-Wojciechowska, A. Gradišek, D. Kruk, N. Maltar-Strmečki, M. Oztop, E. B. Ozvural, and A.-L. Rollet, "Field-dependent nmr relaxometry for food science: Applications and perspectives," *Trends in Food Science & Technology*, 2021.

[44] A. Gradisek, M. Cifelli, D. Ancora, A. Sepe, B. Zalar, T. Apih, and V. Domenici, "Analysis of extra virgin olive oils from two italian regions by means of proton nuclear magnetic resonance relaxation and relaxometry measurements," *Journal of Agricultural and Food Chemistry*, 2021.

[45] D. Ancora, J. Milavec, A. Gradisek, M. Cifelli, A. Sepe, T. Apih, B. Zalar, and V. Domenici, "Sensitivity of proton nmr relaxation and proton nmr diffusion measurements to olive oil adulterations with vegetable oils," *Journal of Agricultural and Food Chemistry*, 2021.

[46] A. G. Redfield, "Shuttling device for high-resolution measurements of relaxation and related phenomena in solution at low field, using a shared commercial 500 mhz nmr instrument," *Magnetic Resonance in Chemistry*, vol. 41, no. 10, pp. 753–768, 2003.

[47] A. G. Redfield, "High-resolution nmr field-cycling device for full-range relaxation and structural studies of biopolymers on a shared commercial instrument," *Journal of biomolecular NMR*, vol. 52, pp. 159–177, 2012.

[48] S. Wagner, T. R. Dinesen, T. Rayner, and R. G. Bryant, "High-resolution magnetic relaxation dispersion measurements of solute spin probes using a dual-magnet system," *Journal of Magnetic Resonance*, vol. 140, no. 1, pp. 172–178, 1999.

[49] C. Charlier, S. N. Khan, T. Marquardsen, P. Pelupessy, V. Reiss, D. Sakellariou, G. Bodenhausen, F. Engelke, and F. Ferrage, "Nanosecond time scale motions in proteins revealed by high-resolution nmr relaxometry," *Journal of the American Chemical Society*, vol. 135, no. 49, pp. 18665–18672, 2013.

[50] C.-Y. Chou, M. Abdesselem, C. Bouzigues, M. Chu, A. Guiga, T.-H. Huang, F. Ferrage, T. Gacoin, A. Alexandrou, and D. Sakellariou, "Ultra-wide range field-dependent measurements of the relaxivity of gd1- xeuxvo4 nanoparticle contrast agents using a mechanical sample-shuttling relaxometer," *Scientific reports*, vol. 7, no. 1, pp. 1–12, 2017.

[51] Z. Wang, S. Pisano, V. Ghini, P. Kaderavek, M. Zachrdla, P. Pelupessy, M. Kazmierczak, T. Marquardsen, J.-M. Tyburn, G. Bouvignies, *et al.*, "Detection of metabolite–protein interactions in complex biological samples by high-resolution relaxometry: Toward interactomics by nmr," *Journal of the American Chemical Society*, vol. 143, no. 25, pp. 9393–9404, 2021.

[52] S. Fallarini, L. Cerofolini, M. Salobehaj, D. Rizzo, G. R. Gheorghita, G. Licciardi, D. E. Capialbi, V. Zullo, A. Sodini, C. Nativi, and M. Fragai, "Site-selective functionalized pd-1 mutant for a modular immunological activity against cancer cells," *Biomacromolecules*, vol. 0, no. 0, p. null, 0.

[53] R. Kimmich, "Principle, purpose and pitfalls of field-cycling nmr relaxometry," *Field-cycling NMR relaxometry: instrumentation, model theories and applications*, pp. 1–41, 2019.

[54] H. Li, G. Parigi, C. Luchinat, and T. J. Meade, "Bimodal fluorescence-magnetic resonance contrast agent for apoptosis imaging," *Journal of the American Chemical Society*, vol. 141, no. 15, pp. 6224–6233, 2019.

[55] M. D. Guillén and A. Ruiz, "High resolution 1h nuclear magnetic resonance in the study of edible oils and fats," *Trends in Food Science & Technology*, vol. 12, no. 9, pp. 328–338, 2001.

[56] W. L. Jorgensen, D. S. Maxwell, and J. Tirado-Rives, "Development and testing of the opls all-atom force field on conformational energetics and

properties of organic liquids," *Journal of the American Chemical Society*, vol. 118, no. 45, pp. 11225–11236, 1996.

[57] A. W. Yee, M. Aldeghi, M. P. Blakeley, A. Ostermann, P. J. Mas, M. Moulin, D. de Sanctis, M. W. Bowler, C. Mueller-Dieckmann, E. P. Mitchell, *et al.*, "A molecular mechanism for transthyretin amyloidogenesis," *Nature communications*, vol. 10, no. 1, p. 925, 2019.

[58] P. Caravan, N. J. Cloutier, M. T. Greenfield, S. A. McDermid, S. U. Dunham, J. W. Bulte, J. C. Amedio, R. J. Looby, R. M. Supkowski, W. D. Horrocks, *et al.*, "The interaction of ms-325 with human serum albumin and its effect on proton relaxation rates," *Journal of the American Chemical Society*, vol. 124, no. 12, pp. 3152–3162, 2002.

[59] R. Sant'Anna, M. R. Almeida, N. Varejāo, P. Gallego, S. Esperante, P. Ferreira, A. Pereira-Henriques, F. L. Palhano, M. De Carvalho, D. Foguel, *et al.*, "Cavity filling mutations at the thyroxine-binding site dramatically increase transthyretin stability and prevent its aggregation," *Scientific Reports*, vol. 7, no. 1, p. 44709, 2017.

[60] C. E. Bulawa, S. Connelly, M. DeVit, L. Wang, C. Weigel, J. A. Fleming, J. Packman, E. T. Powers, R. L. Wiseman, T. R. Foss, *et al.*, "Tafamidis, a potent and selective transthyretin kinetic stabilizer that inhibits the amyloid cascade," *Proceedings of the National Academy of Sciences*, vol. 109, no. 24, pp. 9629–9634, 2012.

[61] J. G. De la Torre, M. Huertas, and B. Carrasco, "Hydronmr: prediction of nmr relaxation of globular proteins from atomic-level structures and hydrodynamic calculations," 2000.

[62] K. Hiraishi, I. Narabayashi, O. Fujita, K. Yamamoto, A. Sagami, Y. Hisada, Y. Saika, I. Adachi, and H. Hasegawa, "Blueberry juice: preliminary evaluation as an oral contrast agent in gastrointestinal mr imaging.," *Radiology*, vol. 194, no. 1, pp. 119–123, 1995.

[63] A. Karantanas, N. Papanikolaou, J. Kalef-Ezra, A. Challa, and N. Gourtsoyiannis, "Blueberry juice used per os in upper abdominal mr imaging: composition and initial clinical data," *European radiology*, vol. 10, no. 6, pp. 909–913, 2000.

[64] E. Ravera, S. Ciambellotti, L. Cerofolini, T. Martelli, T. Kozyreva, C. Bernacchioni, S. Giuntini, M. Fragai, P. Turano, and C. Luchinat,

"Solid-state nmr of pegylated proteins," *Angewandte Chemie*, vol. 128, no. 7, pp. 2492–2495, 2016.

[65] L. Cerofolini, S. Giuntini, A. Carlon, E. Ravera, V. Calderone, M. Fragai, G. Parigi, and C. Luchinat, "Characterization of pegylated asparaginase: new opportunities from nmr analysis of large pegylated therapeutics," *Chemistry–A European Journal*, vol. 25, no. 8, pp. 1984–1991, 2019.

[66] M. Rostkowski, M. H. Olsson, C. R. Søndergaard, and J. H. Jensen, "Graphical analysis of ph-dependent properties of proteins predicted using propka," *BMC structural biology*, vol. 11, pp. 1–6, 2011.

[67] D. H. Powell, O. M. N. Dhubhghaill, D. Pubanz, L. Helm, Y. S. Lebedev, W. Schlaepfer, and A. E. Merbach, "Structural and dynamic parameters obtained from 17o nmr, epr, and nmrd studies of monomeric and dimeric gd3+ complexes of interest in magnetic resonance imaging: an integrated and theoretically self-consistent approach1," *Journal of the American Chemical Society*, vol. 118, no. 39, pp. 9333–9346, 1996.

[68] L. Cerofolini, M. Fragai, and C. Luchinat, "Mechanism and inhibition of matrix metalloproteinases," *Current medicinal chemistry*, vol. 26, no. 15, pp. 2609–2633, 2019.

List of Figures